Jun'ichi Sone · Shinji Tsuji *Editors*

Intelligent Nanosystems for Energy, Information and Biological Technologies

Springer

Intelligent Nanosystems for Energy, Information and Biological Technologies

Jun'ichi Sone · Shinji Tsuji
Editors

Intelligent Nanosystems for Energy, Information and Biological Technologies

Springer

Editors
Jun'ichi Sone
Japan Science and Technology Agency
Tokyo
Japan

Shinji Tsuji
Japan Science and Technology Agency
Tokyo
Japan

ISBN 978-4-431-56427-0 ISBN 978-4-431-56429-4 (eBook)
DOI 10.1007/978-4-431-56429-4

Library of Congress Control Number: 2016947383

Printed on acid-free paper

This Springer imprint is published by Springer Nature
The registered company is Springer Japan KK

Preface

Evolution in nanoscience and nanotechnology has created new opportunities to influence future society through creation and accumulation of wisdom, technological innovations, and applications to society. It is predicted that we will face further deterioration in global warming, exhaustion of natural resources, shortage of food and potable water, and congested cities without that evolution.

In order to solve or mitigate these serious global issues in the future, advanced functions created by nanoscience or nanotechnology should be combined with life, information, and materials science and engineering, which can evolve into integrated intelligent nanosystems. The "Creation of Nanosystems with Innovative Function Through Process Integration" program was launched in 2008 as one of the CREST (Core Research for Evolutional Science and Technology) programs in Japan to pursue the construction of nanosystems, which could be the first step toward the integrated intelligent nanosystems through the integration of top-down and bottom-up processes. One of these has been developed for nanofabrication of large-scale semiconductor integrated circuits and the other is exemplified by self-organization using autonomous chemical reactions. One of the coeditors was assigned as a research supervisor of the program. In the beginning, the nanosystems were envisioned as new functional electron devices with their critical dimensions far less than the miniaturization limit of current semiconductor technology. This was achieved by using the self-organized structures of bio-materials and autonomous chemical reactions. Nano-bio devices with capabilities of handling single cells and molecules also were accomplished by probing their dynamic behaviors using highly advanced semiconductor technology, and thus are expected to bring dramatic progress in diagnosis, clinical treatments, and drug development.

In the project, 16 of many excellent proposals were selected with the aim of realizing intelligent nanosystems over 3 years, and the research based on each proposal has been performed for 5 years. This book is the result of those efforts to realize the nanosystems, which can be classified into the following six groups:

1. Nano-bio devices utilizing advanced semiconductor technology
2. Nano-bio devices utilizing micro- and nano-fluidics technique
3. Advanced electronic and photonic devices utilizing a biotemplate technique
4. Synthesis of unique nanostructured materials and their energy, display, and catalysis applications
5. Electronic and photonic devices on soft substrate
6. Thermal and mechanical application of spintronics.

We understand that there is still a long way to go, but we believe that these attempts are important first steps toward the construction of intelligent nanosystems to resolve issues in the fields of energy, electronics, and health and medical care.

Finally, let us thank Drs. Y. Baba, Y. Bando, T. Degawa, T. Fuyuki, K. Kurihara, K. Matsumoto, S. Nishimoto, K. Ohashi, T. Ono, T. Shimizu, and K. Torimitsu for their valuable advice and their continuous encouragement as advisers to the program. We would like to extend our sincere thanks to Dr. A. Araoka for her great contribution, particularly for the start of the program. We also would like to thank members of the Japan Science and Technology Agency for their continuous 8 years of support for the program.

Tokyo, Japan — Jun'ichi Sone
June 2016 — Shinji Tsuji

Contents

Part I
Introduction

Chapter 1
Evolution of Nanotechnology to Intelligent Nanosystem

Jun'ichi Sone

Abstract The progress of miniaturization and integration of discrete semiconductor devices toward the dimension of nanoscale range according to the Moore's Law has led a dramatic increase in the performance of electronic systems and brought about IT revolution. It has been a major driving force for the progress of nanotechnology these days. Today, we are facing many industrial and social issues, such as physical difficulties of device miniaturization, threats to the environmental sustainability represented by a global warming, and growing demands for medical and health care in an aged society. Nanotechnology is highly expected to provide solutions to these issues through technological innovation. They include further increase in the performance of electronic devices by introducing new nanomaterials or quantum effects occurring in nanoscaled structures, renewable energy generation by using functional nanomaterials, and highly sensitive detection and characterization of biomaterials by microchips. In order to fulfill those demands as a whole, the development of nanotechnology would be required to evolve to the intelligent nanosystem through the pursuit of the technological limit of individual nanotechnologies and their fusion. This book contains the attempts of research members participating in the Core Research for Evolutional Science and Technology programs of the Japan Science and Technology Agency with title of "Creation of Nanosystems with Novel Function through Process Integration" to realize the intelligent nanosystem. While there is still a long way to go, these attempts are important steps without doubt toward effectively applying nanotechnology to resolve issues in the fields of energy, electronics, and medical and health care.

Keywords Nanotechnology · Nanoelectronics · Intelligent nanosystem · Process integration · IT revolution · Sustainability

J. Sone (✉)
Japan Science and Technology Agency, Tokyo 102-0076, Japan
e-mail: junichi.sone@jst.go.jp

J. Sone and S. Tsuji (eds.), *Intelligent Nanosystems for Energy, Information and Biological Technologies*, DOI 10.1007/978-4-431-56429-4_1

1.1 The Historical Evolution of Nanotechnology

Before going to describe how nanotechnology have been evolving historically and why the nanosystem is required as a social demand, the structure of nanotechnology is needed to be clarified. Figure 1.1 shows the whole view of nanotechnology quoted from the report [1] of the Center for Research and Development Strategy in Japan Science and Technology Agency. Nanotechnology is built on nanoscience which is formed by the integration of fundamental sciences such as material science, optics, life science, information science, and mathematical science. Nanoscience has been developed as science dealing with physical, chemical, and structural phenomena occurring at the nanoscale. Common basic technologies, such as manufacturing, measurements, and simulations, are structured on nanoscience, and applications of these technologies to materials lead to the development of devices and components. They form cross-cutting technologies in the field of environment, energy, health and medical care, social infrastructures, information and communication, and electronics. Eventually, nanotechnology is expected to play an important role as an innovation engine in these fields.

The historical evolution of nanotechnology is described schematically in Fig. 1.2. The second half of the twentieth century was a time of dramatic industrial growth driven by the progress of science and technology. This progress started from the emergence of quantum mechanics at the beginning of the century. Based on this new concept, physics and chemistry rapidly evolved, and many new technologies were

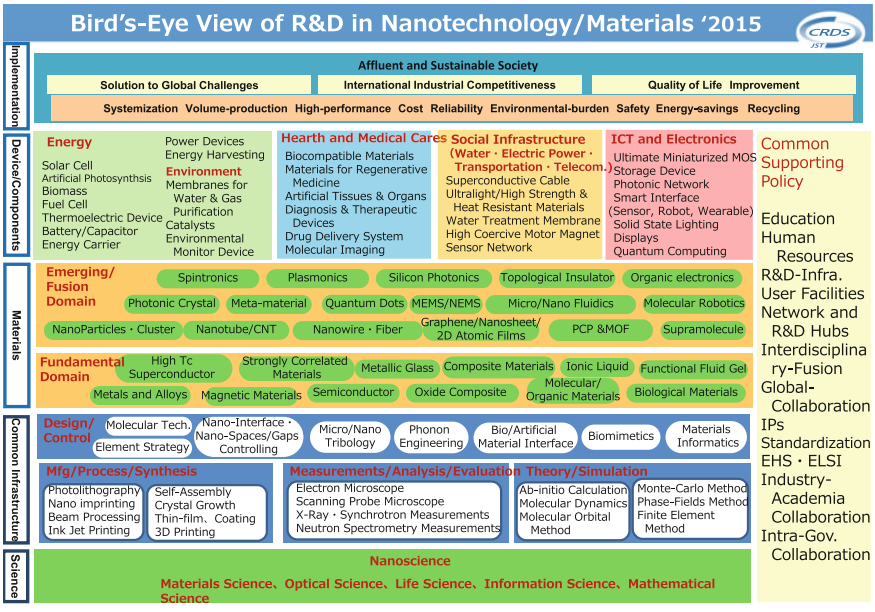

Fig. 1.1 Bird's eye view of R&D in nanotechnology/materials' 2015

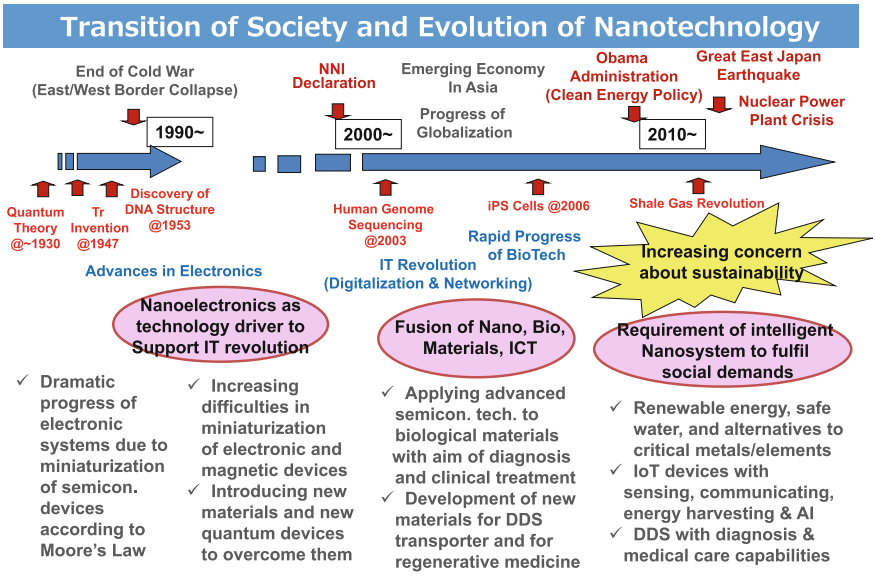

Fig. 1.2 Transition of society and evolution of nanotechnology

created especially after World War II. Consequently, various industries, such as the electronics, automobile, and chemical industries, made significant growth. For instance, in the semiconductor industry, the development of the miniaturization and integration of the discrete semiconductor devices on a chip according to the Moore's Law [2] lead to dramatic improvements in the performance of the electronic devices and their subsequent widespread use in various electronic systems has enriched our life. After 1990, personal computers, mobile phones, and the Internet flourished due to the advancement of the digital processing capability of semiconductor chips, which gave birth to the revolution of the information technology. The research and development of nanoelectronics to support the IT revolution had been a major driving force for the progress of nanotechnology in these days.

Around 2000, technological difficulties in the miniaturization of semiconductor devices became remarkable and the demands to overcome such difficulties increased. Similarly in the magnetic storage system using hard disc drives, miniaturization of the magnetic memory domain, which had been driving the increase of the memory capacity, also came to the point where technological breakthrough was required to further enlarge memory capacity. Various technological challenges have been made to overcome these difficulties. One approach is to utilize new materials in key parts of the devices, for example, high-k gate insulators and metal gates instead of SiO_2/poli-Si gate structure, and CNTs or graphenes as semiconductor channels. Another approach is to utilize quantum effects actively as an operating principle, such as quantum dot devices and spintronic devices. The research and development in the most of these challenges are still under way with expectations to open the new possibilities of nanoelectronics.

Nanotechnologies have also become increasingly important in the advancements of the life sciences. Since the completion of human genome sequencing [3], a large expectation to understand biological phenomena rationally has arisen, and many scientists not only in the life science but also in the material science and the information science have become interested in the progress of life science and have tackled challenging tasks in the life science together. Consequently, many discoveries of new phenomena and developments of new technologies have been made successively. The development of iPS cells was one of those achievements [4]. The core nanotechnologies, such as characterization tools at the atomic and molecular level, molecular level simulation, nanofabrication technology, and material synthesis at the nanoscale range, would accelerate further the progress of the life science as powerful tools for its development.

Increasing concern about environmental sustainability is also a key driving force that makes development of nanotechnology important. In order to solve sustainability issues such as global warming, depletion of natural resources, and shortage of food and water supply due to the explosive increase of human population in the global scale and globalization of the economic activities, nanotechnology is highly expected to play an important role through the fusion with life science, information technology, and material science.

1.2 Social Expectations and the Nanotechnology's Potential

In the future advanced information society, various sensors with networking capability would be deployed in our surrounding. Large amounts of information obtained from sensors would be uploaded in the wireless network, and delivered to a cloud computing system. The massive information collected from a variety of sensors could be processed and analyzed, and new valuable knowledge would be created through their analysis. It would be delivered to persons who need it through various man–machine interface devices. In order to realize such a scheme, it is imperative to develop various devices based on nanotechnologies. What are expected as key devices among them are intelligent sensors with sensory capabilities exceeding human's eyes, noses, ears, and so on, as well as those with the capability of real-time monitoring human's health and environments. Those sensors could be integrated on a silicon chip with compact batteries or energy-harvesting devices to convert various environmental nonelectric energies to electric ones. These integrated devices may be used in a wearable or even implanted form. Thus, we could enjoy convenient and comfortable life in a safe and reliable environment in the advanced information society in future.

On the other hand, issues on environmental sustainability are becoming an international concern and nanotechnologies are also expected to play an important role in this regard. Those are the technologies to produce electric energies or

hydrocarbon chemicals without putting a heavy burden on the environment, such as solar cells, fuel cells, thermoelectric devices, photocatalysis, and artificial photo synthesis. Although the physical mechanisms of these devices have not changed much since their original forms, nanotechnologies can be used to vastly improve their performance, cost, and reliability by introducing new functional materials. Many of these devices also rely on critical metals or rare earth elements in their key parts. Therefore, it is also important to realize equivalent or even better device performance using naturally abundant materials.

Nanotechnology is important also from the standpoint of protecting the environment through technologies that monitor hazardous gases and polluted water and remedy polluted environment, for example, using separation membranes with highly dense nanopores. In fact, ensuring sufficient drinkable water resources is a serious issue globally, particularly in some parts of the Asia, Central America, and Africa where water is heavily contaminated with arsenic [5]. The development of separation membranes and contaminant adsorbents is urgent demands to remove radioactive substances in the water and soil contaminated by the nuclear plant accident at Fukushima in 2011. Those technologies would also be effective to remove contaminants in the large amount of discharged water that result from the hydraulic fracturing methods used to extract shale gas and oil.

Nanotechnology also has great potential in the medical and healthcare sectors. Recent progress in the life sciences is striking, particularly as exemplified in the completion of human genome sequencing or the generation of iPS cells. Innovation is highly expected as a result of the combination of the advanced semiconductor technology and the growing life science, for example through the integration of biological materials such as DNA, proteins, and cells on semiconductor chips. Various researches are currently underway through their combination with the aim of diagnosis and clinical treatment applications. For example, scientists are currently observing the dynamic behavior of biological materials and identifying their characteristics by applying them to artificial nanostructured devices such as 2-dimensional imaging and microfluidic ones. Similarly, scientists are conducting research utilizing nanomaterial as a transporter in a drug delivery. While expectation of the application of iPS cells in regenerative medicine is expanding, scaffold materials are necessary in order to induce differentiation of the iPS cells to a specific organ. Thus, the combination of nanoscience, material science, and life science is highly required to induce progress in the developments of disease diagnosis, drug discovery, and regenerative medicine.

1.3 Toward an "Intelligent Nano-System"

As described above, the technological development of nanotechnology is evolving toward the stage to fulfill social demands. The first step of the nanotechnology evolution is the pursuit of the technological limit of individual technologies, for example, the emergence of the scanning probe microscope that probes individual

atoms and molecules, or ultimate miniaturization of semiconductor devices where innovations of every elements of fabrication including lithography are required.

The second step of the nanotechnology evolution is the fusion of individual technologies, creating new functions. In the semiconductor device development, for example, various functions of photonics, spintoronics, MEMS, or biological materials are integrated on a silicon chip by introducing new materials to link such heterogeneous functions, leading to the emergence of new functional devices.

The final stage of nanotechnology evolution is the creation of nanosystem, where highly advanced elements of nanotechnology are integrated and evolved into an intelligent nanosystem to provide advanced function to fulfill the social demands as a whole. In the electronics sector, it would be an internet of things (IoT) device with sensing, communicating, and energy-harvesting functions, and a microrobot with artificial intelligence. In the biotechnology sector, it is a drug delivery system with a nanoparticle transporter, possessing both diagnosis and medical treatment capabilities, to be used in the clinical application. It could also achieve noninvasive medical treatment through combination with the physical energy generated from an optical beam, ultrasonic wave, or neutron beam.

Figure 1.3 shows a concrete example of the nanosystem to enable advanced information society in future [6]. Various sensors deployed in our surrounding collect massive data continuously, which are transmitted through communication networks to a high-performance computing system in a data center. New

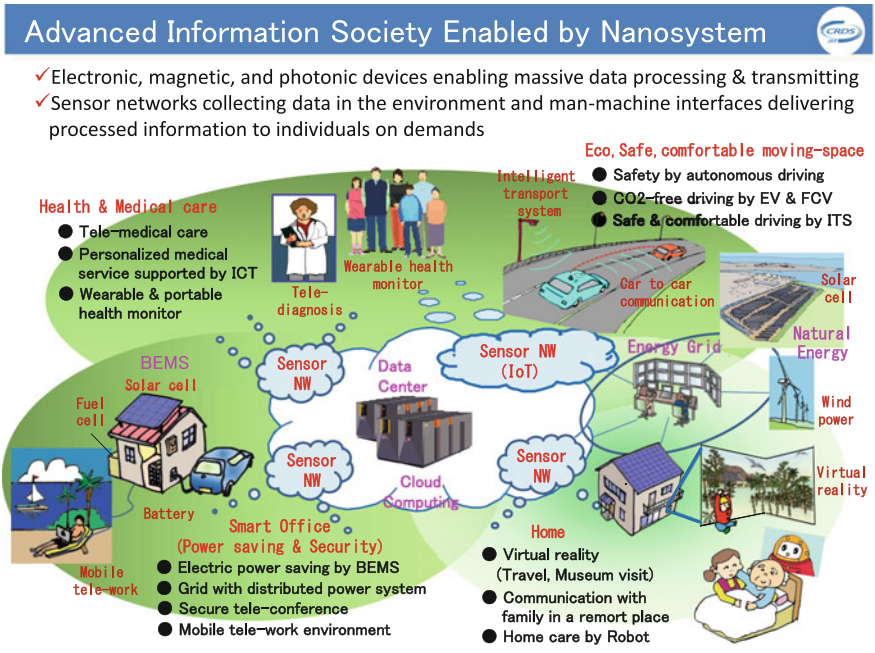

Fig. 1.3 Advanced information society enabled by an intelligent nanosystem

knowledge or information is produced in the data center from the massive data and delivered to individuals on demands through various man–machine interface devices. These services are made possible by the combination of sensor networks, cloud computing system, and man–machine interface devices, where nanoelectronic, magnetic, and photonic devices enable massive data processing, storing, and transmitting. Thanks to these services, one can enjoy safe, secure, and comfortable life at home. It is particularly effective for aged persons at home, in the sense that they can enjoy virtual reality experiences, such as travels or museum visits without going there, and communication with family members in a remote place. Smart robots will take care of those peoples and homes when family is out by notifying the situation to an appropriate person when something irregular or abnormal happens. Such smart robots are composed of sensor devices, actuating devices, batteries, and nanoelectronic processor chips, working together as a nanosystem for robot operation.

In such an advanced information society, health condition for individuals would be monitored continuously by wearable monitors attached on a body and data collected by the monitor will be transmitted to a medical center. One can receive personalized medical service from a doctor when needed, based on the collected data and personal data stored in the center through a remote communication system. The wearable health monitor is composed of various sensing devices, wireless communication devices, and small batteries with high-energy density or energy-harvesting devices integrated on a sheet-like substrate, working as a nanosystem for health and medical care.

One can enjoy safe and comfortable driving with the least environmental load by CO_2-free electric vehicles or fuel cell vehicles. The car navigation is supported by the information obtained from the intelligent transport system (ITS) and from the car-to-car communication. Thus, autonomous driving becomes possible by sensing surrounding traffic conditions, recognizing the present situation, and controlling the drive. The sensing devices of millimeter or laser radars and 2D image sensors, 3D real-time recognition AI chips, and mass storage devices containing road-map data work together as a nanosystem, enabling the autonomous driving.

In the future smart office, electric power consumption is saved by building energy management system (BEMS), and secure ICT environment ensures teleconference meetings and teleworks in remote places using mobile terminals. Solar cells installed on a roof, secondary batteries to store the energy produced by the solar cells, stationary fuel cells for a distributed power supply system, and high-efficient power electronic devices work together as a nanosystem for energy saving in the office building with BEMS.

In order to realize the intelligent nanosystem to resolve the various social challenges, it is imperative that scientists and engineers in various fields compete and collaborate with each other to develop nanotechnology to a higher level.

1.4 Organization of the Book

In this book, various attempts to realize an intelligent nanosystem are described by authors who have engaged in the Core Research for Evolutional Science and Technology (CREST) programs of Japan Science and Development Agency with title of "Creation of Nano-systems with Novel Function through Process Integration." In part II, biosensing, imaging, and cell manipulation are described as an intelligent nano-system based on the fusion of bio and neuroscience and the semiconductor technology with nano and micro fabrication. In part III, original technologies on microfluidics and MEMS are described with their biological applications for single-cell sensing and manipulating as well as their energy device applications. In part IV, original nanofabrication technologies using a biotemplete method and damage-free neutral beam processing are described with emphasis on electronics and photonics applications using quantum dot structures. In part V, fundamental technologies for nanosystem integration are described, which include the unique synthesis of concentrated polymer nanobrushes, metallo-supramolecular polymers, and inorganic subnanoparticles using a dendrimer template with energy and biological applications, electrochromic display applications, and catalysis applications, respectively. They also include electrochemical manipulation of biocells with smart biodevice applications and low temperature growth of gallium and indium nitrides on flexible substrate with electronic and photonic applications. In part VI, a new concept of spintronics is discussed from the standpoint of fundamental physics, which demonstrates the possibility of thermal and mechanical applications of spintronics.

We believe that these attempts described in this book are important steps to build up the concept of an intelligent nanosystem, while there is still a long way to reach the final form. I hope the continued researches on nanotechnology would lead to the development of future intelligent nanosystems, providing the solutions for serious global issues.

References

1. Panoramic View of Nanotechnology/Materials Field. Center for Research and Development Strategy, Japan Science and Technology Agency, April (2015)
2. G.E. Moore, Cramming more components onto integrated circuits. Electronics Magazine, 19 April (1965)
3. Human Genome Sequencing Consortium, Finishing the euchromatic sequence of the human genome. Nature **431**, 931–945 (2004)
4. K. Takahashi, K. Tanabe, M. Ohnuki, M. Narita, T. Ichisaka, K. Tomoda, S. Yamanaka, Induction of pluripotent stem cells from adult human fibroblasts by defined factors. Cell **131**(5), 861–872 (2007)
5. Arsenic in Ground Water. The world's Worst Toxic Pollution Problems Report 2011. http://www.worstpolluted.org/projects_reports/display/92
6. Nanotechnology and Materials R&D in Japan, An overview and analysis. Center for Research and Development Strategy, Japan Research and Development Agency, January 2016 (2015)

Part II
Bio-sensing, Imaging, and Cell Manipulation

Chapter 2
Field-Effect Transistors for Detection of Biomolecular Recognition

Miyuki Tabata, Tatsuro Goda, Akira Matsumoto and Yuji Miyahara

Abstract Electrical biosensors have attracted increasing attention in such fields as point-of-care testing, drug discovery, and healthcare products. In order for next-generation biosensor platforms to become more useful in our daily lives, it will be necessary to significantly improve their sensitivity, specificity, and parallelism. A precisely designed thin layer in molecular dimension on a solid substrate is essential for biosensing. The surfaces of biosensors are designed to capture target bioanalytes. In addition, the solid/liquid interface plays an important role in realizing additional functionalities such as target manipulation, signal stabilization, and switching. A functional interface combined with a field-effect device would enable on-demand label-free biosensing in a portable format. In this chapter, we provide an overview of biomolecular recognition in the context of electrochemical sensing and biosensing. Also, we review recent progress and trends in biosensing, including our own research.

Keywords Biosensor · Biotransistor · ISFET · Sialic acid · Transporter

2.1 Introduction

Since the first ion-sensitive field-effect transistor (ISFET) was reported by Bergveld [1], various types of ISFETs and biochemical FETs have been developed, some of which have been commercialized as pH-sensors for laboratory, medical, and food applications.

Biosensors generally consist of transducers and membranes on which biologically active substances are immobilized. In the transducer, physical and chemical changes at the membrane, which occur as a result of biochemical reactions, are converted into electrical signals. These devices can record electrical, thermal, or

M. Tabata · T. Goda · A. Matsumoto · Y. Miyahara (✉)
Institute of Biomaterials and Bioengineering, Tokyo Medical and Dental University,
2-3-10 Kanda-Surugadai, Chiyoda-Ku, Tokyo 101-0062, Japan
e-mail: miyahara.bsr@tmd.ac.jp

J. Sone and S. Tsuji (eds.), *Intelligent Nanosystems for Energy, Information and Biological Technologies*, DOI 10.1007/978-4-431-56429-4_2

optical outputs from biological reactions on a sensing surface. For practical applications, biosensors have been developed for detecting ions [2, 3], molecules [4], proteins [5, 6], DNA [7–9], viruses [10], etc. In general, bioassays rely on tedious labeling processes involving fluorescent dyes [2, 11], radioactive labeled probes [12, 13], or digoxigenin [14]. By contrast, label-free methods make systems simple, cost efficient, portable, and user-friendly. Several label-free methods have been proposed to date, including surface plasmon resonance (SPR) [15–17], quartz crystal microbalance (QCM) [18, 19], and electrochemical methods [20, 21]. A pH-sensitive ISFET has been used as a transducer in combination with enzymes that produce or consume hydrogen ions during enzyme–substrate reactions. As a result, a pH change is induced around the immobilized enzyme membrane, and this change is detected by the ISFET. Biochemical FETs have several advantages, including small size, low cost, and large-scale integration with other sensors and signal-processing circuits on a single chip. The type of target biomolecule to be detected and its selectivity can be determined by receptor molecules and materials coated on the surface of the gate insulator of the FET. The design and fabrication of functional interfaces on transistor gates are keys to achieving efficient molecular recognition and its transduction to electrical signals in a solid-state substrate.

With the rapid growth of knowledge in the fields of medicine and biology, the number of biomolecules to be detected and the types of information to be gathered are also increasing. Meanwhile, advanced micro- and nanotechnologies in electronics have been applied to these fields to facilitate parallel processing of information, miniaturization of analytical devices, and exploration of molecular mechanisms in biological systems. Solid-state biosensors, in which semiconductor devices are used as the transducer, are typical examples of fusion between biotechnology and microelectronics.

In this chapter, we introduce design and fabrication of functional nanointerfaces for biomolecular recognition and its transduction to electrical signals, as well as their application to field-effect transistors for biomolecular sensing. So-called “bio-FETs” have advantages over any conventional sensors in terms of miniaturization and integration due to the compatibility to established semiconductor fabrication technology. A key challenge for bio-FETs is development of sensing surfaces that can capture a wide variety of target species from ‘dirty’ real-world samples. Therefore, it is very important to create methods for designing functional interfaces.

2.2 Working Principles of FET-Based Biosensors (Bio-FETs)

2.2.1 Principles of Bio-FETs

A great deal of attention has been paid to bio-FETs in the field of bioanalytical applications. Bio-FETs detect biological events such as nucleic acid hybridization, protein–protein interactions, antigen–antibody binding, and enzyme–substrate

reactions. An FET consists of three electrodes: source, drain, and gate. The positive gate voltage attracts electrons from the bulk to the surface of the substrate. A sufficient number of electrons induced form a thin n-channel by electrically bridging the source and drain. Otherwise, when a specific molecular recognition occurs on the gate, the bio-FET detects the change of charge density at the interface by an electrostatic interaction with the electrons in the n-channel (Fig. 2.1).

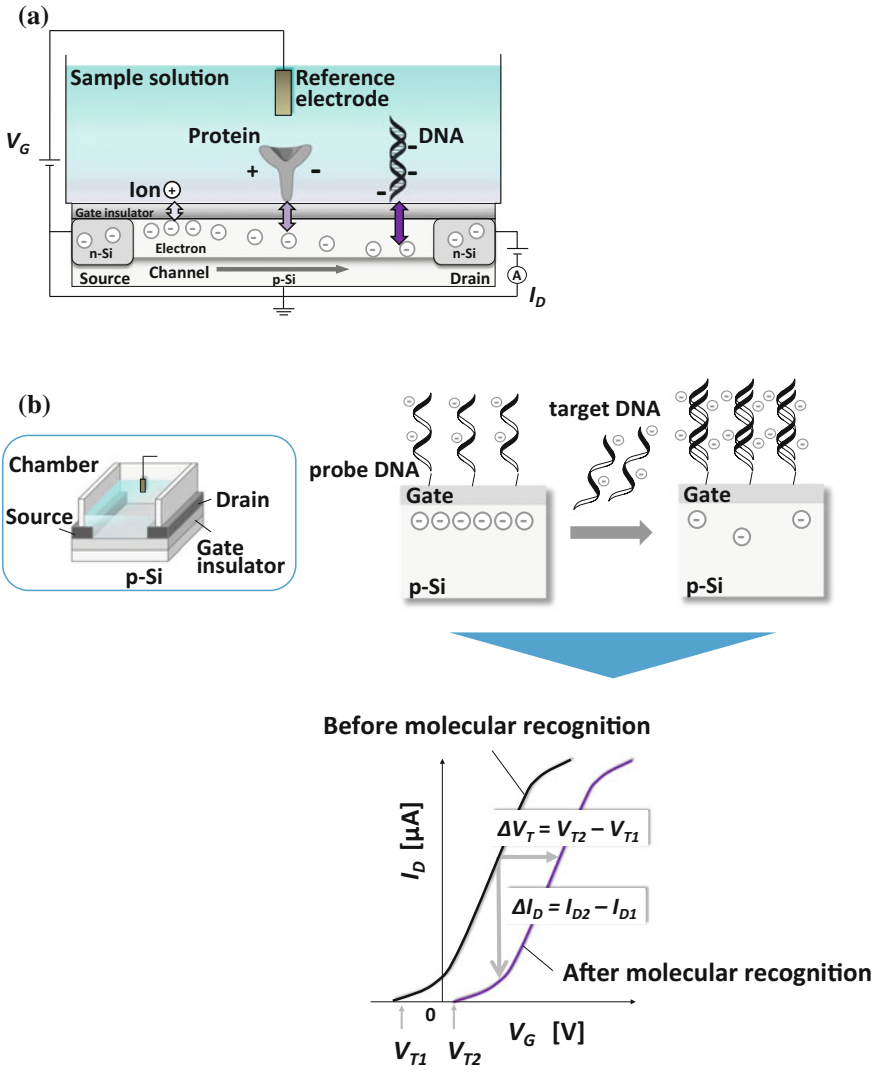

Fig. 2.1 Schematic illustrations of FET-based biosensors. **a** FET-based biosensor composed of a functional interface and signaling transducer. **b** Working principle of a device for detecting DNA hybridization. V_T–I_D characteristics of biotransistor changes before and after molecular recognition

As shown in Fig. 2.1a, the bio-FET detects the change in charge density, occurring within the electrical double layer of the gate/solution interface, as a shift in the threshold gate voltage (V_T). The Debye length, an index of the thickness of the double layer, is given by the following Eq. (2.1):

$$\delta = (\varepsilon\varepsilon_0 kT/2q^2 I)^{1/2} \tag{2.1}$$

where ε is the relative permittivity, ε_0 is the permittivity of the vacuum, kT is the thermal energy, q is the electric charge, and I is the ionic strength of the solution. The change in charge density based on molecular recognition must occur within the Debye length, whereas the change in charge density induced outside the Debye length is shielded by counter ions and cannot be detected with the bio-FET. The Debye length on the gate is considered to be a few nanometers in the physiological sample solution; therefore, the design of the solid/liquid interface plays a critical role in the development of the bio-FET.

2.2.2 *Ion-Sensitive FETs (ISFETs) and Their Application to a Bio-FET*

The ion-sensitive field-effect transistor (ISFET), a pH-sensor, is the first miniaturized silicon-based chemical sensor. In general, the gate used in such pH-sensors consists of dielectric materials, such as SiO_2, Si_3N_4, Ta_2O_5, and Al_2O_3, and the selectivity and pH sensitivity of an ISFET depend on the properties of the solid/liquid interface. A nucleic acid primer-extension reaction has been detected using an ISFET [22, 23]. In this approach, single-stranded oligonucleotide probes immobilized on a gate surface were hybridized with their target DNA molecules, followed by sequential addition and washing steps with each individual deoxynucleotide triphosphate (dCTP, dATP, dGTP, or dTTP) in the presence of DNA polymerase. This process allows an unknown sequence to be determined, because extension by DNA polymerase produces additional negative charges and protons in a template-dependent manner. The increase in negative charges resulting from primer extension can be detected as a V_T shift. The reaction can be monitored at single-base resolution. Based on this fundamental mode of detection, a next-generation high-throughput DNA sequencer was commercialized by Ion Torrent (Life Technologies) in 2012 (Fig. 2.2). High-throughput reading and highly parallel analysis are achieved by integrating millions of ISFETs on a chip in a high-density array format using nanofabrication technology [24]. The sequencer employs microbeads bearing a template DNA, amplified by emulsion PCR, to perform accurate sequencing on a transistor. The extension reaction occurs on the surface of the bead mounted on each ISFET, which detects the protons released during the extension reaction. Currently, this technology is being further developed for applications in tailored medicine.

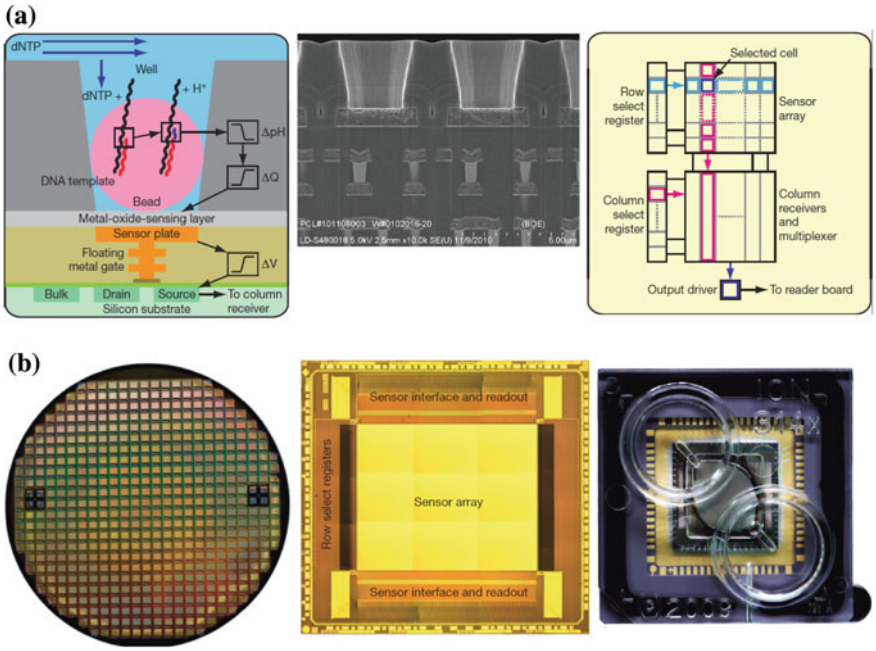

Fig. 2.2 Commercialized ISFET-based DNA sequencer. **a** Schematic illustration of sequencing mechanism and electron micrograph showing wells. **b** Ion chip on wafer, die, and chip packaging. Reprinted by permission from Macmillan Publishers Ltd: Ref. [24], copyright 2011

2.3 Sialic Acid Detection Using Phenylboronic Acid SAM Modified FETs

Bio-FETs offer great potential for addressing major medical challenges in the fields of diagnostics, therapy, and drug delivery. Fortunately, an electrical biosensor platform composed of a target-capturing element and a semiconductor device (used as a signal transducer) is compatible with high-throughput analysis via miniaturization and integration into a small chip, which can then be used for decentralized bioanalytical applications. We have successfully achieved a sialic acid (SA) detection transistor using SA–boronic acid molecular recognition.

SA is present at the ends of sugar chains on the cell surface, and its density and distribution are influenced by disease development and differentiation. Although sialylated glycoproteins are abundant on the surface of cancer cells, their levels are reduced on the erythrocytes of patients with insulin-dependent diabetes. Therefore, quantitative analysis of SA on the cell surface serves as a powerful index for diagnosis of metastatic tumors or diabetes. Phenylboronic acid (PBA) is generally used as a probe molecule for capture of various sugars due to the covalent bond that form between dissociated PBA and diols; even nondissociated PBA interacts strongly with SA [25]. We recently proposed an FET-based SA detection as a new

technique for label-free live-cell cytology [26]. To evaluate the ability of PBA to recognize SA, a self-assembled monolayer (SAM) of PBA derivative (p*K*a = 9), which has a thiol group at the end, was formed on an extended gold electrode gate surface. Over a wide range of pH (5–9), only SA caused a significant increase of V_T (+40 mV), and no significant signal was acquired in the case of mannose or galactose. On the other hand, when similar measurements were performed at pH ≥ 9, PBA could recognize mannose or galactose. In this configuration, the anionic charges of SA (due to carboxyl groups) bound to the electrode could be detected as positive shifts in the threshold voltage (V_T) of the FET. Consequently, it became clear that SA could be directly quantitated using PBA derivatives under physiological conditions.

This PBA-modified FET was then tested for its ability to directly capture the glycan component SA present on the cell surface [27] (Fig. 2.3). The device was capable of quantitatively analyzing SA in rabbit erythrocytes in a type I diabetes model, as well as in lungs into which mouse melanoma had been transferred as a

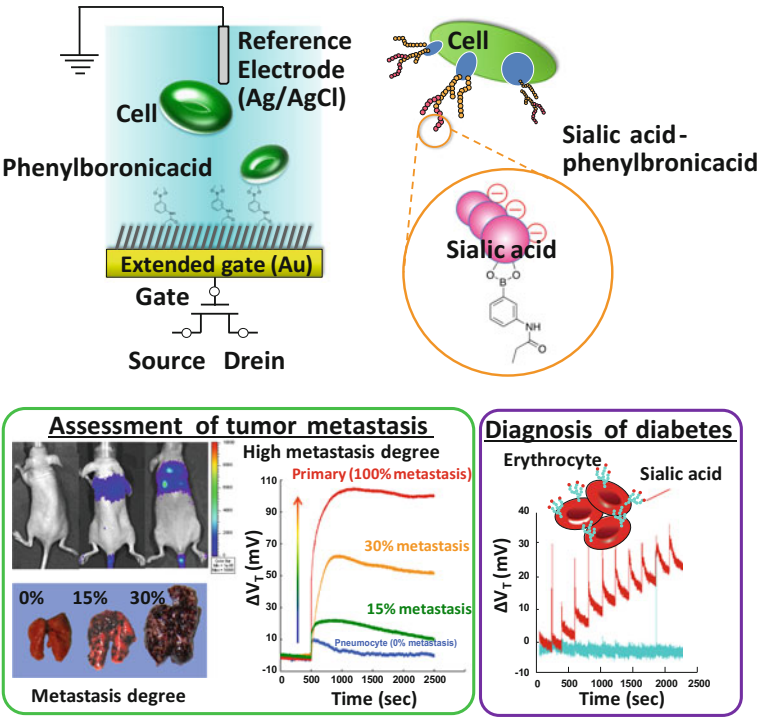

Fig. 2.3 Quantitative analysis of sialic acid using a bio-FET functionalized with phenylboronic acid. Assessment of tumor metastasis based on differentiation of the (pneumocyte) surface-expressed (Reproduced from Ref. [26] by permission of John Wiley & Francis Ltd.), and detection of sialic acid on the surface of rabbit erythrocytes as a relevant technique for the diagnosis of diabetes (Reprinted with the permission from Ref. [27]. Copyright 2009 American Chemical Society.)

model of metastatic cancer. Therefore, we predict that this approach could be applied in a simple device capable of quantitatively evaluating the degree of cancer metastasis.

2.4 Monitoring of Kinetics for Transporter–Substrate Interaction

In drug design, medical treatment, and cosmetics, it is necessary to screen for highly active compounds from among vast numbers of candidate substances, such as libraries of natural or de novo synthesized compounds. In general, various toxicity tests and in vivo pharmacokinetic studies are performed in mammals to determine the efficacy of such compounds. From the standpoint of animal protection, however, various alternatives to animal experiments have been advocated, and analytical technologies using cultured cells are becoming mainstream. Because novel compounds are often precious, it is desirable to use small amounts of such samples for analysis. Therefore, it is necessary to miniaturize the reaction field and the detection space, both of which are possible using an evaluation device combined with our transistor.

Membrane transport proteins can be regarded as gateways that connect the cytosol to the extracellular environment. They play crucial roles in metabolic processes and signal transduction that define the physiological functions in cellular systems. So, the investigation of membrane transport proteins is important not only in the field of cell biology but also in drug screening and development. *Xenopus laevis* oocytes, eggs from a clawed frog native to South Africa, have become widely used for studying membrane proteins such as ion channels and transporters. Transporter is a membrane protein or peptide allowing for passage of specific substrates such as ions and low molecular weight chemical species into or out of the cell. When heterologous expression of a membrane protein is required, RNA or cDNA encoding the target protein is injected into the oocyte. This *X. laevis* expression system is useful for electrophysiolosical studies of the membrane protein and drug development where a potential drug is screened against specific ion channels or transporters expressed in the membrane of *X. laevis* oocytes. Binary response, “hit-or-miss”, can be obtained to evaluate the efficacy of potential drug candidates. Membrane transport activity can be detected using electrical conductance measurement, if the transport process results in a net transfer of charge. This is usually achieved with the voltage clamp or patch clamp methods using a single cell expressing the membrane protein to be investigated. Microelectrodes and their precise manipulation are required for the electrical conductance measurements. Insertion of intracellular microelectrodes into an oocyte is an invasive process and glass microelectrodes with a very fine tip are typically used to reduce the disruption of the cell membrane. A higher degree of experience and skill is required to achieve stable and reliable measurements.

We developed an integrated microdevice for measuring proton-dependent membrane activity at the surface of *X. laevis* oocytes. By culturing an oocyte (female *X. laevis* frogs) on the surface of the ISFET gate, the kinetics of transporter–substrate interactions on the cell membrane can be monitored noninvasively. An overview of this microdevice is shown in Fig. 2.4. The output voltage of this system at varying pH buffer solutions was −58.0 mV/pH. This value is close to the ideal Nernstian slope (−59.2 mV/pH at 25 °C), demonstrating the excellent pH-sensitive material of Ta_2O_5. To evaluate this sensing platform as a cell-based FET, we conducted transport experiments on oocytes heterologously expressing various membrane transport proteins. These heterologously expressed oocytes were prepared by injecting of mouse, flounder or human-derived cRNA according to cell engineering techniques. The protons delivered and received through the cell membrane are used as tracers, due to the much higher lateral diffusion rate of protons relative to other solutes [28].

Assays on oocytes heterologously expressing the proton-driven amino acid transporter (PAT1) revealed a significant potential decrease upon exposure of the cells to a 1 mM proline solution, reflecting the local pH increase at the ISFET interface associated with intracellular inflow of a proton and proline. On the other hand, for oocytes heterologously expressing the electrogenic sodium-coupled phosphate cotransporter (NaPi-IIb), the signal deflection was reversed, indicating a decrease in the surface pH of the ISFET. This phenomenon occurred because divalent (HPO_4^{2-}) and monovalent ($H_2PO_4^-$) phosphate species with an assumed $pK_a = 6.8$ are held in equilibrium under physiological conditions, according to Eq. (2.2).

$$HPO_4^{2-} + H^+ \leftrightarrow H_2PO_4^- \tag{2.2}$$

As a result of taking up divalent P_i (HPO_4^{2-}), the above equilibrium shifted to the left hand side and protons were newly generated due to the depletion of the divalent species. Similarly, it became clear that the transporter activity of NaP_i-IIc and PiT-2 could be evaluated by proton sensing. In addition, the signal was not detected in cells expressing GAT1 and ENaC, which do not change proton concentration. Thus, electrical phenomena at the cell membrane can be monitored using an ISFET with high sensitivity ($\Delta pH = 0.01$) and high time resolution ($\Delta t = 100$ ms). The cell-based transistors are expected to contribute to high-throughput screening in pharmaceutical fields.

2.5 Nanointerfaces for Signal Transduction Using Nanotubes and Nanowires

Functional chemical modification and fabrication of nanostructures at the surface of the gates of FETs, described in the previous sections, can be applied to new types of electron devices. Nanotubes and nanowire transistors are very attractive for highly sensitive biosensing devices [29–32].

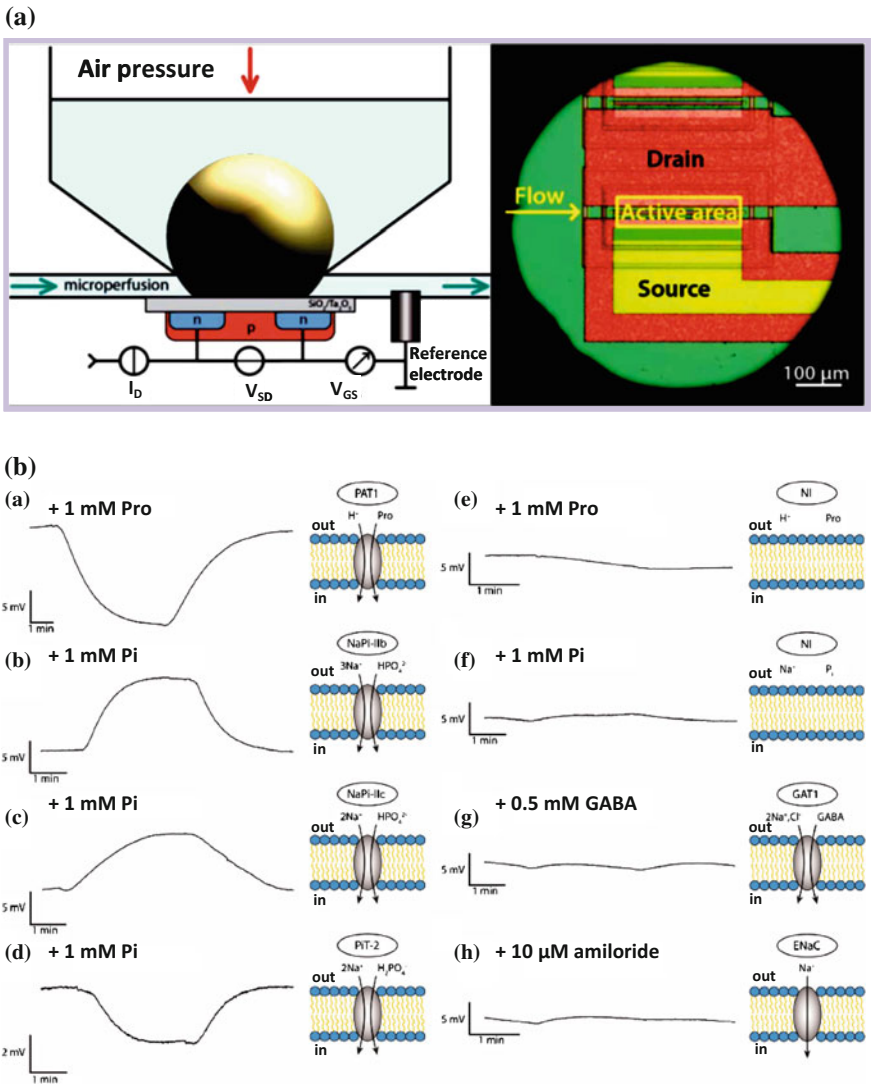

Fig. 2.4 Evaluation of proton transport from oocytes heterologously expressing various membrane transport proteins using ISFET. **a** A simplified illustration of a cross-sectional view of the device and a micrograph of the sensor are shown. **b** Cell membrane transport experiments were conducted on oocytes and their respective controls in noninjected (NI) oocytes. Sensor readout (V_{SG}) is shown as a function of time: *a* PAT1; *b* NaPi-IIb; *c* NaPi-IIc; *d* PiT-2; *e* proline control; *f* P_i control; *g* GAT1; and *h* ENaC. *Bars* indicate the duration of application of the indicated activating and blocking agents. *Arrows* indicate the flux direction of the substrate according to the assumed driving force conditions. Reproduced from Ref. [28]

Carbon nanotubes (CNTs) possess many unique properties such as high aspect ratios, high mechanical strength, high surface areas, excellent chemical and thermal stability, and rich electronic and optical properties, all of which are potentially useful in electronics. Therefore, there has been an explosion of interest in the use of CNTs for the development of biosensors. The high surface area of single-walled CNTs (SWNTs), estimated to be 1600 $m^2\ g^{-1}$, is of particular interest, because it can provide a route to obtaining an impressively high density of biomolecules at the detection interface. Since the first appearance of the SWNT-based FETs (SWNT-FETs) [33], a large number of attempts have been made to apply the SWNT-FET to a range of biomolecular targets. To fabricate SWNT-FETs, a semiconducting-SWNT must be selectively (i.e., out of a mixture of metallic-SWNTs) manipulated to ensure it contacts and bridges between the source and the drain materials. SWNT-FETs are composed of either individual SWNTs or dispersed networks of multiple SWNTs. The chemical vapor deposition (CVD) growth method is typically employed for the fabrication of dispersed SWNT networks on the gate surface, whereas microlithography and electron beam (e-beam) lithography are common techniques for pattern source and drain contacts [29]. At the detection interface, the SWNT not only provides dense surface area for immobilization of biological receptors, but also serves as an electrical modulator of the (SWNT-bridged) source–drain channel. The main factor causing changes in the channel conductance is still controversial, and at least four possible mechanisms have been proposed so far: electrostatic gating, capacitance modulation, Schottky barrier effects, and carrier mobility change [34]. A variety of biological targets have been successfully detected based on the SWNT-FET format, including protons and small molecules such as, NH_3 and NO_2, as well as relatively large targets such as DNA (hybridization) and proteins.

Nanowires are solid, rod-like materials with diameters in the 5–100 nm range, and are most often made from metals or semiconducting metal oxides. Silicon nanowire (SiNW)-FETs have also emerged as powerful biosensors. The sensing mechanism of SiNW-FET can be understood in terms of the change in charge density at the SiNW surface after molecular recognition, as well as typical bio-FETs. This charge sensitivity is affected by many factors, including SiNW size [35], Debye screening [36], surface chemistry [37], distance of the charge layer from the SiNW surface [38], and so on. However, SiNW-FETs can achieve highly sensitive detection of biological species by a complementary metal oxide semiconductor (CMOS)-compatible approach. The performance of SiNW-FETs has been extensively studied in regard to detection of DNA [39] and protein [40]. Since the fabrication process of SiNW-FETs is compatible with the current CMOS processing technologies, the gate region of the FET can be designed and defined precisely and reproducibly. By combining nanowire transistors with our approaches described previously (DNA or PBA-modified FET and cell-based FET), it is expected that the further miniaturized and arrayed biotransistors would be realized for functional analyses of a single molecule and a single cell, while we have to develop a method that functional modification and nanostructure can be formed selectively and separately on each gate.

2.6 Future Perspectives

This chapter described several types of FETs for biosensing, focusing on design and fabrication of functional nanointerfaces at the gate. Particularly for clinical applications, such nanointerfaces could play a crucial role in capturing a wide variety of target biomolecules with high specificity and sensitivity, without nonspecific binding, in 'dirty' real-world samples.

Using the FETs described in this chapter for detection of biomolecular recognition events, it should be possible to develop a small instrument for use in point-of-care testing. Indeed, a DNA sequencer employing an integrated transistor chip has already been applied to cancer genome analysis in the context of tailored medicine. These devices can be used not only in large hospitals but also in smaller medical facilities or physicians' offices, or even in a patient's home. In addition, we can take the small instrument out of the laboratory to detect nucleic acids of viruses or microorganisms on site for the purpose of infectious disease testing. Thus, transistor-based biosensing technology represents a useful and effective means for real-time monitoring of the biosecurity level in our environment. In advanced countries such as Japan, society is aging rapidly, and medical needs are increasing, even while the capacities of hospitals and medical doctors remain limited. We believe that one approach to improving this situation is to develop a system in which medical treatment and clinical diagnostics can be performed on patients at home. Such a system would require a simple, small, and highly sensitive detection system for point-of-care testing.

2.7 Conclusion

In this chapter, we described the fundamental principles and present the use of biotransistors with various sensing interfaces, including a discussion of our own research. Many researchers are now addressing a range of challenges in biosensing: miniaturization, parallelization for high-throughput analysis, integration, functionalization, and increasing the *S*/*N* ratio. A fusion of nanobiotechnologies will enable breakthroughs in biology and biotechnology, especially in fields such as drug design and screening, nanomedicine, and genome-based tailored medicine. We expect that biosensors with functional nanointerfaces will play important roles in developing new modes of clinical care.

Acknowledgments Our work in this chapter was supported in part by the Japan Science and Technology Agency (JST), Core Research of Evolutional Science and Technology (CREST), and by the Japan Society for the Promotion of Science (JSPS) through the "Funding Program for World-Leading Innovative R&D on Science and Technology (FIRST Program)," initiated by the Council for Science and Technology Policy (CSTP).

References

1. P. Bergveld, Development of an ion-sensitive solid-state device for neurophysiological measurements. IEEE Trans. Biomed. Eng. **BM17**(1), 70–71 (1970)
2. P. Jiang, Z. Guo, Fluorescent detection of zinc in biological systems: recent development on the design of chemosensors and biosensors. Coord. Chem. Rev. **248**(1–2), 205–229 (2004)
3. J. Janata, S. Moss, Chemically sensitive field-effect transistors. Biomed. Eng. **11**(7), 241–245 (1976)
4. S. Hrapovic, Y.L. Liu, K.B. Male, J.H.T. Luong, Electrochemical biosensing platforms using platinum nanoparticles and carbon nanotubes. Anal. Chem. **76**(4), 1083–1088 (2004)
5. T. Goda, Y. Miyahara, Label-free and reagent-less protein biosensing using aptamer-modified extended-gate field-effect transistors. Biosens. Bioelectron. **45**, 89–94 (2013)
6. M. Lohndorf, U. Schlecht, T. Gronewold, A. Malave, M. Tewes, Microfabricated high-performance microwave impedance biosensors for detection of aptamer–protein interactions. Appl. Phys. Lett. **87**(24), 243902 (2005)
7. C. Kataoka-Hamai, Y. Miyahara, Label-free detection of DNA by field-effect devices. IEEE Sens. J. **11**(12), 3153–3160 (2011)
8. T. Goda, A. Singi, Y. Maeda, A. Matsumoto, M. Torimura, H. Aoki et al., Label-free potentiometry for detecting DNA hybridization using peptide nucleic acid and DNA probes. Sensors **13**(2), 2267–2278 (2013)
9. M. Tsutsui, M. Taniguchi, K. Yokota, T. Kawai, Identifying single nucleotides by tunnelling current. Nat. Nanotechnol. **5**(4), 286–290 (2010)
10. F. Patolsky, G. Zheng, O. Hayden, M. Lakadamyali, X. Zhuang, C. Lieber, Electrical detection of single viruses. Proc. Natl. Acad. Sci. USA **101**(39), 14017–14022 (2004)
11. S. Thomas, G. Joly, T. Swager, Chemical sensors based on amplifying fluorescent conjugated polymers. Chem. Rev. **107**(4), 1339–1386 (2007)
12. P. Maroney, S. Chamnongpol, F. Souret, T. Nilsen, Direct detection of small RNAs using splinted ligation. Nat. Protoc. **3**(2), 279–287 (2008)
13. J. Jin, M. Cid, C. Poole, L. McReynolds, Protein mediated miRNA detection and siRNA enrichment using p 19. Biotechniques **48**(6), XVII–XXIII (2010)
14. G. Liu, Y. Wan, V. Gau, J. Zhang, L. Wang, S. Song et al., An enzyme-based E-DNA sensor for sequence-specific detection of femtomolar DNA targets. J. Am. Chem. Soc. **130**(21), 6820–6825 (2008)
15. T. Endo, K. Kerman, N. Nagatani, Y. Takamura, E. Tamiya, Label-free detection of peptide nucleic acid-DNA hybridization using localized surface plasmon resonance based optical biosensor. Anal. Chem. **77**(21), 6976–6984 (2005)
16. L. He, M. Musick, S. Nicewarner, F. Salinas, S. Benkovic, M. Natan et al., Colloidal Au-enhanced surface plasmon resonance for ultrasensitive detection of DNA hybridization. J. Am. Chem. Soc. **122**(38), 9071–9077 (2000)
17. M. Estevez, M. Otte, B. Sepulveda, L. Lechuga, Trends and challenges of refractometric nanoplasmonic biosensors: a review. Anal. Chim. Acta **806**, 55–73 (2014)
18. J. Fritz, M. Baller, H. Lang, H. Rothuizen, P. Vettiger, E. Meyer et al., Translating biomolecular recognition into nanomechanics. Science **288**(5464), 316–318 (2000)
19. K. Marx, Quartz crystal microbalance: a useful tool for studying thin polymer films and complex biomolecular systems at the solution-surface interface. Biomacromolecules **4**(5), 1099–1120 (2003)
20. A. Steel, T. Herne, M. Tarlov, Electrochemical quantitation of DNA immobilized on gold. Anal. Chem. **70**(22), 4670–4677 (1998)
21. C. Shan, H. Yang, J. Song, D. Han, A. Ivaska, L. Niu, Direct electrochemistry of glucose oxidase and biosensing for glucose based on graphene. Anal. Chem. **81**(6), 2378–2382 (2009)
22. T. Sakata, Y. Miyahara, Detection of DNA recognition events using multi-well field effect devices. Biosens. Bioelectron. **21**(5), 827–832 (2005)

23. T. Sakata, Y. Miyahara, DNA sequencing based on intrinsic molecular charges. Angew. Chem. Int. Ed. **45**(14), 2225–2228 (2006)
24. J. Rothberg, W. Hinz, T. Rearick, J. Schultz, W. Mileski, M. Davey et al., An integrated semiconductor device enabling non-optical genome sequencing. Nature **475**(7356), 348–352 (2011)
25. H. Otsuka, E. Uchimura, H. Koshino, T. Okano, K. Kataoka, Anomalous binding profile of phenylboronic acid with *N*-acetylneuraminic acid (Neu5Ac) in aqueous solution with varying pH. J. Am. Chem. Soc. **125**(12), 3493–3502 (2003)
26. A. Matsumoto, H. Cabral, N. Sato, K. Kataoka, Y. Miyahara, Assessment of tumor metastasis by the direct determination of cell-membrane sialic acid expression. Angew. Chem. Int. Ed. **49** (32), 5494–5497 (2010)
27. A. Matsumoto, N. Sato, K. Kataoka, Y. Miyahara, Noninvasive sialic acid detection at cell membrane by using phenylboronic acid modified self-assembled monolayer gold electrode. J. Am. Chem. Soc. **131**(34), 12022–12023 (2009)
28. D. Schaffhauser, M. Patti, T. Goda, Y. Miyahara, I. Forster, P. Dittrich, An Integrated field-effect microdevice for monitoring membrane transport in *Xenopus laevis* oocytes via lateral proton diffusion. PLoS ONE **7**(7), e39238 (2012)
29. S. Kim, J. Rusling, F. Papadimitrakopoulos, Carbon nanotubes for electronic and electrochemical detection of biomolecules. Adv. Mater. **19**(20), 3214–3228 (2007)
30. B. Allen, P. Kichambare, A. Star, Carbon nanotube field-effect-transistor-based biosensors. Adv. Mater. **19**(11), 1439–1451 (2007)
31. A. Gao, N. Lu, Y. Wang, P. Dai, T. Li, X. Gao et al., Enhanced sensing of nucleic acids with silicon nanowire field effect transistor biosensors. Nano Lett. **12**(10), 5262–5268 (2012)
32. W. Yang, K. Ratinac, S. Ringer, P. Thordarson, J. Gooding, F. Braet, Carbon nanomaterials in biosensors: should you use nanotubes or graphene? Angew. Chem. Int. Ed. **49**(12), 2114–2138 (2010)
33. S. Tans, A. Verschueren, C. Dekker, Room-temperature transistor based on a single carbon nanotube. Nature **393**(6680), 49–52 (1998)
34. P. Hu, J. Zhang, L. Li, Z. Wang, W. O'Neill, P. Estrela, Carbon nanostructure-based field-effect transistors for label-gree chemical/biological sensors. Sensors **10**(5), 5133–5159 (2010)
35. N. Elfstrom, R. Juhasz, I. Sychugov, T. Engfeldt, A. Karlstrom, J. Linnros, Surface charge sensitivity of silicon nanowires: Size dependence. Nano Lett. **7**(9), 2608–2612 (2007)
36. E. Stern, R. Wagner, F. Sigworth, R. Breaker, T. Fahmy, M. Reed, Importance of the debye screening length on nanowire field effect transistor sensors. Nano Lett. **7**(11), 3405–3409 (2007)
37. Y. Bunimovich, Y. Shin, W. Yeo, M. Amori, G. Kwong, J. Heath, Quantitative real-time measurements of DNA hybridization with alkylated nonoxidized silicon nanowires in electrolyte solution. J. Am. Chem. Soc. **128**(50), 16323–16331 (2006)
38. G. Zhang, G. Zhang, J. Chua, R. Chee, E. Wong, A. Agarwal et al., DNA sensing by silicon nanowire: charge layer distance dependence. Nano Lett. **8**(4), 1066–1070 (2008)
39. J. Hahm, C. Lieber, Direct ultrasensitive electrical detection of DNA and DNA sequence variations using nanowire nanosensors. Nano Lett. **4**(1), 51–54 (2004)
40. E. Stern, J. Klemic, D. Routenberg, P. Wyrembak, D. Turner-Evans, A. Hamilton et al., Label-free immunodetection with CMOS-compatible semiconducting nanowires. Nature **445** (7127), 519–522 (2007)

Chapter 3
BioImaging System with High Resolution and Sensitivity for Biological Science and Medical Application

Kazuaki Sawada, Fumihiro Dasai, Koichi Okumura, Masato Futagawa and Toshiaki Hattori

Abstract Bioimaging technology has been focused on medical and biological field, and it is getting more important and necessary to achieve 2- or 3-dimensional information of organic activity. By using solid-state type biosensor technology and LSI technology, solid-state type bioimage sensors that are based on charge-coupled device/complementary metal–oxide–semiconductor technology have been developed as semiconductor-based chemical imaging tools. These chemical imaging tools are devices that not only determine quantity of analyte ions, but also acquire label-free images of the local distribution of the ions, and chemical species in liquid solution and cells with real time. By using this non-label bioimage sensor system, real-time observation of neurotransmitters (Acetylcholine: ACh) and ions (K^+, Na^+, Ca^{2+}) in cells was carried out. Significant changes in K^+ were detected underneath the hippocampal slices. K^+ ion was detected by the glutamate stimulation associated with gating through potassium ion channels in hippocampal neurons without a labeling process.

Keywords CMOS image sensor · Bioimaging · CCD · ISFET

3.1 Introduction

An ion sensor is one of the most important devices among biosensors because ion is a basic parameter for medical and biological field. The most familiar pH sensor using semiconductor technology is an ion-sensitive field-effect transistor (ISFET), which detects the variation of current through the transistor when the ion concentration changes in solution. The ISFET for neurophysiological measurement in 1970 was introduced [1] and a lot of fundamental researches have been performed on these devices and various applications were proposed [2, 3]. The ISFET is

K. Sawada (✉) · F. Dasai · K. Okumura · M. Futagawa · T. Hattori
Toyohashi University of Technology, 1-1 Hibarigaoka,
Tempaku-Cho, Toyohashi 441-8580, Japan
e-mail: sawada@ee.tut.ac.jp

J. Sone and S. Tsuji (eds.), *Intelligent Nanosystems for Energy, Information and Biological Technologies*, DOI 10.1007/978-4-431-56429-4_3

constructed an ion-selective electrode (ISE) and a metal–oxide–semiconductor field-effect transistor (MOSFET). The normal metal or polysilicon gate electrode of MOSFET is replaced by the electrochemical reference electrode in electrolyte solution and an ion-sensitive membrane on the top of the gate insulator. For proper operation of the ISFET, a gate voltage is applied to the gate insulator via the reference electrode and the electrolyte solution. An electrochemical potential by ions is modified on the surface of the ion-sensitive membrane and can be measured as a shift in drain current or threshold voltage of the ISFET. The sensitivity of the ISFET is derived from site-biding model. From this model, the maximum sensitivity is 59.2 mV/pH for monovalent reaction at 25 °C, which is well known the Nernst value [2].

Bioimaging technology has been focused on medical and biological field, and it is getting more important and necessary to achieve 2- or 3-dimensional information of organic activity. Bioimaging tools are an effective way to visualize these. The bioimaging technology is able to apply, such as health care, food administration, ion distribution with cellular activity, especially, cell exchange inside and outside ions [4, 5]. It is important to detect the ion movement for understanding cellular activity [6]. Fluorescence detection method is generally used in the field of life science for bioimaging. This is because fluorescence detection method has several merits such as sensitivity and possibility of multi-staining procedure.

On the other hand, imaging technique without fluorescent labels to understand information of organic activity in human body for the regenerative medicine is demanded. Chemical microscopes can be used to obtain clear images that display localized chemical and biochemical materials. Various types of chemical microscopes with micrometer-scale resolution have been applied to biological systems [7]. Evolution of the microscope has yielded techniques, such as light-addressable potentiometric sensor (LAPS) [8], which belong to a contact-type sensor and which is label-free and noninvasive, in contrast with a fluorescence microscope. By using solid-state type biosensor technology and LSI technology, solid-state type bioimage sensors that are based on charge-coupled device (CCD) [9, 10] have been recently developed as semiconductor-based chemical imaging tools. These chemical imaging tools are devices that not only determine quantity of analyte ions, but also acquire label-free images of the local distribution of ions and chemical species in liquid solution with real time. In this section, we introduce developments and applications of the CCD based bioimage sensor.

3.2 Principle of Array-Type CCD Ion Image Sensor

Charge-transfer-type ion image sensors with a photo-image acquisition function have been studied [11, 12], and have applied them to the field of biochemical analyses [13, 14]. These sensors, which have a 32 × 32 pixel arrangement [15], have achieved outputs with lower variability between each pixel than those achieved by other groups. Ion image sensors, which use a smaller pixel pitch, more

pixels, and a higher frame rate, are required for the analysis of cell membranes and for the responses of neural networks. We focused on the fabrication of an advanced charge-transfer-type hydrogen ion image sensor [16] with a photo-image actuation function, which has a 128 × 128 pixel configuration, a high pixel density, and high frame rate performance. In order to meet these requirements, a specific fabrication process for an ion image sensor based on complementary metal–oxide–semiconductor (CMOS) large-scale integration (LSI) circuits was developed. A new scanning method and output circuits with low output impedance were adopted to realize a higher frame rate. The proposed sensor was performed to measure hydrogen ion sensitivity, output signal variation, and hydrogen ion imaging.

3.2.1 Sensor Structure and Sensing System

The sensor includes a 128 × 128 pixel array, and an advanced read-out system was adopted for the hydrogen ion sensor to achieve a higher frame rate. The basic sensing principle is described here. A sensing element for hydrogen ions using the charge-transfer technique is shown in Fig. 3.1. Figure 3.1a shows a cross-sectional view in the case of the hydrogen ion measurement. Figure 3.1b–d show hydrogen ion measurement procedures using the charge-transfer technique. The hydrogen ions are adsorbed on a sensing membrane consisting of a Si_3N_4 film. The ions affect the Si surface potential in the sensor area. Input control gate (ICG) and transfer gate (TG) electrodes are used to control the potential level and the gating. Their gates were applied −2.5/+2.5 V. The input diode (ID) and floating diffusion (FD) are pn junctions which supply charge and which detect the charge quantity. The supply voltages of elements were 0/+5 V. The potential level in the FD is reset as shown in Fig. 3.1b. In Fig. 3.1c, the charge in sensor area corresponds to the potential level, which is varied by hydrogen ion concentration (pH), and is maintained under the sensor area by the 'fill and spill' technique [17]. In Fig. 3.1d, the charge is transferred to the FD by increasing the potential of the TG electrode, and the potential of FD is also changed. An output signal is obtained from the variation of the FD potential through a source follower circuit. When the procedures shown in Fig. 3.1c, d are repeated again, the signal charges in the FD region can double. Use of the accumulation method for the signal charges is a big advantage for our sensor, because the accumulation method is capable of signal amplification [17, 18].

The CCD type pH image sensor is able to be operated in charge accumulation method (signal integration mode). Charges corresponded to pH value is transferred from a sensing part to the floating diffusion region on several times as mentioned as explained in Fig. 3.1d, and the signal charges are accumulated in the floating diffusion region. It is expected that the signal-to-noise ratio (SNR) of the pH value information increases by accumulating the signal charges. As a pH signal S_0 is accumulated n times, total quantity of the signal S is described as follows;

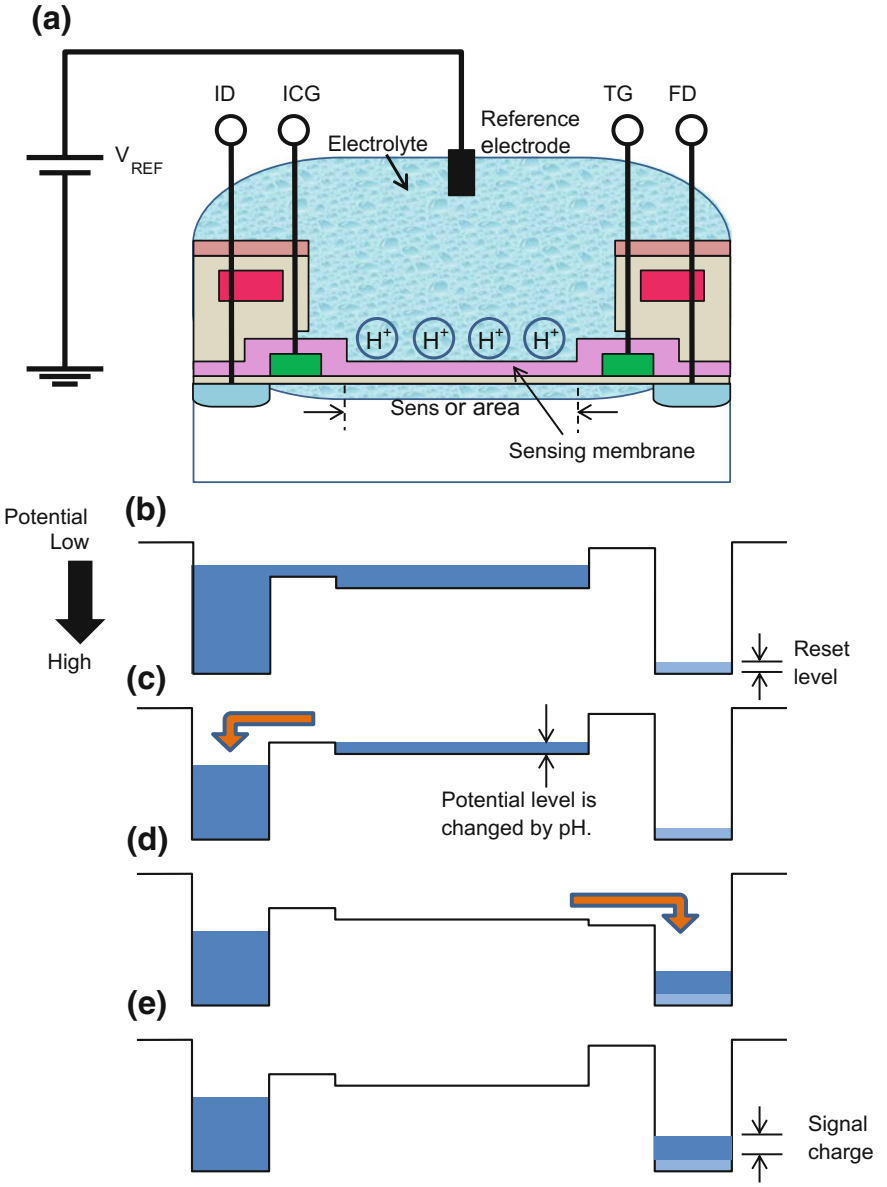

Fig. 3.1 Potential images of pH sensing method using the charge-transfer technique. **a** A cross-sectional view at the time of hydrogen ion measurement with a reference electrode. **b** Read-out reset level. **c** Filling up the charge according to the potential level of the sensor area. **d** Charge-transfer to FD. **e** Read-out signal level [16, Figure 1]

$$S = n \cdot S_0 \tag{3.1}$$

The total quantity of the noise N is described as follows,

$$N = \sqrt{N_1^2 + N_2^2 + \cdots + N_n^2} \tag{3.2}$$

where N_1, N_2, … N_n are noise components on each integration stage. If these components are same, above equation is simplified.

$$N = \sqrt{n \cdot N_0^2} \tag{3.3}$$

where $N_0 = N_1 = N_2 = \cdots = N_n$. Therefore, total SNR is given by

$$\frac{S}{N} = \frac{n \cdot S_0}{\sqrt{n \cdot N_0^2}} = \sqrt{n}\frac{S_0}{N_0} \tag{3.4}$$

From this equation, SNR increases $n^{0.5}$ times, as the signal is integrated n times. The $1/f$ noise component of the source flower circuits is not influenced, because the input signals of the source flower circuit increases by the integration.

The output signal and its noise power level of a charge-transfer-type pH sensor are shown in Fig. 3.2, a noise level of an ISFET is superimposed on it. The sampling rate of the charge-transfer-type pH sensor was varied in 1–5 kHz, which depended on the accumulation cycle. The output signal is proportional to accumulation cycles and the noise power level increases in proportion to (the gain of the sensor)$^{1/2}$. Thus, the noise converted pH, which is fluctuation of pH output signal, is reducing as shown in Fig. 3.3. In a case of 1 accumulation cycle, noise converted pH is 0.0052 pH, which is the same level of the ISFET. The noise is reduced by

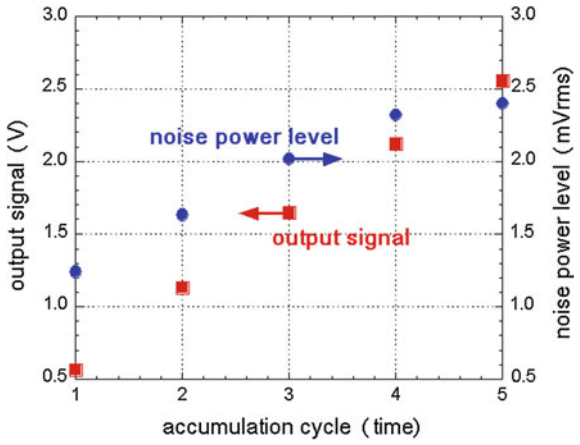

Fig. 3.2 The output signal and the noise power level of a charge-transfer-type pH sensor [32, Figure 4]

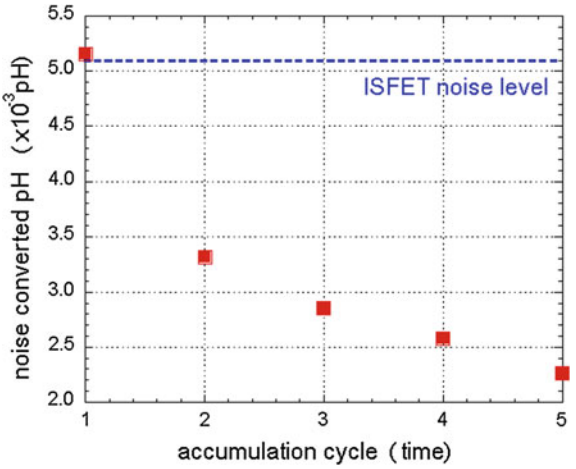

Fig. 3.3 The noise converted pH as input-referred value of a charge-transfer-type pH sensor [32, Figure 5]

increment of accumulation cycles and the noise converted pH of 0.0023 pH is realized in 5 accumulation cycles [19].

A sensor system including the 128 × 128 sensor pixel array with a 23 μm pixel pitch was fabricated using CMOS technology. A new scanning system and high-performance drive buffer circuits were adopted in order to achieve high frame rates. For miniaturization of the sensor pixels, we developed an advanced new fabrication process.

3.2.2 Measurement Results

A hydrogen ion image sensor was fabricated by using a 2 μm process including a 'specialty' process. Photographs of the sensor chip and sensor pixel are shown in Fig. 3.4. The sensor area with 128 × 128 pixels was 3 mm × 3 mm square. The pixel size was 23.55 μm × 23.55 μm and included a hydrogen ion sensing area with an exposed Si_3N_4 sensing membrane.

The sensitivity, including read-out circuit and charge-transfer amplification, was 35.8 mV/pH. The standard deviation of the sensitivity of whole pixel was achieved of 6.5 %. For the stability assay, the pH output signal of a pixel was continuously monitored and $\pm 3\ \sigma$ pH variation was 0.107 pH. A demonstration of real-time hydrogen ion imaging using the sensor chip was carried out. Snapshots from a video showing ion movement and a photo image that was taken simultaneously are shown in Fig. 3.5. First, a solution at pH 9.18 was introduced onto the surface of the chip and uniformly covered the sensor area, as shown in Fig. 3.5a. A snapshot of the dropping of a pH 4.01 solution 10 s after the image in Fig. 3.5a is shown in Fig. 3.5c. The dropping solution was discharged in the direction diagonal to the vertical direction. Therefore, the positions of the silhouette in the photo image and

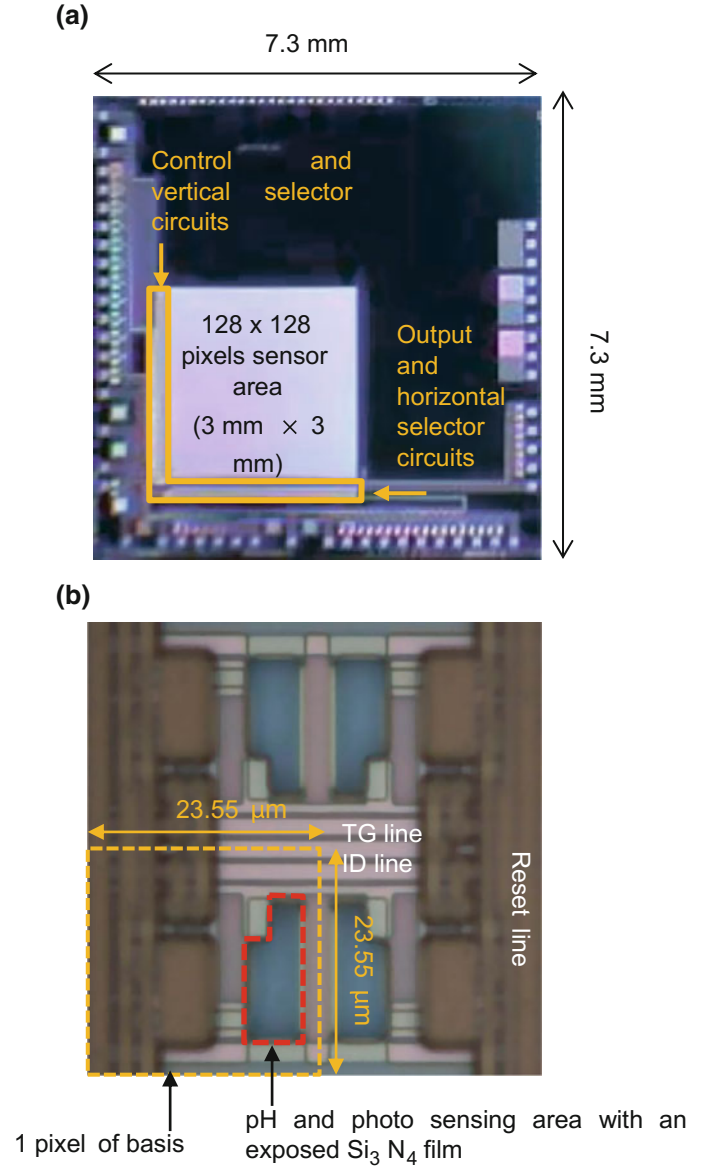

Fig. 3.4 Chip overview of the new sensor. **a** Photograph of the sensor chip. **b** Micrograph of the sensor pixels [16]

hydrogen ion signal appear in different areas. The images captured 1 second after Fig. 3.5c are shown in Fig. 3.5d. The dropped solution diffused and spread out over the area of the sensor. The frame rate obtained was 58 frame/s, which is almost same as conventional Television rate.

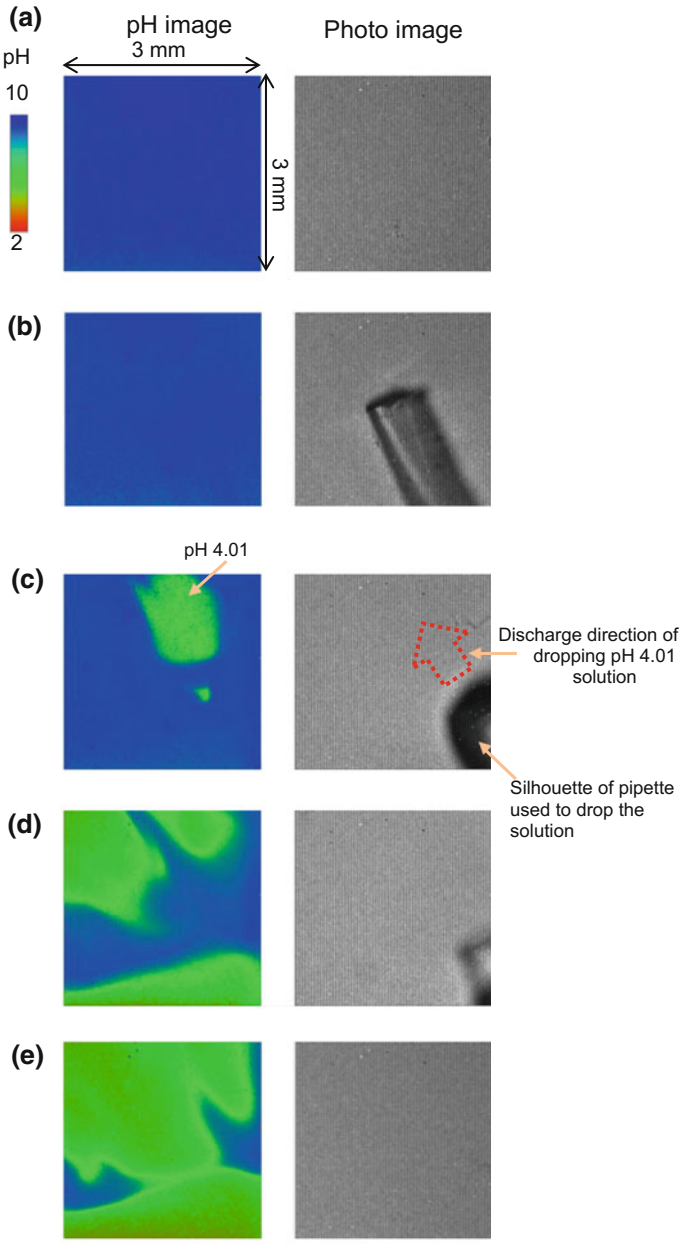

Fig. 3.5 pH and photo images using new sensor chip. **a** Initial image after dropping a pH 9.01 standard solution. **b** Moving the tip of pipette on the sensor area (5 s after image **a**). **c** Instant images of dropping a pH 4.01 solution (10 s after image **a**). **d** Images of pH 4.01 diffusion (11 s after image **a**). **e** Diffusing the pH 4.01 solution further after removing the pipette (16 s after image **a**) [16, Figure 10]

3.3 Chemical Imaging

Each sensing pixel of CCD pH image sensor measures the activity of hydrogen ion in the local region, and the sensor displays a global image of pH distribution over the whole region. The functional component responsible to hydrogen ion is Si_3N_4 which was laid on the surface contacted with the solution. Any different membrane which responds to a different ion can be piled up onto Si_3N_4. Various ion-sensitive membranes have been developed and there are many reports in common ion-selective electrodes (ISE). Although there is a classification for ISE by the nomenclature of IUPAC [20], here, a common classification [21] is applied; solid membrane with fixed ion-exchange site and liquid membrane with mobile ion-exchange site. Several typical ion-sensitive membrane electrodes are shown in Fig. 3.6. Type-I of a typical crystalline electrode is a solid-state membrane which is a crystal of insoluble salts. A fluoride electrode consists of a crystal of lanthanum fluoride doped with trace amount of europium, which increases the conductivity of the membrane substance. Since the solid membrane performs as a mixed conductor of ion and electron, it can be directly contacted with a metal line connected from its electronics. A well-known Ag^+ electrode that is made from Ag_2S responds to Ag^+, but also responds to S^{2-}. When AgX (X; halide ion) or CuS or CdS is mixed into Ag_2S homogeneously, the mixture membrane electrodes respond also to its additive ion. For instance, the solid electrode doped with AgI responds to I^-. Type-II of a glass electrode is a noncrystalline solid electrode that has rigid charged sites. The glass electrode has an internal solution and an internal reference electrode. The chemical composition of the glass determines the selectivity of the membrane, which responds to hydrogen ion and monovalent cations. Type-III of a liquid membrane is made of an immiscible organic liquid supported by polymers or porous materials. The liquid membrane contains a mobile carrier which selectively binds with analyte ion into the membrane. In particular, a selective ion-transport compound called neutral ionophore is an excellent ligand to analyte ion. The liquid

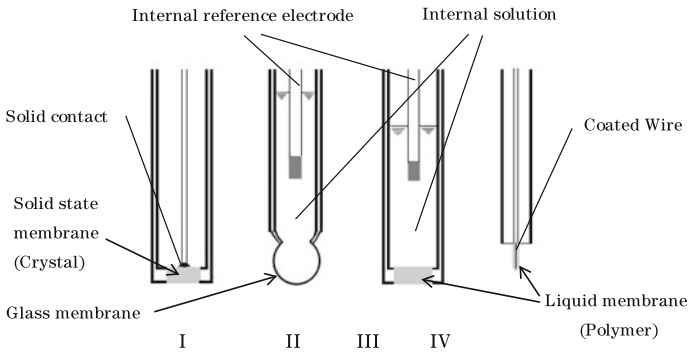

Fig. 3.6 Typical ion-sensitive membrane electrodes; *I* solid-state membrane electrode, *II* glass membrane electrode, *III* liquid membrane electrode with an internal solution, *IV* liquid membrane electrode directly coated

membrane can be used for such a coated wire electrode of type-IV [22]. It is free from the internal solution, and the liquid membrane directly contacts with a metal wire.

On the semiconductor ion sensors, it is difficult to have internal solutions, and directly contacted membranes are favorable. Among the directly contacted membranes, plasticized poly(vinyl chloride) (PVC) is one of the most useful membrane materials for the semiconductor sensor. The plasticized PVC membrane is prepared in room temperature. After the sensor chips cut from silicon wafer was bonded in a package, a heating treatment often destroyed the sensor. The heatless treatment was favorable to the post processing of the packaging. Moreover, the plasticized PVC membranes have abundant variety of its applications. In 1994, a 20 × 20 (400 pixels) array-type ISFET sensor with plasticized PVC membranes which allow chemical imaging of ammonium ions and urea had been reported [23]. However, the response time of the array image sensor was too slow to perform a real-time imaging. As far as we know, there were few reports about fast-response array ISFET ion image sensor with many numbers of pixels, except for the developments of light-addressable potentiometric sensor (LAPS) [24]. We developed a 1K-pixels CCD potassium ion image sensor using the plasticized PVC membrane [25]. The membrane consisted of PVC as a based polymer, di-octylphthalate as a plasticizer, bis[(benzo-15-crwon-5)-4-methyl] pimelate as a potassium ion ionophore, potassium tetrakis(*p*-chlorophenyl)borate as an ion-exchanger, and a polyhedral oligomeric silsesquioxanes (POSS) as a nano-filler. The choices of the ionophore and the plasticizer are important, and these materials determine the ion selectivity for analyte ion. In addition, the semiconductor sensors require adhesion between the semiconductor and the plasticized PVC membrane. The addition of the one of POSSs was very useful to improve the adhesion of the membrane on Si_3N_4. A plasticized PVC membrane tends to absorb water. When the membrane contacted with water, water got into the surface between Si_3N_4 and the membrane. Then, the membrane floated on the sensor lost the potential response to the analyte ion. The POSS protected the invasion of water, and its durability was improved. After the pre-equilibrium process of the membrane with 1 mM of potassium ion solution for 6 h (conditioning), the potential slope to potassium ion was linear from 10^{-2} to 10^{-5} M logarithmic concentration of potassium ion. The selectivity coefficient of potassium ion was larger than other alkali metal ions. The selectivity coefficient indicates the degree of the exchange reaction between the membrane material and the ion in solution [26].

Using the 1K-pixels CCD potassium ion image sensor, we took the video that displayed the leakage of KCl from a reference electrode consisting of KCl saturated Ag/AgCl [26]. After a neutral pH buffer solution without potassium ion was added, the solution set the reference electrode was monitored. Several images captured from the video of the potassium ion releasing are shown in Fig. 3.7. The region of high concentration of potassium ion spread out with time. When a common Vycor glass was used at its junction, the high concentration reached to some pixels within 10 s. It was surprised that the leakage was faster and larger than expected.

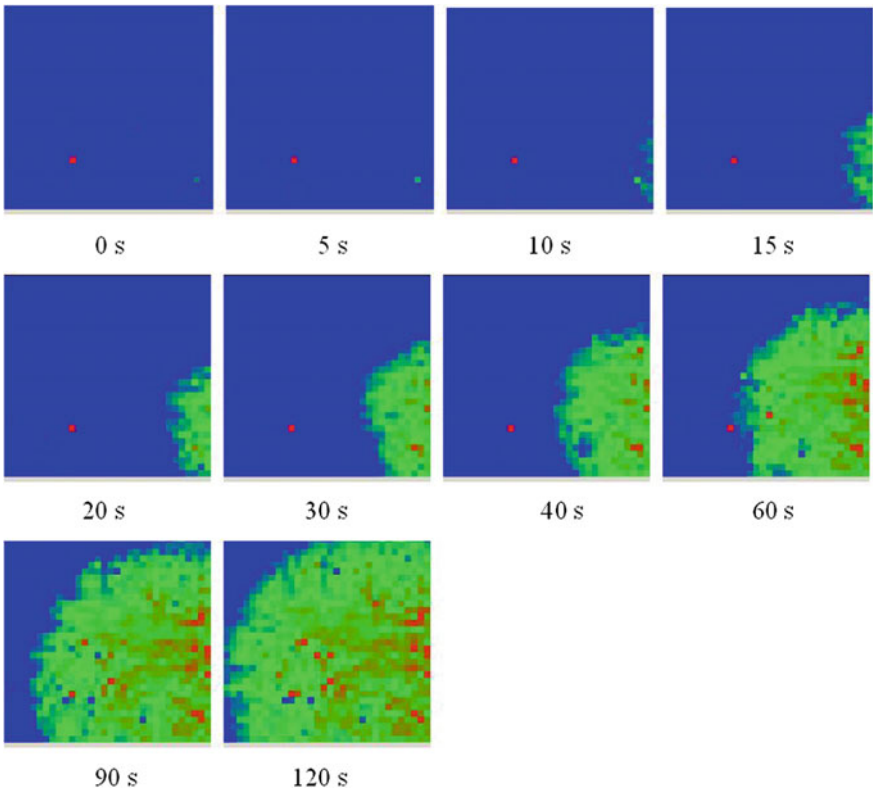

Fig. 3.7 Real-time images of potassium ion concentration during monitoring of KCl solution leakage from Ag/AgCl electrode [25, Figure 7]

A 1K-pixels CCD sodium ion image sensor with the plasticized PVC membrane containing bis [(12-crown-4) methyl)-2-dodecyl-2-methyl malonate] as a sodium ion ionophore also was developed [25]. The composition of the sodium ion-selective membrane including the same nano-filler was optimized. The potential response of the sodium ion image sensor was characterized. The calibration curve indicated the region of linear response was in the concentration region from 10^{-5} to 10^{-1} M. The selectivity coefficient of sodium ion was significantly larger than calcium ion and barium ion. In addition, its time response was evaluated. When a small amount of a high concentration solution of sodium ion was added to a lower concentration solution of sodium ion, the CCD sensor displayed a quick increase in the read-out potential corresponding to the change in concentration of sodium ions. In contrast, when a small amount of the lower concentration solution was added to the high concentration solution, the sodium ion concentration decreased momentarily in certain areas, and then rapidly increased. The ability to catch such the sudden change of signals indicated that the CCD sensor exhibited a quick time response to changes in sodium ion concentration. Ion-exchange reaction of a single

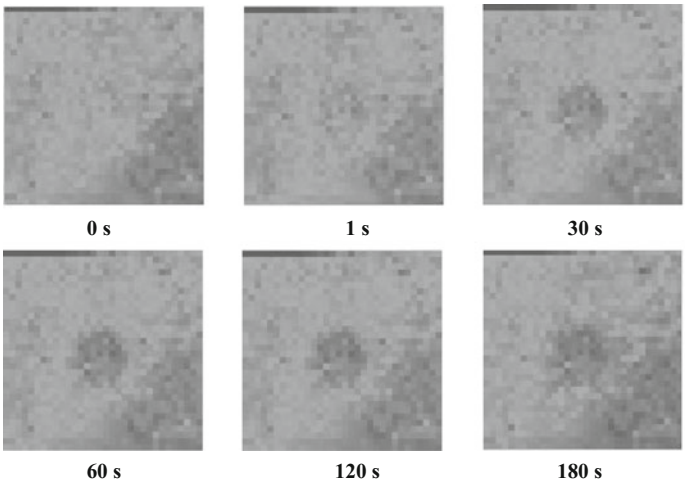

Fig. 3.8 Sodium ion concentration images obtained during the ion-exchange reaction of an Amberlite IR 120 B single resin bead after the addition of a solution containing calcium ions. The *dark areas* indicate a high concentration of sodium ions [26, Figure 3]

resin was easily monitored as a video using the 1K-pixels CCD sodium ion image sensor [27]. Several images captured from a video of Na^{+}–Ca^{2+} ion-exchange reaction are shown in Fig. 3.8. A single bead of Na-type cation exchange resin with a diameter of about 0.7 mm was placed at the center of the CCD sensor, and the CCD sensor was filled with 0.01 M NaCl solution. A small amount of 0.1 M of $CaCl_2$ or $BaCl_2$ solution was added to the solution containing the bead, the concentration of sodium ions increased around the bead. Addition of $BaCl_2$ solution released sodium ions significantly faster than the addition of $CaCl_2$ solution. The different speed of their ion-exchanges indicated a key factor in the flux equation of Nernst–Plank in the initial ion-exchange period.

3.4 Applications of BioImaging

There are several roots to do the bioimaging with CCD pH image sensor, as shown in Fig. 3.9. The key technology is based on the modification of ion-sensitive membranes and the utilization of enzymes. It can be applied to bioimaging even without the modification and enzymes. For instance, a 100-pixels CCD pH ion image sensor had demonstrated that a root of a rice plant released citric acid [28]. The pH around the root was observed to increase with time. The unmodified CCD pH sensor also can monitor a biological interaction on which a change of the surface potential is produced. If a certain poly-charged material such as a DNA is adsorbed onto Si_3N_4, the surface charge on the substrate would be changed.

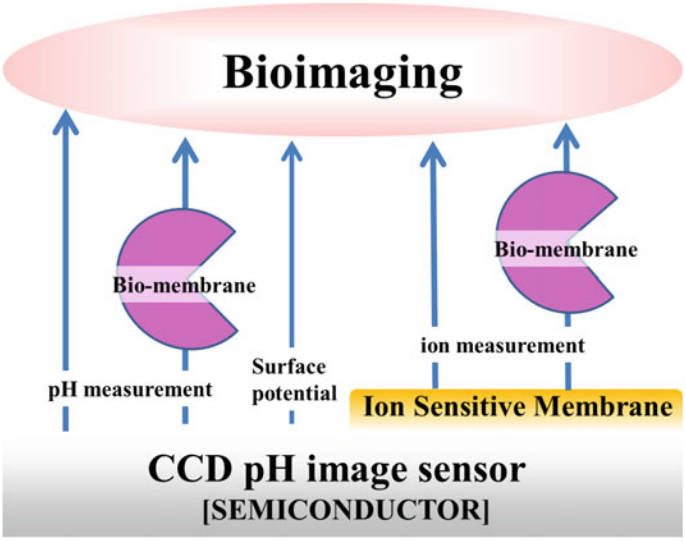

Fig. 3.9 Several methods of bioimaging using CCD pH image sensor [33, Figure 5]

As the use of the enzyme, we developed a 1K-pixels CCD acetylcholine (ACh) image sensor by use of acetylcholine esterase (AChE) [14]. The enzyme-type image sensor detected a concentration change of hydrogen ion generated by the ACh-AChE enzyme reaction according to the followings,

$$\mathrm{ACh} + \mathrm{H_2O} \rightarrow \mathrm{choline} + \mathrm{CH_3COO^-} + \mathrm{H^+}$$

A uniform enzyme membrane was prepared on the Si_3N_4 using a polyion complex method. AChE was concentrated and trapped into the polyion complex between positively charged poly(L-lysine) and negatively charged poly (4-styrenesulfonate). The working curve of ACh was linear from 1 to 10 mM, and the slope was 4.2 mV/mM. The detection limit of ACh was 20 μM. Since the enzyme reaction was fast on the optimum membrane, the real-time imaging of the concentration change of ACh was achieved.

The other is the utilization of the chemical imaging membranes. We applied 16 K-pixels CCD ion image sensors with plasticized membranes to bioimaging of tissue. A potassium ion-sensitive image sensor with plasticized PVC membrane contained valinomycin as the ionophore was applied to bioimaging of brain tissue of a rat [29]. After a hippocampal slice was cultured for 4 days at 37 °C in a 5 % CO_2 incubator, the hippocampal slice was placed onto the sensor filled with a recording medium containing several cell-culture materials. Then, the extracellular potassium ion concentration ($[K^+]_{out}$) including of the hippocampal slice was monitored. When the hippocampal slice was just placed onto the sensor, the changes in $[K^+]_{out}$ were immediately detected underneath the hippocampal slices.

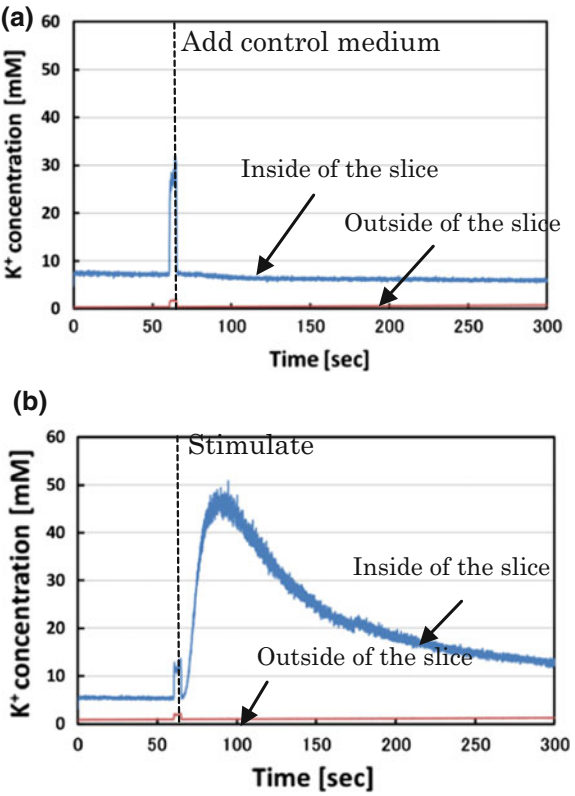

Fig. 3.10 Time course of $[K^+]_{out}$ of the hippocampal slices. **a** Control (no stimulation). **b** Glutamate stimulation. *Dot lines* indicate the time of addition of solutions [29, Figure 6], **a** Control (addition of recording medium), **b** stimulation (addition of recording medium containing 1 mM glutamate)

Moreover, after glutamate was induced, the large changes in $[K^+]_{out}$ was observed in the only position associated with the gating through potassium ion channels in hippocampal neurons. Its change in $[K^+]_{out}$ stimulated with glutamate was from 10 to 50 mM as shown in Fig. 3.10.

A 16K pixels ion image sensor also was applied to bioimaging of rat mast cells stimulated. For the sake we developed a 16K pixels biogenic amine image sensor [30]. Since biogenic amines are positively charged ammonium ions at neutral pH, they can be measured by an ion-sensitive electrode with plasticized PVC membrane. An amine sensitive membrane was prepared from plasticized polyvinyl chloride including a hydrophobic anion which allowed the sensor to detect amines such as histamine and serotonin. Since the image sensor was free from enzyme, the selectivity of the ion-sensitive membrane is inferior to an enzyme biosensor. However, it can circumvent enzyme biosensor drawbacks, which include slow reaction, poor durability, and enzyme heterogeneities in the membrane. Sequential snapshots of biogenic amine concentration in a Tyrode's solution with mast cells are shown in Fig. 3.11. The picture at each time revealed marked differences after the addition of a trace amount of Compound 48/80 as a stimulus. Spots indicated that concentrations of amines increased to a maximum at 4–6 s and then

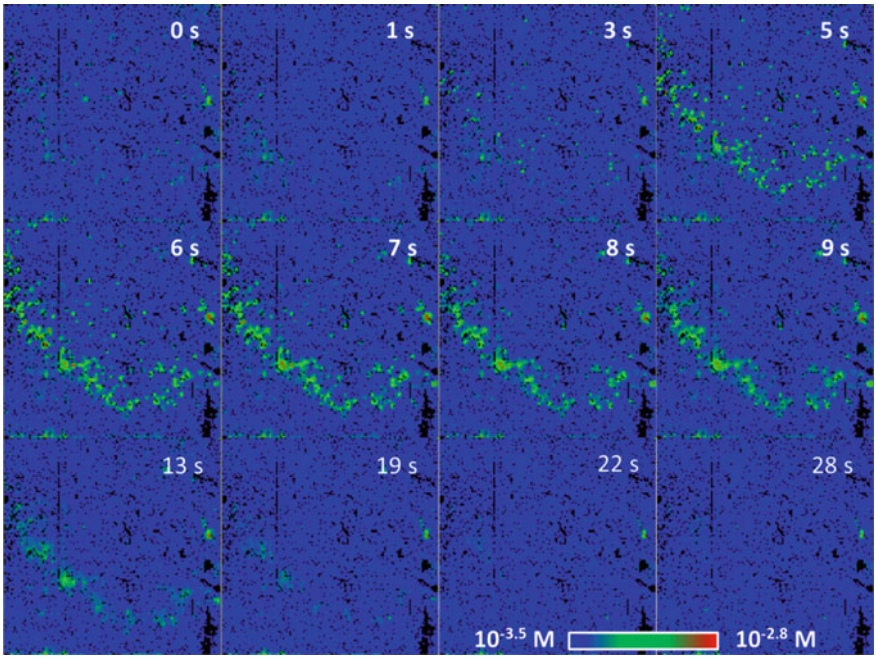

Fig. 3.11 Snapshots of chemical imaging using biogenic amine concentration before and after addition of compound 48/80 solution to sensing well containing rat mast cells [30, Figure 3]

disappeared after about 30 s, with these changes in the spots apparently synchronized. Since mast cells were larger in diameter than the pixel hollows, some pixels monitored amines released from single cells. The 3D figures display the concentration changes of biogenic amine for 2D array including a pixel under a single cell and its surrounding pixels, as shown in Fig. 3.12. Thus, the present biogenic amines image sensor reveals a whole tendency of mast cells by the stimulus addition, and moreover, it can catch local change of each mast cell.

On the other hand, the membrane directly contacts with living cells and tissues. Therefore, the properties of the membrane contents affect living cells and tissues. We examined the influence of use of PVC membranes on culture of cells in order to use array-type semiconductor calcium ion image sensor [31]. Two plasticized PVC calcium ion-sensitive membranes were prepared from optimal membrane contents. These plasticized membranes were evaluated by potential response to calcium ion concentration and by the leakage amount of plasticizers from the membrane to aqueous solution by gas chromatography. Moreover, the aqueous solutions long contacted with the membranes were examined by culture of HeLa cells. All of the solutions never killed the cells. However, the first contact solutions contacted with the membranes inhibit cell proliferation in the culture to 24 h, while the cells grew up to form a cluster at more than 48 h similar to the control experiment. The second contact solution with the membrane that was left from the first contact solution was

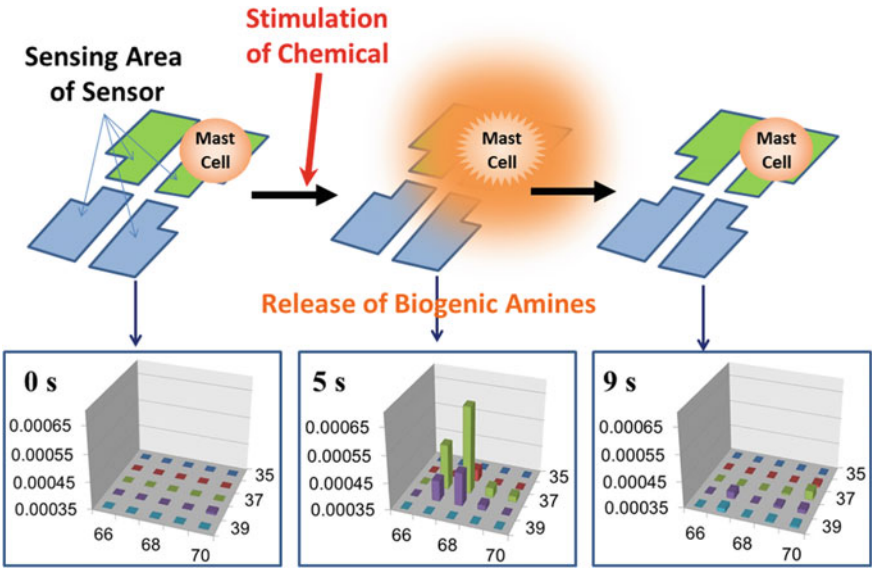

Fig. 3.12 Schematic image of a mast cell on pixels, and 3D figures of the concentration changes for 2D array including a pixel under a single cell and its surrounding pixels [30, Abstract Figure]

an initial inhibition weaker than the first contact solution. In addition, the plasticized PVC calcium ion image sensor with the leak-less feature hardly affects the cell proliferation.

3.5 Summary

Semiconductor-based bioimaging sensors provide a high spatial and time resolutions as well as sensitivity to analyte ion, due to the semiconductor microfabrication technology and LSI technology. The CCD/CMOS image sensor is highest density sensor and it can be fabricate by most refined fabrication process. A pixel size of light image sensor which is fabricated by state-of-the-art technology is about 1 μm pitch. A size of human cell and synapse is about 20 μm and 1–2 μm, respectively. It means that the image sensor technology have a potential to visualize single cell activity without fluorescent label. We are certain that the bioimaging sensors have a potential to be applied in the microbiological and medical field and might help to observe micro-scaled structures, such as single cells, cell groups, and neuronal networks.

Acknowledgments We would like to thank Dr. Takashi Sakurai and Prof. Susumu Terakawa for giving us valuable comments.

References

1. P. Bergveld, Development of an ion-sensitive solid-state device for neurophysiological measurements. IEEE Trans. Biomed. Eng. **17**, 70–71 (1970)
2. T. Matsuo, M. Esashi, Methods of ISFET fabrication. Sens. Actuators B **1**, 77–96 (1981)
3. P. Bergveld, Future applications of ISFETs. Sens. Actuators Chem. **4**, 125–133 (1991)
4. M.E. Watson, J.R. Brown, *pH and Lime Requirements*, vol. **221** North Central Regional Research Publication, 1998), pp. 13–16
5. J. Mazere, C. Prunier, O. Barret, M. Guyot, C. Hommet, D. Guilloteau, J.F. Dartigues, S. Auriacombe, C. Fabrigoule, M. Allard, In vivo SPECT imaging of vesicular acetylcholine transporter using [123I]-IBVM in early Alzheimer's disease. Neuro Image **40**, 280 (2007)
6. R. Li, Q. Lei, G. Song, X. He, Z. Xie, Calcium near the release site is essential for basal ACh release in Xenopus. Cell Biol. Int. **32**, 1136–1142 (2008)
7. M. Navratil, G.A. Mabbott, E.A. Arriage, Chemical microscopy applied to biological systems. Anal. Chem. **78**, 4005–4019 (2006)
8. D. Hafeman, J. Parce, H. McConnell, Light-addressable potentiometric sensor for biochemical systems. Science **240**, 1182–1185 (1988)
9. K. Sawada, S. Mimura, K. Tomita, T. Nakanishi, H. Tanabe, M. Ishida, T. Ando, Novel CCD based pH Imaging Sensor. IEEE Trans. Electron Devices **46**, 1846–1849 (1999)
10. T. Hizawa, K. Sawada, H. Takao, M. Ishida, Fabrication of a two-dimensional pH image sensor using a charge transfer technique. Sens. Actuators B **117**, 509–515 (2006)
11. H. Nakazawa, M. Ishida, K. Sawada, Progressive-type fused pH and optical image sensor. Jpn. J. Appl. Phys. **49**, 04DL04-1-5 (2010)
12. S. Takenaga, Y. Tamai, M. Ishida, K. Sawada, Charge accumulation type hydrogen ion image sensor with high pH resolution. Jpn. J. Appl. Phys. **50**, 027001 (2011)
13. Y. Maruyama, S. Terao, K. Sawada, Label free CMOS DNA image sensor based on the charge transfer technique. Biosens. Bioelectron. **24**(10), 3108–3112 (2009)
14. S. Takenaga, Y. Tamai, K. Okumura, M. Ishida, K. Sawada, Label-free acetylcholine image sensor based on charge transfer technology for biological phenomenon tracking. Jpn. J. Appl. Phys. **51**, 027001-1-5 (2012)
15. T. Hizawa, J. Matsuo, T. Ishida, H. Takao, H. Abe, K. Sawada, M. Ishida, 32 × 32 pH image sensors for real time observation of biochemical phenomena, in *IEEE Conference Publications on Transducers*, Lyon, (2007), pp. 1311–1312
16. M. Futagawa, D. Suzuki, R. Otake, F. Dasai, M. Ishida, K. Sawada, Fabrication of a 128 × 128 pixels charge transfer type hydrogen ion image sensor. IEEE Trans. Electron Devices **60**, 2634–2639 (2013)
17. K. Sawada, T. Shimada, T. Ohshina, H. Takao, M. Ishida, Highly sensitive ion sensors using charge transfer technique. Sens. Actuators B **98**, 69–72 (2004)
18. T. Hizawa, K. Sawada, H. Takao, M. Ishida, Characteristics of highly sensitive pH sensors with charge accumulation operation. Jpn. J. Appl. Phys. **45**, 9259–9263 (2006)
19. E. Watanabe, T. Hizawa, S. Mimura, T. Ishida, H. Takao, K. Sawada, M. Ishida, Low-noise operation of charge-transfer-type pH sensor using charge accumulation technique, in *μ-TAS 2007, M10F*, Paris (2007)
20. R.P. Buck, E. Lindner, Recommendations for nomenclature of ionselective electrodes. Pure Appl. Chem. **66**(12), 2527–2536 (1994); Pure Appl. Chem. **48**, 127–132. Pergamon Press (1976)
21. D. Ammann, *Ion-Selective Micro-Electrodes* (Springer, Berlin, 1986), pp. 3–8
22. H. Freiser, Coated wire ion-selective electrodes, in *Ion-Selective Electrodes in Analytical Chemistry, Modern Analytical Chemistry* vol. 2, (Springer, New York, 1980), pp. 85–105
23. H. Meyer, H. Drewer, J. Krause, K. Cammann, R. Kakerow, Y. Manoli, W. Mokwa, M. Rospert, Chemical and biochemical sensor array for two-dimensional imaging of analyte distributions. Sens. Actuators B **229–234**, 18–19 (1994)

24. J.C. Owicki, L.J. Bousse, D.G. Hafeman, G.L. Kirk, J.D. Olson, H.G. Wada, J.W. Parce, The light-addressable potentiometric sensor: principle and biological applications. Annu. Rev. Biophys. Biomol. Struct. **23**, 87–114 (1994)
25. T. Hattori, Y. Masaki, K. Atsumi, R. Kato, K. Sawada, Real-time two-dimensional imaging of potassium ion distribution using an ion semiconductor sensor with charged coupled device technology. Anal. Sci. **26**, 1039–1045 (2010)
26. T. Hattori, Y. Masaki, D. Mori, R. Miyamoto, R. Kato, K. Sawada, CCD-type sodium ion image sensor: dynamic observation of ion-exchange reactions of a single Na-type cation-exchange resin bead. Electroanalysis **24**, 114–120 (2012)
27. E. Pungor, K. Toth, A. Hrabeczy-Pali, Selectivity coefficients of ion-selective electrodes. Pure Appl. Chem. **51**, 1913–1980 (1979)
28. K. Sawada, M. Ishida, Developments of 2 dimensional pH imaging system. Oyo Butsuri **77**, 1462–1466 (2008)
29. A. Kono, S. Takashi, T. Hattori, K. Okumura, M. Ishida, K. Sawada, Label free bio image sensor for real time monitoring of potassium ion released from hippocampal slices. Sens. Actuators B **201**, 439–443 (2014)
30. T. Hattori, Y. Tamamura, K. Tokunaga, T. Sakurai, R. Kato, K. Sawada, Two-dimensional microchemical observation of mast cell biogenic amine release as monitored by a 128 × 128 array-type charge-coupled device ion image sensor. Anal. Chem. **86**, 4196–4201 (2014)
31. T. Hattori, T. Sakurai, A. Kato, R. Kato, Y. Hirata, K. Sawada, Safty estimation of two calcium ion-sensitive plasticized poly(vinyl chloride) membrane for bioimaging apparatus. Bunseki Kagaku **63**, 119–125 (2014)
32. K. Sawada et al., EICE Trans. Fundam. Electron. Commun. Comput. Sci. **E97-A**(3), 726–733 (2014)
33. T. Hattori, K. Sakurai, M. Futagawa, K. Hizawa, F. Dasai, K. Okumura, K. Sawada, Electrochemistry **82**, 288–293 (2014)

Chapter 4
Development of High-Throughput Screening Device for Neurodegenerative Diseases

Tsuneo Urisu, Zhi-hong Wang, Hidetaka Uno, Yasutaka Nagaoka, Kei Kobayashi, Miho Goto-Saitoh, Yoshinori Suzuki and Yoko Urabe

Abstract Neurodegenerative diseases such as amyotrophic lateral sclerosis and Alzheimer's disease are intractable diseases, for which neither the cause nor treatment method are known in spite of more than 100 years of research. The reason for this is (1) it is not easy to sample neurons, the affected parts, during the lifetime of the patients and (2) there have never been suitable and precise high-throughput methods for analyzing the function of the neuron network. The first problem is now being solved by iPS technologies. We are now developing several technologies to solve the second problem. The problem of low seal resistance, the weak point of the incubation-type planar patch clamp (by which we can measure the ion-channel current from the neuron network at many measuring points), was overcome by using a salt-bridge Ag/AgCl electrode. The ion-channel current from the neuron network was measured for the first time by a planar patch clamp using this stable electrode. A new type of substrate for the planar patch clamp was developed, and a high density but spatially homogeneous neuron network was successfully formed. By combining these device technologies and the human iPS technology, we are now developing a disease model for neurodegenerative diseases.

Keywords Neurodegenerative disease · High-throughput screening · Neuron network · Planar patch clamp · Ion-channel · iPS

4.1 Introduction

Neurodegenerative diseases such as Alzheimer's disease (AD) and amyotrophic lateral sclerosis (ALS) are intractable diseases for which neither the cause nor reliable treatment methods have been established. The reason why these diseases

T. Urisu (✉) · Z. Wang · H. Uno · Y. Nagaoka · K. Kobayashi · M. Goto-Saitoh · Y. Suzuki · Y. Urabe
Institute of Innovation for Future Society, Nagoya University, Furo-Cho, Chikusaku, Nagoya 464-8603, Japan
e-mail: t.urisu@nanobio.nagoya-u.ac.jp

J. Sone and S. Tsuji (eds.), *Intelligent Nanosystems for Energy, Information and Biological Technologies*, DOI 10.1007/978-4-431-56429-4_4

are so intractable is (1) it is not easy to sample neurons, the affected parts, during the lifetime of the patients and (2) suitable methods for analyzing the function of the neuron network have never been developed. Animal models are generally used to solve the former problem. Unfortunately, however, the medicine developed using animal models is not so effective for human diseases especially neurodegenerative diseases. This is because animals do not suffer from the same neurodegenerative diseases as humans. Recently developed iPS technology is expected to solve this problem. To apply iPS technology to elucidate the cause and/or the novel drug developments of neurodegenerative diseases, the second problem must be solved. Since many and various kinds of ion-channels are the most important parts that realize signal transduction in the neuron network, the measurement of ion-channel current, which contains information about the release of the neurotransmitter molecules at synapses, is considered to be the most useful method for analyzing neuron network function. The pipette patch clamp is the most excellent standard method of ion-channel current measurements. It is, however, not suitable for multi-point measurement, which is necessary in high-throughput screening applications. Therefore, we must first develop a multi-point measurement method for ion-channel current in the neuron network. Furthermore, neurons easily gather and form aggregations through migrations. The formation method of a spatially homogeneous neuron network suitable for long-term incubation must also be developed. We have developed an incubation-type planar patch clamp [1] and recently succeeded in measuring the spontaneous ion-channel current for the first time by using the planar patch clamp in the neuron network of the cerebral cortex of an embryonic rat with gestational day 17 [2]. We have also succeeded in forming the neuron network with good spatial homogeneity. In this chapter, these results are introduced, and the future prospect of high-throughput screening applications using a human disease model chip is discussed.

4.2 Incubation-Type Planar Patch Clamp

It is expected that the weak point of the pipette patch clamp would be overcome by planarization of the device. For the planar ion-channel biosensor, glass [3], Si [4–6], quartz [7], and a silicon elastomer PDMS (polydimethylsiloxane) [8], etc. have been reported as substrate materials. For Si, it has been considered that the background noise current is large due to the free charge carrier density in the substrate. However, we have recently demonstrated that the noise current can be significantly reduced by using a silicon-on-insulator (SOI) substrate [9]. Since commercialized planar patch clamp devices, however, are not equipped with the incubation function, they cannot be used for a system that requires long incubation periods. New functional analysis and/or screening devices could be realized by adding an incubation function, such as an extra-cellular matrix (ECM) coating on the substrate surface to the conventional planar patch clamp method, and these would be especially useful in applications such as in vitro systems of neurons and neuron

networks using dissociated cultured neurons [10–13]. Moreover, the planar patch clamp method enables simultaneous measurement of multi-point ion-channel currents and advanced 2-D bio-imaging. We have developed an incubation-type planar patch clamp device and demonstrated its operation using TRPV1-expressing human embryonic kidney (HEK) 293 cells and capsaicin as a ligand molecule [1, 2, 14]. In this experiment, we have used SOI substrates as the sensor chip material. But the chip fabrication process using diamond drilling followed by focused ion beam for micropore formation was not necessarily suitable for expanding to the multi-point measurement, which was necessary for high-throughput screening applications. The recently developed light-gated ion-channel method is extremely suitable for the investigation of neural cell and/or neuron network functional analysis due to its excellent time and space resolutions [15, 16]. We also think that this noble technology is useful for the performance test of ion-channel biosensors.

In this work, we have newly developed a biosensor chip fabrication process suitable for multi-point measurements using plastic materials, such as polymethylmethacrylate (PMMA) and polycarbonate (PC) substrates, using several advanced photolithographic microfabrication techniques followed by electroforming, ultra-precision machining, hot embossing, and focussed ion beam process. Plastic materials have excellent characteristics as sensor chip material. Noise due to parasitic capacitance is sufficiently low due to their low dielectric constant. Several nano-microstructures can be easily formed by advanced microfabrication techniques. In this work, the ion-channel biosensor with incubation function was constructed using a PMMA or PC sensor chip, and excellent performance equivalent to the pipette patch clamp was confirmed by using a channelrhodopsin (ChR)-wide receiver (ChRWR), which was the light-gated ion-channel developed by Wang et al. [17].

4.2.1 Fabrication of Biosensor Chip

4.2.1.1 Hot Embossing and Metal Mould

The fabrication process using plastic materials and the structure of the sensor chip are shown in Fig. 4.1. The basic structure of the sensor chip was formed by double-sided hot embossing using a machine made by Engineering System Co., Ltd. The brass mould (mould 2 in Fig. 4.1) for forming the pipette solution wells (a in Fig. 4.1) was fabricated by ultra-precision machining equipment, Robonano (FANUC Ltd.). The scanning electron microscopy (SEM) image of the square pillar structure on the brass mould (mould 2) is shown in Fig. 4.1. The thickness of the thin film structure (b in Fig. 4.1) was controlled with good reproducibility by selecting the thickness of the original PMMA or PC substrate, usually 0.2 mm, and the height of the square pillar structure (193 $\pm$ 2 μm). Temperature control of the moulds was important to form a good quality thin film structure for the sensor chip at the pipette solution well. The temperature conditions were investigated using the

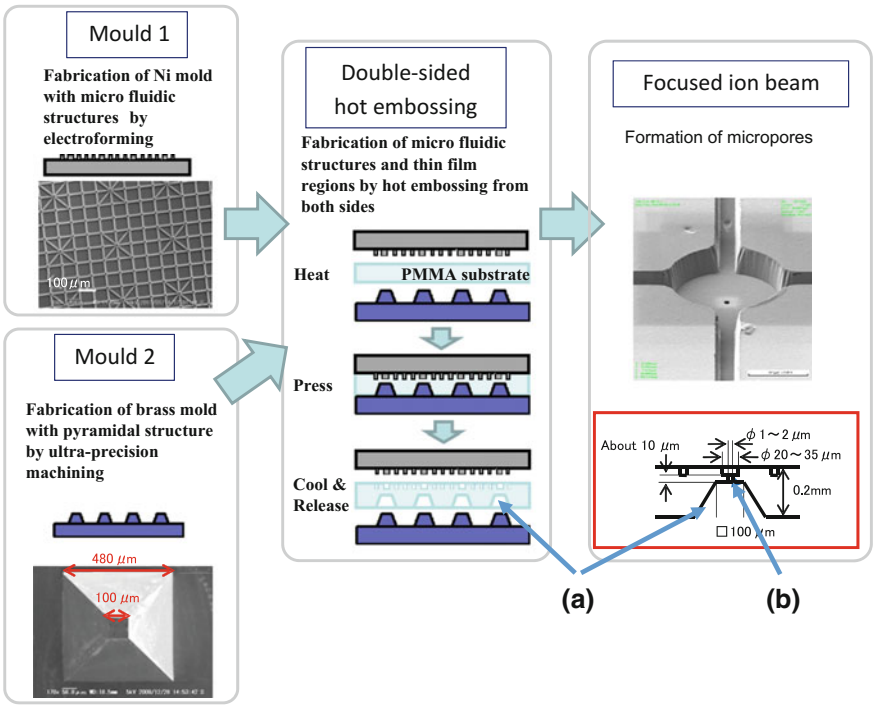

Fig. 4.1 Schematic drawing of fabrication protocol of planar patch clamp substrate by hot embossing. *a* Pipette solution well. *b* Thin film structure

mirror-polished Si wafer as the upper mould. The typical embossing conditions used in the case of PMMA were: upper and lower mould temperatures of 180 and 140 °C, respectively, loading pressure limit of 3500 N, lowering speed of the upper mould 10 μm/s, pressing time of 60 s, and cooling speed of 0.5 °C/s. Mould 1 in Fig. 4.1, which has a lattice pattern on the surface, was used in this work to form the substrate for the HEK293 cells. The lattice pattern forms the microfluidic structure on the substrate surface by embossing. The round areas formed at the crossing points of the lattice pattern of the upper mould were effective to fix the position of the cell. This Ni upper mould was fabricated by electroforming (IKEX Industry Co., Ltd.), for which the master mould was formed by photolithography using positive resist (AZ P4903, AZ Electronic Materials) on the one-side-mirror-polished Si(100) substrate. The electroforming was carried out after forming a thin Ni film on the surface of the resist pattern by sputtering. The Ni mould precisely replicates the resist pattern within the preciseness of the optical microscopy evaluations. It is noted that the side wall of the resist pattern was declined by about 20° from the vertical by baking at 120 °C for 90 min after the development. The upper side mould was aligned to the lower side mould so that the round area for the cell trapping on the upper side mould came into the square

pattern to form the pipette solution well [18]. The structure of the substrate for the neuron network formation is described in Sect. 4.4.

4.2.1.2 Formation of Micropore by Focussed Ion Beam (FIB)

The micropore with diameter of 1.5–2 μm was formed by focused ion beam (FIB) machine (Seiko Instruments Ltd.) at almost the centre of the round area on the pipette solution well. The ion-channel current was measured through this micropore. In the case of the plastic substrate, a Cu thin film was deposited on the surface of both sides of the substrate to reduce the charge-up effects during the FIB processing. This Cu thin film was removed using diluted HNO_3 solution after the micropore formation. The acceleration voltage and the current of the Ga ion beam were 30 keV and 50 pA.

4.2.2 Device Structure of Ion-Channel Biosensor

Figure 4.2a shows the schematic structure of the ion-channel biosensor used in this work. A photograph of the actual device is shown in Fig. 4.2b. The sensor chip was sandwiched between the upper (bath solution side) and the lower (pipette solution side) polydimethylsiloxane (PDMS) plates. Microfluidic circuits were formed inside the lower PDMS plate to supply and exhaust the pipette solutions. The bath solutions were supplied or exhausted through polytetrafluoroethylene (PTFE) tubes (not shown). The weak point of the incubation-type planar patch clamp is the low-seal resistance (Rj in Fig. 4.3a). In the pipette patch clamp, seal resistance larger than 1 GΩ is usually obtained; however, in the case of the incubation-type planar patch clamp, the seal resistance is easily decreased by more than two orders of magnitude due to the extra cellular matrix coated on the sensor chip surface, which makes the gap between the cell membrane and the sensor chip surface larger. Thus, as can easily be understood from Fig. 4.3a, fluctuation of the interface potential between the electrolyte solution and the Ag/AgCl electrode surface causes

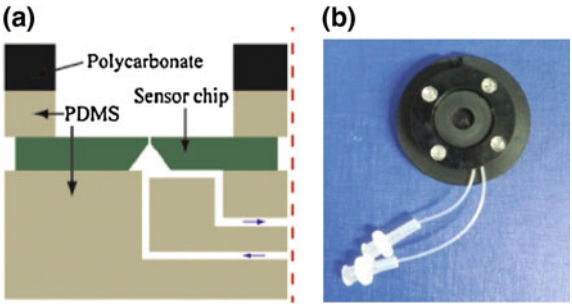

Fig. 4.2 **a** Schematic drawing of planar patch clamp ion-channel biosensor and **b** top view of the device

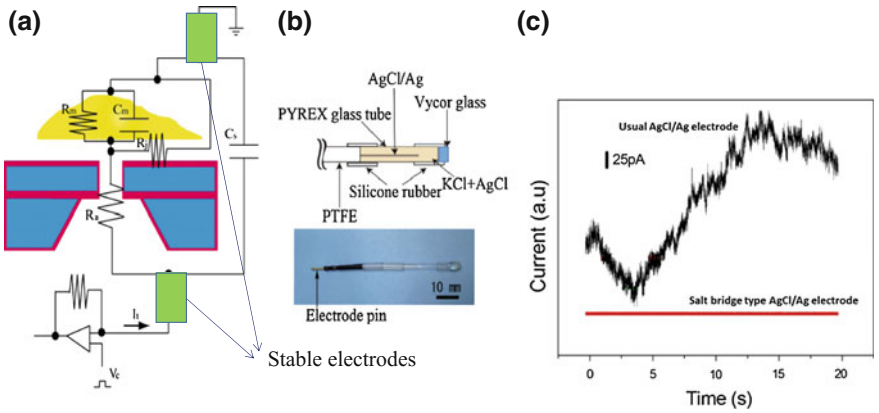

Fig. 4.3 **a** Equivalent electric circuit of incubation-type planar patch clamp, **b** structure of salt-bridge stable electrode, and **c** example of noise reduction data by using stable electrode

a large fluctuation in the base line. The stable electrodes of the salt-bridge structure (Fig. 4.3b) were used both for the bath solution side as a ground and the pipette solution side as the membrane voltage electrode [2]. The Ag/AgCl wire of the stable electrode, which was formed by painting the surface of the Ag wire (0.3 mm diameter) with AgCl ink (BAS Inc.), was inserted into a Pyrex glass tube filled with a saturated KCl and AgCl solution, and the tip was sealed with Vycor glass (Gikenkagaku Co. Ltd.). The Ag/AgCl wire was connected to a gold-plated electrode pin, as shown in Fig. 4.3b. The significant reduction in the noise by using the stable electrode is shown by the red line in Fig. 4.3c as an example.

4.2.3 Expression of ChRWR and TRPV1 on HEK293

Channelrhodopsin is also useful when investigating the performance of the ion-channel biosensor. ChRWR is the name given to the chimeric molecule ChR (ABCDEfg) in Ref. [17], and its plasmid construction is reported in detail in the same Ref. [17]. The HEK293 cells, which were a generous gift from Minoru Wakamori of Tohoku University, were cultured at 37 °C and with 5 % CO_2 in Dulbecco's modified eagle's medium (DMEM) (Sigma-Aldrich Co.) supplemented with 10 % fetal bovine serum (FBS, Biological Industries Ltd.) and transfected using Effectene transfection reagent (Qiagen, Tokyo, Japan) in accordance with the manufacturer's instructions. After cloning twice with the addition of G418 (Gibco) in a 10 cm dish, single colonies with bright Venus fluorescence [19, 20] were selected by using a cloning cylinder IWAKITE-32 (Asahi Glass Co., Ltd.) and cultured in a medium containing G418 until they were confluent in the dish. The TRPV1-expressing HEK293 was a gift from Professor Makoto Tominaga of the

Okazaki Institute for Integrative Bioscience. Details of the transfection procedure are reported in Ref. [21].

4.2.4 Culture of HEK293 Cells in Biosensor

The surfaces of both the sensor chips (Si and PMMA in this case) were coated with ECMs of poly-L-lysine (PLL, Sigma-Aldrich Co.), which showed better performance in the preliminary experiments on the culture in the biosensor than the fibronectin used in our previous experiments [1, 14]. The 50 µl solution (0.005 %) was dropped onto the substrate surface followed by incubation for 1–2 days at room temperature. At this stage, the surface density of the ECM was about 3–5 µg/cm^2. After removal of excess solution, the substrate was rinsed with sterilized water, dried under a gentle nitrogen stream, and kept sterile until use. Cells were cultured in dishes filled with the medium under the conventional incubating conditions, i.e., 37 °C and 5 % CO_2. The culture medium was supplemented with Dulbecco's modified eagle medium (DMEM) to which 10 % (v/v) fetal bovine serum (FBS), 1 % (v/v) Glutamax™ (Gibco), and 0.5 % (v/v) penicillin/streptomycin (Gibco) were added. After cells were detached from the culture dishes, the cell suspension was seeded at a density of 100–300 cells/mm^2 on the ECM-coated chip. The channel current was measured after 5 days of culturing, at which point about 70 % confluence was reached in the case of the no cell trapping pattern, as shown in Fig. 4.4a. In the case of the chip with cell trapping pattern, the

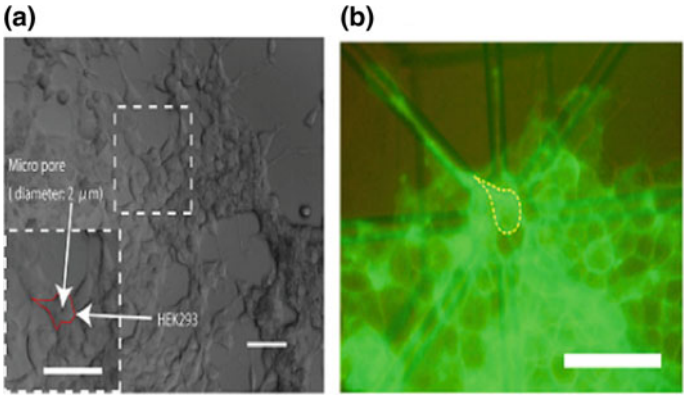

Fig. 4.4 Optical microscopy image of ChRWR expressing HEK293 cells incubated on substrate of incubation-type planar patch clamp biosensor. **a** Bright field image of cells after 5 days incubation on non-patterned substrate. The expanded figure with the cell on the micropore is inserted and **b** fluorescence microscopy image of cells after 3 days incubation on substrate with cell trapping pattern. The cell trapping pattern and the trapped cell is shown by *dotted lines*. The *scale bar* is 50 µm

channel current was measured after about 3 days of culturing when the monolayer colony around the micropore was formed (Fig. 4.4b).

4.2.5 Measurement of Ion-Channel Current

An ion-channel biosensor and preamplifier head stage were set inside the aluminium electromagnetic shield box. The culture medium was replaced with bath and pipette solutions for the upper and lower chambers, respectively. The bath solution in the upper chamber contained: 140 mM NaCl, 3 mM KCl, 10 mM 4-(2-hydroxyethyl)-1-piperazineethanesulfonic acid (HEPES), 2.5 mM $CaCl_2$, 1.25 mM $MgCl_2$, and 10 mM glucose at pH 7.4 (with HCl). The lower chamber solution (pipette solution) contained: 40 mM CsCl, 80 mM $CsCH_3SO_4$, 1 mM $MgCl_2$, 10 mM HEPES, 2.5 mM MgATP, and 0.2 mM Na_2EGTA (pH 7.4) All data were recorded using a patch-clamp amplifier (Axopatch 200B) at room temperature. Data were obtained using a 1 or 2 kHz low-pass filter and output gain of 1 mV/pA, and they were analyzed using pClamp 9.2 software. For whole-cell current recordings, sub-nanometre conductive pores through the cell membrane, which electrically connected the inside of the cell to the lower chamber, were formed by applying the nystatin (Sigma) solution to the lower chamber [22]. The nystatin stock solution was prepared by dissolving nystatin in 1 ml of methanol and successively adding 45 μl of HCl (1 M) and 45 μl of NaOH (1 M), which was then diluted with the lower chamber solution to final concentrations of 100–200 μg/ml before use. The formation of the whole-cell arrangement was confirmed by the observation of a capacitance increase of about 10 pF from 5 to 10 min after the addition of the nystatin solution to the lower chamber.

In the case of the laser-evoked channel current measurements, the laser beam from a semiconductor laser with a 473 nm peak wavelength and 3.2 mW maximum output power (Sumitomo Osaka Cement Co., Ltd) was guided by optical fibre and focused with a microlens with a 26.5 mm focal length under the fluorescence microscope's objective lens (Olympus). The beam diameter at the focal point was 30–100 μm.

4.2.6 Detection of Capsaicin by TRPV1-Expressing HEK293 Biosensor

The ion-channel biosensor could be used in diverse applications ranging from the detection of biological warfare agents to high-throughput screening devices for pharmaceutical development because of its extremely high selectivity and sensitivity. In this work, we constructed a single-channel biosensor shown in Fig. 4.1 using a Si or PMMA sensor chip. First, we constructed the ion-channel biosensor

using TRPV1-expressing HEK293 cells for the detection of capsaicin, which is the main pungent ingredient in hot chili peppers and elicits a sensation of burning pain by selectively activating sensory neurons. Capsaicin stimulation opens the TRPV1 ion-channel, and the non-selective cation flow through the channel is induced. If Ca^{2+} is contained in the extracellular solution, TRPV1 becomes insensitive to capsaicin with prolonged exposure. The mechanism underlying these phenomena is still not clearly understood [21]. The increase in intracellular Ca^{2+} mediates the desensitization, and various signalling pathways are implicated in the desensitization of TRPV1 [21, 23].

To investigate sensitivity for capsaicin, we measured the channel current for the bath solution of several different capsaicin concentrations with draining the bath solution by using a syringe pump (KD Scientific Inc.) at a pumping speed of 12 ml/h. The measurements were carried out at room temperature. The unique inward current followed by desensitization was observed when Ca^{2+} ions were present in the bath solution (Fig. 4.5a). The desensitization was not observed with the Ca^{2+}-free bath solution, as shown in Fig. 4.5a, which agrees well with the reported data measured using a pipette patch clamp [21]. The observed dependence

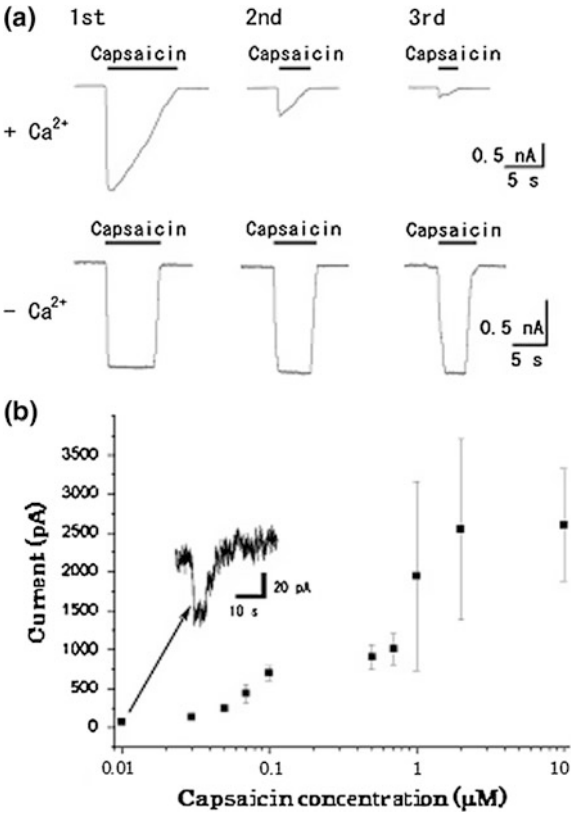

Fig. 4.5 Capsaicin stimulated ion-channel current of TRPV1 expressing HEK293 cells measured by incubation-type planar patch clamp biosensor after 5 days incubation. **a** Current recordings using bath solution containing Ca^{2+} ion (*upper trace*) and not containing Ca^{2+} ion (*lower trace*). **b** Dependence of current on capsaicin concentration. Sensitivity limit is about 10 nM, which is almost equivalent to pipette patch clamp biosensor

of the peak current on the capsaicin concentration is shown in Fig. 4.5b. The lower detection limit was about 0.01 μM. Highly sensitive detection of neurotransmitter molecules and biologically active molecules by the ion-channel biosensor using a pipette patch clamp have been reported [24–26]. In those studies, the noise level including the baseline fluctuations was 5–20 pA (p-p). The noise level of 10–20 pA (p-p) in the present case (Fig. 4.5b) shows that an ion-channel biosensor with almost equivalent performance to the pipette patch clamp can be constructed by using an incubation-type planar patch clamp equipped with a salt-bridge stable electrode, so long as it is the whole-cell mode. In this experiment, use of a stable electrode is essential. The success probability of the device fabrication (number of devices that operated/total number of devices fabricated) was increased from 1 to 2 % (simple Ag/AgCl electrode) to about 60 % (stable electrode).

4.2.7 *Laser-Evoked Channel Current Using ChRWR-Expressing HEK293 Cells and Comparison Between Si and PMMA Sensor Chips*

The performance of the ion-channel biosensor using a PMMA sensor chip was evaluated by measuring the laser-evoked channel current using ChRWR-expressing HEK293 cells. 20 μl of cell suspension (1×10^4 cells/ml) was injected around the cell trapping area and incubated for 3 days. After confirmation of the formation of a single monolayer colony covering the micropore region (Fig. 4.4b), nystatin solution (100–200 μg/ml) was mixed into the pipette solution, and the formation of the whole-cell mode was easily confirmed by the capacitance increase of about 10 pF caused by the nystatin perforation. After 3 days of incubation, the seal resistance was 7.4 MΩ, and it increased to 9.4 MΩ when negative pressure ($\sim$10 kPa) was applied to the pipette solution side. We also carried out control experiments. No channel currents were observed for cells without ChRWR expression. The dependence of the channel current profiles on the membrane potentials when ChRWR-expressing HEK293 cells were irradiated by a laser (λ = 473 nm, output power = 1.5 mW) driven by rectangular pulses is shown in Fig. 4.6. Similar channel current profiles were observed with the Si sensor chip. In this case, the cell trapping pattern was formed on the Si chip surface by photolithography using SU8 negative resist [27]. Channel current profiles in the case of the PMMA sensor chip agree well with the reported profile (ABCDEfg in Fig. 6A of Ref. [17]) measured using the pipette patch clamp, for the important points: almost no desensitization in the current profile, relatively sharp *on* profile ($\sim$10 ms), and slower *off* profile ($\sim$20 ms).

Much work has been done on the molecular mechanisms relating to the *on* and *off* profile of the channel current induced by the photo-excitation of channelrhodopsin [17, 28–30]. There are, however, still many unclear points. Widely accepted arguments about the mechanisms of photoexcitation and the following

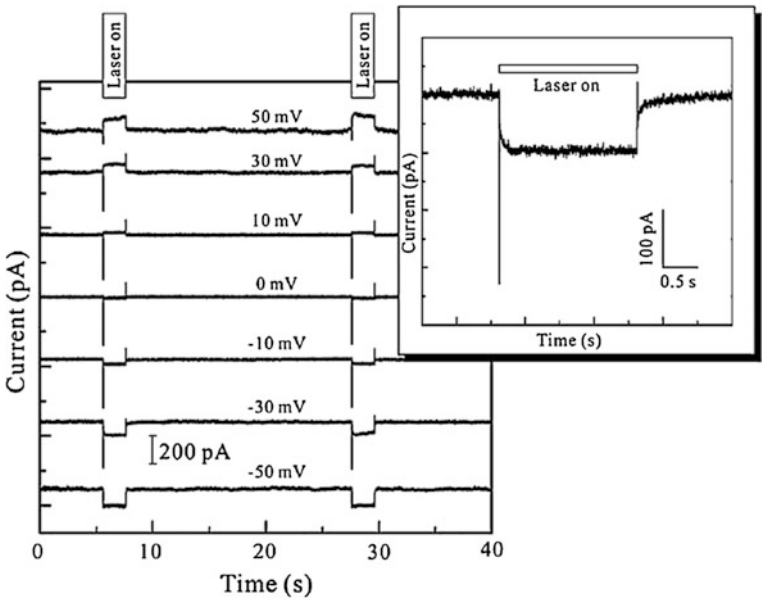

Fig. 4.6 Observed dependence of laser-gated channel current recordings on membrane potential for ChRWR expressing HEK293 cells after 3 days incubation. SOI substrate was used. *Inset* is expanded current profile measured at membrane potential of −30 mV

relaxations are: channelrhodopsin contains a retinal that covalently binds to the apoprotein and the photoisomerization of all-*trans*-retinal to 13-*cis* configuration is coupled to conformational changes in the protein and causes the permeation of ions [17]. Many (∼8) intermediate states including dark states with a lifetime longer than several seconds are observed, and several photocycle models are proposed [17, 28, 31]. The "*on*" transition time to the initial opening state is about 2 ms, and the decay of the photocurrent upon light off strongly depends on the intracellular pH [28]. In the case of the wild-type channelrhodopsin 2 (ChR2), it is excited to the first channel open state by the blue (∼480 nm) light irradiation by the transition time of about 2 ms, and after that it quickly desensitizes to the second channel open state, and then it decays to the dark state by the switching off of the irradiation light with a transition time of about 15 ms [29]. The photocurrent of ChR1 is hardly desensitized during bright light illumination, although that of ChR2 is rapidly desensitized [17, 28]. The *N* terminal segments of ChR2 were replaced with the homologous counterparts of ChR1 and generated several chimeras with different current profiles [17]. In ChRWR, a small desensitization and an almost flat and quite large current profile were realized [17].

In the case of the Si sensor chip, however, the *on* profile was slightly slow (Fig. 4 in Ref. [27]); this may be due to the large capacitance (∼100 pF) of the Si sensor chip compared with the PMMA chip (3–5 pF). Therefore, these data indicate that a current profile with high reliability equivalent to the pipette patch clamp

method can be obtained by using the PMMA sensor chips together with salt-bridge stable electrodes. Without a cell trapping pattern, a long incubation time (>5 days) was necessary to wait for the sensor cell to make stable coverage of the micropore (Fig. 4.4a), and the multiple layers of the sensor cell that were often formed owing to this long incubation time made current measurement impossible. When the cell trapping pattern was present, a single monolayer colony stably covering the micropore was formed in a short incubation time (Fig. 4.4b). Therefore, the cell trapping pattern not only shortened the necessary incubation time (to $\sim$3 days) but also improved the success probability by 10–20 %.

4.3 Ion-Channel Current Recording in Neural Network

4.3.1 Formation of Rat Cerebral Cortex Neuron Network on PC Sensor Chip

Rat embryos of embryonic day 17 were obtained by caesarian section from pregnant mothers, which were anaesthetized with isoflurane (Abbott) and killed by scission of carotid arteries. The use of these animals in the experimental protocols described was approved by the Nagoya University Animal Care Committee. Brains of 8–10 embryos were quickly brought out with surgical scissors, and the cerebral cortex tissue was dissected into small pieces, which were transferred into a 15-ml plastic centrifuge tube with 5 ml Hank's balanced salt solution (HBSS, Gibco) containing 0.25 % trypsin and kept at 37 °C for 20 min in a water bath. HBSS was removed, and neural cells were disassembled by pipetting in 5 ml DMEM with 10 % fetal bovine serum (FBS). The tube was centrifuged at 140*g* for 5 min, and the cell pellet was suspended in 1 ml Neurobasal medium containing B27 (Gibco), 2 mM Glutamax (Gibco), and 5 % FBS. The cells were plated at a density of 1–5 $\times$ 10^4 cells/cm^2 onto an 11 mm square PLL-coated PC sensor chip in 35-mm plastic culture dishes. The cultures were maintained at 37 °C in a humidified atmosphere containing 5 % CO_2 for 10–14 days. After the formation of the neuron network on the PC sensor chip surface, it was set up in the biosensor for the channel current measurements.

4.3.2 Recordings of Spontaneous Ion-Channel Currents in Neural Networks

One of the most important applications of the incubation-type planar patch clamp is the multi-point ion-channel current recordings in neural networks. In this case, the stable electrode is essential since it is more difficult to realize the high-seal resistance due to a very long incubation time. First, we tried to form a neuron network

using a PMMA sensor chip with cell trapping pattern as shown in Fig. 4.1. It was, however, difficult to form a long-term stable neuron network. It was found that the viability of the neuron cells in the cell trapping area was much lower than those outside that area (Fig. 4.7). Stable incubation inside the cell trapping area was observed in PC12 and HEK293 cells. On the other hand, in the case of the primary culture neurons that form a network by making a huge number of synapses, almost all neurons died in our case if they could not form synapses with surrounding neurons within about 1 week. We consider that the cell trapping pattern shown in Fig. 4.1, inside which neurons cannot extend neurites freely, is not suitable for maintaining the neuron network for a long-term culture. Therefore, in this experiment, we seeded rat hippocampal neurons on the PC sensor chip with a flat surface with a density of 1–5 × 10^4 cells/cm^2 and incubated them in the 35-mm dish for 10–14 days. In all sensor chips, inhomogeneous gathering of neurons due to migration was observed, as shown in Fig. 4.8a, and in 1–2 chips out of 10, it was observed that a neural cell existed on the micropore on the chip. The seal resistance was surprisingly small; it was ∼2.7 MΩ before the suction and ∼3.4 MΩ after the suction (n = 5). The sensor chip with a cell on the micropore was set up on the sensor chip position in the ion-channel biosensor shown in Fig. 4.2, and the upper and lower spaces were filled with bath and pipette solutions, respectively. The network formed was already very complex. A large number of multi-synaptic contacts and autaptic contacts [32] were formed. Therefore, we have considered that the measurements of spontaneous channel currents are more important than those of evoked currents induced by artificial stimulation, which makes the network structure much more complex due to synaptic plasticity [33]. Before the nystatin perforation, no channel currents were observed under the voltage clamp, but immediately after the injection of nystatin into the pipette solution, a channel current that depended on the membrane voltage was observed with good

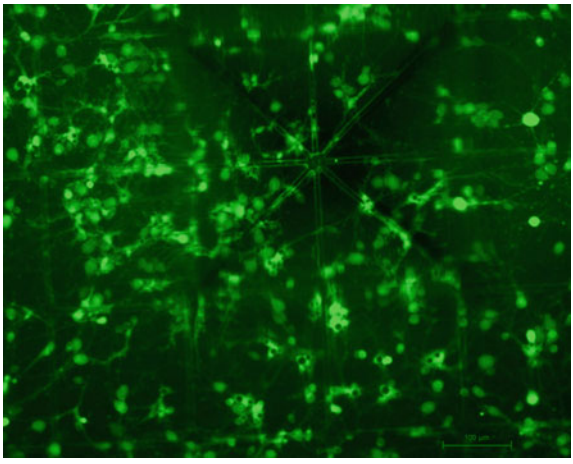

Fig. 4.7 Fluorescence microscopy image of rat cerebral cortex neuron network formed on PMMA substrate after about 2 weeks incubation. Groove pattern is formed and round cell trapping area is formed at crossing point of grooves. The viability of the cell was low inside of the groove or the cell trapping area

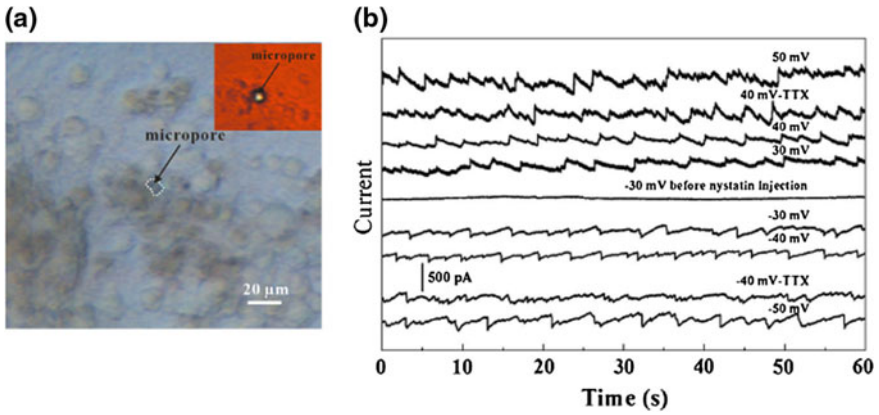

Fig. 4.8 Spontaneous channel current measurements in in vitro neuron network of rat hippocampus. **a** Neuron network of 10 day culture formed on Si-SOI sensor chip with flat surface. **b** Spontaneous channel current observed for various membrane potential value. Effects of TTX addition were investigated for membrane potential at −40 mV and +40 mV. *Smooth line* around centre is recording at membrane potential at −30 mV before nystatin injection to pipette solution. All other recordings were measured after nystatin injection

reproducibility as shown in Fig. 4.8b. It is clear that these signals are due to spontaneous activity of the neural network. By adding tetrodotoxin (TTX), which is a typical antagonist of the Na^+ channel [10, 33]; some unique changes of the channel current profile were observed. At −40 mV, pulse-like current disappeared by adding TTX, but at +40 mV pulse-like current was still observed. Therefore, it is concluded that the observed channel currents are a mixture of many post-synaptic currents evoked by the spontaneous firing of presynaptic neurons and post-synaptic currents induced by the spontaneous neurotransmitter emission, which are called miniature excitatory post-synaptic currents (mEPSC) and miniature inhibitory post-synaptic currents (mIPSC) [33]. It is entirely due to the stable electrodes that the spontaneous channel currents were successfully observed. Since inhomogeneous gathering of neurons due to migration makes meaningful multi-point measurements impossible, we are now developing a new type of cell trapping pattern and cell seeding technique that hinders cell migration and enables the formation of more homogeneous neural networks.

4.4 Future Prospects and Disease Model Chip

For neurodegenerative diseases, such as ALS and AD, many mutated genes that cause the onset of the disease have already been discovered. Therefore, considering that neurodegenerative diseases such as ALS and AD are unique to humans, the in vitro neural network containing mutated genes is considered to be the most useful

disease model, which can be used for developing new drugs that are effective in treating the diseases. We can make the disease model by making the neuron network from human iPS cells and transfecting the mutated genes. In this case, however, this disease model has a limitation; it cannot be used to investigate the cause of diseases, that is, to investigate how the mutations are introduced.

As already mentioned, neurons easily aggregate due to the nature of migrations, especially in the case of high density cultures, which are close to the real brain neuron network, and spontaneous firing is observed with a frequency of about 2–3/s in frequent cases [34]. Therefore, it is necessary to develop a technology to form an in vitro neuron network without inhomogeneous aggregations. Furthermore, the soma of the neuron must be set on the micropore of the substrate, in the case of the planar patch clamp. As the first step to the realization of a disease model, we have developed the substrate for an incubation-type planar patch clamp suitable for long term incubation of a neuron network (Fig. 4.9). The cell trapping area is surrounded by several pillars that are 30 μm in diameter and about 8 μm in height, by which cell migration is limited, but axon and dendrites can extend through the gap between the pillars. Micropores with a diameter of about 2 μm for the ion-channel current measurements are formed inside the several cell trapping area. The network of the rat cerebral cortex neuron formed by seeding the cells selectively inside the cell trapping area is shown in Fig. 4.9b. In the near future, we are going to form complex neuron networks on this substrate consisting of several kinds of brain cells such as motor neurons, cerebral cortex neurons, and glia cells formed from human iPS cells by differentiation.

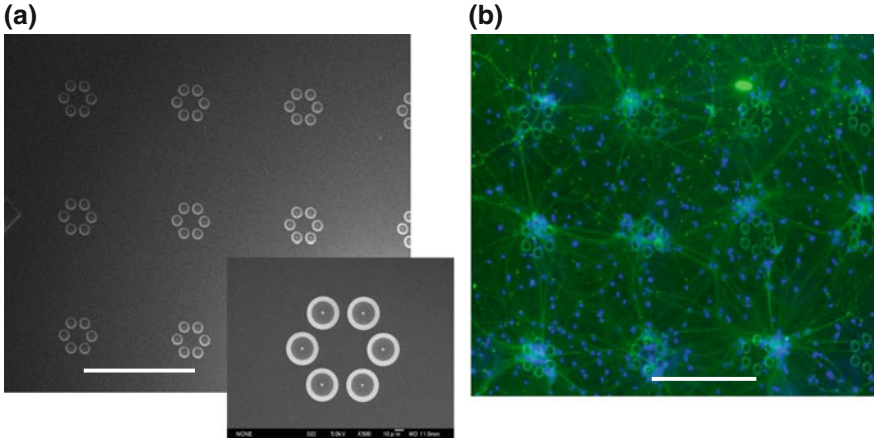

Fig. 4.9 **a** Scanning microscopy image of PC substrate developed for homogeneous neuron network formation. Many cell trapping areas surrounded by six pillars are observed. Diameter and height are ∼30 and ∼8 μm, respectively. Gap between neighbouring pillars is ∼9 μm. **b** Fluorescence microscopy image of rat cerebral cortex neuron network after 13 day incubation. Cells were seeded on cell trapping pattern area selectively. *Green* and *blue* are tubulin and DAPI staining, respectively. *Scale bar* is 300 μm

4.5 Summary

Optogenetic tools, such as channelrhodopsin and halorhodopsin, are useful to investigate the function of neuron networks due to their high spatial and temporal resolutions. In this chapter, however, another application of channelrhodopsin is introduced. We are developing a high-throughput screening device, which is necessary for investigation of the cause and new drag development of neurodegenerative diseases. Since ion-channel current measurement is considered to give the most important information to analyze the neuron network functions, we have developed a planar patch clamp device with incubation function using ChRWR for the performance test of the device. In the development, the large noise due to the low-seal resistance of the incubation-type planar patch clamp was significantly reduced, and we succeeded in taking ion-channel current measurements in the in vitro neuron network of rat cerebral cortex for the first time. We are now developing a disease model of a neurodegenerative disease, such as ALS and/or AD based on the in vitro neuron network formed from human iPS cells. We believe that a new important way to elucidate the cause and development of the treatment method of these intractable diseases can be found by combining these disease models of neuron networks and the high-throughput screening device.

Acknowledgments The authors thank the staff of the Equipment Development Centre of the Institute for Molecular Science, especially Ms. Noriko Takada, Mr. Masaki Aoyama, and Mitsukazu Suzui, for their support with device fabrication. The authors also thank the group leaders of the CREST team, Profs. Yugo Fukazawa, Toru Ishizuka, Yuji Furutani, Tetsunari Kimura, and Yuki Sudo, for their support with channelrhodopsin and meaningful discussions.

References

1. T. Urisu, T. Asano, Z. Zhang, H. Uno, R. Tero, H. Junkyu, I. Hiroko, Y. Arima, H. Iwata, K. Shibasaki, M. Tominaga, Incubation type Si-based planar ion channel biosensor. Anal. Bioanal. Chem. **391**, 2703–2709 (2008)
2. H. Uno, Z.-H. Wang, Y. Nagaoka, N. Takada, S. Obuliraj, K. Kobayashi, T. Ishizuka, H. Yawo, Y. Komatsu, T. Urisu, Improvement of performances in incubation-type planar patch clamp biosensor by using salt bridge electrode and plastic (PMMA) substrates. Sens. Actuators, B Chem. **193**, 660–668 (2014)
3. N. Fertig, R.H. Blick, J.C. Behrends, Whole cell patch clamp recording performed on a planar glass chip. Biophys. J. **82**, 3056–3062 (2002)
4. T. Sordel, F. Kermarrec, Y. Sinquin, I. Fonteille, M. Labeau, F. Sauter-Starace, C. Pudda, F. de Crécy, F. Chatelain, M. De Waard, C. Arnoult, N. Picollet-D'hahan, The development of high quality seals for silicon patch-clamp chips. Biomaterials **31**, 7398–7410 (2010)
5. B. Matthews, J.W. Judy, Design and fabrication of a micromachined planar patch-clamp substrate with integrated microfluidics for single-cell measurements. J. Microelectromech. Syst. **15**, 214–222 (2006)
6. R. Pantoja, J.M. Nagarah, D.M. Starace, N.A. Melosh, R. Blunck, F. Bezanilla, J.R. Heath, Silicon chip-based patch-clamp electrodes integrated with PDMS microfluidics. Biosens. Bioelectron. **20**, 509–517 (2004)

7. A. Stett, C. Burkhardt, U. Weber, P.V. Stiphout, T. Knott, CYTOCENTERING: a novel technique enabling automated cell-by-cell patch clamping with the CYTOPATCH chip. Recept. Channels **9**, 59–66 (2003)
8. X. Li, K.G. Klemic, M.A. Reed, F.J. Sigworth, Microfluidic system for planar patchclamp electrode arrays. Nano Lett. **6**, 815–819 (2006)
9. H. Uno, Z.-L. Zhang, K. Suzui, R. Tero, Y. Nonogaki, S. Nakao, S. Seki, S. Tagawa, S. Oiki, T. Urisu, Noise analysis of Si-based planar-type ion-channel biosensors. Jpn. J. Appl. Phys. **45**, L1334–L1336 (2006)
10. H.-Z.W. Tao, L.I. Zhang, G.-Q. Bi, M.-M. Poo, Selective presynaptic propagation of long-term potentiation in defined neural networks. J. Neurosci. **20**, 3233–3243 (2000)
11. A.M. Taylor, D.C. Dieterich, H.T. Ito, S.A. Kim, E.M. Schuman, Microfluidic local perfusion chambers for the visualization and manipulation of synapses. Neuron **66**, 57–68 (2010)
12. A. Reska, P. Gasteier, P. Schulte, M. Moeller, A. Offenhäusser, J. Groll, Ultrathin coatings with change in reactivity over time enable functional in vitro networks of insect neurons. Adv. Mater. **20**, 2751–2755 (2008)
13. J. Erickson, A. Tooker, Y.C. Tai, J. Pine, Caged neuron MEA: a system for long-term investigation of cultured neuronal network connectivity. J. Neurosci. Methods **175**, 1–16 (2008)
14. T. Asano, H. Uno, K. Shibasaki, M. Tominaga, T. Urisu, A cell culture type planar ion-channel biosensor. Trans. Mater. Res. Soc. **33**, 767–770 (2008)
15. F. Zhang, L.-P. Wang, E.S. Boyden, K. Deisseroth, Channelrhodopsin-2 and optical control of excitable cells. Nat. Methods **3**, 785–792 (2006)
16. L. Petreanu, D. Huber, A. Sobczyk, K. Svoboda, Channelrhodopsin-2-assisted circuit mapping of long-range callosal projections. Nat. Neurosci. **10**, 663–668 (2007)
17. H.Y. Wang, Y. Sugiyama, H. Hikima, E. Sugano, H. Tomita, T. Takahashi, T. Ishizuka, H. Yawo, Molecular determinants differentiating photocurrent properties of two channelrhodopsins from chlamydomonas. J. Biol. Chem. **284**, 5685–5696 (2009)
18. N. Takada, M. Aoyama, M. Suzui, Y. Hachisu, H. Ohmori, Z.-H. Wang, S. Obuliraju, Y. Nagaoka, M. Goto-Saitoh, T. Urisu, Microfabrication of PMMA sensor chips for an incubation type planar patch clamp. Int. J. Nanomanuf. **10**, 281–294 (2014)
19. A. Rekas, J.R. Alattia, T. Nagai, A. Miyawaki, M. Ikura, Crystal structure of Venus, a yellow fluorescent protein with improved maturation and reduced environmental sensitivity. J. Biol. Chem. **277**, 50573–50578 (2002)
20. T. Nagai, K. Ibata, E.S. Park, M. Kubota, K. Mikoshiba, A. Miyawaki, A variant of yellow fluorescent protein with fast and efficient maturation for cell-biological applications. Nat. Biotechnol. **20**, 87–90 (2002)
21. M.J. Caterina, M.A. Schumacher, M. Tominaga, T.A. Rosen, J.D. Levine, D. Julius, The capsaicin receptor: a heat-activated ion channel in the pain pathway. Nature **389**, 816–824 (1997)
22. N. Akaike, N. Harata, Nystatin perforated-patch recording and its applications to analyses of intracellular mechanisms. Jpn. J. Physiol. **44**, 433–473 (1994)
23. L. Vyklický, K. Nováková-Toŭsová, J. Benedikt, A. Samad, F. Toŭska, V. Vlachová, Calcium-dependent desensitization of vanilloid receptor TRPV1: a mechanismpossibly involved in analgesia induced by topical application of capsaicin. Physiol. Res. **57**, S59–S68 (2008)
24. E.A. Schwartz, Depolarization without calcium can release gamma-aminobutyric acid from a retinal neuron. Science **238**, 350–355 (1987)
25. Y. Kataoka, H. Ohmori, Activation of glutamate receptors in response to mem-brane depolarization of hair cells isolated from chick cochlea. J. Physiol. **477**, 403–414 (1994)
26. A. Hazama, S. Hayashi, Y. Okada, Cell surface measurements of ATP release fromsingle pancreatic beta cells using a novel biosensor technique. Pflug. Arch. **437**, 31–35 (1998)
27. Z.-H. Wang, N. Takada, H. Uno, T. Ishizuka, H. Yawo, T. Urisu, Positioning of the sensor cell on the sensing area using cell trapping pattern in incubation type planar patch clamp biosensor. Colloids Surf., B **96**, 44–49 (2012)

28. G. Nagel, T. Szellas, W. Huhn, S. Kateriya, N. Adeishvili, P. Berthold, D. Ollig, P. Hegeman, E. Bamberg, Channelrhodopsin-2 a directly light-gated cation-selective membrane channel. Proc. Natl. Acad. Sci. USA **100**, 13940–13945 (2003)
29. T. Ishizuka, M. Kakuda, R. Araki, H. Yawo, Kinetic evaluation of photosensitivity in genetically engineered neurons expressing green algae light-gated channels. Neurosci. Res. **54**, 85–94 (2006)
30. C. Bamann, T. Kirsch, G. Nagel, E. Bamberg, Spectral characteristics of the pho-tocycle of channelrhodopsin-2 and its implication for channel function. J. Mol. Biol. **375**, 686–694 (2008)
31. K. Stehfest, P. Hegemann, Evolution of the channelrhodopsin photocycle model. ChemPhysChem **11**, 1120–1126 (2010)
32. B.R. Rost, J. Breustedt, A. Schoenherr, G. Grosse, G. Ahnert-Hilger, D. Schmitz, Autaptic cultures of single hippocampal granule cells of mice and rats. Eur. J. Neurosci. **32**, 939–947 (2010)
33. K.S. Wilcox, J. Buchhalter, M.A. Dichter, Properties of inhibitory and excitatory synapses between hippocampal neurons in very low density cultures. Synapses **18**, 128–151 (1994)
34. B.-Q. Mao, F. Hamzei-Sichani, D. Aronov, R. C. Froemke, R. Yuste, Dynamics of Spontaneous Activity in Neocortical Slices. Neuron **32**, 883–898 (2001)

Part III
Micro Fluidics/MEMS and Their Application

Chapter 5
Extended-Nano Scale Fluidics and Applications to Bioanalysis

Hisashi Shimizu, Kazuma Mawatari, Yutaka Kazoe, Yuriy Pihosh and Takehiko Kitamori

Abstract Extended-nano space, which is in 10–1000 nm scale, is a transitional region from single molecules to continuous fluid. Even though many specific effects are expected, device engineering of extended-nano space has not been developed so far due to the lack of basic technologies for fluidic engineering. Previously, our group established a strategy of device integration for microchemical systems called continuous flow chemical processing and applied the strategy to various analytical systems. In addition, we have succeeded in developments of basic technologies including fabrication, fluidic control and detection for extended-nano space to find very unique effects such as higher viscosity, lower dielectric constant and higher proton mobility. In this chapter, the uniqueness, device engineering of extended-nano space and its application to bioanalytical devices are introduced. Especially, we focus on an ultimate chromatography using extended-nano space and its innovative performances to break the limits of conventional technologies.

Keywords Microfluidics · Nanofluidics · Immunoassay · Chromatography · Fuel cell · Photothermal spectroscopy

5.1 Introduction

Over a couple of decades, nanotechnology has made a huge impact on the research of materials, electronics, and biotechnology. Microfluidics which integrate experimental operations of chemistry and biochemistry on a plane substrate, has also made great progress to realize a small, fast, and efficient analysis. The concept of microfluidics which is also called miniaturized total analytical system (μTAS) was firstly introduced by Manz et al. in 1990 [1]. The group developed an integrated liquid chromatography device using microfabrication technology of silicon [2], which was followed by many researchers to develop miniaturized analytical devices

H. Shimizu · K. Mawatari · Y. Kazoe · Y. Pihosh · T. Kitamori (✉)
School of Engineering, The University of Tokyo, 7-3-1, Hongo, Bunkyo, Tokyo, Japan
e-mail: kitamori@icl.t.u-tokyo.ac.jp

J. Sone and S. Tsuji (eds.), *Intelligent Nanosystems for Energy, Information and Biological Technologies*, DOI 10.1007/978-4-431-56429-4_5

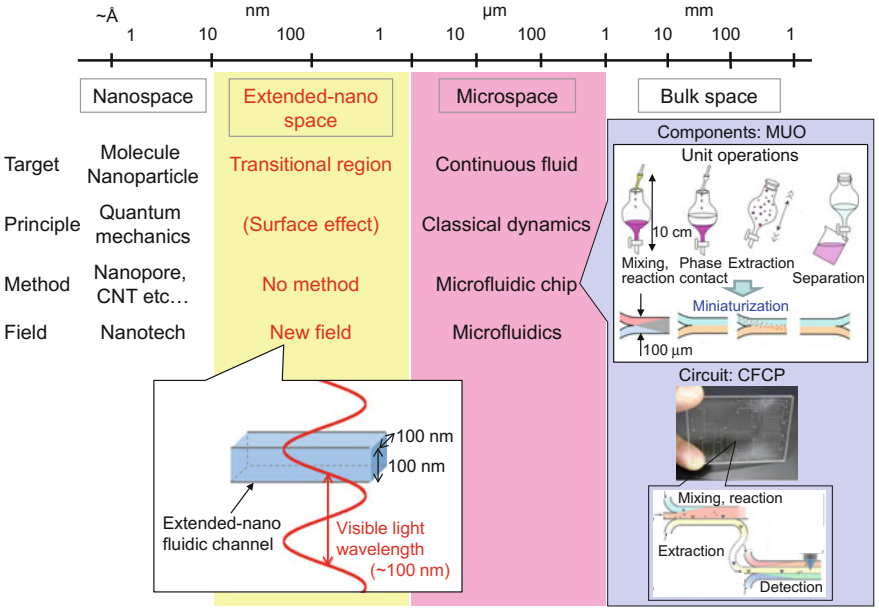

Fig. 5.1 Overview (target substance, dominant principle, methodology, and technology region) of nano, micro and extended-nano space. Strategy of micro/nano integration (MUO and CFCP) is shown in *right hand side*

such as electrophoresis [3], polymerase chain reaction (PCR) [4] and immunoassay [5]. Owing to the use of microspace which is 10–100 μm scale, microfluidics can dramatically decrease the volume of sample and reagents, which decreases environmental load and cost for analyses. Furthermore, microfluidics realizes faster analyses due to the efficient mixing and reaction in the microspace. At present, various microfluidic analytical devices including enzyme-linked immunosorbent assay (ELISA) [6] and cell analysis system [7] have been commercialized for biological research. Application to clinical diagnosis is also ongoing targeting for point-of-care testing (e.g. instant blood test on bedside from one drop of blood) [8].

On the contrary, the *extended-nano* space, which is in 10–1000 nm scale, is a transitional region between nanospace and microspace. The size scale of nanospace, microspace, and extended-nano space is shown in Fig. 5.1. The size of nanospace is basically a single nm that is dominated by quantum mechanics. Therefore, novel nanomaterials utilizing DNA molecules, nanoparticles, and carbon nanotubes (CNTs) are intensively studied to realize expression of novel functions [9] and they are called nanotechnology. In case of conventional microfluidic devices, the scale is from several to hundreds microns that are completely dominated by classical and thermal dynamics so that the target medium is continuous fluid [10, 11]. Here, only the increase of surface-to-volume ratio contributes to dramatic improvements of their performances. Then, extended-nano space is a transitional region from single

molecule to continuous fluid and various specific properties due to its surface are expected. A typical example of the specificities is electric double layer (EDL) [12] that is generated by the surface charge. Utilizing the EDL effect, some primitive functional devices have been proposed such as DNA separation [13, 14], preconcentration [15] and rectification device [16]. However, the extended-nano space has still been a frontier for fluidic engineering due to the size that is smaller than the wavelength of visible light. It is necessary to combine top–down and bottom–up approaches for fabrication and detect molecules at single molecule level. Fluidic control techniques are also limited to electrokinetic and electrophoretic method because high pressure ($\sim$MPa) is necessary for pressure-driven fluidic control that is very easy and useful in microfluidics. Therefore, our group has established basic technologies such as fabrication, detection and pressure-driven fluidic control method for the extended-nano space [17]. As a result, we have discovered unique properties of water confined in the extended-nano space including higher viscosity, lower dielectric constant [18], and higher proton mobility [19, 20] which are clearly different from the EDL effect as explained above. Then, we conceived that novel device engineering using the unique properties of extended-nano space could be created for analysis and energy applications which contribute to biotechnology and energy innovations. In this chapter, we introduce a strategy, basic fabrication technologies and an application of the extended-nano space for chemical analysis, giving special attention to the description of separation analysis (chromatography) using an extended-nano fluidic channel. The innovative performance of the extended-nano chromatography was also discussed. Finally, a perspective of the extended-nano analytical devices is introduced.

5.2 Strategy for Device Integration

Previously, our group has proposed a concept of a continuous flow chemical processing (CFCP) [21] for microfluidic analytical devices as shown in the right hand side of Fig. 5.1. In the concept of CFCP, an analysis is divided into the series of procedures such as mixing, reaction, phase contact, and separation which are called unit operations. Then, each unit operation is miniaturized using microfluidic channels on a glass substrate as micro unit operations (MUOs) and the MUOs are connected to make a fluidic circuit. This is an analogy of electronic integrated circuit that many transistors and other components are integrated on a semiconductor substrate. The feature of the CFCP is the use of pressure-driven fluidic control, although most of microfluidic research uses electrophoresis for fluid control. In addition, we have developed thermal lens microscope (TLM) that is a sensitive detection method of nonfluorescent molecules, although fluorescent spectroscopy is generally used for detection in microspace. The pressure-driven fluidic control and TLM make possible to use various solvents and molecules for research of chemistry and our group has developed many analytical and chemical synthesis devices including immunoassay [6], metal ion [22] and gas monitoring

system [23] based on the CFCP strategy. Therefore, the general strategy is supposed to be also applicable to extended-nano space, although the unique properties should be considered in each unit operation. For example, in case of mixing that is the easiest unit operation, the increase of viscosity has influences on the decrease of flow rate and difference of mixing ratio. Therefore, the first step to create an extended-nano analytical device is to establish extended-nano unit operations (ENUOs). Second, the ENUOs are integrated on a glass substrate combining top–down and bottom–up fabrications. Finally, the function of the integrated device is confirmed and its performance is optimized.

5.3 Basic Technologies

5.3.1 Micro/Nanofabrication

Extended-nano channels were fabricated by electron beam (EB) lithography and reactive ion etching (plasma etching) on a silica glass substrate. Figure 5.2 shows the schematic of the nanofabrication. Firstly, EB resist, and electroconductive

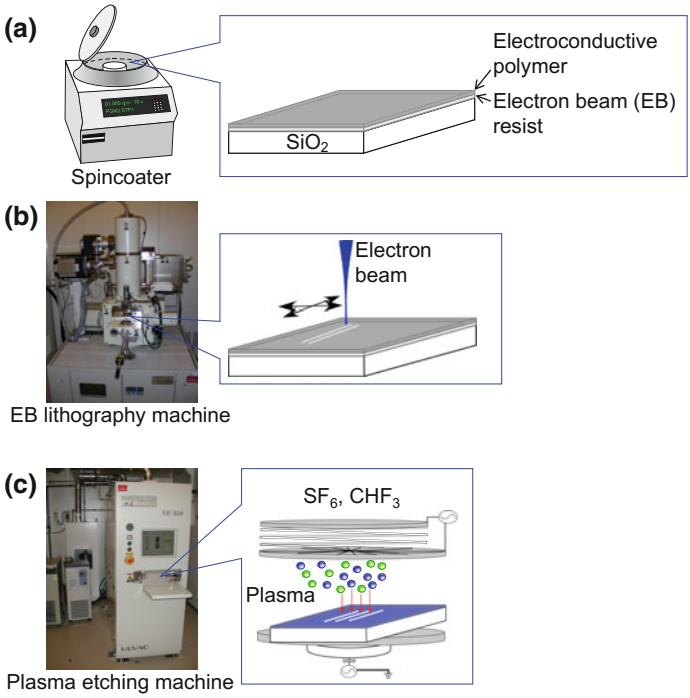

Fig. 5.2 Schematic of nanofabrication. **a** Spincoating, **b** EB lithography and **c** plasma etching

polymer were spincoated on a fused silica substrate. Then, a pattern of nanochannel was transferred onto the substrate by EB lithography and developed. Next, the substrate was anisotropically etched by plasma of CHF_3 and SF_6 to make a nanochannel with rectangular cross-section. The width and depth of the nanochannel were determined by the pattern width and etching time, respectively. Microchannels were fabricated by UV photolithography and plasma etching similarly.

5.3.2 Thermal Fusion Bonding and Surface Modification

Surface chemistry is the most important in creation of bioanalytical and functional devices in micro/nanospace. Therefore, we developed surface modification methods for extended-nano space. One of them is a modification using silane agents after thermal fusion bonding. Firstly, the micro/nanofabricated glass substrate was laminated with a cover glass substrate and fused into one chip at 1080 °C [24]. After that, silane agents with various functional groups, such as hydrophobic octadecyl group and hydrophilic polyethylene glycol, were introduced to react with surface silanol group on glass. This method allows fabrication of robust chips for high pressure, though it is difficult to modify the surface of extended-nano space partially.

5.3.3 Surface Patterning and Room Temperature Bonding

In order to realize the partial modification in extended-nano space, we have developed a new chemical patterning method and room temperature bonding to keep chemical functions [25].

Figure 5.3 shows the schematic of the modification method as an example of antibody patterning for immunochemical reaction. First, a fused silica substrate was modified by aminopropyltriethoxysilane (APTES) gas to add amino group on the surface. Second, the substrate was irradiated under vacuum UV light (VUV) through a photomask, which partially turned the surface into hydrophilic via decomposition of amino group by oxygen radical. As a result, only a part of surface with amino group which was covered by the photomask remained on the substrate so that the substrate was patterned with amino group. Thirdly, the patterned substrate was bonded with a micro/nanofabricated substrate using low temperature bonding as explained later. Finally, polyethylene glycol (PEG)-silane agent was modified on the unpatterned area to prevent nonspecific adsorption and antibody

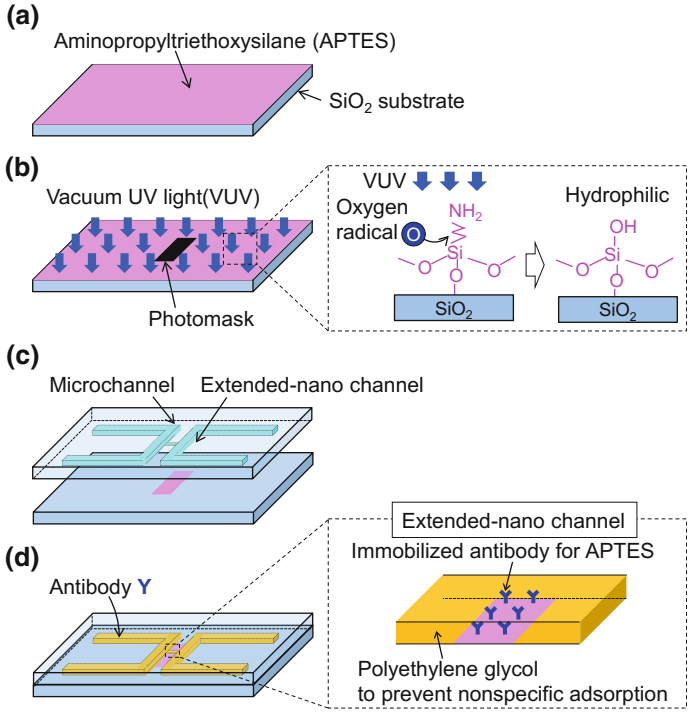

Fig. 5.3 Schematic of antibody patterning in extended-nano channel. **a** Surface modification of glass substrate, **b** VUV patterning, **c** room temperature bonding and **d** antibody immobilization

was immobilized only on the patterned area. Using this method, molecules can be patterned in extended-nano space, even if they are sensitive to high temperature. Thus, introduction of chemical function into extended-nanospace was realized.

In this technique, low temperature bonding was used to keep the functionality of amino group [26]. Figure 5.4 shows the schematic of low temperature bonding. First, silanol groups on the surface of substrate were activated by oxygen plasma and hydrophilicity was optimized by fluorine plasma. In particular, a piece of Teflon was put into the oxygen plasma chamber to generate moderate amount of fluorine. Secondly, the two substrates were bonded using pressure at low temperature to make one chip.

The strength of the bonding was evaluated by a pressure test as shown in Fig. 5.5. Water solution of a fluorescent dye (rhodamine) was introduced into nanochannel by applying pressure (~MPa) using a pressure controller and leakage of the solution was checked under the nanochannel from fluorescent image. Notably, a microchip bonded at 25 °C, 24 atm and 48 h showed no leakage of the

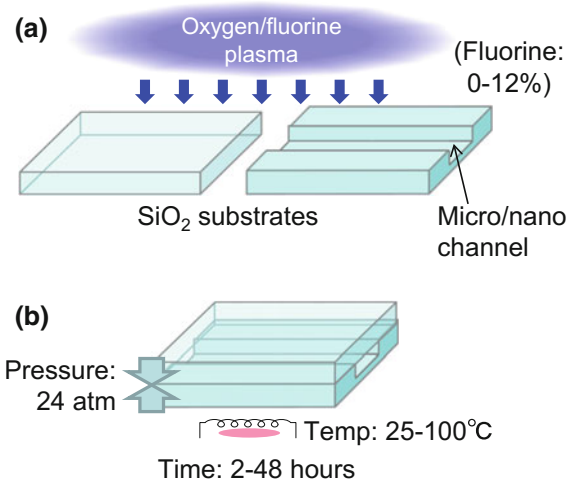

Fig. 5.4 Schematic of room temperature bonding of glass substrates. **a** Surface activation using oxygen plasma with fluorine for hydrophilicity control, **b** pressure bonding at room temperature

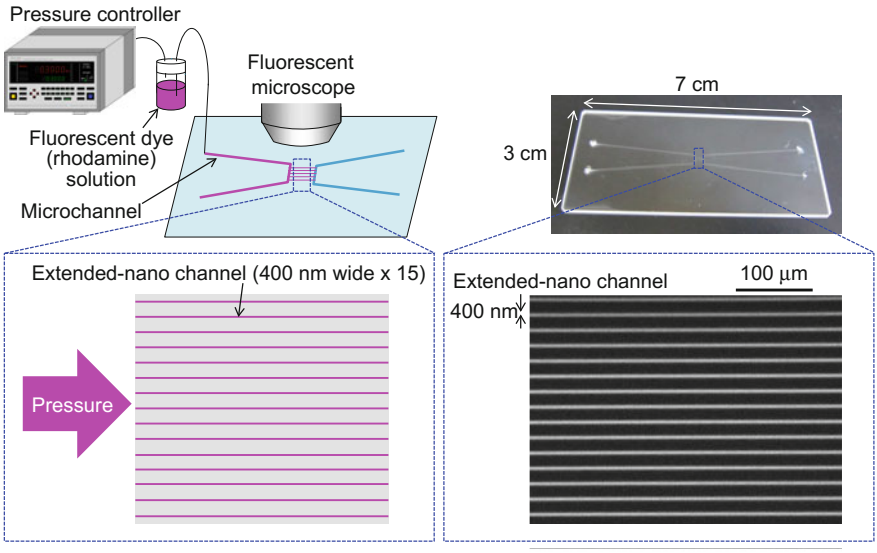

Fig. 5.5 Pressure test of microchip device fabricated by low temperature bonding. Schematic of experiment (*left*) and result (*right*) shows that no leakage of fluorescent solution

solution from nanochannels up to 4 MPa. The pressure resistance was sufficient for almost all of nanofluidic experiments, which suggests that this technique is highly useful in many kinds of chemical experiments in extended-nano space.

5.4 Application of Extended-Nanospace to Chromatography

5.4.1 Concept and Theory

Liquid chromatography, which separates and purifies samples, is an essential technology for sample analysis. In the research of separation analysis, a smaller sample volume and higher separation efficiency have been mainly targeted for a long time although conventional technology has limitations both in terms of volume and efficiency. Therefore, our group proposed using an extended-nano channel as a separation column for chromatography [27]. The principles of a conventional packed column and extended-nano chromatography are illustrated in Fig. 5.6. The conventional technology uses a column packed with porous particles (a few microns in diameter) which have interspaces of 10–100 nm scale. Molecules are separated by interactions between the surface (stationary phase) and liquid (mobile phase) in the interspace. On the other

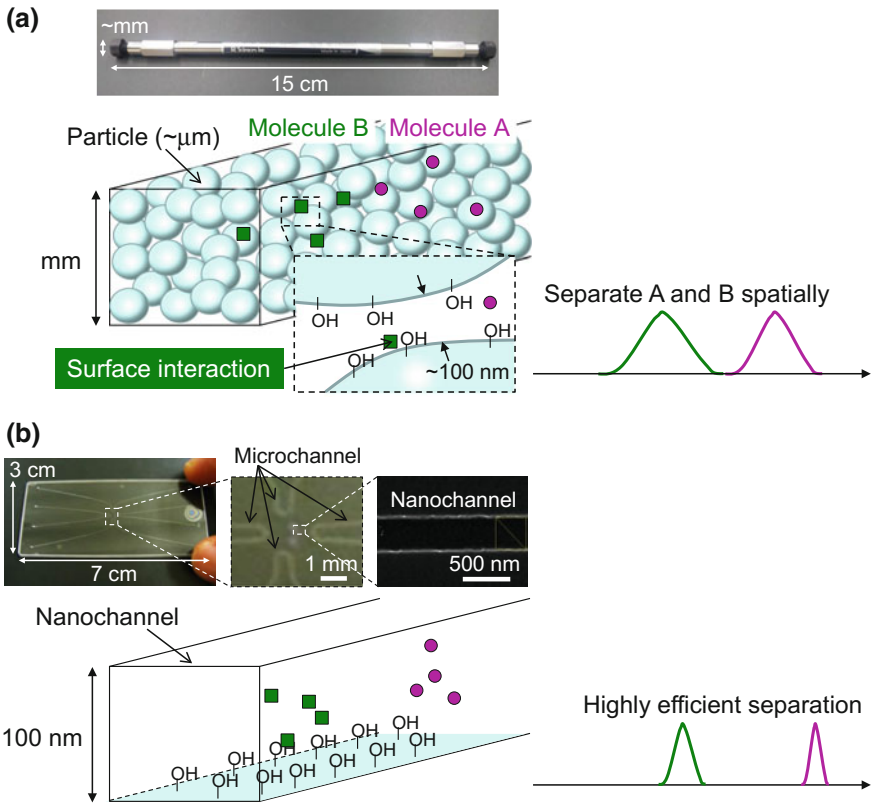

Fig. 5.6 Concepts of **a** conventional packed column and **b** extended-nano chromatography for highly efficient separation

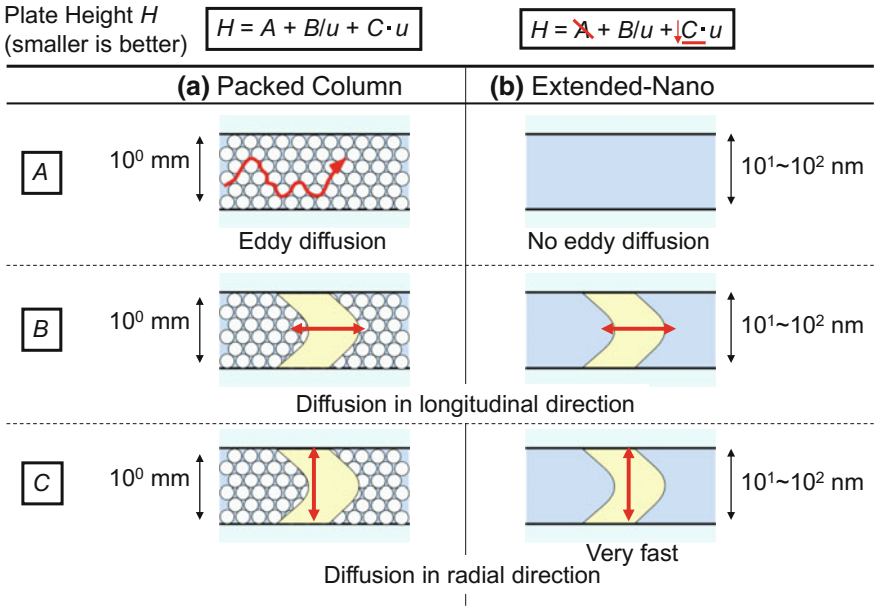

Fig. 5.7 Plate height H and terms A, B, and C in **a** conventional packed column and **b** extended-nano chromatography

hand, extended-nano chromatography uses the extended-nano space itself instead of the particles' interspace. By using the extended-nano channel as a separation column, sample volume could be dramatically decreased. Furthermore, the size-regulated extended-nano space offers a strong and homogeneous surface interaction, which could lead to ultrahigh separation efficiency.

In terms of the theory of chromatography, the advantage of an extended-nano channel is shown in Fig. 5.7. Here, a theoretical plate height H is introduced to evaluate the separation efficiency of a column. The value of H is theoretically expressed as follows and a lower H is better.

$$H = A + B/u + C \cdot u$$

Here, the A term corresponds to broadening of sample bands due to the eddy diffusion which comes from random pathways of molecules. The B term and C term correspond to diffusion of molecules in longitudinal and radial directions, respectively, and u is a flow rate of a mobile phase. In case of an extended-nano channel, the A term is eliminated because there is no particle in the nanochannel. In addition, the C term could be also reduced significantly because the diameter of a nanochannel is so small that the band broadening due to the diffusion in radial direction is negligibly small. Eventually, the plate height H becomes small to realize high efficiency.

In order to realize chromatography in an extended-nano channel, the analysis procedures were divided into three extended-nano unit operations (ENUOs). The

first ENUO is a sample injection into the nanochannel. Here, the point is to use a fluidic control method to cut a sample of a constant volume avoiding a severe effect of molecular diffusion. Also, high pressure is necessary for the fluidic control due to the large pressure loss in an extremely small channel. The second ENUO is a column separation in the nanochannel, which has a point of verification of highly efficient separation. The final ENUO is detection that is easily achieved by fluorescence, although a sensitive detection of nonfluorescent species in the nanospace smaller than wavelength is challenging. In this section, the developments of the three ENUOs are introduced respectively.

5.4.2 *Experimental*

Figure 5.8a shows an experimental setup for extended-nano chromatography [28]. The left-hand side of the setup is pressure controlling part which consists of a compressor, solenoid valves, and a control panel. The sample in the liquid reservoir was introduced into a glass chip by compressed air (up to 4 MPa) and observed by a fluorescence microscope. Figure 5.8b is the glass chip which has microchannels and nanochannels which was bonded by the thermal fusion method. The size of the

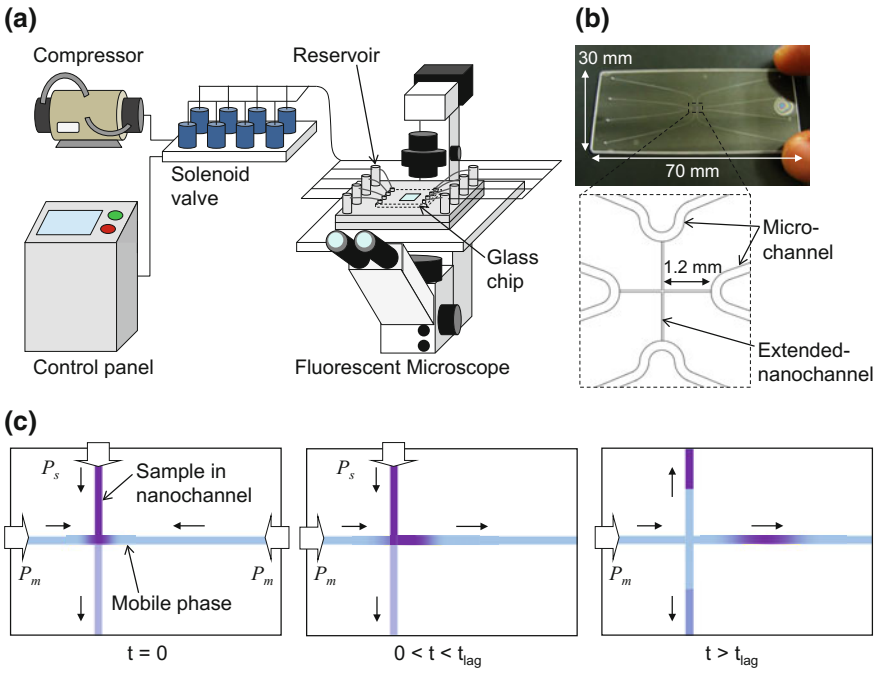

Fig. 5.8 **a** Experimental setup and **b** glass chip used for extended-nano chromatography. **c** Injection procedure using pressure switching. *Arrows* show the direction of flow

nanochannel was 910 nm wide, 220 nm deep and 1.2 mm long. Figure 5.8c shows a procedure of sample injection using pressure switching. First, the sample and a mobile phase were introduced from the top, right, and left side. Then, after an injection time t_{lag}, the pressure of the right side was turned off and the sample was injected into the right channel. Finally, the pressure of the top side was turned-off to cut the sample band. In this procedure, the broadening of the sample band due to the molecular diffusion of the sample becomes a serious problem. For example, a small molecule, which has a diffusion coefficient of $\sim 10^{-9}$ (m^2/s), diffuses 100 μm in ~ 1 s, which leads to large band broadening and makes the separation difficult. Therefore, solenoid valves which have a time response of 50 ms were used to switch the pressures.

5.4.3 Result and Discussion

Figure 5.9 shows the result of the sample injection with different injection times t_{lag} using a toluene solution of a fluorescent dye (Pyrromethene 597) as a sample. The fluorescence was observed at 50 μm from the intersection of nanochannels. The increase and decrease due to the passage of the sample was recorded with good reproducibility, which verified that the injection procedure to cut the sample solution was successful. The injection volume could be controlled by t_{lag} from 180 attoliter (aL) at minimum to ~ 10 femtoliter (fL). Thus, a platform of chromatography at aL-fL was established utilizing the extended-nano space.

Figure 5.10 shows a chromatogram of two fluorescent dyes (Pyrromethene 597, P597 and Coumarin 460, C460) separated using a normal phase mode that utilizes a polar stationary phase (surface) and a nonpolar mobile phase (liquid). In order to make the polar surface, the nanochannel was washed with a sodium hydroxide solution, hydrochloric acid and ultrapure water to expose silanol group on the surface. Then, a nonpolar solvent, toluene, and ethanol were used as a mobile phase. The fluorescence of P597 and C460 was observed separately because they have different emission wavelengths. The result shows the two fluorescent dyes were clearly separated in four

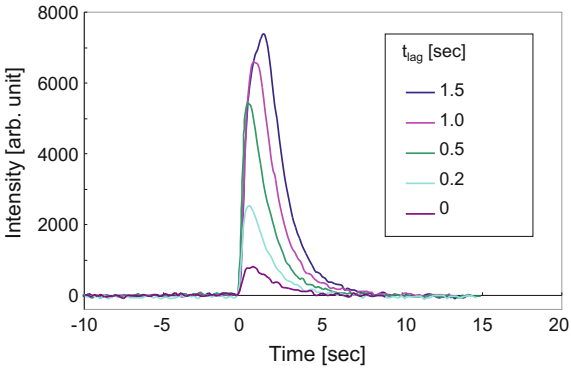

Fig. 5.9 Result of sample injection with different injection time t_{lag}. The injection volume was the minimum (180 aL) when $t_{lag} = 0$

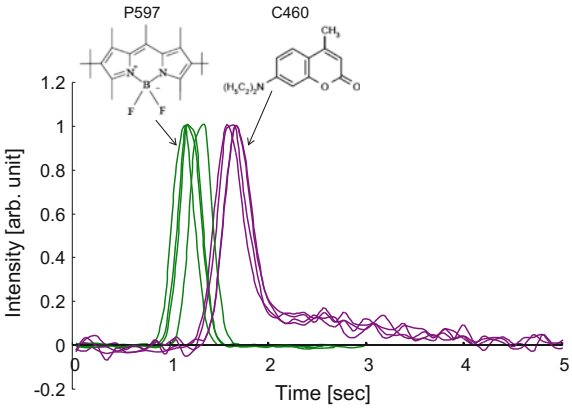

Fig. 5.10 Chromatograms of P597 and C460 by a normal phase mode. The chromatograms of each sample were overlaid 4 time, respectively

repeated experiments in several seconds, while separation of the same dyes using a conventional high performance liquid chromatography (HPLC) system using a packed column took 10 min. Note that the length of nanochannel was merely 1.2 mm, while the length of HPLC column was 15 cm.

In addition, the peak area was verified to be proportional to concentration of each fluorescent dye from Fig. 5.11. From these two results, separation analysis was confirmed to be possible and we concluded that extended-nano chromatography was created.

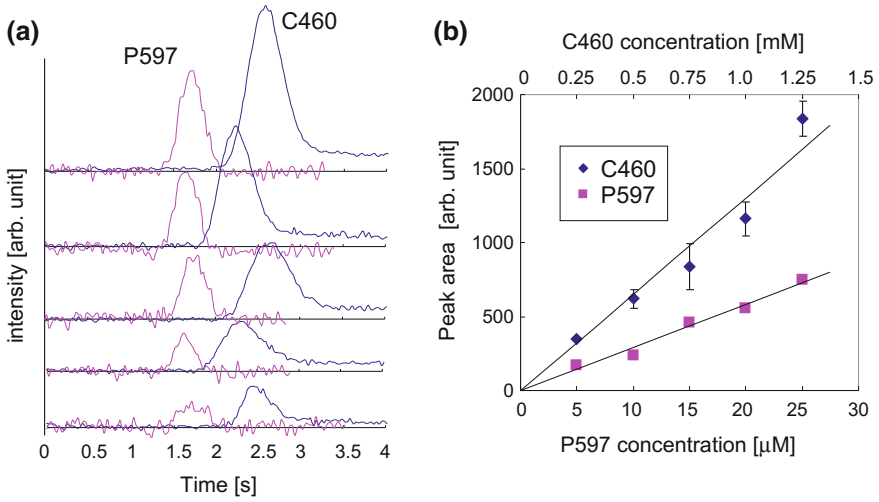

Fig. 5.11 **a** Chromatograms of P597 and C460 for different concentrations from 5 to 30 μM (P597) and 0.25 to 1.5 mM (C460), respectively. **b** Calibration curves of peak area of P597 and C460

In order to evaluate the separation efficiency, plate height H was investigated. The plate height H was experimentally derived from the following equation:

$$H = \frac{\sigma_{\text{det}}^2 - \sigma_{\text{inj}}^2}{L}$$

where σ_{det} and σ_{inj} are standard deviations of Gaussian approximations of the peaks at detection point and injection point. L is the distance between the detection point and the injection point. Figure 5.12 is a plot of plate height H with different flow rates (the so-called "Van Deemter plot") for P597 and C460. The minimum plate heights were 2.8 and 2.3 μm that correspond to the theoretical plate number (*1/H*, theoretical plate number per unit length) of 360,000 and 440,000 plates/m, respectively. These theoretical plate numbers were one order higher compared to the values of a conventional packed column. Furthermore, to discuss the theoretical plate height deeply, the experimental results were compared to a theoretical curve. The theoretical plate height H is expressed in the following equation in the theory of a traditional open tubular chromatography [29],

$$H = \frac{2D_{\text{m}}}{u} + \frac{f_0}{105} D_{\text{m}} \cdot u$$

where D_{m} is a molecular diffusion coefficient and f_0 is the aspect ratio (width-to-depth ratio) of the nanochannel. Here, D_{m} of P597 measured in the nanochannel was 1.06×10^{-9} (m^2/s) and f_0 was 5.36, which gave a theoretical curve as shown in Fig. 5.12. The theoretical curve for P597 was well-accorded with the experimental results, which suggests that the theoretical plate height could be improved further at a higher flow rate. The theoretical value of H becomes the minimum value of 0.14 mm which corresponds to 7,100,000 plates/m at a flow rate of 30 mm/s. Thus, an ultrahigh separation efficiency that is two orders higher than the conventional technology was indicated.

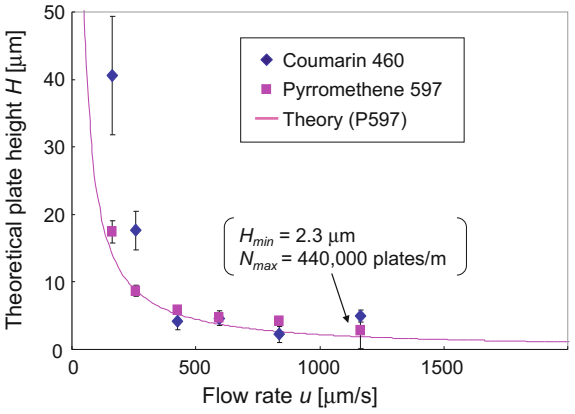

Fig. 5.12 Van Deemter plot of C460, P597, and theoretical curve for P597

Then, the reason why the ultrahigh separation efficiency could be realized was discussed. In Fig. 5.7, the elimination of the *A* term and a significant decrease of the *C* term were expected to decrease the theoretical plate height *H* compared to HPLC using packed columns. The theoretical expression of *H* for the packed column is as follows [30]:

$$H = A + \frac{B}{u} + C \cdot u = d_\mathrm{p} + 1.6\frac{D_\mathrm{m}}{u} + \frac{0.37}{D_\mathrm{m}} d_\mathrm{p}^2 u$$

where d_p is the diameter of packed particles. Figure 5.13 compares the theoretical curves of HPLC and extended-nano chromatography. The terms *A*, *B*, and *C* in HPLC are also drawn separately. The theoretical curve of extended-nano chromatography was well-accorded with the *B* term of HPLC, which verifies the elimination of the *A* term and *C* term leading to a lower theoretical plate height and higher separation efficiency. From these results, we concluded that extended-nano chromatography succeeded in breaking the limitation of a conventional packed column.

Because the theoretical plate height of extended-nano chromatography was revealed to agree with the theory, performance of separation could be easily designed and improved. So far, we revealed a 1–2 orders higher theoretical plate number per unit length of extended-nano chromatography, though a total theoretical plate number, that is a theoretical plate number over the column, was short due to the short nanochannel. (For example, the total theoretical plate number for P597 in Fig. 5.13 was 440,000 plates/m × 1.2 mm = 530 plates.) To solve this problem, we designed the size of the nanochannel and a total theoretical plate number according to the theoretical expression [31]. Figure 5.14a shows a nanochannel design which has a long, serpentine shape. The size of the nanochannel was designed as 1 μm wide, 400 nm deep and 5.2 mm long. The serpentine shape might produce an unwanted broadening of a sample band, though the effect of a corner was negligible due to the very small width of the nanochannel compared to the molecular diffusion. As a result, the performance of separation was clearly

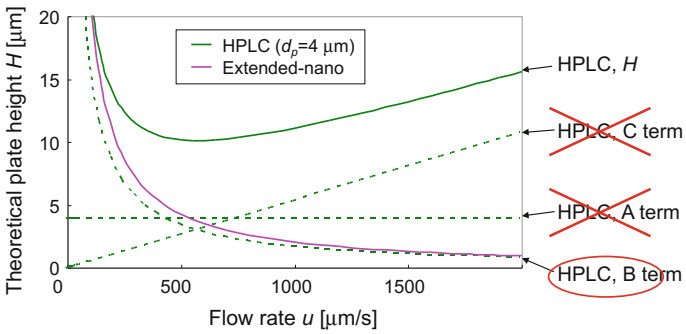

Fig. 5.13 Theoretical curves of theoretical plate heights *H* for extended-nano chromatography, HPLC, *A*, *B*, and *C* term of HPLC

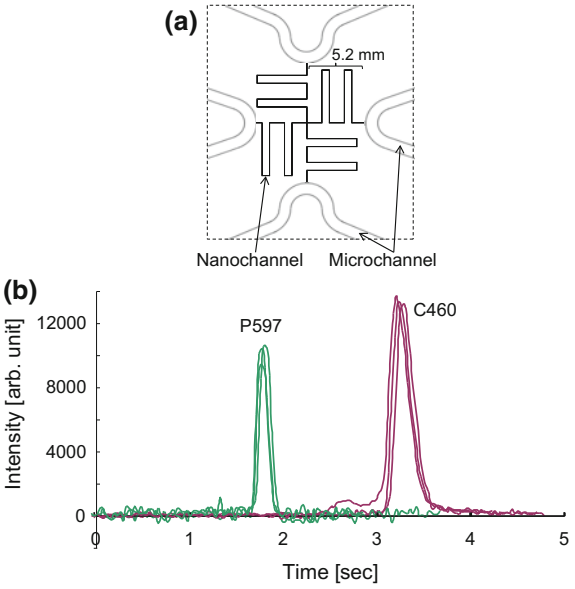

Fig. 5.14 **a** Design of serpentine nanochannel and **b** chromatogram of P597 and C460 with improved separation

improved as shown in a chromatogram of P 597 and C460 (Fig. 5.14b). The total plate number was improved from 530 to 2100 plates. Thus, extended-nano chromatography can design and improve the separation performance more and more using a longer nanochannel. Most of microfluidic chromatography techniques have the problem of band broadening due to the corner and curve effect, while it has no influence in the extended-nanochannel.

5.4.4 Combination with Thermal Lens Microscope

Due to the extremely small volume, detection techniques are quite important in the extended-nano channel because the absolute number of detected molecules is very low. For example, in a 100 nm cube, 1 μM solution contains only 0.6 molecules on average, which indicates single molecule detection is necessary for the extended-nano space. In the experiments of extended-nano chromatography so far, a fluorescent microscope was used for detection. Although fluorescence methods have a very high sensitivity, such as single molecule detection using laser induced fluorescence, most of molecules in the world show no fluorescence. Therefore, our group has developed a thermal lens microscope (TLM) based on thermal lens spectroscopy [32, 33] for sensitive detection of nonfluorescent molecules in the microspace and used the TLM in many microfluidic applications [34]. However, the conventional TLM could not be applied to the extended-nanospace due to a problem in principle. Figure 5.15a shows a principle of the conventional TLM. First, a sample is heated by an excitation beam through the sample molecule's light

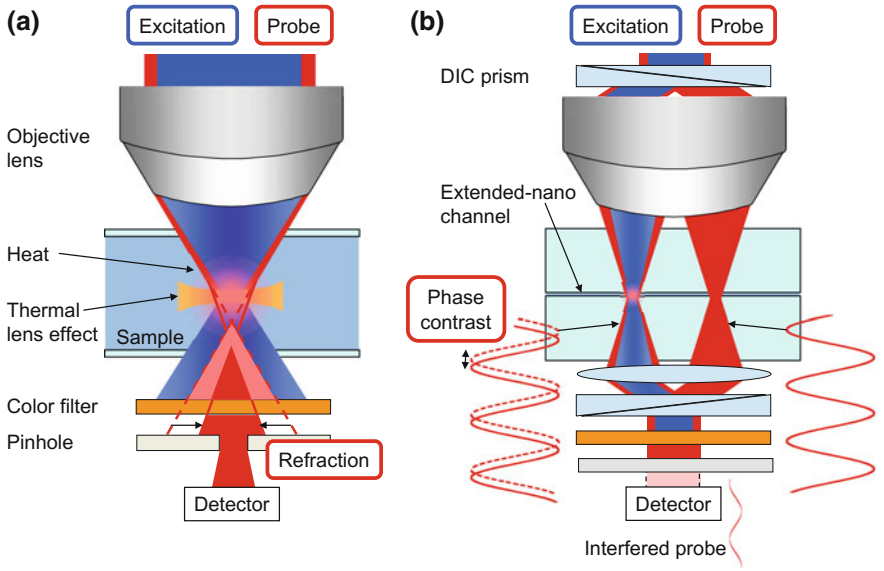

Fig. 5.15 Principle of **a** conventional TLM and **b** DIC-TLM

absorption and nonradiative relaxation. Then, a change in refractive index was locally induced around the excitation focus. This is called a thermal lens effect because it has a distribution of refractive index change which corresponds to a concave lens. Therefore, a coaxially introduced probe beam is refracted by the thermal lens, which produces an intensity change of the probe beam through a pinhole. However, this principle is not effective in the nanospace that is smaller than the wavelength of visible light because the refraction is an effect based on geometrical optics. In order to overcome this problem, a differential interference contrast thermal lens microscope (DIC-TLM) was developed, as shown in Fig. 5.15b. In DIC-TLM, the probe beam is separated into two beams and integrated again using a pair of DIC prisms to make interference. The excitation beam is not separated by controlling its polarization, which induces a change in the refractive index only in the left side and produces phase contrast between the two probe beams. Finally, the phase contrast makes a change of the probe intensity after interference to be detected. Because the interference is based on wave optics, the principle is available in extended-nanospace that is smaller than the wavelength.

Figure 5.16 is a chromatogram of two nonfluorescent dyes (Sudan I and Sudan Orange G) separated by a normal phase mode and detected by DIC-TLM in a nanochannel of 2.3 mm wide, 350 nm deep and 1.2 mm long [35]. For the separation, silica surface and hexane/2-propanol were used as a stationary and a mobile phase, respectively. The detection was performed using the 488 nm excitation laser and the 633 nm probe laser. The detection limit of Sudan I was 370 molecules in the detection volume of 170 aL. Thus, it was revealed that high efficient separation and sensitive detection were possible even for nonfluorescent molecules.

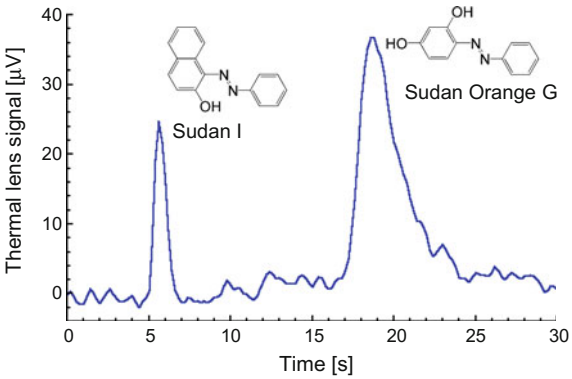

Fig. 5.16 Chromatogram of nonfluorescent molecules detected by DIC-TLM

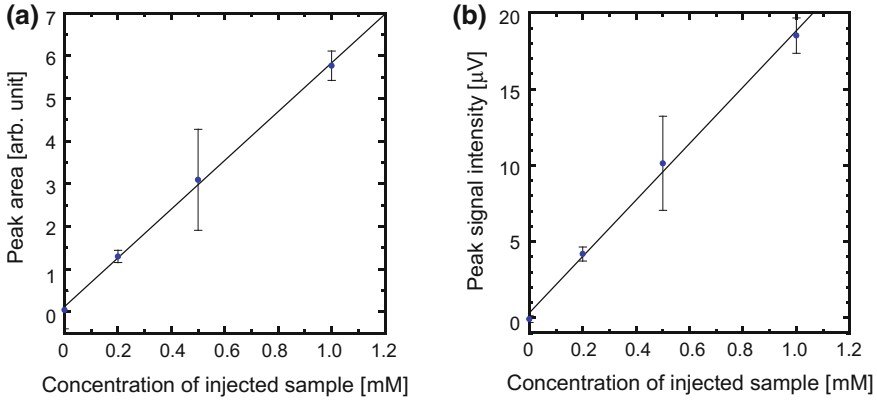

Fig. 5.17 Calibration curve of **a** peak area and **b** peak signal intensity of Sudan I

Finally, detection limit of DIC-TLM and injection volume is discussed. Figure 5.17 shows calibration curves of peak area and height of Sudan I. The limit of detection calculated from the peak height was 12 μM. Because the injection volume calculated from the peak area was 21 fL, the concentration at the limit of detection corresponds to 250 zmol in 21 fL. This result indicates that DIC-TLM is very sensitive and useful for the detector of extended-nano chromatography.

5.5 Summary and Perspectives

In this chapter, creation of bioanalytical device utilizing extended-nano space, especially an ultrasmall, highly efficient chromatography was introduced. The extended-nano chromatography made a separation analysis of 180 aL at minimum

and high efficiency of 440,000 plates/m possible. The sample volume and separation efficiency were in different orders of magnitude compared to the conventional packed column technology. In addition, target molecules of separation could be expanded vastly by the sensitive detection method of nonfluorescent molecules, differential interference contrast thermal lens microscope (DIC-TLM).

The extended-nano chromatography was composed of three extended-nano unit operations (ENUOs) of the injection, separation and detection. Similarly, more complicated analytical methods, such as enzyme-linked immunosorbent assay (ELISA), can be divided into ENUOs such as capturing of molecules, chemical amplification, and detection to be integrated in the extended-nano channel using the chemical patterning and low-temperature bonding method. The further integration of ENUOs has a potential of developing a more complicated analysis, such as a single cell analysis. For example, making a single cell chamber before the immunoassay and chromatography would realize the analysis of cell secretions [36]. Because the volume of the extended-nano channel is aL-fL, which is 10^3 times smaller than the cell, the extended-nano analytical platform might enable analyzing the cell without killing it. Thus, the ultimate analytical tool using the extended-nano space would contribute to the state-of-the-art research in biology. Moreover, developments of the next-generation analytical instruments would explore a new market on the world scale.

References

1. A. Manz, N. Graber, H.M. Widmar, Miniaturized total chemical analysis systems: a novel concept for chemical sensing. Sens. Actuators B Chem. **1**, 244–248 (1990)
2. A. Manz, Y. Miyahara, J. Miura, Y. Watanabe, H. Miyagi, K. Sato, Design of an open-tubular column liquid chromatograph using silicon chip technology. Sens. Actuators B Chem. **1**, 249–255 (1990)
3. J.C. Fister, S.C. Jacobson, L.M. Davis, J.M. Ramsey, Counting single chromophore molecules for ultrasensitive analysis and separations on microchip device. Anal. Chem. **70**, 431–437 (1998)
4. M.U. Kopp, A.J. de Mello, A. Manz, Chemical amplification: continuous-flow PCR on a chip. Science **280**, 1046–1048 (1998)
5. K. Sato, M. Tokeshi, T. Odake, H. Kimura, T. Ooi, M. Nakao, T. Kitamori, Integration of an immunosorbent assay system: analysis of secretory human immunoglobulin a on polystyrene beads in a microchip. Anal. Chem. **72**, 1144–1147 (2000)
6. T. Ohashi, K. Mawatari, K. Sato, M. Tokeshi, T. Kitamori, A micro-ELISA system for the rapid and sensitive measurement of total and specific immunoglobulin E and clinical application to allergy diagnosis. Lab Chip **9**, 991–995 (2009)
7. S.L. Spurgeon, R.C. Jones, R. Ramakrishnan, High throughput gene expression measurement with real time PCR in a microfluidic dynamic array. PLoS ONE **3**, e1662 (2008)
8. H. Jiang, X. Weng, D. Li, Microfluidic whole-blood immunoassays. Microfluid Nanofluidics **10**, 941–964 (2011)
9. E. Katz, I. Willner, Integrated nanoparticle-biomolecule hybrid systems: synthesis, properties, and applications. Angew. Chem. Int. Ed. **43**, 6042–6108 (2004)
10. D.R. Reyes, D. Iossifidis, P.A. Auroux, A. Manz, Micro total analysis systems. 1. Introduction, theory, and technology. Anal. Chem. **74**, 2623–2636 (2002)

11. P.A. Auroux, D. Iossifidis, D.R. Reyes, A. Manz, Micro total analysis systems. 2. Analytical standard operations and applications. Anal. Chem. **74**, 2637–2652 (2002)
12. M. Napoli, J.C.T. Eijkel, S. Pennathur, Nanofluidic technology for biomolecule applications: a critical review. Lab Chip **10**, 957–985 (2010)
13. J. Han, H.G. Craighead, Separation of long DNA molecules in a microfabricated entropic trap array. Science **288**, 1026–1029 (2000)
14. N. Kaji, Y. Tezuka, Y. Takamura, M. Ueda, T. Nishimoto, H. Nakanishi, Y. Horiike, Y. Baba, Anal. Chem. **76**, 15–22 (2004)
15. Y.C. Wang, A.L. Stevens, J. Han, Million-fold preconcentration of proteins and peptides by nanofluidic filter. Anal. Chem. **77**, 4293–4299 (2005)
16. R. Karnik, C. Duan, K. Castelino, H. Daiguji, A. Majumdar, Nano Lett. **7**, 547–551 (2007)
17. T. Tsukahara, K. Mawatari, T. Kitamori, Integrated extended-nano chemical systems on a chip. Chem. Soc. Rev. **39**, 1000–1013 (2010)
18. A. Hibara, T. Saito, H.B. Kim, M. Tokeshi, T. Ooi, M. Nakao, T. Kitamori, Nanochannels on a fused-silica microchip and liquid properties investigation by time-resolved fluorescence measurements. Anal. Chem. **74**, 6170–6176 (2002)
19. T. Tsukahara, A. Hibara, Y. Ikeda, T. Kitamori, NMR study of water molecules confined in extended nanospaces. Angew. Chem. Int. Ed. **46**, 1180–1183 (2007)
20. H. Chinen, K. Mawatari, Y. Pihosh, K. Morikawa, Y. Kazoe, Enhancement of proton mobility in extended-nanospace channels. Angew. Chem. Int. Ed. **51**, 3573–3577 (2012)
21. M. Tokeshi, T. Minagawa, K. Uchiyama, A. Hibara, K. Sato, H. Hisamoto, T. Kitamori, Continuous flow chemical processing on a microchip by combining micro unit operations and a multiphase flow network. Anal. Chem. **74**, 1565–1571 (2002)
22. T. Minagawa, M. Tokeshi, T. Kitamori, Integration of a wet analysis system on a glass chip: determination of Co(II) as 2-nitroso-1-naphthol chelates by solvent extraction and thermal lens microscopy. Lab Chip **1**, 72–75 (2001)
23. S. Hiki, K. Mawatari, A. Aota, M. Saito, T. Kitamori, Sensitive gas analysis system on a microchip and application for on-site monitoring of NH3 in a clean room. Anal. Chem. **83**, 5017–5022 (2011)
24. B. Renberg, K. Sato, T. Tsukahara, K. Mawatari, T. Kitamori, Hands on: thermal bonding of nano- and microfluidic chips. Microchim. Acta **166**, 177–181 (2009)
25. K. Shirai, K. Mawatari, T. Kitamori, Extended nanofluidic immunochemical reaction with femtoliter sample volumes. Small **10**, 1514–1522 (2014)
26. Y. Xu, C. Wang, L. Li, N. Matsumoto, K. Jang, Y. Dong, K. Mawatari, T. Suga, T. Kitamori, Bonding of glass nanofluidic chips at room temperature by a one-step surface activation using an O_2/CF_4 plasma treatment. Lab Chip **13**, 1048–1052 (2013)
27. M. Kato, M. Inaba, T. Tsukahara, K. Mawatari, A. Hibara, T. Kitamori, Femto liquid chromatography with attoliter sample separation in the extended nanospace channel. Anal. Chem. **82**, 543–547 (2010)
28. R. Ishibashi, K. Mawatari, T. Kitamori, Highly efficient and ultra small volume separation by pressure driven liquid chromatography in extended nanochannels. Small **8**, 1237–1242 (2012)
29. H. Poppe, Mass transfer in rectangular chromatographic channels. J. Chromatogr. A **948**, 3–17 (2002)
30. G. Desmet, G.V. Baron, On the possibility of shear-driven chromatography: a theoretical performance analysis. J. Chromatogr. A **855**, 57–70 (1999)
31. R. Ishibashi, K. Mawatari, T. Kitamori, High resolution separation by pressure-driven liquid chromatography in meander extended-nanochannels. J. Chromatogr. A **1238**, 152–155 (2012)
32. S.E. Bialkowski, *Photothermal Spectroscopy Methods for Chemical Analysis* (Wiley, New York, 1996)
33. R.D. Snook, R.D. Lowe, Thermal lens spectrometry: a review. Analyst **120**, 2051–2068 (1995)
34. T. Kitamori, M. Tokeshi, A. Hibara, K. Sato, Thermal lens microscopy and microchip chemistry. Anal. Chem. **76**, 52A–60A (2004)

35. H. Shimizu, K. Mawatari, T. Kitamori, Femtoliter-scale separation and sensitive detection of nonfluorescent samples in an extended-nano fluidic device. Analyst **139**, 2154–2157 (2014)
36. K. Jang, H.T.T. Ngo, Y. Tanaka, Y. Xu, K. Mawatari, T. Kitamori, Development of a microfluidic platform for single-cell secretion analysis using a direct photoactive cell-attaching method. Anal. Sci. **27**, 973–978 (2011)

Chapter 6
Microfluidic Approach to Cell Handling and Measurement

Jiro Kawada, Shohei Kaneda, Soo Hyeon Kim and Teruo Fujii

Abstract Microfluidic technologies enable us to analyze cells with much higher resolution in space and time. The approaches are mostly realized by making use of numerous advantageous features of microfluidic systems, such as relatively small dimensions, low Reynolds number flow, etc. In this chapter, the examples of microfluidic approach to cell handling and measurement highlighting its advantageous features will be described. It will be shown that the microfluidic approach is among the promising methods for the future experimentation in biomedical applications.

Keywords Microfluidics · Pluripotent stem cells · Differentiation · Circulating tumor cells (CTCs) · Single-cell analysis

6.1 Introduction

Microfluidic technologies enable us to analyze cells with much higher resolution in space and time. We can even handle cells at the single-cell level in microfluidic systems. The microfluidic approaches are mostly realized by making use of numerous advantageous features of microfluidic systems, such as relatively small dimensions of the microfabricated structure which could be almost comparable to the dimension of cells, confinement of molecules into a small space leading to higher concentration than in regular experimental formats, etc. The specific characteristics of the low Reynolds number flow could also be useful to form laminar flow streams over a micrometer-sized space to culture cells. Thus, local culture conditions can be controlled flexibly and stably by the laminar flow streams containing different types of soluble factors affecting on, for example, the cell fate, such as differentiation versus undifferentiated (pluripotent) state.

J. Kawada · S. Kaneda · S.H. Kim · T. Fujii (✉)
Institute of Industrial Science, The University of Tokyo,
4-6-1 Komaba, Meguro-ku, Tokyo 153-8505, Japan
e-mail: tfujii@iis.u-tokyo.ac.jp

J. Sone and S. Tsuji (eds.), *Intelligent Nanosystems for Energy, Information and Biological Technologies*, DOI 10.1007/978-4-431-56429-4_6

In this chapter, the examples of microfluidic approach to cell handling and analysis highlighting its advantageous features will be described;

- Microfluidic Techniques for Stem Cell Culture
- Capture and Analysis of Circulating Tumor Cells (CTCs)

With these examples, it will be shown that the microfluidic approach is among the promising methods for the future experimentation in biomedical applications.

6.2 Microfluidic Techniques for Stem Cell Culture

Pluripotent stem cells (PSCs) have the potentials to infinitely proliferate and differentiate into derivatives from three germ layers (endoderm, mesoderm, and ectoderm). Recently it has been shown that in vivo-like tissues can be formed by self-organization [1, 2]. In developmental biology, it has been shown that specific distributions of morphogens are necessary to form highly organized tissues [3, 4]. So in order to realize more complex tissues in vitro through stem cell culture, it is important to reconstruct in vivo-like situation.

In conventional culture methods, however, cells are usually exposed to uniform distributions of soluble factors and adhered on one type of ECM coated over the bottom of a culture vessel. On the other hand, by adopting microfluidic methods, we can control the spatial distribution of soluble factors and the surface property over the culture space. In the following sections, we show spatially controlled culture techniques for PSCs in two-dimensional and three-dimensional formats, followed by the techniques to pattern the surface property for cell adhesion using two kinds of specific ECMs.

Controlling the distribution of differentiation factors in culture environment is a highly effective method to realize spatially nonhomogeneous situation for PSCs culture in vitro. As described above, it is difficult to form specific distribution of factors in a dish, because the distribution is, in principle, depending on the molecular diffusion and even in the case there is a preformed specific distribution in a dish, it would finally become equalized during the culture. Thus, the microfluidic devices have been proposed for exposing cells to spatially patterned distribution of soluble factors in culture space [5–9]. In their works, cells or single cells are exposed to chemical gradient formed by multi-laminar flow or diffusion in microenvironment. However, it is known that laminar flow damages cells attached in a channel [10] and also it is difficult to maintain the chemical gradient for a longer term required for stem cell differentiation.

Table 6.1 shows the comparison between diffusion-based and flow-based techniques. In the case of flow-based techniques, it is necessary to make the situation of "low physical damage".

In the discussions above, formation of soluble factor distribution is mostly considered for two-dimensional cell culture formats, that is, the cells are cultured

Table 6.1 Advantageous and negative points of diffusion- and flow-based technique for spatially exposing to soluble factors

	Diffusion-based technique	Flow-based technique
Controllability of chemical distribution	No good	Good
Physical damage by shear stress	Good	No good

mostly in adhered conditions. We also have to consider three-dimensional formats for the culture of PSCs to realize more complex tissue constructs.

Embryonic stem cells (ESCs) and induced pluripotent stem cells (iPSCs) form a spherical structure, which is called embryoid body (EB), by floating culture, that is, with a non-adherent condition. It was shown that the EB formation could be an initialization step of differentiation procedures [11, 12]. Some studies showed that differentiation procedures of EB have similarities to developmental process in vivo [13]. Microfluidic techniques have already been proposed to induce spatially different differentiation states in an EB by applying multi-laminar flow containing different chemicals to the EB culture [14]. In this case, however, it is hard to transfer the EB to downstream analyses because it is so difficult to collect it from the microchannel due to its increased size after the culture for a certain term. It is, therefore, expected that there should be a room in the device for the EB to grow and it should also be capable to pick the EB up for the downstream analyses. Thus, totally new concept is required for the EB culture in spatially heterogenous (nonuniform) conditions, that is, in three-dimensional formats.

6.2.1 Spatially Controlled Differentiation

Device Design

We used a membrane-based microfluidic device made of polydimethylsiloxane (PDMS) to expose cells to a specific distribution of soluble factors in a microchannel and to keep it stably for a long time. The microfluidic device has upper and lower channels with a semipermeable porous membrane in between (Fig. 6.1a). To start the cell culture in the device, first the cells are seeded in the upper channel, and then the device is put in an incubator overnight to let the cells completely attach to the membrane. After incubation overnight, two different kinds of culture media are injected into the lower channel. The specific distribution of soluble factors, corresponding to the laminar flow pattern, is formed in the lower channel. The factors included in the media are carried by advection from the lower channel to the upper channel through the membrane (Fig. 6.1b). During this transportation to the upper channel, the cells take up the factors flowing through the membrane (Fig. 6.1c). Thus, the cells cultured on the membrane are exposed to the specific distribution of soluble factors according to the laminar flow pattern. The factors transported from the lower channel are, in fact, not accumulated in the upper

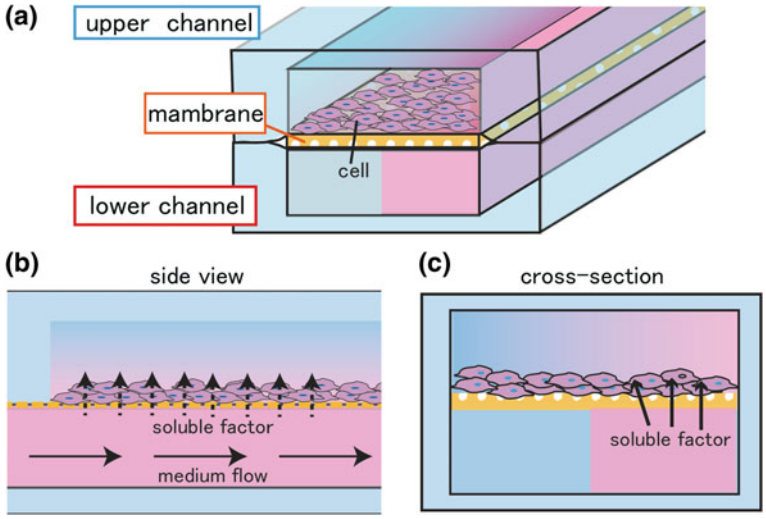

Fig. 6.1 Concept of device for spatially cellular exposure to factors. **a** The device consists of the upper and lower channels and the porous membrane in between. **b** When the culture medium is injected into the lower channel, the contained factors are also transported to the upper channel through the membrane by advection. **c** When the laminar flow pattern is formed in the lower channel, the cells on the membrane are exposed to the specific chemical distribution depending on the laminar flow pattern. (Reproduced from Ref. [15] by permission of The Royal Society of Chemistry.)

channel due to the existence of slight flow through the membrane. This mechanism is different from the diffusion-based techniques as mentioned above. It is confirmed that the flow velocities in the upper channel are approximately 9 and 24 % of that in the lower channel with and without cells seeded on the membrane, respectively. This feature of the device allows a long-term culture under spatially heterogenous (nonuniform) condition.

Experimental

The effectiveness of the present method was examined through the experiments using mouse iPSCs (iPS-MEF-Ng-20D-17 cell line provided by Kyoto University). We used two types of media, which are maintenance medium and differentiation medium. The maintenance medium contains leukemia inhibitory factor (LIF), which retains the undifferentiated state of miPSCs. The differentiation medium contains retinoic acid (RA), which is a differentiation factor. The cell line expresses Green Fluorescent Protein (GFP) as a reporter of pluripotency marker Nanog. A cell expressing GFP is in the undifferentiated state and a cell not expressing GFP is already differentiated. After the cells attachment on the membrane, both media were injected into the lower channel at 2 μL/min each (Fig. 6.2a). 4 days later, fluorescence intensities (FIs) of GFP and DAPI (4′,6-diamidino-2-phenylindole, dihydrochloride) from miPSCs were measured. Figure 6.2b shows the result of measuring the FIs. It was confirmed by the FI of DAPI that the cells were

homogenously distributed over the microchannel. And the FI of GFP on the side of the maintenance medium was higher than that on the side of the differentiation medium. This means that on the side where the maintenance medium was flown there are more undifferentiated cells, while on the other side there are more differentiated cells.

We could also try a different pattern of tri-laminar flow to control the differentiation state of the miPSCs. We injected the maintenance medium into the center channel and the differentiation medium into both of the side channels at 2 μL/min each (as depicted in Fig. 6.2c). As the result, the FI of GFP in the central area of the channel was higher than that on the both side, while the cell distribution was homogenous as shown by the FI of DAPI (Fig. 6.2d).

These results show that the differentiation of a cell population cultured in a two-dimensional format can be spatially controlled by the laminar flow pattern in the lower channel.

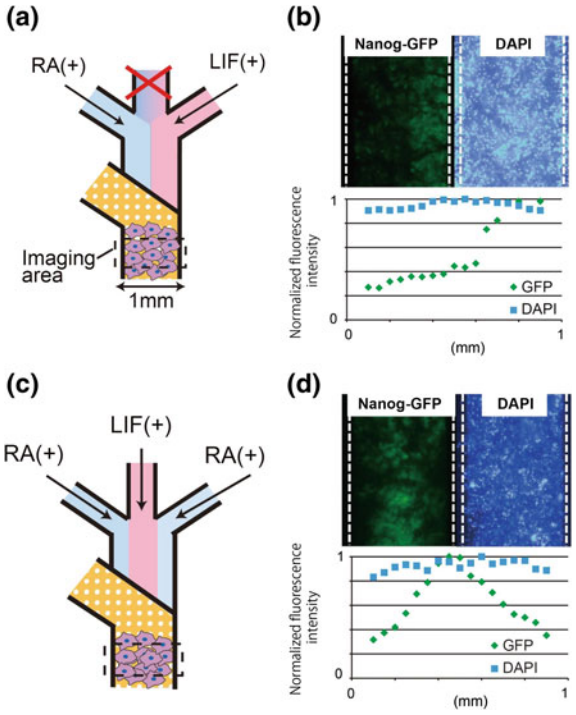

Fig. 6.2 Schematics of experiments and measured FIs of GFP and DAPI from miPSs. **a** To conduct spatially controlled differentiation, the maintenance and differentiation media were injected into each of the two side inlets at 2 μL/min. **b** The result of measuring FIs of DAPI and GFP on the day 4. **c** The pattern of tri-laminar flow was applied to the cells. The maintenance medium was injected into the center channel and the differentiation medium was injected into both of the side channels at 2 μL/min each. **d** The result of measuring FIs of DAPI and GFP on the day 4. (Reproduced from Ref. [15] by permission of The Royal Society of Chemistry.)

6.2.2 Culture Insert-Type Device

Device Design

Here, we show a simple technique for three-dimensional formats, that is, to culture an EB in spatially heterogeneous conditions. We use a culture insert with a PDMS-made membrane at the bottom, where there is a through-hole with a few hundred micrometers in diameter [Fig. 6.3a(i)]. First, an EB is injected into the insert with additional culture medium [Fig. 6.3a(ii)], and then the EB settles down by the gravity force on the bottom. And when the medium level in the insert is higher than that in the well, flow is generated from the insert to the well through the through-hole by hydrostatic pressure. Hence, the EB is moved with the flow and immobilized on the through-hole (Fig. 6.3b). Then, the EB can be exposed to different factors above and below the membrane by changing the media into different ones depending on the purposes (Fig. 6.3c). We confirmed that the EB was transformed into a specific shape by this culture method. After the immobilization of the EB on the through-hole, each of the two portions of the EB above and below the membrane gradually grows to a larger size because the cells contained in the EB still have the potential to proliferate. Finally the EB becomes an articulated shape as if the EB consists two spheroids. This transformation of an EB has two advantages; the EB can be fixed on the through-hole steadily because the two portions of the EB pinch the through-hole up and down. The EB culture can, therefore, be maintained stably for a long time. Another advantage is that the EB can be exposed to different factors with a clear boundary. Thus, two different portion of a single EB can be cultured in different conditions and analyzed at the same time.

Experimental

We cultured an EB derived from miPSCs (same cell line as in the previous section) with two different media. The media are the maintenance medium, which contains LIF, and the neural differentiation medium. First the miPSCs were seeded and reaggregated in a 96 well-plate with the maintenance medium for 2 days. And the generated EB is injected into the insert and then we introduced the maintenance medium and the neural differentiation into the insert and the well, respectively (Fig. 6.4a). On the day 4 of the culture, the EB was transported to a dish and the GFP fluorescence was observed. We injected the EBs generated from 5000 cells and 10,000 cells into the inserts with 200 and 300 μm through-hole in diameter, respectively.

The results of the culture are shown in Fig. 6.4. When the EB was removed from 200 μm through-hole by pipetting, the upper and the lower parts of the EB were separated from each other (Fig. 6.4b). It was confirmed that the GFP fluorescence of the upper part was higher than that of the lower part, where the upper part was exposed to the maintenance medium and the lower part to the differentiation medium (Fig. 6.4c). The EB could be transported to the dish while maintaining the articulated shape in the case of 300 μm through-hole (Fig. 6.4d). We observed

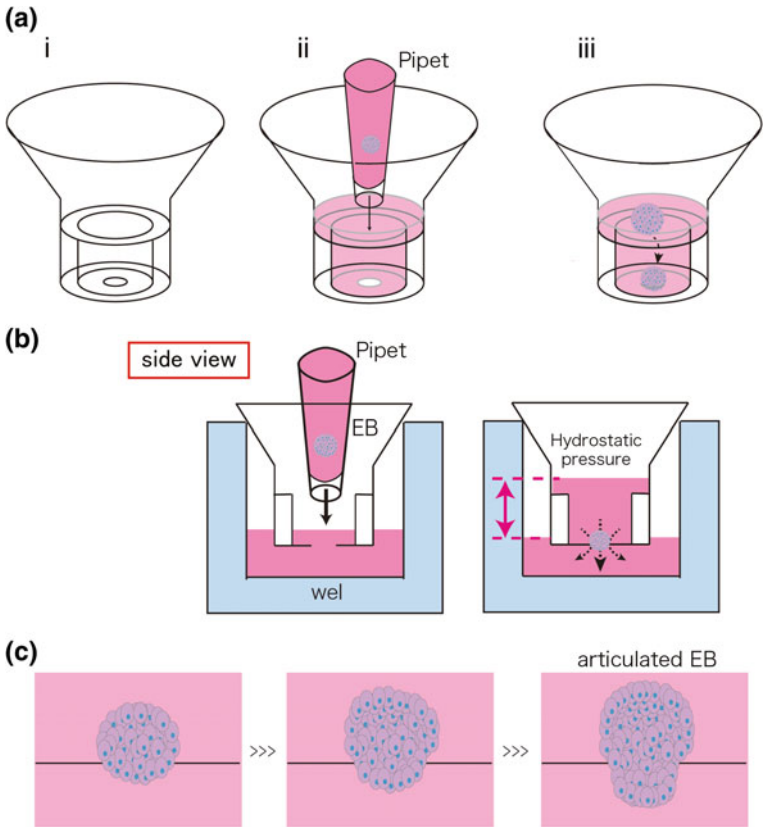

Fig. 6.3 Culture insert-based technique for spatially heterogeneous culture of an EB. **a** Procedure for culturing a EB in the insert. (*i*) The insert has a through-hole on the bottom. (*ii*) To start the culture, the EB is injected into the insert with culture medium. (*iii*) After injecting the EB, it settles down on the bottom. **b** When the liquid surface in the insert is higher than that in the well, flow is generated from the insert to the well through the through-hole by hydrostatic pressure. The EB is moved to and immobilized on the through-hole. **c** The EB cultured on the through-hole is gradually forming articulated shape, art-EB

clearly that the GFP fluorescence of the lower part is higher than that of the upper part, where the upper part was exposed to the differentiation medium and the lower part to the maintenance medium in this case (Fig. 6.4e). These results show that the differentiation states of the portions of an EB can be controlled in a three-dimensional format by the present culture insert-based technique.

6.2.3 Controlling Surface Conditions

Signals from extracellular matrix (ECM) for cell adhesion of stem cell are one of the parameters that regulates stem cell fate [16]. Therefore, controlled stem cell

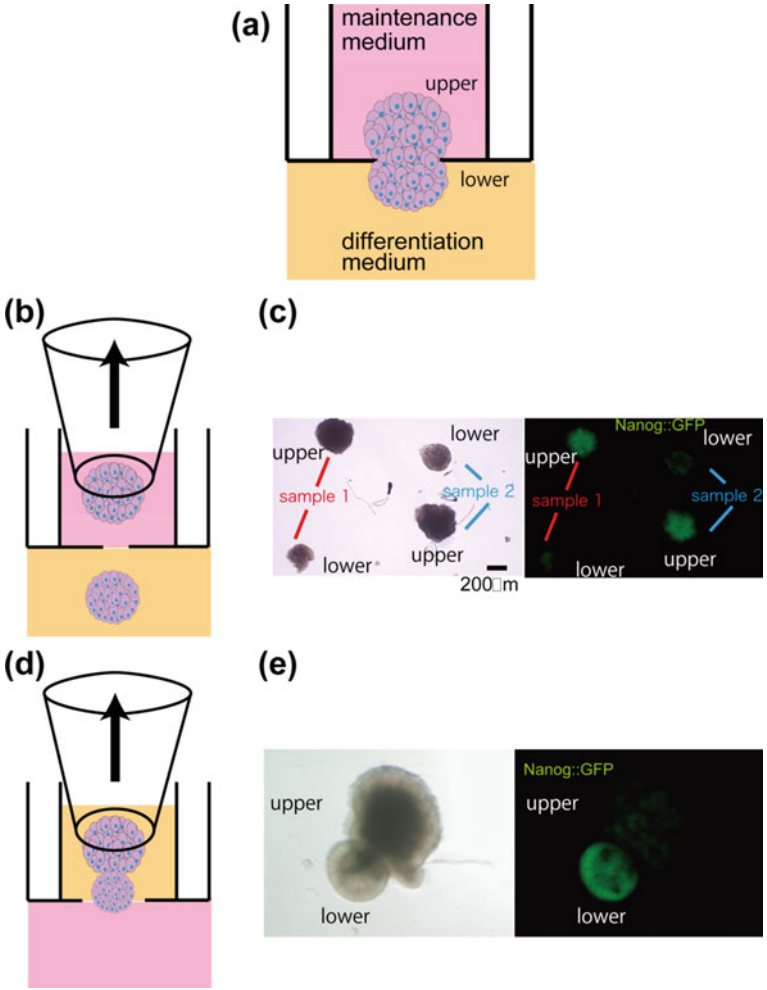

Fig. 6.4 Experimental setup and the results of the EB culture. **a** To spatially control differentiation states, the maintenance medium and the differentiation medium are introduced in the insert and the well, respectively. **b** In the case of the 200 μm through-hole, the EB was divided into two parts when it was removed from the through-hole. **c** GFP fluorescence of the *upper part* is higher than that of the *lower part*. **d** In the case of the 300 μm through-hole, the EB could be transported to a dish keeping its articulated shape. **e** It is confirmed that the GFP fluorescence of the *lower part* is higher than that of the *upper part*

differentiation by the specific surfaces coated with spatially defined heterogeneous ECM (as shown in, e.g., Fig. 6.5) could be one of the key technologies to achieve complex tissues consisting of various types of cells derived from PSCs. Microcontact printing [17] and microfluidic patterning [18] are the methods currently available to form spatially defined heterogeneous ECM-coated surfaces.

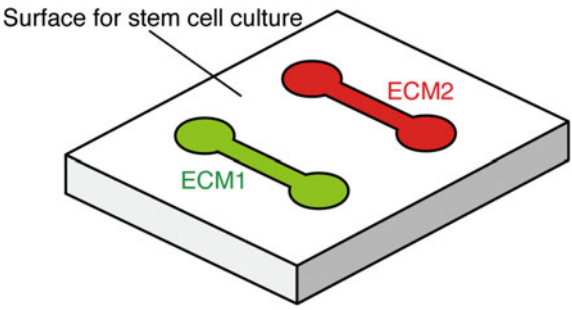

Fig. 6.5 Schematic drawing of spatially defined heterogeneous ECM-coated surfaces for stem cell culture

Although microcontact printing offers spatial resolution in submicron scale [19], special equipment is required for the alignment process of PDMS stamps for every different type of ECM to pattern. On the other hand, microfluidic patterning is an easier way to from the surfaces, however two different microfluidic chips, one for pattering of ECM and another one for cell culture, have to be prepared in the conventional microfluidic approaches [20].

To resolve this bothersome issue, here we propose the use of a single microfluidic chip containing capillary stop valves with a partial barrier structures [21] for the formation of spatially defined heterogeneous ECM-coated surfaces and for the positioning of the EB in between the heterogeneous surfaces.

The developed microfluidic device consists of a PDMS microfluidic chip with microgrooves (150-μm height) and micropillar structures (a square 50 μm on a side), and a glass substrate. Both the PDMS microfluidic chip and the glass substrate were oxidized with an oxygen plasma treatment by a RIE machine to make the surfaces of the chip and the substrate hydrophilic to fill liquids into the side microchannels (100-μm width) in the device using capillary action. The micropillar in the central microchannel are used for positioning of an EB formed from miPSCs (Fig. 6.6a) and the micropillars with partial barrier structure (5-μm width) in the side microchannels are used as capillary stop valves that can prevent intrusion of liquids from the side microchannels into the central microchannel. To validate the performance of the device, solutions of two different BSA fluorescent conjugates (FITC and Texas Red tags) used as a model of ECM solutions were introduced into the side microchannels (Fig. 6.6b, c). The BSA solutions are flushed out by introducing PBS solution from the port of the central channel. After the removal process, spatially defined BSA-coated surfaces could be successfully formed in the device (Fig. 6.6d, e).

As a demonstration, stem cell cultures of miPSCs on the surfaces coated with two different ECM proteins, such as a recombinant human laminin (BioLamina) and a vitronectin (Lifetechnologies) was conducted in the devices. EBs (200 cells/EB) formed from Nanog-GFP miPSCs (iPS-MEF-Ng-20D-17 cell line)

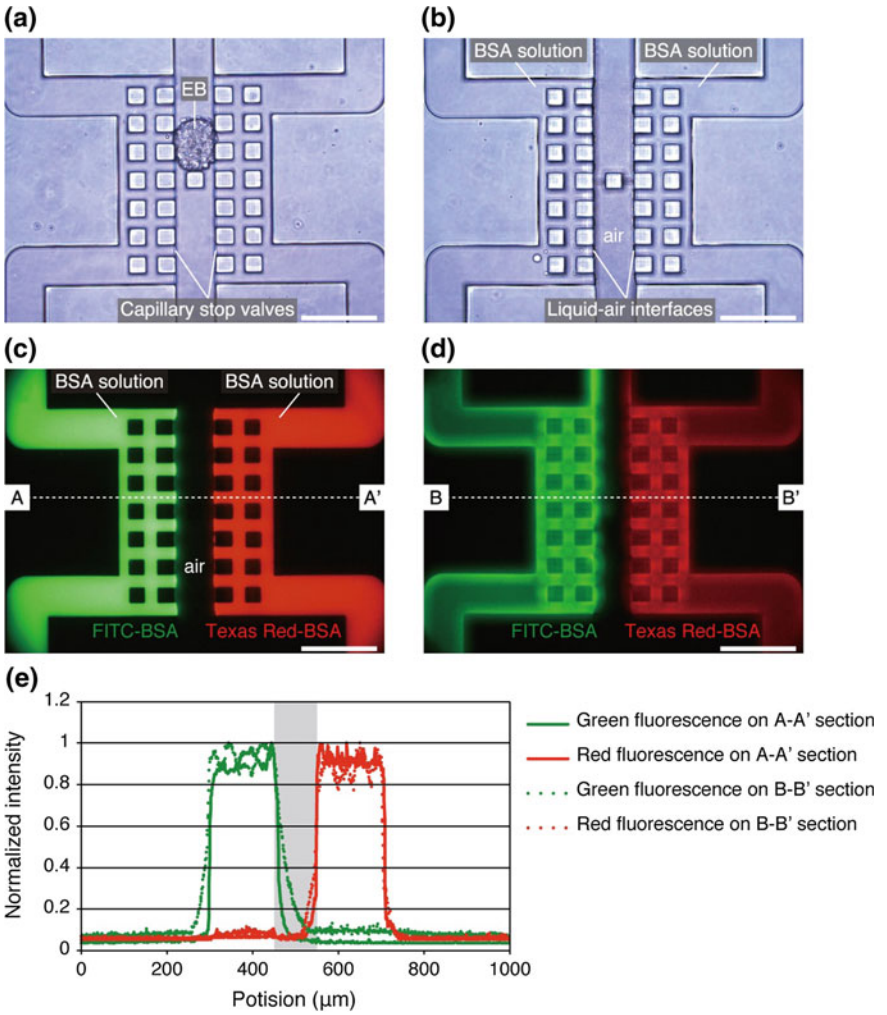

Fig. 6.6 Developed microfluidic device. **a** EB positioned in the central microchannel. **b** Liquid–air interfaces of two different fluorescent BSA (FITC and Texas Red tags) solutions formed by capillary stop valves. **c** Florescence image of (**b**). **d** Patterned BSA-coated surfaces after the removal of the fluorescent BSA solutions. **e** Profiles of *green* and *red* fluorescence on A–A′ section in (**c**) and B–B′ section on (**d**). The *gray-colored* are in the graph shows the region of the central microchannel in the device. All *scale bars* are 200 μm

were positioned in the central microchannel and cultured in the device with a defined serum-free medium (Millipore).

We preliminarily confirmed that the glass surface in the device is non-cell adhesive surface (data not shown). As shown in Fig. 6.7a, cell adhesions could not be observed on both sides with laminin-coated surfaces (as control culture),

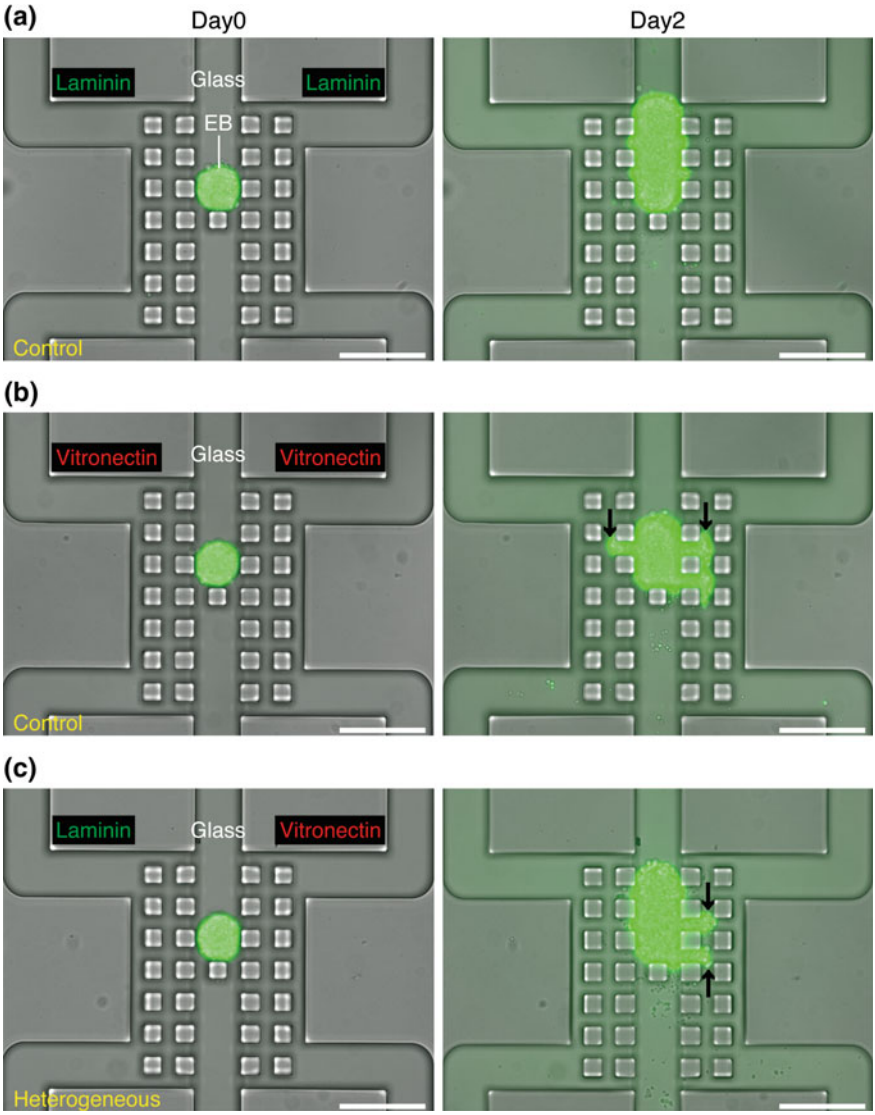

Fig. 6.7 Results of cell culture of EBs formed from Nanog-GFP miPSCs on both sides with laminin-coated surfaces as control culture (**a**), on both sides with vitronectin-coated surfaces as control culture (**b**) and on the laminin- and vitronectin-coated surfaces (**c**). Cell adhesive areas were observed only vitronectin-coated surfaces (indicated by *black-colored arrows* shown in (**b**, **c**). All *scale bars* are 200 μm

whereas the adhesions could be observed on both sides with vitronectin-coated surfaces (as a control culture, indicated by arrows in Fig. 6.7b). In the heterogeneous ECM-coated surfaces, cell adhesions could be observed only on the side of

virtonectin-coated surfaces (indicated by arrows in Fig. 6.7c). This result corresponds to the cell adhesion property of the laminin and vitronectin-coated surfaces shown in control cultures (Fig. 6.7a, b). Thus we conclude that cell adhesion property of the surface can be controlled by spatially defined heterogeneous coating of ECMs realized by the capillary stop valves in the developed device.

6.3 Capture and Analysis of Circulating Tumor Cells (CTCs)

Tumor cells shed from a primary tumor and circulating in peripheral blood is called circulating tumor cells [22] (CTCs). Despite the importance of CTCs for understanding the biological process of metastasis, and for predicting the response of anticancer treatment and disease progression, detection, and characterization of CTCs are still major technological challenges in the field of cancer research because CTCs are extremely rare and admixed with numerous blood cells (e.g., one CTC exists in billion normal blood cells) [23]. In this section, we focus on a trend of development of microfluidic devices for detection and analysis of CTCs and then report a microfluidic device to separate CTCs by combining cell size-based and immunoaffinity-based cell separation, and a microfluidic device with microwell array for CTC analyses at the single-cell level.

6.3.1 CTC Capture Device

Generally, there are two ways to separate CTCs from blood cells, one way utilizes cell size of CTCs that are bigger than blood cells [24] and the other way utilizes their specific surface antigen derived from epithelial cancer cells such as EpCAM [25] (epithelial cell adhesion molecule). Today, an automated processing system for immunomagnetic cell separation with anti-EpCAM antibody-coated magnetic beads is the only one apparatus that approved by U.S. Food and Drug Administration (FDA), however its capture efficiency is not enough ($\sim$80 %), and the captured CTCs are no longer viable [26].

Microfluidic technologies for CTC separation have recently been attracting enormous attentions and various microfluidic approaches to separate CTCs based on cell size [27] and immunoaffinity [28] were reported. However it is pointed out that variation of the expression level of EpCAM on CTCs surfaces and its cell size sometimes make capture efficiency low, however there are a few reports about the methods that take it into consideration [29]. Thus, we propose here a simple method to separate CTCs by utilizing both cell size and immunoaffinity as shown in Fig. 6.8. In the proposed method, a microfilter structure consists of antibody-coated surfaces that is used for CTC separation.

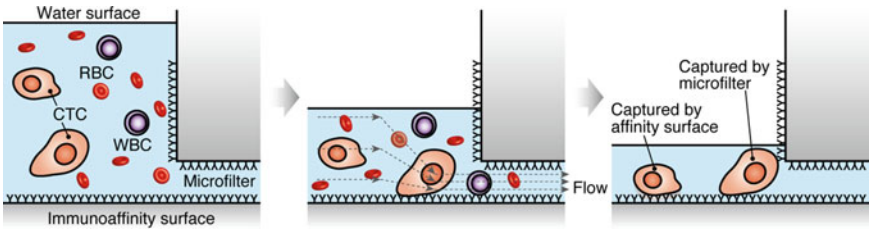

Fig. 6.8 Schematic illustration of proposed CTC separation method combining both cell size-based and immunoaffinity-based cell separation. RBC and WBC are abbreviation of red blood cell and white blood cell, respectively. By aspiration of blood containing CTCs via the microfilter structure coated with antibody, separation of CTCs is conducted

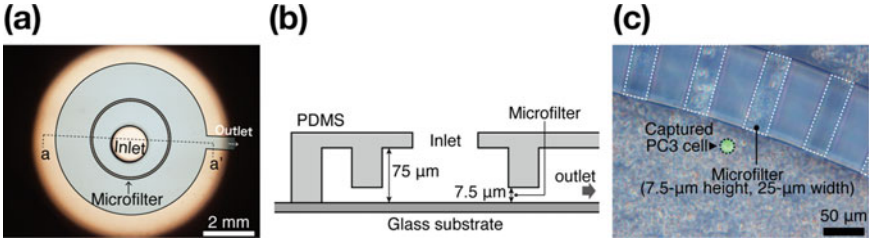

Fig. 6.9 A developed microfluidic device for CTC separation. **a** The microfluidic device consists of microfluidic chip made of PDMS and glass substrate. The surfaces of the microfilter structures (7.5-µm height and 25-µm width) are coated with antibody. The number of the microfilter is 128. **b** The a–a′ section in (**a**). **c** PC3 cell (prostate cancer cell line) separated from a blood sample in the device

To validate the feasibility of the proposed method, a microfluidic device was fabricated (Fig. 6.9a). It consists of a PDMS microfluidic chip and a glass substrate. The microfilters in the device has anti-EpCAM antibody (eBiosciences, Inc) surfaces (Fig. 6.9b). The height and width of the microfilter are 7.5 and 25 µm, respectively (Fig. 6.9b, c). A prostate cancer cell (PC3 cell) spiked into a blood sample was successfully captured by the device (Fig. 6.9c).

The effectiveness of antibody-coating on the microfilters for capture efficiency of CTCs was estimated using a PBS solution containing PC3 cells as a model of CTC at different flow rate conditions (Fig. 6.10a). The capture efficiency of PC3 cells was kept at around 100 % with anti-EpCAM antibody-coated surface independently of the present flow rate conditions, whereas the efficiency with Glass-PDMS surface (without antibody-coating) decreases depending on the increasing of flow rate. Thus effectiveness of the antibody-coating on the microfilters is validated. The influence of the separation process on the cell viability was evaluated using a live-cell stain (Calcein-AM) and dead-cell stain (PI). The viability before and after separation process are 97.2 ± 0.1 % and 94.7 ± 2.4 %, respectively, and this result shows the separation process in the device does not cause considerable loss of

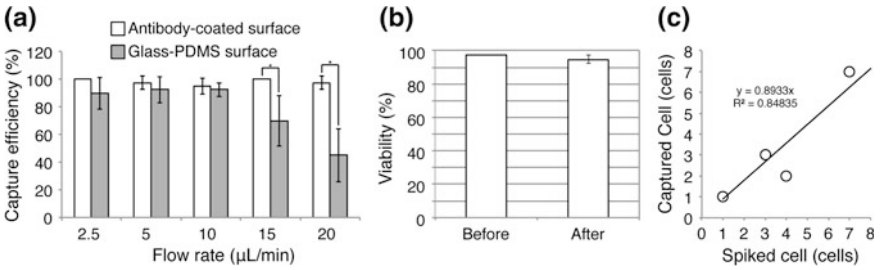

Fig. 6.10 Performance evaluation of the device. **a** The capture efficiency of PC3 cells using the developed device with the microfilters coated with or without antibody at the different flow rate conditions ($N = 4$, $^*p < 0.05$). **b** The effect on cell viability by the separation process of PC3 cells in PBS solution on the device ($N = 4$, flow rare = 20 μL/min). The viability was evaluated using a live-cell stain (Calcein-AM) and a dead-cell stain (PI). **c** Result of the capturing PC3 cells spiked in blood samples. The blood samples containing known number of PC3 cells were prepared by mixing 10 μL of whole blood with 10 μL of PBS containing EDTA

cell viability. The result of capture efficiency of PC3 cells spiked into blood samples is shown in Fig. 6.10c. The capture efficiency is about 89 % and thus we conclude that the developed device can be available for CTC separation from blood sample.

6.3.2 Single CTC Analysis Device

6.3.2.1 CTC Analysis at the Single-Cell Level

Counting the number of CTCs in peripheral blood makes it possible to monitor therapeutic effect and prognosis [30]. However, little is known about the CTCs such as mechanism of metastasis, their functional properties, etc. Since understanding the diversity of tumor is an important clue for cancer therapy [31], revealing CTCs' biological heterogeneity at the single-cell level has been highly required to suppress heterogeneous metastasis. In recent years, it has become possible to elucidate heterogeneity of single cell by the development of analytical techniques with a focus on flow cytometry [32] and microfluidic device [33, 34]. However, the method is not suitable for CTC analysis at the single-cell level because the existence of CTCs is extremely rare as described above (1 in 10^9 blood cells) and mixed with normal blood components. Microfluidic devices are suitable for sorting and analyzing rare cells because one can efficiently handle complex cellular fluids. Several groups have been developing microfluidic devices to isolate CTCs from normal blood components, for example, cell trapping using antibody-coated microposts, size-based separation by a microfilter, etc. [35]. Although previous methods using microfluidic devices successfully demonstrated separation of CTCs, the separated cells have to be collected for the downstream analysis.

To analyze individual CTCs, sorted cells should be arrayed at the single-cell level. Hydrodynamic single-cell arraying methods are widely used for the observation of cellular response [36]. The device, utilizing microfluidic channels, has advantages on the fluorescent array and sample preparation, which are manual and intensive operations of incubation, centrifugation, and resuspension in conventional techniques. The practical problem of the system is that the trapped cell can be easily deformed due to the hydrodynamic pressure and the microfluidic channels can be easily get clogged because the dimension of the channel is comparable with that of single cells. Microwell array is also common method for single-cell arraying without damage on the cells [37]. Although microwell arrays show good efficiency for single-cell arraying, a drawback of the system lies in the difficulty to change reagents for various chemical stimuli. Moreover, the gravity, usually used for trapping single mammalian cells, cannot attract a single cell without any loss of samples; the cell recovery rate is quite low.

In order to overcome the drawbacks of the microwell array platform, we have developed a new method for single-cell analysis using electroactive microwell array [38] (EMA) and demonstrated single cancer cell analysis using the device [39]. EMA contains patterned thin-film electrodes on the bottom of each microwell for single-cell trapping with dielectrophoresis (DEP). Since DEP force provides fast, active and stable trapping, we could efficiently trap single cells suspended in sample solution, which is quite important for the CTC analysis. Moreover, trapped cells can be stably held in the microwell by DEP, allowing rapid exchange of reagents with an extremely small sample volume (10 μL). These features of the EMA device facilitate high-throughput biochemical assays for arrayed single cells. We demonstrated the feasibility of our approaches by carrying out two kinds of assays; cancer cell identification by immunostaining and viability/apoptosis assay. The whole process for assays requires just sequential injection of cell suspension and reagents for the analyses without complicated valve or tubing systems.

6.3.2.2 Electroactive Microwell Array

Dielectrophoresis

The time averaged DEP force, $\boldsymbol{F}_{\mathrm{DEP}}$, acting on a spherical particle of radius, a, is approximated by

$$\boldsymbol{F}_{\mathrm{DEP}} = 2\pi\varepsilon_{\mathrm{e}} a^3 \mathrm{Re}[K(2\pi f)]\nabla \boldsymbol{E}^2 \tag{6.1}$$

$$K(2\pi f) = \frac{\varepsilon^*_{\mathrm{cell}} - \varepsilon^*_{\mathrm{e}}}{\varepsilon^*_{\mathrm{cell}} + 2\varepsilon^*_{\mathrm{e}}}, \tag{6.2}$$

where ε_{e}, f and $\boldsymbol{E}$ are permittivity of the external medium, frequency of the applied electric field and the applied electric field strength, respectively, and $\varepsilon^*_{\mathrm{cell}} = \varepsilon_{\mathrm{cell}} - j\frac{\sigma_{\mathrm{cell}}}{2\pi f}$ is the complex electrical permittivity of the cell (σ is electrical

conductivity and $j = \sqrt{-1}$). The direction of DEP force depends on the sign of the Clausius–Mossotti (CM) factor given by the real part of $K(2\pi f)$, which can be controlled by adjusting the conductivity of the external medium and the frequency of the applied electric fields. When the CM factor is bigger than 0, the particle will be attracted toward the strong field, positive DEP (pDEP). In the meanwhile, when CM factor is smaller than 0, the particle will be directed away from the strong field, negative DEP (nDEP). Positive DEP is widely used to attract the particle to the edge of the electrodes, where the electric field strength is highly localized.

The dielectrophoretic velocity $\boldsymbol{V}_{\mathrm{DEP}}$ of the particles results from the equilibrium between $\boldsymbol{F}_{\mathrm{DEP}}$ and the viscous drag force, $\boldsymbol{F}_{\mathrm{drag}} = 6\pi\eta a\boldsymbol{V}_{\mathrm{DEP}}$, where η is a fluid viscosity, where $\boldsymbol{V}_{\mathrm{DEP}}$ is given by

$$\boldsymbol{V}_{\mathrm{DEP}} = \frac{2\pi\varepsilon_{\mathrm{e}}a^3\mathrm{Re}[K(2\pi f)]\nabla\boldsymbol{E}^2}{6\pi\eta a}. \tag{6.3}$$

Since $\boldsymbol{V}_{\mathrm{DEP}}$ is proportional to real part of CM factor, the real part of CM factor should be controlled for the efficient single-cell manipulation. Strong pDEP force can be induced to the typical mammalian cells with high frequency (several megahertz) of the applied electric fields with low conductivity (several tenth of millisiemens per meter) of the medium. Moreover, different sizes of the cells can be manipulated with the different force since the $\boldsymbol{V}_{\mathrm{DEP}}$ is proportional to square radius of a target cell, which would allow us to selectively manipulate based on the size of the target cells.

Design of the Electroactive Microwell Array

In the EMA device, ITO electrodes are patterned on a glass substrate to attract single cells using pDEP (Fig. 6.11a). The through-hole structure, fabricated with the photoresist, is aligned with the interdigitated ITO electrodes in order to locate a pair of electrodes (anode and cathode) at the bottom of each microwell. Since the photoresist is a good insulation material, the electric fields are well blocked except for the hole. Since the direction of the gradient of the electric fields is toward the inside of the microwell, the cells above the microwell will be pulled down into the bottom of the microwell by the pDEP force. The diameter of the hole is slightly bigger than that of the target cells, which physically restrict the available space for cells during trapping by DEP.

The EMA is bonded to a patterned PDMS membrane to form a microfluidic channel (Fig. 6.11b). The suspension of target cells and reagents for the subsequent analyses are dripped on an access port using a pipet and delivered into the microfluidic channel using laminar flow induced by the negative pressure. The relatively large contact angle of the aqueous solutions on the PDMS surface allows us to keep the position of the drop of reagents at the access ports. This design facilitates rapid exchange of reagents with quite small volumes (10 μL) since additional reagent is easily added into the access port and the dead volume is quite small.

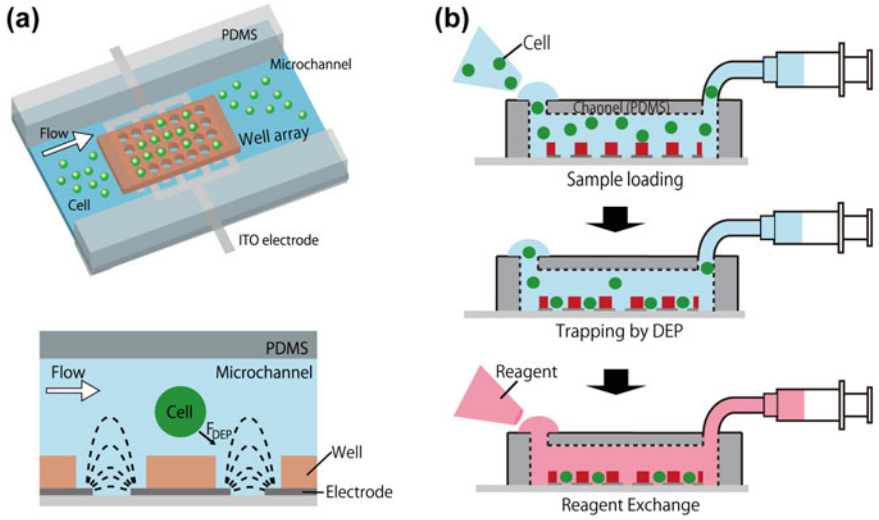

Fig. 6.11 Concept of single CTC analysis using EMA [39]. **a** Configuration of the device. Positive DEP force attracts the cell to the edge of the electrodes at the bottom of the well. **b** Cell trapping and reagent exchange for CTC analysis. Sorted cell suspension is introduced into the microfluidic channel on the device and cells are trapped into the microwells using pDEP. After cell trapping, cell analysis is performed by introducing required reagents into the microchannel

Device Fabrication

The glass substrate was coated with ITO, and the shape of the electrodes were patterned using positive photoresist, followed by etching of ITO using 0.2 M $FeCl_3$ + 6 M HCl solution for 30 min at room temperature. The substrate was cleaned and rinsed to remove the photoresist remaining on the ITO using acetones and isopropyl alcohol, respectively. To make a microwell array on the patterned electrodes, the negative photoresist was spin-coated on the electrodes, and a chromium photo-mask patterned for the microwell array was aligned with the patterned ITO electrodes. The photoresist was exposed to ultraviolet light through the photo-mask, followed by development and rinsing.

The PDMS fluidic chip is fabricated through the standard replica molding process. The negative photoresist, which serves as a mold, was patterned on a silicon wafer. The mold was thoroughly cleaned with isopropanol and deionized water. PDMS was mixed with curing agent (10:1 mass ratio) and poured over the mold. Then, the PDMS was baked at 75 °C for 2 h, followed by peeling off the polymerized PDMS from the mold. Holes as access ports to the flow channel were punched out.

In order to bond the microwell array and PDMS fluidic chip, they were exposed to O_2 plasma to activate opposing surfaces using reactive ion etching machine. Also O_2 plasma treatment makes the microwell structures and the PDMS channel hydrophilic, which ensures easy injection of aqueous reagents into the channel and the microwells.

6.3.2.3 Single-Cell Analyses Using EMA

Single-Cell Trapping

The feasibility of the single-cell arraying with EMA was demonstrated by trapping single U937 cells [38]. The U937 cells, introduced into the PDMS microfluidic channel, were attracted into the edge of the electrodes of the EMA with pDEP by applying 2 Vp-p sinusoidal electric potential at 1 MHz. The EMA was gradually occupied by single U937 cells. Since the size of the microwells of EMA is comparable with that of single U937 cells, the device allows efficient single-cell trapping. After 3 min almost all the wells contained single U937 cells (Fig. 6.12a).

The single-cell trapping efficiency can be affected by several parameters such as diameter of the microwell, flow rate of the cell supply solution, and DEP force.

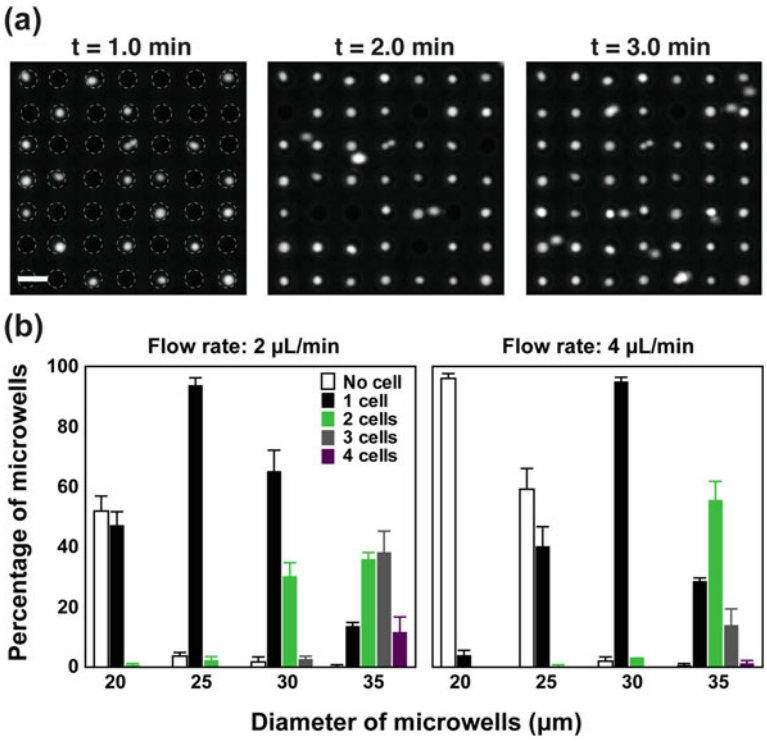

Fig. 6.12 **a** The time-lapse images of 25-μm microwell array during U937 cell trapping by applying 2 Vp-p at 1 MHz sinusoidal AC voltage to the electrodes at $t = 0$ min. *White dotted circles* indicate the positions of microwells. Cells are continuously introduced into the microfluidic channel with the flow late at 2 μL/min. With DEP, single cells gradually occupy microwells. *Scale bar* is 50 μm. **b** The ratio of microwells is plotted versus the diameter of microwells for the occupancy of the cell. The sinusoidal electric potential is applied for 3 min with the flow rate at 2 and 4 μL/min. (Reprinted with modifications from Ref. [38], where sub labels are removed from the original figure and the flow rate for each histogram is added.)

Figure 6.12b shows the rate of cell occupancy plotted versus the diameter of the microwells for flow rate at 2 or 4 μL/min. Since large diameter of microwell allows more available space for cell occupancy, the percentage of microwells containing two or three cells increased with the diameter of the microwells, where the 25-μm microwell shows good trapping efficiency for single cells (about 95 %) for the flow rate at 2 μL/min. Meanwhile, 30-μm microwell shows best result for the flow rate at 4 μL/min because higher velocity shortened exposure time of the electric fields to the cells flowing over the microwells. The two histograms in Fig. 6.12b illustrate how we can trap single cells in different size of microwells by controlling experimental conditions.

On-chip Analyses

The cells trapped in EMA can be easily identified and analyzed by labeling the cells using specific reagents. Since the microfluidic EMA device allows rapid exchange of reagents and stable trapping of the single cells, one can efficiently apply various analytical reagents to the trapped cells. By observing the response of the trapped cells to the reagents, cancer cells can be identified and analyzed at the single-cell level. For the demonstration of the feasibility of the on-chip CTC analyses, we carried out immunostaining and viability and apoptosis assay on a microfluidic chip using cultured cancer cells.

To identify the cells trapped in the EMA, immunostaining was carried out by applying fluorescently labeled antibodies to the cells. For the demonstration, two different cell lines including U937 cells (a model of white blood cell, WBC) and DU145 cells (a model of CTC) were trapped in EMA and identified with immunostaining.

The cell suspension of U937 and DU145 was introduced into the EMA device and trapped using pDEP. The cells were fixed with 4 % paraformaldehyde and permeabilized with 0.2 % Triton X-100. Cells were stained with Hoechst33342 for DNA, with FITC (fluorescein isothiocyanate) for epithelial cells, and with PE (phycoerythrin) for leukocytes. The trapped cells were successfully stained with blue for DNAs, green for epithelial cells, and red for leukocyte cells (Fig. 6.13a). In this way, identification of cancer cells and WBCs can be done only by immunostaining operation on the EMA device.

We investigated the viability of trapped cancer cells to detect and selectively analyze viable cells that could be involved in metastasis. Since almost all of the cells in the blood are killed by cytotoxic cells such as T-cells, etc., and dead due to the anoikis or the damage caused by shear stress, it is highly required to identify viable cells among a population of cells for further analysis. To check the viability of cancer cell, DU145 cells were trapped into the microwells and cultured in the device by introducing culture medium. Trapped cells were exposed to Annexin V Alexa Fluor 488 at room temperature in the dark room for 30 min followed by exchanging the reagents into mixed reagents of Annexin binding buffer, Propidium Iodide, and Calcein blue for 10 min. Viable cells were stained with calcein, and dead cells were stained annexin or PI. Almost all of the trapped cells (85 %) emit

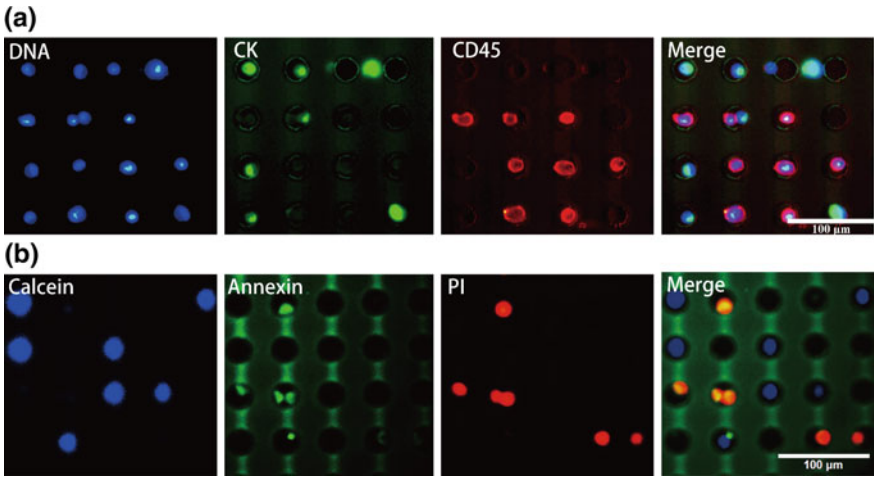

Fig. 6.13 On-chip analyses of single cancer cells. **a** Cancer cell identification by immunostaining. Trapped DU145 cells and U937 cells stained with Hoechst33342 (*blue*), Anti-cytokeratin antibody (*green*) and Anti-CD45 antibody (*red*). Merged image identifies DU145 cells as a model of CTC (*blue* + *green*). **b** Viability and apoptosis assay. Annexin V (*green*) stains apoptotic cell, PI (*red*) stains dead cell and Calcein (*blue*) stains viable cells. Merged image identify both apoptotic and dead cell (*green* + *red*). Images of cells trapped in the microwells after 6 h of incubation

blue fluorescence, indicating that the cells are viable even after 6 h of incubation on the device (Fig. 6.13b).

6.4 Concluding Remarks

Microfluidic approaches enable us to control stem cell differentiation by the spatial distribution of soluble factors and/or patterned surfaces treated with specific ECMs. The approaches could also be applied to a new domain of biological analysis on the rare cells for minimally invasive cancer diagnostics. This could be extended even to the multicomponent analysis at the single-cell level. Although there should be the conventional and routine methods for stem cell biology and medical diagnostics, the methods presented here could become one of the new ways to improve or to expand the potentiality of engineered biomedical systems based on micro- and nanoscale technologies that would be of help in future medical and healthcare practices.

Acknowledgments The authors are grateful to their collaborators; Dr. Kiyotaka Shiba at Cancer Research Foundation (Tokyo, Japan), Dr. Hidenori Akutsu at National Center for Child Health and Development (Tokyo, Japan) for their kind help, and fruitful discussions.

References

1. M.A. Lancaster et al., Cerebral organoids model human brain development and microcephaly. Nature **501**, 373–379 (2013). doi:10.1038/nature12517
2. M. Eiraku et al., Self-organizing optic-cup morphogenesis in three-dimensional culture. Nature **472**, 51–56 (2011). doi:10.1038/nature09941
3. H.L. Ashe, J. Briscoe, The interpretation of morphogen gradients. Development **133**, 385–394 (2006). doi:10.1242/dev.02238
4. J.B. Gurdon, P.Y. Bourillot, Morphogen gradient interpretation. Nature **413**, 797–803 (2001). doi:10.1038/35101500
5. D. Irimia et al., Microfluidic system for measuring neutrophil migratory responses to fast switches of chemical gradients. Lab Chip **6**, 191–198 (2006). doi:10.1039/b511877h
6. V.V. Abhyankar, M.A. Lokuta, A. Huttenlocher, D.J. Beebe, Characterization of a membrane-based gradient generator for use in cell-signaling studies. Lab Chip **6**, 389–393 (2006). doi:10.1039/b514133h
7. J. Diao et al., A three-channel microfluidic device for generating static linear gradients and its application to the quantitative analysis of bacterial chemotaxis. Lab Chip **6**, 381–388 (2006). doi:10.1039/b511958h
8. H. Mao, P.S. Cremer, M.D. Manson, A sensitive, versatile microfluidic assay for bacterial chemotaxis. Proc. Natl. Acad. Sci. USA **100**, 5449–5454 (2003). doi:10.1073/pnas.0931258100
9. B.G. Chung et al., Human neural stem cell growth and differentiation in a gradient-generating microfluidic device. Lab Chip **5**, 401–406 (2005). doi:10.1039/b417651k
10. Y. Tanaka, M. Yamato, T. Okano, T. Kitamori, K. Sato, Evaluation of effects of shear stress on hepatocytes by a microchip-based system. Meas. Sci. Technol. **17**, 3167–3170 (2006). doi:10.1088/0957-0233/17/12/S08
11. S.M. Dang, M. Kyba, R. Perlingeiro, G.Q. Daley, P.W. Zandstra, Efficiency of embryoid body formation and hematopoietic development from embryonic stem cells in different culture systems. Biotechnol. Bioeng. **78**, 442–453 (2002). doi:10.1002/Bit.10220
12. L. Larue et al., A role for cadherins in tissue formation. Development **122**, 3185–3194 (1996)
13. G. Keller, Embryonic stem cell differentiation: emergence of a new era in biology and medicine. Genes Dev. **19**, 1129–1155 (2005). doi:10.1101/Gad.1303605
14. W.T. Fung, A. Beyzavi, P. Abgrall, N.T. Nguyen, H.Y. Li, Microfluidic platform for controlling the differentiation of embryoid bodies. Lab Chip **9**, 2591–2595 (2009). doi:10.1039/b903753e
15. J. Kawada, H. Kimura, H. Akutsu, Y. Sakai, T. Fujii, Spatiotemporally controlled delivery of soluble factors for stem cell differentiation. Lab Chip **12**, 4508–4515 (2012). doi:10.1039/c2lc40268h
16. F.M. Watt, B.L. Hogan, Out of Eden: stem cells and their niches. Science **287**, 1427–1430 (2000)
17. C.S. Chen, M. Mrksich, S. Huang, G.M. Whitesides, D.E. Ingber, Geometric control of cell life and death. Science **276**, 1425–1428 (1997)
18. E. Delamarche, A. Bernard, H. Schmid, B. Michel, H. Biebuyck, Patterned delivery of immunoglobulins to surfaces using microfluidic networks. Science **276**, 779–781 (1997)
19. S.A. Ruiz, C.S. Chen, Microcontact printing: a tool to pattern. Soft Matter **3**, 168–177 (2007). doi:10.1039/B613349e
20. A. Tourovskaia, X. Figueroa-Masot, A. Folch, Long-term microfluidic cultures of myotube microarrays for high-throughput focal stimulation. Nat. Protoc. **1**, 1092–1104 (2006). doi:10.1038/nprot.2006.123
21. K. Ono, S. Kaneda, T. Fujii, Single-step CE for miniaturized and easy-to-use system. Electrophoresis **34**, 903–910 (2013). doi:10.1002/elps.201200365

22. D. Wirtz, K. Konstantopoulos, P.C. Searson, The physics of cancer: the role of physical interactions and mechanical forces in metastasis. Nat. Rev. Cancer **11**, 512–522 (2011). doi:10.1038/nrc3080
23. M. Yu, S. Stott, M. Toner, S. Maheswaran, D.A. Haber, Circulating tumor cells: approaches to isolation and characterization. J. Cell Biol. **192**, 373–382 (2011). doi:10.1083/jcb.201010021
24. G. Vona et al., Isolation by size of epithelial tumor cells: a new method for the immunomorphological and molecular characterization of circulatingtumor cells. Am. J. Pathol. **156**, 57–63 (2000). doi:10.1016/S0002-9440(10)64706-2
25. W.J. Allard et al., Tumor cells circulate in the peripheral blood of all major carcinomas but not in healthy subjects or patients with nonmalignant diseases. Clin. Cancer Res. **10**, 6897–6904 (2004). doi:10.1158/1078-0432.CCR-04-0378
26. P. Li, Z.S. Stratton, M. Dao, J. Ritz, T.J. Huang, Probing circulating tumor cells in microfluidics. Lab Chip **13**, 602–609 (2013). doi:10.1039/c2lc90148j
27. S. Zheng et al., 3D microfilter device for viable circulating tumor cell (CTC) enrichment from blood. Biomed. Microdevices **13**, 203–213 (2011). doi:10.1007/s10544-010-9485-3
28. S.L. Stott et al., Isolation of circulating tumor cells using a microvortex-generating herringbone-chip. Proc. Natl. Acad. Sci. USA **107**, 18392–18397 (2010). doi:10.1073/pnas.1012539107
29. Y. Dong et al., Microfluidics and circulating tumor cells. J. Mol. Diagn. **15**, 149–157 (2013). doi:10.1016/J.Jmoldx.2012.09.004
30. J.S. de Bono et al., Circulating tumor cells predict survival benefit from treatment in metastatic castration-resistant prostate cancer. Clin. Cancer Res. **14**, 6302–6309 (2008). doi:10.1158/1078-0432.CCR-08-0872
31. S. Bhatia, J.V. Frangioni, R.M. Hoffman, A.J. Iafrate, K. Polyak, The challenges posed by cancer heterogeneity. Nat. Biotechnol. **30**, 604–610 (2012). doi:10.1038/nbt.2294
32. S.C. Bendall, G.P. Nolan, From single cells to deep phenotypes in cancer. Nat. Biotechnol. **30**, 639–647 (2012). doi:10.1038/nbt.2283
33. U. Dharmasiri et al., Highly efficient capture and enumeration of low abundance prostate cancer cells using prostate-specific membrane antigen aptamers immobilized to a polymeric microfluidic device. Electrophoresis **30**, 3289–3300 (2009). doi:10.1002/elps.200900141
34. E. Ozkumur et al., Inertial focusing for tumor antigen-dependent and -independent sorting of rare circulating tumor cells. Sci. Transl. Med. **5**, 179ra147 (2013). doi:10.1126/scitranslmed.3005616
35. Y. Chen et al., Rare cell isolation and analysis in microfluidics. Lab Chip **14**, 626–645 (2014). doi:10.1039/c3lc90136j
36. D. Di Carlo, L.Y. Wu, L.P. Lee, Dynamic single cell culture array. Lab Chip **6**, 1445–1449 (2006). doi:10.1039/b605937f
37. J.R. Rettig, A. Folch, Large-scale single-cell trapping and imaging using microwell arrays. Anal. Chem. **77**, 5628–5634 (2005). doi:10.1021/ac0505977
38. S.H. Kim, T. Yamamoto, D. Fourmy, T. Fujii, Electroactive microwell arrays for highly efficient single-cell trapping and analysis. Small **7**, 3239–3247 (2011). doi:10.1002/smll.201101028
39. M. Kobayashi, S.H. Kim, H. Nakamura, S. Kaneda, T. Fujii, Cancer cell analyses at the single cell-level using electroactive microwell array device. PLoS One **10**, e0139980 (2015). doi:10.1371/journal.pone.0139980.g001

Chapter 7
Digital Bioassay with Femtoliter Reactor Array

Takao Ono and Hiroyuki Noji

Abstract Number of a molecule is discrete by its nature. Therefore, upon better detection sensitivity of analytical methods approaching the single-molecule level, the measured concentration and number of analytes show intrinsic discreteness. An emerging analytical method that makes use of this intrinsic discreteness is digital counting. When an analyte solution is partitioned into many small reaction compartments, such that each molecule is individually encapsulated into a compartment, the analyte quantification is inevitably digitized; each compartment contains none or one molecule of analyte. When a solution of enzyme or enzyme-conjugated molecule is partitioned into such small reactors with fluorogenic substrate, one can count the number of the molecule as that of fluorescent reactors under an optical microscope. We refer to this strategy as "digital counting." One of the most successful examples of digital counting is digital ELISA, in which target molecules are individually encapsulated in a water-in-oil droplet after bound to enzyme-conjugated antibody. Although the chemistry of digital ELISA; antibody and enzyme is common to conventional ELISA, the detection sensitivity of digital ELISA is higher than that of conventional ELISA by 4–6 orders of magnitude. In this review, we introduce recent achievements in digital ELISA and similar methods.

Keywords ELISA · Lab-on-a-chip · Biochemical · Single-molecule · Microreactor

7.1 Introduction

An emerging trend in biochemical analysis is digitization. The word "digitization" here does not refer to automatization of instruments nor data analysis. Rather, we use it to describe the conversion of target objects into a temporal and/or spatial

T. Ono · H. Noji (✉)
Department of Applied Chemistry, School of Engineering, The University of Tokyo, 7-3-1 Hongo, Bunkyo-ku, Tokyo 113-8656, Japan
e-mail: hnoji@appchem.t.u-tokyo.ac.jp

J. Sone and S. Tsuji (eds.), *Intelligent Nanosystems for Energy, Information and Biological Technologies*, DOI 10.1007/978-4-431-56429-4_7

distribution of quantized signals. Biochemical substances and their reactions are generally regarded as continuous, but in reality they show discrete and quantized behavior at the single-molecule level. A classic example is the single channel recording reported in 1976 [1]. In this experiment, channel current was quantized by the opening or closing of a single membrane ion channel. In the late twentieth century, single-molecule imaging in aqueous solution demonstrated that the presence or absence of a fluorescence signal correlated with the respective association and dissociation of a fluorescently labeled ligand to a single enzyme molecule [2]. We have conducted single-molecule imaging of rotation of F_1-ATPase and demonstrated that discrete 120° stepping rotations are coupled with the single turnover of ATP hydrolysis, where the angular velocity represents on and off, or digital, behavior [3]. These reports are just a few examples that show how single-molecule resolution has revealed an intrinsic discreteness in molecular behavior. At the beginning of this century, the concept of digitalization was extended to the quantification of enzymatic biomolecules by the use of micron-sized (fL volume) reactor chamber systems (hereafter simply called, "reactor chamber"). Successful examples of this approach include digital PCR and digital ELISA [4–6]. In these assays, a sample solution is partitioned into a massive number of reactor chambers and then the number of chambers that show signs of DNA amplification (for digital PCR) or enzymatic activity (for digital ELISA) are counted. We refer to this strategy as "digital counting." Digital counting requires handling micron-sized aqueous solution, which is now possible because of "Lab-on-a-chip" technology.

7.2 Lab-on-a-Chip Technology for Biochemical Analysis

Lab-on-a-chip (LOC), also called micro total analysis system (μTAS) or biodevice, has become an invaluable instrument for biochemical analysis. After the first LOC report by Terry and coworkers in 1979 [7], Manz et al. [8] provided a comprehensive review on the concept of LOC technology in the early stage of the field. Over the following quarter-century, LOC technology has provided novel methods for cell biology, molecular biology, and other research fields [9]. Essential to LOC technology is miniaturization, which has benefited from gains in micro/nanofabrication technologies of the semiconductor industry. In the past half century, advancement in semiconductor devices have been driven by a sophistication in highly precise and efficient fabrication such as photolithography and plasma etching. To handle minute sample solutions, a variety of microstructures, including not only microreactors and capillaries, but also micropumps and microvalves, are fabricated onto a chip [10–12]. For easy microfabrication and replication of the device structure, simple fabrication methods, such as molding using silicone rubber poly(dimethylsiloxane) (PDMS), have been developed [13].

What advantageous features does LOC technology bring to biochemistry? These devices allow for the precise control of those factors that regulate microscale

biological phenomena. Such factors include laminar flow, electroosmotic flow, the diffusion-limited step, and temperature [8]. Moreover, miniaturization enables a small amount or small size of sample to be treated in parallel [14–16], thus enhancing the throughput of the assay. High-throughput analysis using LOC has proven extremely useful in combinatorial chemistry [17] and directed evolution [18], which require huge libraries, and for epigenome analysis [19] and proteome analysis [20], which exemplify a new trend of biology. Another important feature of LOC is that it reduces the sample consumption, device size, and device cost. These features enable it to be applied to point-of-care testing (POCT) for personalized medicine at home or clinical use in developing countries [21].

Miniaturization especially has important implications for single-molecule assays. The size reduction of the reaction volume magnifies the concentration change of analyte molecules. For enzymatic reactions, single-molecule enzymatic assays can be done using reactor chambers. For example, when two identical enzymes that have a turnover rate of 10 s^{-1} are separately encapsulated into 1 μL (1 mm^3) or 1 fL (1 μm^3) reactors, the ensuing reaction product reaches 10 fM and 10 μM, respectively, after 10 min incubation. Note that volume time concentration gives a constant value (quantity of reaction product molecule). While 10 fM is almost undetectable, 10 μM is reliably detectable. Thus, the signal/background ratio is improved to a level that permits the digital counting of enzyme molecules. Large-scale integration of the reactor chambers increases the binary digit (bit) of the measurement, which further improves the sensitivity and dynamic range. Accordingly, we have developed reactor chamber devices for biochemical analysis at the single-molecule level.

7.3 Femtoliter Droplet Array and Its Application to Single-Molecule Measurements

The Nobel Prize in Chemistry 2014 was awarded to S. W. Hell, E. Betzig, and W. E. Moerner for the development of super-resolved fluorescence microscopy. Among the three laureates, Betzig and Moerner laid the foundation for photoactivated localization microscopy (PALM) using single-molecule fluorescence imaging [22, 23]. Prior to the development of PALM, they separately demonstrated direct optical detection of single-molecules circa 1990 [24, 25]. In contrast, single-molecule detection by enzymatic products was realized using microdroplets as early as the 1960s [26]. This fact underscores the easiness and robustness of single-molecule detection using microdroplets. Nevertheless, this method had not been utilized for digital counting due to heterogeneities in droplet size and shape until LOC technology, which has enabled the generation of monodisperse microdroplets [27, 28]. Recently, such monodisperce microdroplets were employed for digital PCR [29]. For parallel and successive imaging of a massive number of microdroplets, a microdroplet array immobilized on a substrate has been used. Using reactor chamber, we have explored various techniques for the measurement of single

biomolecules (Fig. 7.1). As an early example, we encapsulated single F_1-ATPase into a reactor chamber and rotated it clockwise using magnetic tweezers. After release from the tweezers, the F_1-ATPase rotated counterclockwise, indicating that ATP accumulated in the reactor chamber and was utilized for the autonomous counterclockwise rotation. From the counterclockwise rotation speed, it was revealed that ATP synthesis by F_1-ATPase was efficiently coupled with the rotating motion [30]. We also demonstrated digital counting for β-galactosidase (β-gal),

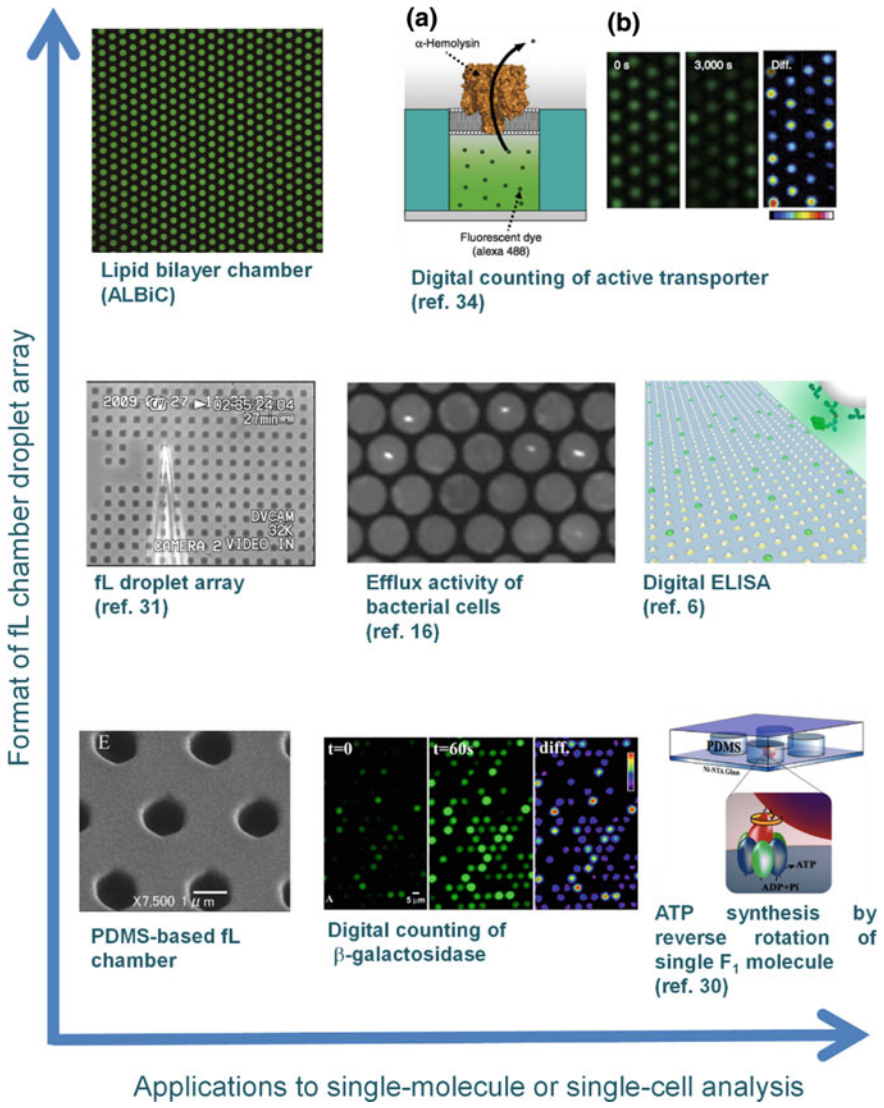

Fig. 7.1 Schematic illustration of our recent achievements using reactor chambers

which catalyzes hydrolysis of a fluorogenic substrate; fluorescein di-β-D-galactopyranoside (FDG) into fluorescein [31]. Here, the average number of β-gal encapsulated into single reactor chamber was determined from the β-gal concentration and chamber volume. When several pM of β-gal was distributed into the reactor chambers, each chamber randomly showed fluorescence and the ratio of fluorescent chambers increased linearly with β-gal concentration. Additionally, the rate of the fluorescence increase took discretized values of chambers. Thus, the reactor chamber enables measurement of very small, gradual changes in single biomolecules. This advantageous feature of reactor chamber was utilized for efflux activity measurement of single bacterial cell [16].

7.4 Digital ELISA

Enzyme-linked immunosorbent assay (ELISA) is one of the most widely used methods for diagnostic assays. ELISA that captures a particular target molecule via specific antigen-antibody interaction can detect the target molecule even in a mixture of biomolecules. In a typical procedure of sandwich ELISA, one of the most common types of ELISA, the minimum constituents of assay mixture are; capture antibody that is immobilized on a solid surface, such as a plastic plate or plastic beads, detection antibody that is conjugated to enzyme as a reporter, and reaction substrate for the conjugated enzyme that produces reaction product molecule with different color (colorimetric assay) or fluorescence (fluorogenic assay) from the reaction substrate. The target molecules are at first captured on the capture antibody and then subject to reaction with detection antibody to form the sandwich structure; antibody-antigen-antibody. The quantity of the captured target molecule is determined from the enzymatic activity.

ELISA is a remarkable method, as it can easily obtain high sensitivity and specificity and is widely used in biochemistry and medical studies. However, its sensitivity remains insufficient for the detection of many important biological substances such as the influenza virus in the early phase of infection and biomarkers in early cancer stages. In digital ELISA [4, 6], extremely high sensitivity is achieved by the use of femtoliter reactor chambers. Figure 7.2 shows the schematic image of digital ELISA from Ref. 7, where antigen molecules are reacted with capture antibodies immobilized on microbeads. Because the excess amount of microbeads are mixed with antigen molecules, each microbead carries none or one antigen molecule. After reacted with the detection antibody that is conjugated with β-galactosidase (β-gal), the beads are individually encapsulated in a reactor chamber with the aforementioned fluorogenic substrate of β-gal, FDG. After incubation for a few tens of minutes, some chambers emit distinctive fluorescent signal while the others remain dark, giving clear bimodal peaks in fluorescent histogram of chambers. Thus, when set a threshold to discriminate the fluorescent and nonfluorescent chamber, one can readily count the number of trapped antigen molecules as the number of fluorescent chamber. The probability that a reactor chamber encapsulates two or

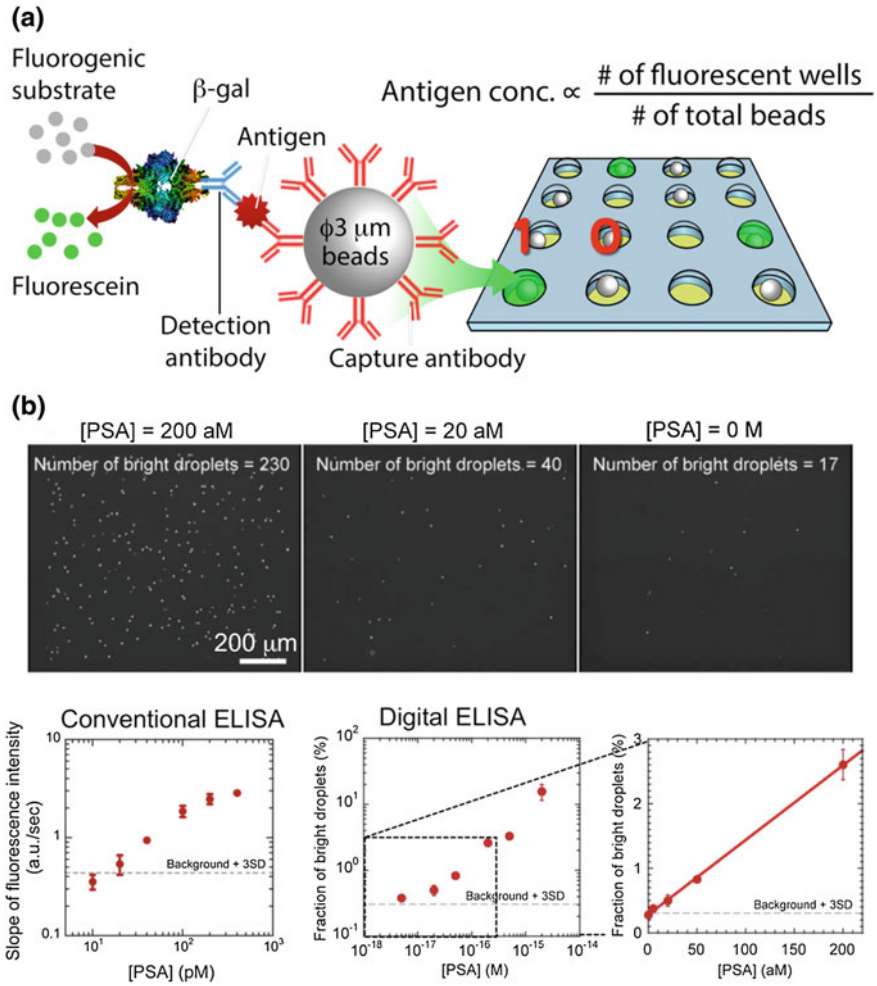

Fig. 7.2 Digital ELISA. **a** Schematics of digital ELISA. A single sandwich complex is encapsulated into a reactor chamber. The antigen is detected by the fluorescent product of β-gal. The initial concentration of the antigen can be determined by the ratio of fluorescent chambers to the total number of beads. **b** Digital ELISA for prostate specific antigen (PSA). In the fluorescence images, most bright spots correspond to single PSA molecules. The concentration of PSA was in proportion to the ratio of fluorescent chambers at low concentrations, i.e., less than 200 aM. In this assay, the limit of detection (LOD) was 2 aM, more than one million times lower than that of conventional ELISA. The nonzero fraction at 0 M indicates nonspecific adsorption of the detection antibody

more antigen molecule in a reactor chamber is negligible due to the extremely low ratio of antigen to beads (typically less than 0.05).

For the proof of concept, digital ELISA for prostate specific antigen (PSA), a biomarker for prostate cancer, was conducted [6]. We determined the number of

bright chambers at different PSA concentrations. The fraction of bright chamber showed a good linearity to the PSA concentration from atto- to femto-molar. Thus, digital ELISA of PSA showed a wide dynamic range of 3 digits. The determined limit of detection (LOD) was as low as 2 aM (60 ag/mL), which was a millionfold lower than that of conventional ELISA. It is noteworthy that digital ELISA has no LOD in principle, when any fluorescent chamber is not observed in the absence of target molecule. In the case of digital ELISA for PSA, even in the absence of PSA, 0.2 % of chambers showed fluorescence mainly due to nonspecific absorption of detection antibody on the microbeads.

Digital ELISA would enable early diagnostics of diseases such as influenza, cancer and neurodegenerative diseases. Furthermore, it has the potential to discover new biomarkers that are not currently detectable and to the development of new diagnostic technologies. The reduction of the nonspecific binding is one of the main challenges for improvement of digital ELISA.

7.5 Future Perspectives

Digital ELISA is a promising analytical method for presymptomatic testing, but several challenges remain for its practical application. The first challenge involves the detection of multiple types of biomarkers in a single assay. Such a feature would improve the specificity of diagnosis and reduce the amount of sample, such as blood, required from a patient. Multicolored digital ELISA, in which multiple types of antibodies are conjugated to distinct enzymes, may be useful for this purpose. Multicolor detection has already been demonstrated with β-gal and alkaline phosphatase, which produces resorufin [32].

The second challenge is the reduction of the assay time. The observation of a massive number of reactor chambers requires wide-field imaging with a low-power objective lens, which weakens the fluorescence incidence on the lens. For example, the digital counting of β-gal using 60 fL chambers and a 10× objective lens takes several tens of minutes even with a scientific CMOS camera due to the slow increase of fluorescence intensity. Moreover, in multicolored digital ELISA, enzymes would function in nonoptimum conditions and take a longer time, because optimum buffer contents and pH are different among enzymes. Thus, a technological advancement that achieves more rapid detection of single enzyme activity is still required. For rapid detection, reactor chambers were further miniaturized to submicron scale and aL volume using nanoimprint technology. We named this aL-droplet array “Nanocell.” In Nanocell, the concentration of fluorescent products rapidly increased and reached detectable levels (Ono et al. unpublished).

The third challenge is to reduce the background noise from nonspecific adsorption to the microbeads. In addition to Poisson noise, nonspecific adsorption of the detection antibody increases background noise and reduces the sensitivity of the assay. Strategies include blocking the microbeads surface with bovine serum

albumin or modifying it with polyethylene glycol, but better reductions are still needed.

Finally, the fourth challenge is the miniaturization of the whole ELISA system. In the present digital ELISA system, the reactor chamber chip is as small as several square centimeters, but a conventional microscope is used for the fluorescence detection. To bring POCT to the home or small clinics, a portable imaging unit is needed. We are therefore developing a digital ELISA system that includes a CMOS image sensor behind the chip [33]. Using this system, we have detected single molecule in reactor chambers and expect a convenient and cost-effective diagnostic system will appear in the near future.

Aside from digital ELISA, reactor chambers can be used to measure the activity of single-molecule membrane transporters, which are in general very promising drug targets. Active transport by these transporters is quite slow, less than one ten-thousandth of the passive transport rate done by membrane channels. The significant difference in transport rate between active and passive transporters is due to the intrinsic difference of their working principle; in active transport, transporter proteins undergo a large conformational change accompanying main chain rearrangement, to pump substrate molecules one-by-one against substrate concentration gradient or membrane voltage. Such a large conformational change occurs in tens of milliseconds that determines the overall transport rate. In contrast, passive transporter proteins just facilitate substrate diffusion along concentration gradient or voltage by forming nanometer-sized pore. In some ion channel proteins, each ion takes only submicroseconds to travel across the membrane-spanning pore, allowing electrical recording of the ion current by a single ion channel protein. Thus, single-molecule detection of active transporter proteins requires completely different detection principles from single ion channel recording. To address the technical challenge, we developed a new type of femtoliter reactor array in which each reactor is sealed with lipid bilayer [34]. In our arrayed lipid bilayer chamber (ALBiC) system, membrane transporters are reconstituted into a lipid bilayer that covers the upper side of the reactor chamber. When an active transporter protein pumps substrate molecules into the reactor, substrate molecules quickly accumulate in the reactor, enabling the detection of single transporter proteins. We have demonstrated detection of active proton pump activity by single F_oF_1-ATPase molecules that pump proton, hydrolyzing ATP [34]. This system is now being developed for other transporters and drug screening [35, 36].

7.6 Conclusion

In our CREST project, we have developed biochemical analysis methods based on digital methodologies for the measurement of biological phenomena at the single-molecule level. More specifically, using our unique LOC devices, we have successfully measured the reaction activity of single F_1 motor proteins, enzyme activity and membrane transporter protein. Moreover, we have incorporated digital

counting into ELISA format, which has drastically improved the sensitivity (more than one million times higher than that of conventional ELISA). We see these digital methods as the beginnings of a "Digitization Revolution" in biochemical analysis.

References

1. E. Neher, B. Sakmann, Nature **260**, 799 (1976)
2. T. Funatsu, Y. Harada, M. Tokunaga, K. Saito, T. Yanagida, Nature **374**, 555 (1995)
3. H. Noji, R. Yasuda, M. Yoshida, K. Kinoshita Jr., Nature **386**, 299 (1997)
4. D.M. Rissin, C.W. Kan, T.G. Campbell, S.C. Howes, D.R. Fournier, L. Song, T. Piech, P.P. Patel, L. Chang, A.J. Rivnak, E.P. Ferrell, J.D. Randall, G.K. Provuncher, D.R. Walt, D.C. Duffy, Nat. Biotechnol. **28**, 595 (2010)
5. Y. Men, Y. Fu, Z. Chen, P.A. Sims, W.J. Greenleaf, Y. Huang, Anal. Chem. **84**, 4262 (2012)
6. S.H. Kim, R. Iino, S. Iwai, S. Araki, S. Sakakihara, H. Noji, Lab Chip **12**, 4986 (2012)
7. S.C. Terry, J.H. Jerman, J.B. Angell, IEEE Trans. Electron Device **26**, 1880 (1979)
8. A. Manz, N. Graber, H.M. Widmer, Sens. Actuators B **1**, 244 (1990)
9. E.K. Sackmann, A.L. Fulton, D.J. Beebe, Nature **507**, 181 (2014)
10. T. Thorsen, S.J. Maerkl, S.R. Quake, Science **298**, 580 (2002)
11. H.T.G. van Lintel, F.C.M. van De Pol, S. Bouwstra, Sens. Actuators **15**, 153 (1988)
12. M. Esahsi, S. Shoji, A. Nakano, Sens. Actuators **20**, 163 (1989)
13. D.C. Duffy, J.C. McDonald, O.J.A. Schueller, G.M. Whitesides, Anal. Chem. **70**, 4974 (1998)
14. D.D. Carlo, L.Y. Wu, L.P. Lee, Lab Chip **6**, 1445 (2006)
15. L. Cai, N. Friedman, X.S. Xie, Nature **440**, 358 (2006)
16. R. Iino, K. Hayama, H. Amezawa, S. Sakakihara, S.H. Kim, Y. Matsumono, K. Nishino, A. Yamaguchi, H. Noji, Lab Chip **12**, 3923 (2012)
17. M.C. Mitchell, V. Spikmans, A. Manz, A.J. de Mello, J. Chem. Soc. Perkin Trans. **15**, 514 (2001)
18. J.J. Agresti, E. Antipov, A.R. Abate, K. Ahn, A.C. Rowat, J.-C. Baret, M. Marquez, A.M. Klibanov, A.D. Griffiths, D.A. Weitz, Proc. Natl. Acad. Sci. USA **107**, 4004 (2010)
19. J. Clarke, H.-C. Wu, L. Jayasinghe, A. Patel, S. Reid, H. Bayley, Nat. Nanotechnol. **4**, 265 (2009)
20. Y. Taniguchi, P.J. Choi, G.-W. Li, H. Chen, M. Babu, J. Hearn, A. Emili, X.S. Xie, Science **329**, 553 (2010)
21. C.D. Chin, T. Laksanasopin, Y.K. Cheung, D. Steinmiller, V. Linder, H. Parsa, J. Wang, H. Moore, R. Rouse, G. Umviligihozo, E. Karita, L. Mwambarangwe, S.L. Braunstein, J. van de Wijgert, R. Sahabo, J.E. Justman, W. El-Sadr, S.K. Sia, Nat. Med. **17**, 1015 (2011)
22. R.M. Dickson, A.B. Cubitt, R.Y. Tsien, W.E. Moerner, Nature **388**, 355 (1997)
23. E. Betzig, G.H. Patterson, R. Sougrat, O.W. Lindwasser, S. Olenych, J.S. Bonifacino, M.W. Davidson, J. Lippincott-Schwartz, H.F. Hess, Science **313**, 1642 (2006)
24. W.E. Moerner, L. Kador, Phys. Rev. Lett. **62**, 2535 (1989)
25. E. Betzig, R.J. Chichester, Science **262**, 1422 (1993)
26. B. Rotman, Proc. Natl. Acad. Sci. USA **47**, 1981 (1961)
27. P.B. Umbanhowar, V. Prasad, D.A. Weitz, Langmuir **16**, 347 (2000)
28. T. Thorsen, R.W. Roberts, F.H. Arnold, S.R. Quake, Phys. Rev. Lett. **86**, 4163 (2001)
29. B.J. Hindson, K.D. Ness, D.A. Masquelier, P. Belgrader, N.J. Heredia, A.J. Makarewicz, I.J. Bright, M.Y. Lucero, A.L. Hiddessen, T.C. Legler, T.K. Kitano, M.R. Hodel, J.F. Petersen, P.W. Wyatt, E.R. Steenblock, P.H. Shah, L.J. Bousse, C.B. Troup, J.C. Mellen, D.K. Wittmann, N.G. Erndt, T.H. Cauley, R.T. Koehler, A.P. So, S. Dube, K.A. Rose, L. Montesclaros, S. Wang, D.P. Stumbo, S.P. Hodges, S. Romine, F.P. Milanovich, H.E.

White, J.F. Regan, G.A. Karlin-Neumann, C.M. Hindson, S. Saxonov, B.W. Colston, Anal. Chem. **83**, 8604 (2011)
30. Y. Rondelez, G. Tresset, T. Nakashima, Y. Kato-Yamada, H. Fujita, S. Takeuchi, H. Noji, Nature **433**, 773 (2005)
31. S. Sakakihara, S. Araki, R. Iino, H. Noji, Lab Chip **10**, 3355 (2010)
32. Y. Obayashi, R. Iino, H. Noji, Analyst **140**, 5065 (2015)
33. K. Sasagawa, K. Ando, T. Kobayashi, T. Noda, T. Tokuda, S.H. Kim, R. Iino, H. Noji, J. Ohta, Jpn. J. Appl. Phys. **51**, 02BL01 (2012)
34. R. Watanabe, N. Soga, D. Fujita, K.V. Tabata, L. Yamauchi, S.H. Kim, D. Asanuma, M. Kamiya, Y. Urano, H. Suga, H. Noji, Nat. Commun. **5**, 4519 (2014)
35. R. Watanabe, N. Soga, T. Yamanaka, H. Noji, Sci. Rep. **4**, 7076 (2014)
36. N. Soga, R. Watanabe, H. Noji, Sci. Rep. **5**, 11025 (2015)

Part IV
Nano-fabrication Using Biotemplate

Chapter 8
Biotemplates and Their Application to Electronic Devices

Yukiharu Uraoka, Mutsunori Uenuma, Yasuaki Ishikawa, Shinya Kumagai, Satoshi Tomita, Heiji Watanabe and Ichiro Yamashita

Abstract In the development of semiconductor device which is facing the difficulties of miniaturization, introduction of material with self-assembling ability is one of the most important methods to overcome those difficulties. In this study, we propose a nanosystem utilizing biosupramolecules as biotemplate. Biosupramolecules have many fascinating features such as size uniformity and self-assembling ability, which cannot be realized in conventional inorganic materials. Various inorganic materials that are very important materials for fabricating semiconductor devices can be incorporated inside the molecules. This meritorious technique is called biomineralization. It can be performed at room temperature. We established the technique to place the above-mentioned material accurately from one (linearly) to three (sterically) dimensions on the semiconductor substrate. In this chapter, we introduce several examples of application to electron device, such as floating gate memory, resistive memory, thin film transistor, MEMS sensor, solar cell, and metamaterials. We successfully demonstrated the new function by utilizing these unique features. This technique will open the door to next generation semiconductor devices.

Keywords Ferritin · Self-assembling · Biomineralization · Electron device · Semiconductor device · Memory · Thin film transistor · MEMS · Solar cell

8.1 Introduction

More than 60 years has passed since the transistor was invented by W.B Shockley, John Bardeen, Walter Brattain in 1949 [1]. During this period, semiconductor technology has greatly advanced. John Atalla and Dawon Kahng demonstrated the first successful MOS field-effect amplifier in 1960 [2]. General Microelectronic Corporation introduced the first commercial MOS IC at 1964. Intel's first micro-

Y. Uraoka (✉) · M. Uenuma · Y. Ishikawa · S. Kumagai · S. Tomita
H. Watanabe · I. Yamashita
Nara Institute of Science and Technology, Takayama, Ikoma, Nara 630-0192, Japan
e-mail: uraoka@ms.naist.jp

J. Sone and S. Tsuji (eds.), *Intelligent Nanosystems for Energy, Information and Biological Technologies*, DOI 10.1007/978-4-431-56429-4_8

processor, the 4004, was realized in 1968. A system On Chip (SOC) integrated circuit incorporates all electronic components in 1974. As this history show, miniaturization and integration of mainly memory and central processing units (CPUs) have rapidly progressed. Nowadays, the size of one transistor is smaller than an influenza virus of 100 nm. The speed of miniaturization follows Moore's law, reducing four times in size in 3 years. As a result, the advent of computers, displays, and mobile phones, and their improvement in performance has made our life more convenient than ever before. Semiconductor technology has been very unique and lucky, because the performance is enhanced by the scaling down of the transistors. This is one of the great drivers of development in technology. However, as miniaturization comes to the nanometer scale, several such serious problems reveal themselves, as the increased fabrication cost, lowering of yield, and increase in size fluctuation. In this way, top–down processing, which makes smaller structures by thinning the film or shortening gate length, is reaching its limit [3].

In this situation, the fabrication techniques of nanoscale structures by utilizing bottom–up technology based on the self-assembling is necessary. As one of these techniques, biotechnology is very promising. In the field of biotechnology, nanoscale structure is abundant, and the synthesis of nanomaterials, location control, functionalization, hierarchic structure, and self-healing are commonly occurred and these are the special features for fabricating electron devices [4, 5].

This chapter consists of four sections. After the introduction of background and purpose of this study, bottom–up process using biotemplates is described in Sect. 8.2. Special features of bio material are discussed in this section. In Sect. 8.3, semiconductor devices fabricated using bio-nanoprocesses are outlined. Mainly focusing on memory devices (floating gate memory and resistive memory), high performance semiconductor devices achieved first by employing the bio-nanoprocess are introduced in this section. In Sect. 8.4, as unique applications of bio-nanoprocess, crystallization of Si thin film for TFT and MEMS, solar cells, plasmon biosensor and single electron transistors are introduced. In Sect. 8.5, as photonic application, metamaterial fabricated by bio-nanoprocess is introduced. In the final section, this chapter was summarized and future prospect is described.

8.2 Bottom–Up Process Using Biotemplates

8.2.1 Supramolcules as Biotemplates

Supramolecules have various nanoscale shapes. Here, supramolecules are defined as an ordered assembly of molecules combined by weak interaction such as hydrogen bonding or coordinate bond. As shown in Fig. 8.1, various kinds of supramolecules with different shapes and different sizes exist in biofield. Not only sphere shape but also rods or wires are available as nanobuilding blocks. For example, ferritin is a cage-shaped protein including iron oxide inside its shell, which controls iron transport in the body of mammals. Inside of the ferritin, approximately 3000 iron atoms are

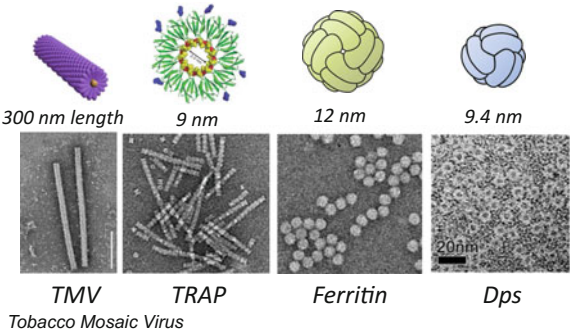

Fig. 8.1 Various kinds of supramolecules with nano scales used in this study. They have fascinating feature such as uniform or self-assembling ability and can be nano block for electron device

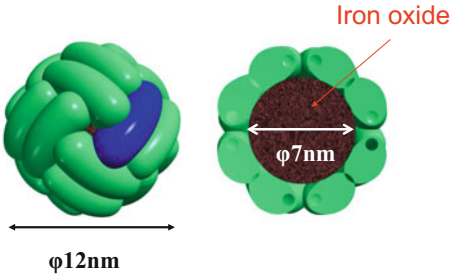

Fig. 8.2 Ferritin protein used in this study. Ferritin comprises 24 monomers with an outer and inner diameter of 12 and 7 nm, respectively

incorporated. Ferritin comprises 24 monomers of 18,500 molecular weight, with an outer and inner diameter of 12 and 7 nm, respectively, as shown in Fig. 8.2 [6]. Size dispersion is very small (standard deviation: $\sigma = 0.59$ nm). This protein is commonly included in not only animal or plant but also bacteria. By employing different kinds of supramolecules, smaller nanoparticles with various sizes are available.

In this study, we propose a bottom–up process to successfully create new semiconductor devices utilizing biosupramolecules with their fascinating properties such as size uniformity or self-assembling ability. Integration of semiconductor fabrication and biotechnology, which is referred to herein as a "bio-nanoprocess," is being developed and opening up a new academic field.

8.2.2 *Features of Supramolecule for Application in Electronic Devices*

The protein molecule works interactively in tissue. However, if we focus on specific kinds of protein, quite similar features such as size uniformity or self-assembling ability can be observed in any tissue of the body. Proteins with different functions are synthesized chemically. This is because proteins are synthesized based on the same genetic information. In other words, as a result of evolution, living things have established a synthetic method for proteins with no duplicating errors by using genetic information.

The diversity and similarity of living things seems to be contradicted. However, diversity is secured by increasing the kinds of interaction or multi-functionalization. In this way, living things synthesize the same proteins by stable genetic information. This gives us a very important engineering message. That is the reason why proteins are a massively fabricated standard product. We can fabricate periodic structures or large-scaled nanostructures by using structured proteins as a nanoblock [7]. We can also fabricate them at economically lower cost when we use their self-assembling capability.

As mentioned above, biomolecules such as proteins have many fascinating features which cannot be observed in inorganic material; such as the following:

(1) As they are designed based on DNA, fluctuation in composition or structure is small.
(2) They have self-assembling capability, which help nanostructures assemble by themselves.
(3) They have a biomineralization power which crystallizes inorganic material inside or outside.
(4) They have an ability to recognize specific inorganic materials.
(5) They can be synthesized by solution process at room temperature without high temperature annealing.

The features mentioned above are all necessary to fabricate nanostructures well at low cost and with high yield in semiconductor device fabrication. They also have high potential to create new structures. This is precisely what is required in the semiconductor device fabrication technology, which is currently approaching its limits.

8.2.3 *Biomineralization*

Precipitation of inorganic material by using biosupramolecules, such as protein, is called biomineralization (as shown in Fig. 8.3) [8–19]. Particularly to fabricate

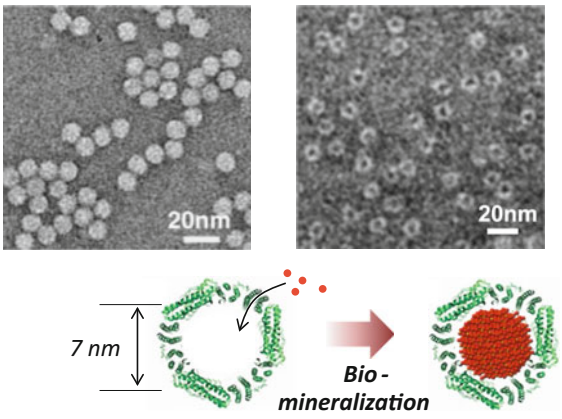

Fig. 8.3 Biomineralization is performed utilizing precipitation of inorganic material by bio- supramolecules, such as protein

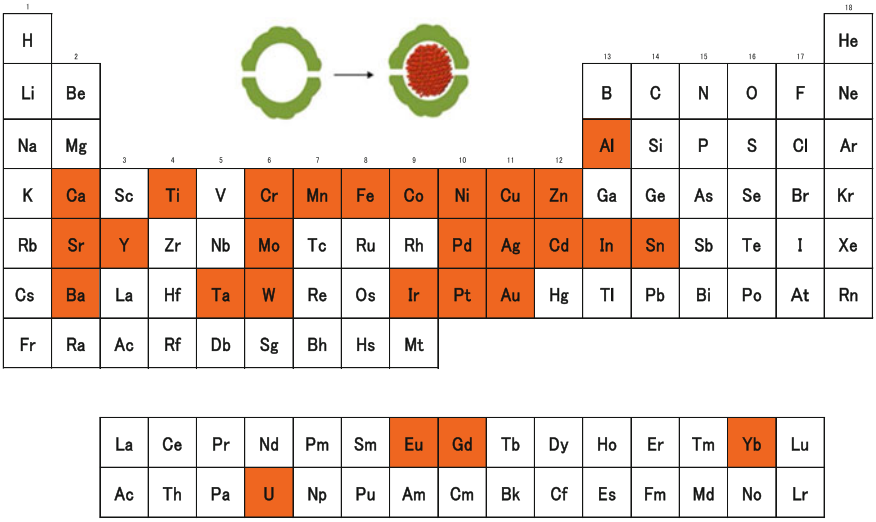

Fig. 8.4 Nanomaterials synthesized in the ferritin using biomineralization. So far so many materials have been synthesized. Atoms colored in the figure are previously synthesized in the protein

nanoparticles and nanowires, we utilize cage-shaped proteins and tube-shaped proteins. Depending on the purpose of the fabrication, we can select various kinds of inorganic materials synthesized in recombinant apoferritin. As described later, metal nanoparticles, semiconductor nanoparticles, and oxide nanoparticles are fabricated to adjust the work function in electronic devices.

Biomineralization using ferritin protein is performed as follows. In the cage-shaped protein, channels with three or four rotation symmetry axes exist. Through these channels, inorganic material in ionic state penetrates to crystalize internally in a specific position by electrostatic interactions. Due to this mechanism, polycrystalline solids are formed. Magnetic materials such as Fe, Co, Ni are easily synthesized. Size can be controlled by controlling the crystallization time. So far, so many nanodots have been synthesized as shown in Fig. 8.4. Atoms colored in the figure are previously synthesized in the protein [20].

8.2.4 Location Control of Biosupramolecule

Location control in nanoscale accuracy is inevitable regarding nanomaterial application in electron devices. We have proposed a number of control methods. We were successful in fabricating crystalized mono and multilayers on a semiconductor, insulator, or metal film, as well as single nanodot arrays with precise location control. Furthermore, we were able to succeed in dispersive location control of a single nanodot and its adsorption on specific materials.

The PBHL (PBLH; Poly-1-benzyl-L-histidine) method is widely used to develop monolayers on semiconductors or insulating film [4, 21]. As shown in Fig. 8.5, a positively charged PBLH layer is developed on the surface of the ferritin solution. Negatively charged ferritin gathers on the layer and is crystallized by electrostatic interaction. By dipping the silicon wafer into the solution, a monolayer is transferred on the surface of the wafer as shown in Fig. 8.6.

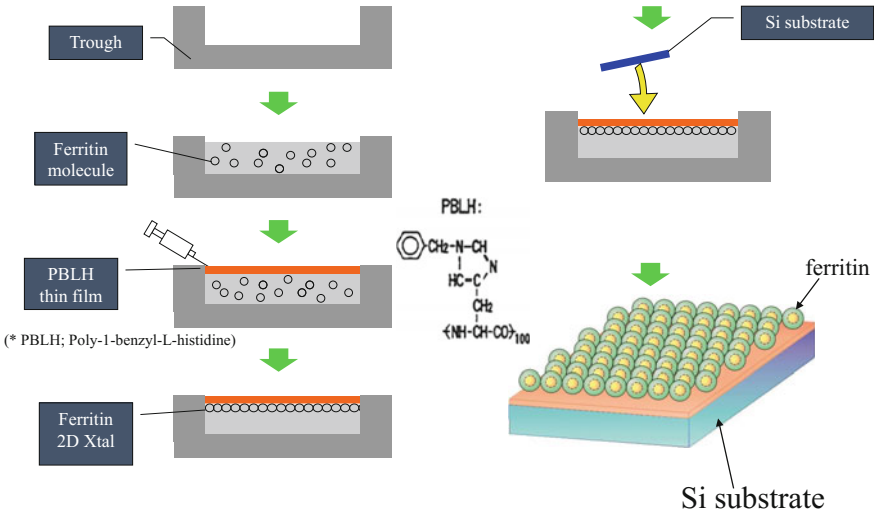

Fig. 8.5 PBHL(PBLH; Poly-1-benzyl-L-histidine)method used to obtain monolayer of the protein on the semiconductor substrate

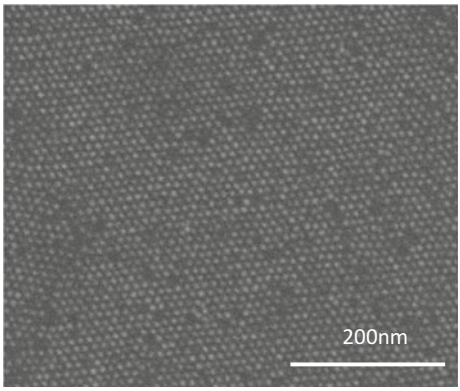

Fig. 8.6 Monolayer of ferritin on the silicon substrate obtained using PBLH method. Completely arrayed nanodots can be confirmed. By selecting different size protein, density can be controlled

We can locate single or plural nanodots by using electrostatic interaction between the charge of the protein molecule and film [22, 23]. As shown in Fig. 8.7, negatively charged particles are adsorbed on the patterned film with a positive charge, such as APTES (Aminopropyl triethoxysilane) film.

Another way of location control is as follows. As shown in Fig. 8.8 [24, 25], we can adsorb the molecule on a specific location by modifying the surface of the supramolecule with peptides, which recognize specific inorganic materials. Such peptides can be obtained using biopanning. In contrast, by decorating surface of the molecule with polyethylene glycol (PEG), we can develop monolayers with dispersive location control [26]. The distance between each nanodot can be controlled by the length of PEG.

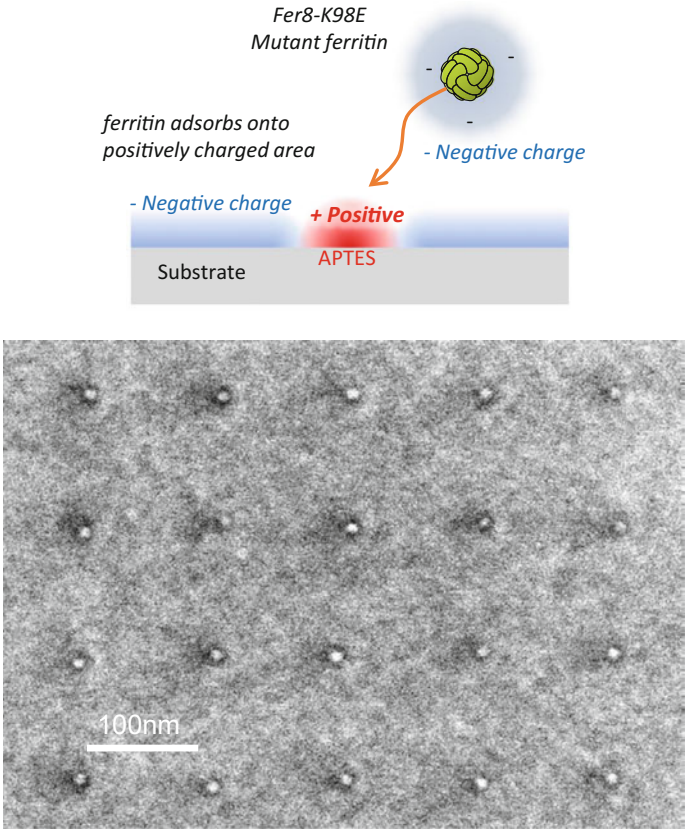

Fig. 8.7 Location controlled nanodots placed on the substrate. Precise location control can be performed using electrostatic interaction between negatively charged dots and APTES (Aminopropyl triethoxysilane) with positive charge

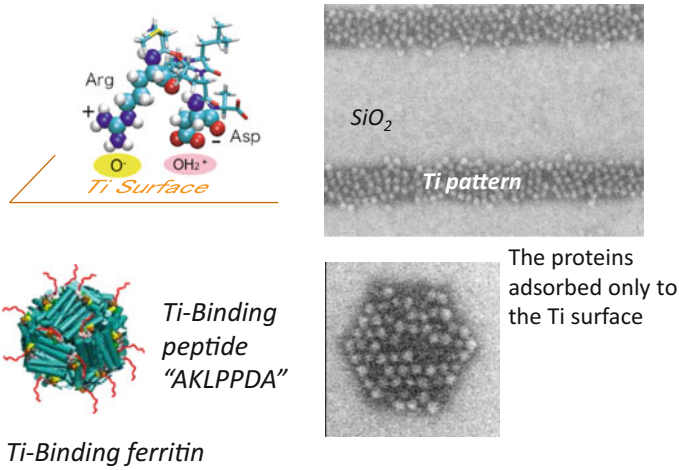

Fig. 8.8 Location control of nanodots using peptide which can recognize specific inorganic materials. Ti-binding peptide is obtained using biopanning. By decorating ferritin the peptide, nano dots can be placed on the Ti film

8.3 Semiconductor Devices Fabricated Using Bio-Nanoprocess

8.3.1 Floating Gate Memory

To demonstrate the effectiveness of the material for electron device application, we tried to fabricate a floating gate memory, which is widely used as a Universal Serial Bus (USB) memory. This memory is nonvolatile even if the electric source is switched off, and reading and writing speeds are very fast. They have high scalability for large integration.

Threshold voltage can be controlled by the charge injection with electrons or holes into the nanodots embedded in the insulating film. Assigning different threshold voltage with discrete values, a functional memory can be obtained. Embedded nanodots are called as a floating gate, because these nanodots are electrically isolated. For this floating gate, we employed biologically synthesized nanodots. Requirements for the nanodots used for floating gate are small in size with high density, uniform with low-size fluctuation, and electrically isolated. Biologically synthesized nanodots completely meet these requirements.

We tried to fabricate a floating gate memory with ferritin protein including various nanoparticles such as Fe, Co [27–33]. Depending on the metal nanoparticle, work function can be adjusted to control the memory properties such as writing and erasing speed or retention time. As we described above, we developed a high-density monolayer on the semiconductor. Synthesis of the nanoparticles is quite compatible with the conventional semiconductor fabrication process. Therefore, we employed a conventional process except for the nanodot fabrication, as shown in Fig. 8.9.

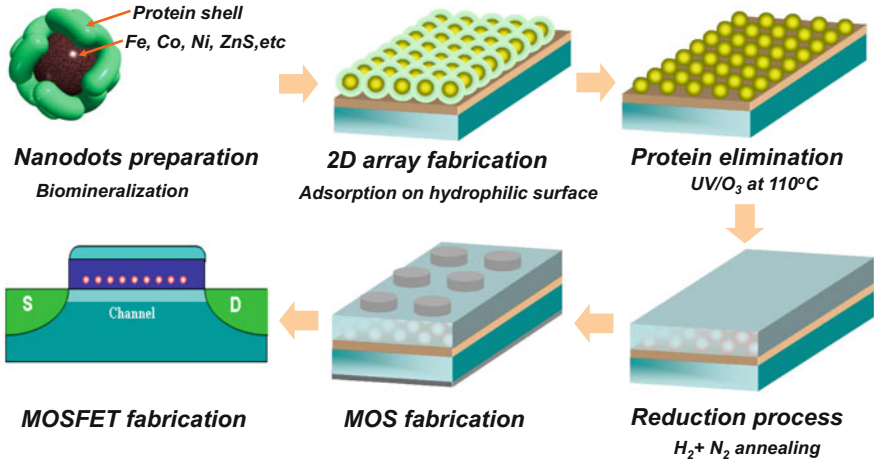

Fig. 8.9 Fabrication method for floating gate memory using bio-nanoprocess. The monolayer is developed on the gate insulator followed by UV/ozone to remove outer protein. After embedding nanodots with insulator, annealing in the hydrogen or nitrogen ambient is performed to reduce the nanodots. By depositing and patterning gate metal, MOS structure is completed

Before embedding the dots, the outer protein should be removed. We found that the outer protein can be removed completely by ozone treatment. Remaining protein can be a cause of contamination; therefore complete removal is very important. UV-ozone treatment can remove the outer protein without destructing the array. After embedding the dots with insulating film such as silicon dioxide, the nano dot array was quite stable after very high-temperature treatment over 800 °C. Not only silicon dioxide, but high-dielectric constant film such as HfOx was successfully employed for the performance improvement [31–33].

We confirmed that the floating gate memory fabricated with bionanodots has higher performance and reliability. Figure 8.10 illustrates clear hysteresis (memory

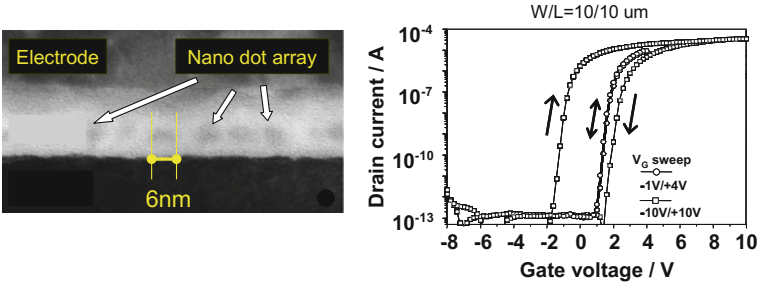

Fig. 8.10 TEM image of MOS structure with embedded nanodots (*left*). Hysteresis of transfer curve of floating gate transistors. Hysteresis suggests that charging and discharging are occurred in the dots embedded in the gate insulator. By increasing gate voltage sweep range, the window is increased

window) and stability against erasing more than one hundred thousand times. Furthermore operation of the floating gate memory fabricated on silicon on insulator (SOI) substrate or glass substrate was also demonstrated [35]. This demonstration suggests that the bio-nanoprocess is very promising for wide electron device application.

8.3.2 *Multilayer Floating Gate Memory Fabricated Using Bio Layer by Layer*

The peptide which can recognize specific inorganic material has an ability to crystalize inorganic material. For example, ferritin modified with titanium cognitive peptide has an ability to precipitate the titanium oxide outside the ferritin. We successfully fabricated the stack structure layer by layer by utilizing the both abilities of recognition and precipitation on the titanium pattern [35]. This method is called "bio layer by layer". Figure 8.11a, b shows the principle of the process and TEM image of three-dimensional stack structure, respectively.

Ferritin protein can uptake various kinds of nanoparticles as described above. Therefore, by preparing ferritin of different kinds, we can fabricate the stacked structure with different kinds of nanoparticle such as Fe, Co, CdSe. There is no limit on the number of layers, and so far we have succeeded to stack 12 layers using this technique. We confirmed stacked Co nanodots on the tunneling oxide by biolayer by layer [36]. Input transfer curve is shown in Fig. 8.12. Clear hysteresis was also confirmed and hysteresis window were increased depending on the number of

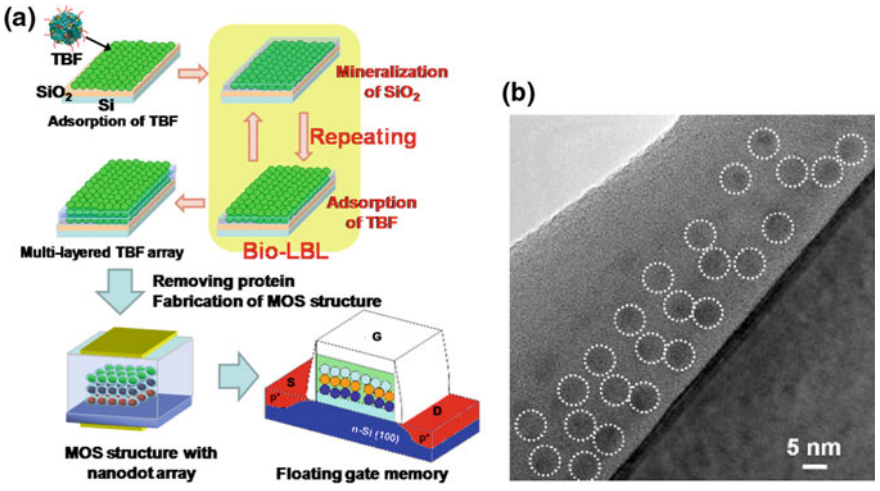

Fig. 8.11 Floating gate memory with 3-Dstacked nanodots. Stacked structure can be fabricated using bio layer by layer (bio-LBL) (**a**). TEM image of stacked structure obtained using bio LBL (**b**)

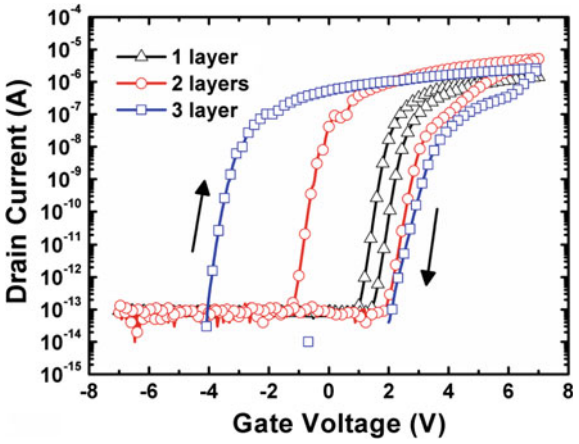

Fig. 8.12 Hysteresis properties of floating gate memory with three dimensionally stacked nanodots. By increasing number of layers, the window increased due to increased nanodots density

layers. With the increase of Co nanodot layers, density of nanodots per unit area increased. Hence memory window increased due to the increase of injected charge.

Furthermore, measurements such as retention time, writing speed, and reliability against repetitive writing and erasing demonstrated the effectiveness of this memory. Here we discuss the effectiveness of the bio-nanoprocess on the floating gate memory by comparing with previous device fabricated by conventional top–down process. In the conventional floating gate memory with plate-type gate, operation voltage was high due to thick gate oxide film. By using uniform and high-density nanodots fabricated with bio-nanoprocess, much lower voltage operation was found to be possible. This is due to increased reliability and decreased film thickness of gate oxide. Therefore, this low voltage operation will lead to low power consumption device which is strongly required as future devices.

8.3.3 Resistive Memory

Resistive memory is now widely studied as nonvolatile memory for next generation. Due to its simple structure, higher speed and lower power operation can be expected [37–40]. Resistive material is sandwiched by metal electrode; therefore resistive memory has high scalability as shown in Fig. 8.13. Scalability is the most advantageous point; for example, operation of memory device with a size of 10 nm has been reported [41]. However, in the previous semiconductor process, the most meritorious scalability has not been used due to insufficient nano fabrication technique.

We tried to fabricate resistive memory using bio-nanoprocess [42–46]. Iron oxide nanoparticle with a size of 7 nm was synthesized in the ferritin and they were employed as resistive layer in the resistive memory. It is considered that the resistive memory works because the generation and breakdown of the filament

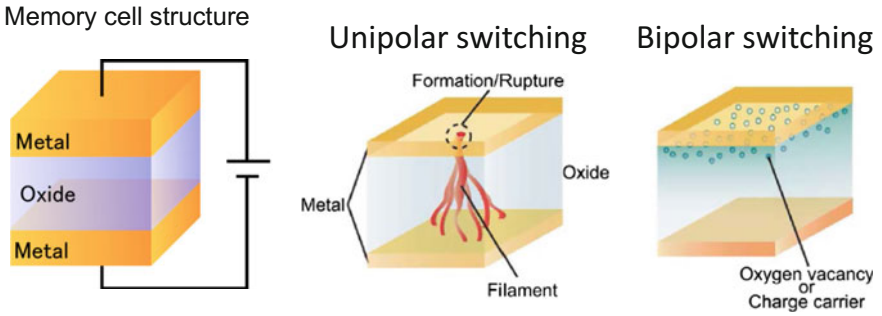

Fig. 8.13 Theory of resistive memory operation. For the resistive change, two models are proposed. Filament path is generated due to reduction of metal oxide results in unipolar switching (*center*). Accumulation of oxygen vacancy of charged carriers at the interface between metal oxide and electrode results in bipolar switching (*left*)

occur in the resistive layer. Generation and breakdown of the filament are related to the movement of oxygen ions or oxygen vacancy caused by the electric field in the resistive layer. In the resistive memory fabricated using iron oxide, it is reported that resistivity is changed by the forming of iron oxide layer of different oxygen compositions at the interface caused by the movement of oxygen ion [47]. In addition, according to the recent report, oxygen deficient region of 10 nm generated in the TaOx film works as the filament [48]. As a method of electrical measurement of local area in the resistive memory, we use Conductive Atomic Force Microscope (C-AFM) which enables us to measure local memory properties by writing and erasing using cantilever of AFM [43].

In our study, we used C-AFM to evaluate the resistive behavior of single oxide nanoparticle synthesized using bio-nanoprocess. Figure 8.14 shows the current

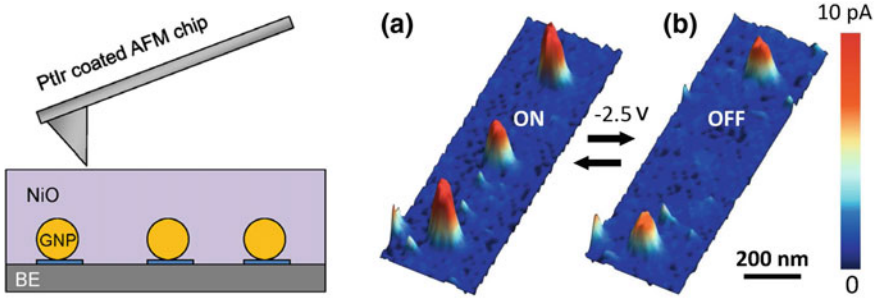

Fig. 8.14 Demonstration of resistive change in the memory with nanodot electrode. Cross sectional view (**a**). Forming filament path on each electrode (**b**). Filament is disappeared at only center electrode (**c**). This result indicates that the control of filament position is possible in nano scale

distribution obtained by C-AFM measurement. Comparison between surface morphology and current distribution indicates that current spot was formed on the nanoparticle. By applying set voltage (Vset), reset voltage (Vreset), and reading voltage (Vread), set and reset operations can be controlled. These results clarified that nanoparticle with a diameter of 7 nm fabricated by biomineralization is applicable to the memory device. In addition, resistive change occurs in the single nanoparticle, thus miniature memory of 7 nm is available.

Memory property of nanoparticle was evaluated using metal–insulator–metal (MIM) structure as shown in Fig. 8.15. Current-voltage measurement indicated bipolar-type resistive memory behavior after forming process. By repetitive test by applying pulse voltage, switching behavior more than 10^3 times were observed. On the contrary, devices without nanoparticles showed breakdown effect after forming process with high voltage, hence stable switching property was not obtained. Results obtained in this experiment clarified that inorganic material obtained by biomineralization is applicable to memory device. Mechanism of switching can be considered as follows: By applying plus voltage to top electrode, negative oxygen ions move up to the top electrode leaving electrons, thus a conductive path is formed and the resistivity changes from high resistive state (HRS) to low resistive state (LRS). Next by applying negative voltage to the top electrode, negative oxygen diffuse back to nanoparticle, thus conductive path is broken and resistivity changes from HRS to LRS.

As demonstrated in this section, a single nanoparticle of 7 nm synthesized in protein was found to work as memory. This is the smallest memory in the world. As described in Sect. 8.2.1, there is possibility to make smaller nanodots using different cage-shaped protein. Therefore, ultimately small memory less than 3 nm will be realized using bio-nanoprocess in the future.

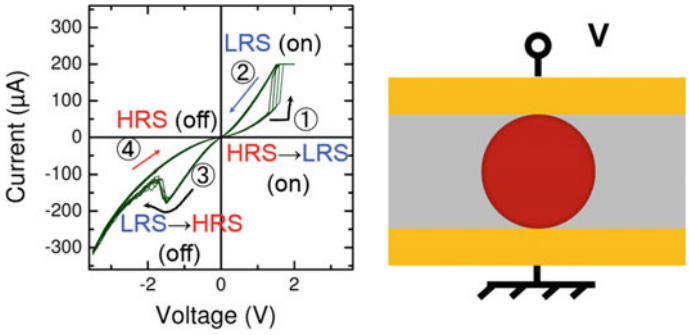

Fig. 8.15 Resistive memory using single nanodot. Current-voltage measurement indicated bipolar-type resistive memory behavior after forming process. *HRS* and *LRS* indicates high resistance state and low resistance state, respectively

8.4 Unique Applications of Bio-Nanoprocess to Electron Device

8.4.1 Crystallization of Silicon Film

When we closely look at the pixel of liquid display, there is small device called thin film transistor (TFT) which is a switching device to control the direction of liquid molecule [49]. This is considered to be a part of large-scale integration (LSI) fabricated on the glass substrate. Therefore, if the performance is high enough, we can fabricate not only the pixel, but CPU and memory on the glass or plastic substrate called system on panel. To achieve this purpose, high quality of silicon film is crucial. However, unlike the silicon LSI process, low-temperature process is required, because the high-temperature process more than 1000 °C cannot be accepted for substrates such as glass or plastic film.

Crystallization of silicon thin film at low temperature using metal catalyst is called Metal-Induced Lateral Crystallization (MILC) and it has been studied for long time [50, 51]. Transition metal like Ni is highly reactive with silicon, hence silicidation ($SiNi_2$) occurs at low temperature. Crystallized silicon film can be obtained using this phenomenon. Compared with the case without catalysts, crystallization occurs at much lower temperature. However, catalytic metal should be removed after the annealing because residual metal act as contamination. Furthermore, under this condition, grain size is not enough and has a problem in quality.

We tried to crystalize silicon film utilizing ferritin with Ni nanoparticle as catalytic metal as shown in Fig. 8.16 [52–54]. Ni is synthesized using biomineralization described previously. After the adsorption of ferritin on the amorphous silicon, outer protein is removed by UV-ozone treatment. Crystal nuclei can be formed by the interaction between Ni nanoparticle and silicon and crystal grows by the thermal treatment. Our experiment demonstrated large grain size more than 10 μm and ten times lower impurity concentration than conventional MILC method. By using this film we fabricated high performance thin film transistor.

By performing location control of Ni ferritin, position of crystal nucleus can be controlled; hence silicon film with neatly arrayed grains is available. Ge film can also be crystallized using this method [55]. By using ferritin protein, the film with controlled grain position and with very low impurity (contamination) is available as shown in Fig. 8.17.

8.4.2 MEMS Device as an Application of Bio Crystallization

Polycrystalline Si (poly-Si) thin films are widely used in micro-electromechanical systems (MEMS). Poly-Si thin film, however, has defects such as grain boundary, vacancy, and dislocation. Such defects affect mechanical properties of poly-Si film.

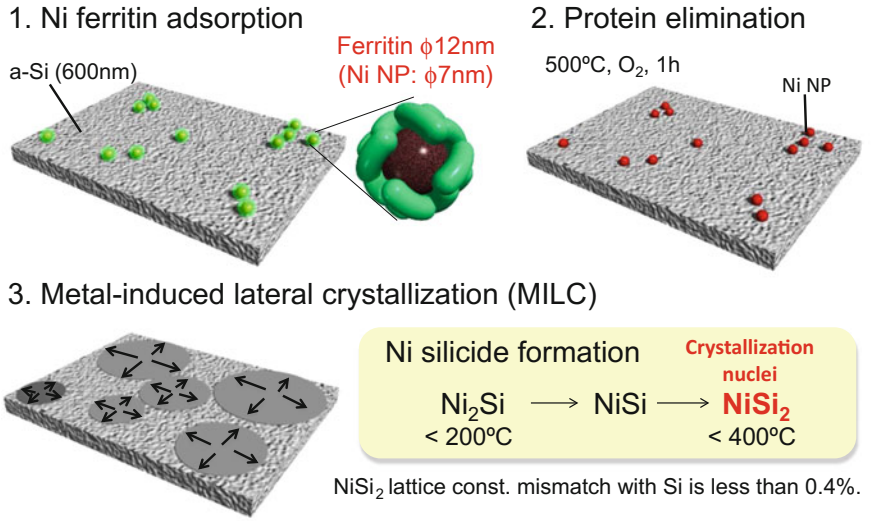

Fig. 8.16 Crystallization of silicon thin film using metal-induced lateral crystallization (MILC). Ferritin incorporating Ni inside is deposited on the amorphous silicon. After removing outer protein, Ni nanoparticle is annealed at lower than 500 °C. Ni reacts with amorphous silicon at lower temperature to form $NiSi_2$. Lattice mismatch of $NiSi_2$ is less than 4 % for crystalline Si. Therefore, large and high quality Si grain can be obtained using this method

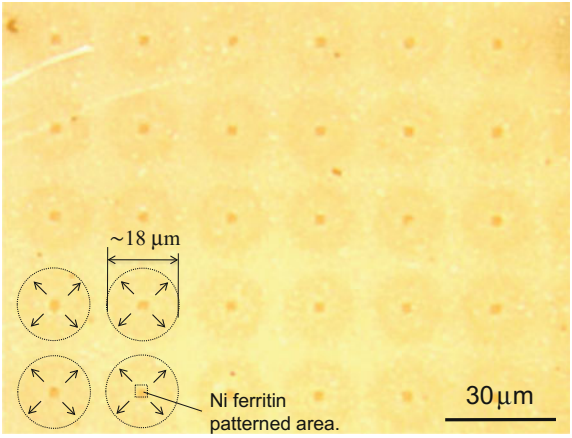

Fig. 8.17 Si film with large grain obtained by MILC with bio-nanoprocess. Depending on the interval of $NiSi_2$ nuclei, grain size can be controlled. Large grain with 18 μm diameter is obtained. Very low impurity of Ni is one of the big features of this methods

While actuating a MEMS device made from poly-Si thin film, energy supplied for actuation is dissipated by the internal friction at defects. Here, let us consider the actuation of MEMS resonator. The performance of the resonator can be characterized by the quality (Q) factor, which is defined by the ratio of stored energy to the dissipated energy per one cycle. A MEMS resonator made from single crystalline Si achieved $Q = 10^4$–10^6 [54–58], while those made of poly-Si thin film achieved

$Q = 10^3$–10^4 [61–63]. If defects in the poly-Si thin film are decreased, the low-energy loss characteristics are expected in the poly-Si thin film MEMS resonator, and the device can achieve a high Q factor, which is needed for sensitive measurement.

Using Ni nanoparticles which were synthesized within apoferritin supramolecules, metal-induced lateral crystallization (MILC) was conducted to define the positions of crystallized area in Si thin film [63]. The crystallized area was used to make the body of the MEMS resonator. Therefore, grain boundaries, which degrade the resonance characteristics, can be excluded from the MEMS resonator. Four MEMS cantilever resonators were designed and fabricated (Fig. 8.18a–d). Resonator 1 was a reference device, which was fabricated without MILC. Resonator 2 was crystallized from the side of cantilever body. Resonator 3 was crystallized along axial direction of the cantilever. Resonator 4 had a grain boundary, which ran across the cantilever body along 45° direction to the cantilever axis. Optical microscopy revealed no significant differences for the resonators 1, 2, and 3. However, for the resonator 4, grain boundary which was generated by the collision of two crystallization growth was clearly observed. Crystallization structures of the resonators were analyzed by electron backscatter diffraction (EBSD) method. Resonator 1 had small grains (less than 1 μm) which were not able to be detected by EBSD measurement. Resonators 2, 3, and 4 had larger grains on the order of 10 μm [64].

Characteristics of the fabricated resonators were measured under vacuum of 3.0×10^{-3} Pa to minimize the damping by air. Q factors were calculated from the resonance frequency ratio to the full width at 3 dB below the resonant peak ($Q = f_{res}/\Delta f_{-3dB}$). Resonator 1 (reference) achieved $Q = 12{,}100$ (Fig. 8.19a).

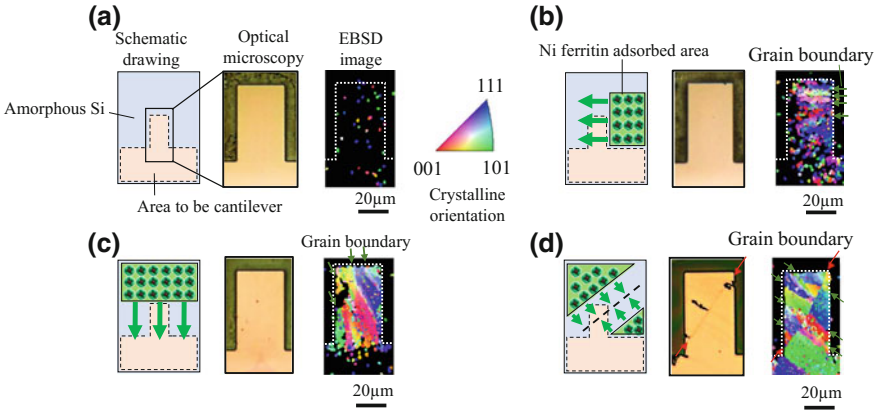

Fig. 8.18 Images of MEMS cantilever resonators by schematic, optical microscopy, and EBSD. **a** Resonator 1. A reference device fabricated without MILC. **b** Resonator 2. Crystallized from the side of cantilever body. **c** Resonator 3. Crystallized along axial direction of cantilever body. **d** Resonator 4. Grain boundary, which is formed by the collision of two crystallization growths, is included in the cantilever body

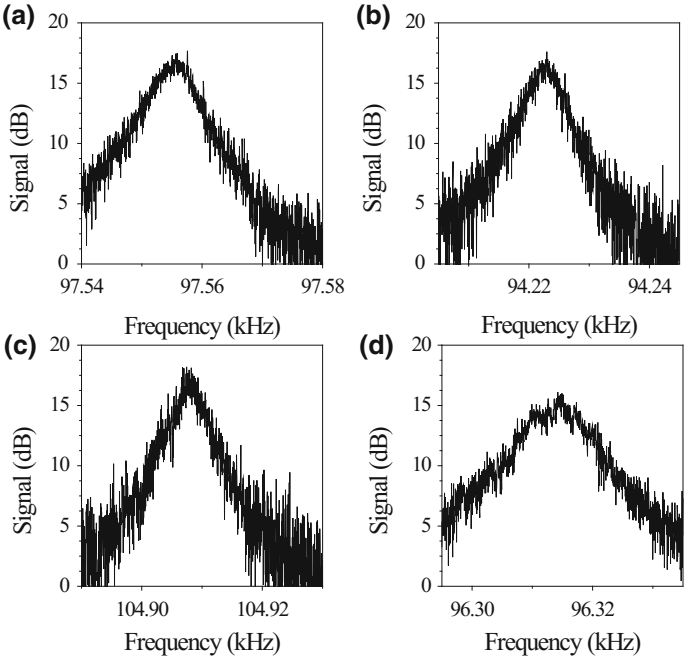

Fig. 8.19 Resonance characteristics of the fabricated resonators. **a** Resonator 1. **b** Resonator 2. **c** Resonator 3. **d** Resonator 4

Resonator 2 had larger grains. Q factor was calculated to Q = 13,400 (Fig. 8.19b). Only 1.1 times greater than that of resonator 1. Maximum of Q factor was observed for resonator 3. Q = 26,200 was achieved (Fig. 8.19c). Twofold increase was observed. The Q factor difference between resonator 2 and 3 was direction of crystallization growth. In contrast, although resonator 4 had larger grains than the resonator 1, the Q factor was decreased to Q = 6400 (Fig. 8.19d), which was caused by the energy loss at the grain boundary [11]. For the low-energy loss thin film MEMS devices, we must consider to improve the crystallinity and tune crystallization directions in the device structure.

8.4.3 Dye-Sensitized Solar Cell Fabricated Using Bio Supramolecule

Dye-sensitized solar cell gathers much attention as wet type solar cell because they are fabricated using solution process at low cost [65, 66]. Mechanism of the cell is as follows: When the light is irradiated, electrons are generated at dye adsorbed on the TiO_2 and the electrons are collected to cathode through TiO_2. Oxidized dye

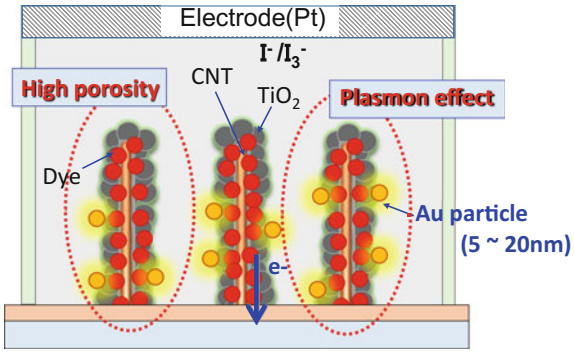

Fig. 8.20 Dye-sensitized solar cell (DSSC) fabricated using bio nano process. On the transparent electrode, carbon nanotube (CNT) was grown by using nano dots as nuclei and modified protein with high density was adsorbed on the CNT. TiO_2 was precipitated by the protein by biomineralization. By the thermal treatment we, TiO_2 as anatase of porous electrode film can be formed

losing electrons are reduced by getting electron from iodine in electrolyte. Iodine is recovered by getting electron from anode.

One of the problems of the cell is low efficiency. We considered that this problem would be solved by increasing the surface area for light irradiation using bio-nanoprocess. We tried to introduce the following cathode electrode as shown in Fig. 8.20 [67]. On the transparent electrode, carbon nanotube (CNT) was grown by using nanodots as nuclei and modified protein with high density was adsorbed on the CNT. TiO_2 was precipitated by the protein by biomineralization. By the thermal treatment, we can utilize TiO_2 as anatase of porous electrode film. We are aiming to enhance the cell efficiency by introducing nanomaterial with large surface area and low resistive CNT as electron path.

8.4.4 Plasmon Biosensor Fabricated Using Bio-Nanoprocess

In this study, as an application of bio-nanoprocess, we tried to realize a sensing device using gold nanoparticle as plasmonic antenna as shown in Fig. 8.21a [68]. On the transparent oxide semiconductor (Nb-doped TiO_2) against visible light, high density gold nanoparticle was synthesized using porter protein technique. Modulated channel current by surface plasmon effect was utilized as sensing parameter. In conventional sensing devices such as biosensor, plasmon effect was detected by the change of transmitted light. However, in our system, plasmon effect can be detected by the current without detecting light. We compared the photo current flowing between electrodes with and without nanoparticle. In the system with gold nanoparticle, obvious photo current increase was observed at wavelength

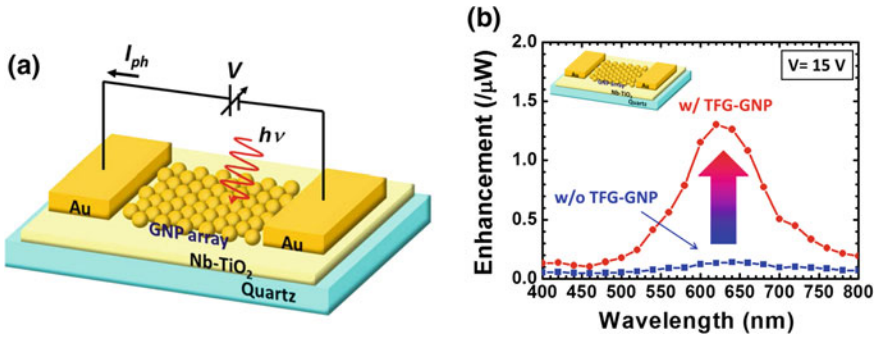

Fig. 8.21 **a** Concept of the proposed photoelectronic hybrid device utilizing GNPs, which act not only as the plasmon antenna but also as the sensing part. **b** Enhancement of photocurrent in the devices plotted as a function of the wavelength of monochromatic incident light. *Red circles* and *blue squares* indicate the obtained enhancement factor of the devices with and without GNP arrays on the Nb-doped TiO_2 channels, respectively

of 640 nm as shown in Fig. 8.21b. This wavelength indicates the generation of surface plasmon resonance. This is due to an increase of hot carrier flowing over the Schottky barrier at the Au/Nb-TiO_2 interface. By monitoring channel carrier, plasmon signal derived by gold nanoparticle was directly detected without optical signal.

8.4.5 Single Electron Transistor Fabricated Using Bio-Nanoprocess

Single electron transistor (SET) which operates by the charging and discharging by single electron gathers attention as ultimately low power consumption device [69, 70]. However, nano fabrication is necessary and their size fluctuation becomes a serious problem. Hence we tried to apply core of ferritin to the electrode confining electron [71]. Here, we used modified protein with peptide which recognizes Ti. We successfully placed single protein between Ti electrodes by utilizing an effect that the modified protein is adsorbed only on Ti surface as shown in Fig. 8.22. Fortunately, thickness of the outer shell of protein corresponds to distance that electron can tunnel. We successfully demonstrated the behavior of single electron transistor. At low temperature, we could observe Coulomb oscillation. It is verified that nanoparticles synthesized by bio-nanoprocess work as electrode of SET. This is a successful device example that can demonstrate the effectiveness of peptide and self-assembling ability.

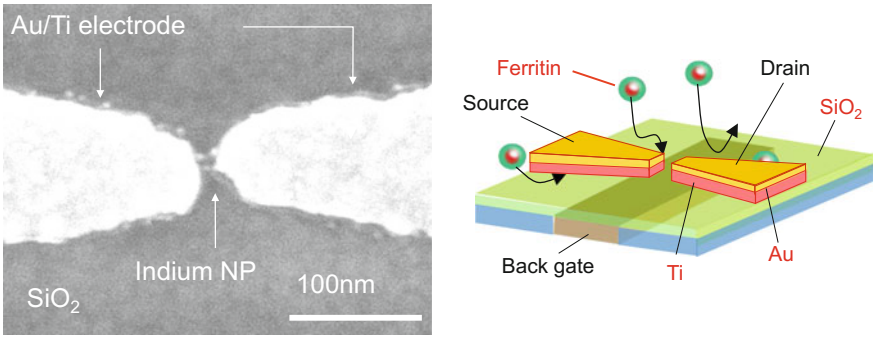

Fig. 8.22 Single electron transistors fabricated using bio nano dot. Ferritin decorated with Ti-binding peptide can be placed between each Ti electrode. We successfully demonstrated the behavior of single electron transistor

8.5 Metamaterial Fabricated Using Bio-Nanoprocess

Metamaterials consisting of building blocks much smaller than the wavelength of light are a rich and rapidly growing area in optics and photonics [72]. To realize metamaterials operating at optical frequencies, a scaling law suggests that the size of the building blocks, i.e., meta-atoms which compose metamaterials, must be smaller than several tens of nanometers. Biomolecules, for example, subunits of proteins, are smaller than several tens of nanometers [73] and have identical structures determined by genomic information. Especially, virus proteins are able to self-assemble into three dimensional (3-D) structures. Hence, virus proteins are promising meta-atoms to construct 3-D optical metamaterials. We demonstrate here a chiral meta-molecule in the visible regions using a complex of Au nanodots and rod-shaped tobacco mosaic virus (TMV).

TMV is a rod-shaped plant virus consisting of a right-handed helical single-strand ribonucleic acid (RNA) surrounded by 2130 coat proteins [74] (Fig. 8.23a). We genetically fused a titanium-binding peptide (TBP; Arg-Lys-Leu-Pro-Asp-Ala) [75], which has been shown to promote mineralization of plasmonic metals [76], to the outer surface of the virus (Fig. 8.23b). We call this engineered virus, tbpTMV. Wild-type TMV (wtTMV) was used as a reference. For Au deposition, potassium chloroaurate ($KAuCl_4$) was mixed with the TMV in the presence of 5 % acetic acid, and the solution was reduced by 5 mM sodium borohydride ($NaBH_4$) for 20 min at ambient conditions [77, 78]. Figure 8.23c shows a transmission electron microscopic (TEM) image of wtTMV after Au deposition (wtTMV-Au). White rods correspond to the TMV. Black patches attached to the TMV correspond to the Au nanodots of 4.78 ± 2.18 nm in diameter. Figure 8.23d shows a TEM image of tbpTMV after Au deposition (tbpTMV-Au). Au nanodots more uniform in diameter of 4.96 ± 1.06 nm were deposited using tbpTMV as a scaffold.

Figure 8.24a shows absorption spectra for wtTMV-Au and tbpTMV-Au in solution [79]. An absorption peak around 540 nm was observed, which is attributed to

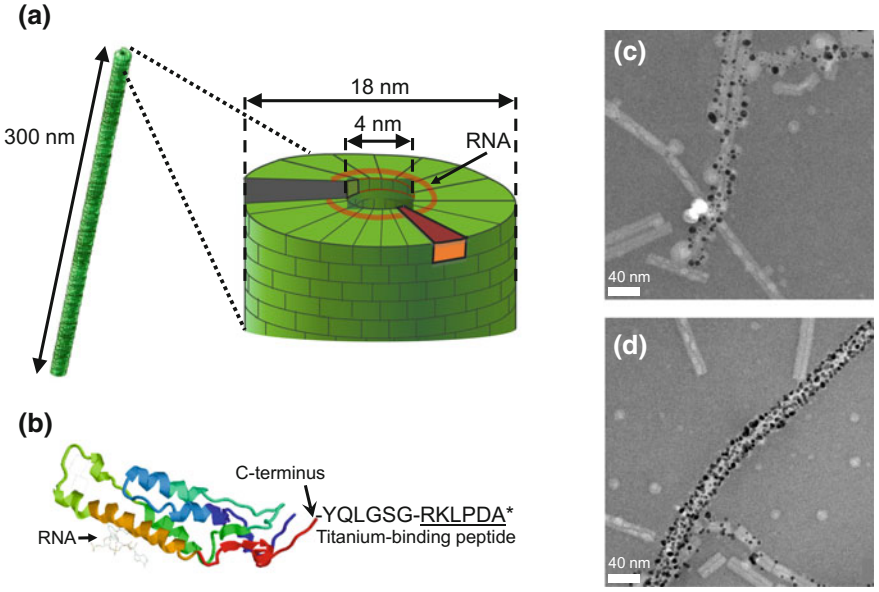

Fig. 8.23 **a** Schematic representation of TMV. **b** Atomic coordination of a coat protein subunit of the virus. TEM images of **c** wtTMV-Au and **d** tbpTMV-Au

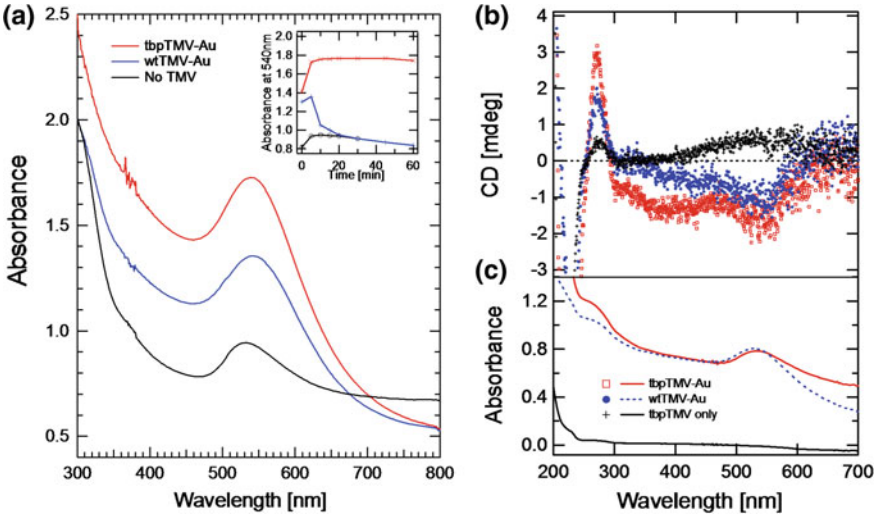

Fig. 8.24 **a** Absorption spectra of tbpTMV-Au (*red*), wtTMV-Au (*blue*), and reaction mixture without virus (*black*) in solution. *Inset* shows time dependence of absorbance at 540 nm. **b** CD spectra of the dried tbpTMV-Au (*red*), wtTMV-Au (*blue*), and tbpTMV only (*black*). **c** Simultaneously measured absorption spectra

localized surface plasmon of Au nanodots. Because tbpTMV-Au showed a larger absorbance at 540 nm, tbpTMV is a better scaffold for constructing TMV-Au complexes. In addition, tbpTMV-Au can be dispersed in solution for a longer period (inset of Fig. 8.24a). The tbpTMV-Au has thus improved dispersion in solution.

Figure 8.24b shows circular dichroism (CD) spectra, which is caused by the absorption difference between left-/right-handed circularly polarized light, of the dried samples of the TMV-Au complexes [79]. In the region between 300 and 700 nm of Fig. 8.24b, tbpTMV without Au nanodots (black crosses) shows no obvious CD peak. Contrastingly, for the tbpTMV-Au (red squares), a negative CD peak at about 540 nm was observed whereas optical activity in this region is negligible for TMV or Au nanodots themselves. A similar negative CD peak was observed for the wtTMV-Au (blue circles). It is noteworthy that the absorption peak derived from localized surface plasmon of Au nanodots in the dried samples was also observed around 540 nm as shown in Fig. 8.24c. This indicates the interaction of plasmonic resonance and optical activity. A strong electric field owing to localized surface plasmons probably enhances the CD signals of chiral molecules at plasmon wavelength [80]. The meta-molecule—structurally defined complex of Au nanodots and an engineered TMV—constructed here is a promising building block for 3-D chiral metamaterials at optical frequencies.

8.6 Summary

As described above, integration of semiconductor nano fabrication and biotechnology could be an innovative solution for the problems encountered in the previous top–down method. In this chapter, we described fascinating feature of bio nano process and demonstrated the various kinds of electron devices fabricated using the bio nano process such as memory, TFT, MEMS, Solar cell, etc. In addition, sensor or meta-material were also demonstrated to show their possibility for new optic devices.

Due to the development of internet society, integration and multifunctionality and low power consumption will be more and more required. At the same time, as their power source, energy harvesting devices such as solar cell or thermal transducer are also required. To meet these requirements, bio nano process will be a powerful tool for their fabrication. We can conclude that this technique is one of the promising methods that can meet the requirements in the future. This technique will open up the new world.

References

1. http://www.nobelprize.org/nobel_prizes/physics/laureates/1956/
2. U.S. Patent No. 3, 102, 230 (Filed 31 May 31, 1960, issued 27 Aug, 1963)

3. International Technology Roadmap for Semiconductors, http://www.itrs.net/links/2013ITRS/Home2013.htm
4. I. Yamashita, Thin Solid Films **393**(1–2), 12–18 (2001)
5. T. Hikono, Y. Uraoka, T. Fuyuki, I. Yamashita, Novel method for making nanodot arrays using a cage-like protein. Jpn. J. Appl. Phys. **42**, L398–L399 (2003)
6. F.C. Meldrum, B.R. Heywood, S. Mann, Science **257**, 522–523 (1992)
7. K. Sugimoto, S. Kanamaru, K. Iwasaki, F. Arisaka, I. Yamashita, Angew. Chem. **45**(17), 2725–2728 (2006)
8. D. Price, J.G. Joshi, Proc. Natl. Acad. Sci. **79**, 3116–3119 (1982)
9. F.C. Meldrum, V.J. Wade, D.L. Nimmo, B.R. Heywood, S. Mann, Nature **349**, 684–687 (1991)
10. J.F. Hainfeld, Proc. Natl. Acad. Sci. **89**, 11064–11068 (1992)
11. S. Mann, Nature **365**, 499–505 (1993)
12. F.C. Meldrum, T. Douglas, S. Lei, P. Arosio, S. Mann, J. Inorg. Biochem. **58**, 59–68 (1995)
13. T. Douglas, P.E.D. Dickson, S. Betteridge, J. Charnock, D.C. Garner, S. Mann, Science **269**, 54–56 (1995)
14. T. Douglas, V.T. Stark, Inorg. Chem. **39**, 1828–1830 (2000)
15. K. Iwahori, K. Yoshizawa, M. Muraoka, I. Yamashita, Inorg. Chem. **44**, 6393–6400 (2005)
16. R. Tsukamoto, K. Iwahori, M. Muraoka, I. Yamashita, Bull. Chem. Soc. Jpn. **78**(11), 2075–2081 (2005)
17. K. Yoshizawa, K. Iwahori, K. Sugimoto, I. Yamashita, Chem. Lett. **35**(10), 1192–1193 (2006)
18. K. Iwahori, I. Yamashita, J. Phys. Conf. Ser. **61**, 492–496 (2007)
19. K. Iwahori, I. Yamashita, J. Clust. Sci. **18**(2), 358–370 (2007)
20. I. Yamashita, J. Hayashi, M. Hara, Chem. Lett. **33**(9), 1158–1159 (2004)
21. T. Furuno, H. Sasabe, K.M. Ulmer, Thin Solid Films **180**, 23–30 (1989)
22. S. Kumagai, S. Yoshii, K. Yamada, N. Matsukawa, T. Fujiwara, K. Iwahori, I. Yamashita, Appl. Phys. Lett. **88**, 153103 (2006)
23. S. Kumagai, S. Yoshii, K. Yamada, N. Matsukawa, K. Iwahori, I. Yamashita, Jpn. J. Appl. Phys. **45**(10B), 8311–8316 (2006)
24. B. Zheng, I. Yamashita, M. Uenuma, K. Iwahori, M. Koayashi, Y. Uraoka, Site-directed delivery of ferritin-encapsulated fold nanoparticles. Nanotechnology **21**(4), 045305 (2010)
25. B. Zheng, N. Zettsu, M. Fukuta, M. Uenuma, T. Hashimoto, K. Gamo, Y. Uraoka, I. Yamashita, H. Watanabe, Versatile protein-based bifunctional nano-systems (encapsulation and directed assembly): Selective nanoscale positioning of gold nanoparticle-viral protein hybrids. Chem. Phys. Lett. **506**(1–3), 76 (2011)
26. C. He, M. Uenuma, Y. Shinoda, N. Okamoto, R. Honda, H. Kamitake, I. Yamashita, Y. Uraoka, *Improved Thermoelectric Properties by Control of Nanoparticles in Thin Film*. International Thermoelectric Society, A5, Nashville (2014)
27. A. Miura, T. Hikono, T. Matsumura, H. Yano, T. Hatayama, Y. Uraoka, T. Fuyuki, S. Yoshii, I. Yamashita, Floating nanodot gate memory devices based on biomineralized inorganic nanodot array as a storage node. Jpn. J. Appl. Phys. **45**(01), L1–L3 (2006)
28. T. Hikono, T. Matsumura, A. Miura, Y. Uraoka, T. Fuyuki, M. Takeguchi, S. Yoshii, I. Yamashita, Appl. Phys. Lett. **88**, 023108 (2006)
29. A. Miura, R. Tanaka, Y. Uraoka, N. Matsukawa, I. Yamashita, The characterization of a single discrete bionanodot for memory device application. Nanotechnology **20**, 125702-1–125702-9 (2009)
30. Y. Tojo, A. Miura, Y. Uraoka, T. Fuyuki, I. Yamashita, Controlled reduction of bionanodots for better charge strage characteristics of bionanodots flash memory. Jpn. J. Appl. Phys. **48**, 04C90-1–04C90-5 (2009)
31. K. Ohara, I. Yamashita, T. Yaegashi, M. Moniwa, H. Yoshimaru, Y. Uraoka, Floating gate memory with biomineralized nanodots embedded in High-k gate dielectric. Appl. Phys. Express **2**, 095001 (2009)

32. K. Ohara, Y. Uraoka, T. Fuyuki, I. Yamashita, T. Yaegashi, M. Moniwa, M. Yoshimaru, Floating gate memory based on ferritin nanodots with High-k gate dielectrics. Jpn. J. Appl. Phys. **48**(4), 04C153-1–04C153-4 (2009)
33. K. Ohara, Y. Tojo, I. Yamashita, T. Yaegashi, M. Moniwa, M. Yoshimaru, Y. Uraoka, Floating gate memory with biomineralized nanodots embedded in HfO_2. IEEE Trans. Nanotechnol. **10**(3), 576 (2011)
34. K. Ohara, I. Yamashita, Y. Uraoka, Thin-film transistor type flash memory with biomineralized Co nanodots on silicon-on-insulator. Jpn. J. Appl. Phys. **49**, 04DJ05 (2010)
35. K. Sano, H. Sasaki, K. Shiba, J. Am. Chem. Soc. **128**, 1717–1722 (2006)
36. K. Ohara, B. Zheng, M. Uenuma, Y. Ishikawa, K. Shiba, I. Yamashita, Y. Uraoka, Three dimensional nanodot-type floating gate memory fabricated by bio-layer-by-layer. Appl. Phys. Express **4**, 085004 (2011)
37. M.-J. Lee, S. Han, S.H. Jeon, B.H. Park, B.S. Kang, S.-E. Ahn, K.H. Kim, C.B. Lee, C.J. Kim, I.-K. Yoo, D.H. Seo, X.-S. Li, J.-B. Park, J.-H. Lee, Y. Park, Nano Lett. **9**, 1476 (2009)
38. S. Spiga, A. Lamperti, C. Wiemer, M. Perego, E. Cianci, G. Tallarida, H.L. Lu, M. Alia, F.G. Volpe, M. Fanciulli, Microelectron. Eng. **85**, 2414 (2008)
39. K. Kinoshita, K. Tsunoda, Y. Sato, H. Noshiro, S. Yagaki, M. Aoki, Y. Sugiyama, Appl. Phys. Lett. **93**, 033506 (2008)
40. H. Inoue, S. Yasuda, H. Akinaga, H. Takagi, Phys. Rev. B **77**, 035105 (2008)
41. B. Govoreanu, G.S. Kar, Y-Y. Chen, V. Paraschiv, S. Kubicek, A. Fantini, I.P. Radu, L. Goux, S. Clima, R. Degraeve, N. Jossart, O. Richard, T. Vandeweyer, K. Seo, P. Hendrickx, G. Pourtois, H. Bender, L. Altimime, D. J. Wouters, J.A. Kittl, M. Jurczak. 10×10 nm^2 Hf/HfOx crossbar resistive RAM with excellent performance, reliability and low-energy operation, in *Tech. Dig. Int. Electron Devices Meeting*, Washington DC (2011), pp. 729–732
42. M. Uenuma, K. Kawano, B. Zheng, N. Okamoto, M. Horita, S. Yoshii, I. Yamashita, Y. Uraoka, Resistive memory utilizing ferritin protein with nano particle. Nanotechnology **22**, 215201 (2011)
43. M. Uenuma, B. Zhen, K. Kawano, M. Horita, Y. Ishikawa, I. Yamashita, Y. Uraoka, Guided filament formation in NiO-resistive random access memory by embedding gold nanoparticles. Appl. Phys. Lett. **100**, 083105 (2012)
44. M. Uenuma, K. Kawano, B. Zheng, M. Horita, S. Yoshii, I. Yamashita, Y. Uraoka, Resistive memory utilizing ferritin protein with nano particle. Key Eng. Mater. **470**, 92–97 (2011)
45. M. Uenuma, T. Ban, N. Okamoto, B. Zheng, Y. Kakihara, M. Horita, Y. Ishikawa, I. Yamashita, Y. Uraoka, Memoristive nanoparticles formed using biotemplate, in *RCS Advances* (2013)
46. M. Uenuma, T. Ban, N. Okamoto, B. Zheng, Y. Kakihara, M. Horita, Y. Ishikawa, I. Yamashita, Y. Uraoka, Memristive nanoparticles formed using a biotemplate. R. Soc. Chem. Adv. **3**, 18044–18048 (2013)
47. K. Eriguchi, Z. Wei, T. Takagi, K. Ono, J. Appl. Phys. **107**(1), 013507 (2010)
48. K. Wei, Y. Kanzawa, K. Arita, Y. Katoh, K. Kawai, S. Muraoka, S. Mitani, S. Fujii, K. Katayama, M. Iijima, T. Mikawa, T. Ninomiya, R. Miyanaga, Y. Kawashima, K. Tsuji, A. Himeno, T. Okada, R. Azuma, K. Shimakawa, H. Sugaya, T. Takagi, R. Yasuhara, K. Horiba, H. Kumigashira, M. Oshima, Highly reliable TaOx ReRAM and direct evidence of redox reaction mechanism, in *IEEE International Electron Devices Meeting, IEDM 2008* (2008)
49. Y. Uraoka, T. Hatayama, T. Fuyuki, T. Kawamura, Tsuchihashi, Reliability of high-frequency operation of low-temperature polysilicon thin film transistors under dynamic stress. Jpn. J. Appl. Phys. **39**, L1209–L1212 (2000)
50. R.C. Cammarata, C.V. Thomson, C. Hayzelden, K.N. Tu, J. Mater. Res. **5**, 2133 (1990)
51. C. Hayzelden, J.L. Batstone, J. Appl. Phys. **73**, 8279 (1993)
52. H. Kirimura, Y. Uraoka, T. Fuyuki, M. Okuda, I. Yamashita, Study of low-temerature crystallization of amorphous Si film obtained using ferritin with Ni nanoparticles. Appl. Phys. Lett. **86**, 262106 (2005)

53. Y. Tojo, A. Miura, I. Yamashita, Y. Uraoka, Positional control of crystal grains in silicon thin film utilizing cage-shaped protein. Jpn. J. Appl. Phys. **50**, 04DL12 (2011)
54. Y. Tojo, A. Miura, Y. Ishikawa, I. Yamashita, Y. Uraoka, Polycrystalline silicon thin-film transistor utilizing self-assembled monolayer for crystallization. Thin Solid Films **540**, 266–270 (2013)
55. M. Uenuma, B. Zheng, K. Bundo, M. Horita, Y. Ishikawa, H. Watanabe, I. Yamashita, Y. Uraoka, Crystallization of amorphous Ge thin film using Cu nanoparticle synthesized and delived by ferritin. J. Cryst. Growth **382**, 31–35 (2013)
56. J.E.-Y. Lee, Y. Zhu, A.A. Seshia, J. Micromech. Microeng. **18**, 064001 (2008)
57. K. Nakamura, Y. Naito, K. Onishi, H. Kawakatsu, J. Miromech. Microeng. **22**, 125028 (2012)
58. S. Nitzan, C.H. Ahn, T.-H. Su, M. Li, E.J. Ng, S. Wang, Z.M. Yang, G. O'Brien, B.E. Boser, T.W. Kenny, D.A. Horsley, in *Proceedings of the 26th IEEE International Conference on Micro Electro Mechanical Systems*, Tapipei (2013), p. 625
59. J. Yang, T. Ono, M. Esashi, Appl. Phys. Lett. **77**, 3860 (2000)
60. D.F. Wang, T. Ono, M. Esashi, Appl. Phys. Lett. **83**, 3189 (2003)
61. V.T. Srikar, S.D. Senturia, J. Microelectromech. Syst. **11**, 499–504 (2002)
62. J. Gaspar, V. Chu, J.P. Conde, J. Appl. Phys. **97**, 094501 (2005)
63. M. Villarroya, J. Verd, J. Teva, G. Abada, E. Forsen, F.P. Murano, A. Uranga, E. Figueras, J. Montserrat, J. Esteve, A. Boisen, N. Barniol, Sens. Actuators A **132**, 154 (2006)
64. S. Kumagai, T. Tomikawa, S. Ogawa, I. Yamashita, Y. Uraoka, M. Sasaki, Appl. Phys. Lett. **103**, 223103 (2013)
65. B. O'Regan, M. Grätzel, A low-cost high-efficiency solar cell based on dye-sensitized colloidal TiO_2 thin films. Nature **353**, 737–740 (1991)
66. M. Grätzel, Photoelectrochemical cells. Nature **414**, 338–344 (2001)
67. I. Inoue, K. Watanabe, H. Yamauchi, Y. Ishikawa, H. Yasueda, Y. Uraoka, I. Yamashita, Biological construction of single-walled carbon nanotube electron transfer pathways in dye-sensitized solar cells. ChemSusChem (2014). doi:10.1002/cssc.201402514
68. T. Hashimoto, Y. Fukunishi, B. Zheng, Y. Uraoka, T. Hosoi, T. Shimura, H. Watanabe, Electrical detection of surface plasmon resonance phenomena by a photoelectronic device integrated with gold nanoparticle plasmon antenna. Appl. Phys. Lett. **102**, 083702 (2013)
69. Y. Takahashi, H. Namatsu, K. Iwadate, M. Nagase, K. Murase, IEEE Trans. Electron Devices **43**, 1213–1217 (1996)
70. J. Shirakashi, K. Matsumoto, N. Miura, M. Konagai, Appl. Phys. Lett. **72**, 1893–1895 (2009)
71. S. Kumagai, S. Yoshii, N. Matsukawa, R. Tsukamoto, K. Nishio, I. Yamashita, Ext. Abst. SSDM, D-8-5,956-957 (2007)
72. D.R. Smith, J.B. Pendry, M.C.K. Wiltshire, Science **305**, 788 (2004)
73. A.D. Malay, J.G. Heddle, S. Tomita, K. Iwasaki, N. Miyazaki, K. Sumitomo, H. Yanagi, I. Yamashita, Y. Uraoka, Nano Lett. **12**, 2056 (2012)
74. M. Kobayashi, M. Seki, H. Tabata, Y. Watanabe, I. Yamashita, Nano Lett. **10**, 773 (2010)
75. K. Sano, K. Shiba, J. Am. Chem. Soc. **125**, 14234 (2003)
76. K. Sano, S. Yoshii, I. Yamashita, K. Shiba, Nano Lett. **7**, 3200 (2007)
77. K.M. Bromley, A.J. Patil, A.W. Perriman, G. Stubbs, S. Mann, J. Mater. Chem. **18**, 4796 (2008)
78. M. Kobayashi, I. Yamashita, Y. Uraoka, K. Shiba, S. Tomita, Proc. SPIE **8070**, 8070C (2011)
79. M. Kobayashi, S. Tomita, K. Sawada, K. Shiba, H. Yanagi, I. Yamashita, Y. Uraoka, Opt. Express **20**, 24856 (2012)
80. A.O. Govorov, Z. Fan, P. Hernandez, J.M. Slocik, R.R. Naik, Nano Lett. **10**, 1374 (2010)

Chapter 9
Fabrication of 3D Quantum Dot Array by Fusion of Bio-Template and Neutral Beam Etching I: Basic Technologies

Seiji Samukawa

Abstract The direct formation of a uniform, closely packed, and high density two-dimensional array of ferritin molecules is realized on Si and GaAs substrates using our developed neutral beam oxidation (NBO) technique to prepare the surface oxide. The NBO process is applied to form thin films by slight surface oxidations, which have negative zeta potential and highly hydrophilic surfaces. It is experimentally proven that surface hydrophilicity is essential for the mechanism of uniform and high density ferritin arrangement. Uniform and defect-free 2D and 3D array of Si-NDs with ND density of more than 7×10^{11} cm^{-2} were realized as Si-QDSLs using combination of bio-templates and NBE processes. The diameter of Si-ND can be controlled by changing the conditions under which surface-oxide removal was conducted. 2D array of GaAs-NDs with ND density of 7×10^{11} cm^{-2} has been also developed successfully. Each step of the process, i.e., ferritin protein shell removal, NBE, and iron core removal, has been investigated and several novel solutions have been developed that do not damage the GaAs substrate. O-radicals are first found to eliminate the protein shell effectively at a low temperature of 280 °C without deteriorating surface roughness or moving the iron oxide cores. NBE with a 22 % chlorine and 78 % argon gas mixture and 16 W RF bias power can etch a GaAs nanostructure with a diameter of about 10 nm, atomic-level surface roughness of less than 1 nm and vertical taper angle of 88°.

Keywords Bio-template · Neutral beam etching · 2D array of ferritin molecular · Nanodisk

S. Samukawa (✉)
Institute of Fluid Science, Tohoku University, Sendai 980-8577, Japan
e-mail: samukawa@ifs.tohoku.ac.jp

J. Sone and S. Tsuji (eds.), *Intelligent Nanosystems for Energy, Information and Biological Technologies*, DOI 10.1007/978-4-431-56429-4_9

9.1 Introduction

As material size shrinks to a nanometer scale, the materials start to show specific electrical and optical characteristics based on the quantum confinement of conduction band electrons, valence band holes or excitons in several nanoscales. Recently, super lattices with closely packed quantum dots (QDSLs) with high-uniformity, and high density have been received great attention to develop high-performance optoelectronic devices, including lasers and solar cells. Bandgap energy (E_g) of the QDs is engineered by adjusting the size of the QDs [1–4]. In super lattices with close-packed and well-aligned QDs, wave functions of QDs overlap each another, and discrete energy levels of each QD merge to form broadened mini-bands [5–9]. For photovoltaic applications, such engineered QDs can be used as an adjustable absorber layers with intermediate bandgap energy and applied to tandem solar cells [9–12]. Highly efficient solar cells is expected using SiC as interlayer material instead of SiO_2 and SiN, because carrier wave function easily spreads into the interlayers due to its lower bandgap energy. Quantum dot (QD) of III–V compounds has also been formed by bottom-up process such as Stranski–Krastanov growth based on self-organization [13] and attractive to develop optoelectronic devices including high-performance QD lasers [1–4]. In this method, there is some limitation in forming QDs with high density and separation enough to avoid the coupling of wave functions to realize high gain laser. However, it is difficult to fabricate defect-free nanostructures using conventional top-down process technologies such as epitaxy followed by photolithography, plasma etching, co-sputtering, and annealing [14–17].

In this chapter, to break-through the above problems, our innovative processes for fabrication of uniform and closely packed arrays of sub-10-nm Si and GaAs nanodisks (GaAs-ND) was realized using a damage-free neutral beam (NB) etching technology combined with a bio-template process to address these issues.

9.2 Top-Down Process for the Fabrication of Sub-10-nm Structure

To address the problems in the process technologies discussed above, we proposed a new fabrication method of uniform and closely packed arrays of sub-10-nm Si and GaAs nanodisks (GaAs-ND) which combines a bio-template [18] and damage-free neutral beam etching [19]. We employ ferritins to make a nano-etching mask. The ferritins produced from DNA information can make uniform 7-nm iron oxide (Fe_2O_3) cores in their cavities. A high density 2D-ordered array of ferritin on a substrate provides an array of independent cores with distances that are roughly twice the protein shell thickness after selective protein shell elimination. By using the iron core as an etching mask, our developed neutral beam etching processes could fabricate 2D array of defect free nanodisk on any kind of materials.

9.2.1 Neutral Beam Sources for Damage-Free Etching and Surface Oxidation

For the development of damage-free etching processes, neutral beam (NB) sources have been investigated as substitutes for conventional plasma source. Using the sources, damage-free etching processes can be achieved by eliminating charged particles (ions and electrons). During etching, energetic neutral beams, rather than ions, bombard the wafer surface where radicals absorb, resulting in the removal of the materials. In particular, Samukawa has developed practical NB sources for high-performance neutral beam etching. Figure 9.1 provides a schematic representation of a NB source that consists of an ICP and parallel carbon plates [19–21]. The process chamber is separated from the plasma chamber by a bottom electrode made of carbon, which has the low sputtering yield under high-energy bombardment and does not contaminate semiconductor devices. Neutral beams are extracted from the plasma through numerous high-aspect-ratio apertures in the bottom electrode. The NB sources employ pulse-time-modulated ICPs to generate large quantities of negative ions, which are more effectively neutralized than positive ions because the detachment energy of electrons from negative ions is much smaller than the charge transfer energy of positive ions. In previous-generation neutral beam sources, where neutral beams are obtained through the charge transfer of positive ions, the neutralization efficiency is at most 60 % and the beam energy must be greater than 100 eV to obtain a large degree of neutralization of positive ions. On the other hand, a NB source using Cl_2 plasma with pulsed operation can obtain a neutralization efficiency of almost 100 % and high neutral beam flux of more than 1 mA/cm^2. At the same time, because of the presence of apertures, UV radiation

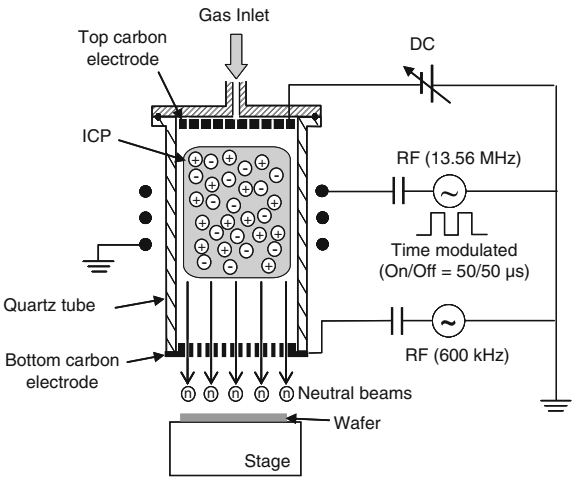

Fig. 9.1 Schematics of neutral beam system

from the plasma is shaded and/or absorbed in the bottom electrode; consequently, UV radiation damage can be eliminated. The NB process is a promising solution for next-generation nanoscale device fabrication, which requires damage-free etching conditions [19–25]. Additionally, we also developed damage-free neutral beam oxidation (NBO) for the fabrication of ultrathin oxide films on Si and GaAs surfaces at a temperature of less than 300 °C using energy-controlled oxygen neutral beam [22–24]. In this system, the Si aperture was used for neutral beam generation to eliminate carbon contamination at the interface.

9.2.2 High Density Ferritin Arrangement

A uniform, closely packed, and high density 2D array of ferritin molecules was directly formed on a Si and GaAs substrate with preparation of surface oxide. The NBO process [22–25] was applied to form both SiO_2 and GaAs oxide thin films that have negative zeta potential and highly hydrophilic surfaces [26, 27]. To form the high density 2-dimensional ferritin array, two interactions should be considered, i.e., ferritin–ferritin and ferritin–substrate interaction. The former interaction is an attractive force due to the hydrophobic interaction between ferritins derived from the carbonaceous binding peptides [28, 29]. Therefore, the interaction between ferritin and surface plays an important role in this study. When the ferritin solution is dropped onto a hydrophilic surface, ferritin molecules spread over the substrate and are then absorbed onto the surface oxide [28]. When the surface oxide is highly hydrophilic, such as with Si-NBO or GaAs-NBO, the surface hydrophilicity would reduce the absorption force of the ferritin, as shown in Fig. 9.2. A negative zeta potential would also weaken the interaction between the ferritin and NBO surfaces. Therefore, soft absorption between ferritin molecules and the oxide surface was realized, and the ferritin could attain sufficient degree-of-freedom of movement and then easily reform the arrangement to make a closely packed array. In other words, absorption force between ferritin and substrate was weak enough to allow ferritins to be rearranged by attractive protein–protein interaction. A repulsive force due to the negative charge of ferritin and the negative potential of the oxide surface may also help prevent multilayer generation of ferritins on the substrate. On the other hand, if the absorption force is stronger in the case of using thermal oxide (TO), ferritin will not move again once it absorbs to the surface, which results in a disordered arrangement. This might be what happened with the TO. The reason the adsorption force is strong with TO is not clear, but the difference in hydrophilicity might explain it. There might be an attractive force between the hydrophobic surface patches of ferritin and the TO substrate. To prove this hypothesis, we need to conduct more studies on ferritin adsorption behavior.

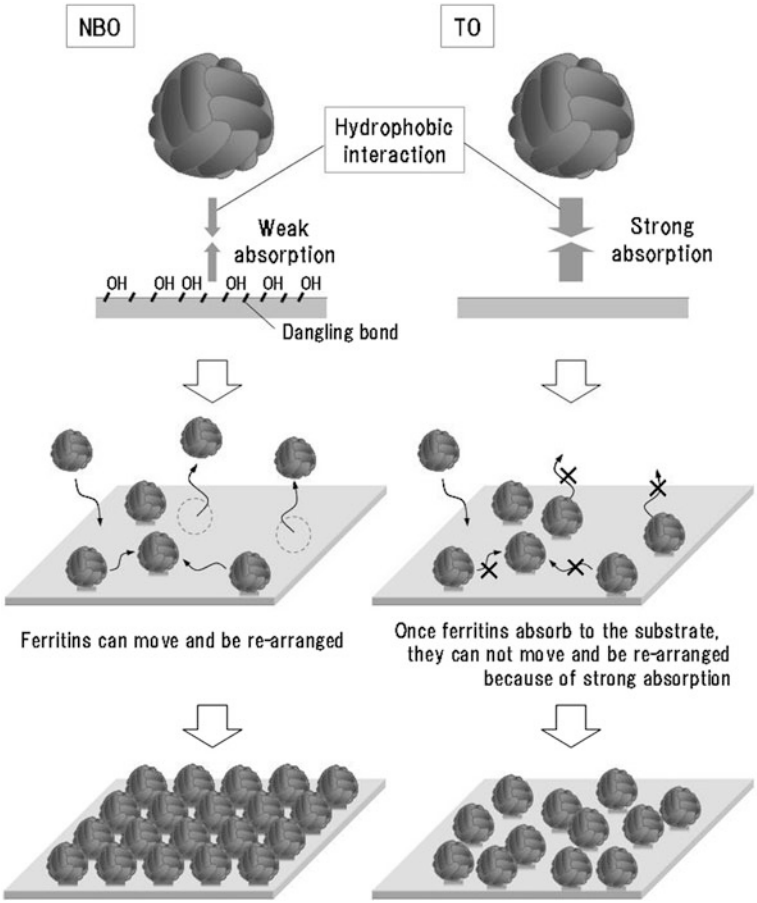

Fig. 9.2 Schematic image of uniform and high density arrangement mechanism [23]

9.3 Fabrication of Silicon Nanodisks

9.3.1 Process Flow

To measure optical transmittances, we prepared 2D arrays of Si-NDs with SiO_2 or SiC matrix on quartz substrate. The fabrication of a 2D Si-ND array structure using the two types of bio-template of ferritin and Listeria-Dps (Lis-Dps) and damage-free NB etching is schematically shown in Fig. 9.3a–i. The fabrication steps are as follows. First, 2–12 nm-thick poly-Si and 3-nm-thick Si-NBO (SiO_2) layers were fabricated on a 10 × 10 mm^2 quartz substrate as shown in Fig. 9.3b, c. The poly-Si

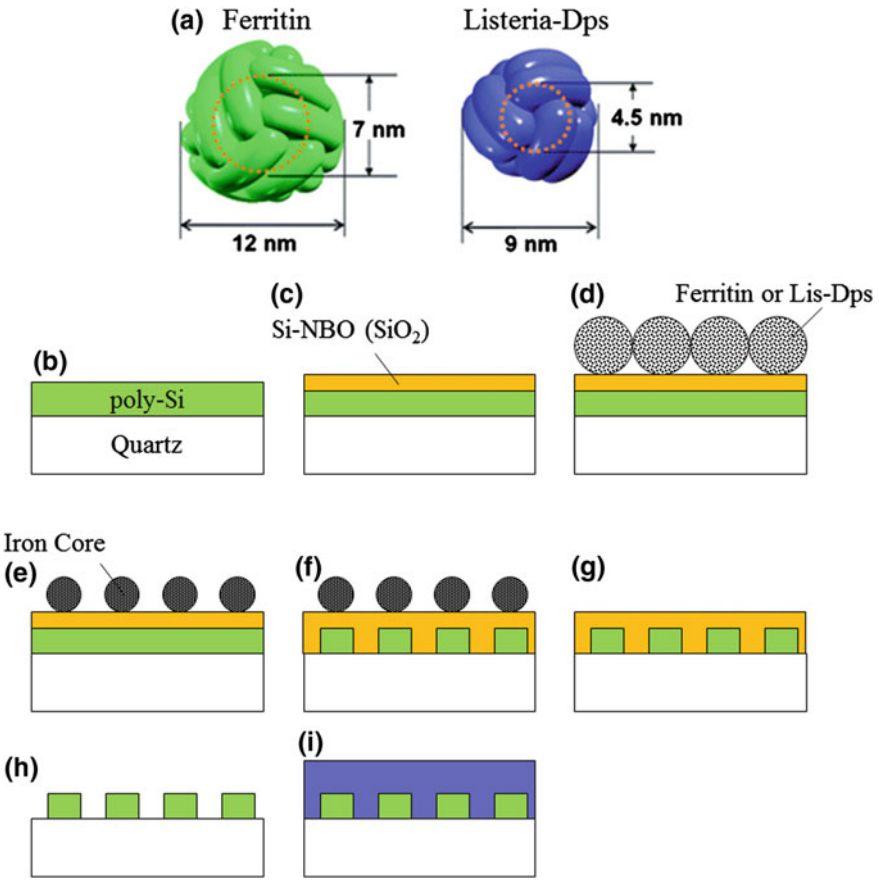

Fig. 9.3 Flow of sample preparation

layer was prepared using molecular beam epitaxy with a controlled deposition rate of 0.05 nm/min followed by annealing in argon atmosphere at 600 °C for 16 h. By in situ monitoring the poly-Si deposition thickness we could precisely control the thickness of the Si-ND. Then a 3 nm SiO_2 layer was fabricated using our developed neutral beam oxidation process at a low temperature of 300 °C as a surface oxide (Si-NBO) [22–24]. Second, a new bio-template of a 2D array of ferritin (a 7.0 nm diameter iron oxide core in the cavity) or Lis-Dps (a 4.5 nm diameter iron oxide core) molecules was formed as shown in Fig. 9.3d. Lis-Dps is a Dps protein that is synthesized from Listeria bacteria. It has a spherical protein shell with an external diameter of 9.0 nm and a cavity diameter of 4.5 nm, and biomineralizes iron as a hydrate iron oxide core (diameter: 4.5 nm) in the cavity and stores it. Using iron oxide core as the 4.5 nm diameter etching mask, we would like to realize a much smaller diameter size of the Si-ND structure. Next, protein shells were removed by heat treatment in oxygen atmosphere at 500 °C for 1 h to obtain a 2D array of iron

oxide cores as the etching masks, as shown in Fig. 9.3e. Etching was carried out by combination between NF_3/H-radicals treatment at 100 °C [30, 31], and anisotropic etching of poly-Si using Cl_2 NB, respectively, as shown in Fig. 9.3f [23]. During the etching process by changing the NF_3/H-radicals treatment time to 15 and 40 min we could change the diameter of ND due to the side etching of Si-NBO. Then, the 2D iron oxide core array was removed using hydrochloric solution to obtain a 2D Si-ND array structure, as shown in Fig. 9.3g. Because the native oxide grows between Si-NDs, we call this structure simply a 'Si-ND array structure with a SiO_2 matrix.' For fabrication of the Si-NDs with SiC matrix, finally, the SiO_2 matrix was removed by the NF_3/H-radicals treatment and then a 3-nm-thick SiC was deposited on Si-NDs by sputtering system as shown in Fig. 9.3h, i.

Figures 9.4a and 9.5a show a top-view SEM image of the 2D Si-ND array structure fabricated using Ferritin and Lis-Dps as the etching mask, which consisted of a closely packed array of 7 and 4.5 nm diameter iron oxide cores on the Si-NBO surface. As the figure shows, this array structure had a high density (7×10^{11} and 1.4×10^{12} cm^{-2} respectively), uniform size (Si-ND diameter: 6.4 and 10 nm) and well-ordered arrangement (quasi-hexagonal ordered arrays). The density of the 2D Si-ND array structure fabricated using Lis-Dps increased to two times that of the array fabricated using ferritin, while the diameter of the Si-ND shrunk to 61 % of that obtained using ferritin with 40 min NF_3/H-radicals treatment. To confirm regularity in this array, we measured the center-to-center distance between adjacent Si-NDs, as shown in the SEM image in Figs. 9.4b and 9.5b. These figures show that the standard deviation of the center-to-center distance was less than 10 %. The results show that the 2D Si-ND array structure fabricated using a Ferritin and Lis-Dps etching mask with a 4.5 and 7 nm diameter iron oxide core formed a 2D superlattice structure with a highly density and well-ordered arrangement, making it a suitable quantum dot structure.

9.4 Photoluminescence in Silicon Nanodisk

To analyze defects at the interface between a Si-ND and the SiO_2 matrix, high-sensitivity electron spin resonance (ESR) analysis was performed to quantify the presence of any paramagnetic defects. We used Si-NBO grown onto a p-type Si wafer with a (111) surface orientation and a high resistivity of more than 1000 Ω cm. ESR measurement was performed on the samples at 4 K using a Bruker-ESP300E spectrometer. The microwave frequency and power were approximately 9.62 GHz and 0.1 mW, respectively. The paramagnetic (P_b) center density at the Si-ND/Si-NBO (SiO_2) interface was 5.0×10^{10} cm^{-2}. Incidentally, the surface areas of the (7 nm in diameter) Si-NDs with thicknesses of 4 and 8 nm were 1.6×10^{-12} and 2.5×10^{-11} cm^2, respectively. Therefore, we were able to estimate the number of defects in 4 and 8 nm-thick Si-NDs at 0.08 and 0.16, respectively. In achieving these results, we found that the interface between the Si-NDs and the SiO_2 matrix was almost completely defect-free.

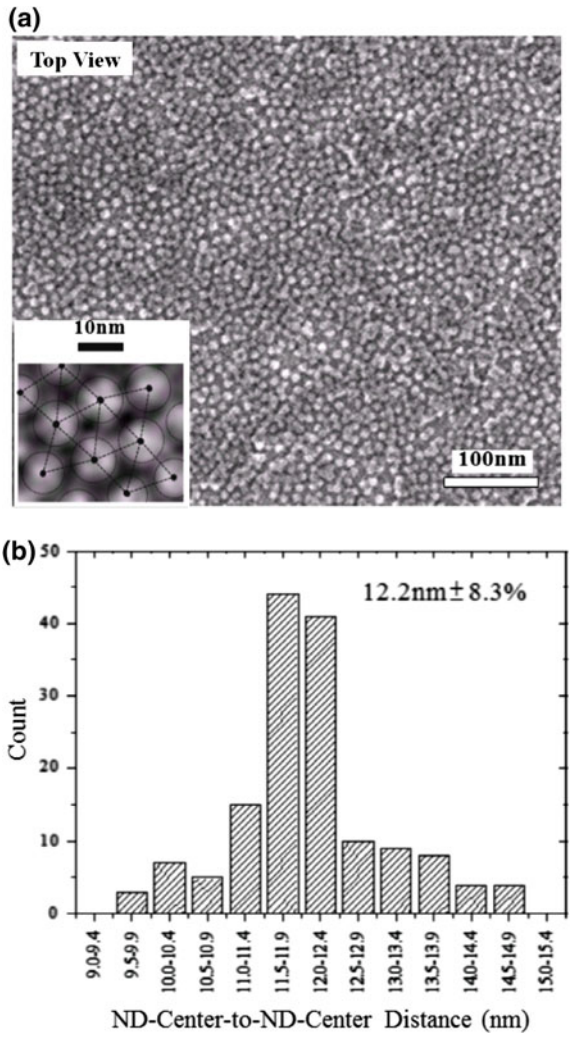

Fig. 9.4 **a** SEM picture of 2D array of Si-NDs. **b** Distribution of ND-Center-to-ND-Center distances

Silicon is basically an indirect band gap semiconductor and thus its optical absorption and radiative recombination efficiencies are markedly low. On the other hand, with a QD structure, the surface effect and size effect, which modify the carrier wave function, can improve radiative recombination efficiency [32–34]. However, in the conventional fabrication processes, a large amount of defect-induced and interfacial local energy levels can be formed easily. As a result, the majority of experiments on Si nanostructures have shown extremely slow decaying PL with decay times ranging from several tens of nanoseconds to microseconds. This can be attributed to carriers recombining at the defect states rather than the nanostructure itself [33]. With this in mind, we researched photo-excited emissions from the Si-ND array structure. Figure 9.6 shows time-integrated PL spectra of a 2D array of 8-nm-thick Si-NDs with

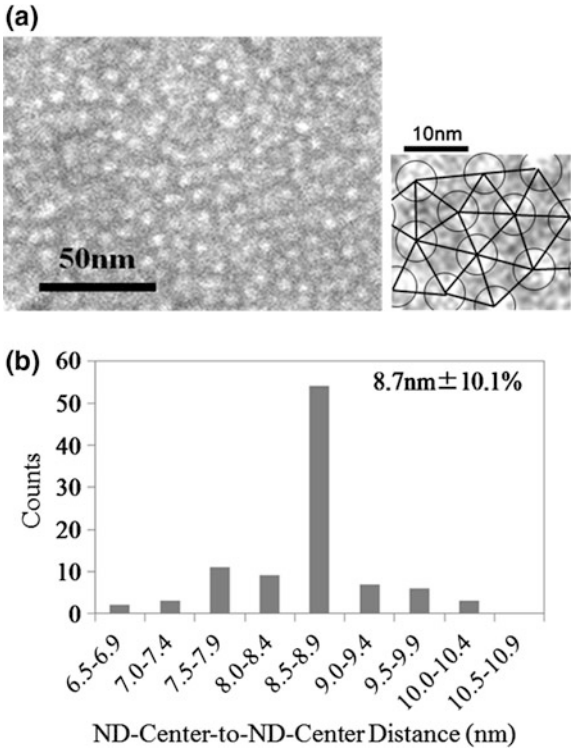

Fig. 9.5 **a** SEM image of 2D Si-NDs array using Lis-Dps. **b** Distribution of ND-center-to-ND-center distances

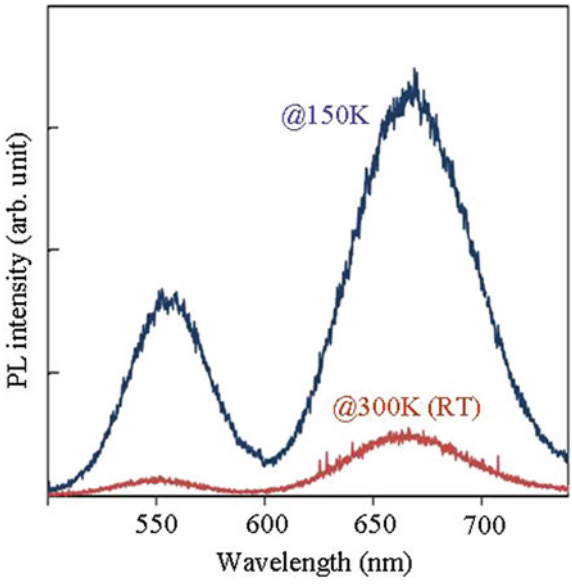

Fig. 9.6 Time-integrated PL spectra of a 2D array of 8-nm-thick Si-NDs with a SiO_2 interlayer for an excitation power of 50 mW

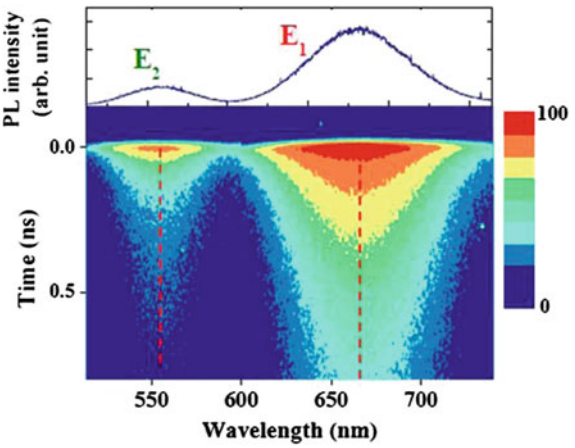

Fig. 9.7 Time-integrated and time-resolved PL spectra of a 2D array of 8-nm-thick Si-NDs measured at a temperature of 150 K

a SiO_2 interlayer for an excitation power of 50 mW. We performed the measurement from 10 to 300 K. The result shows two PL emissions centered at wavelengths of 665 nm (E_1: 1.86 eV) and 555 nm (E_2: 2.23 eV), and the highest peak of PL intensity was observed at 150 K. Moreover, PL emission of 2D array of Si-NDs structure also could be observed even in the room temperature. Figure 9.7 shows time-integrated and time-resolved PL spectra of a 2D array of 8-nm-thick Si-NDs measured at a temperature of 150 K. While the decay characteristic of two PL bands is slow in the case of conventional self-assembled QD, i.e., the microsecond region originating in local states in Si and SiO_2 induced by a defect or interface state [33], both peaks in our structure show short lifetimes of 3 ns or less. Therefore, we can rule out assigning the emission bands to defect-related emissions.

9.5 Control of Bandgap Energy by Geometric Parameters of Nanodisk

Figure 9.8a shows the results of E_g as a function of Si-ND thickness. We found that, for the 2D array of Si-NDs, E_g can be controlled from 2.3 to 1.3 eV when the ND thickness is changed from 2 to 12 nm. We also saw that, when the poly-Si thin film thickness changes from 2 to 8 nm, E_g varies from 1.6 to 1.1 eV, which is the E_g of bulk Si. From these results, as shown in Fig. 9.8a, we know that the controllable E_g range of a 2D array of Si-NDs is much larger than that of poly-Si thin film. Figure 9.8b shows the results of E_g as a function of Si-ND diameter controlled by the bio-templates and NF_3/H-radicals treatment. By shrinking the Si-ND diameter from 12.5 to 6.4 nm, the E_g increased from 1.9 to 2.1 eV even at a ND thickness of 4 nm. We found that the E_g could be controlled by both Si-ND thickness and diameter. The diameter from 6.4 to 12.5 nm allowed the E_g to be changed in the range of 0.1 eV, while controlling the thickness from 2 to 12 nm

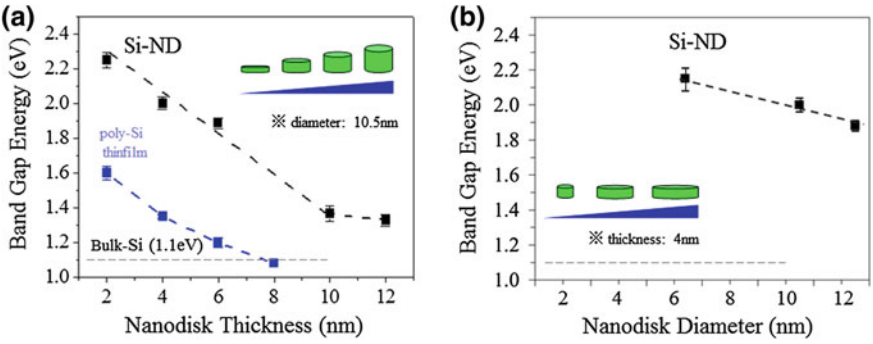

Fig. 9.8 Bandgap control by changing thickness and diameter

allowed the gap to change in the range of 0.5 eV. This result also suggests that stronger quantum confinement occurs in the thickness direction. These results made it clear that independently changing the geometric parameters of thickness and diameter in our proposed Si-ND array structure enables the optical band gap energy to be precisely designed within a wide range. This wide controllable range of E_g is very suitable for developing all-Si tandem solar cells. For the three cells of all-Si tandem solar cells, the E_g of the top and middle cells requires 2.0 and 1.5 eV, respectively [35].

9.6 Fabrication of Gallium Arsenide Nanodisks

9.6.1 Process Flow

The process flowchart is shown in Fig. 9.9 and described next. (1) The GaAd substrate was sequentially cleaned using acetone, ethanol, and deionized water for 5 min, respectively, in an ultrasonic bath (Fig. 9.9a). (2) The surface native oxide of GaAs was removed through a hydrogen-radical treatment at 280 °C with a hydrogen flow rate of 40 sccm, process pressure of 40 Pa, and 2.45 GHz microwave power of 200 W (Fig. 9.9b). (3) After native oxide removal, the GaAs substrate was transferred to a neutral beam oxidation (NBO) chamber in a vacuum environment and then sequentially oxidized to form a 1-nm-thick GaAs–NBO film at room temperature with an O_2 flow rate of 5 sccm, process pressure of 0.14 Pa and 13.56 MHz RF power of 500 W (Fig. 9.9c). (4) Ferritin molecules were spin-coated on the GaAs-NBO surface for 500 rpm in 2 s and 3000 rpm in 30 s to form the 2D array monolayer (Fig. 9.9d). (5) The protein shell of the ferritin was removed through an O-radicals treatment with a temperature of 280 °C, O_2 flow rate of 30 sccm, process pressure of 50 Pa and 2.45 GHz microwave power of 200 W (Fig. 9.9e). (6) After removal of the ferritin protein shell, the iron oxide cores inside the ferritin remain as the etching mask and then GaAs was etched by a

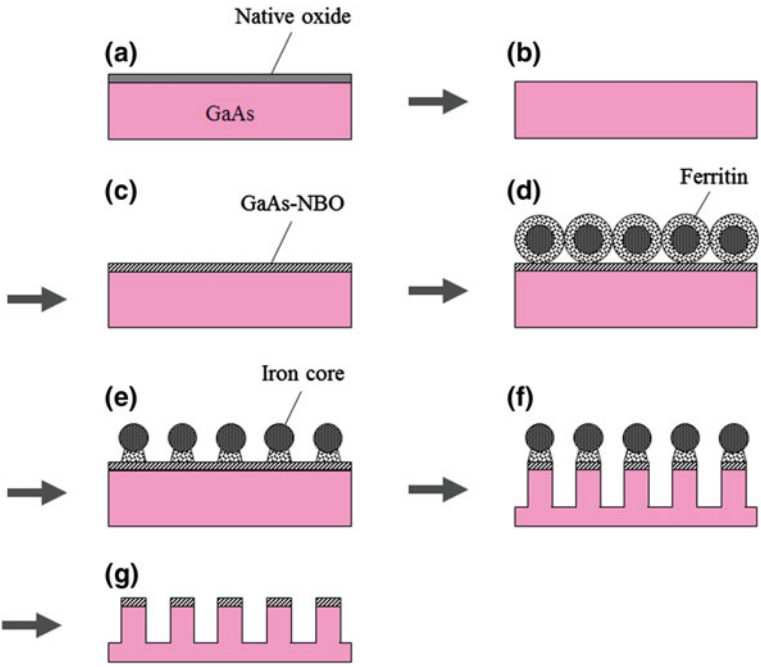

Fig. 9.9 Process flow for fabricating 2D array of GaAs-QDs

neutral beam process (Fig. 9.9f). (7) Finally, the iron oxide cores were removed using a diluted hydrogen chloride solution (HCl:H_2O = 1:10), resulting in the 2D array of GaAs-QDs (Fig. 9.9g).

There are two conventional approaches to removing the ferritin protein shell: ultraviolet (UV) ozone treatment at 150 °C and oxygen annealing at a high temperature of 500 °C. The UV ozone treatment produces UV irradiation damage that would seriously damage the GaAs QD crystalline structure, and the high temperature oxygen annealing would cause severe surface roughness because of desorption of As. Therefore, a low temperature process without UV light needs to be developed for removing the ferritin protein shell. In this work, we first developed an O-radicals treatment approach to removing the ferritin protein shell. The O-radicals system consists of a plasma chamber and treatment chamber that are connected by a φ2 mm aperture (Fig. 9.10). The O-radicals are extracted from plasma generated by a 2.45 GHz RF power source and are passed through the aperture into the treatment chamber. Meanwhile, the UV light from the plasma would be eliminated by the φ2 mm aperture.

In this condition, we found that 280 °C O-radicals treatment was confirmed to remove protein shells effectively. Then, top-view SEM images were observed to check whether the iron oxide cores were still arranged as well as before the treatment. Three different treatment times were investigated: 30, 45, and 60 min.

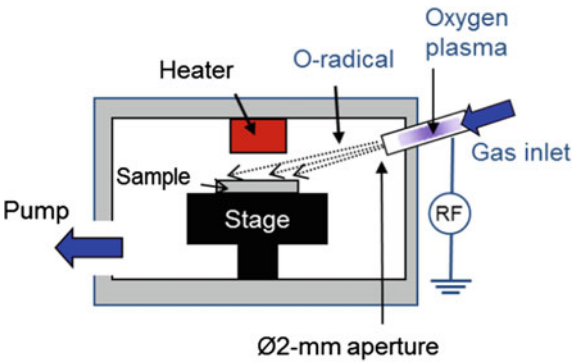

Fig. 9.10 Illustration of O-radicals system

After the 30 min treatment, in a comparison with the SEM image of 2D array ferritins, the iron oxide cores were still arranged in order of high density, as shown in Fig. 9.11a. However, after the 45 min treatment, part of the iron oxide cores moved and some locations were not occupied by iron cores (Fig. 9.11b). Furthermore, after the 60 min treatment, many of the iron cores not only moved but also aggregated together (Fig. 9.11c)

Initially, the O-radicals only contact and react with the upper parts of the protein shell. As treatment time increases, most of the upper part of the protein shell would be removed while the bottom part still exists. The iron core would be exposed

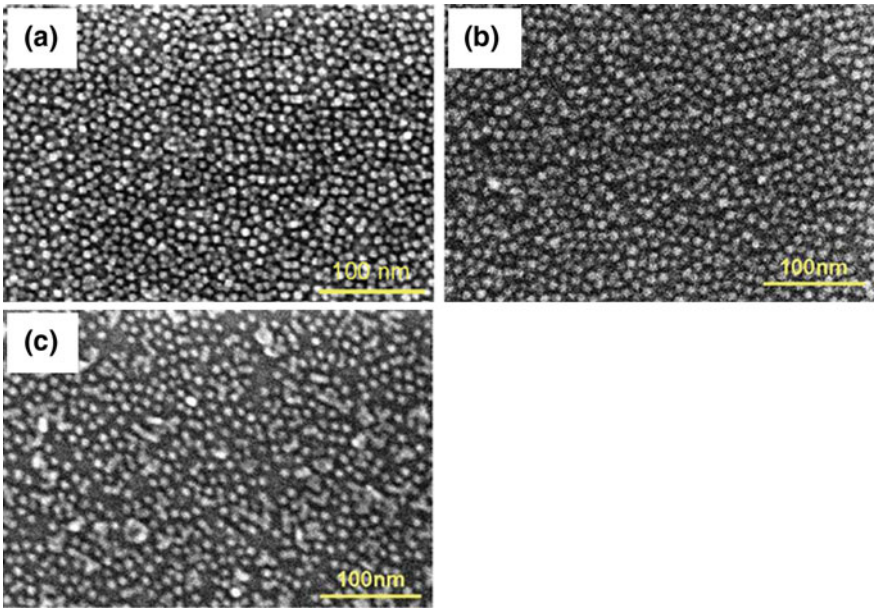

Fig. 9.11 Top-view SEM images after 280 °C O-radicals treatment with different treatment time: **a** 30 min, **b** 45 min, and **c** 60 min

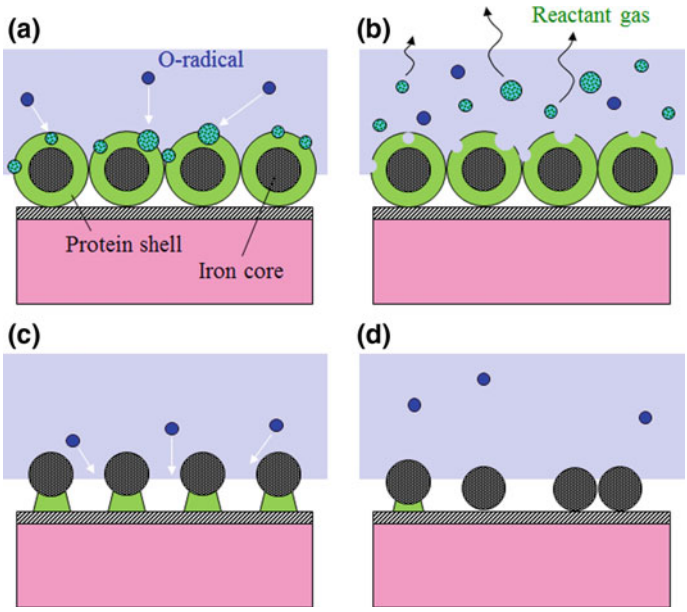

Fig. 9.12 Schematic of ferritin protein shell removal with oxygen-radical treatment at 280 °C (from **a** to **d**)

without moving because it is supported by the residual protein shell (Fig. 9.12c). This situation is similar to the experiment results after the 30 min O-radicals treatment at 280 °C (Fig. 9.11a). However, when the treatment time is longer than 30 min, the bottom part of the protein shell would also be eliminated by the O-radicals. Finally, the iron oxide core loses all protein shell support and thus moves easily (Fig. 9.12d), as in the experimental results of the 45 min (Fig. 9.11b) and 60 min (Fig. 9.11c) treatments. To summarize and to maintain the arrangement of a 2D array iron core, a suitable treatment time at 280 °C is necessary. Although FTIR analysis cannot detect the C=O and N–H bond signals of ferritin protein after treatment for 30 min at 280 °C, it is believed that the small bottom parts of the residual protein, which fixed the iron oxide cores in order as shown in Fig. 9.9e, were very few and cannot be detected. In this work, the O-radicals treatment for 30 min at 280 °C can remove the ferritin protein shell without changing the arrangement of a high density 2D array of iron oxide cores.

9.6.2 GaAs Nanostructure Etching by Neutral Beam

After O-radicals treatment, an atomic-level smooth surface with well-arranged iron oxide cores can be obtained for the etching process. The next step is to investigate the etching conditions of the neutral beam process. Quantifying the cross-sectional

etching profile of single GaAs nanostructures inside the 2D array is very difficult by SEM or transmission electron microscopy because the high in-plane density of the GaAs-NDs array causes an indistinct background. Therefore, we tried to reduce the density of the GaAs-NDs by diluting a ferritin solution by 400 times with deionized water. Following the process steps from Fig. 9.9a–d, the diluted ferritin solution can be spin-coated on the GaAs-NBO surface and arranged randomly with a low in-plane density.

In GaAs etching, the gallium and arsenic components have different chemical reactions during the etching process. Their different reaction rates would increase the etched surface roughness. Therefore, in previous work [36], we used chlorine and argon gas mixture as the reaction gas in the NBE process. The addition of an argon neutral beam (Ar-NB) can buffer the different chemical reaction rates of Ga-Cl and As-Cl from a chlorine neutral beam (Cl-NB). An atomic-level etched surface roughness can be obtained. In this work, the mixed gas ratio and 600 kHz RF bottom bias power were optimized for etching sub-10 nm GaAs nanodisk structure. The other process conditions of plasma source RF power, plasma RF time-modulated ratio, top electrode bias, and substrate temperature were fixed as 800 W, 50 μs ON/50 μs OFF (duty ratio: 50 %), 100 Vdc and −16 °C, respectively.

SEM images for samples etched by NB with different mixtures of gas and bias power are shown in Fig. 9.13. Etching results of pure chlorine gas and 6 W RF bias power are shown in Fig. 9.13a. The etched surface roughness was higher than

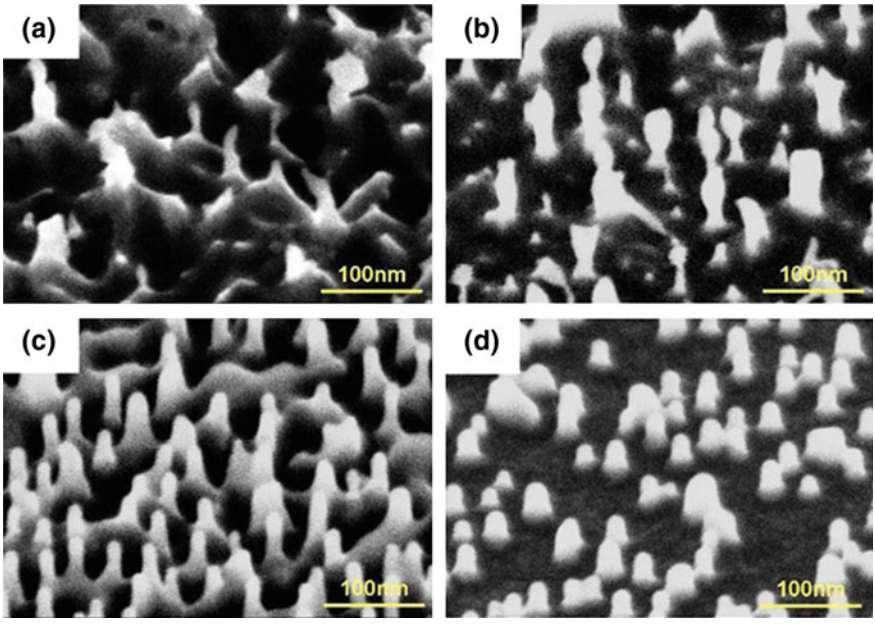

Fig. 9.13 SEM images with 40° tilt angle of neutral beam etched GaAs nanostructures with different gas and bias power conditions

20 nm and only a few GaAs nanocolumn structures remained distinct. These results show that a pure chemical reaction at low bias power not only causes serious surface roughness but also has a serious problem of undercut etching. The undercut etching would easily eliminate nanocolumns whose diameters were less than 10 nm. The results of pure chlorine gas again being used but RF bias power increased to 16 W are in Fig. 9.13b. More nanocolumn structures remained after etching and the surface roughness was improved, but the sidewalls of the nanocolumns were not vertical. These pure chlorine gas etching results indicate that the undercut etching and surface roughness problems happened at low bias power and for pure chemical etching. Pure chemical etching with low ion bombardment energy performs more like isotropic etching, which causes a serious undercut problem.

On the basis of these results and previous work [36, 37], a high argon mixed ratio was expected to reduce the etching surface roughness and buffer the chemical reaction from Cl-NB. Figure 9.13c shows a sample that was etched with a Cl_2: Ar = 22:78 (total flow rate was 40 sccm) gas mixture and 10 W RF bias power. The undercut etching problem was dramatically reduced, but the bottom surface roughness was still larger than 10 nm. The etching conditions of the sample shown in Fig. 9.13d were a 78 % Ar mixed ratio and 16 W RF bias power. The undercut phenomenon was eliminated and the bottom surface was smooth. In Fig. 9.13d, the SEM image was taken with a tilt angle of 20° and the electron charge problem was serious on the surface of the GaAs nanocolumns. Hence, the diameters of the nanocolumns seem larger than 10 nm. The cross-sectional SEM image was observed to investigate more precise dimensions, as shown in Fig. 9.14 [38–40]. The top diameters of the nanocolumns and etching depth were ∼10 and ∼45 nm, respectively. The taper angle of a nanocolumn was about 88°. In the results, the top diameter of a nanocolumn was a little larger than an iron oxide core's diameter of 7 nm. Since the flux of NB near the iron oxide core mask is lower than that in wide space without the iron core, the etching rate of GaAs oxide is lower than that of

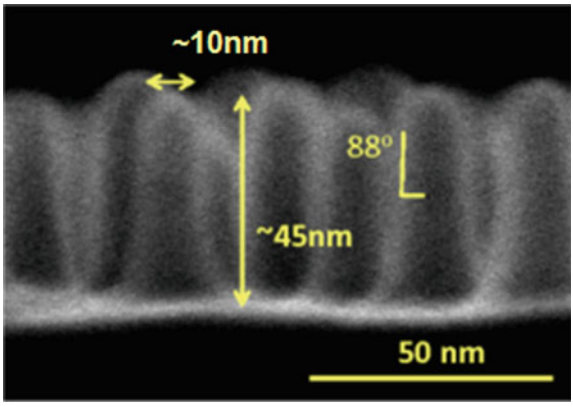

Fig. 9.14 Cross-sectional SEM images of GaAs-etched sample in Fig. 9.18d

GaAs. In the real etching process, a certain amount of GaAs was etched in the wide space before the GaAs oxide was completely etched near the iron oxide core mask. Therefore, a nanocolumn with a larger diameter was fabricated.

9.6.3 *Fabrication of High Density Dispersed GaAs Nanodisks with AlGaAs Matrix*

In this experiment, we used PEG ferritin (Fig. 9.15a) which was the ferritin modified with poly ethylene glycol (PEG) as the bio-template in order to realize large distance between ferritins. Considering laser devices, the coupling of wave-functions between GaAs-NDs should be avoided to confine carriers strongly into each QDs and enhance probability of radiative recombination. Figure 9.15b shows SEM images ferritin arrangement. Using PEG ferritin, a high density (more than 10^{11} cm^{-2}) and large distance (ferritin-to-ferritin distance is around 25 nm) PEG ferritin array were formed on the GaAs substrate [41].

Cross-section SEM profile of etched sample was shown in Fig. 9.16a. We could achieve the fabrication high-aspect ratio nanopillars which include GaAs nanodisks using a GaAs/AlGaAs structure. Further experiments revealed that the etching rates for GaAs and $Al_{0.3}GaAs$ bulk materials were 30 and 20 nm/min, respectively, which mean a low etching-selectivity (GaAs/AlGaAs) of 1.5. This low etching-selectivity resulted in a vertical and high-aspect ratio nano-pillar etching through the GaAs/AlGaAs structure without creating defects in the nanodisk structure [42]. Atomic-level transmission electron microscopy (TEM) picture was shown in Fig. 9.16b to further evaluate nanopillars crystal quality. We found that our nanopillars exhibit highly ordered and well-aligned atomic alignments at the etched side-wall, an ideal single-crystal structure; even none of any disordered atoms induced by defects were observed at the distinct and smooth interfaces. Theses result clarified that defect-free, atomically flat side-wall, and anisotropic GaAs etching have been achieved using our new processes.

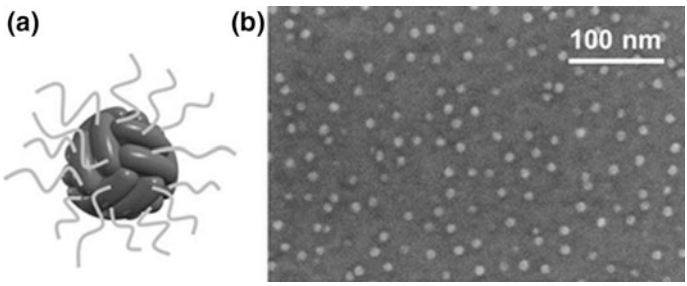

Fig. 9.15 **a** Illustration of PEG ferritin, **b** top-view SEM image of PEG ferritin arranged on GaAs substrate

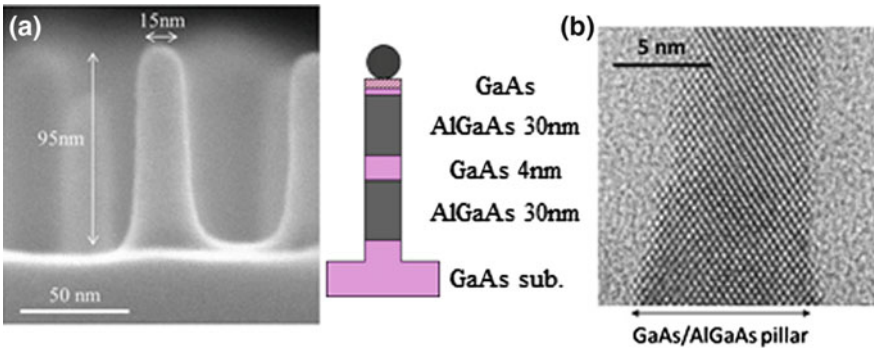

Fig. 9.16 **a** SEM image of GaAs/AlGaAs nanopillar including GaAs nanodisk, **b** TEM picture of nanopillar

9.7 Photoluminessence in Gallium Arsenide Nanodisks

Then, photoluminescence (PL) measurement was performed for the GaAs-NDs. Figure 9.17 shows the SEM images after NBE and GaAs regrowth. As we can see conformal capping layer were regrown on the pillars.

PL spectra were measured to evaluate exciton states and optical transitions in our GaAs-ND as shown in Fig. 9.18a; sample-A and B include GaAs nanodisks with the thickness of 4 and diameter of 15 nm, thickness of 4 and diameter of 10 nm, respectively. As the reference, we measured double-QW sample including two QW layers; 4 and 8 nm GaAs-QW.

Samples were excited by second harmonic light pulses from a mode-locked Ti: sapphire laser at a wavelength of 400 nm that provided ultrashort pulses with a time width of 150 fs and an excitation density of 0.3 μJ/cm^2. The time-resolved PL spectra were detected by a synchroscan streak camera. The time width of the

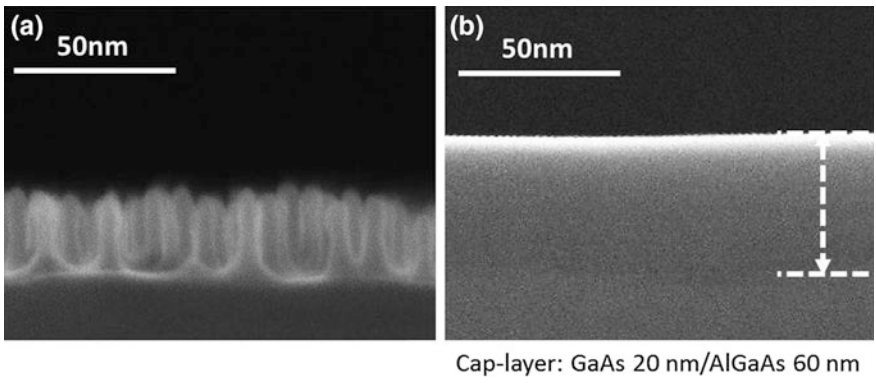

Fig. 9.17 Cross-section SEM images, **a** after neutral beam etching, **b** after regrowth

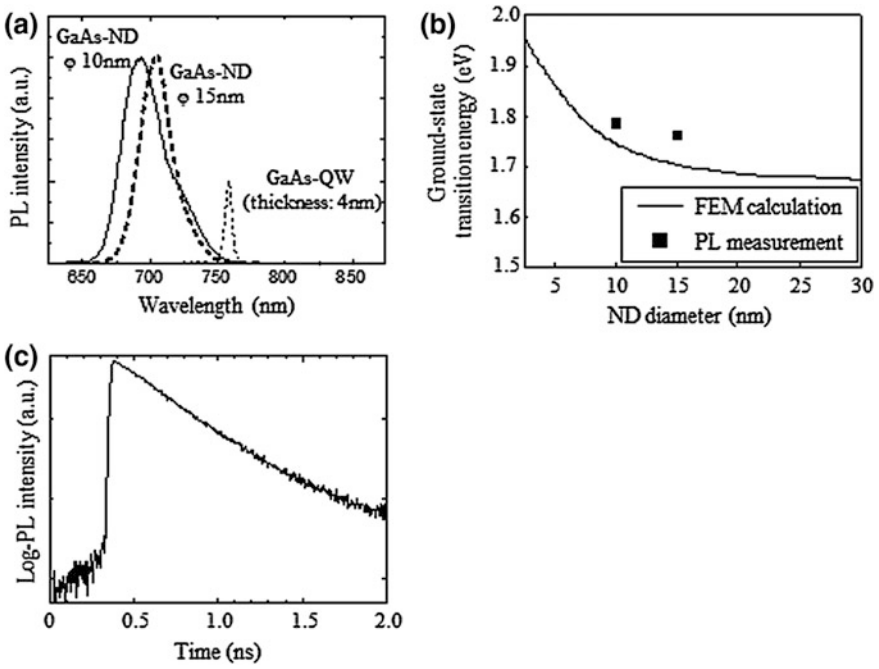

Fig. 9.18 **a** PL spectra of sample-A (ND thickness: 4 nm, diameter: 15 nm), sample-B (ND thickness: 4 nm, diameter: 10 nm) and GaAs-QW (thickness: 4 nm). **b** Calculated and measured ground state transition energy of GaAs-ND. **c** Transient PL profile of GaAs-ND sample

instrumental response curve was 15 ps. From the reference double-QW sample, PL originated from the GaAs bulk and QW of 4 nm were observed at 824 (=1.50 eV) and 758 nm (=1.63 eV), respectively. In addition to this, we observed a weak PL peak from the AlGaAs barrier layer at 636 nm (=1.95 eV). On the other hand, from GaAs nanodisk sample, we could obtain a strong photoemission between GaAs band edge and $Al_{0.3}GaA$ band edge in all of GaAs-ND samples; the peak positions are following; sample-A: 693 nm (=1.79 eV), sample-B: 706 nm (=1.76 eV). Compared with the same thickness GaAs-QW, their emissions wavelengths remarkably blue-shift due to quantum confinement. With the classic envelop-function theory, we solve the one band Schrodinger equations to get the electronic structure. We adopted the finite element method (FEM) to describe our NDs shape, size, and component. The calculation results were shown as the solid line, and PL measurement data were shown as the solid square in Fig. 9.18b. Our calculations reveal that due to classic quantum localization effect, the NDs state gradually decreases with increasing diameters which matches with experimental data very well. We want to mention it that the atomic H-regrowth process removed 1–2 nm (2–4 layers atomics) native oxidation GaAs to shrink the GaAs-ND diameter. If including this 2–4 nm diameter shrink, the above calculation was almost consistent with experimental results. This indicates that the emission form the ND was

corresponding to the ground state transition. As we know, only our group reported this convincible photoluminescence originated from quantum dot fabricated with the plasma-based top-down process.

Then, the carrier lifetime was investigated by the time-resolved PL spectrometry with sample-A at around 693 nm to understand a crystal structure (Fig. 9.18c). Lifetime analysis obtains information about non-radiative relaxation of carriers through defect states. The PL decay profile was fitted by a single-exponential function, and the decay time was 300 ps. The observed PL lifetime of the GaAs-ND is in same order to the values compared with the same thickness GaAs-QW. This lifetime is similar to that of GaAs-QD fabricated by a droplet epitaxy of 150–400 ps [42, 43]. In addition, long lifetime component due to defect-related relaxation process could not be observed in these spectra. These results indicate a satisfactory crystalline structure of our GaAs-NDs. We obtained a strong PL spectrum from the 15 nm diameter GaAs nanodisk structures fabricated using the combination of bio-template technique, NBE, and atomic hydrogen-assisted MBE because of internal defect-free and surface dangling bond-free nanostructures.

9.8 Summary

In this chapter, the novel fabrication processes of Si and GaAs nanodisk arrays by combination of bio-template and neutral beam etching processes were discussed.

The direct formation of a uniform, closely packed, and high density two-dimensional array of ferritin molecules was realized on Si and GaAs substrates using our developed NBO technique to prepare the surface oxide. The neutral beam oxidation process was applied to form both SiO_2 and GaAs oxide thin films that have negative zeta potential and highly hydrophilic surfaces. It was experimentally proven that surface hydrophilicity is essential for the mechanism of uniform and high density ferritin arrangement.

Uniform and defect-free 2D and 3D array of Si-NDs with ND density of more than 7×10^{11} cm^{-2} were realized as Si-QD super lattice structure using combination of bio-templates and NBE processes. The defect-free process with our top-down concept was verified by ESR measurement and PL spectra. The diameter of Si-ND could be controlled by changing the conditions under which surface-oxide removal was conducted.

2D array of GaAs-NDs with ND density of 7×10^{11} cm^{-2} has been developed successfully. Each step of the process, i.e., ferritin protein shell removal, NBE, and iron core removal, has been investigated and several novel solutions have been developed that do not damage the GaAs substrate. O-radicals were first found to eliminate the protein shell effectively at a low temperature of 280 °C without deteriorating surface roughness or moving the iron oxide cores. NBE with a 22 % chlorine and 78 % argon gas mixture and 16 W RF bias power can etch a GaAs nanostructure with a diameter of about 10 nm, atomic-level surface roughness of less than 1 nm and vertical taper angle of 88°.

References

1. S. Baskoutas, A.F. Terzis, Size-dependent band gap of colloidal quantum dots. J. Appl. Phys. **99**, 013708 (2006)
2. H. Yu, J. Li, R.A. Loomis, P.C. Gibbons, L.W. Wang, E.W. Buhro, Cadmium selenide quantum wires and the transition from 3D to 2D confinement. J. Am. Chem. Soc. **125**, 16168 (2003)
3. A. Kongkanand, K. Tvrdy, K. Takechi, M. Kuno, P.V. Kamat, Quantum dot solar cells. Tuning photoresponse through size and shape control of CdSe–TiO_2 architecture. J. Am. Chem. Soc. **130**, 4007 (2008)
4. B. Pejova, I. Grozdanov, Three-dimensional confinement effects in semiconducting zinc selenide quantum dots deposited in thin-film form. Mater. Chem. Phys. **90**, 35 (2005)
5. L. Goldstein, F. Glas, J.Y. Marzin, M.N. Charasse, G. Le Roux, Growth by molecular beam epitaxy and characterization of InAs/GaAs strained-layer superlattice. Appl. Phys. Lett. **47** (10), 1099–1101 (1985)
6. A. Luque, A. Marti, Increasing the efficiency of ideal solar cells by photon induced transitions at intermediate levels. Phys. Rev. Lett. **78**, 5014 (1997)
7. A.A. Konakov, V.A. Burdov, Optical gap of silicon crystallites embedded in various wide-band amorphous matrices: role of environment. J. Phys. Condens. Matter **22**, 215301 (2010)
8. L.H. Thamdrup, F. Persson, H. Bruu, A. Kristensen, H. Flyvbjerg, Experimental investigation of bubble formation during capillary filling of SiO_2 nanoslits. Appl. Phys. Lett. **91**, 163505 (2007)
9. G. Conibeer, M.A. Green, R. Corkish, Y. Cho, E.C. Cho, C.W. Jiang, T. Fangsuwannarak, E. Pink, Y. Huang, T. Puzzer, T. Trupke, B. Richards, A. Shalav, K.L. Lin, Silicon nanostructures for third generation photovoltaic solar cells. Thin Solid Films **511/512**, 654 (2006)
10. E.C. Cho, S. Park, X. Hao, D. Song, G. Conibeer, S.C. Park, M.A. Green, Silicon quantum dot/crystalline silicon solar cells. Nanotechnology **19**, 245201 (2008)
11. Y. Okada, R. Oshima, A. Takata, Characteristics of InAs/GaNAs strain-compensated quantum dot solar cell. J. Appl. Phys. **106**, 024306 (2009)
12. R.B. Laghumavarapu, M. El-Emawy, N. Nuntawong, A. Moscho, L.F. Lester, D.L. Huffakerb, Improved device performance of InAs/GaAs quantum dot solar cells with GaP strain compensation layers. Appl. Phys. Lett. **91**, 243115 (2007)
13. R.P. Raffaelle, S.L. Castro, A.F. Hepp, S.G. Bailey, Quantum dot solar cells. Prog. Photovolt. Res. Appl. **10**, 433 (2002)
14. G. Conibeer, M.A. Green, E.C. Cho, D. König, Y.H. Cho, T. Fangsuwannarak, G. Scardera, E. Pink, Y. Huang, T. Puzzer, S. Huang, D. Song, C. Flynn, S. Park, X. Hao, D. Mansfield, Silicon quantum dot nanostructures for tandem photovoltaic cells. Thin Solid Films **516**, 6748 (2008)
15. X.J. Hao, A.P. Podhorodecki, Y.S. Shen, G. Zatryb, J. Misiewicz, M.A. Green, Effects of Si-rich oxide layer stoichiometry on the structural and optical properties of Si QD/SiO_2 multilayer films. Nanotechnology **20**, 485703 (2009)
16. Y. Kurokawa, S. Tomita, S. Miyajima, A. Yamada, M. Konagai, Photoluminescence from silicon quantum dots in Si quantum dots/amorphous SiC superlattice. Jpn. J. Appl. Phys. **46**, L833 (2007)
17. X. Wen, L.V. Dao, P. Hannaford, Temperature dependence of photoluminescence in silicon quantum dots. J. Phys. D Appl. Phys. **40**, 3573 (2007)
18. I. Yamashita, Fabrication of a two-dimensional array of nano-particles using ferritin molecule. Thin Solid Films **393**, 12 (2001)
19. S. Samukawa, K. Sakamoto, K. Ichiki, Generating high-efficiency neutral beams by using negative ions in an inductively coupled plasma source. J. Vac. Sci. Technol. A **20**, 1566 (2002)

20. S. Samukawa, K. Sakamoto, K. Ichiki, High-efficiency low energy neutral beam generation using negative ions in pulsed plasma. Jpn. J. Appl. Phys. **40**, L997 (2001)
21. S. Samukawa, K. Sakamoto, K. Ichiki, High-efficiency neutral-beam generation by combination of inductively coupled plasma and parallel plate DC bias. Jpn. J. Appl. Phys. **40**, L779 (2001)
22. M. Yonemoto, T. Ikoma, K. Sano, K. Endo, T. Matsukawa, M. Masahara, S. Samukawa, Low temperature, beam-orientation-dependent, lattice-plane-independent, and damage-free oxidation for three-dimensional structure by neutral beam oxidation. Jpn. J. Appl. Phys. **48**, 04C007 (2009)
23. C.H. Huang, M. Igarashi, M. Wone, Y. Uraoka, T. Fuyuki, M. Takeguchi, I. Yamashita, S. Samukawa, Two-dimensional Si-nanodisk array fabricated using bio-nano-process and neutral beam etching for realistic quantum effect devices. Jpn. J. Appl. Phys. **48**, 04C187 (2009)
24. A. Wada, K. Sano, M. Yonemoto, K. Endo, T. Matsukawa, M. Masahara, S. Yamasaki, S. Samukawa, High-performance three-terminal fin field-effect transistors fabricated by a combination of damage-free neutral-beam etching and neutral-beam oxidation. Jpn. J. Appl. Phys. **49**, 04DC17 (2010)
25. S. Samukawa, Ultimate top-down etching processes for future nanoscale devices. Jpn. J. Appl. Phys. **45**, 2395 (2006)
26. M.F. Hochella Jr., A.H. Carim, A reassessment of electron escape depths in silicon and thermally grown silicon dioxide thin films. Surf. Sci. Lett. **197**, 260 (1988)
27. Z.H. Lu, B. Bryskiewicz, J. McCaffrey, Z. Wasilewski, M.J. Graham, Ultraviolet-ozone oxidation of GaAs(100) and InP(100). J. Vac. Sci. Technol. B **11**, 2033 (1993)
28. T. Matsui, N. Matsukawa, K. Iwahori, K. Sano, K. Shiba, I. Yamashita, Realizing a two-dimensional ordered array of ferritin molecules directly on a solid surface utilizing carbonaceous material affinity peptides. Langmuir **23**, 1615 (2007)
29. T. Matsui, N. Matsukawa, K. Iwahori, K. Sano, K. Shiba, I. Yamashita, Direct production of a two-dimensional ordered array of ferritin-nanoparticles on a silicon substrate. Jpn. J. Appl. Phys. **46**, L713 (2007)
30. H. Nishino, N. Hayasaka, H. Okano, Damage-free selective etching of Si native oxides using NH_3/NF_3 and SF_6/H_2O down-flow etching. J. Appl. Phys. **74**, 1345 (1993)
31. J. Kikuchi, M. Iga, H. Ogawa, S. Fujimura, H. Yano, Native oxide removal on Si surfaces by NF_3-added hydrogen and water vapor plasma downstream treatment. Jpn. J. Appl. Phys. Part 1 **33**, 2207 (1994)
32. L. Pavesi, L.D. Negro, C. Mazzoleni, G. Franzo, F. Priolo, Optical gain in silicon nanocrystals. Nature **408**, 440 (2000)
33. K. Kůsová, O. Cibulka, K. Dohnalova, I. Pelant, J. Valenta, A. Fučíková, K. Zıdek, J. Lang, J. Englich, P. Matějka, P. Štěpánek, S. Bakardjieva, Brightly luminescent organically capped silicon nanocrystals fabricated at room temperature and atmospheric pressure. ACS Nano **4**(8), 4495 (2010)
34. W. Boera, H. Zhangb, T. Gregorkiewicz, Optical spectroscopy of carrier relaxation processes in Si nanocrystals. Mater. Sci. Eng. B **159–160**, 190 (2003)
35. I.A. Walmsley, Looking to the future of quantum optics. Science **29**, 1211 (2008)
36. X.Y. Wang, C.H. Huang, Y. Ohno, M. Igarashi, A. Murayama, S. Samukawa, Defect-free etching process for GaAs/AlGaAs heteronanostructure using chlorine/argon mixed neutral beam. J. Vac. Sci. Technol. B **28**, 1138 (2010)
37. T. Yoshikawa, Y. Sugimoto, S. Kohmoto, S. Kitamura, K. Makita, Y. Nambu, K. Asakasa, Dry etching and consequent burring regrowth of nanosize quantum wells stripes using an in situ ultrahigh vacuum multichamber system. J. Vac. Sci. Technol. B **16**, 1 (1998)
38. X.Y. Wang, Y. Ohno, M. Igarashi, M. Murayama, S. Samukawa, Damage-free top-down processes for fabricating two-dimensional arrays of 7 nm GaAs nanodiscs using biotemplates and neutral beam etching. J. Vac. Sci. Technol. B **28**, 1138 (2010)

39. X.Y. Wang, C.H. Huang, R. Tsukamoto, P.A. Mortemousque, K.M. Itoh, Y. Ohno, S. Samukawa, Damage-free top-down processes for fabricating two-dimensional arrays of 7 nm GaAs nanodiscs using bio-templates and neutral beam etching. Nanotechnology **22**, 365301 (2011)
40. M. Igarashi, R. Tsukamoto, C.H. Huang, I. Yamashita, S. Samukawa, Direct fabrication of uniform and high density sub-10-nm etching mask using ferritin molecules on Si and GaAs surface for actual quantum-dot superlattice. Appl. Phys. Expres. **4**, 015202 (2011)
41. R. Tsukamoto, M. Muraoka, Y. Fukushige, H. Nakazawa, T. Kawaguchi, Y. Nakatsuji, I. Yamashita, Improvement of Co_3O_4 nanoparticle synthesis in apoferritin cavity by outer surface PEGylation. Bull. Chem. Soc. Jpn **81**, 1669 (2008)
42. Y. Tamura, T. Kaizu, T. Kiba, M. Igarashi, R. Tsukamoto, A. Higo, W. Hu, C. Thomas, M. E. Fauzi, T. Hoshii, I. Yamashita, Y. Okada, A. Murayama, S. Samukawa, Quantum size effects in GaAs nanodisks fabricated using a combination of the bio-template technique and neutral beam etching, Nanotechnology **24**, 285301 (2013)
43. I. Yamashita, A. Murayama, S. Samukawa, Light-emitting devices based on top-down fabricated GaAs quantum nanodisks. Scientific Reports **5**, 9371 (2015)

Chapter 10
Fabrication of 3D Quantum Dot Array by Fusion of Biotemplate and Neutral Beam Etching II: Application to QD Solar Cells and Laser/LED

Seiji Samukawa

Abstract We investigated the controllable range of bandgap energy, E_g and optical absorption characteristic of silicon quantum nanodisks (QNDs) formed by a top-down method described in previous chapter, which enables precise control of geometrical parameters. By embedding by Silicon Carbides, the wave function of the QNDs overlaps each other, and a wide miniband was formed, which enhance only the photon absorption but carrier transport in the stacked QNDs. The high optical absorption and conductivity properties were verified by fabricating p–i–n solar cells with Si-NDs, and efficient carrier generation and high electrical conductivity in our Si-ND structure were surely clarified. The top-down process was also applied to form quantum dots photonic devices based on III–V compound semiconductors. We fabricated GaAs nanodisks (NDs) with a diameter of sub-20 nm. The GaAs NDs were embedded with AlGaAs regrown by metal organic vapor phase epitaxy. Light emitting diodes were fabricated using the NDs, exhibiting a narrow spectral width of 38 nm with high-intensity as a result of small size deviation of NDs and superior quality of GaAs/AlGaAs surface formed by neutral beam etching.

Keywords Neutral beam etching · Quantum nanodisk · GaAs · MOVPE · Photoluminescence · LED

10.1 Introduction

Semiconductor quantum dots (QDs) have high potential in the fabrication of new quantum effect devices such as QD solar cells and QD laser/LED [1–8]. Semiconductor material has to be scaled down to the nanometer level comparable to the Bohr radius (Si Bohr radius: 4.9 nm) to generate quantum effect. In this case,

S. Samukawa (✉)
Institute of Fluid Science, Tohoku University, Sendai 980-8577, Japan
e-mail: samukawa@ifs.tohoku.ac.jp

J. Sone and S. Tsuji (eds.), *Intelligent Nanosystems for Energy, Information and Biological Technologies*, DOI 10.1007/978-4-431-56429-4_10

carrier wave functions are localized in nanomaterials and continuum bands are reduced to discrete quantum levels (the quantum size effect), which provide the opportunity to engineer the optical band gap by adjusting the carrier confinement in spatial dimensions from the size control [9–11].

All-Si tandem solar cells and intermediate band solar cells comprising QDs have attracted much attention for their potential to break through the Shockley–Queisser limit and their compatibility with current Si technology [12, 13]. Moreover, the SiC for the interlayer is one of the most promising materials to be used to form minibands that anticipate enhanced photon absorption and conductivity in Si-QD solar cells [14]. Carrier wave functions more easily spread into the SiC interlayer to form minibands to achieve Si-QD solar cells because of its lower bandgap energy compared with other insulating materials such as SiO_2 and SiN.

Quantum dots (QDs) have also attracted considerable interests due to their potential device applications for the next generation quantum cryptosystem such as single-photon source, light emitting diodes, detectors, and laser diodes [15]. The active gain medium of QD semiconductor has numerous merits that are not available in a form of bulk or quantum wells [16, 17]. For example, high-speed modulation, low-power consumption, and temperature independence have been demonstrated based on the QD technology [18, 19]. In this chaper, the application of our fabricated 3D nano disk structures to QD Solar Cells and Laser/LED is reviewed.

10.2 Application to Solar Cells [20]

We have developed a sub-10 nm Si nanodisk (Si-ND) structure using a biotemplate and damage-free neutralbeam (NB) etching [21, 22]. In this study, we firstly investigated the controllable range of E_g and optical absorption characteristic of Si-NDs by changing the geometric parameters of Si-ND and matrix material, and discussed the mechanism of band gap energy by comparing the experimental result with the simulation result. Secondary, we observed an enhancement of conductivity in Si-NDs by formation of minibands. Within the envelop function theory and Anderson Hamiltonian method, we also calculated electronic structures and the current transport, which theoretically proved that minibands enhanced the conductivity. Finally, we verified the high optical absorption and conductivity properties by fabricating p–i–n solar cells with Si-NDs and clarified carrier generation and carrier collection in our Si-ND structure.

10.2.1 Control of Absorption Coefficient by Miniband Formation

We prepared 2D arrays of Si-NDs with a SiC or SiO_2 interlayer whose ND thickness, diameter, and average ND-center-to-ND-center distance corresponded to

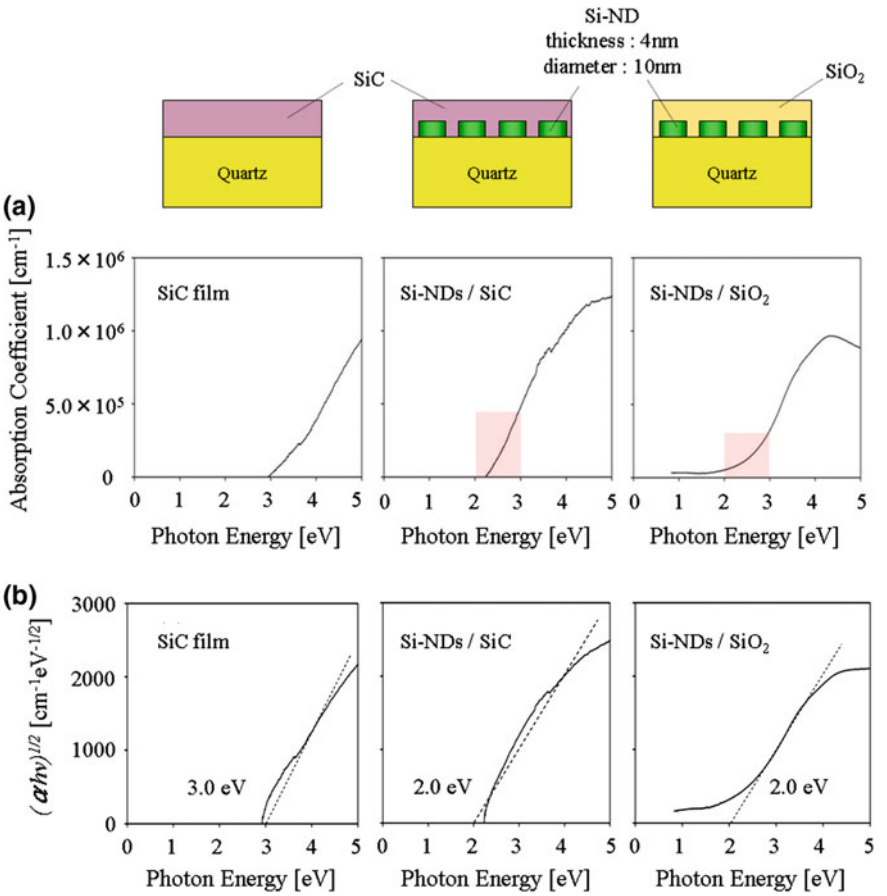

Fig. 10.1 **a** Absorption coefficients of Si-NDs with SiC, Si-NDs with SiO_2 and SiC thin film, and **b** Tauc plot $((\acute{a}hv)^{1/2}$ versus photon energy (hv)) for each sample

4, 10, and 12 nm. Figure 10.1a presents the results for the absorption coefficients of the Si-NDs with SiC, Si-NDs with SiO_2, and SiC interlayer on the substrate, and Fig. 10.1b has the $(\acute{a}hv)^{1/2}$ versus photon energy (hv). The absorption coefficient of the 2D Si-ND array with the SiC interlayer was higher than that of the SiO_2 matrix because of the higher photon absorption in the SiC layer. The absorption edge of the Si-ND array with a SiC interlayer was also blue shifted more than the SiO_2 interlayer. Moreover, even though the E_g of the SiC layer was 3.0 eV, the absorption coefficient from 2 to 3 eV also increased when using SiC as the interlayer compared with using SiO_2 and only SiC film. These results would have originated in variations in the band offset that changed the localization of the wave function and the electronic states in Si-ND; the typical conduction band offset of a Si/SiO_2 interface is 3.2 eV and that of a Si/SiC interface is 0.5 eV [14]. Therefore, this indicates that the coupling of wave functions strengthens and forms a wide

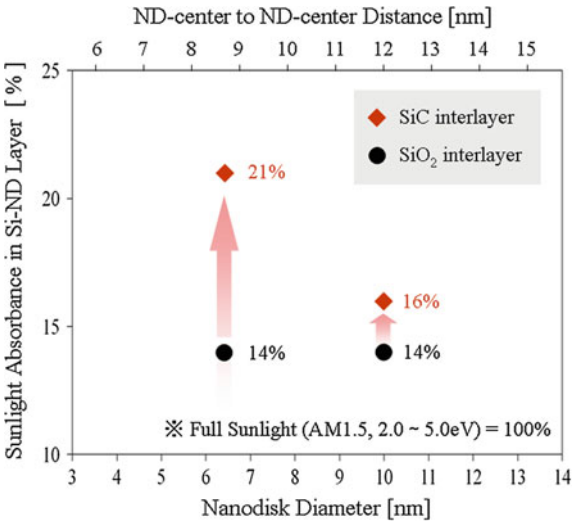

Fig. 10.2 One-sun illuminated photon absorbance from E_g (2.0 eV) to 5.0 eV in 2D array of Si-NDs with SiC and SiO_2 matrix

miniband due to the lower bandgap energy of the SiC interlayer, which enhanced photon absorption in the structure. We estimated the one-sun (photon intensity: AM1.5, 1000 W/m^2) illuminated photon absorbance from E_g (2.0 eV) to 5.0 eV in one layer of the Si-ND array (Fig. 10.2) to better understand the efficiency of photon utilization. We found that when the interlayer was changed from SiO_2 to SiC, the photon absorbance in the 2D array of Si-NDs increased from 14 to 16 % of sunlight from 2.0 to 5.0 eV. We also prepared a 2D array of small diameter (6.4 nm) Si-NDs with a SiC interlayer to investigate the optical absorption properties. In this case, the one-sun illuminated photon absorbance from E_g (2.0 eV) to 5.0 eV in one layer of the Si-ND above 100 K, as shown above 100 K, as shown also shown in Fig. 10.2. The photon absorbance in the 2D array of Si-NDs was clearly increased to 21 % due to a combination of the small diameter of the Si-ND array and the SiC interlayer. It means that shrinking the Si-ND diameter simultaneously increased the optical absorption coefficient.

These interesting phenomena can perhaps be attributed to the lateral coupling of the NDs. There are not only strongly coupled wave functions at the discrete initial quantum level but they also relax selection rules to induce additional transitions, which commonly means an increased state density that leads to enhanced total absorption. We solved one-band Schrödinger equations with classic envelope function theory to obtain the electronic structure of our Si NDs and the electron spatial probability (square wave function)

$$-\nabla \cdot \left(\frac{\hbar}{2m^*}\nabla\phi\right) + V\phi = \mathrm{E}, \tag{10.1}$$

where $\hbar$, m^*, V, E, and φ correspond to Planck's constant divided by 2π, the effective mass, the position-dependent potential energy, the quantum levels, and the

electron envelope function. The finite element method was used to finely describe our complex structures. Electron spatial probability in three neighboring NDs is indicated by the logarithmic axis in Fig. 10.3. Using the SiC interlayer effectively enhanced wave function coupling more than using the SiO_2 interlayer because the energy potential well at the SiC/Si interface is lower than that in the SiO_2 interlayer (Fig. 10.3a). Moreover, wave function coupling is also effectively enhanced by decreasing the diameter (Fig. 10.3b). A possible reason is that, by decreasing diameters, the center-to-center distance between NDs is decreased so that wave functions more easily spread to the neighboring NDs and are coupled with each other. These enhanced wave function coupling will enhance total photon absorption and conductivity in the 2D array of Si-ND structures.

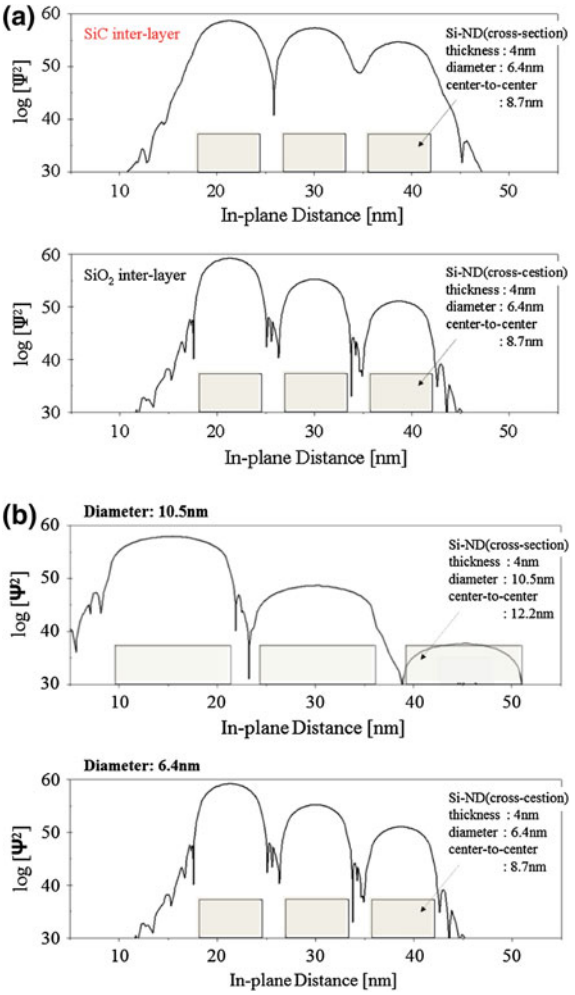

Fig. 10.3 Simulation results for electron spatial possibilities (*square* wave function) in three lateral coupled NDs in accordance with our samples structures

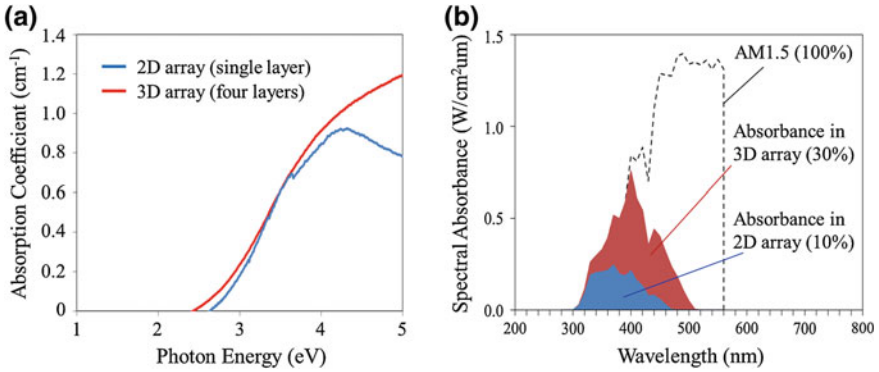

Fig. 10.4 **a** Absorption coefficients of 2D and 3D arrays of Si-NDs with SiC matrix. **b** One-sun illuminated photon absorbance from E_g to 5.0 eV in 2D and 3D array of Si-NDs

Then, we measured optical absorption coefficient in 3D array of Si-NDs to investigate the effect of 3D miniband formation on the optical absorption. Figure 10.4 shows absorption coefficients in 2D and 3D array of Si-NDs samples prepared on transparent quartz substrates. The absorption coefficient in 3D array was almost the same as that in 2D array and the calculated E_g of the both samples was 2.2 eV, and the total photon absorbance in 3D array was increased to 30 %. Following the results, we calculated a width of miniband in 2D and 3D array of Si-NDs by Eq. 10.1, and a change in miniband width between the samples was estimated as 3.85 meV (single layer: 0.95 meV, four layers: 4.80 meV). Therefore, it seems that the change of 3.85 meV in miniband width is not large enough to affect the photon absorption.

10.2.2 Enhancement of Electron Conductivity Due to Miniband Formation in Silicon Nanodisk Superlattices

Theoretical discussion was carried out to investigate enhancement of the conductivity due to miniband formation. Our developed top-down nanotechnology achieves great flexibility in designing parts of the quantum structure, such as the independently controllable diameter and thickness, high-aspect ratio, different matrix materials, and so on. The finite element method very suitably describes complex quantum structures. Within the envelope function theory, the electronic structure and wave function are presented as Eq. 10.1. Here, we mainly consider the matrix material, realistic geometry structure, and the number of stacking layers. Results are shown in Fig. 10.5. A distinct feature is that, due to the higher band offset of Si/SiO_2 interface, electron wave functions are more strongly confined in

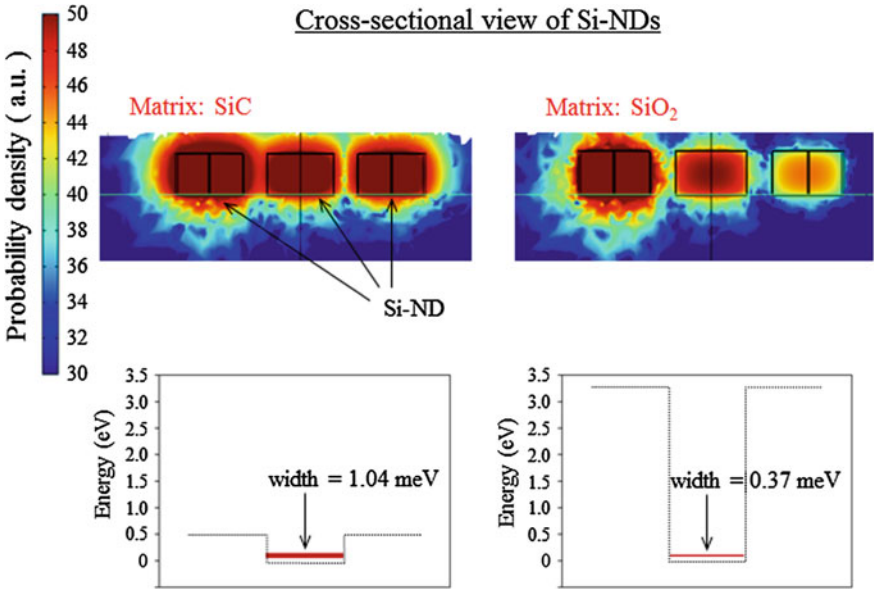

Fig. 10.5 Calculated results of electron spatial possibilities (square wave function) in three lateral coupled NDs and miniband width in 2D array of Si-NDs

Fig. 10.6 Calculated results of miniband width in 3D array of Si-NDs

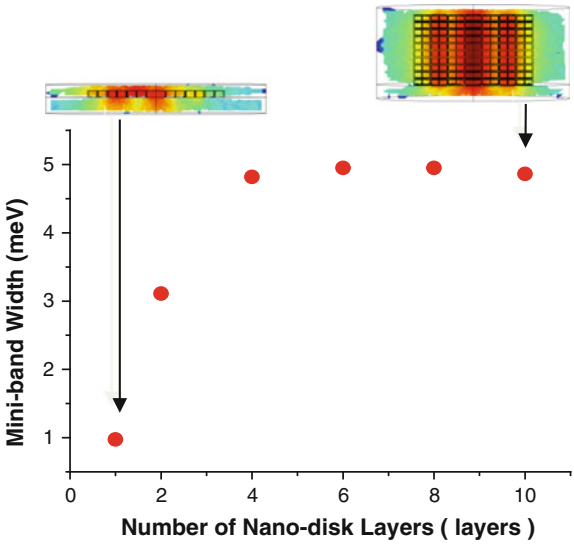

the Si-NDs in SiO_2 matrix. Thus, they result in the higher quantum levels. In addition, in the same geometry alignment, the stronger confinement means the weaker coupling of wave function and narrower miniband. In Fig. 10.6, by stacking our NDs from 1 layer to 10 layers, the miniband gradually broadens; and at around

4–6 layers, the broadening width seems to saturate. The probability of wave function diffusing into barrier exponentially reduces with distance, which indicates that wave function coupling saturates as the number of layers increases. Perhaps 4- or 6-layer NDs are enough to maximize the advantage of minibands.

With the Anderson Hamiltonian model, Chang et al. considered interdot coupling to deduce the tunneling current density as shown in detail in [23].

As shown in Fig. 10.7, calculated results also reveal that the wider miniband in SiC matrix brings a better transport property than that in SiO_2 matrix. A simplified, but not too distorted, explanation is that miniband formation broadens the resonance levels to increase the joint state density. The carrier transport in this two-barrier structure mainly depends on the resonant tunneling. Miniband formation broadens resonant peak to allow more states to approach the maximum, which results in the enhanced current. Thus, the wider miniband means a higher current density and lower threshold voltage, as shown in the Si-NDs in the SiC matrix. In addition, the 2D array of Si-NDs in the SiC matrix has a lower miniband level, E_0, which also shifts the I–V curves to a lower threshold voltage. This tendency closely matches our experimental results, and due to the larger tunneling resistance in the SiO_2 interlayer, the threshold voltage (V) is further increased in realistic I–V curves. Moreover, the conductivity in 2D and 3D array of Si-NDs were enhanced due to the

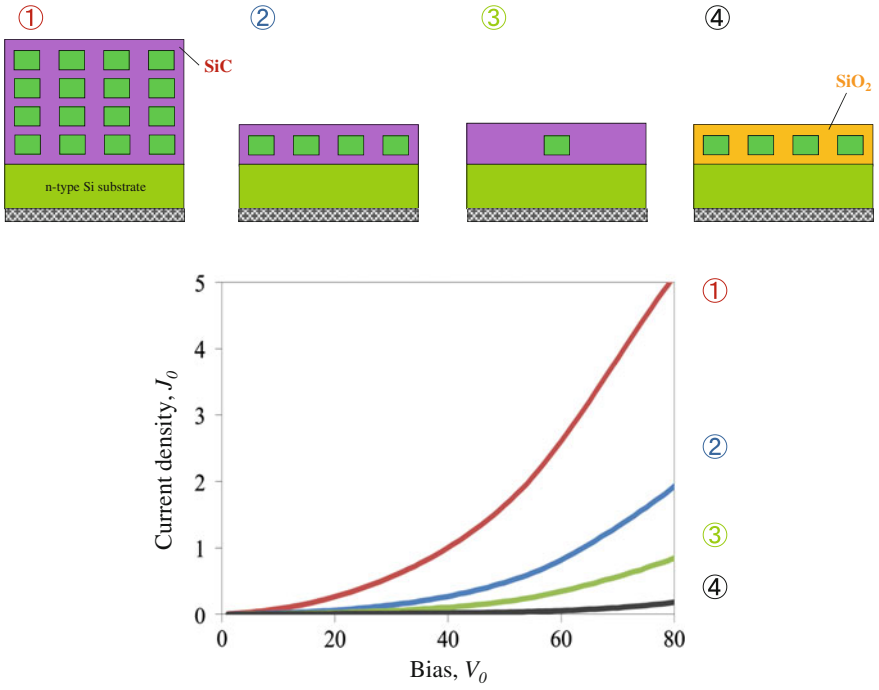

Fig. 10.7 Simulation results for I–V properties of our samples structures

same mechanism of broadening of the wave functions and formation of wider minibands. These were also very consistent with the trend in our experimental results, so it is clarified that miniband formation in both in-plane and out-of-plane could enhance the carrier transport in QDSL. The enhanced conductivity is very significant for electronic/optoelectronic devices, which indicates high charge injection efficiency in lasers and carriers collection efficiency in solar cells.

10.2.3 Investigation of Silicon Nanodisk Superlattices for High Efficiency Multi-Stacked Solar Cells

Quantum dot solar cells are very promising devices to break the frustrating Schockley–Queisser limit. Many exciting results have been reported to verify the key operating mechanism, the preparation of various materials, and the fabrication of prototype devices. However, these researches, unsurprisingly, is still insufficient to optimize these novel devices after exciting developments with conventional cells. One critical problem has been the lack of ideal QDSLs and basic understanding of their electrical/optical properties, especially key optical absorption and electrical conductivity.

The 2D array of Si-NDs fabricated by using a combination of an etching mask of Listeria-Dps (Lis-Dps) iron cores and a SiC interlayer was the most effective structure to enhance conductivity and optical absorption in the Si-ND layer. The SiC interlayer could enhance the conductivity in the 2D array of Si-NDs due to the strong coupling of wave functions. By using a 2D array of an etching mask with a Lis-Dps iron core, a 2D array of Si-NDs with an ND-center-to-ND-center distance of 8.7 nm could be achieved enhanced optical absorption due to the strong overlap of wave functions. Hence, we designed solar cell structures with a 2D array of Si-ND layers fabricated by using a Lis-Dps biotemplate and a SiC interlayer (Fig. 10.8). The diameter, space between NDs, and average ND-center-to-ND-center distance corresponded to 6.4, 2.3, and 8.7 nm. We fabricated Si-ND solar cells with different Si-ND thicknesses of 2 and 4 nm to clarify how the Si-ND layer contributed to the performance of solar cells. Four types of structures were prepared (Fig. 10.8) to clarify the effects of the Si-ND array structure: a solar cell with a 2-nm-thick-SiC/2-nm-thick-Si-ND/2-nm-thick-SiC layer, a 2-nm-thick-SiC/4-nm-thick-Si-ND/2-nm-thick-SiC layer, a 2-nm-thick SiC layer, and a p–n junction without a Si-ND structure. The p–n junction solar cell without any structures inserted could be used as a sample, which is established as a criterion to evaluate current generation in Si-NDs and carrier collection through them. All samples were fabricated on a 400-nm-thick, 1–1.5-Ω p-type Si substrate. After that, 30-nm-thick undoped epitaxial (epi)-Si was grown by electron beam evaporation at 600 °C. An n-type phosphorus-doped Si emitter was formed with a method of diffusion by rapid thermal annealing [12, 13]. We deposited 70-nm-thick indium tin oxide by sputtering to use it as an antireflective film. The backsurface field contact was formed by printing it with aluminum paste and subsequent annealing, and the front finger contact was formed by firing silver paste

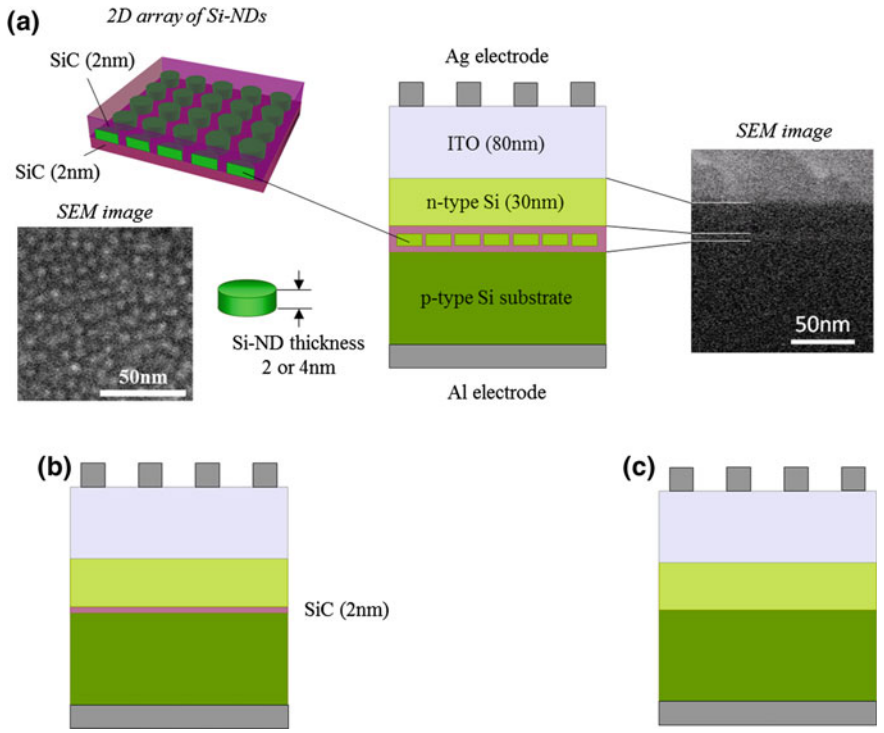

Fig. 10.8 Schematics and SEM image of structures of solar cells **a** our fabricated Si-ND/SiC solar cells, **b** SiC thin film solar cells and **c** Single layer PN junction solar cells

through an ITO film. There is a cross-sectional SEM image of Si-ND array solar cells in Fig. 10.8. Figure 10.9 shows the photon absorbance for each layer in the actual structure of a solar cell (Fig. 10.8a, b) as a function of the light wavelength calculated from the absorption coefficient in each layer. The results indicate that the SiC/4-nm-thick Si-ND/SiC structure (Fig. 10.8a) has a more efficient absorption of photons that entered from the top of the solar cell than the SiC thin film.

We measured the cell properties by using a characterization system (Jasco, YQ-250BX) with an AM1.5 solar simulator (100 mW/cm^2) as a light source at room temperature (RT). Figure 10.10a plots the one-sun illuminated I–V curves of Si-ND solar cells with 2-nm- and 4-nm-thick Si-NDs, a solar cell with 2-nm-thick SiC film, and a pn junction solar cell. Here, the contributions and reduction in cell performance in inserted layers (Si-ND or SiC thin film) could be evaluated by comparing them with the cell performance of a standard sample of a p–n junction solar cell. The solar cell with the 2-nm-thick SiC film had a conversion efficiency (η) of 5.4 % with an open-circuit voltage (V_{oc}) of 0.544 V, short circuit current density (J_{sc}) of 29.0 mAcm^{-2}, and a fill factor (FF) of 34 %, due to large resistivity in SiC thin film that resulted in reductions in current and FF (Table 10.1).

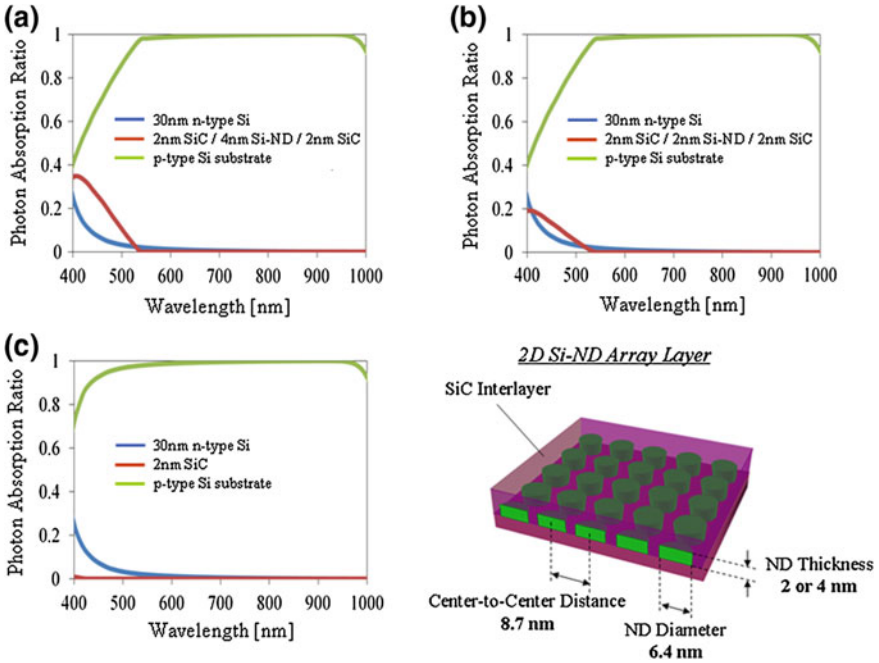

Fig. 10.9 Photon absorbance for each layer in actual solar cell structure (Fig. 10.8a, b, c) as a function of light wavelength calculated from absorption coefficient in each layer

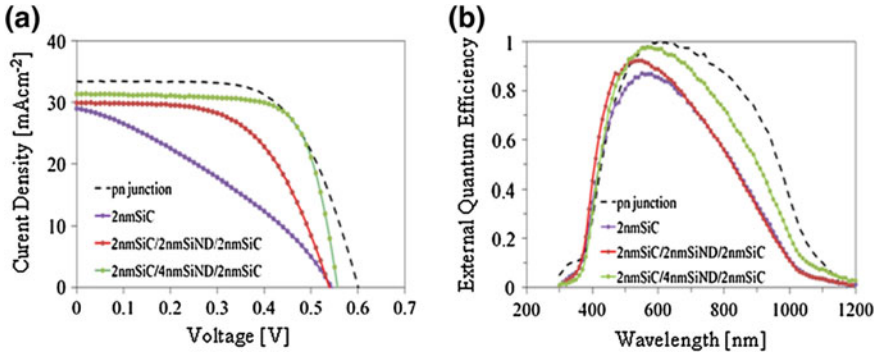

Fig. 10.10 Properties of solar cells. **a** One-sun illuminated I–V curves of Si-ND solar cells with 2-nm- and 4-nm-thick Si-NDs and solar cell with 2-nm-thick SiC film measured at RT. **b** External quantum efficiency (EQE) of three different solar cell structures

Interestingly, despite the two types of quantum dot solar cells having the same SiC film thickness (2 nm), the cell with 2-nm-thick-SiC/4-nm-thick-Si-ND/2-nm-thick SiC had superior performance with V_{oc} of 0.556 V, J_{sc} of 31.3 mAcm^{-2}, *FF* of 72.4 %, and η of 12.6 % (Table 10.1). The cell parameters including conversion

Table 10.1 One-sun illuminated cell parameters of three different solar cells measured at RT

Type of solar cell	Saturation current, J_{SC} (mA/cm^2)	Open circuit voltage, V_{OC} (V)	Fill factor, FF	Conversion efficiency, η (%)
pn junction	33.4	0.601	0.634	12.7
2 nm SiC	29	0.544	0.34	5.4
2 nm SiC/2 nm Si-ND/2 nm SiC	29.9	0.539	0.578	9.3
2 nm SiC/4 nm Si-ND/2 nm SiC	31.3	0.556	0.724	12.6

efficiency had good values close to those of the p–n junction solar cell by comparing them with those of the solar cell with SiC film. This demonstrated that the photogenerated carriers in the substrate were efficiently transported through the Si-ND structure without generating any reductions in cell performance. Figure 10.10b plots the external quantum efficiency (EQE) of the three different solar cell structures. The spectrum EQE of the Si-ND solar cell had a good response at ~620 nm, while the EQE peak of photon absorption when 2-nm-thick Si-NDs (E_g: 2.2 eV) were used was observed at a shorter wavelength (570 nm) than that (620 nm) when 4-nm-thick Si-NDs (E_g: 2.0 eV) were used. That is, the EQE peak was blue shifted by increasing E_g due to the decreasing thickness of Si-NDs. From the results of the absorption coefficient in the Si-ND structure, the largest possible contribution of the Si-ND structure to the total current density can be calculated as

$$J_{\mathrm{Si-ND}} = \frac{q}{hc} \cdot \int I_{\mathrm{AM1.5}}(\lambda) \cdot A_{\mathrm{Si-ND}}(\lambda) \cdot \lambda \cdot \mathrm{d}\lambda, \tag{10.2}$$

where $I_{\mathrm{AM1.5}}$, $A_{\mathrm{Si\text{-}ND}}$, q, and c correspond to the solar spectral irradiance of AM1.5, the absorption ratio in the Si-ND layer (see Fig. 10.10), the elementary charge, and the speed of light. The contribution of the Si-ND layer can be estimated at 1.2 mA/cm^2 when using 4-nm-thick Si-NDs. Although the absorption of photons in the Si substrate contributed to a large fraction of the current, this suggests that a Si-ND array also can play a key role in the efficient absorption of photons as well as in power generation in solar cells.

However, the EQE spectra of the Si-ND solar cells decreased at wavelengths from 600 to 1100 nm, which might result in lower J_{sc} and V_{oc} than that for the pn junction solar cell. We concluded from the bandgap energy of each layer (Si-ND: 2.0 eV and bulk Si: 1.1 eV) that the EQE from 600 to 1100 nm belonged to carriers generated in the Si substrate. Therefore, this could be attributed to still low conductivity vertically even in the 2D array of Si-NDs. This indicates that the electrons generated in the p-type Si substrate could not be completely extracted to the n-type Si layer through the Si-ND layer compared with the pn junction solar cell. Namely, the conductivity in our single layer Si-ND array structure was still lower than that in

the bulk Si pn junction. We speculated that this problem could be solved by generating minibands both vertically and laterally using a 3D Si-ND array structure.

10.3 Application to Laser/LED [24]

Quantum dots (QDs) have attracted considerable interests due to their potential device applications for the next generation quantum cryptosystem such as single-photon source, light emitting diodes, detectors, and laser diodes. The active gain medium of QD semiconductor has numerous merits that are not available in a form of bulk or quantum wells. For example, high-speed modulation, low-power consumption, and temperature stability have been demonstrated based on the QD technology. Current research efforts focus on the lattice-mismatched QD systems such as InAs/GaAs grown in Stranski–Krastanov (SK) mode. While these systems are promising for application to telecommunication devices in the near-infrared wavelength range, the structures are usually complex due to the strained, heavy intermixing, and wetting layers (WLs). Besides, the WLs under QDs behave as a carrier trap layer for QDs. These structures make noncontiguous energy bands drop to the quantum energy level of QDs, and hence the carrier relaxation is strongly affected by the ground states of QDs, obscuring the intrinsic properties of QD devices. Due to these fundamental reasons and also to the intention to create prototype devices, it is desirable to develop a GaAs/AlGaAs system in a lattice-matched condition, where strain-free QDs without WLs can be formed as an ideal quantum structure. To this end, we have investigated a GaAs/AlGaAs system by using the ultimate top-down technique, and recently observed a photoluminescence (PL) emission from the GaAs/AlGaAs nanodisks (NDs). Reactive ion etching (RIE) is conventionally used to pattern optoelectronic devices without the active layer such as nanowire waveguide, distributed Bragg reflector (DBR), and distributed feedback (DFB) structures. On the other hand, RIE process for the quantum nanostructures of III–V compound semiconductor still remains inapplicable due to the generation of defects after the irradiation of charged particles and the vacuum ultraviolet (UV) photons. The RIE damage in GaAs is known to penetrate to a depth of several tens of nanometers from the surface.

10.3.1 GaAs Quantum Dot Fabrication

The sample was grown on a GaAs (001) substrate using the metal-organic vapor phase epitaxy (MOVPE). At first, MQWs structure consisted of a 100-nm-thick $Al_{0.15}Ga_{0.85}As$ and MQWs of three pairs of 8-nm-thick GaAs well and 12-nm-thick $Al_{0.15}GaAs$ barrier for PL measurement, a single QW structures consisted of a 100-nm-thick $Al_{0.25}Ga_{0.75}As$ and QW of a 4-nm- and an 8-nm-thick GaAs well, a 20-nm-thick $Al_{0.275}GaAs$ barrier and 5-nm-thick capping layer for high energy

level offset for strong quantum energy level confinement for various temperature measurement, and MQWs device structure consisted of a 1.4-μm-thick $Al_{0.35}Ga_{0.65}As$ bottom cladding layer and a 100-nm-thick $Al_{0.25}Ga_{0.75}As$ separated confinement heterostructure (SCH) layer, and MQWs of six pairs of 8-nm-thick GaAs well and 12-nm-thick $Al_{0.15}GaAs$ barrier. The NDs in the active layer were formed by the ultimate top-down combination processes of the biotemplate and the neutral beam (NB) etching for LED [24–29].

Figure 10.11a, b shows SEM images of the as-etched pillars. The images in Fig. 10.1b clearly show that high-aspect-ratio nanopillars (diameter <20 nm and height 100 nm) were obtained by Cl_2–NBE using metal oxide core masks. After etching, clear lattice images were visible on the sidewalls, suggesting that no significant critical physical damage had occurred. The surface of the nanopillars was then passivated by hydrogen radical treatment at room temperature to prevent surface oxidation. To confirm the ND crystal quality, we also inspected a sample using cross-sectional high-angle annular dark field scanning transmission electron microscope (HAADF-STEM). Figure 10.11c shows HAADF-STEM images for checking the stacked structure of the NDs. MQWs of 8-nm-thick GaAs well and 4-nm-thick $Al_{0.275}GaAs$ barrier was grown and shaped into nanopillars, and then an $Al_{0.15}GaAs$/GaAs cap was regrown to clearly observe the GaAs NDs that was

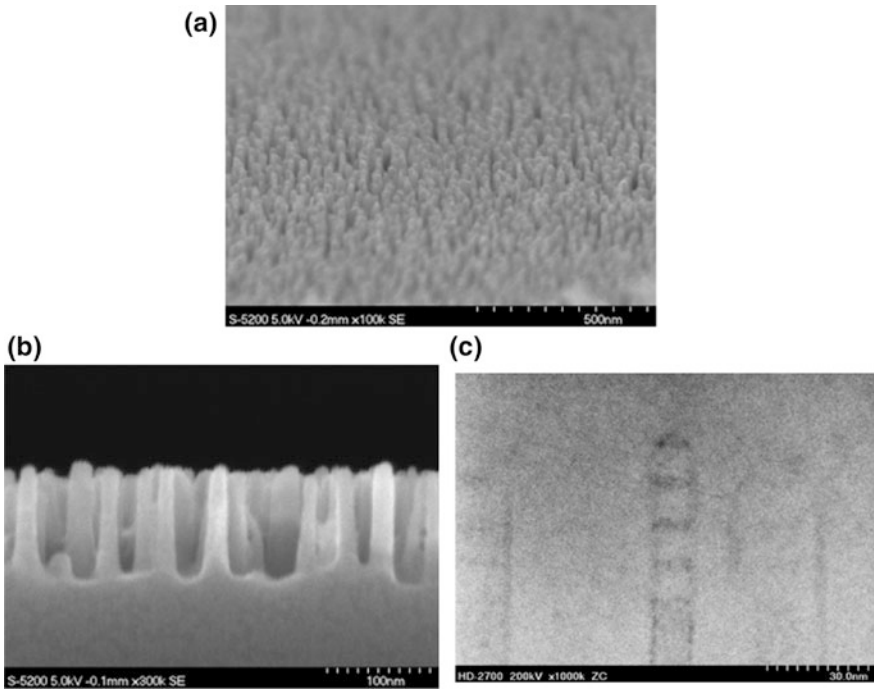

Fig. 10.11 SEM and TEM pictures of as-etched GaAs/AlGaAs nanopillars by ultimate top-down process. **a** Bird's eye view, **b** cross-section, and **c** TEM image after AlGaAs regrowth

embedded in a low Al concentration in the AlGaAs layer. Because of lattice-matched systems, it was difficult to clearly observe the NDs structure, and the Al concentration was controlled between 0.15 at MQWs barriers and 0.275 at regrown barriers.

10.3.2 PL Measurement and Its Analysis

The time-resolved PL spectra of the fabricated structures were obtained. The samples were excited using second-harmonic ultrashort pulses with a time width of 150 fs from a mode-locked Ti:sapphire laser operating at a wavelength of 400 nm (=3.10 eV). The excitation density was 0.084 μJ/cm^2, and the typical spot diameter on the sample surface was approximately 100 μm. PL was dispersed spectrally using a monochromator and detected using a streak camera. The sample was mounted on the surface of a low-temperature stage controlled using a closed-cycle helium cryostat, which enabled measurement of the temperature dependence of PL at temperatures ranging from 7 to 200 K.

Four different samples as respective reference materials were prepared and subjected to PL analysis: thin (4-nm-thick GaAs NDs) and thick ND (8-nm-thick GaAs NDs) samples and thin QW (4-nm-thick-QW) and thick QW (8-nm-thick-QW) samples. The time-integrated PL spectra of the thin and thick ND samples and the thin and thick QW reference samples at 7 K are measured in Fig. 10.12. The PL emissions from the thin and thick GaAs QW samples were observed at 1.62 eV (=764 nm) and 1.55 eV (=800 nm), respectively. In contrast, PL bands centered at 1.74 eV (=713 nm) and 1.66 eV (=747 nm) were observed for the thin and thick ND samples, respectively. The latter PL bands were clearly distinguished from those observed in the PL spectra of the GaAs QWs and were shifted to higher energies by 120 and 110 meV compared with those of the thin and thick GaAs QW samples, respectively. These significant shifts in the energies of the

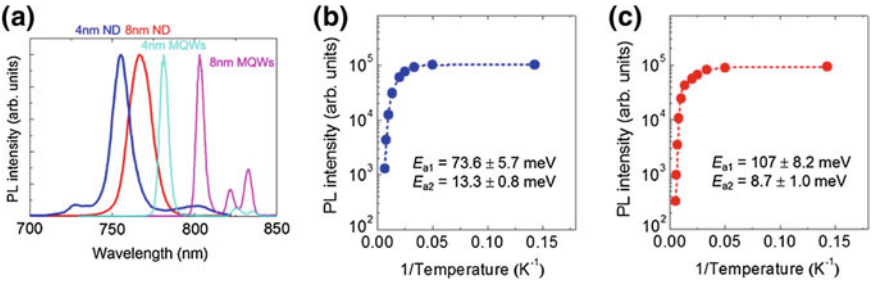

Fig. 10.12 Temperature-dependent PL spectra of the **a** 4-nm-thick and 8-nm-thick GaAs quantum NDs and MQWs at 7 K. Integrated PL intensities of the **b** 4-nm-thick and **c** 8-nm-thick GaAs quantum NDs as a function of the inverse temperature. The *dashed lines* are fitting results obtained using Eq. (10.2)

PL bands of the NDs were attributed to three-dimensional quantum confinement effects. A reduction in PL intensities was observed, because the volume of gain media shrank after realizing NDs. GaAs gain volume was reduced to 1/100 as compared with MQWs. Namely, it is estimated that PL intensity degradation of NDs were as the same order of that of MQWs.

To gain insight into the optical properties of the new ND structures, the temperature dependence of the PL spectra of both the thin and the thick ND samples were measured over the range of 7–200 K, as shown in Figs. 10.13a, and 10.14b, respectively. With increasing temperature, the PL intensities for both ND samples decreased monotonically, while the PL peak energies shifted to the lower energy region. The integrated spectral intensities of the thin and the thick ND samples were then semi-logarithmically plotted as a function of the inverse temperature (Fig. 10.13c, d, respectively), and similar behavior was observed for both samples, with the PL intensity decreasing moderately down to 100 K and rapidly above 100 K. These temperature-dependent PL intensities suggest the presence of non-radiative recombination processes.

Next, the temperature dependence of the PL intensity was analyzed using the following Arrhenius-type equation [30–32].

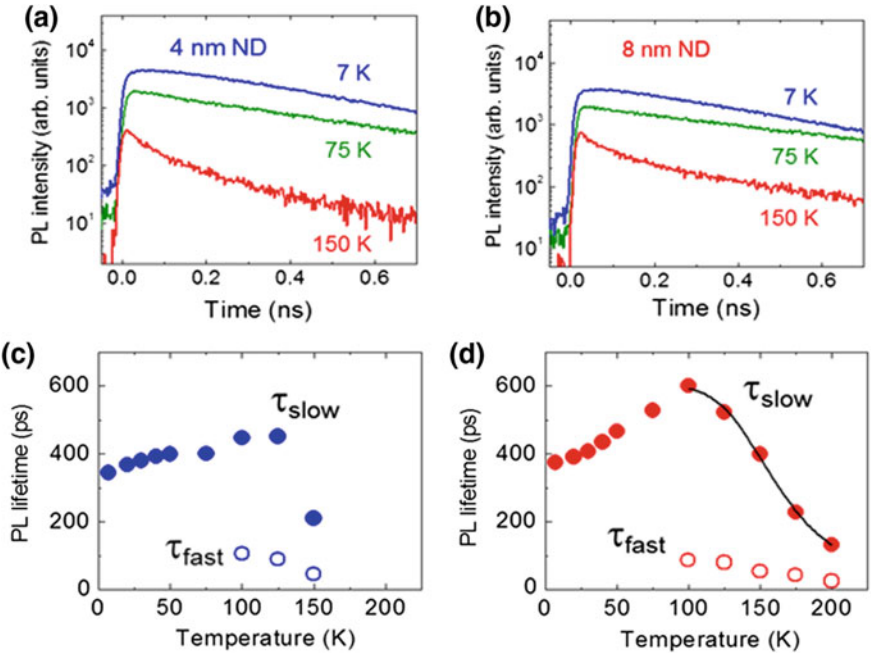

Fig. 10.13 PL time profiles of the **a** 4-nm-thick and **b** 8-nm-thick quantum NDs as a function of temperature (7, 75, and 150 K), and temperature dependence of the PL life times **c** and **d** for the respective samples in **a** and **b**. The *closed* and *open circles* correspond to slower and faster PL life times, respectively

$$I(T) = \frac{I_0}{1 + B_1 \exp\left(-\frac{E_{a1}}{kT}\right) + B_2 \exp\left(-\frac{E_{a2}}{kT}\right)}, \tag{10.3}$$

where I_0 is the PL intensity at 0 K, E_{a1} and E_{a2} are the thermal activation energies for the PL-quenching processes, and B_1 and B_2 are coefficients relating to the number of nonradiative centers for the respective processes. The fitting results for the two ND samples with different thicknesses are shown in Fig. 10.13a, b. Here, the two exponential terms in Eq. (10.3) are necessary to reproduce the experimental data, thereby indicating two different types of nonradiative recombination mechanisms.

Time-resolved PL spectra of the samples at temperatures ranging from 7 to 200 K were then observed in order to gain more insight into the carrier dynamics, including the nonradiative quenching processes. The time-resolved PL spectra were recorded using a synchroscan streak camera (Hamamatsu photonics, C4334) with a time resolution of approximately 5 ps after the deconvolution analysis. Typical PL time profiles of the thin and thick ND samples were measured at 7 K, as shown in Fig. 10.13a, b. Below 100 K, the PL transients were well fitted using a single exponential function, whereas the double exponential components were required for the fitting above 100 K. The decay times obtained are plotted as a function of temperature for the thin and thick ND samples in Fig. 10.13c, d, respectively. The temperature dependence of the PL decay time for the two samples is similar, with a slower decay time that increases as the temperature increases up to 100 K and then decreases above 100 K.

To study the relationship between measured activation energies and ND structures, the ND energies were estimated using known parameters, such as the temperature dependence of semiconductor energy levels as determined using the Varshini empirical equation [33], effective masses [34], ND profiles, and measured optical transition energies. The ND confinement energies were calculated by solving Schrodinger's equation for the GaAs/AlGaAs finite potential well using the three-dimensional finite element method (FEM) [35]. The calculated band parameters are shown in Table 10.2.

The fitting coefficients for B_1 determined to be 16 and 8.7 which is responsible for E_{a1}, were found to be significantly lower than those for B_2 determined to be 1.86×10^4 and 9.69×10^4 for the thin and thick ND samples, suggesting that the nonradiative process in the low-temperature regime plays a minor role in determining the overall PL behavior of the NDs. Therefore, the origin of activation energy E_{a2} was explored.

The larger activation energies E_{a2} were determined to be 73.6 and 107 meV for the thin and thick ND samples, respectively. These activation energies explain the rapid quenching of PL above 100 K and can be attributed to the effective barrier height for thermal leakage of excitons or carriers from the confined ND states. This conclusion is supported by the fact that E_{1a} for the thin ND sample was lower than that for the thick ND sample because of the stronger confinement resulted in quantum states of higher energies.

Table 10.2 Three-dimensional FEM simulated and measured activation energies of the unstrained GaAs/$Al_{0.275}$ GaAs quantum ND structure at 7 K

	Thin ND (4-nm-thick ND)	Thick ND (8-nm-thick ND)
GaAs bandgap level E_{GaAs} (eV)	1.519	
$Al_{0.275}$ GaAs bandgap level E_{AlGaAs} (eV)	1.865	
Ground state electron confinement energy E_e^1 (meV)	126	80
First excited state electron confinement energy E_e^2 (meV)	176	134
Ground state heavy hole confinement energy E_{hh}^1 (meV)	29	15
First excited state heavy hole confinement energy E_{hh}^2 (meV)	38	24
$E_{hh}^2 - E_{hh}^1$ (meV)	9	9
Transition energy		
$E_T = E_e^1 + E_{hh}^1 + E_g$ (eV)	1.674	1.614
Activation energy for valence band (meV)	99	145
Activation energy for conduction band (meV)	92	106
Measured activation energy (meV)	73.6 ± 5.7	107 ± 8.2
Energy of conduction band offset: energy of valence band offset = 0.65:0.35		

The energy differences (187 meV for the thin ND sample and 248 meV for the thick ND sample) between the transition energies of the confined states (corresponding to the PL emission peaks) and the band gap energy of the AlGaAs barrier were much larger than the obtained activation energies. Therefore, thermal escape of excitons cannot account for the nonradiative process. In addition, for the thin ND sample, the calculated barrier height for an electron at the ground state was 99 meV and that for a heavy hole was 88 meV, while the experimentally obtained value of the activation energy E_{a2} was 73.6 ± 5.7 meV, which was close to the barrier height calculated for the valence band rather than that for the conduction band. For sample B (the thick ND), the calculated barrier height for an electron was 145 meV and that for a heavy hole was 103 meV. Therefore, the E_{a2} value of 107 ± 8.2 meV was again well in accordance with the barrier height for the valence band. Based on these results, we concluded that the nonradiative recombination process described by the activation energy E_{a2} can be attributed to the thermal escape of heavy holes from the confined ground states to the valence band of the AlGaAs barrier.

The results of the time-resolved PL measurements for the thick ND sample further confirmed this hypothesis for the thermal quenching of PL in the QDs. The PL decay time decreased at 100 K, which coincided with rapid decrease in the PL intensity beginning at 100 K. The observed temperature dependence of the PL decay time above 100 K for the thick ND sample was analyzed using a similar Arrhenius-type equation, as follows [36].

$$\tau_{PL}(T) = \frac{\tau_{max}}{1 + \left(\frac{\tau_{max}}{\tau_{esc}}\right) \exp\left(-\frac{E_a}{kT}\right)}, \tag{10.4}$$

where τ_{max} is the maximum decay time at 100 K, E_a is the activation energy, and τ_{esc} is the escape time of the carriers from the ND states to the barrier. From the fitting calculations, the activation energy E_a was found to be 97 ± 5 meV, with an escape time τ_{esc} of approximately 0.6 ps. The value of E_a deduced from the PL decay time was close to that obtained from the temperature dependence of the PL intensity (approximately 107 meV). This agreement again suggests that the nonradiative recombination process, which causes rapid decreases in the PL intensity and decay time above 100 K, can be attributed to the thermal escape of heavy holes from the confined ground states of ND to the valence band of the barrier.

We note that a faster decay was also observed in the high temperature range above 100 K, as shown in Fig. 10.13c, d. The time constants (τ_{fast}) were similar for both ND samples; therefore, this fast process can be attributed to the extrinsic, rather than intrinsic, nature of NDs. In addition, the presence of this fast decay indicates that, in some sample areas, nonradiative recombination centers may exist in the barrier at the GaAs–AlGaAs interface of the sidewalls of NDs. Thermally excited carriers may be rapidly trapped by nonradiative centers in the barrier with high impurity level of oxygen and carbon which were still existed between the interface of NDs and regrown barrier, which then exhibit fast decay.

The lower activation energies (E_{a1}) were determined to be 13.3 and 11.1 meV for the thin and thick ND samples, respectively. These activation energies describe the moderate decrease in the PL intensity at temperature above 75 K. The values of E_{1a} agreed well with the energy difference between the ground and first excited states (eigenvalues) of the valence bands ($E^2_{hh} - E^1_{hh}$), which were calculated to be 12 and 11 meV for the thin and thick ND samples, respectively. Therefore, the nonradiative process described by E_{1a} is attributed to the thermally excited excitons ($E^1_e - E^2_{hh}$) as an optically inactive dark state with slightly higher energy [37]. The overlapping integral of the wave functions of the ground state electron and the first excited heavy hole is nearly zero in the present calculation. Thereforethe oscillator strength of this electron–hole pair is also nearly zero, thereby indicating that the optically inactive exciton states are nonradiative. The low difference in the value of E_{a1} for the 2 samples may be explained by the difference in the strength of the quantum confinement; when the size of the ND decreases, the energy interval of the confinement states increases.

This assignment of E_{a1} is also consistent with the temperature dependence of the PL decay times. In general, the radiative recombination time is determined by the net and effective oscillator strengths of the ND, reflecting the density of states and thermal distribution of the excitons [38–40]. In a stronger quantum confinement regime, because the effect of the thermal excitation at higher energy-confined states is significantly reduced due to the discrete energy separation, the net oscillator strength nearly equals that of the ground state, and the radiative recombination time remains constant with increasing temperature. When the quantum confinement is

not strong enough, the excitons can populate the higher energy states that have lower oscillator strengths as the temperature increases, resulting in a gradual increase in the radiative recombination time with increasing temperature. For the thin ND sample, the PL decay time moderately increased from 350 ps at 7 K to 440 ps at 100 K. On the other hand, in the thick ND sample, the PL decay time significantly increased from 380 ps at 7 K to 600 ps at 100 K. Therefore, the incremental increase in the PL decay time with increasing temperature in both samples can be attributed to thermal excitation of excitons into optically inactive exciton states with lower oscillator strengths. The significant increase in the PL decay time for the thick ND sample compared with the moderate increase for the thin ND sample can be explained by the difference in the strengths of the quantum confinements. In the thin ND sample, the density of states is more discrete, thus, the energy separation is larger, preventing thermal excitation to the higher optically inactive states. As a result, the PL decay time is insensitive to the temperature for the thinner NDs. This thermal excitation to the optically inactive states is also consistent with the moderate decrease in the PL intensity with a low activation energy (E_{a1}).

10.3.3 LED Fabrication and Its Properties

After the regrowth process, we made an LED structure. First, we deposited a 300-nm-thick SiO_2 layer and opened a window with a width from 20 to 100 μm. Next, we deposited a 20-nm-thick Ti and a 300-nm-thick Au to make the top electrodes. Third, lapping of the GaAs substrate was performed to a thickness of 150 μm, and a 20-nm-thick AuGe and a 100-nm-thick Au was deposited on the rear side. For the LED emission experiments, we cleaved the sample into a bar piece without a subsequent coating process on the edge.

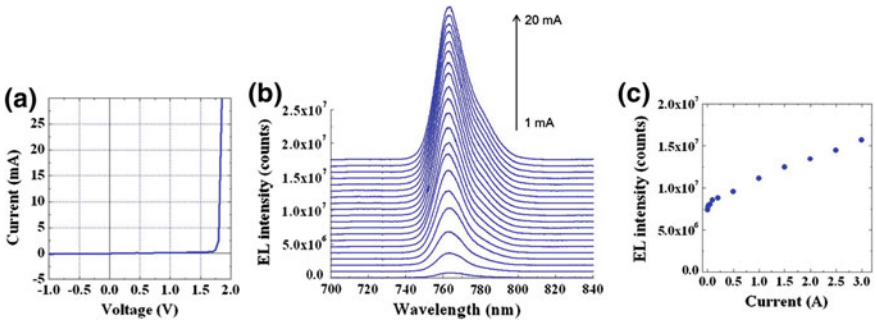

Fig. 10.14 I–V and I–L characteristics of GaAs ND-LED. **a** I–V characteristic, **b** ND-LED emission spectrum, and **c** I–L characteristics of ND-LED

To induce device excitation, we used a continuous wave current source. The optical emission normal to the cleaved surface was detected by a spectrometer equipped with a charge-coupled device. Figure 10.14a shows the I–V curve of the ND-LED operated at 7 K. The width of the stripe electrode was 20 μm, and a threshold voltage of 1.8 V was observed. Figure 10.14b shows the emission spectrum taken from the cleaved edge of the LED structure for various current injection conditions at 7 K. The spectra show a smooth and narrow curve, corresponding to the emissions from the ND ensemble. The center energy of the line ensemble was 763 nm, which agreed well with that of the ND emissions. This observation suggests that the emission was originated from the ground state of the NDs, which was attributed to the formation of the high-density NDs at high uniformity. Figure 10.14c plots the emission intensity profile measured at various current values at a 10 kHz pulse current injection. An offset emission was observed at an offset direct current (DC) of 4 mA. As pulse current was increased, emission power increased linearly as usually seen in a typical LED behavior.

10.4 Summary

Recently, quantum dot super lattices (QDSLs) with uniform dot size, uniform inter-dot-spacing and high-density QDs have been widely used to develop new generation devices, such as QD lasers, QD solar cells, and QD electronic devices. Quantum size effect in QDs provides an opportunity to engineer the bandgap energy (E_g) by adjusting the size of the QD. Carrier wave functions with close-packed and well-aligned QDs overlap one another and discrete confined energy levels merge into broadened minibands. Such nanoengineered QDs in photovoltaic applications have great potential as novel adjustable absorber layers to achieve intermediate band solar cells and tandem solar cells. Moreover, for Si-QDSLs, the SiC for the interlayer is one of the most promising materials to be used to form minibands that anticipate enhanced photon absorption and electrical conductivity in Si-QD solar cells. Carrier wave functions more easily spread into the SiC interlayer to form minibands to achieve Si-QD solar cells because of its lower E_g compared with other insulating materials such as SiO_2 and SiN. However, it is difficult to fabricate defect-free and sub-10 nm nanostructures by using conventional methods such as plasma processes with photolithography techniques and co-sputtering techniques with annealing and molecular beam epitaxy processes. Furthermore, a fabrication process with a high degree of control is also required for different QD materials in different applications. Our aim in this paper was to develop a uniform and closely packed array of sub-10-nm Si structure as realistic QDSL using a new process that combines a biotemplate and damage-free neutral beam (NB) etching to address these problems, and investigated and controlled optical and electronic properties due to quantum effects for future devices. We firstly investigated the controllable range of E_g and optical absorption characteristic of Si-NDs by changing the geometric parameters of Si-ND and matrix material, and discussed the mechanism by comparing the

experimental result with the simulation result. It was clarified that independently changing the geometric parameters of thickness and diameter in our proposed Si-ND array structure enables the optical E_g to be precisely designed within a wide range from 1.3 to 2.3 eV. It was demonstrated that the coupling of wave functions strengthens and forms a wide miniband due to the lower E_g of the SiC or decreasing of the center-to-center distance between NDs, which enhanced photon absorption in the structure. Then, an enhancement of conductivity in Si-NDs by formation of minibands was investigated. Within the envelop function theory and Anderson Hamiltonian method, we also calculated electronic structures and the current transport, which theoretically proved that minibands enhanced the conductivity. Finally, the highly optical absorption and electrical conductivity were verified by fabricating p–i–n solar cells with Si-NDs, and effective carrier generation and transport in our Si-ND structure were surely clarified.

We demonstrated the current injection operation of a GaAs ND-LED developed by the ultimate top-down process and MOVPE regrowth. By using the damage-free NB etching, we achieved high-density GaAs/AlGaAs QDs at high uniformity and quality, thereby realizing an intense narrow PL emission from the ensemble of NDs. The ND-LED structure of these NDs exhibited a narrow emission with a clear threshold at 7 K. The strain-free GaAs/AlGaAs system has a definite advantage in enabling a large number of QD layers, while keeping a high crystallographic quality since there is no strain-induced dislocation. Therefore, this developed manufacturing process is thought to be a promising method to produce high-performance ND optical devices in the lattice-matched compound semiconductor systems.

References

1. L. Zhuang, L. Guo, S.Y. Chou, Silicon single-electron quantum-dot transistor switch operating at room temperature. Appl. Phys. Lett. **72**, 1205 (1998)
2. R.L. Sellin, C. Ribbat, M. Grundmann, N.N. Ledentsov, D. Bimberg, Lithographic alignment to site-controlled quantum dots for device integration. Appl. Phys. Lett. **78**, 1207 (2001)
3. C. Schneider, M. Strauß, T. Sunner, A. Huggenberger, D. Wiener, S. Reitzenstein, M. Kamp, S. Hofling, A. Forchel, Lithographic alignment to site-controlled quantum dots for device integration. Appl. Phys. Lett. **92**, 183101 (2001)
4. H. Ishikuro, T. Hiramoto, Quantum mechanical effects in the silicon quantum dot in a single-electron transistor. Appl. Phys. Lett. **71**, 3691 (1997)
5. V. Wood, M.J. Panzer, J.M. Caruge, J.E. Halpert, M.G. Bawendi, V. Bulovic, Air-stable operation of transparent, colloidal quantum dot based LEDs with a unipolar device architecture. Nano Lett. **10**, 24 (2010)
6. S. Chakrabarti, M.A. Holub, P. Bhattacharya, T.D. Mishima, M.B. Santos, M.B. Johnson, D.A. Blom, Spin-polarized light-emitting diodes with Mn-doped InAs quantum dot nanomagnets as a spin aligner. Nano Lett. **5**, 209 (2005)
7. A. Luqu, A. Marti, Photovoltaics: towards the intermediate band. Nat. Photon. **5**, 137 (2011)
8. A. Luque, A. Marti, The intermediate band solar cell: progress toward the realization of an attractive concept. Adv. Mater. **22**, 160 (2009)

9. H. Yu, J. Li, R.A. Loomis, P.C. Gibbons, L.W. Wang, W.E. Buhro, Cadmium selenide quantum wires and the transition from 3D to 2D confinement. J. Am. Chem. Soc. **125**, 16168 (2003)
10. A. Kongkanand, K. Tvrdy, K. Takechi, M. Kuno, P.V. Kamat, Quantum dot solar cells. Tuning photoresponse through size and shape control of CdSe–TiO_2 architecture. J. Am. Chem. Soc. **130**, 4007 (2008)
11. B. Pejova, I. Grozdanov, Three-dimensional confinement effects in semiconducting zinc selenide quantum dots deposited in thin-film form. Mater. Chem. Phys. **90**, 35 (2005)
12. W. Pan, N. Usami, K. Hara, N. Arifuku, M. Matsui, S. Matsushima, *PVSEC21, 2D-1P-04* (Hukuoka, Japan, 2011)
13. S. Yamada, Y. Kurokawa, S. Miyajima, A. Yamada, M. Konagai. High open-circuit voltage oxygen-containing silicon quantum dots superlattice solar cells, in *Proceeding of the 35th IEEE Photovoltaic Specialists Conference*, 317, Honolulu, HI (2010)
14. G. Conibeer, M.A. Green, E.C. Cho, D. König, Y.H. Cho, T. Fangsuwannarak, G. Scardera, E. Pink, Y. Huang, T. Puzzer, S. Huang, D. Song, C. Flynn, S. Park, X. Hao, D. Mansfield, Silicon quantum dot nanostructures for tandem photovoltaic cells. Thin Solid Films **516**, 6748 (2008)
15. D. Bimberg, *Semiconductor Nanostructures* (Springer, Berlin, 2008)
16. Y. Arakawa, H. Sakaki, Appl. Phys. Lett. **40**, 939 (1982). doi:10.1063/1.92959
17. M. Asada, Y. Miyamoto, Y. Suematsu, IEEE J. Quantum Electron. **QE-22**, 1915 (1986). doi:10.1109/JQE.1986.1073149
18. P.G. Eliseev, H. Li, A. Stintz, G.T. Liu, T.C. Newell, K.J. Malloy, L.F. Lester, Appl. Phys. Lett. **77**, 262 (2000). doi:10.1063/1.126944
19. K. Otsubo, N. Hatori, M. Ishida, S. Okumura, T. Akiyama, Y. Nakata, H. Ebe, M. Sugawara, Y. Arakawa, Jpn. J. Appl. Phys. Part **2**(43), L1124 (2004). doi:10.1143/JJAP.43.L1124
20. M. Igarashi, M.F. Budiman, W. Pan, W. Hu, Y. Tamura, M.E. Syazwan, N. Usami, S. Samukawa, Nanotechnology **24**, z015301 (2013)
21. S. Samukawa, K. Sakamoto, K. Ichiki, Generating high-efficiency neutral beams by using negative ions in an inductively coupled plasma source. J. Vac. Sci. Technol. A **20**, 1566 (2002)
22. S. Samukawa, K. Sakamoto, K. Ichiki, High-efficiency low energy neutral beam generation using negative ions in pulsed plasma. Jpn. J. Appl. Phys. **40**, L997 (2001)
23. D.M.T. Kuo, G.Y. Guo, Y.C. Chang, Tunneling current through a quantum dot array. Appl. Phys. Lett. **79**, 3851 (2001)
24. A. Higo, T. Kiba, Y. Tamura, C. Thomas, J. Takayama, Y. Wang, H. Sodabanlu, M. Sugiyama, Y. Nakano, I. Yamashita, A. Murayama, S. Samukawa, *Scientific Reports*, vol. 5 (2015), p. 9371
25. S. Samukawa, Ultimate top-down etching processes for future nanoscale devices: advanced neutral-beam etching. Jpn. J. Appl. Phys. **45**, 2395 (2006)
26. X.Y. Wang, C.H. Huang, R. Tsukamoto, P.A. Mortemousque, K. Itoh, Y. Ohno, S. Samukawa, Damage-free top-down processes for fabricating two-dimensional arrays of 7 nm GaAs nanodiscs using bio-templates and neutral beam etching. Nanotechnology **22**, 365301 (2011)
27. Y. Tamura, T. Kaizu, T. Kiba, M. Igarashi, R. Tsukamoto, A. Higo, W. Hu, C. Thomas, M.E. Fauzi, T. Hoshii, I. Yamashita, Y. Okada, A. Murayama, S. Samukawa, Quantum size effects in GaAs nanodisks fabricated using a combination of the bio-template technique and neutral beam etching. Nanotechnology **24**, 285301 (2013)
28. C. Thomas, Y. Tamura, M.E. Syazwan, A. Higo, S. Samukawa, Oxidation states of GaAs surface and their effects on neutral beam etching during nanopillar fabrication. J. Phys. D: Appl. Phys. **47**, 215203 (2014)
29. R. Tsukamoto, M. Godonoga, R. Matsuyama, M. Igarashi, J.G. Heddle, S. Samukawa, I. Yamashita, Langmuir **29**, 12737 (2013)
30. R. Heitz, I. Mukhametzhanov, A. Madhukar, A. Hoffmann, D. Bimberg, J. Electron. Mater. **28**, 520 (1999)

31. G. Gelinas, A. Lanacer, R. Leonelli, R.A. Masut, S. Raymond, P.J. Poole, Phys. Rev. B **81**, 235426 (2010)
32. N.A. Jahan, C. Hermannstadter, J.H. Huh, H. Sasakura, T.J. Rotter, P. Ahirwar, G. Balakrishnan, K. Akahane, M. Sasaki, H. Kumano, I. Suemune, J. Appl. Phys. **113**, 033506 (2013)
33. M.E. Levinshtein, S.L. Rumyantsev, M.S. Shur (eds.) 1996 *Handbook Series of Semiconductor Parameters*, vol. 2: *Ternary and Quaternary III–V Compounds* (World Sci Publ Co)
34. M. Grundmann, D. Bimberg, Phys. Rev. B **55**, 9740 (1997)
35. COMSOL Multiphysics. http://www.comsol.com/
36. G. Raino, A. Salhi, V. Tasco, R. Intartaglia, R. Cingolani, Y. Rouillard, E. Tournie, M. De Giorgi, Appl. Phys. Lett. **92**, 101931 (2008)
37. G. Trevisi, L. Seravalli, P. Frigeri, C. Bocchi, V. Grillo, L. Nasi, I. Suarez, D. Rivas, G. Muñoz-Matutano, J. Martinez-Pastor, Cryst. Res. Technol. **46**, 801 (2011)
38. H. Gotoh, H. Ando, T. Takagahara, J. Appl. Phys. **81**, 1785 (1997)
39. H. Gotoh, H. Kamada, H. Ando, J. Temmyo, Jpn. J. Appl. Phys. **42**, 3340 (2003)
40. M. Gurioli, A. Vinattieri, M. Zamfirescu, M. Colocci, S. Sanguinetti, R. Notzel, Phys. Rev. B **73**, 085302 (2006)

Part V
Fundamental Technologies for Nanosystem Integration

Chapter 11
Development of Novel Nano-systems for Electrochemical Devices by Hierarchizing Concentrated Polymer Brushes

Yoshinobu Tsujii, Yohei Nakanishi, Ryohei Ishige, Kohji Ohno, Takashi Morinaga and Takaya Sato

Abstract This chapter provides an overview of the fundamental concepts concerning the synthesis and properties of a "concentrated" polymer brush (CPB) followed by our recent research topics regarding self-organization of CPB-modified nanoparticles, their application to solid electrolytes along with ionic liquids, and then their practical use in various electrochemical devices including a lithium ion battery, an electric double-layer capacitor, a dye-sensitized solar cell, and a polymer electrolyte fuel cell. A CPB is one type of polymer brushes, and its controlled synthesis and hence systematic study were achieved by living radical polymerization (LRP) or reversible-deactivation radical polymerization. Since the graft chains of CPB have a highly elongated and oriented conformation in a good solvent, and hence potentially, the CPB exhibits favorable characteristics on their own. However, the LRP method has a limitation in the range of the controllable molecular weight of thereby synthesized polymers and hence the thickness of CPBs, i.e., on the order of 100 nm, limiting their use for a wider range of applications. In order to overcome this issue, CPBs have recently been successfully built up to a new hierarchical nano-system via self-ordering, as building blocks, nanoparticles/rods/sheets with CPBs on their surfaces. Among others, we here focus on the science and technology of CPB from the viewpoint of above-mentioned applications, otherwise difficult to achieve high performance.

Keywords Living radical polymerization · Polymer brush · Colloidal crystal · Ionic liquid · Solid electrolyte · Electrochemical device

Y. Tsujii (✉) · Y. Nakanishi · R. Ishige · K. Ohno
Institute for Chemical Research, Kyoto University, Gokasho, Uji, Kyoto 611-0011, Japan
e-mail: tsujii@scl.kyoto-u.ac.jp

T. Morinaga · T. Sato (✉)
National Institute of Technology, Tsuruoka College, 104 Sawada, Inooka, Tsuruoka, Yamagata 997-8511, Japan
e-mail: takayasa@tsuruoka-nct.ac.jp

J. Sone and S. Tsuji (eds.), *Intelligent Nanosystems for Energy, Information and Biological Technologies*, DOI 10.1007/978-4-431-56429-4_11

11.1 Introduction

Since surfaces and interfaces play an extremely important role in determining the interaction with external environment or other substances, their precise control is directly linked to improved functionality. To date, various methods of surface modification have been devised with the objective of controlling the surface morphology as well as characteristics of substances. Among them, the method of tethering polymer chains to a surface (surface grafting) has enabled us to fabricate a stable surface layer with a thickness as much as nanometer to micrometer scale, and hence it has been widely used for modifying and functionalizing organic and inorganic materials [1–3]. The function of such a polymer-tethered (grafted) surface is strongly linked to the conformation of the graft chain (see Fig. 11.1) [4–6]. A polymer chain swollen in a good solvent takes a random coil conformation. Once one end is fixed to a solid surface, it becomes somewhat distorted in the vertical direction to the surface ("mushroom" regime). When the surface density of graft chain increases and neighboring mushrooms overlap each other, osmotic pressure extends graft chains in the vertical direction to avoid an increase in concentration. This type of molecular organization is called a "polymer brush." A polymer brush with a relatively low surface density (σ) is called a semi-dilute polymer brush (SDPB), and according to the scaling theory based on a "blob" concept [7–10], it has a swollen thickness L_e represented as follows:

$$L_e \sim \beta L_c \sigma^{1/3} \tag{11.1}$$

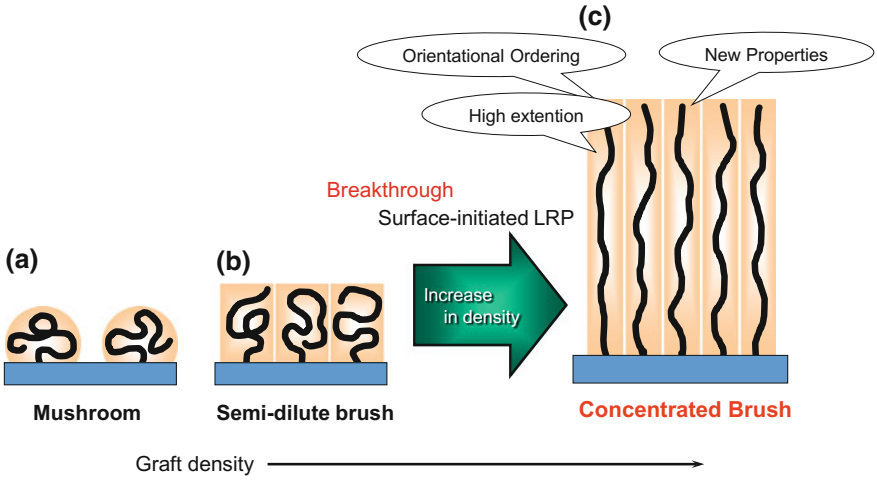

Fig. 11.1 Schematic illustrations of tethered polymer chains and polymer brushes; **a** mushroom, **b** semi-dilute brush, and **c** concentrated brush

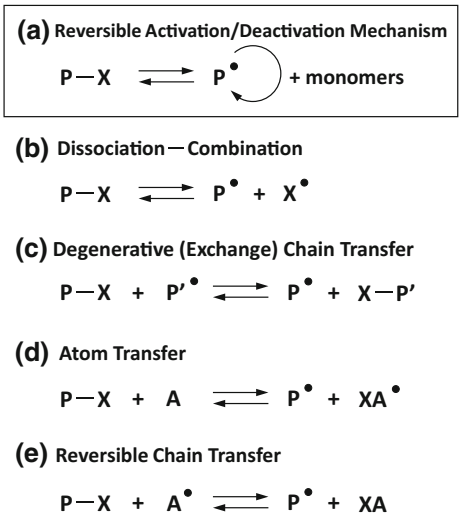

Scheme 11.1 Basic mechanisms of living radical polymerization

where L_c is the total chain length (fully extended length) and β is a constant dependent on the solvent strength. This SDPB theory is based on the approximations of a two-body interaction between segments as well as a Gaussian model for a graft chain. This graft-density regime has been extensively studied not only from the viewpoint of fundamental science but also from the practical issue of colloidal dispersion, and Eq. (11.1) has been experimentally verified.

Further increase in surface density achieves a so-called "concentrated" polymer brush (CPB), in which long-range interactions between graft chains are screened out and the above-mentioned SDPB theory can be no more applied. In this regime, L_e is believed to have a higher σ-dependency as follows [9, 10]:

$$L_e \sim L_c \sigma^{1/2} \tag{11.2}$$

However, conventional synthetic methods had achieved only the SDPB regime but not the CPB one with a surface occupancy (σ^*) of graft chain exceeding 10 %, where σ^* is the surface density normalized by the cross-sectional area of a polymer chain and the maximum value is unity. The structure and properties of the CPB had remained practically unknown/unexperienced until recently. Application of LRP to the surface graft polymerization enabled the controlled synthesis of CPB and systematic studies on its properties.

11.2 Living Radical Polymerization (LRP) and Concentrated Polymer Brush (CPB)

11.2.1 LRP Mechanism and Recent Advances

As indicated in Scheme 11.1a, the basic mechanism of LRP includes the temporary covalent bonding of a propagating radical ($P^{\bullet}$) with a suitable protecting group (X), giving a dormant species (P–X) in a quasi-equilibrium [11]. The following cycle is repeated, regenerating $P^{\bullet}$ (activation) by breaking the covalent bond → adding monomers (propagation) → returning to the dormant state (deactivation). The main mechanisms for "reversible" activation are the thermal (optical) dissociation and bonding (Scheme 11.1b), the degenerative (exchanging) chain transfer between the propagating radical and P–X (Scheme 11.1c), and the halogen-atom transfer catalyzed by a transition metal complex (Scheme 11.1d). These mechanisms correspond to nitroxide-mediated polymerization (NMP), reversible addition-fragmentation chain transfer (RAFT) polymerization, and atom transfer radical polymerization (ATRP), respectively. Recently, further progress has been achieved via the development of high-performance protecting groups as well as the introduction of novel catalytic cycles. Goto et al. [12] developed a LRP using iodine as a protecting group and a non-metallic compound as a catalyst. This polymerization method was named "reversible chain transfer catalyzed polymerization" (RTCP) due to a new type of reaction mechanism (Scheme 11.1e), i.e., catalytic radical mediation. To date, this method has achieved controlled polymerization of various functional monomers (styrenes, methacrylates, etc.) containing epoxy groups, hydroxyl groups, amino groups, carboxyl groups, and others. In addition to the metal-free system, many of its catalysts have low toxicity, hence being highly expected for application in batteries and electronic materials as well as in bio-inspired systems. Yamago et al. [13–15] focused on the kind of elements of the protecting group and developed LRPs using organotellurium (group 16), organoantimony (group 15), and organobismuth (group 15). This type of LRP methods features not only high versatility and tolerance of monomers and functional groups but also highly efficient convertibility of terminal groups. It should be noted that this method was applicable to monomers with acidic protons, whose polymerization is difficult to be controlled, as a result, successfully leading to the controlled synthesis of a proton-conducting CPB (discussed below) [16].

11.2.2 Surface Grafting and CPB

By applying LRP after fixing polymerization-initiating groups to the surface of various materials (surface-initiated LRP), a structurally well-defined CPB was potentially synthesized (see Fig. 11.2) [17, 18]. This grafting-from method achieved a dramatic increase (up to an order of magnitude) in graft density via

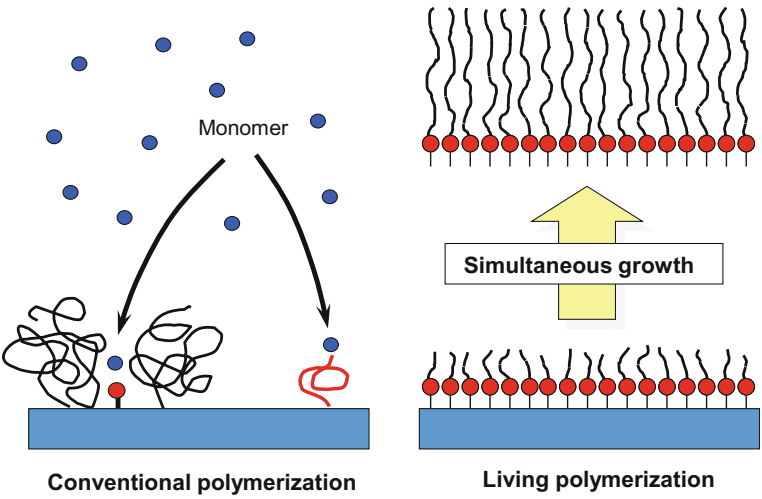

Fig. 11.2 Schematic illustration of surface-initiated polymerization (grafting-from technique) producing polymer brushes

highly efficient initiation of polymerization and uniform growth, resulting in a CPB system [19]. Figure 11.3 summarizes the dependence of swollen thickness (L_e) as a function of normalized graft density, i.e., surface occupancy (σ^*) in a good solvent for various polymer brushes, including CPBs of poly(methyl methacrylate) (PMMA) synthesized via surface-initiated ATRP [20, 21] as well as others [22–24]. With increasing σ^*, the L_e value increased exceeding the prediction of Eq. (11.1) for SDPB and approaching to the prediction of Eq. (11.2). This suggests that the CPB regime could be successfully reached. Detailed experimentation and

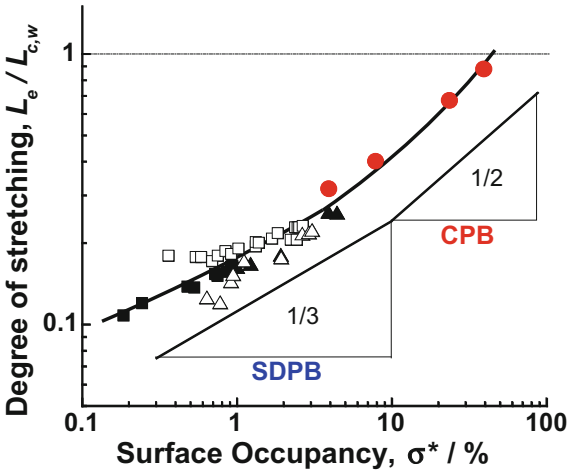

Fig. 11.3 Plot of normalized swollen thickness $L_e/L_{c,w}$ vs surface occupancy σ^*; the data for SDPB from the references [22–24]

consideration on the basis of Eqs. (11.1) and (11.2) revealed that the crossover surface density between SDPB and CPB was approximately $\sigma^* = 10$ %. This crossover density is an important factor for designing various CPBs. Surprisingly, the swollen thickness of the highest-density brush reached 80–90 % of the fully extended chain length, like a literal "polymer brush" as schematically indicated in Fig. 11.1. This was exceptional contrast to conventionally synthesized SDPBs having L_e values of at most 20–30 % of the fully extended chain length.

Swelling of a polymer brush in a solvent can be understood by the balance of osmotic pressure and elastic stress, related to mixing entropy and conformational entropy, respectively. In other words, graft chains are swollen and elongated due to the osmotic pressure, reaching equilibrium at a degree of swelling when the osmotic pressure is balanced with the elastic stress (increasing with elongation). Such a CPB system involves a huge stress inside owing to exceptionally high osmotic pressure and elastic stress and thus exhibits an exceptionally large resistance against compression beyond the prediction of the conventional SDPB theory. This large repulsion would impart a high stability in dispersion of colloidal particles with the CPB on their surface. Below is an introduction to lubricating and size-exclusion properties as fascinating surface functions.

The coefficient of friction (COF) between PMMA brushes in a good solvent was measured using a colloid-probe technique of atomic force microscopy (AFM). As a result, it was discovered that while the SDPB system exhibited a transition from a low- to high-friction regimes in a small range with increasing applied load, the CPB one constantly exhibited ultralow friction (COF < 0.0005) regardless of the magnitude of loading [25]. In the latter system, a large osmotic pressure caused as a concentrated-solution system supports a large load, and confronting polymer brushes do not interpenetrate each other (non-interpenetrating interaction) due to the gain in conformational entropy at any compression (even in bulk). Takahara et al. investigated the friction as well as wear properties of CPBs from the viewpoints of machine lubrication systems [26, 27]. Recently, we successfully synthesized a significantly thicker CPB via a high-pressure ATRP method and demonstrated macro-level low-friction properties and high applicability to practical systems [28].

In addition, a swollen CPB exhibits marked selectivity in interactions with other molecules in solution (size-exclusion effect). As above illustrated, the intermolecular distance (positional ordering) between neighboring chains in the CPB should be defined by the graft points and preserved favorably even at the outermost surface. Therefore, the incursion of a larger molecule would force a large loss of entropy on the graft chains, affording a clear size-exclusion effect at approximately the distance between neighboring graft points, as illustrated in Fig. 11.4. Using hydrophilic CPBs, the non-specific adsorption/adhesion of proteins and cells were demonstrated to be effectively suppressed, which was primarily understood by this size-exclusion effect [29, 30]. Additionally, the molecular dynamics in the brush and the structuring of water are also attracting attention. These characteristics of CPBs were entropy-driven, assuring generality under good solvent conditions.

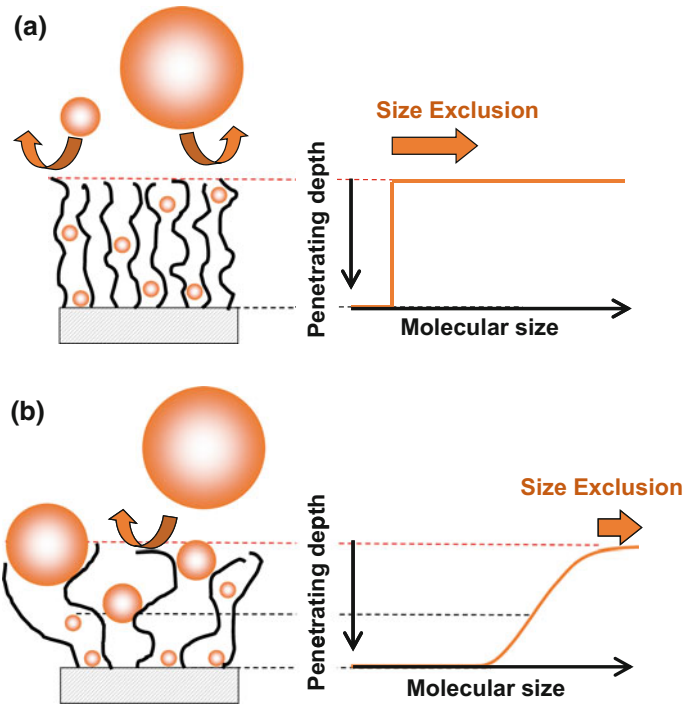

Fig. 11.4 Schematic illustration of size-exclusion effect of polymer brushes

11.2.3 Synthesis of CPB-Afforded Nanoparticle and Its Formation of Colloidal Crystal

As discussed above, high-density grafting is possible even on colloidal particles via graft polymerization from their surface. A broad range of particles have been used as cores, specifically silica particles (SiP) as well as various metal nanoparticles, semiconductor nanoparticles, metal oxide particles, carbon nanotubes, carbon nanoparticles, and the like. We succeeded in synthesizing a series of SiPs modified with a CPB of PMMA (PMMA-SiP) with high uniformity and high dispersibility (confirmed via a dynamic light scattering method) by developing the methodology for the introduction of initiating group and the polymerization on SiP and first demonstrated that these polymer-grafted hybrid nanoparticles (PSiP) were crystallized at a certain concentration of a dispersed solution (see Fig. 11.5) [31–34]. Additionally, this system was confirmed to have a coexisting zone of liquid and crystal phases and hence verified to be a thermodynamically stable colloidal crystal. The driving force behind crystallization is the three-dimensional (repulsive)

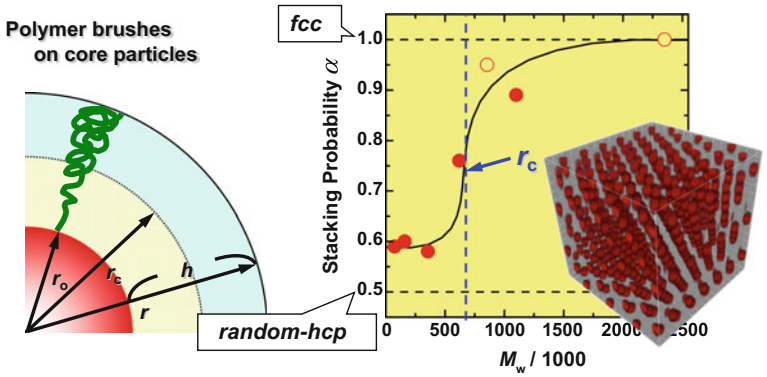

Fig. 11.5 Colloidal crystal of silica particles with concentrated brushes of poly(methyl methacrylate) in good solvents. Reproduced from Ref. [32] and [33]

interaction between graft chains swollen and extended to a high degree at the nanoparticle core surface. In contrast to the well-known hard and soft colloidal crystals formed specifically by rigid sphere and electrostatic potentials, respectively, this new system was classified as a "quasi-soft" or "semi-soft" colloidal crystal. As illustrated in Fig. 11.5, the effective graft density of polymer-grafted layer on a spherical-particle surface should decrease with increasing thickness. On the basis of the Daoud-Cotton scaling model, the polymer brush layer was revealed to be divided into the inner CPB and outer SDPB layers at a virtual interface of certain critical radius. Correspondingly, there was observed a change in the structure of colloidal crystals, at a narrow region of molecular weights (and hence chain lengths) of graft chains, from a random hexagonal close-packed (rhcp) structure at a lower region to a face-centered cubic (fcc) structure at a higher region (see Fig. 11.5). This was considered to stem from changes in inter-particle potential. Interestingly, this boundary of molecular weight corresponded to a surface occupancy of 10 % at a virtual surface formed by completely elongated chains. This was eventually identical to the above-mentioned density boundary between SDPB and CPB. The CPB-modified colloidal system is characterized not only by widely controllable structural factors such as the type and length of graft chains, the type and size of core particles, the type of solvent, and others, but also by a variety of thereby controlled crystal structures and lattice parameters. This would lead to the development of novel devices with high performance and functionality. Currently, an investigation is also underway regarding many applications including drug delivery system, bio-imaging, and laser devices via fluorescent labeling of CPB.

11.3 Composite of CPB-Afforded Nanoparticle with Ionic Liquid

11.3.1 Order/Disorder States as a Function of Some Parameters

Main factors affecting the ordering of colloidal particles are the inter-particle potential and the concentration of particle. In the case of a PSiP system in a good solvent, the former factor is related with the surface graft density, the molecular weight (the chain length) and its distribution, and the core-particle size (as above discussed for SDPB and CPB systems). When an ionic liquid (IL) is used as a dispersion medium, it is possible to achieve uniform mixing at concentrations from low to high regimes by means of the casting method using a volatile solvent (dispersing/dissolving a desired ratio of PSiP and IL into a volatile solvent). In recent years, ILs have been subjected to a variety of research and development as functional materials owing to their non-volatility, non-combustibility, high ion conductivity, and other characteristics. Higher order structures formed using ILs hold promise not only in fundamental science but also in applications as highly functionalized materials.

In order to verify the mechanism and process of structural formation of colloidal particles, three types of CPB-modified SiP (core diameter; 130 nm) were mixed with a predetermined concentration of *N*,*N*-diethyl-*N*-methyl-*N*-(2-methoxyethyl) ammonium bis(trifluoromethanesulfonyl)imide (DEME) via the casting method using acetonitrile or tetrahydrofuran as a volatile solvent. DEME is an aliphatic-quaternary-ammonium type of ILs and a good solvent for the polymer brushes discussed below. DEME (and consequently, its polymer type, PDEMM) has a wide potential window in addition to other characteristic properties and is gathering attention as a high-performance electrolyte. Figure 11.6 shows the chemical structures of brush components and ILs discussed in this chapter, and Table 11.1

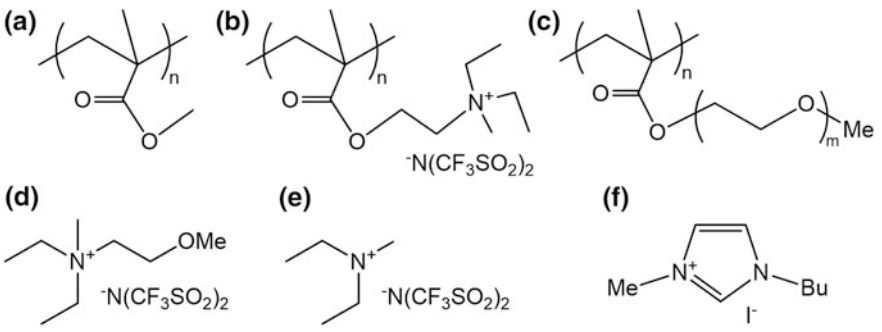

Fig. 11.6 Molecular structures of **a** PMMA, **b** PDEMM, **c** PPEGMA, **d** DEME, **e** DEMH, and **f** BMII

Table 11.1 Molecular characteristics of PSiPs and modeled potential of their swollen shell

PSiP	Comp.	M_n (DP_n)	M_w/M_n	σ/chains nm^{-2} (σ^*/%)	Brush-type	Coulombic interaction
1	PDEMM	27,800 (58)	1.08	0.17 (39)	CPB	○
2	PMMA	6600 (66)	1.27	0.32 (18)	CPB	–
3	PMMA	164,000 (1640)	1.29	0.66 (36)	SDPB	–

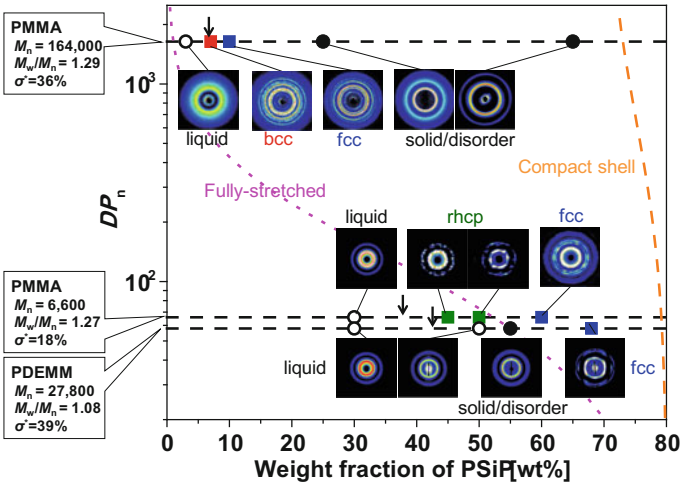

Fig. 11.7 Two-dimensional images of small-angle X-ray scattering (SAXS) intensity and identified structures as a function of the type and chain length of polymer brushes and the particle concentration; the *open*, *filled*, *circle* and *square symbols* represent a liquid, solid, disorder and order states, respectively

summarizes the molecular characteristics of the PSiPs discussed below and the modeled potential of their swollen shell. The type of polymer brushes was judged from the above-mentioned critical value (10 %) in σ^* at the outermost surface assumed by the fully extended chain. For PDEMM, unlike PMMA, the Coulomb interaction may conceivably contribute at a close range; a so-called electrical double-layer repulsion can be ignored due to a high ionic strength of IL. The following discussion will be based on these hypotheses.

Figure 11.7 shows the two-dimensional images of intensity obtained by the small-angle X-ray scattering measurement (collected by the BL19B2 and BL03XU beamlines of a large synchrotron radiation facility SPring-8, Japan) and thereby identified structures as a function of the type and chain length of polymer brushes on the vertical axis (related to the inter-particle potential) and the particle concentration on the horizontal axis. The dotted and dashed lines in the figure represent the concentration of particles closely packed assuming that the graft chain is radially and fully extended (fully extended shell model) and non-swollen

(compact shell model), respectively. If the deformation of the shell layer is ignored, the closely packed concentration in the compact shell model can be the maximum value for uniform mixing.

At low concentrations, the systems are in a liquid/disordered state. Here, a "liquid" state means that one can observe a flow in a certain time. An ordered arrangement arises at a particular (threshold) concentration. For the PSiP with larger molecular weight, i.e., larger size, the ordering occurs at a lower concentration, and the threshold is close to the separately determined concentration at equilibrium crystallization (the ↓ symbol in Fig. 11.7). Interestingly, the PMMA-SiP gave an rhcp structure in the CPB system (of a hard core potential; PSiP ***2***) and a body-centered cubic (bcc) structure in the softer SDPB system (PSiP ***3***). In the former, the ordering was achieved even at a concentration lower than the closed packed value for the fully extended shell model, suggesting a correlation with an Alder transition. Owing to the softer shell, the latter was analogous to a structure in which star polymers or block copolymer micelles are formed at an equilibrium state in a solvent [35, 36]. We have not yet observed an ordered structure at around an equivalent concentration for the CPB system with PDEMM (PSiP ***1***), and it is currently under investigation whether this is due to the Coulomb interaction or simply to a kinetic problem (more time necessary for crystallization). The difference between the CPB and SDPB systems was also seen in the higher concentration region. Specifically, while in the SDPB system (PSiP ***3***), a glassy state (solid/disordered state) was observed even at a PSiP concentration of 65 wt%, the fcc ordering (colloidal crystal solid: solid/ordered state) was achieved in the CPB system. This was presumably because a stable structure can be formed more rapidly due to the above-mentioned size-exclusion and low-friction properties of the CPB. On the other hand, the SDPB system possibly gives an interpenetration between polymer brushes and hence an attracting interaction. The difference between fcc and hcp structures is in the pattern of layering the closely packed plane. As indicated in Fig. 11.8, when putting a particle on the closely packed plane (the middle layer B in the figure), the fcc and hcp stackings select the positions A (case 1) and C (case 2), respectively, depending on whether a particle exists in the underlying (bottom) layer A. The rhcp randomly selects one of the two regardless of the bottom layer. Two possibilities are conceivable for the formation of the fcc structure. One is an ordering (non-equilibrium) resulting from the shear force (during vaporization of a volatile solvent) observed in many colloidal systems. The other is responsible for the CPB effect, which helps easily forming a stable structure, i.e., a (quasi)equilibrium state. In the latter hypothesis, the CPB is expected to form the rhcp according to the case 1 since it behaves like a rigid sphere around the critical concentration, and it may form the fcc according to the case 2 at higher concentration where the shell layer be deformed by compression. Although, of course, the effect of solvent flow during the course of solvent casting will be considered, the ordering of polymer brush-afforded colloidal particles markedly differs depending on the inter-particle potential (particularly the CPB and SDPB systems).

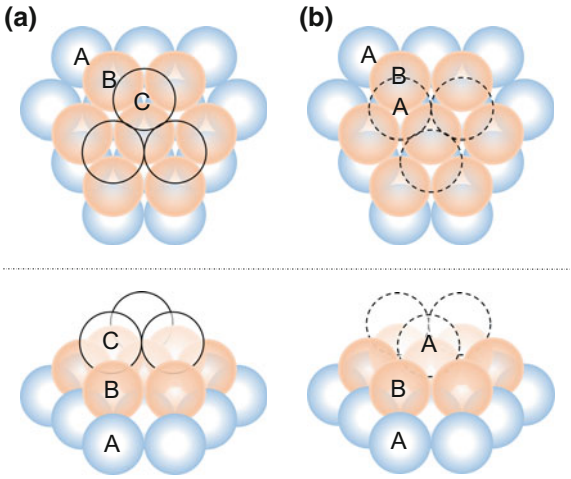

Fig. 11.8 Schematic illustration of particle stacking in **a** fcc (ABC-stacking) and **b** hcp (ABA-stacking) structures

This system is believed to be a good model for discussing the process of crystallization/vitrification and thermodynamic equilibrium structure (phase diagram) of colloid suspensions. Further investigation on these issues is now undergoing.

11.3.2 Application to Solid Electrolyte

Detailed structural analysis was made on the above-mentioned solid/ordered structure, which the PSiP with the CPB of PDEMM (PSiP ***1***) formed at a particle concentration of 75 wt% (with DEME as a dispersion medium or plasticizer) from the viewpoint of applicability as a solid electrolyte [37, 38]. Figure 11.9 shows the highly oriented ultra-small-angle X-ray scattering (USAXS) images for the casting film obtained by the X-ray incident perpendicular to the through and edge planes and their scattering profiles, i.e., the circular average of scattering intensity as a function of the scattering vector. The observed spots in the 2D image were reasonably assigned to the fcc structure, and no evidence was observed for other crystalline structures. In addition to this, the scattering profiles were well fitted by the simulation curve assuming that the closed packed plane, the (111) plane, was highly oriented parallel to the membrane surface: we successfully estimated the order parameter to be high by another analysis of the X-ray scattering data. Such a highly oriented fcc structure was also confirmed by the scanning electron microscopic (SEM) observation of a cross section of the solid membrane. Two types of PSiP arrangements, a hexagonal and square lattices, were observed (with a domain size exceeding tens of micrometers), corresponding to the (111) and (100) planes of the fcc structure, respectively. The fcc structure was directly verified by means of SEM observation of a single-crystalline domain from different

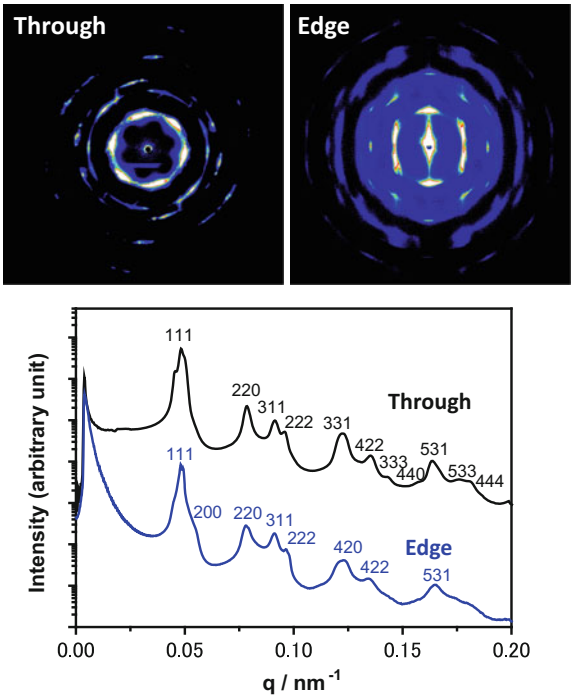

Fig. 11.9 Ultra-small-angle X-ray scattering (USAXS) images and their circularly averaged profile; the data were obtained by the X-ray incident perpendicular to the through and edge planes of the sample

directions (Fig. 11.10). The application of a dip-coating method was also investigated for preparing the PSiP-laminate solid membrane, successfully giving a uniform ultrathin membrane in the order of 10 μm. As discussed below, this would be a useful method to fabricate electrochemical devices by directly coating such a pseudo-solid electrolyte on electrode.

The ion conductivity, as an electrical conductivity, of this solid membrane was evaluated via a so-called complex impedance method. An extremely high conductivity (0.2 mS/cm at 30 °C) for a solid was obtained. This was reasonably ascribed to the well-ordered PSiP arrangement forming an interconnected network structure of IL-swollen CPB layers and functioning as a highly efficient ion-conducting nanochannel. It should be noted that the obtained value of ion conductivity was at least three orders of magnitude greater than conventional polymer–solid electrolytes by coupling with the CPB effect enhancing the ion diffusion (discussed below). As mentioned above, the LPR technique enables a variety of molecular designs of polymer brushes and hence affords a variety of functionality. We succeeded in improving the mechanical property of the pseudo-solid electrolytes of self-assembled PSiPs by intermolecularly cross-linking polymer brushes in the presence of crosslinkable binder polymers and finally in developing flexible as well as high ion-conducting membrane by controlling the cross-linking density. This membrane is of great interests, being put to practical use in the near future.

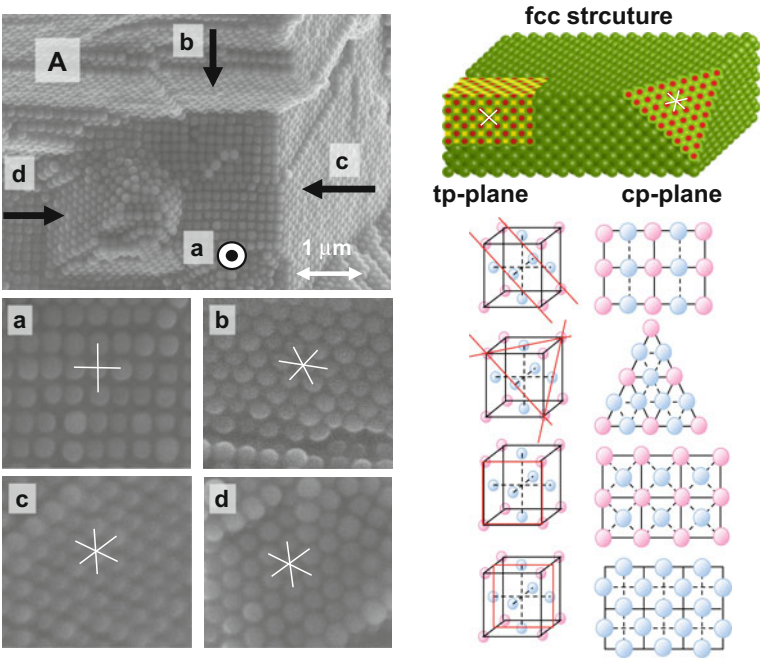

Fig. 11.10 Scanning electron microscopic (SEM) images of a single-crystalline domain from different directions and corresponding crystalline planes in fcc. Reproduced from Ref. [38]

11.4 Application in Electrochemical Devices

11.4.1 Bipolar Lithium Ion Battery

We attempted to develop a novel lithium ion battery (LIB) using the above-mentioned solid electrolyte of the self-assembled PDEMM-SiPs (M_n = 25,000, M_w/M_n = 1.13, σ = 0.15 chains/nm^2, σ^* = 33 %; PSiP ***1′*** in the same category of PSiP ***1***) with DEME [38]. For the operation of LIB, lithium bis(trifluoromethanesulfonyl) imide (Li-TFSI) was added to the casting solution of PSiP and IL, giving a homogeneous and solid membrane without precipitation of added salt. The final concentration of Li ion in the membrane was adjusted to be 0.3 mol/kg. Table 11.2 summarizes the self-diffusion coefficients (D) of ions in this solid electrolyte estimated by the pulsed field-gradient nuclear magnetic resonance (NMR) technique. It should be noted that the addition of Li-TFSI to DEME (in bulk) heavily depressed the D value of Li^+ and $TFSI^-$, which was understood by the formation of Li-ion clusters and hence the increase in viscosity as was observed for many ILs. This is

Table 11.2 Self-diffusion coefficients (D) of ions estimated by the pulsed field-gradient nuclear magnetic resonance (NMR) technique

Electrolytes	D /10^{-11} m^2s^{-1}		
	Li^+	$DEME^+$	$TFSI^-$
DEME (bulk)	–	1.7	1.6
DEME + Li-TFSI (0.3 mol/kg)	0.49	1.0	0.81
DEME + Li-TFSI + PDEMM (28 wt%)	0.11	0.27	0.15
PDEMM-SiP (75 wt%) + DEME + Li-TFSI (0.3 mol/kg)	2.1	1.9	1.3

one of serious problems for practical use of ILs as LIB electrolytes. On the other hand, the solid PSiP-assembled membrane with Li-TFSI gave the D values of $DEME^+$ and $TFSI^-$ approximately the same as those in bulk DEME without Li-TFSI. This means that the clustering of Li ion was effectively inhibited. More interestingly, the D value of Li^+ was 4.2 times larger than that in DEME with Li salt and 19 times larger than that in DEME containing Li salt as well as PDEMM. In the solid electrolyte, Li ion must exist in the domain of PDEMM brush swollen in DEME. Except for the portion of SiP cores into which the ions cannot penetrate, the average concentration of PDEMM was estimated to 28 wt%. It was reasonably concluded that the CPB at the surface of SiPs not only promote the self-assembling of PSiP and hence the formation of ion-conducting network channel owing to its low-friction and high-repulsion characteristics but also greatly contribute to increasing ion conductivity.

Then, we developed, as a prototype, a bipolar high-voltage cell as well as a unit cell of LIB using this novel solid electrolyte (see Fig. 11.11). A bipolar cell has many advantages including high-voltage operation, but it is difficult to be fabricated using a liquid electrolyte because of the problem of inter-liquid shorting. In order to overcome this issue, a liquid sealing is needed, giving another problem against downsizing of a cell. In our system, a bipolar cell was fabricated by a simple method; a bipolar electrode, i.e., the cathode and the anode on the front and back sides of a metal foil collector, was directly coated with a solid electrolyte membrane and just laminated, giving multiple cells connected in series and mounted in a single package. The prototyped 3-stack bipolar battery achieved almost triple characteristics of a single cell battery, i.e., a discharge/charge potential between 9.0 V and 4.5 V as well as a charging/discharging efficiency of 98 % after six charge/discharge cycles. The developed solid electrolyte was demonstrated to have a high ion conductivity as well as a sufficient mechanical strength and moldability, enabling a bipolar design. In addition to this, this LIB cell does not contain any volatile component, attracting much attention on its much improved safety without sacrificing performance.

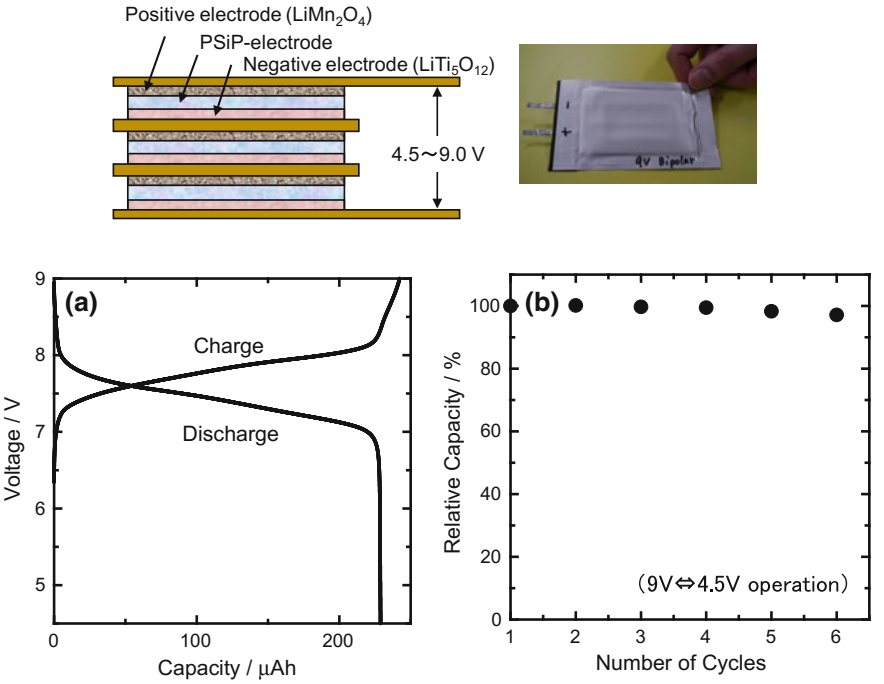

Fig. 11.11 Schematic illustration, photo charge/discharge curves, and cycle performance of a bipolar high-voltage lithium ion battery (LIB) using PSiP-assembled solid electrolyte

11.4.2 Bipolar Electric Double-Layer Capacitor

The technology established for the bipolar laminated high-voltage LIB was applied to an electric double-layer capacitor (EDLC). A 3-stack EDLC using bipolar electrodes and PSiP ***1'***-assembled solid electrolytes was designed and fabricated [39]. The addition of a lithium salt is unnecessary for EDLCs. Figure 11.12 shows the cell structure and charge/discharge characteristics of the EDLC. Each composing unit cell had nearly the same charge/discharge behavior and gave little difference in voltage. Figure 11.13 shows the relative capacity as a function of C rate and number of charge/discharge cycles for 3-stack bipolar and 1-stack EDLCs using the PDEMM-SiP-assembled solid electrolyte as well as 1-stack EDLCs using an organic liquid and DEME. Here, the C-rate value is used as a measure of the charge/discharge rate, and 1 C is a rate at which the fully charged capacitor is completely discharged for 1 h. In general, with increasing discharge current, the ion mobility becomes rate-determining, and the capacitance decreases. Especially in this situation, the increase in viscosity negatively greatly impacts the rate characteristics. Figure 11.13a revealed that at a discharge rate of 10 C (at which all the stored energy is discharged for 6 min), this bipolar EDLC (7.5 V) gave the discharge characteristics almost the same as a conventional EDLC (2.5 V) using

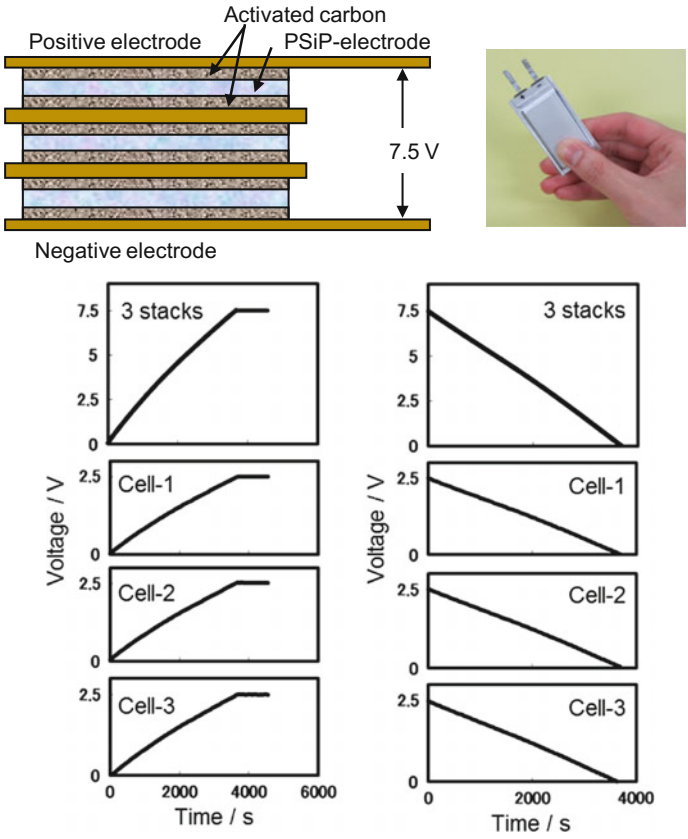

Fig. 11.12 Schematic illustration and performance of bipolar electric double-layer capacitor (EDLC) using PSiP-assembled solid electrolyte

organic liquid electrolytes. As shown in Fig. 11.13b, little deterioration in capacitance was observed in a test of a thousand charge/discharge cycles. Thus, a prototype EDLC shown in Fig. 11.12 was designed as a device that could be subjected to industrial production processes for practical use. Its cell performance was confirmed to be equivalent to that of the above-mentioned laboratory-made device.

11.4.3 Dye-Sensitized Solar Cell (DSSC)

The PSiP-assembled solid electrolyte was applied for a dye-sensitized solar cell (DSSC) by introducing an iodine redox system [37]. For this, the above-mentioned PDEMM-SiP (PSiP ***1***) was solidified with a mixture of *N*-butyl-*N*'-methyl imidazolium iodide (BMII) and DEME (BMII : DEME = 38 : 62 by weight) using casting and dip-coating methods. Figure 11.14b shows the cross-sectional image observed

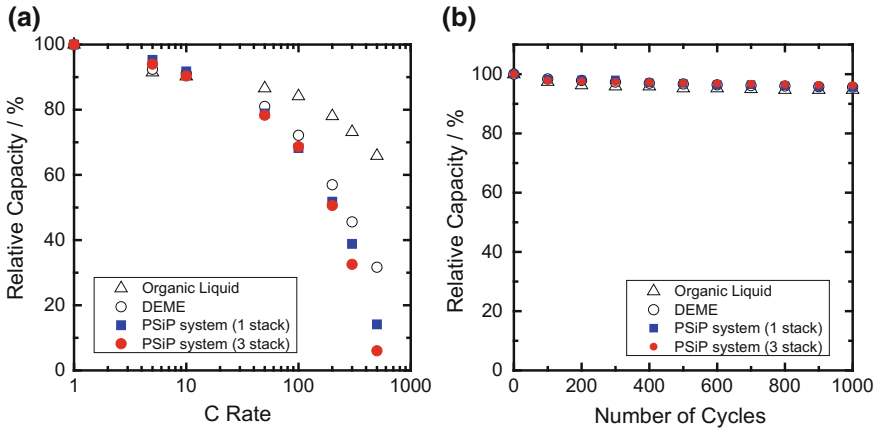

Fig. 11.13 Relative capacities as a function of **a** C rate and **b** number of cycles for charge/discharge operation of electric double-layer capacitors (EDLCs) using different electrolytes; the relative capacity is the capacity relative to the initial value observed at 1C rate. Reproduced from Ref. [39]

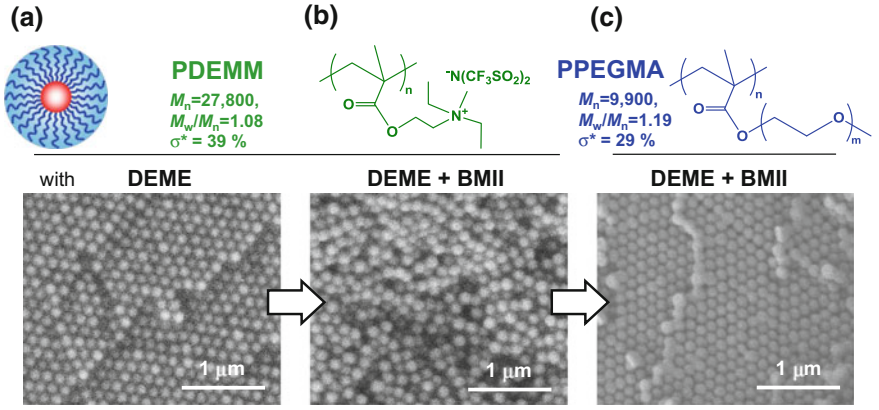

Fig. 11.14 Cross-sectional scanning electron microscopic (SEM) images of PSiP-assembled solid electrolytes with different polymer components, **a**, **b** PDEMM and **c** PPEGMA, in the presence of DEME and/or BMII

by SEM for the membrane (prepared by dip-coating using acetonitrile (65 wt%) containing PSiP/(DEME + BMII) of 74/26 by weight). A regular ordering of PSiP has never been achieved even under various conditions we tried. This is quite contrast to the fact that the same PSiP sample was well assembled in DEME only, as indicated in Fig. 11.14a. This problem was resolved by replacing the CPB-configuring component with an amphipathic polymer poly(oligo(ethylene glycol) methacrylate) (see Fig. 11.6c, PPEGMA; M_n = 9900, M_w/M_n = 1.19, σ = 0.09 chains/nm^2, σ^* = 29 %) having a higher affinity to BMII. Figure 11.14c shows the cross-sectional SEM image of the membrane fabricated using PPEGMA-SiP,

revealing well ordering. Similar to the discussion in Sect. 11.3.2, only hexagonal and square two-dimensional lattices were observed, suggesting an fcc structure. As mentioned above, PSiP ordering must be assisted by the CPB effect, especially high-repulsion and extremely low-friction characteristics, which is considered to be effective under a good solvent condition. Actually, this is one of good examples to verify our concept. In other words, the design of CPB is very important for a variety of novel PSiP-assembled solid electrolytes, which can be versatilely achieved by the LRP. By controlling the dip-coating conditions (proportion of volatile solvent, etc.), it was possible to control the membrane thickness with maintaining regular ordering. We prepared a composite membrane on the substrate with a line-pattern electrode and measured the ionic conductivity via the complex impedance method. This solid membrane was demonstrated to have a high conductivity equivalent to that of the electrolyte membrane already discussed. In order to dope iodine (I_2) into this solid electrolyte membrane, the addition of I_2 into the dip-coating solution as well as I_2 vapor processing after membrane formation were investigated. Both gave a satisfactory result to dope I_2 without disturbing the PSiP arrangement.

Finally, in order to build a DSSC cell, the iodine-redox composite membrane was directly fabricated on a TiO_2 electrode (with a thickness of 4 μm), to which a dye (N-719) was pre-adsorbed. The SEM observation revealed that the composite electrolyte was closely adhered to the TiO_2 electrode and the PSiPs were regularly arranged. As a preliminary experiment, photoelectric conversion characteristics were confirmed along with the formation of a well-ordered and networked ion-conducting nanochannel. This would open up a new route to a flame-resistant, all-solid DSSC for practical use.

11.4.4 Fuel Cell

A PSiP-assembled solid electrolyte using a proton-conducting IL and thereby a novel polymer electrolyte fuel cell (PEFC) were developed. As a proton-conducting IL, *N*,*N*-diethyl-*N*-methylammonium bis(trifluoromethanesulfonyl)imide was used. Thus obtained solid electrolyte exhibited an ion conductivity approximately three orders of magnitude higher than that of IL-polymer films. The reaction mechanism at an electrode of IL systems was reported to differ from conventional aqueous system, and the detailed mechanism in our system is now under investigation. Until now, we confirmed that our system could operate under a non-humidified condition, achieving a maximum output density of 25 mW/cm^2 at 80 °C. For a stable operation at higher temperature, it is important to improve the physical property of the electrolyte membrane. For this, we succeeded in greatly improving the open-circuit voltage at 120 °C by introducing a cross-linked structure between the CPBs of the PSiP. Although some technical problems still remain unresolved especially regarding the interface between the electrolyte and the electrode, these results demonstrate the possibility for the practical application of an IL type of PEFC

achieving mid-to-high temperature, non-humidified operation. Currently, an improvement in characteristics is being devised using composite particles imparted with proton-conducting CPBs using the TERP method discussed above.

11.5 Future Prospective

Although not discussed in this chapter, many research groups including ours are vigorously engaged with continuing studies such as controlling the sequence and three-dimensional structure using LRP, and polymerization control of unconjugated monomers. In addition, taking into consideration the novelty of the structures and characteristics of the CPBs that can be synthesized via surface-initiated LRP, there are high hopes for novel methods of surface modification. Here, the fundamentals and application, especially to some electrochemical devices, were described. In addition, nanofibers and nanosheets have attracting more attention as building blocks for hierarchizing CPB, thereby developing next-generation devices. We expect that, in the future, there will be a great expansion in the diversity of material design resulting from LRP, and that the development of high-functionality and high-performance polymer materials with controlled structures will be accelerated. We hope to go beyond the previous scope of material design limited by synthetic strategy, enabling innovative ideas to be realized and creating new materials based on novel material design.

References

1. D.H. Napper, *Polymeric Stabilization of Colloidal Dispersions* (Academic Press, London, 1983)
2. E. Raphael, P.G. Degennes, J. Phys. Chem. **96**, 4002 (1992)
3. J. Klein, Annu. Rev. Mat. Sci. **26**, 581 (1996)
4. J.N. Israelachvili, *Intermolecular and Surface Forces*, 2nd edn (Academic Press, London, 1992)
5. A. Halperin, M. Tirrell, T.P. Lodge, Adv. Polym. Sci. **100**, 31 (1992)
6. M. Kawaguchi, A. Takahashi, Adv. Colloid Interface Sci. **37**, 219–317 (1992)
7. S. Alexander, J. Phys. (Paris) **38**, 983 (1997)
8. P.G. de Gennes, Macromolecules **13**, 1069 (1980)
9. M. Daoud, J.P. Cotton, J. Phys. (Paris) **43**, 531 (1982)
10. T.M. Birstein, E.B. Zhulina, Polymer **25**, 1453 (1984)
11. N.V. Tsarevsky, B.S. Sumerl, *Fundamentals of Controlled/Living Radical Polymerization* (Royal Society of Chemistry, London, 2013)
12. A. Goto, Y. Tsujii, T. Fukuda, Polymer **49**, 5177 (2008)
13. S. Yamago, K. Iida, J. Yoshida, J. Am. Chem. Soc. **124**, 2874 (2002)
14. S. Yamago, B. Ray, J. Yoshida, T. Tada, K. Yoshizawa, Y. Kwak, A. Goto, T. Fukuda, J. Am. Chem. Soc. **126**, 13908 (2004)
15. S. Yamago, E. Kayahara, M. Kotani, B. Ray, Y. Kwak, A. Goto, T. Fukuda, Angew. Chem. Int. Ed. **46**, 1304 (2007)

16. Y. Nakamura, K. Nakanishi, S. Yamago, Y. Tsujii, K. Takahashi, T. Morinaga, T. Sato, Macromol. Rapid Commun. **35**, 642 (2014)
17. Y. Tsujii, K. Ohno, S. Yamamoto, A. Goto, T. Fukuda, Adv. Polym. Sci. **197**, 1 (2006)
18. K. Matyjaszewski (ed.), *Macromolecular Engineering: Precise Synthesis, Materials Properties, Applications* (Wiley-VCH, Weinheim, 2007), p. 1137
19. M. Ejaz, S. Yamamoto, K. Ohno, Y. Tsujii, T. Fukuda, Macromolecules **31**, 5934 (1998)
20. S. Yamamoto, M. Ejaz, Y. Tsujii, M. Matsumoto, T. Fukuda, Macromolecules **33**, 5602 (2000)
21. S. Yamamoto, M. Ejaz, Y. Tsujii, T. Fukuda, Macromolecules **33**, 5608 (2000)
22. D.F.K. Shim, M.E. Cates, J. Phys. (Paris) **50**, 3535 (1989)
23. P.Y. Lai, A. Halperin, Macromolecules **24**, 4981 (1991)
24. H.D. Bijsterbosch, V.O. Dehaan, A.W. Degraaf, M. Mellema, F.A.M. Leermakers, M.A.C. Stuart, A.A. Vanwell, Langmuir **11**, 4467 (1995)
25. Y. Tsujii, A. Nomura, K. Okayasu, W. Gao, K. Ohno, T. Fukuda: *J. Phys., Conf. Ser.*, **184**, 012031 (2009)
26. H. Sakata, M. Kobayashi, H. Otsuka, A. Takahara, Polym. J. **37**, 767 (2005)
27. M. Kobayashi, A. Takahara, Chem. Lett. (Jpn.) **34**, 1582 (2005)
28. Y. Tsujii, S.Y. Hsu, K. Sakakibara, K. Ohno, Ann. Rep. Res. Inst. Chem. Fib. (Jpn.) **73**(3), 11 (2016)
29. C. Yoshikawa, A. Goto, N. Ishizuka, K. Nakanishi, A. Kishida, Y. Tsujii, T. Fukuda, Macromol. Symp. **248**, 189 (2007)
30. C. Yoshikawa, Y. Hashimoto, T. Honda, S. Hattori, D. Terada, A. Kishida, Y. Tsujii, H. Kobayashi, Chem. Letters **39**, 142 (2010)
31. K. Ohno, T. Morinaga, K. Koh, Y. Tsujii, T. Fukuda, Macromolecules **38**, 2137 (2005)
32. T. Morinaga, K. Ohno, Y. Tsujii, T. Fukuda, Macromolecules **41**, 3620 (2008)
33. K. Ohno, T. Morinaga, S. Takeno, T. Tsujii, T. Fukuda, Macromolecules **40**, 9143 (2007)
34. K. Ohno, Polym. Chem. **1**, 1545 (2010)
35. G.A. McConnell, A.P. Gast, J.S. Huang, S.D. Smith, Phys. Rev. Lett. **71**, 2102 (1993)
36. A.P. Gast, Langmuir **12**, 4060–4067 (1996)
37. Y. Tsujii, Y. Nakanishi, Y. Kawano, K. Ohno, Ann. Rep. Res. Inst. Chem. Fib. (Jpn.) **69**, 14 (2012)
38. T. Sato, T. Morinaga, S. Marukane, T. Narutomi, T. Igarashi, Y. Kawano, K. Ohno, T. Fukuda, Y. Tsujii, Adv. Mater. **23**, 4868 (2011)
39. T. Sato, S. Marukane, T. Morinaga, T. Kamijo, H. Arafune, Y. Tsujii, J. Power Sources **295**, 108 (2015)

Chapter 12
Metallo-Supramolecular Polymers: Design, Function, and Device Application

Masayoshi Higuchi

Abstract This chapter introduces synthesis of multi-topic ligands, design and preparation of metallo-supramolecular polymers, the electro- and photo-chemical properties including electrochromism and vapoluminescence, the humidity-responsive ionic properties, and the device fabrication toward the applications to color electronic paper, smart window, digital signage, and sensors.

Keywords Metallo-supramolecular polymer · Organic–metallic hybrid polymer · Electrochromism · Vapoluminescence · Device fabrication

12.1 Introduction

Organic polymers such as plastics and rubbers have made our lives comfortable as light and durable materials. The polymer chains, which are prepared by polymerization of the monomers, are consisted of (strong) covalent bonds. Organic–metallic hybrid polymers, in which organic compounds and metallic components are fused in nano-size scale, have recently received much attention as a new polymer material due to their unique electronic, photonic, magnetic, and catalytic properties, which are caused by the electronic interaction between the organic and metallic parts. Metallo-supramolecular polymers, which are composed of (weak) coordination bonds between metal ions and multi-topic organic ligands, are a typical organic–metallic hybrid polymer. Metallo-supramolecular polymers with a linear structure are synthesized by the 1:1 complexation of metal ions and ditopic organic ligands (Scheme 12.1). Metallo-supramolecular polymers are obtained by mixing of metal ions and multi-topic organic ligands in solution without any additives such as a catalyst. Therefore, diverse combinations of metal ion species and organic ligands are possible in the synthesis of metallo-supramolecular polymers. Each polymer exhibits different properties due to the different interactions between the metal ions

M. Higuchi (✉)
National Institute for Materials Science (NIMS), Tsukuba 305-0044, Japan
e-mail: HIGUCHI.Masayoshi@nims.go.jp

J. Sone and S. Tsuji (eds.), *Intelligent Nanosystems for Energy, Information and Biological Technologies*, DOI 10.1007/978-4-431-56429-4_12

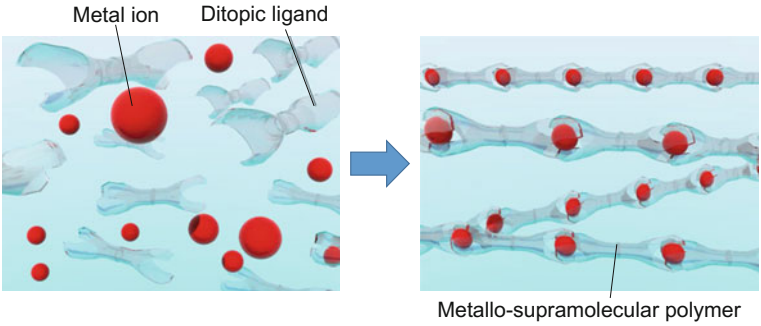

Scheme 12.1 Formation of the metallo-supramolecular polymer via the 1:1 complexation of metal ions and ditopic organic ligands

and the organic ligands. Since the complexation is an equilibrium reaction, the complexation and de-complexation in the polymer chains occur in solution. However, the polymer chains become free themselves from restraint of the equilibrium by removal of the solvent. As the result, the metallo-supramolecular polymers serve as a functional material.

12.2 Synthesis of Multi-topic Organic Ligands

Metallo-supramolecular polymers are synthesized by the complexation of metal ions and multi-topic organic ligands bearing several coordination sites. This section introduces synthesis of multi-topic organic ligands including bis(terpyridine)s, bis(phenanthroline)s, carboxylate-substituted bis(terpyridine), asymmetrical ditopic ligands with two different coordination sites, and tris(terpyridine).

12.2.1 Bis(terpyridine)s

2,2′:6′,2″-Terpyridine forms a 2:1 complex with transition metal ions bearing an octahedral coordination structure such as Fe(II) and Co(II). The two terpyridines cross at right angles in the complex [1]. Bis(terpyridine)s, in which two terpyridines are connected through a π-conjugated linear spacer, are a ditopic ligand and used in the synthesis of Fe(II)-, Co(II)-, Ru(II)-, and Zn(II)-metallo-supramolecular polymers. The bis(terpyridine)s are synthesized by two methods: (1) C–C bond formation between two terpyridine moieties using a coupling reaction and (2) synthesis of terpyridine moieties by the Kröhnke procedure (Scheme 12.2). The Kröhnke procedure [2] was suitable to introduce substituents such as an electron releasing or withdrawing group at the 6-position of the terpyridine moieties.

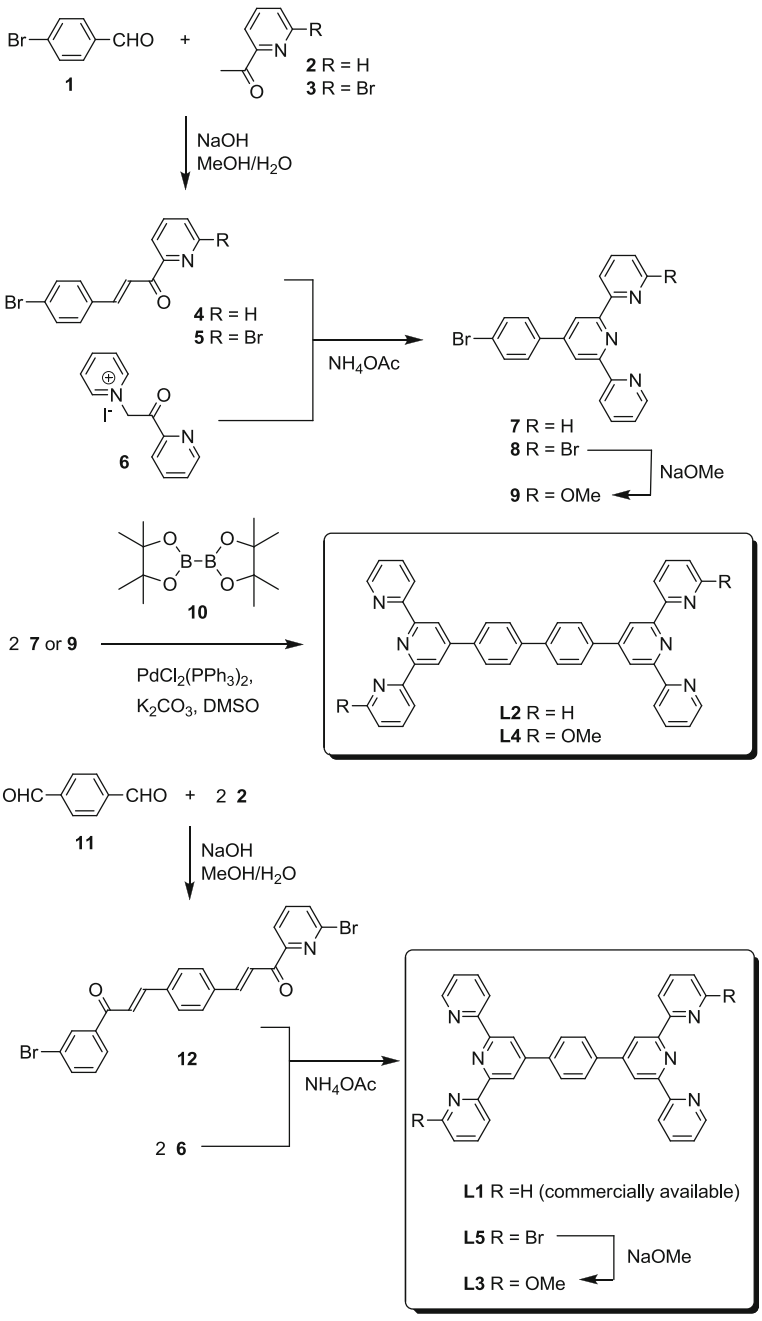

Scheme 12.2 Synthesis of bis(terpyridine)s (**L1–5**) [3, 4]

Bis(terpyridine)s with a 1,4-phenyl or 4,4′-biphenyl group as the spacer connecting the two terpyridines were synthesized [3, 4], because the rigid and linear structures of spacers are anticipated to prevent macro-cyclization of the metallo-supramolecular polymer chain during the polymerization. 1,4-Bis(2,2′:6′,2″-terpyridine-4′-yl)benzene (**L1**) is commercially available in Ardrich. 4,4′-Bis(2,2′:6′,2″-terpyridine-4′-yl)biphenyl (**L2**) was prepared via the Suzuki–Miyaura coupling reaction of 4′-(4-bromophenyl)-2,2′:6′,2″-terpyridine (**7**). In order to introduce a bromo group at the 6-position of the terminal pyridine ring in **7**, the two-step Kröhnke procedure was used: an aldol condensation of 4-bromobenzaldehyde (**1**) and 2-acetyl-6-bromotpyridine (**2**), followed by the Michael addition of the resultant azachalcone (**5**) with pyridinium iodide (**6**). Nucleophilic substitution of the obtained 2-bromo-4′-(4-bromophenyl)-2,2′:6′,2″-terpyridine (**8**) by NaOMe yielded 2-methoxy-4′-(4-bromophenyl)-2,2′:6′,2″-terpyridine (**9**) preferentially, though **8** has two bromo groups. 4,4′-Bis(6-methoxy-2,2′:6′,2″-terpyridine-4′-yl)biphenyl (**L4**) was obtained via the Suzuki–Miyaura coupling reaction of **9**. 1,4-Bis(6-bromo-2,2′:6′,2″-terpyridine-4′-yl)benzene (**L5**) was prepared by the two-step Kröhnke procedure: an aldol condensation of benzene-1,4-dicarboxaldehyde (**11**) and **2**, followed by a Michael addition of the resultant azachalcone (**12**) with **6**. Nucleophilic substitution of **L5** by NaOMe yielded 1,4-bis(6-methoxy-2,2′:6′,2″-terpyridine-4′-yl)benzene (**L3**).

12.2.2 Bis(phenanthroline)s

1,10-Phenanthroline is a bidentate coordination molecule and forms 2:1 complexes with transition metal ions bearing a tetrahedral or squire planer coordination structure such as Ni(II), Cu(II), and Pt(II) [5, 6]. Bis(1,10-phenanthroline)s with two 1,10-phenanthrolines linked at the 2-position have been already reported [7, 8].

5,5′-Linked bis(phenanthroline)s were synthesized as a new ditopic ligand. The 5,5′-linked bis(phenanthroline)s are expected to have less steric hindrance than that in the 2,2′-linked ones in the metallo-supramolecular polymer formation [9, 10]. 5-Bromo-1,10-phenanthrolines (**13** and **14**) were synthesized in the same manner as a previously reported procedure [11]. 5,5′-Linked bis(1,10-phenanthroline)s (**L6–11**) were prepared by the Suzuki–Miyaura cross-coupling reaction (Scheme 12.3) [12, 13]. For instance, **L9** was obtained by the reaction of 9,9-dioctylfluorene-2,7-diboronic acid bis (1,3-propanediol) ester (**16**) with two equivalents of 5-bromo-1,10-phenanthroline (**14**), in dehydrated DMSO for 24 h in the presence of $PdCl_2(PPh_3)_2$ and K_2CO_3 in a 35 % yield.

12.2.3 Bis(terpyridine) with Carboxylic Acids

Unlike transition metal ions characterized by *d*-electrons, lanthanide metal ions have the high coordination number (8–10) due to their *f*-electrons. In addition,

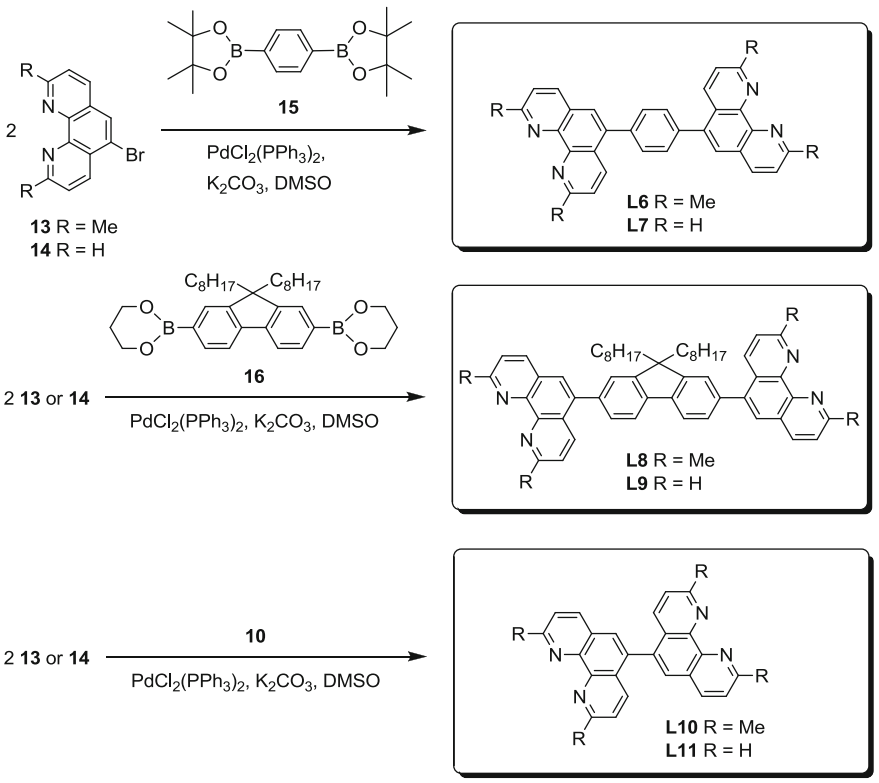

Scheme 12.3 Synthesis of bis(phenanthroline)s (**L6–11**) [12, 13]

lanthanide metal ions show strong affinity to oxygen. Bis(terpyridine) with four carboxylic acids at the 6,6′-positions of the two terpyridine moieties (**L12**) was synthesized as a ditopic ligand for the complexation with lanthanide metal ions (Scheme 12.4) [14]. Terpyridine with two ethyl esters at the 6,6′-positions (**18**) was converted from the cyano compound (**17**). A boronic ester of **18** (**19**) was dimerized by the Suzuki–Miyaura cross-coupling reaction with a spacer. The spacer with tetra (ethylene glycol) chains was necessary to improve the solubility of the ligand. Finally, **L12** was obtained by dehydration of the ethyl ester (**19**).

12.2.4 Asymmetrical Ditopic Ligands and a Tritopic Ligand

Ditopic organic ligands with same, two coordination sites such as bis(terpyridine)s and bis(phenanthroline)s are proper to introduce one kind of metal ion species to the

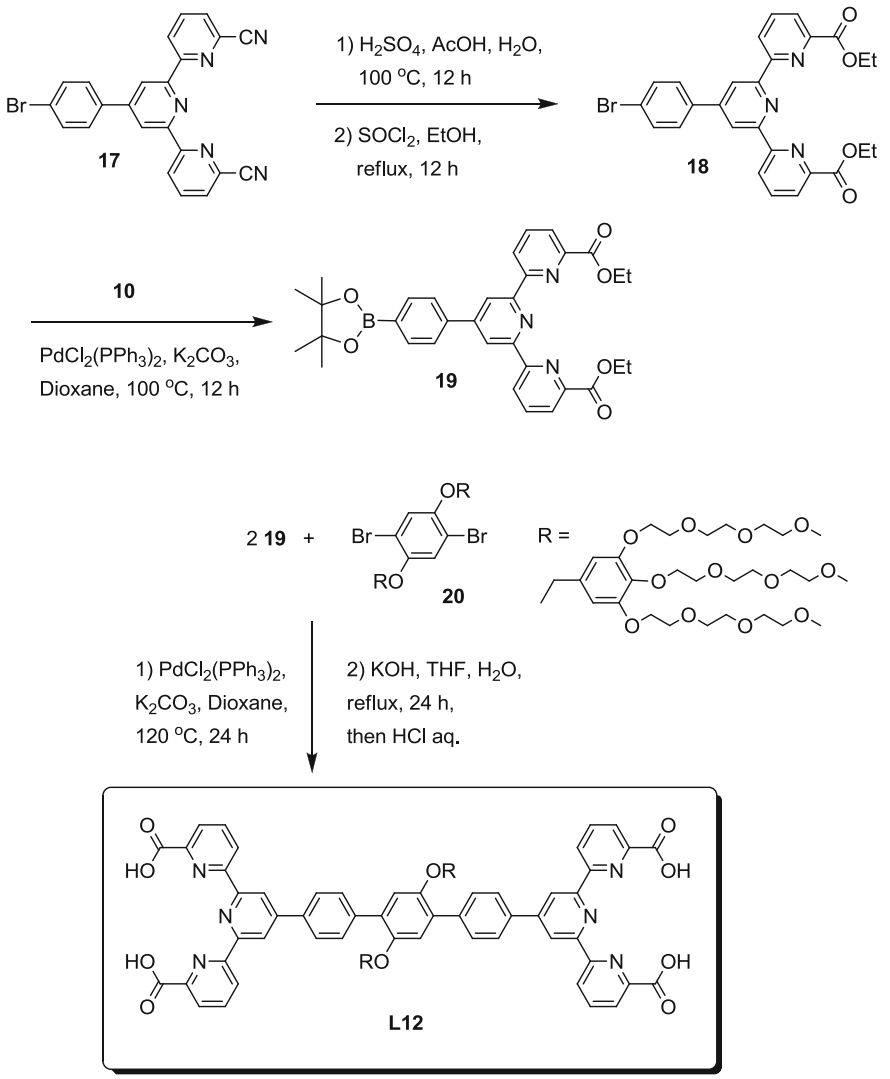

Scheme 12.4 Synthesis of bis(terpyridine) bearing carboxylic acids (**L12**) [14]

metallo-supramolecular polymer backbone. Asymmetrical ditopic ligands with two different coordination sites, on the other hand, have possibility to introduce two metal ion species alternately to a metallo-supramolecular polymer backbone, because of the different coordination properties to metal ions.

An asymmetrical ditopic ligand with a phenanthroline moiety and a terpyridine moiety (**L13**) was synthesized by the Suzuki–Miyaura cross-coupling reaction

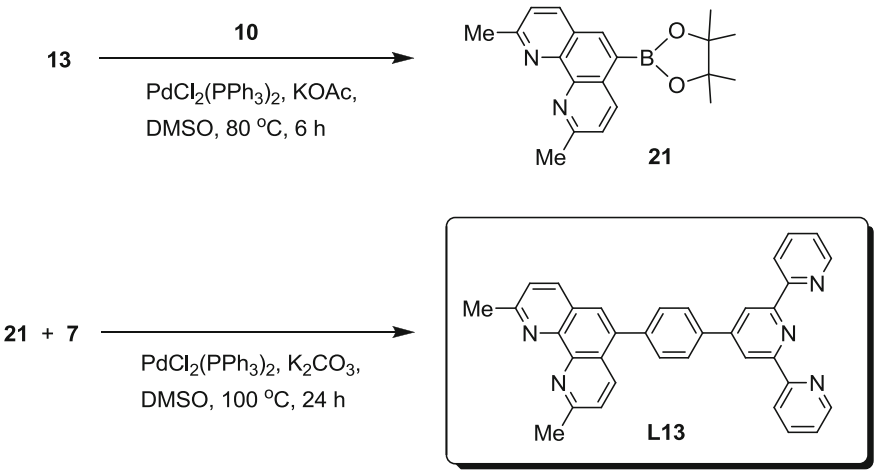

Scheme 12.5 Synthesis of an asymmetrical ditopic ligand bearing a phenanthroline and terpyridine moieties (**L13**) [15]

(Scheme 12.5) [15]. The Miyaura–Ishiyama borylation reaction [16] between 5-bromo-2,9-dimethyl-1,10-phenanthroline (**13**) [17, 18] and bis(pinacolato)diboron (**10**) (molar ratio: 1:1) was done in the presence of $PdCl_2(PPh_3)_2$ as a catalyst for 6 h at 80 °C in DMSO to provide a boronic ester (**21**) as a light yellow solid (80 %). Bis(phenanthroline), which was generated as a homo-coupled byproduct during the reaction, was removed by alumina column chromatography and preparative HPLC [3, 19]. It was found that KOAc is a good, moderate base in this reaction: the stronger bases such as K_2CO_3 accelerated the formation of bis (phenanthroline). **L13** was obtained as a white solid (65 %) by the Suzuki–Miyaura cross-coupling reaction of **21** with 4′-(4-bromophenyl)-2,2′:6′,2″-terpyridine (**7**).

Another asymmetrical ditopic ligand with a none-substituted terpyridine and a terpyridine bearing two carboxylic acids (**L14**) was also synthesized by the Suzuki–Miyaura cross-coupling reaction of dicarbonyl ester groups containing terpyridine (**18**) and 4′-(4-(4,4,5,5-tetramethyl-1,3,2-dioxaborolan-2-yl)phenyl)-2,2′:6′,2″-terpyridine (**22**), followed by hydrolysis (Scheme 12.6) [20].

The 1:1 complexation of metal ions and ditopic ligands results in the formation of linear metallo-supramolecular polymers. When metal ions and a tritopic ligand with three coordination sites are further added to the linear polymer solution, the linear polymer structure is expected to become a hyperbranched and/or cross-linked one by the connection among the linear polymers at the terminals, through the tritopic ligand. Tris(terpyridine) (**L15**) was prepared by the Suzuki–Miyaura cross-coupling reaction of 1,3,5-tribromobenzene with three equivalents of **22** (Scheme 12.7) [21, 22].

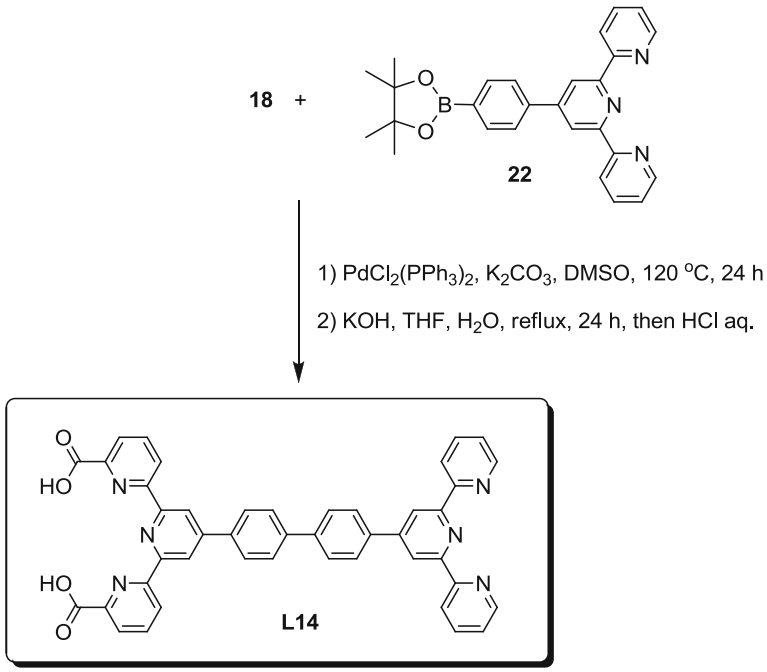

Scheme 12.6 Synthesis of an asymmetrical ditopic ligand bearing a none-substituted terpyridine and a terpyridine bearing two carboxylic acids (**L14**) [20]

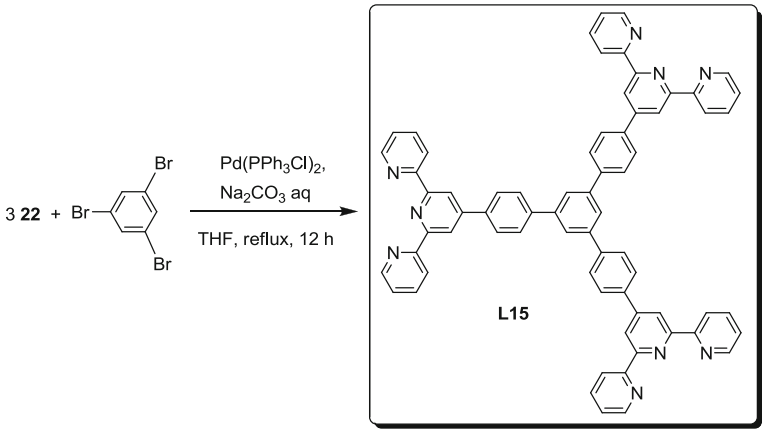

Scheme 12.7 Synthesis of tris(terpyridine) (**L15**) [21, 22]

12.3 Synthesis of Metallo-Supramolecular Polymers

Metallo-supramolecular polymers are synthesized by the complexation of metal ions and multi-topic organic ligands. A high coordination constant between the metal ions and the multi-topic ligands is necessary to the formation of high molecular weight polymers. Tridentate ligands such as terpyridine form a 2:1 complex with transition metals bearing an octahedral coordination structure. It is well known that the coordination ability of multi-dentate ligands to metal ions is much higher than that of mono-dentate ligands such as pyridine. The 1:1 complexation of bis(terpyridine)s (**L1–5**) and transition metal ions such as Fe(II), Ru (II), and Co(II) results in the formation of linear metallo-supramolecular polymers. Bidentate ligands including phenanthroline are complexed with transition metal ions having a tetrahedral or square-planer structure at a 2:1 molar ratio. The 1:1 complexation of bis(phenanthroline)s (**L6–11**) and transition metal ions such as Ni (II) and Cu(II) also gives linear metallo-supramolecular polymers. Terpyridine with two carboxylic acids is complexed with lanthanide metal ions at a 2:1 molar ratio. For this reason, the linear polymers are obtained by the 1:1 complexation of bis (terpyridine) with four carboxylic acids (**L12**) and Eu(III) ions.

The molar ratio of metal ions and organic ligands in the complexation is confirmed by the titration experiments using UV–Vis spectroscopy. For instance, bis (terpyridyl)benzene (**L1**) has no absorption in the visible light region between 400 and 800 nm. When Fe(II) ions are added to the ligand solution, a new absorption around 580 nm appears. This is based on the metal-to-ligand charge transfer (MLCT) absorption, which is an evidence of the complexation between **L1** and Fe (II). Absorbance of this absorption is linearly enhanced with increasing the amount of the metal ions added to the ligand solution due to the complexation. Finally, the absorption is saturated when all the ligand is complexed with Fe(II) ions. Absorbance of this absorption does not change any more by the further addition of Fe(II) ions, because no un-complexed ligands remain in the solution. The molar ratio in the saturation point suggests the molar ratio of the metal ions and the ligand in the complexation. The complexation constant is also estimated by the theoretical curve fitting of the titration plot. In the complexation of bis(terpyridyl)benzene and Fe(II) ions the complexation constant was found to be more than 1.0×10^7.

Heterometallo-supramolecular polymers with two metal ion species are prepared by the complexation of a ditopic ligand and two different metal ion species. In order to obtain the linear polymer, the molar ratio between the ligand and the total amount of the two metal ion species should be 1:1. In the case of heterometallo-supramolecular polymers with two metal ion species, careful investigation in the titration measurements is required to determine the molar ratio, because exchange of the two metal ion species may happen in solution. The position of two metal ion species in the heterometallo-supramolecular polymer is controlled using asymmetrical ligands (**L13–14**). The use of tritopic ligands (**L15**) changes the polymer structure from linear to hyperbranched or cross-linked one.

12.3.1 *Fe(II)-, Ru(II)-, and Co(II)-Based Metallo-Supramolecular Polymer*

Fe(II)-, Ru(II)-, and Co(II)-based metallo-supramolecular polymers (**polyFeL*n***, **polyRuL*n*,** and **polyCoL*n***) (n = 1–5) were synthesized by the 1:1 complexation of bis(terpyridine)s (**L1–5**) and the corresponding metal ions (Scheme 12.8) [4, 23].

For the synthesis of **polyFeL*n*** (n = 1–5), an equimolar amount of **L1–5** and Fe $(OAc)_2$ was refluxed in an argon-saturated acetic acid (ca. 10 mL solvent per mg of ligand) for 24 h. The reaction solution was cooled down to room temperature and filtered to remove a small amount of insoluble residues. The filtrate was moved to a petri dish and the solvent was evaporated slowly to dryness. The brittle film was collected and dried further in vacuo overnight to afford **polyFeL*n*** (n = 1–5) (>90 %). For the synthesis of **polyRuL*n*** (n = 1–5), an equimolar amount of **L1–5** and $RuCl_2(DMSO)_4$ was refluxed in an argon-saturated absolute ethylene glycol (ca. 10 mL solvent per mg of ligand) for 24 h. After the reaction solution was cooled down to room temperature, THF was added until the solution was colorless. The precipitated polymers were collected by filtration and washed with THF, and then dried in vacuo overnight to afford **polyRuL*n*** (n = 1–5) (95 % ~quant.). For the synthesis of **polyCoL*n***, an equimolar amount of **L1–5** and $Co(OAc)_2$ was refluxed in an argon-saturated absolute methanol (ca. 10 mL solvent per mg of ligand) for 24 h. The reaction solution was cooled to room temperature and filtered to remove a small amount of insoluble residues. The filtrate was moved to a petri dish and the solvent was evaporated slowly to dryness. The brittle film was collected and dried further in vacuo overnight to afford **polyCoL*n*** (n = 1–5) (>90 %). The polymers show high solubility in polar solvents such H_2O, MeOH, EtOH, and HOAc, because they are poly-cation bearing metal ions with positive charges. In addition, the solubility was changed by exchanging the counter anion species: the solubilities of their PF_6^- and ClO_4^- forms are much poorer.

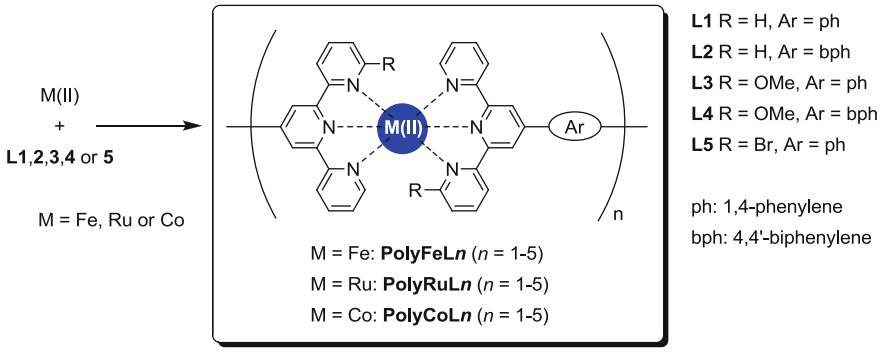

Scheme 12.8 Synthesis of Fe(II)-, Ru(II)-, and Co(II)-based metallo-supramolecular polymers (**polyFeL*n***, **polyRuL*n*,** and **polyCoL*n***) (n = 1–5) [4, 23]

12.3.2 Cu(II)- and Ni(II)-Based Metallo-Supramolecular Polymers

Cu(II)- and Ni(II)-based metallo-supramolecular polymers (**polyCuL*n***) and **polyNiL*n***) (*n* = 6–11) were synthesized by the 1:1 complexation of bis(phenanthroline)s (**L6–11**) and the corresponding metal ions (Scheme 12.9) [12, 13].

L6 or **L7** (0.03 mmol) was dissolved in CH_2Cl_2 (5 mL) under nitrogen atmosphere. In the meantime, $Ni(ClO_4)_2{\cdot}6H_2O$ or $Cu(ClO_4)_2{\cdot}6H_2O$ (0.03 mmol) dissolved in MeCN (5 mL) was added drop by drop over a 30 min. The mixture is stirred for 1–3 h at room temperature. The solvent was slowly evaporated by leading a stream of nitrogen over the reaction mixture. During this procedure, precipitate formed and rinsed thoroughly with Et_2O (20 mL), filtered off, and dried in vacuo at room temperature to afford **polyNiL6** and **polyCuL7**. **L9** (0.026 mmol) was dissolved in of MeCN (5 mL) under nitrogen atmosphere. In the meantime, $Cu(ClO_4)_2{\cdot}6H_2O$ (0.026 mmol) dissolved in MeCN (5 mL) was added drop by drop over a 30 min. The mixture is stirred for 1 h at room temperature. The CH_3CN was slowly evaporated from the green solution by leading a stream of nitrogen over the reaction mixture. During that procedure a green precipitate formed and rinsed thoroughly with 20 mL of Et_2O, filtered off, and dried in vacuo at room temperature to afford **polyCuL9** (yield: 90 %). **L8–11** (0.026 mmol) was dissolved in CH_2Cl_2 (5 mL) under a nitrogen atmosphere. $Ni(ClO_4)_2{\cdot}6H_2O$ (0.026 mmol) dissolved in MeCN (5 mL) was added dropwise over a 30 min to the ligand solution. The mixture was stirred for 1 h at room temperature. The solvent was slowly evaporated from the pink solution by leading a stream of nitrogen over the reaction mixture. During this procedure, precipitate was formed and rinsed thoroughly with Et_2O (20 mL), filtered off, and then dried in vacuo at room temperature to afford **polyNiL8–11** (**polyNiL8**: pink solid; yield: 92 %. **polyNiL9**: pink solid; yield: 95 %. **polyNiL10**: pink solid; yield: 90 %. **polyNiL11**: pink solid; yield: 93 %).

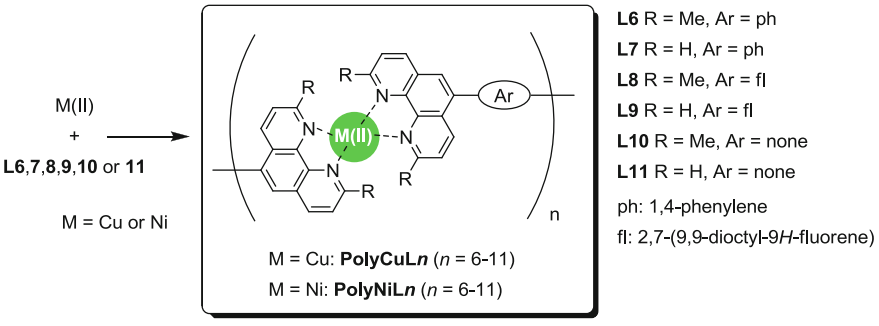

Scheme 12.9 Synthesis of Cu(II)- and Ni(II)-based metallo-supramolecular polymers (**PolyCuL*n*** and **PolyNiL*n***) (*n* = 6–11) [12, 13]

12.3.3 A Eu(III)-Based Metallo-Supramolecular Polymer

A Eu(III)-based metallo-supramolecular polymer (**polyEuL12**) was synthesized as a yellow solid in a 93 % yield by the 1:1 complexation of $Eu(NO_3)_3$ and bis (terpyridine) bearing four carboxylic acides (**L12**) in the presence of KOH as a base (Scheme 12.10) [14]. The complexation was performed by refluxing an equimolor amount of **L12** with $Eu(NO_2)_3$ in MeOH. **PolyEuL12** was isolated as a yellow solid in 93 % yield. **PolyEuL12** was dissolved in methanol but insoluble in common organic solvents such as hexane, chloroform, and THF. The molecular weight of **polyEuL12** was confirmed by the SEC-Viscometry/RALLS method ($Mn = 7.8 \times 10^4$, $Mw/Mn = 1.7$).

The complexation behavior of **L12** with $Eu(NO_2)_3$ was investigated by UV–Vis spectroscopic titration measurements. $Eu(NO_2)_3$ was added to a solution of **L12** in the presence of a stoichiometric amount of KOH for the deprotonation of **L12**. An increase in the absorbance around 380 nm and a decrease in the absorbance at 260 nm were observed with an isosbestic point at 293 nm during the addition of 0–0.5 equiv. of $Eu(NO_2)_3$. The isosbestic point was then shifted to 303 nm at between 0.6 and 1.0 equiv. of $Eu(NO_2)_3$ added. The shift of the isosbestic point suggests that two different complexations happen successively upon addition of $Eu(NO_2)_3$, indicating that the polymerization process progresses in a two-step fashion from mono-complex formation to the supramolecular polymer. Furthermore, plotting of the absorbance at 378 nm versus the ratio of metal to ligand showed a linear increase and a sharp end point at the ratio of 1:1 (**L12**: $Eu(NO_2)_3$), indicating that the metallo-supramolecular polymer was successfully formed. Evidently, the presence of PEG chains at the pendant does not affect the binding ratio between the ligand and the Eu(III) ions.

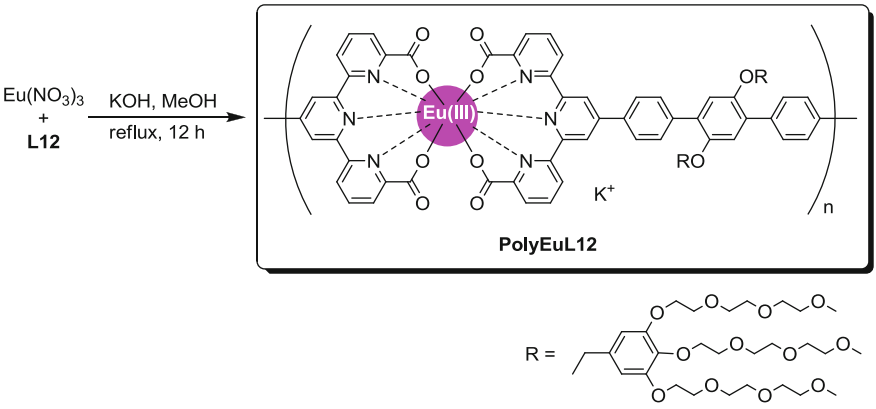

Scheme 12.10 Synthesis of a Eu(III)-based metallo-supramolecular polymer (**polyEuL12**) [14]

12.3.4 *Fe(II)/Ru(II)-Based Heterometallo-Supramolecular Polymers*

In general, it is difficult to achieve the precisely alternate introduction of two metal ion species in the metallo-supramolecular polymer backbone, because symmetrical ditopic ligands such as bis(terpyridine)s cannot recognize the difference of the two metal ion species in the complexation. However, when the complexation conditions of the two metal ion species are greatly different, the alternate introduction of two metal ion species becomes possible by stepwise complexation of the two metal ion species to the ligand.

Fe(II) and Ru(II) ions were introduced alternately in the polymer backbone during the stepwise complexation utilizing different complexation conditions for the metal ions (Scheme 12.11) [24]. By changing the molar ratio of Fe(II) and Ru(II) to 1:0, 0.75:0.25, 0.5:0.5, 0.25:0.75, and 0:1, a series of the heterometallo-supramolecular polymers (**polyFeL1**, **polyFe$_{0.75}$Ru$_{0.25}$L1**, **polyFe$_{0.5}$Ru$_{0.5}$L1**, **polyFe$_{0.25}$Ru$_{0.75}$L1**, and **polyRuL1**, respectively) were obtained. **polyFe$_{0.75}$Ru$_{0.25}$L1**, **polyFe$_{0.5}$Ru$_{0.5}$L1**, and **polyFe$_{0.25}$Ru$_{0.75}$L1** were synthesized by seeding calculated molar ratios of $Fe(BF_4)_2$ to $RuCl_2(DMSO)_4$. First, **L1** and $RuCl_2(DMSO)_4$ were added in argon-saturated absolute ethylene glycol and stirred at 130 °C for 24 h. After reaction, $Fe(BF_4)_2$ dissolved in EG was added into the reaction bottom and stirred at 80 °C for 24 h. They were obtained in >90 % yields. When the molar ratio of Fe(II) and Ru(II)

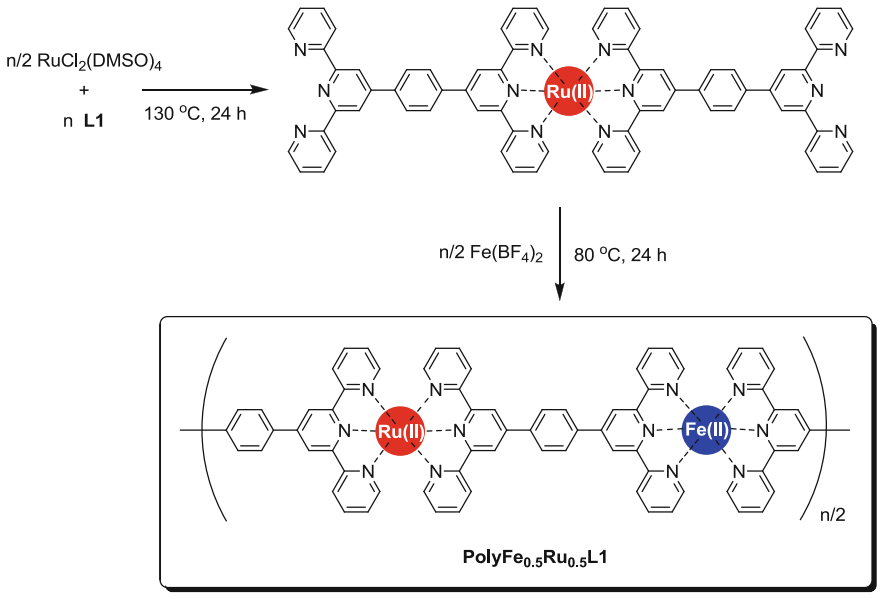

Scheme 12.11 Synthesis of the Fe(II)/Ru(II)-based heterometallo-supramolecular polymer (**PolyFe$_{0.5}$Ru$_{0.5}$L1**) [24]

was a value other than 0.5:0.5, the polymers had a block copolymer structure with oligomeric Fe(II) [or Ru(II)] units.

12.3.5 A Cu(II)/Fe(II)-Based Heterometallo-Supramolecular Polymer

Two metal ion species can be precisely introduced to the metallo-supramolecular polymer backbone by utilizing their different complexation conditions. However, after the polymer formation, exchange of the two metal ion species may occur in solution, because the complexation is an equilibrium reaction. Another way to control two metal ion species is using asymmetrical ligands with two different coordination sites in the polymer synthesis. Complexation behavior of an asymmetrical ligand **L13** with Cu(I) and Fe(II) ions was monitored by UV–Vis spectrophometric titration experiments. When $Cu(CH_3CN)_4OTf$ was added to an **L13** solution, an MLCT absorption of the Cu(I)-phenanthroline complex appeared around 465 nm. The absorbance increased linearly to [Cu(I)]/[**L13**] during the addition of 0.5 equivalent of Cu(I). Then when $Fe(ClO_4)_2 \cdot 6H_2O$ was added to the solution, another MLCT absorption based on the Fe(II)-terpyridine complex emerged around 575 nm. While the Fe(II) salt was added up to 0.5 equivalent amount of **L13**, the absorbance of the peak around 575 nm increased linearly to [Fe(II)]/[**L13**]. These spectral changes indicate that first Cu(I) ions formed a 1:2 complex with **L13** and then Fe(II) ions were complexed with the Cu(I) complex at the 1:1 molar ratio. It means that Cu(I) and Fe(II) ions were preferentially complexed with the bidentate phenanthroline and tridentate terpyridine moieties of **L13**, respectively, based on the different (tetrahedral or octahedral) coordination structures. A heterometallo-supramolecular polymer with Cu(I) and Fe(II) ions introduced alternately (**polyCuFeL13**) was one-pot prepared in a 97 % yield by simple mixing of an anhydrous dichloromethane solution of **L13**, anhydrous acetonitrile solutions of $Cu(CH_3CN)_4OTf$, and $Fe(ClO_4)_2 \cdot 6H_2O$ (molar ratio: 1:0.5:0.5) (Scheme 12.12) [15].

12.3.6 A Eu(III)/Fe(II)-Based Heterometallo-Supramolecular Polymer

An asymmetrical ligand with a none-substituted terpyridine and a terpyridine bearing two carboxylic acids (**L14**) introduces transition metal ions and lanthanide metal ions alternately to the metallo-supramolecular polymer backbone.

The complexation of **L14** with $Eu(NO_3)_3$ and $Fe(BF_4)_2$ was investigated by UV–Vis spectroscopic titration measurement. The spectrum of a methanol solution of **L14**, which was deprotonated by the addition of two equivalents of

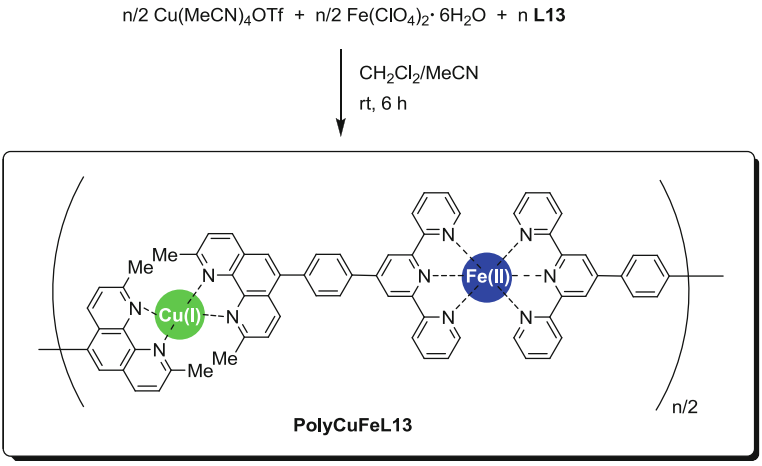

Scheme 12.12 Synthesis of the Cu(I)/Fe(II)-based heterometallo-supramolecular polymer (**polyCuFeL13**) [15]

tridodecylamine, was changed by the addition of $Eu(NO_3)_3$ until a molar ratio of $[Eu(NO_3)_3]$/[**L14**] became 0.5: the absorption around 345 nm increased and one at 303 nm decreased. Absorbance change of the absorption at 345 nm and the molar ratio of $[Eu(NO_3)_3]$/[**L14**] showed a linear relationship. Then, when $Fe(BF_4)_2$ was added to the solution (**L14-Eu-L14**), a new absorption at 570 nm based on the MLCT band appeared. The MLCT absorption was clearly saturated, when the molar ratio of $[Fe(BF_4)_2]$/[**L14**] became 0.5. These spectral changes suggest the formation of heterometallo-supramolecular polymer with Eu(III) and Fe(II) ions introduced alternately (**polyEuFeL14**). The spectrum did not change by the further addition of $Eu(NO_3)_3$, indicating that **polyEuFeL14** was stable in solution. **PolyEuFeL14** was obtained by complexation of **L14** with the addition of 0.5 equiv. of $Eu(NO_3)_3$ and the further addition of 0.5 equiv. of $Fe(BF_4)_2$ in the presence of tridodecylamine in a 36 % yield (Scheme 12.13) [20].

12.3.7 Three-Dimensional (3-D) Metallo-Supramolecular Polymers

Metallo-supramolecular polymers with a 3-D structure (**polyFeL1$_{95\%}$L15$_{5\%}$**, **polyFeL1$_{90\%}$L15$_{10\%}$**, **polyFeL1$_{85\%}$L15$_{15\%}$**, **polyFeL1$_{82\%}$L15$_{18\%}$**, and **polyFeL1$_{80\%}$L15$_{20\%}$**) were synthesized by the stepwise complexation of an Fe(II) salt with different ratios of bis(terpyridine) (**L1**) and tris(terpyridine) (**L15**) (Scheme 12.14) [22]. First, the 1-D polymer chains were prepared by the 1:1 complexation of Fe^{2+} and **L1**, and then **L15** and Fe^{2+} were added to the solution to make a 3-D structure. The successive addition should first lead to linear polymers,

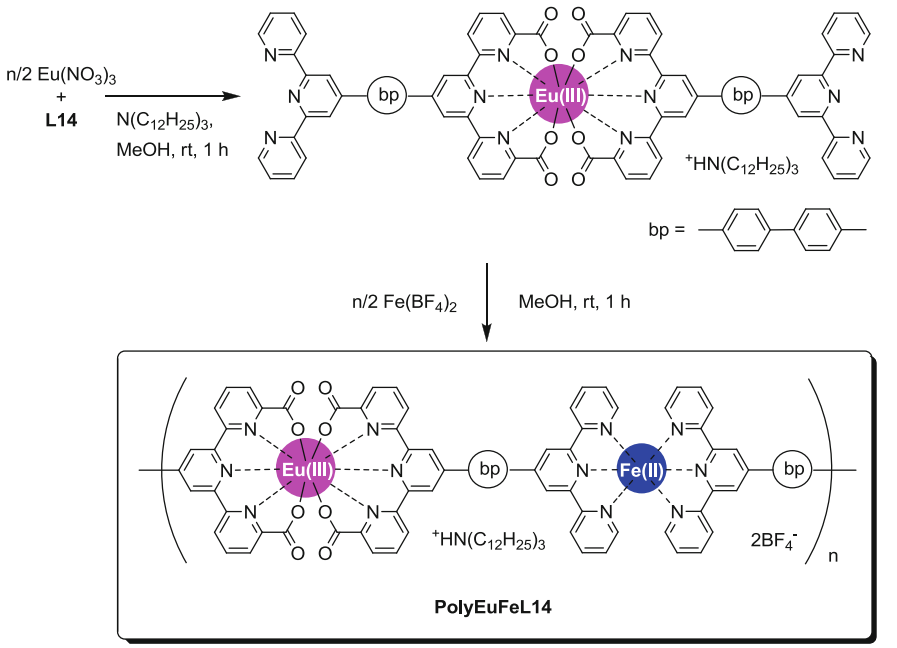

Scheme 12.13 Synthesis of the Eu(III)/Fe(II)-based heterometallo-supramolecular polymer (**polyEuFeL14**) [20]

followed by formation of highly cross-linked polymers. The degree of branching was controlled by changing the molar ratio of **L1** and **L15** from 95:5 to 80:20.

12.4 Electronic Properties

Electronic properties based on the redox of metal ions are expected in metallo-supramolecular polymers including transition metal ions. The oxidation state of transition metal ions is controlled electrochemically in the thin polymer film prepared on a working electrode. This section introduces electrochromic properties of metallo-supramolecular polymers.

12.4.1 Electrochromism in Metallo-Supramolecular Polymers

UV–Vis spectra of **polyFeL1–5** and **polyRuL1–5** solutions showed an MLCT absorption around 580 and 520 nm, respectively (Table 12.1) [4, 23–28].

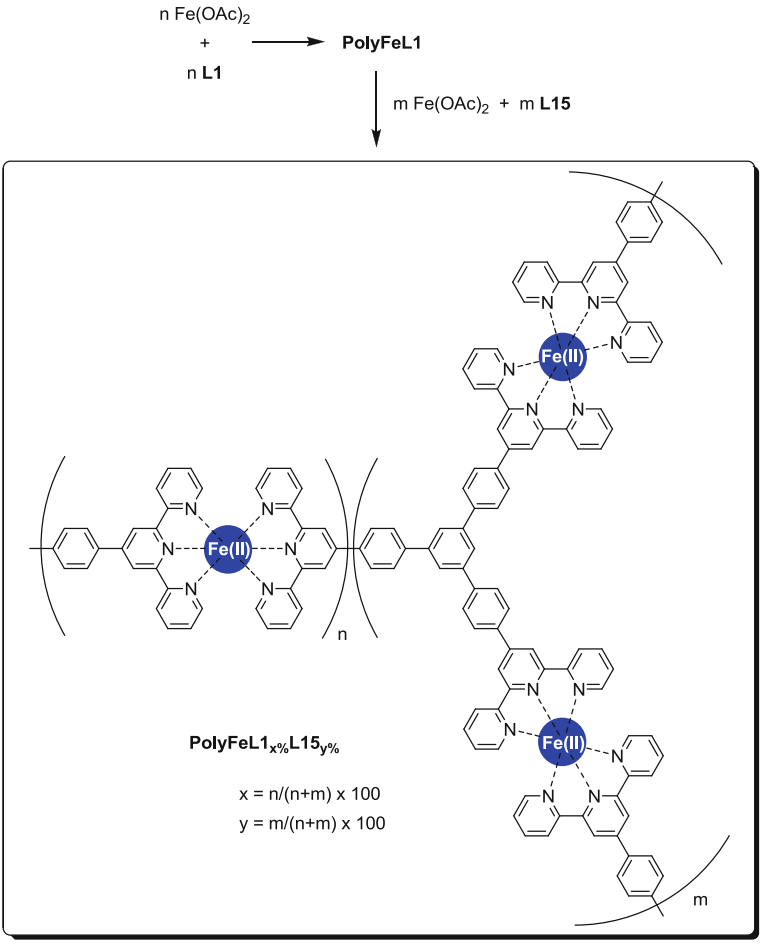

Scheme 12.14 Synthesis of the 3-D Fe(II)-based metallo-supramolecular polymer (**polyFeL1**$_{x\%}$ **L15**$_{y\%}$)

The absorption in **polyRuL1–5** appeared shorter wavelength and have higher ε than that in **polyFeL1–5** due to the stronger π-backbonding of **L1–5** to Ru(II) than Fe(II) [29] and a stronger dynamic chelate effect of **L1–5** to Ru(II) than Fe(II) [30]. In cyclic voltammograms (CVs) of **polyFeL1–5** and **polyRuL5**, a reversible redox wave based on Fe(II)/(III) and Ru(II)/(III) was observed. The CV results clearly show the shift to less oxidative potential by the introduction of electron donating groups (methoxy groups) and the shift to more oxidative potential by the introduction of electron withdrawing groups (bromo groups), because the strong electron donation of the methoxy groups stabilized the oxidized Fe(III) state and the electron deficiency of the bromo groups unstabilized the state. The same trend was observed in **polyRuL1–5**.

Table 12.1 The MLCT absorption and redox potential of **polyFeL1–5** and **polyRuL1–5** [23]

	Maximum wavelength (λ_{max})[a], nm	Absorption coefficient (ε)[a], $\times 10^4$	Redox potential ($E_{1/2}$)[b], V versus Ag/AgCl
PolyFeL1	585 [24]	3.06 [24]	0.77
PolyFeL2	579	2.57	0.78
PolyFeL3	585	1.43	0.70
PolyFeL4	578	1.67	0.70
PolyFeL5	612	0.77	0.93
PolyRuL1	513	4.10	0.95
PolyRuL1 in MeOH	508 [24]	4.00 [24]	–
PolyRuL2	502	3.55	0.95
PolyRuL3	536	2.54	0.84
PolyRuL4	524	2.25	0.85
PolyRuL5	507	3.25	1.16

[a]Solvent: MeOH for **polyFeL1–5**; MeOH/H_2O (4:1) for **polyRuL1–5**
[b]Working electrode: glassy carbon; counter electrode: Pt wire; reference electrode: Ag/AgCl; electrolyte: 0.10 M *n*-Bu_4NClO_4/MeCN; scan rate: 100 mV/s

We found electrochromism in the metallo-supramolecular polymer by chance [25]: the blue film of **polyFeL1** cast on a working electrode in an electrolyte solution changed to colorless upon applying more positive potential than 0.8 V versus Ag/AgCl. The colorless film returned to the colored state again upon applying a negative potential. The color change was reversible. Such electrochemical color changes are called electrochromism. The electrochromism in a **polyFeL1** film can be explained by the energy diagram (Fig. 12.1). Fe(II) ions have four *d*-electrons and the band structure is changed by the complexation with the ligand. The blue color of **polyFeL1** is based on the MLCT absorption from the *d*-electron of the Fe(II) ion in the HOMO (the highest occupied molecular orbital) potential to the π^* orbital of the ligand in the LUMO (the lowest unoccupied molecular orbital) potential in the metal complex moiety (Fig. 12.1a). The bandgap of MLCT is estimated to be 2.12 eV from the maximum wavelength (585 nm) of the absorption. When the Fe(II) ions are oxidized to be Fe(III) electrochemically, the MLCT absorption disappeared, because the *d*-electron contributed to the MLCT absorption is removed (Fig. 12.1b). The mechanism was supported by in situ UV–Vis spectral measurement while applying a voltage: a thin film of **polyFeL1** cast on an ITO glass was inserted into a quartz cuvette bearing necks to introduce counter and reference electrodes and argon gas. UV–Vis spectra of the polymer film were measured while applying a voltage. The MLCT absorption around 585 nm disappeared at an oxidative potential more than 1.0 V versus Ag/AgCl. On the other hand, the MLCT absorption reappeared by applying 0.0 V versus Ag/AgCl. From the comparison with the redox potential of Fe ions (0.77 V versus Ag/AgCl) in **polyFeL1**, it is concluded that the disappearance/reappearance of the MLCT

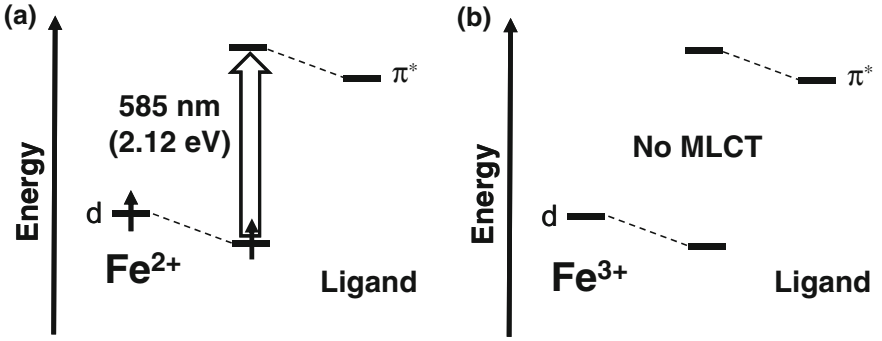

Fig. 12.1 A proposed mechanism for the electrochromism in a **polyFeL1** film: **a** the original (reduced) and **b** oxidized states

absorption was caused by the electrochemical redox between Fe(II) and Fe(III) states.

Color of the metallo-supramolecular polymers is a complemental color of the MLCT absorption. The bandgap of MLCT is decided by the HOMO and LUMO potentials. Metal ions and ditopic ligands have different band structures. Therefore, diverse combinations of metal ions and ditopic ligands are expected to give various colors of metallo-supramolecular polymers. **PolyFeL1–5**, **polyRuL1–5,** and **polyCuL9** showed blue-, red-, and green-colored electrochromism, respectively, due to the different bandgaps of MLCT [4, 12, 23–28].

12.4.2 Multi-color Electrochromism in Metallo-Supramolecular Polymers

Heterometallo-supramolecular polymers with two transition metal ion species show multi-color electrochromism, because of the different redox potentials of the two metal ion species [15, 24]. Redox potentials of **polyFeL1**, **polyFe$_{0.75}$Ru$_{0.25}$L1**, **polyFe$_{0.5}$Ru$_{0.5}$L1**, **polyFe$_{0.25}$Ru$_{0.75}$L1,** and **polyRuL1** are revealed by cyclic voltammetry (CV) (Table 12.2) [24]. The thin polymer films were prepared on ITO glass by spray coating. The results exhibit the positive shift of redox potential of Fe (II)/(III) from 755 to 769 mV with increasing the ratio of Ru(II) ions in the polymer and the negative shift of redox potential of Ru(II)/(III) from 933 to 913 mV with increasing the ratio of Fe(II) ions in the polymer. These changes are explained as the interaction between Fe(II) and Ru(II) ions through the π-conjugated ditopic ligand. The shift toward the more (or less) oxidative potential indicates a decrease (or increase) of electron donation from the ligand to the metal ion. In **polyFe$_{0.5}$Ru$_{0.5}$L1**, it is expected that Fe(II) and Ru(II) ions are introduced to the

Table 12.2 Redox potentials of Fe(II)/Ru(II)-based heterometallo-supramolecular polymers [24]

	Redox potential ($E_{1/2}$) of Fe(II)/(III), mV versus Ag/Ag^+	Redox potential ($E_{1/2}$) of Ru(II)/(III), mV versus Ag/Ag^+
PolyFeL1	755	–
PolyFe$_{0.75}$Ru$_{0.25}$L1	759	913
PolyFe$_{0.5}$Ru$_{0.5}$L1	764	919
PolyFe$_{0.25}$Ru$_{0.75}$L1	769	927
PolyRuL1	–	933

Working electrode: glassy carbon; counter electrode: Pt wire; reference electrode: a homemade Ag/Ag^+ electrode in ACN with 0.1 M n-Bu_4NClO_4 + 0.01 M $AgNO_3$; electrolyte: 0.10 M $LiClO_4$/MeCN; scan rate: 20 mV/s

polymer backbone in an alternate manner. However, the different potentials of Fe (II)/(III) between **polyFe$_{0.5}$Ru$_{0.5}$L1** and **polyFe$_{0.25}$Ru$_{0.75}$L1** or the different potentials of Ru(II)/(III) between **polyFe$_{0.75}$Ru$_{0.25}$L1** and **polyFe$_{0.5}$Ru$_{0.5}$L1** indicate that the order of Fe(II) and Ru(II) is not perfectly alternate in **polyFe$_{0.5}$Ru$_{0.5}$L1**.

An asymmetrical ligand enables the perfectly alternate introduction of two metal ion species in the metallo-supramolecular polymer backbone. Cu(I) and Fe(II) ions are aligned alternately in **polyCuFeL13**. The redox potentials of **polyFeL1**, **polyCuFeL13,** and **polyCuL6** were measured under the same conditions by CV (Table 12.3) [15]. The redox potential of **polyFeL1** (0.82 V) was different from those shown in Tables 12.1 and 12.2 (0.77 V and 755 mV, respectively) due to a different solvent (MeOH). In Fe(II)/Ru(II)-based heterometallo-supramolecular polymers, the redox potential of Fe(II)/(III) was positively shifted and the redox potential of Ru(II)/(III) was negatively shifted, compared to the redox potentials in the homo-metal polymer, because of the interaction between the two metal ion species (Table 12.2). On the other hand, in **polyCuFeL13**, the redox potential of Fe (II)/(III) was shifted negatively from 0.82 to 0.79 V, but the redox potential of Cu (I)/Cu(II) was also shifted negatively from 0.41 to 0.28 V. The results indicate the influence of the different ligands among the polymers as well as the interaction between the metal ions. The terpyridine moiety of **L13** stabilized the Cu(II)-phenanthroline complex probably by the electron donation to the phenanthroline moiety.

Table 12.3 Redox potentials of a Cu(I)/Fe(II)-based heterometallo-supramolecular polymer [15]

	Redox potential ($E_{1/2}$) of Cu(I)/(II), V versus Ag/Ag^+	Redox potential ($E_{1/2}$) of Fe(II)/(III), V versus Ag/Ag^+
PolyCuL6	0.41	–
PolyCuFeL13	0.28	0.79
PolyFeL1	–	0.82

Working electrode: glassy carbon; counter electrode: Pt wire; reference electrode: Ag/Ag^+; electrolyte: 0.10 M TBAP/EtOH; scan rate: 50 mV/s

Heterometallo-supramolecular polymers with two transition metal ion species have two MLCT absorptions. The multi-color electrochromism in these polymers was observed due to stepwise disappearance/appearance of the two absorptions, which was triggered by changing the applied potential. The spectral change can be monitored by in situ UV–Vis spectral measurements at different applied potentials. For example, two MLCT absorptions based on the Ru(II) and Fe(II) complex moieties appear at 508 and 585 nm, respectively, in the UV–Vis spectrum of a **polyFe$_{0.5}$Ru$_{0.5}$L1** film. When 0.9 V versus Ag/Ag$^+$ was applied to the film, the absorption at 585 nm almost disappeared, because of the oxidation of Fe(II) to Fe (III). The absorption at 508 nm also disappeared at 1.2 V versus Ag/Ag$^+$ due to the oxidation of Ru(II) to Ru(III). As the result, color change from reddish purple, orange, to colorless (pale green) was observed by changing the applied potential from 0, 0.9 to 1.2 V versus Ag/Ag$^+$, respectively. **PolyCuFeL13** has two absorptions at 465 and 575 nm and the color change from purple, blue to colorless was confirmed by applying 0, 1.6, and 2.2 V versus Ag/Ag$^+$ in the solid-state device.

The electrochromic properties of **polyFe$_{0.5}$Ru$_{0.5}$L1** are summarized in Table 12.4. The transmittance change at 508 nm in a **polyFe$_{0.5}$Ru$_{0.5}$L1** film was measured between 0 and 1.1 V with various interval times (20, 10, 5, 2.5, 1.0, and 0.5 s). The transmittance differences (ΔT) were 69.8, 68.3, and 67.2 % in 10, 5, and 2.5 s, respectively. The color change was very rapid: the bleaching time (t_b) and coloring time (t_c) (the time need for 95 % change of ΔT) were calculated to be 1.5 and 0.4 s, respectively. The bleached state [Fe(III) and Ru(III)] is less stable that the colored state [Fe(II) and Ru(II)]. Fe(III) and Ru(III) are easily reduced to Fe(II) and Ru(II). Therefore, t_c is much shorter than t_b. The charge/discharge amount for the electrochromic change was 2.72 mC/cm^2 in the bleaching process from 0 to 1.1 V and 2.66 mC/cm^2 in the coloring process from 1.1 to 0 V. Redox behavior of only Fe ions in **polyFe$_{0.5}$Ru$_{0.5}$L1** was also investigated by redox switching between 0 and 0.9 V.

Coloration efficiency (η) is the amount of optical density change (ΔOD) induced as a function of the injected/ejected electronic charge (Q_d) (Eq. 12.1) [31]. It is an important index to evaluate electrochromic materials:

$$\eta = \frac{\Delta \mathrm{OD}}{Q_d} = \log \frac{T_b}{T_c} / Q_d \tag{12.1}$$

Table 12.4 Electrochromic properties of the **polyFe$_{0.5}$Ru$_{0.5}$L1** film when switched between 0 and 0.9 V, 0 and 1.1 V with an interval of 5 s [24]

Applied voltage, V	Maximum wavelength (λ_{max}), nm	Coloring time (t_c), s	Bleaching time (t_b), s	Transmittance change (ΔT), %	Charge/discharge amount (Q), mC/cm^2	Coloration efficiency (η), cm^2/C
0–0.9	585	0.4	1.5	37.93	1.60/2.19	188.2
0–1.1	508	0.4	1.5	68.70	2.66/2.72	242.1

where η (cm^2/C) is the coloration efficiency at a given ΔOD and T_b and T_c are the bleached and colored transmittances, respectively. The η is measured by in situ UV–Vis spectral measurement during applying a voltage.

Using Eq. 12.1 and the data in Table 12.4, the η values were estimated to be 242.1 cm^2/C at 508 nm and 188.2 cm^2/C at 585 nm. In general, the η of inorganic electrochromic materials often is less than 100 cm^2/C [32, 33], and the η of organic electrochromic materials lies within a wide range on the order of dozens [34] or more than one thousand [35, 36]. The average η is *ca.* 200 cm^2/C, demonstrated by the values for PEDOT [37, 38], polyaniline [39], and triphenylamine [40, 41] systems, which are all located within these ranges.

12.4.3 Improvement of Electrochromism by the 3-D Structure

Electrochromism in a metallo-supramolecular polymer film is caused by the electron transfer between the polymer film and the electrode. In addition, anion transfer between the polymer film and an electrolyte also happens during the electrochromic change in order to compensate the charge unbalance caused by the electrochemical redox in the polymer film. Therefore, the morphology change of the polymer film is anticipated to improve the electrochromic properties.

Optical and electrochemical properties of Fe(II)-based metallo-supramolecular polymers with a 3-D structure (**polyFeL1$_{95\%}$L15$_{5\%}$**, **polyFeL1$_{90\%}$L15$_{10\%}$**, **polyFeL1$_{85\%}$L15$_{15\%}$**, **polyFeL1$_{82\%}$L15$_{18\%}$**, and **polyFeL1$_{80\%}$L15$_{20\%}$**) are summarized in Table 12.5 [22]. With increasing the ratio of the tritopic ligand (**L15**) from 0 to 20 % in the polymer, we observed a blue shift of the maximum wavelength (λ_{max}) in the MLCT absorption due to the higher LUMO potential of **L15** than that of **L1**, the increase of peak separation (ΔE) in the cyclic voltammogram because of the decrease of conductivity, the enhancement of thermal stability based on the formation of a cross-linking structure. The decrease of solubility also supports the cross-linking structure formation in the polymers with a high ratio of **L15**.

Atomic force microscopic (AFM) images of the polymer films revealed the surface morphology. The surface of a **polyFeL1** film was discontinuous and had a cotton-like apparent. The root mean square roughness (R_{rms}) measured from the image was small (2.9 nm). A dramatic morphology change was observed in **polyFeL1$_{90\%}$L15$_{10\%}$** and **PolyFeL1$_{85\%}$L15$_{15\%}$**; many holes approximately 30–50 nm in diameter appeared on the surface and the number of holes increased with increasing the ratio of **L15**. The R_{rms} increased to 5.8 nm in **polyFeL1$_{90\%}$L15$_{10\%}$**. The surface of the **polyFeL1$_{85\%}$L15$_{15\%}$** film had a highly porous 3-D structure, probably due to the formation of hyperbranched polymer chains, and the R_{rms} reached 6.0 nm. However, the large holes and porous structure disappeared in **polyFeL1$_{82\%}$L15$_{18\%}$** and **polyFeL1$_{80\%}$L15$_{20\%}$** and the film surfaces became rigid and solid. The 3-D structure improved electrochromic properties of the polymers

Table 12.5 Optical and electrochemical properties of Fe(II)-based metallo-supramolecular polymers with a 3-D or 1-D structure [22]

3-D or 1-D polymers	λ_{max} (nm)[a]	E_{pa} (V)[b]	ΔE (V)[c]	T_d (°C)[d]	Solubility[e]
PolyFeL1	585.2	0.765	0.055	367.9	+++
PolyFeL1$_{95\%}$L2$_{5\%}$	582.8	0.780	0.065	378.6	+++
PolyFeL1$_{90\%}$L2$_{10\%}$	582.5	0.780	0.065	398.5	+++
PolyFeL1$_{85\%}$L2$_{15\%}$	580.2	0.785	0.070	399.2	++
PolyFeL1$_{82\%}$L2$_{18\%}$	579.5	0.790	0.080	403.9	+
PolyFeL1$_{80\%}$L2$_{20\%}$	578.7	0.795	0.090	420.1	+

The symbol "+++" means the polymer was totally dissolved in methanol and there was no precipitation after 72 h. The symbol "++" means the polymer was totally dissolved in methanol but precipitation happened within 72 h. The symbol "+" means the polymer was partially dissolved in methanol

[a]Maximum wavelength (λ_{max}) of the MLCT absorption. The polymer films were prepared by spray coating a 1 mg/mL methanol solution of the polymer onto an ITO glass (working area: 1 × 1.5 cm). All the polymer films had the same thickness of approximately 500 ± 34 nm, which was estimated using a surface profiler (Alpha-step IQ, KLA Tencor)

[b]Anodic peak potential (E_{pa}). The polymer films used in the UV–Vis spectral measurements were also used for the cyclic voltammetry measurements (electrolyte: an MeCN solution of 0.1 M $LiClO_4$; counter electrode: platinum wire; reference electrode: Ag/Ag^+; scan rate: 10 mV s^{-1}) at room temperature

[c]The peak separation in the redox (ΔE). The differences in the redox potentials ($E_{ox} - E_{red}$)

[d]Thermal stability (T_d). The temperature for the 5 % weight loss in the thermogravimetric analysis (TGA) (the temperature increase rate: 10 °C min^{-1})

[e]The solubility was examined by dissolving 1 mg of the polymer into 1 mL of methanol

(Table 12.6). The most highly porous film (**polyFeL1$_{85\%}$L2$_{15\%}$**) exhibited the best electrochromic performance; as compared with the 1-D linear polymer (**polyFeL1**), the switching times were improved from 0.31 to 0.19 s for the coloring and from 0.58 to 0.36 s for the bleaching. The transmittance change (ΔT) increased from 41.6 to 50.7 %. The coloration efficiency (η) was enhanced from 263.8 to 383.4 cm^2/C. It is considered that the porous structure of the 3-D polymer films contributed to improvement of the electrochromic properties due to the smooth ion transfer during the redox.

12.5 Emission Properties

Metallo-supramolecular polymers with lanthanide metal ions such as Eu(III) ions are expected to show emission properties. This section introduces vapoluminescence and electrochemical emission switching of metallo-supramolecular polymers.

Table 12.6 The electrochromic properties of the 3-D and 1-D polymer films [21]

3-D or 1-D polymers	$T_{bleached}$ (%)[a]	$T_{colored}$ (%)[a]	ΔT (%)[a]	$t_{coloring}$ (s)[b]	$t_{bleaching}$ (s)[b]	Charge/discharge (mC)[c]	η (cm^2/C)[d]
PolyFeL1	93.2	51.6	41.6	0.31	0.58	1.46/1.44	263.8
PolyFeL1$_{95\%}$L2$_{5\%}$	92.5	43.9	48.6	0.21	0.51	1.69/1.65	287.2
PolyFeL1$_{90\%}$L2$_{10\%}$	94.0	46.5	47.5	0.23	0.52	1.38/1.35	332.2
PolyFeL1$_{85\%}$L2$_{15\%}$	91.6	40.9	50.7	0.19	0.36	1.37/1.34	383.4
PolyFeL1$_{82\%}$L2$_{18\%}$	78.8	54.8	24.0	0.37	0.60	1.69/1.65	140.0
PolyFeL1$_{80\%}$L2$_{20\%}$	81.6	54.4	27.2	0.37	0.62	2.02/1.97	130.7

[a]Transmittances of the MLCT absorption (λ_{max}) in the bleached ($T_{bleached}$) and colored states ($T_{colored}$) of the polymer film coated on an ITO glass were measured by in situ UV–Vis spectroscopy at 0 or 1.2 V versus Ag/Ag^+ with an interval time of 5 s (electrolyte: 0.1 M $LiClO_4$/MeCN; the ITO working area: 1 × 1.5 cm). Transmittance difference (ΔT) was calculated from $T_{bleached}$ and $T_{colored}$

[b]The times for coloring and bleaching ($t_{coloring}$ and $t_{bleaching}$) were defined as the time taken for 95 % of ΔT to change

[c]Charge/discharge values were calculated from the integration of the coulomb number in the current response during the redox

[d]Coloration efficiency (η) was defined as the relationship between the electron charge used and the change of ΔT. All the values of the electrochromic properties, including transmittance ($T_{bleached}$ and $T_{colored}$), transmittance change (ΔT), switching time ($t_{coloring}$ and $t_{bleaching}$), and coloration efficiency (η), were averaged from three data points of the polymer films. The errors of these values were less than ±5 %

12.5.1 Vapoluminescence

Vapoluminescence is emission change triggered by vapor. Some Pt or Au complexes have been reported to show vapoluminescence [42–44], but the change is slow and often irreversible because the large structural change in a crystal state of the complexes is required. A Eu(III)-based metallo-supramolecular polymer (**polyEuL12**) showed quick and reversible vapoluminescence for acidic/basic vapor [14]. A **polyEuL12** film showed bright-red emission under UV light (λ_{ex} = 365 nm). In the emission spectrum of the **polyEuL12** film, sharp peaks based on the $^5D_0 \rightarrow {}^7F_{1-4}$ in Eu(III) ions appeared upon the excitation at 365 nm. Especially, the $^5D_0 \rightarrow {}^7F_2$ transition is hypersensitive. The excitation wavelength (365 nm) is overlapped with a broad absorption (200–400 nm) of **L12**. Therefore, it is considered that red emission of the Eu(III) ion is caused by the energy transfer from the ligand to the Eu(III) ion in the polymer. The PL quantum yield (Φ_{FL}) of **polyEuL12** was 0.24 in the film state. Interestingly, a free-standing film of **polyEuL12** showed vapoluminescence: the ON/OFF switching of the photoluminescence occurred by exposure to basic/acidic vapor. The red emission was quenched by the exposure of HCl vapor for 5 s. The quenched film showed red emission again by the exposure of Et_3N vapor for 5 s. The switching in the film state was reversible at least up to eight times. It is considered that the partial protonation of the ligand moiety in **polyEuL12** causes the quenching of the emission (Scheme 12.15), because the energy transfer to Eu(III) ions is prevented by the energy transfer to the CT band.

12.5.2 Electrochemical ON/OFF Switching of Luminescence

A Eu(III)/Fe(II)-based heterometallo-supramolecular polymer (**polyEuFeL13**) in ethylene glycol showed emission around 550–720 nm of the Eu(III) ion [19].

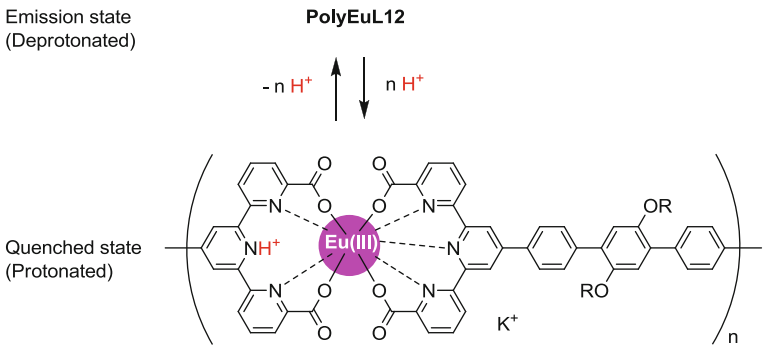

Scheme 12.15 A possible quenching mechanism by protonation in **polyEuL12** [14]

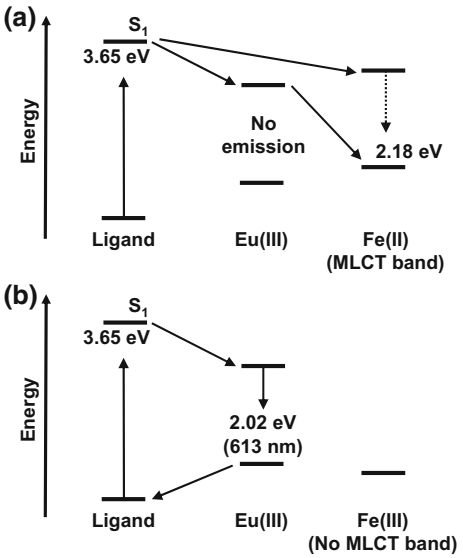

Fig. 12.2 Possible electrochemical switching mechanisms of emission in **polyEuFeL13** [19]: **a** the original (quenched) state and **b** the oxidized (emissive) state

The emission is very weak [absolute quantum yield (Φ) = 0.07] compared to that of **polyEuL12** (Φ = 0.27), probably due to the energy transfer to the MLCT band of the Fe(II) complex moiety. This polymer film also exhibited redox activity based on the redox of Fe(II)/(III) at 0.8 V versus Ag/AgCl and reversible electrochromism. It was found that the emission at 613 nm greatly enhanced by applying 2.0 V versus Ag/AgCl. The red emission was quenched by applying 0 V versus Ag/AgCl. The electrochemical ON/OFF switching of emission was repeated at least for 10 times. The emission change clearly corresponds to the electrochromic change: the quenching and emitting occur simultaneously with the coloring and bleaching of the polymer film based on the redox of Fe ions, respectively. The possible quenching mechanisms are shown in Fig. 12.2: (i) the energy transfer from the excited state of the ligand to the MLCT band of the Fe(II) moiety and the subsequent quenching in the MLCT band or (ii) the energy transfer from the excited state of the ligand to Eu(III) and the quenching by the energy transfer to Fe(II). When Fe(II) is oxidized to Fe(III) electrochemically, the unfavorable energy transfer for the emission of Eu(III) does not occur due to disappearance of the MLCT absorption and/or lowing of the HOMO potential of Fe ions.

12.6 Ionic Conductivity

Ionic conductive materials such as Nafion [45] have received much attention for energy-related applications including fuel cells and secondary batteries. This section introduces ionic conductivity of Ni(II)-based metallo-supramolecular polymer films at high humidity [46, 47].

12.6.1 Ionic Conductivity of Metallo-Supramolecular Polymer Films

Ionic conductivity of Ni(II)-based metallo-supramolecular polymer (**polyNiL8–10**) films greatly enhanced with increasing the humidity [46]. The ionic conductivity of **polyNiL8–10**, which was calculated from the diameter of the semicircle at the high-frequency region of the Nyquist plots in the ac impedance measurement, reached 1.44×10^{-6}, 3.2×10^{-5}, and 0.75×10^{-3} S/cm, respectively, at room temperature and 98%RH (relative humidity). The order of hydrophobicity in the ligands [**L8** (with alkyl chains and methyl groups) >**L9** (with alkyl chains) >**L10** (with methyl groups)] of **polyNiL8–10** was completely in agreement with the order of low ionic conductivity. This result indicates that the hydrophobicity of the ligand prevents the ionic conduction in the polymer film. The activation energy for the ionic conduction in **polyNiL10** was investigated by the dc current measurement at different temperatures and 98%RH and determined from the Arrhenius plot to be 0.43 eV. The low activation energy indicates that the ionic conduction includes proton conduction based on the Grotthuss mechanism [48, 49], probably due to the proton channel formation through the polymer chains (Fig. 12.3).

12.6.2 Improved Ionic Conduction in Metallo-Supramolecular Polymer Films

Ni(II)-based metallo-supramolecular polymers with different counter anions (chloride (Cl^-), nitrate (NO_3^-), acetate (CH_3COO^-), and acetylacetate ($CH_3C(=O)CH=C(O^-)CH_3$)) (**polyNiL10-Cl**, -**NO_3**, -**ac,** and **-acac**, respectively) were

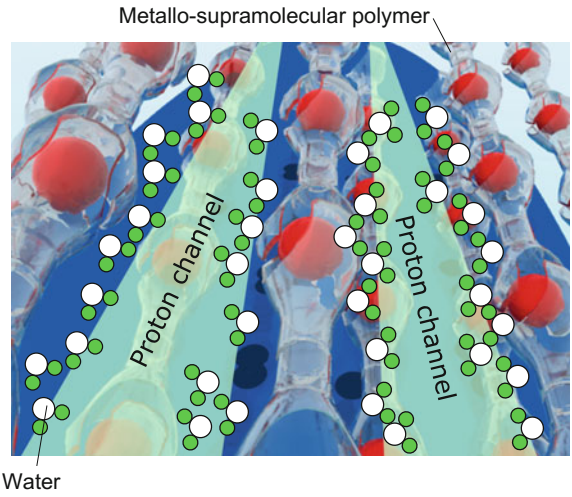

Fig. 12.3 A possible proton channel formation through the polymer chains

Table 12.7 Ionic conductivity of **polyNiL10-Cl**, **-NO_3**, **-ac,** and -**acac** films at room temperature and different %RHs [47]

%RH	Ionic conductivity (S/cm)			
	polyNiL10-Cl	**polyNi2**	**polyNi3**	**polyNi4**
30	5.0×10^{-6}	5.4×10^{-7}	4.5×10^{-8}	4.0×10^{-8}
40	3.8×10^{-5}	3.1×10^{-6}	4.5×10^{-7}	5.3×10^{-7}
50	1.2×10^{-4}	9.1×10^{-6}	2.6×10^{-6}	3.7×10^{-6}
60	2.8×10^{-4}	3.3×10^{-5}	1.2×10^{-5}	1.4×10^{-5}
70	6.5×10^{-4}	9.5×10^{-5}	3.7×10^{-5}	3.9×10^{-5}
80	1.6×10^{-3}	1.9×10^{-4}	1.6×10^{-4}	1.0×10^{-4}
90	4.6×10^{-3}	1.0×10^{-3}	5.2×10^{-4}	2.2×10^{-4}
100	5.0×10^{-2}	2.4×10^{-3}	1.0×10^{-3}	6.1×10^{-4}

prepared by the 1:1 complexation of the corresponding Ni(II) salts and **L10** [47]. The Nyquist plots of the polymer films were obtained by the ac impedance measurement at 25 °C and 98%RH. The ionic conductivities of **polyNiL10-Cl**, **-NO_3**, **-ac,** and **-acac** were calculated from the diameter of the semicircle at the high-frequency region of the Nyquist plots to be 5.0×10^{-2}, 2.4×10^{-3}, 1.0×10^{-3}, and 0.6×10^{-3} S/cm, respectively. The results indicate the influence of the counter anion to the ionic conductivity of the polymer films. Interestingly, the polymer with "harder" anions showed higher ionic conductivity: the order of the hardness in the anions (chloride > nitrate > acetate > acetylacetate) [50] was in good agreement with the order of the ionic conductivity of the polymers (**polyNiL10-Cl** > **polyNiL10-NO_3** > **polyNiL10-ac** > **polyNiL10-acac**).

The ionic conductivity of the polymer films greatly depends on the humidity and increased by about four orders of magnitude while increasing the humidity from 30 to 98%RH (Table 12.7). *I–V* properties of **polyNiL10-Cl**, **-NO_3**, **-ac,** and -**acac** were measured at 98%RH and different temperatures (20–80 °C). Their activation energies for the ionic conductivity were estimated using the Arrhenius plots (logarithm of current as a function of 1/T) to be 0.21, 0.31, 0.32, and 0.80 eV, respectively. It is known that an activation energy less than 0.4 eV suggests the Grotthuss-type mechanism, in which protons pass along the hydrogen bonds.[38] These results indicate that the high ionic conductivity in **polyNiL10-Cl**, **-NO_3**, **-ac** films at high humidity is achieved by efficient proton transfer through the ion channels formed by water molecules, which were assembled along the polymer chains with the help of the positive charge of Ni(II) ions and/or the negative charge of the counter anions.

12.7 Device Application

Metallo-supramolecular polymers are suitable to device applications because of the amorphous film formation properties. This section introduces solid-state electrochromic devices and real-time humidity sensors using the polymer films.

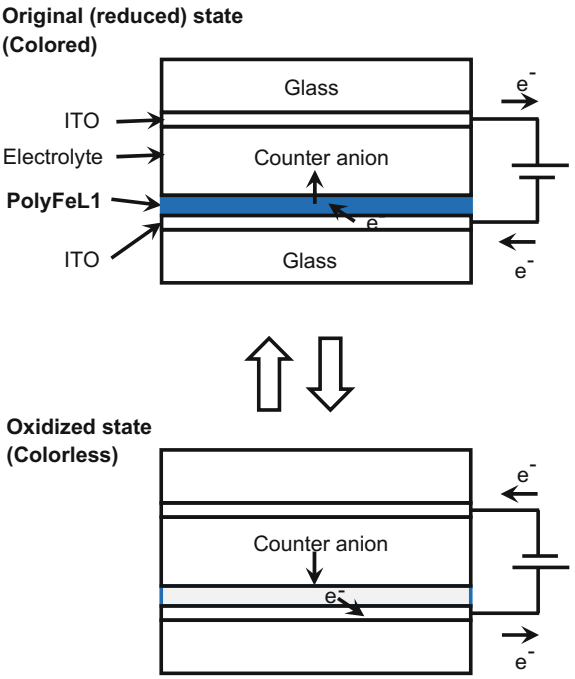

Fig. 12.4 The electrochromic device structure with a **polyFeL1** film and a mechanism of the color change

An electrochromic solid-state device with a **polyFeL1** film was successfully fabricated by combining with a gel electrolyte [51–58]. A **polyFeL1** film was prepared on an ITO glass by spin-coating the methanol solution (2.0 mg/mL). An gel electrolyte, which was composed of poly(methylmethacrylate) (PMMA) (7.0 g), propylene carbonate (PC) (20 mL), and $LiClO_4$ (3.0 g), was coated on another ITO glass. The solid-state device was fabricated by stacking the **polyFeL1** film on an ITO glass and the gel electrolyte layer on an ITO glass (Fig. 12.4). When a voltage more than 2.5 V was applied between two ITO electrodes of the device, the color of the device changed from blue to colorless, because Fe(II) ions in the **polyFeL1** film were oxidized to Fe(III) electrochemically. It was found that the device has a memory property: the colorless state was maintained after turning off the power. The bleaching/coloring speed and the memory time greatly depended on the applied voltage and the thickness of the gel electrolyte layer, respectively. When the opposite voltage was applied, the colorless state was changed to the original colored state. The behavior means that Fe(III) ions were reduced to Fe(II) electrochemically. When flexible ITO glasses were used as the electrodes of the device, the device itself showed flexibility (Fig. 12.5).

When an insulating film in which an arbitrary image was cut off was inserted between the electrolyte layer and the metallo-supramolecular polymer film layer, the colorless image appeared immediately on the blue screen by applying a positive potential to the polymer side in the device. The insulating film was important to exhibit an image, because the film prevents the ion transfer between the gel

Fig. 12.5 A flexible solid-state electrochromic device using a **polyFeL1** film

electrolyte layer and the **polyFeL1** film in the device. When the color of **polyFeL1** in the device changes from blue to colorless, electron transfer happens from the **polyFeL1** film to the ITO electrode. At the same time, anion transfer occurs from the gel electrolyte layer to the **polyFeL1** film to neutralize the change in the positive charge of the metal ions. Therefore, the **polyFeL1** part covered with the insulating film did not show any color changes even when a voltage was applied to the device, because the anion transfer did not occur.

Capacitive, thermal, and resistive methods have been used for humidity sensing so far [59–64]. It was revealed that Ni(II)-based metallo-supramolecular polymer films serve as a humidity sensor owing to the highly humidity-responsive ionic conductivity. A **polyNiL10-Cl** film was prepared on an interdigitated electrode composed of 65 pairs of Pt wires printed on quartz substrate with 10 μm gap between the paired Pt electrodes. The current of the film was measured with changing humidity (bias voltage: 1.0 V). With increasing the humidity from 25 to 90 %RH, the conductance (1/R) of the film enhanced simultaneously. The real-time humidity sensing property of the film was also confirmed by the following experiment, too. When the humidity was changed stepwise from 30%RH to 50, 70, 90, 98, 90, 70, 50, and 30%RH (duration: 30 min), a stepwise change of the conductance can be monitored corresponding to the humidity change.

12.8 Summary

Metallo-supramolecular polymers are prepared by complexation of metal ions and multi-topic organic ligands. The multi-topic ligands such as bis(terpyridine)s, tris (terpyridine), and bis(phenanthroline)s are synthesized via the Suzuki–Miyaura cross-coupling reaction. The Fe(II)-, Ru(II)-, and Co(II)-based metallo-supramolecular polymers are obtained by the combination of the metal salts and

bis(terpyridine)s. The Cu(II)- and Ni(II)-based polymers are synthesized by the complexation of the metal salts with bis(phenanthroline)s. The Eu(III)-based polymer is prepared through the 1:1 complexation of the metal salt and bis(terpyridine) bearing carboxylic acids in the presence of a base. By utilizing the different complexation behaviors of the two different metal ion species to bis(terpyridine), Fe(II) and Ru(II) ions are alternately introduced to the polymer chain. Asymmetrical ditopic ligands with two different coordination sites enable the precise introduction of two kinds of metal ions to the polymer backbone in an alternate manner: the Cu(I)/Fe(II)- and Eu(III)/Fe(II)-based heterometallo-supramolecular polymers are obtained with asymmetrical ditopic ligands. The use of a tritopic ligand changes the polymer structure to a hyperbranched one. The Fe(II)-, Ru(II)-, and Cu(II)-based polymers show reversible electrochromism between a blue-, red-, or green-colored state and a colorless one, respectively. The Ru(II)/Fe(II)- and Cu(I)/Fe(II)-based heterometallo-supramolecular polymers exhibit multi-color electrochromism based on the different MLCT absorptions and different redox potentials between the two metal ion species. The Eu(III)-based polymer displays vapoluminescence and the Eu(III)/Fe(II)-based polymer demonstrates luminescence switching triggered by electrochemical redox of Fe ions. A film of the Ni(II)-based polymer shows humidity-sensitive ionic conduction. As for applications of these polymers, electrochromic devices are fabricated using the Fe(II)- and Ru(II)-based polymers. Real-time humidity sensing is also achieved using the Ni(II)-based polymer.

References

1. W. Huang, H. Qian, J. Mol. Struct. **874**, 64 (2008)
2. I. Eryazici, C.N. Moorefield, S. Durmus, G.R. Newcome, J. Org. Chem. **2006**, 71 (1009)
3. F.S. Han, M. Higuchi, D.G. Kurth, Org. Lett. **9**, 559 (2007)
4. F.S. Han, M. Higuchi, D.G. Kurth, Adv. Mater. **19**, 3928 (2007)
5. P.G. Sammes, G. Yahioglu, Chem. Soc. Rev. **23**, 327 (1994)
6. T. Cardinaels, J. Ramaekers, P. Nockemann, K. Driesen, K. Van Hecke, L. VanMeervelt, G. Wang, S. De Feyter, E.F. Iglesias, D. Guillon, B. Donnio, K. Binnemans, D.W. Bruce, Soft Matter **4**, 2172 (2008)
7. U. Velten, B. Lahn, M. Rehahn, Macromol. Chem. Phys. **198**, 2789 (1997)
8. U. Velten, M. Rehahn, Chem. Commun. **23**, 2639 (1996)
9. S.V. Pakhomova, M.A. Proskurnin, V.V. Chernysh, M.Y. Kononets, E.K. Ivanova, J. Anal. Chem. **56**, 910 (2001)
10. M.A. Proskurnin, V.V. Chernysh, S.V. Pakhomova, M.Y. Kononets, A.A. Sheshenev, Talanta **57**, 831 (2002)
11. C. Reichardt, Chem. Rev. **94**, 2319 (1994)
12. M.D. Hossain, T. Sato, M. Higuchi, Chem. Asian J. **8**, 76 (2013)
13. M.D. Hossain, M. Higuchi, Synthesis **45**, 753 (2013)
14. T. Sato, M. Higuchi, Chem. Commun. **48**, 4947 (2012)
15. J.P.W. Eggert, U. Luning, C. Nather, Eur. J. Org. Chem. **2005**, 1107 (2005)
16. M. Hissler, W.B. Connick, D.K. Geiger, J.E. McGarrah, D. Lipa, R.J. Lachicotte, R. Eisenberg, Inorg. Chem. **39**, 447 (2000)

17. T. Ishiyama, M. Murata, N. Miyaura, J. Org. Chem. **60**, 7508 (1995)
18. T. Ishiyama, Y. itoh, T. Kitano, N. Miyaura, Tetrahedron Lett. **38**, 3447 (1997)
19. T. Sato, M. Higuchi, Chem. Commun. **49**, 5256 (2013)
20. M. Cavazzini, S. Quici, C. Scalera, F. Puntoriero, G. La Ganga, S. Campagna, Inorg. Chem. **48**, 8578 (2009)
21. C.-W. Hu, T. Sato, J. Zhang, S. Moriyama, M. Higuchi, A.C.S. Appl, Mater. Interfaces **6**, 9118 (2014)
22. F. Han, M. Higuchi, D.G. Kurth, J. Am. Chem. Soc. **130**, 2073 (2008)
23. C.-W. Hu, T. Sato, J. Zhang, S. Moriyama, M. Higuchi, J. Mater. Chem. C **1**, 3408 (2013)
24. M.D. Hossain, J. Zhang, R.K. Pandey, T. Sato, M. Higuchi, Eur. J. Inorg. Chem. **2014**, 3763 (2014)
25. M. Higuchi, D.G. Kurth, Chem. Rec. **7**, 203 (2007)
26. M. Higuchi, Kobunshi Ronbunshu **65**, 399 (2008)
27. T. Ikeda, M. Higuchi, D.G. Kurth, Trans. Mater. Res. Soc. J. **33**, 403 (2008)
28. M. Higuchi, J. Nanosci. Nanotechnol. **9**, 51 (2009)
29. H. Hofmeier, U.S. Schubert, Chem. Soc. Rev. **33**, 373 (2004)
30. M. Maestri, N. Armoroli, V. Balzani, E.C. Constable, A.M.W.C. Thompson, Inorg. Chem. **34**, 2759 (1995)
31. M. Fabretto, T. Vaithianathan, C. Hall, P. Murphy, P.C. Innis, J. Mazurkiewicz, G.G. Wallace, Electrochem. Commun. **9**, 2032 (2007)
32. D.A. Wruck, M.A. Dixon, M. Rubin, S.N. Bogy, J. Vac. Sci. Technol. **9**, 2170 (1991)
33. S.K. Deb, Sol. Energy Mater. Sol. Cells **92**, 245 (2008)
34. C.W. Hu, K.M. Lee, K.C. Chen, L.C. Chang, K.Y. Shen, S.C. Lai, T.H. Kuo, C.Y. Hsu, L.M. Huang, R. Vittal, K.C. Ho, Sol. Energy Mater. Sol. Cells **99**, 135 (2012)
35. C.G. Wu, M.I. Lu, S.J. Chang, C.S. Wei, Adv. Funct. Mater. **2007**, 17 (1063)
36. S.A. Sapp, G.A. Sotzing, J.R. Reynolds, Chem. Mater. **10**, 2101 (1998)
37. M. Deepa, A. Awadhia, S. Bhandari, Phys. Chem. Chem. Phys. **11**, 5674 (2009)
38. C.L. Gaupp, D.M. Welsh, R.D. Rauh, J.R. Reynolds, Chem. Mater. **14**, 3964 (2002)
39. S.J. Yoo, J. Cho, J.W. Lim, S.H. Park, J. Jang, Y.E. Sung, Electrochem. Commun. **12**, 164 (2010)
40. G.S. Liou, C.W. Chang, Macromolecules **41**, 1667 (2008)
41. C.W. Chang, C.H. Chung, G.S. Liou, Macromolecules **41**, 8441 (2008)
42. W. Lu, M.C.W. Chan, N. Zhu, C.-M. Che, Z. He, K.-Y. Wong, Chem. Eur. J. **9**, 6155 (2003)
43. J. Ni, Y.-H. Wu, X. Zhang, B. Li, L.-Y. Zhang, Z.-N. Chen, Inorg. Chem. **48**, 10202 (2009)
44. S.H. Lim, M.M. Olmstead, A.L. Balch, J. Am. Chem. Soc. **133**, 10229 (2011)
45. K.S. Rohr, Q. Chen, Nat. Mater. **7**, 75 (2008)
46. R.K. Pandey, M.D. Hossain, S. Moriyama, M. Higuchi, J. Mater. Chem. A **1**, 9016 (2013)
47. R.K. Pandey, M.D. Hossain, S. Moriyama, M. Higuchi, J. Mater. Chem. A **2**, 7618 (2014)
48. M. Sadakiyo, T. Yamada, H. Kitagawa, J. Am. Chem. Soc. **131**, 9906 (2009)
49. T. Yamada, M. Sadakiyo, H. Kitagawa, J. Am. Chem. Soc. **131**, 3144 (2009)
50. R.G. Pearson, J. Am. Chem. Soc. **85**, 3533 (1963)
51. M. Higuchi, Y. Akasaka, T. Ikeda, A. Hayashi, D.G. Kurth, J. Inorg. Organomet. Polym. Mater. **19**, 74 (2009)
52. M. Higuchi, Polym. J. **41**, 511 (2009)
53. M. Higuchi, Kobunshi Ronbunshu **67**, 368 (2010)
54. M. Higuchi, J. Synth. Org. Chem Jpn. **69**, 229 (2011)
55. A. Bandyopadhyay, M. Higuchi, Eur. Polym. J **49**, 1688 (2013)
56. http://www.youtube.com/watch?v=cRI5bK_-FRo
57. M. Higuchi, J. Mater. Chem. C **2**, 9331 (2014)
58. M. Higuchi, Kobunshi Ronbunshu **71**, 624 (2014)
59. Z. Chen, C. Lu, Sens. Lett. **3**, 274 (2005)
60. R. Demir, S. Okur, M. Seker, Ind. Eng. Chem. Res. **51**, 3309 (2012)
61. R.-J. Wu, Y.-L. Sun, C.-C. Lin, H.-W. Chen, M. Chavali, Sens. Actuaters B **145**, 174 (2010)
62. R. Xuan, Q. Wu, Y. Yin, J. Ge, J. Mater. Chem. **21**, 3672 (2011)
63. B. Cheng, B. Tian, C. Xie, Y. Xiao, S. Lei, J. Mater. Chem. **2011**, 21 (1907)
64. J. Liu, F. Sun, F. Zhang, Z. Wang, R. Zhang, C. Wang, S. Qiu, J. Mater. Chem. **21**, 3775 (2011)

Chapter 13
Feasibility of Fabricating Large-Area Inorganic Crystalline Semiconductor Devices

Jitsuo Ohta, Kohei Ueno, Atsushi Kobayashi and Hiroshi Fujioka

Abstract Generally, group III–V compound semiconductor devices are believed to exhibit high performance; however, their applications are limited because of their high fabrication costs. This problem primarily stems from the fact that the fabrication process involves low-throughput and high-temperature metalorganic chemical vapor deposition growth on expensive bulk single-crystal substrates. To fabricate high-performance, large-area III–V semiconductor devices, such as solar cells or displays, at a reasonable cost, development of a high-throughput, low-temperature growth technique on low-cost substrates is important. We have recently discovered that using pulsed sputtering deposition as a growth technique allows the synthesis of device-quality III–V semiconductors even at room temperature. This reduction in the growth temperature allows utilization of various large-area, low-cost substrates that have not previously been used for the growth of III–V compound semiconductors. This chapter describes the feasibility of fabricating large-area inorganic crystalline devices based on group III nitrides.

Keywords Low-temperature epitaxial growth · Group III nitrides · Pulsed sputtering deposition · Light-emitting diodes · Electron devices

13.1 Introduction

This chapter describes the feasibility of fabricating large-area inorganic crystalline devices based on group III nitrides. Generally, group III–V compound semiconductor devices are believed to exhibit high performance; however, their applications are limited because of their high fabrication costs. This problem primarily stems from the fact that the fabrication process involves low-throughput and high-temperature metalorganic

J. Ohta · K. Ueno · A. Kobayashi · H. Fujioka (✉)
Institute of Industrial Science, The University of Tokyo, Tokyo 153-8505, Japan
e-mail: hfujioka@iis.u-tokyo.ac.jp

J. Sone and S. Tsuji (eds.), *Intelligent Nanosystems for Energy, Information and Biological Technologies*, DOI 10.1007/978-4-431-56429-4_13

chemical vapor deposition (MOCVD) growth on expensive bulk single-crystal substrates. To fabricate high-performance, large-area III–V semiconductor devices, such as solar cells or displays, at a reasonable cost, development of a high-throughput, low-temperature growth technique on low-cost substrates is important. We have recently discovered that using pulsed sputtering deposition (PSD) as a growth technique allows the synthesis of device-quality III–V semiconductors even at room temperature. In this technique, surface migration of the film precursors is enhanced, and therefore, the temperature for epitaxial growth is dramatically reduced. This reduction allows utilization of various large-area, low-cost substrates that have not previously been used for the growth of III–V compound semiconductors because of their chemical vulnerability. Among the various III–V compound semiconductors, III nitrides, such as GaN and InGaN, are most suitable for large-area applications because they can accommodate the high density of crystalline defects that are generated because of using foreign large-area substrates without causing serious device degradation.

The first half of this chapter discusses the advantages of the low-temperature PSD, including suppression of phase separation reactions in InGaN during growth. Suppression of phase separation is important for fabricating devices that utilize high-in-concentration InGaN, such as solar cells and long-wavelength LEDs. The other advantage of using a low-temperature PSD is alleviation of thermal stress, which is crucial for the heterostructures formed between materials with different thermal expansion coefficients. The first half also covers various device fabrication applications for PSD, such as LEDs, high electron mobility transistors (HEMTs), and metal–insulator–semiconductor field-effect transistors (MISFETs). The second half of this chapter describes the characteristics of GaN films grown on low-cost amorphous substrates and their LED applications. Notably, for successfully operating LEDs, suppression of interfacial reactions between GaN and the substrate using low-temperature PSD is essential.

13.2 Low-Temperature Fabrication of Nitride Devices Using PSD

This section includes an overview of the low-temperature heteroepitaxial growth of group III nitride semiconductors via PSD and their applications in optical and electron devices. The structural properties of the low-temperature-grown nitride films and recent advances in the fabrication of LEDs, HEMTs, and MISFETs using PSD are presented.

13.2.1 Low-Temperature Growth of Nitride Films Using PSD

Group III nitride semiconductors have been grown via conventional epitaxial growth techniques, such as MOCVD and molecular beam epitaxy (MBE).

However, in these techniques, growth is performed at high temperatures, i.e., above 800 °C, which results in degradation of the substrate surfaces and/or the formation of interfacial layers between the films and the substrates. Therefore, the substrates that can be used for the epitaxial growth of group III nitrides are limited to chemically and thermally stable materials, such as Al_2O_3, SiC, and Si. To address this issue and enable the fabrication of nitride-based optoelectronic devices on various substrates, the development of a low-temperature growth technique is highly sought. Recently, the use of pulsed laser deposition (PLD), which is capable of supplying high kinetic energies to the film precursors via excimer laser irradiation, enabled a significant reduction in the growth temperature [1–3]. However, while it is true that using PLD is quite promising for the growth of group III nitride films at low temperature, its low throughput must be improved before this process can be applied for the mass production of nitride-based devices. PSD, which utilizes pulsed plasma as the excitation source rather than an excimer laser, is quite an attractive technique for driving improvements in throughput because it can supply high-energy film precursors onto large-area substrates. Here we described the recent progress achieved in the low-temperature heteroepitaxial growth of group III nitride films using PSD [4].

As substrate for the low-temperature heteroepitaxial growth of nitride films, 6H-SiC $(000\bar{1})$ was selected because SiC exhibits small mismatches with group III nitride semiconductors with respect to their lattice constants and thermal expansion coefficients. The SiC substrates were annealed in a gaseous mixture of H_2 (4 %) and He (96 %) at 1530 °C for 60 min at atmospheric pressure to obtain atomically flat surfaces. The surfaces of the SiC substrates after annealing had clear stepped and terraced structures with a step height of 1.5 nm [5], which corresponded to the six-bilayer structure of SiC. After dipping into HF (3 %) and HCl (3 %) solutions, the substrates were transferred into a PSD chamber. First, 80-nm-thick AlN films were grown at substrate temperatures of room temperature (RT) and 800 °C on the prepared atomically flat SiC substrates. Sputtering on Al metal target was performed in N_2/Ar at ambient temperature while the pressure was varied from 1 to 3 mTorr. Ambient N_2 activated by the pulsed discharge was used as the nitrogen source for the AlN. During growth, the surfaces of the films were monitored using reflection high-energy electron diffraction (RHEED). To investigate the thermal stability of the heterointerfaces between the RT-grown AlN films and the SiC substrates, annealing of the samples was performed at 1200 °C for 10 min under an N_2 ambient at atmospheric pressure. The structural properties of the AlN films were characterized via high-resolution X-ray diffraction (HRXRD) analysis, and the surface morphologies of the films were investigated using atomic force microscopy (AFM).

The AlN films grown at RT on the SiC substrates showed clear RHEED diffraction patterns that were characteristic of *c*-plane AlN, indicating that the AlN films had grown epitaxially, even at RT, likely because of the enhanced surface migration of Al atoms caused by the pulsed supply of the high-energy Al species. Figure 13.1a, b shows AFM images of AlN films grown at 800 °C and RT,

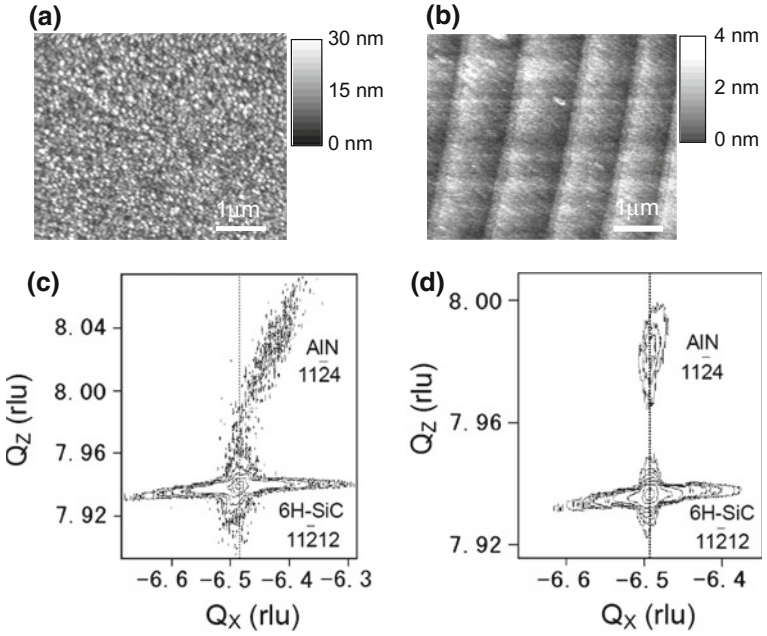

Fig. 13.1 AFM images of the AlN films grown at **a** 800 °C and **b** RT. RSM for the asymmetric 11$\bar{2}$4 diffractions of AlN films grown at **c** 800 °C and **d** RT. Sato et al. [4]. Copyright 2009, The Japan Society of Applied Physics

respectively. A large number of randomly distributed three-dimensional islands could be observed on the surface of the AlN film grown at 800 °C. On the other hand, the surface morphology of the RT-grown AlN film was quite smooth. Straight steps and atomically flat terraces were clearly observed in the AFM image. The step height in this image was estimated to be approximately 1.5 nm, which corresponds to 6 MLs of AlN. This observation indicated that the step height of the SiC substrate was preserved during the growth of AlN at RT. In addition, the $2\theta/\omega$ curves of the XRD measurements for the AlN films grown at RT had a clear AlN 0002 diffraction peak at 35.8°. Because the 0002 diffraction for bulk AlN appeared at 36.0°, and in fact, AlN films grown at 800 °C have a clear diffraction peak at this angle, it can be concluded that the RT-grown AlN film was highly strained. Reciprocal space mapping (RSM) measurements for the asymmetric 11$\bar{2}$4 diffractions of the AlN films grown at 800 °C and RT were also performed to investigate the lattice strain in the AlN films, and the results are shown in Fig. 13.1c, d, respectively. Although a large portion of the lattice strain was relaxed in the AlN film grown at 800 °C, the *a*-axis lattice parameter of the RT-grown AlN film was 0.308 nm, which is the same as that for SiC. These results indicated that the introduction of misfit dislocations at the AlN/SiC heterointerfaces was suppressed by reducing the growth temperature to RT. Although the critical thickness of the AlN films on the SiC substrates was

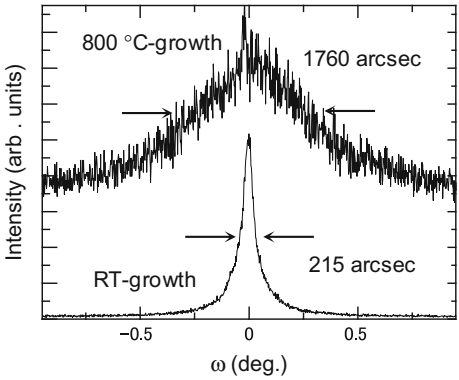

Fig. 13.2 XRCs of the $10\bar{1}2$ diffractions for AlN films grown at 800 °C and RT. Sato et al. [4]. Copyright 2009, The Japan Society of Applied Physics

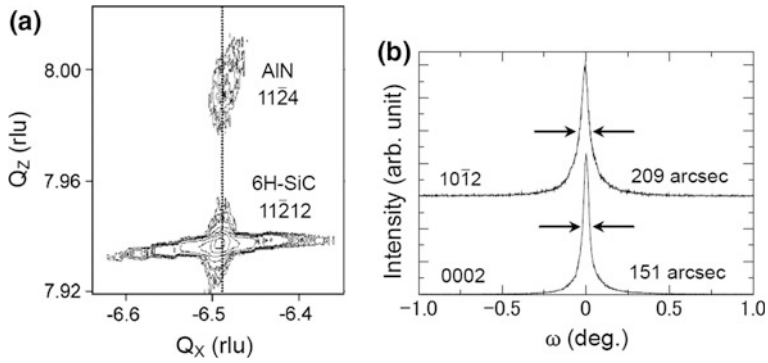

Fig. 13.3 **a** RSM and **b** XRCs for an RT-grown AlN film after annealing at 1200 °C. K. Sato et al. [4]. Copyright 2009, The Japan Society of Applied Physics

calculated to be 27 nm according to the "force balance" model proposed by Fischer et al. [6], in this study, the lattice strain in the AlN film grown at RT was not released, even at a film thickness of 80 nm. This result indicated that the activation energy for the introduction of misfit dislocations was too large to be overcome for growth at RT. The crystalline quality of the AlN films was also evaluated by measuring their X-ray rocking curves (XRCs). The full-width at half-maximum (FWHM) values for the 0004 and $10\bar{1}2$ XRCs for the RT-grown AlN film were 150 and 215 arcsec, respectively. Notably, the FWHM value of the $10\bar{1}2$ diffraction for the AlN film grown at 800 °C was as large as 1760 arcsec, as shown in Fig. 13.2. This dramatic improvement in crystalline quality by reducing the growth temperature can be attributed to suppression of the introduction of misfit dislocations.

To investigate the thermal stability of the heterointerface between the RT-grown AlN and SiC, annealing of RT-grown samples was performed at 1200 °C. As shown in the RSM in Fig. 13.3a, the position of Qx for the $11\bar{2}4$ diffraction of AlN

still coincided with that for the SiC $11\bar{2}12$ diffraction, even after annealing at 1200 °C. In addition, the *a*-axis lattice parameter for the RT-grown AlN annealed at 1200 °C was calculated to be 0.308 nm, which is the same as that before annealing. This result indicated that misfit dislocations were not introduced in the AlN film, even after annealing at 1200 °C, and that the activation energy for the introduction of misfit dislocations is thus quite high. Interestingly, misfit dislocations were introduced in the AIN grown at 800 °C. This difference is likely due to the rough surface of the AlN grown at 800 °C, which possibly reduces the activation energy for the introduction of misfit dislocations. Finally, as shown in Fig. 13.3b, the FWHM values of the 0002 and $10\bar{1}2$ XRCs for the RT-grown AlN after annealing were 151 and 209 arcsec, respectively, which were nearly the same as those before annealing. These results indicated that the heterointerface between the RT-grown AlN and SiC is highly stable once it is formed. This thermal robustness makes the RT-AlN/SiC samples promising as templates for the fabrication of various nitride devices.

In summary, it was found that PSD use allows the growth of epitaxial AlN films on SiC substrates even at RT, which is likely due to the supply of highly energetic film precursors via pulsed sputtering. The FWHM values of the XRCs for the 0004 and $10\bar{1}2$ diffractions of RT-grown AlN films on SiC substrates were as low as 150 and 215 arcsec, respectively. Also, the introduction of misfit dislocations is revealed to be suppressed during RT growth, which is likely the reason for the improvement in the crystalline quality with the reduction of the growth temperature. In addition, misfit dislocations were not introduced even after annealing at 1200 °C, indicating that the activation energy for the introduction of dislocations is considerably high for the AlN/SiC structure. These combined results suggest that using PSD is promising for the low-temperature fabrication of nitride-based optical and electronic devices.

13.2.2 Low-Temperature Fabrication of Nitride LEDs Using PSD

InGaN LEDs have been fabricated using well-established MOCVD technology. The process temperature of MOCVD growth typically exceeds 1000 °C; however, this limits the substrate choice to expensive single-crystal materials, such as sapphire and Si. Recently, amorphous glass, typically used in liquid crystal displays (LCDs), has attracted much attention as a substrate material for the growth of nitrides [7] because it is available in sizes greater than 2×2 m^2, which is much larger than the sizes of sapphire and Si substrates. However, such glass is not stable in the MOCVD growth process because the growth temperature is much higher than the glass softening temperature of approximately 500 °C. Therefore, to extend the application of nitride-based optoelectronic devices on large-area glass, reduction in the growth temperature plays an important role.

Pulsed sputtering is a promising candidate for the low-temperature growth of nitride devices because it enables the growth of epitaxial nitride films, even at RT because of the enhanced surface migration of the growth precursors generated using a pulsed supply of group III metals. In fact, as mentioned in the previous section, nitride films grown using PSD at RT exhibit excellent structural properties. However, despite the potential of PSD for the fabrication of device-quality group III nitride films at low temperatures, their electrical and optical properties are yet to be fully explored. In particular, p-type doping in GaN at low temperatures remains problematic because films grown at low-temperature generally suffer from the incorporation of donor-like native defects and residual impurities, such as oxygen. Therefore, understanding the influence of PSD growth parameters on the structural and electrical properties of Mg-doped GaN grown at low temperatures is quite important.

This section focuses on the methodology for achieving p-type conduction in low-temperature-grown GaN using PSD and demonstration of the fabrication of InGaN LEDs at the low temperature of 480 °C [8].

All nitride layers were grown in a conventional PSD chamber at a temperature of 480 °C. First, tests on an Mg-doped sample were performed using semi-insulating GaN on sapphire templates for optimizing the growth conditions.

In the low-temperature growth of Mg-doped GaN, the Ga/N growth stoichiometry significantly affects its structural and electrical properties. Thus, to achieve p-type conductivity in low-temperature-grown GaN, precise control of the Ga/N growth stoichiometry and balance between the Ga and nitrogen supply is quite important. Figure 13.4 shows the AFM surface image of Mg-doped GaN with different Ga/N growth stoichiometries. Table 13.1 also summarizes the carrier concentrations and mobilities estimated from Hall measurements. For the N-rich growth condition, surface roughing occurred because of insufficient Ga migration, which likely caused significant incorporation of residual donors, such as oxygen. In fact, this film exhibited significant n-type conductivity with an electron concentration greater than 10^{19} cm^{-3}. On the other hand, for the Ga-rich condition, although enhanced Ga migration on the growth surface led to improvement in the

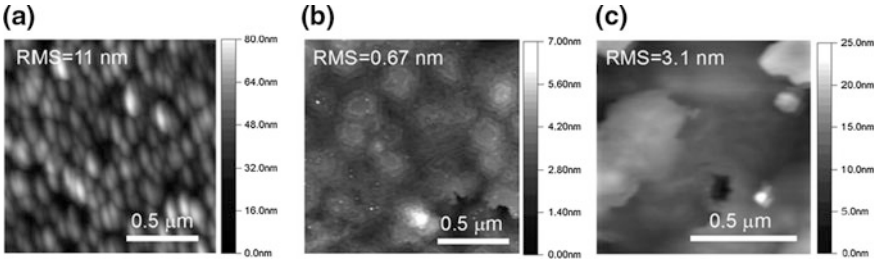

Fig. 13.4 AFM surface images of Mg-doped GaN grown at 480 °C under **a** N-rich, **b** near stoichiometric, and **c** Ga-rich condition. Reprinted with permission from Nakamura et al. [8]. Copyright 2014, AIP Publishing LLC

Table 13.1 Carrier concentrations and mobilities of Mg-doped GaN grown at 480 °C with different growth stoichiometries

Growth condition	Carrier type	Carrier concentration (cm^{-3})	Mobility ($cm^2\ V^{-2}\ s^{-1}$)
N-rich	n-type	1.5×10^{19}	22
Near stoichiometric	p-type	3.0×10^{17}	3.1
Ga-rich	n-type	4.7×10^{18}	42

surface morphology, the Mg-doped film still exhibited n-type conductivity with an electron concentration in the mid 10^{18} cm^{-3}. This behavior is likely due to the introduction of nitrogen vacancies that act as compensating donors. Theoretical calculations indicated that under Ga-rich conditions, nitrogen vacancies are likely to be incorporated into Mg-doped GaN because of a reduction in their formation energy [9]. In addition, at such a low growth temperature, Ga-rich conditions led to significant Ga accumulation during growth of the GaN layer due to negligible Ga desorption. In fact, after growth, high-density Ga droplets with diameters of several microns were observed on the surface. On the other hand, at near stoichiometric conditions, an atomically flat, clear step, and terrace structure was observed for the GaN layer, and the root-mean-square (RMS) value of its surface roughness was as low as 0.67 nm. In addition, only this sample exhibited p-type conductivity with a hole concentration and mobility of 3.0×10^{17} cm^3 and 3.1 $cm^2\ V^{-1}\ s^{-1}$, respectively. This result was likely due to the improvement in the surface morphology and a reduction in the number of point defects. Temperature-dependent Hall measurements yielded an estimated activation energy for the Mg acceptor of 153 meV, which is comparable to values obtained for Mg-doped GaN grown via conventional high-temperature MOCVD [10]. Furthermore, after annealing at high temperature, which is advantageous for the reduction of the process temperature for LED fabrication, the as-grown sample exhibited clear p-type conductivity without activation. Overall, these results demonstrated that for low-temperature growth of Mg-doped GaN using PSD, precise control of the growth stoichiometry is critical for suppressing the incorporation of intrinsic and extrinsic point defects and consequently achieving p-type doping.

Using these results, InGaN LEDs were fabricated at a process temperature of below 500 °C. The LED epitaxial structures consisted of a 4-m-thick n-GaN layer, 0.03-m-thick $In_{0.33}Ga_{0.67}N$ active layer, and a 0.3-m-thick p-GaN layer. This sample showed a bright photoluminescence (PL) emission peak near 640 nm at RT. Temperature-dependent PL measurements also gave an internal quantum efficiency of 24 %, which was estimated from the ratio of the integrated PL intensity at 293 and 15 K, assuming that the efficiency at 15 K was 100 %. During current–voltage measurements, the LED mesa-structures exhibited good rectifying characteristics with a leakage current of 3×10^{-5} A at −5 V. Figure 13.5 shows the electroluminescence (EL) spectra with forward currents ranging from 5 to 20 mA and a photograph at a forward current of 20 mA. A clear orange emission was observed near 640 nm, and the intensity of the EL emission increased with the forward

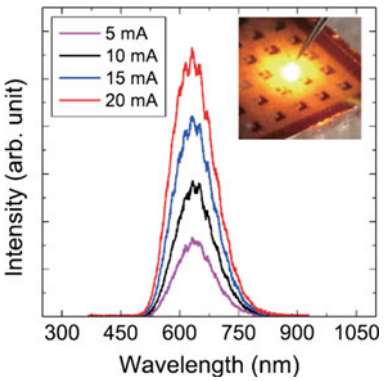

Fig. 13.5 EL spectra of LED structure grown at 480 °C at forward currents from 5 to 20 mA. *Inset* photograph of orange EL at forward current of 20 mA. Reprinted with permission from Nakamura et al. [8]. Copyright 2014, AIP Publishing LLC

current. These results represent the demonstration of EL emission from a nitride-based LED structure fabricated at a process temperature below the glass softening temperature. These results indicate that this low-temperature PSD growth technique is quite promising for the fabrication of nitride-based light-emitting devices on large-area glass substrates.

13.2.3 Fabrication of HEMTs Using PSD

Heteroepitaxial growth of GaN on Si wafers has attracted much attention for its potential applications in high-power electronic and light-emitting devices [11–15] because the use of Si wafers offers several advantages: high thermal conductivity, availability of low-cost large wafers, and possibility of integration with Si devices. To date, most GaN-based devices on Si substrates have been fabricated using MOCVD. However, the high substrate temperatures (>1000 °C) required during MOCVD growth are known to form cracks in GaN films on Si wafers because of the large mismatch in the thermal expansion coefficients of GaN (5.59×10^{-6} K^{-1}) and Si (3.59×10^{-6} K^{-1}). In addition, this mismatch causes bowing of the Si wafers, which makes the lithography process difficult during device fabrication. Therefore, complicated growth processes, such as the introduction of strain mitigation layers, are used to grow crack-free GaN films on Si wafers with processable bowing using MOCVD [16, 17]. An alternative and straightforward strategy for solving the thermal mismatch problem is to reduce the growth temperature for GaN. PSD is possibly useful for low-temperature epitaxial growth of nitride films in which sputtered species impinge on the sample surface with high kinetic energy. Here, we describe the growth of GaN films on Si substrates using a PSD low-temperature growth technique and its application to the fabrication of AlGaN-/GaN-based HEMTs [18].

Si (111) wafers are typically used for growing GaN because they share threefold rotational symmetry with the most stable (0001) plane of GaN. However, several

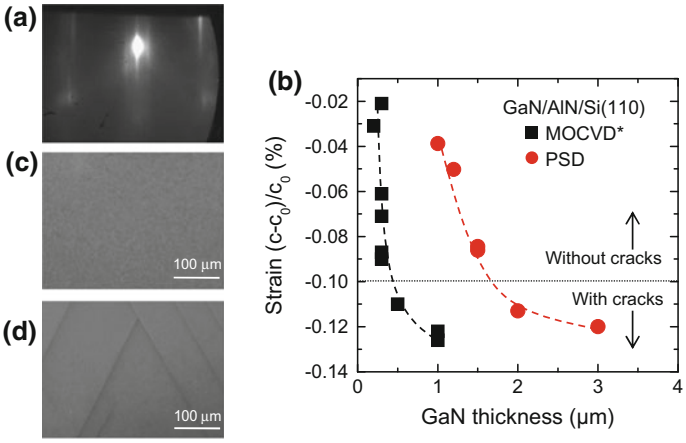

Fig. 13.6 **a** RHEED patterns of GaN films grown on Si (110) using PSD with the electron beam parallel to the [11–20] $_{GaN}$. **b** Strain along the *c*-axis of GaN films on Si (110) substrates as a function of the GaN thickness. *Circles* and *squares* indicate GaN films grown via PSD and MOCVD [7], respectively. SEM images of the GaN films with thicknesses of **c** 1.5 and **d** 2.0 μm. Reprinted with permission from Watanabe et al. [18]. Copyright 2014, AIP Publishing LLC

groups have reported the epitaxial growth of GaN films on Si (110) and fabrication of LEDs and HEMTs using conventional techniques, such as MOCVD [19–21]. Thus, Si (110) wafers were selected in this study as a potential for future integration of GaN devices with Si complementary metal–oxide–semiconductor (CMOS) technology [22]. After the formation of oxide layers on the Si surfaces using a conventional wet chemical cleaning process [23], the substrates were introduced into the PSD chamber. First, 60-nm-thick AlN nucleation layers were grown on the Si substrates, followed by the PSD growth of epitaxial GaN layers at 750 °C. The thickness of the GaN films was varied from 1 to 3 μm to investigate the strain evolution and crack formation in the films. A carbon-doped GaN film was used as a highly resistive buffer layer for an AlGaN/GaN HEMT structure.

Figure 13.6a presents the RHEED pattern of a GaN film grown on a Si (110) substrate with an AlN nucleation layer. The clear streaky pattern with satellite lines just outside the integral order lines, which is known as a "1 × 1" reconstructed pattern [24], indicated the formation of Ga-polarity GaN films. Careful interpretation of the RHEED pattern also revealed that the in-plane alignment of the GaN and Si layers was $[10\bar{1}0]_{GaN}$ parallel to $[001]_{Si}$; this epitaxial relation is consistent with literature reports [21]. The strain states in GaN films of various thicknesses were then studied on the basis of their *c*-axis lengths, which were deduced from corresponding XRD $2\theta/\omega$ curves [17]. Figure 13.6b shows the dependency of strain along the *c*-axis on the GaN film thickness. It can be clearly observed that the *c*-axis length of the GaN films decreased as the GaN thickness increased, indicating the accumulation of tensile strain in the films. In the scanning electron microscopy (SEM) images shown in Fig. 13.6c, d, it can be respectively seen that no cracks formed in the 1.5-m-thick GaN

film, while high-density cracks were observed on the surface of the 2.0-m-thick GaN film. These results indicated that the cracks were generated when the strain along the *c*-axis exceeded approximately −0.1 %. Similar results have been reported for GaN growth via MOCVD [17]. Notably, the critical thickness for crack generation during PSD was much larger than that for MOCVD. This difference can be attributed to the lower growth temperature of PSD because strain accumulation is typically associated with the difference between the growth temperature and room temperature. The FWHM values for the XRCs of the 1.5-m-thick GaN film were 709 and 752 arcsec for the GaN 0002 and $10\bar{1}2$ diffractions, respectively. These values are comparable with those of an MOCVD-grown sample (363 and 993 arcsec for the 0002 and $10\bar{1}0$ diffractions, respectively [19]). In addition, further improvement in the crystalline quality should be possible if special structures are used for dislocation reduction, such as an ultrathin SiN nano-mask layer that blocks the propagation of threading dislocations [25].

Next, carbon doping of the GaN layers was performed to grow highly resistive GaN buffer layers beneath the AlGaN/GaN HEMT structure. Figure 13.7a shows the RT PL spectrum of a carbon-doped GaN buffer layer grown using PSD. The emission near 2.85 eV and the large yellow emission at 2.2 eV likely originated from the carbon incorporated into the GaN buffer layer [26, 27]. It was also found that the as-grown carbon-doped GaN layer exhibited semi-insulating characteristics, and that carbon doping had a negligible impact on the FWHM values of the XRCs and the surface morphology of the GaN. These results indicate that PSD-grown carbon-doped GaN layers are very promising as highly resistive buffer layers for the fabrication of AlGaN/GaN heterostructures on Si. An unintentionally doped GaN layer with a thickness of 120 nm was grown on top of the 1.4-m-thick carbon-doped GaN buffer layer followed by a 20-nm-thick AlGaN barrier layer. The XRD $2\theta/\omega$ curve for the AlGaN/GaN heterostructure exhibited only {0001}-related diffraction peaks (Fig. 13.7b), indicating that the (0001) plane of the nitride

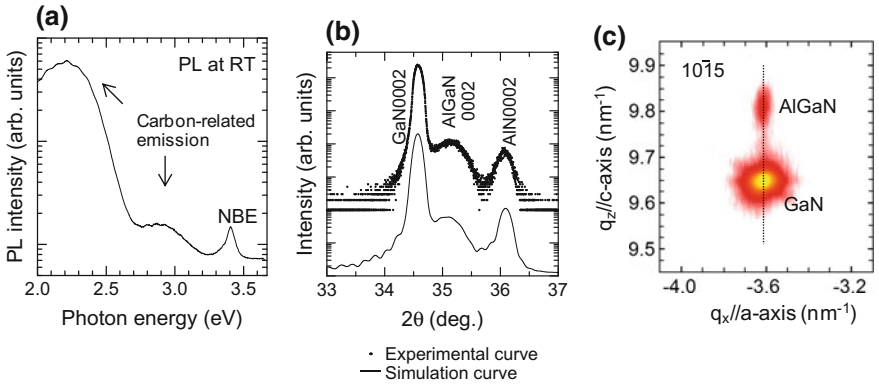

Fig. 13.7 **a** RT photoluminescence spectrum of a carbon-doped GaN buffer layer. **b** XRD $2\theta/\omega$ curve and **c** RSM for the asymmetric 101-5 diffraction of the AlGaN/GaN heterostructure on Si (110). Reprinted with permission from Watanabe et al. [18]. Copyright 2014, AIP Publishing LLC

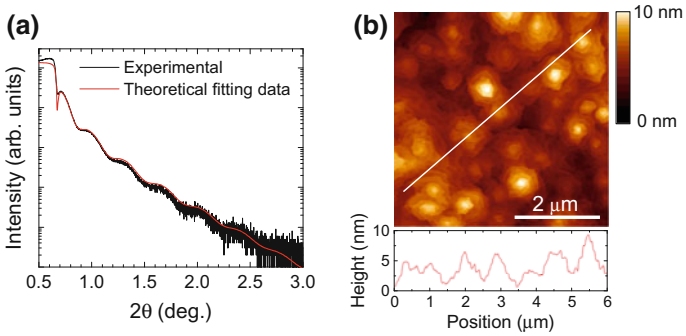

Fig. 13.8 **a** XRR curve and its theoretical fitting based on the Fresnel equation and **b** surface AFM image for the AlGaN/GaN heterostructure. Reprinted with permission from Watanabe et al. [18]. Copyright 2014, AIP Publishing LLC

was parallel to the Si (110) surface. The Al composition in the AlGaN layer was estimated to be 25 % from a simulation assuming that the AlGaN layer was fully strained to the underlying GaN layer. Figure 13.7c presents a reciprocal space map for the asymmetric $10\bar{1}5$ diffractions of the AlGaN/GaN heterostructure. The reciprocal points for AlGaN and GaN were located at the same position q_x, indicating that the AlGaN layer coherently grew on the GaN without lattice relaxation. An X-ray reflectivity (XRR) analysis was also performed to investigate the roughness at the interface and of the surface of the AlGaN/GaN heterostructure. In Fig. 13.8a, the XRR curve and its theoretical fitting based on the Fresnel equation [28, 29] are shown. The experimental XRR curve was well fitted by the AlGaN/GaN two-layer model with an Al composition of 27 ± 3 %, which is consistent with the XRD results. On the basis of the theoretical fitting results, the RMS values for the surface and interface roughnesses were determined to be as little as 1.0 and 1.1 nm, respectively. The surface of the AlGaN/GaN heterostructure observed using AFM is shown in Fig. 13.8b. The stepped and terraced surface typical for spiral growth with an RMS roughness value of 1.6 nm can be clearly seen in the image, which is in agreement with the XRR investigation. These results indicated that the growth of the AlGaN/GaN heterostructure using PSD yielded a smooth surface and abrupt interface. In addition, capacitance–voltage (CV) measurements of this structure uncovered the existence of a two-dimensional electron gas (2DEG) at the heterointerfaces, while room-temperature Hall effect measurements on the van der Pauw configuration revealed that the 2DEG at the AlGaN/GaN heterointerface had a mobility of 1360 $cm^2\ V^{-1}\ s^{-1}$ with a sheet carrier density of $1.3 \times 10^{13}\ cm^{-2}$ and a sheet resistance of 386 $\Omega\ sq^{-1}$. These values are comparable to those reported for AlGaN/GaN heterostructures on Si substrates prepared via MOCVD [30].

An HEMT based on the AlGaN/GaN heterostructure was then fabricated using PSD. Ti/Al/Ni/Au (30/70/40/20 nm) ohmic contacts were formed using a lift-off process followed by rapid thermal annealing at 800 °C for 45 s under 1 atm of

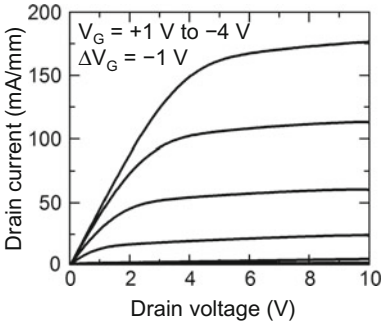

Fig. 13.9 Output characteristics of an AlGaN/GaN HEMT fabricated on Si (110) using PSD. Reprinted with permission from Watanabe et al. [18]. Copyright 2014, AIP Publishing LLC

nitrogen. Device isolation was achieved using a dry etching process with a Cl_2-based inductively coupled plasma. Schottky gate contacts were fabricated via the vacuum evaporation of Au (65 nm) using a lift-off process. Figure 13.9 shows the output characteristics of the HEMT with a gate length and width of 6 and 20 μm, respectively. Thus, operation of this HEMT fabricated using the PSD epitaxial growth technique was confirmed.

In summary, GaN films were grown on Si substrates using a low-temperature growth technique based on pulsed sputtering, and reduction in the growth temperature was found leading to suppression of strain in the GaN films, which in turn allowed an increase in the critical thickness for crack formation. It was also revealed that AlGaN/GaN heterostructures with flat interfaces can be prepared on C-doped insulating GaN buffer layers using PSD. The operation of an HEMT was demonstrated using the AlGaN/GaN, and the presence of a 2DEG with a mobility of 1360 $cm^2\ V^{-1}\ s^{-1}$ and a sheet carrier density of $1.3 \times 10^{13}\ cm^{-2}$ was confirmed. These results indicate that PSD low-temperature epitaxial growth of GaN is promising for fabricating future low-cost GaN power devices on Si substrates.

13.2.4 Fabrication of InN FETs

An InN crystal takes one of two crystallographic structures, the more stable hexagonal (wurtzite) structure or the metastable cubic (zincblende) structure. Theoretical calculations based on optical measurements predict that hexagonal InN possesses a high electron peak velocity exceeding $2 \times 10^8\ cm\ s^{-1}$ [31]. This value is much higher than those for conventional semiconductor materials, such as GaAs and GaN, used in high-speed electronics. This nature of hexagonal InN makes it a promising material for use in high-speed FETs. In fact, an InN-based MISFET with a channel length of 100 nm can be predicted to be theoretically operated at terahertz frequencies [32]. Despite these outstanding transport properties, the performance of FETs fabricated with hexagonal InN has been discouraging [33]. The transistors show poor on/off ratios and lack clear linear-saturation output characteristics. The problems with these InN transistors are believed to stem from the poor quality of

the hexagonal InN films and their interfaces with the surrounding insulators. Hexagonal InN films are typically grown on foreign crystals such as GaN [34, 35] or AlN [33, 36], resulting in considerably large lattice mismatches, which in turn leads to the formation of a high density of misfit dislocations at the interfaces [37]. These dislocations then propagate into the InN films and act as unintentional electron sources [38, 39], making it difficult to modulate the source-drain current (I_{DS}) in FETs via gating. Therefore, a new technique that enables the deposition of InN films with higher structural perfection must be developed for successfully fabricating high-performance InN-based FETs. The use of yttria-stabilized zirconia (YSZ) substrates is a good option for this purpose because there is a very small lattice mismatch (2.7 %) between YSZ and InN, which should provide a reduced defect density at the interface [40, 41]. The other advantage of using YSZ substrates lies in their insulating nature, which is important for the fabrication of FETs, because the use of semiconducting substrates may lead to an increase in the leakage current in the "off" state.

The characteristics of cubic (zincblende) InN, which is a metastable counterpart of stable hexagonal InN, are interesting. Generally, the optical and transport properties of group III nitrides in cubic and hexagonal structures are different due to the differences in their crystal symmetries and electronic band structures [42]. Cubic nitrides are typically believed to possess lower phonon scattering because of their higher crystalline symmetry compared to that of hexagonal nitrides [43]. Notably, a practical device simulation using the Monte Carlo method predicted that cubic GaN-based FETs should outperform hexagonal FETs [44]. Therefore, it is natural to believe that InN follows the same trend as the other group III nitrides.

13.2.4.1 Preparation of Lattice-Matched YSZ Substrates

Prior to film growth, the YSZ (111) substrates were thermally treated at 1000 °C in air such that cubic InN films with atomically flat surfaces could grow on them. During annealing, the substrates were capped with a sapphire wafer. This capping step is essential for reproducibly obtaining high-quality cubic InN films on YSZ. Figure 13.10a, b shows AFM images of YSZ (111) substrates before and after thermal treatment. The annealed surface possessed a clear step-and-terrace structure with a single-step height of approximately 0.6 nm, which roughly corresponded to two monolayers of YSZ (111). Atomically, flat surfaces are critical for epitaxial growth of high-quality InN films and fabricating transistors, because surface roughness often leads to the generation of defects.

13.2.4.2 Structural Characteristics of InN Films Prepared Using PSD

Cubic InN films were grown at 620 °C via PSD [4, 41]. The InN film thickness was controlled by varying the pulse number during sputtering. The average deposition rate of the film precursors was adjusted such that growth of an InN monolayer was

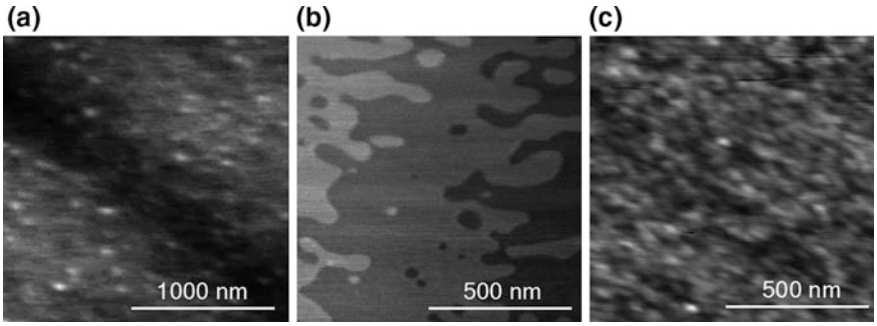

Fig. 13.10 AFM surface images of YSZ (111) and ultrathin InN. **a** As-received YSZ (111) surface. **b** The surface of YSZ became atomically flat after thermal annealing at 1000 °C. Atomic steps appeared on the surface. **c** Epitaxial InN film grown on the atomically flat YSZ (111). The RMS roughness for the InN surface was 0.18 nm. Figure reproduced from M. Oseki, K. Okubo, A. Kobayashi. J. Ohta, and H. Fujioka, Scientific Reports 4, 3951 (2014)

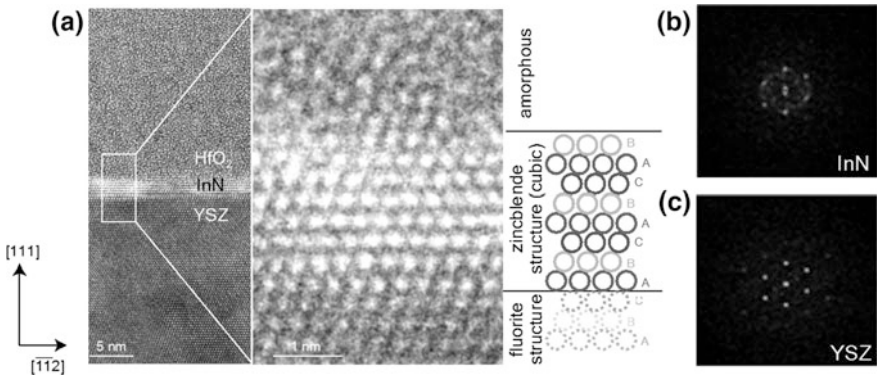

Fig. 13.11 **a** High-resolution TEM image of an amorphous-HfO_2/cubic-InN/YSZ interface. The expanded TEM image reveals that high-quality cubic InN (111) grew on the YSZ (111), and that abrupt HfO_2/InN and InN/YSZ interfaces were formed. The stacking sequence for YSZ is the same as that for InN. **b** Fourier-transformed image of InN and **c** Fourier-transformed image of YSZ in the TEM image. The symmetries in **b** and **c** are the same, indicating that the symmetry of the cubic YSZ was transferred to the InN film. Figure reproduced from M. Oseki, K. Okubo, A. Kobayashi. J. Ohta, and H. Fujioka, Scientific Reports 4, 3951 (2014)

completed in 2.7 s. The epitaxial InN films formed on the YSZ (111) substrates were continuous and without cracks or pits on their surfaces (Fig. 13.10c). The RMS value of the surface roughness for the films was as low as 0.18 nm, which is sufficiently smooth for fabricating an abrupt interface with, for example, a gate oxide insulator used in the fabrication of FETs.

Figure 13.11a shows a cross-sectional TEM image of ultrathin (2 nm) InN grown on a YSZ (111) substrate. Because the sample was intended to be part of an FET, an amorphous HfO_2 gate insulator was deposited on top of the InN film. The

stacking sequences of hexagonal (wurtzite) InN along the <0001> direction and cubic (zincblende) InN along the <111> direction are.*ABABAB*. and.*ABCABC*., respectively, where *A*, *B*, and *C* denote InN layers with different atom positions. Careful interpretation of the TEM image revealed that the stacking sequence for this InN was that of the (111)-oriented cubic (zincblende) structure. In addition, the stacking sequence of the cubic InN replicated that of the YSZ substrate. The successful growth of cubic InN was achieved because of the stacking sequence of the fluorite structure in YSZ, which has a zincblende-like structure. The white dots in the YSZ in Fig. 13.11a represent Zr(Y) atoms stacked in the sequence.*ABCABC*., which is the same as that for cubic InN. Figure 13.11b, c shows the Fourier-transformed images of the InN and YSZ in Fig. 13.11a, respectively. The distribution of spots in Fig. 13.11b is similar to that of Fig. 13.11c, indicating that the InN crystallized in the cubic structure. All of these results support the conclusion that the growth of cubic InN (111) occurred on the cubic YSZ (111) substrate.

13.2.4.3 Characteristics of InN FETs

FETs with cubic InN channel thicknesses of 2 and 5 nm were then fabricated using the newly developed cubic InN growth technique. An optical microscopic image and schematic view of a representative FET are shown in Fig. 13.12. To fabricate the FETs, 100 μm × 50 μm islands substrates were formed in the cubic InN films on the YSZ (111) using photolithography and inductively coupled plasma reactive ion etching techniques. A 50-nm-thick Au layer was then deposited on each of the InN surfaces and used as the source and drain electrodes. A 20-nm-thick HfO_2 gate insulator was then deposited at 200 °C on each FET using atomic layer deposition. The HfO_2 was in the amorphous phase, which was confirmed by analyzing the TEM

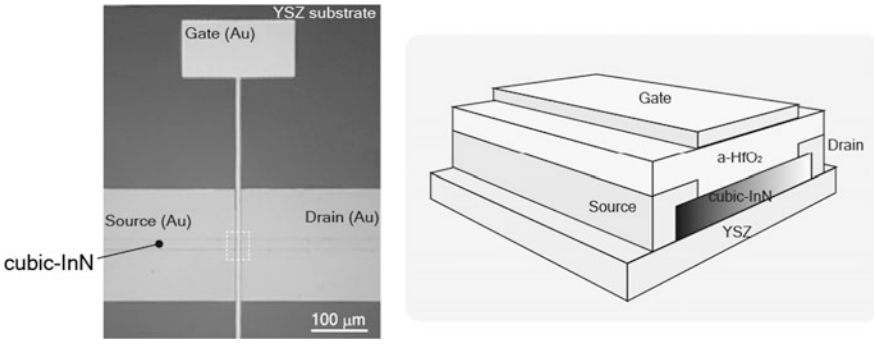

Fig. 13.12 Optical micrograph and schematic of a cubic (zincblende) InN-based FET. Mesa etching of cubic InN epitaxially grown on YSZ substrates was performed using conventional photolithography and dry etching. The cubic InN channel layers were covered with Au (source and drain electrodes) and amorphous HfO_2 (gate insulator). Reproduced from M. Oseki, K. Okubo, A. Kobayashi. J. Ohta, and H. Fujioka, Scientific Reports 4, 3951 (2014)

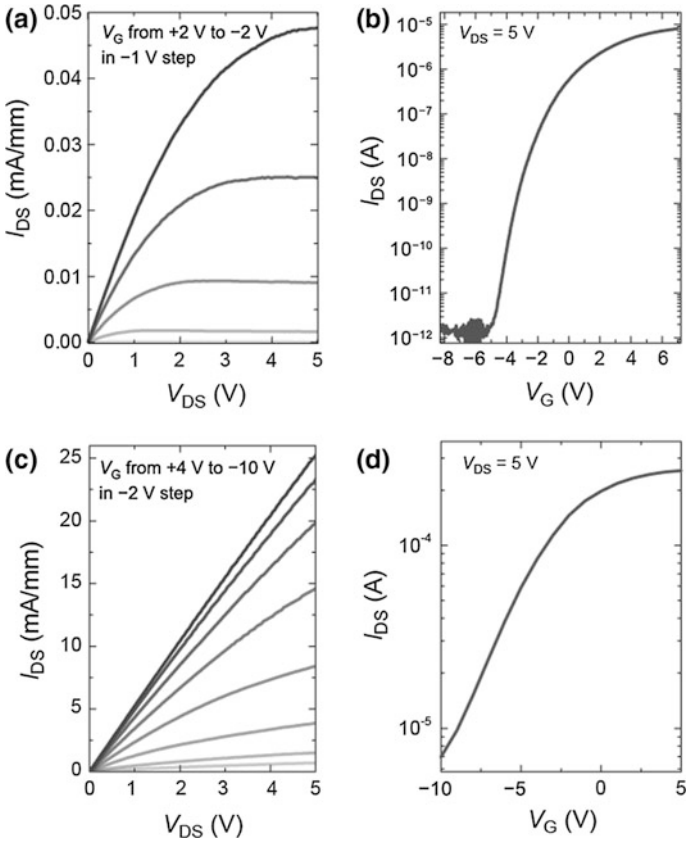

Fig. 13.13 **a** Output and **b** transfer characteristics of a cubic InN FET with a 2-nm-thick channel. The width and length of the gate are 50 and 20 μm, respectively. The I_{DS} on/off ratio at V_{DS} = 5 V is approximately 5 × 10^6. **c** Output and **d** transfer characteristics of a cubic InN FET with a 5-nm-thick channel. The width and length of the gate are 10 and 50 μm, respectively. The field-effect mobility in the linear region is calculated to be 44 cm^2 V^{-1} s^{-1}. Reproduced from M. Oseki, K. Okubo, A. Kobayashi. J. Ohta, and H. Fujioka, Scientific Reports 4, 3951 (2014)

images (Fig. 13.11a). The quality of the heterointerfaces between the gate insulators and semiconductors is critically important for fabricating high-performance FETs. Notably, the HfO_2/InN interface was found to be abrupt. Finally, an Au film was deposited on the HfO_2 and used as a gate electrode. The gate length L_G and width W_G of the FETs varied from 5 to 50 μm.

Figure 13.13a presents the output characteristics of the HfO_2/2-nm-cubic-InN/YSZ FET. The current through the cubic InN was seen to be well controlled by changing V_G, which clearly exhibited linear and saturation regions, indicating that the characteristics of this FET follow conventional, simple FET theory. In addition, the FET operated in the depletion mode, indicating that the ultrathin cubic InN had a conduction channel for electrons, even at zero bias.

Figure 13.13b shows the transfer characteristics of the 2-nm-thick device. The on/off current ratio was approximately 5×10^6. In this sample, the electrons were well depleted by the negative gate bias in the "off" state, and I_{DS} decreased to the order of pA. The off-state characteristics of this FET were thus better than those of SiO_2/hexagonal-InN/AlN FETs, whose off current is at a level of nA [6], indicating that high-quality HfO_2/cubic-InN/YSZ interfaces were formed using the newly developed process. The field-effect mobility (μ_{FE}) calculated using the relation for the linear region ($I_{DS} = (\mu_{FE} C_i W_G / L_G)\ (V_{GS} - V_{TH})\ V_{DS}$) was 0.17 $cm^2\ V^{-1}\ s^{-1}$. Figure 13.13c, d shows the output and transfer characteristics of the FET, respectively, with a channel thickness of 5 nm. The drain current was approximately two orders of magnitude larger than that of the 2-nm-thick InN FET. Maximum values for the I_{DS} and μ_{FE} in this study were 61 mA mm^{-1} and 58 $cm^2\ V^{-1}\ s^{-1}$, respectively, which were obtained for an FET with a channel thickness of 5 nm, $W_G = 20$ μm, and $L_G = 50$ μm. These values increased nonlinearly with an increase in the channel thickness, indicating that FETs' fabrication with thicker cubic InN channel layers should lead to an improvement in the driving performance of the FETs.

13.3 Preparation of Nitride Devices on Amorphous SiO_2 Substrates

InGaN-based LEDs have been widely accepted as highly efficient light sources capable of replacing incandescent bulbs. However, applications of InGaN LEDs are limited to small devices because their fabrication process involves expensive epitaxial growth of InGaN via MOCVD on single-crystal wafers. If a low-cost epitaxial growth process, such as sputtering on large-area substrates, is developed, fabrication of large-area InGaN light-emitting displays should be possible. In this section, recent progress in the growth of group III nitride films on amorphous SiO_2 using PSD is described [45, 46], and the application of PSD to the fabrication of flexible and large-area LEDs is reviewed.

13.3.1 Growth of GaN on Amorphous SiO_2 Substrates

Numerous attempts have been made to replace single-crystal substrates for the growth of group III nitrides with low-cost, large-area materials such as glass, metal, and various oxides [1, 2, 13, 47, 48]. Among these candidates, glass is an ideal substrate material for large-area, low-cost LEDs because of its transparency and compatibility with existing LCD fabrication processes. Despite these advantages, GaN films grown on glass have not been practical because of two serious problems. The first is the amorphous nature of glass, which leads to poor crystalline quality of

the overlaid nitride semiconductor layer. To overcome this problem, a highly oriented crystalline buffer layer can be inserted between the substrate and nitride film. Graphene is one of the most suitable materials because large-area graphene films with highly oriented structures can be easily deposited using chemical vapor deposition (CVD) [49, 50] and are easily transferred onto various substrates that have not previously been used as semiconductor growth materials [51–53]. The other problem is a low softening temperature (500–700 °C) for glass substrates. Because the substrate temperature for GaN growth typically exceeds 1000 °C for conventional MOCVD, using glass substrates for GaN growth via MOCVD is impossible. Nevertheless, recent progress in epitaxial growth techniques based on PSD has enabled the high-quality group III nitride crystals growth, even at room temperature. The successful reduction in the growth temperature was achieved because of the high kinetic energy and pulsed supply of group III atoms, which assist the surface migration of film precursors at substrate surfaces [4]. Successful fabrication of 640 nm InGaN LEDs via PSD at a maximum process temperature of 480 °C has been reported [8]. Here we show the structural properties of group III nitride films grown on amorphous SiO_2 using graphene buffer layers.

The graphene layers were grown using CVD on Ni foil and transferred onto amorphous fused silica substrates or amorphous SiO_2 prepared via thermal oxidation of Si [52, 54]. Before growth of the group III nitride films, the graphene layers on the amorphous SiO_2 were heated at 600 °C for 30 min in a vacuum. The GaN and AlN films were grown on the cleaned substrates in a PSD chamber. The group III and V sources were group III metal targets and nitrogen gas, respectively. The GaN and A1N films were grown to thicknesses of 600 and 50 nm, respectively.

Figure 13.14a shows an SEM image of a GaN film grown without a graphene buffer layer. The surface consisted of randomly oriented grains with sizes in the order of several hundred nanometers. In contrast, as shown in Fig. 13.14b, the GaN film with the graphene buffer layer had a smooth surface morphology. The crystal orientations of the GaN films were then investigated using electron backscatter diffraction (EBSD). Figure 13.15 shows {0002} and $\{10\bar{1}2\}$ EBSD pole figures for a 20 × 20 μm^2 area on GaN films grown on SiO_2 (a) without and (b) with graphene buffer layers. The GaN film prepared without the graphene buffer layer showed broad spots in the {0001} pole figure and ring-shaped patterns in the $\{10\bar{1}2\}$ pole

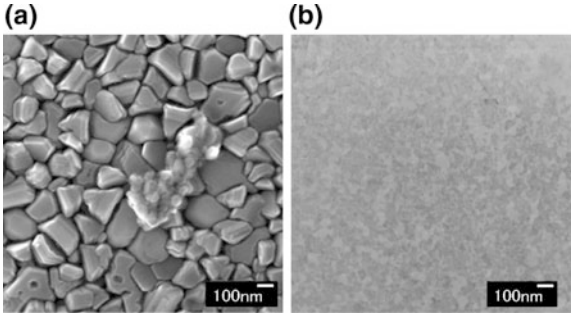

Fig. 13.14 SEM images of a GaN film grown on an amorphous SiO_2 substrate **a** without and **b** with a graphene buffer layer. Reproduced from Shon et al. [46]

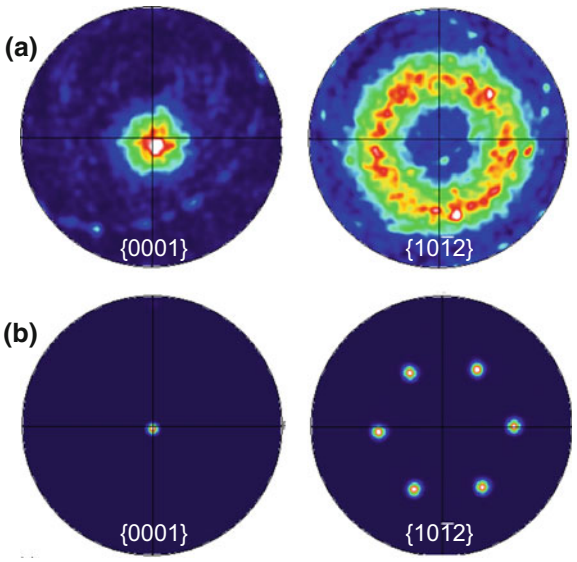

Fig. 13.15 {0002} and {101-2} EBSD pole figures for GaN films grown on amorphous SiO_2 **a** without and **b** with a graphene buffer layer. Reproduced from Shon et al. [46]

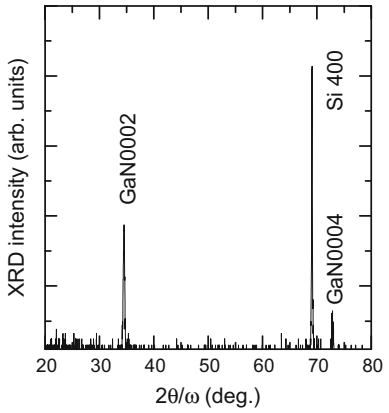

Fig. 13.16 XRD pattern for the GaN film grown on graphene/SiO_2. Shon et al. [45]. Copyright 2014, The Japan Society of Applied Physics

figure, which are consistent with the random orientation of small grains observed using SEM. In contrast, the {0001} spots for the GaN film prepared with a graphene buffer layer were small, and the $\{10\bar{1}2\}$ pole figure showed a clear sixfold rotational symmetry. This result indicated that the crystalline quality of the GaN films was drastically improved because of using the graphene buffer layer and can be attributed to the epitaxial growth of GaN on the highly oriented graphene. The epitaxial growth of GaN on graphene occurs with the epitaxial relation GaN (0001)/graphene(0001) [54]. Figure 13.16 shows an XRD $2\theta/\omega$ curve for the GaN film grown at 750 °C on graphene/SiO_2. The diffraction peaks observed at approximately 34.5°, 69.1°, and 72.9° coincide with diffractions for GaN 0002,

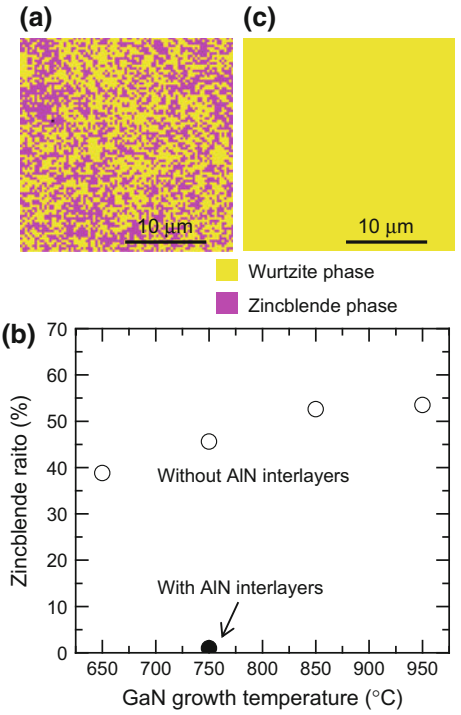

Fig. 13.17 EBSD phase maps of GaN films grown on graphene **a** without and **c** with AlN interlayers. **b** Zincblende phase ratio of the GaN films as a function of the growth temperature. Shon et al. [45]. Copyright 2014, The Japan Society of Applied Physics

Si 400, and GaN 0004, respectively. These results therefore indicated that GaN grew along the c-axis, which agreed well with the EBSD measurements.

Next, the phase purity of GaN films on graphene was investigated using EBSD. Figure 13.17a shows the phase map of a GaN film grown at 750 °C. Wurtzite and zincblende phases coexisted in the GaN film directly grown on graphene, and the proportion of the zincblende phases was as high as 45 %. In Fig. 13.17b, the percentage of the zincblende phase in GaN films with and without an AlN interlayer is plotted as a function of the growth temperature. Although the zincblende phase was reduced at lower growth temperatures, its proportion remained above 38 %, even at the lowest growth temperature (650 °C). In addition, carbon-related signals were detected using the X-ray photoelectron spectrum of the GaN film directly grown on graphene (data not shown), indicating the formation of an interfacial layer between the GaN and graphene. Because the zincblende phase apparently arises because of interfacial reactions at the GaN/graphene heterointerface [55], it should be effectively suppressed by inserting a blocking layer between the GaN and graphene. To test this theory, a 50-nm-thick AlN interlayer was deposited prior to GaN growth. Figure 13.17c shows the EBSD phase map of a GaN film grown at 750 °C with an AlN interlayer. The zincblende phase in this film was negligible, and the percentage of the zincblende phase was nearly zero, as evident from the figure. The optical properties of the GaN films grown on graphene were then investigated using

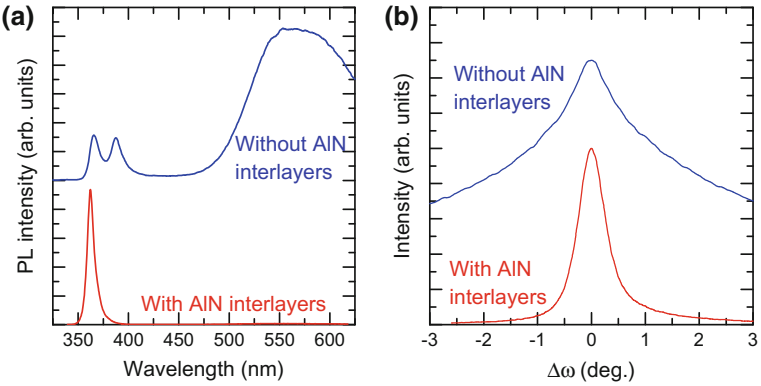

Fig. 13.18 **a** PL spectra and **b** XRC curves of GaN 0002 diffractions for the GaN films grown on MLG/thermally oxidized Si with (*red*) and without (*blue*) an AlN interlayer. Shon et al. [45]. Copyright 2014, The Japan Society of Applied Physics

RT PL measurements. The PL spectra of the GaN films with and without an AlN interlayer are shown in Fig. 13.18a. Without the AlN interlayer, the GaN film exhibited both clear excitonic emission from the zincblende phase at approximately 380 nm [56] and near-band-edge emission from the wurtzite phase at approximately 360 nm. The broad peak at 550 nm was a defect-related yellow luminescence, likely attributable to Ga vacancies or carbon impurities [57]. On the other hand, the GaN film grown with the AlN interlayer exhibited a strong near-band-edge emission from the wurtzite phase and negligible emission from the zincblende phase or deep levels. Figure 13.18b shows the XRCs of the 0002 diffractions of the GaN films with and without the AlN interlayer. The interlayer reduced the FWHM from 144 to 37 arcmin. These results indicated that interfacial reactions were suppressed and the quality of the GaN film was improved by inserting an AlN interlayer between the GaN and the graphene.

The performance of GaN-based devices also critically depends on the polarity of the *c*-axis-oriented GaN films [58, 59]. Therefore, the polarity of the GaN films was also investigated. An SEM image of the chemically etched surface of a GaN film grown on graphene with an AlN interlayer is shown in Fig. 13.19a. Etching considerably roughened the GaN surface, indicating the growth of N-polar GaN [60]. To fabricate a variety of GaN devices on graphene, such as LEDs and transistors, a technique is required that inverts the polarity from N to Ga. Recently, Ga-polar GaN was grown by forming an AlO_x layer on an N-polar GaN substrate [61]. For the present N-polar AlN/GaN grown on graphene, an AlO_x layer was formed by thermally oxidizing the AlN interlayer in air at 200 °C. As revealed by SEM observations (see Fig. 13.19b), the surface morphology of the GaN film on the oxidized AlN interlayer was unaltered by wet chemical etching. Because chemical resistance to KOH etching is a characteristic of Ga-polar GaN, the GaN polarity can be concluded to be reversed from N- to Ga-polarity due to the oxidation of the AlN

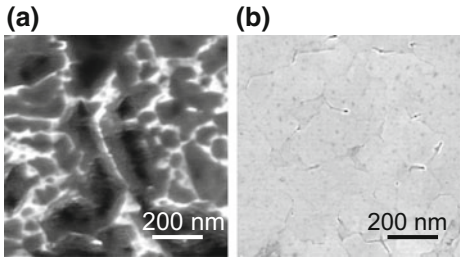

Fig. 13.19 SEM images of the GaN films on graphene after wet etching: **a** without and **b** with thermal oxidation of the AlN interlayer. Shon et al. [45]. Copyright 2014, The Japan Society of Applied Physics

interlayer. Therefore, by manipulating the polarity of GaN films on graphene, it should be possible to realize the design of highly efficient GaN-based devices.

In summary, GaN films were grown on graphene/amorphous SiO_2 stacks using PSD, and their structural properties were investigated. XRD and EBSD analyses revealed a high *c*-axis orientation of the GaN film on graphene. Both zincblende and wurtzite phases were observed in the GaN films grown on graphene, whereas the zincblende phase was diminished by inserting an AlN interlayer between the GaN and the graphene. The polarity of the GaN film was then controlled by altering the oxidation state of the AlN interlayer. The present technique may improve the quality and substrate versatility of graphene-grown GaN films. The technique is also potentially expandable to large-area GaN-based optical and electronic devices.

13.3.2 Fabrication of Full-Color LEDs on Amorphous SiO_2 Substrates

To confirm the high crystallinity of nitride films prepared on amorphous substrates via PSD, LEDs were fabricated on the AlN/graphene/SiO_2 structures. For an InGaN LED, five periods of InGaN/GaN multiple quantum wells (MQWs) were grown on a 1-m-thick n-type GaN layer and topped with an Mg-doped p-type GaN layer. The thicknesses of the MQW periodic structure and p-type GaN layer were 70 and 600 nm, respectively. The thick p-type layer was used to keep the surfaces of the LED structures smooth. Clear satellite peaks near the GaN 0002 diffraction peak in the XRD pattern in Fig. 13.20a indicated the smoothness and abruptness of the heterointerfaces in the MQWs. The fitting of the experimental XRD curves to the theoretical curves revealed that the MQWs consisted of 3.1-nm-thick $In_{0.21}Ga_{0.79}N$ wells and 8.6-nm-thick GaN barriers. Figure 13.20b shows a typical room-temperature PL spectrum obtained using a 405-nm violet laser as the excitation source. Green PL was clearly observed with a peak wavelength of 520 nm. The temperature dependence of the PL spectrum from 300 to 13 K for the green MQW prepared on amorphous SiO_2 with a multilayer graphene buffer layer was then investigated. Figure 13.20c shows the temperature dependence of the integrated PL intensity. The ratio of the integrated PL intensity at 13 K to that at 300 K was 7.4 %, which is comparable to the value for conventionally fabricated

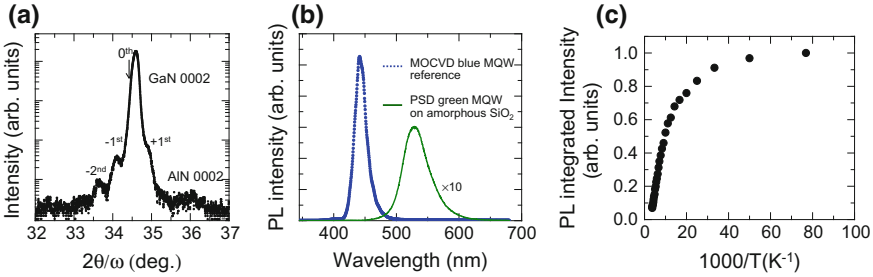

Fig. 13.20 **a** XRD $2\theta/\omega$ curve and **b** RT *green* PL spectrum for an LED structure fabricated on amorphous SiO_2 with a graphene buffer layer. A PL spectrum for a commercially available *blue* LED on a single-crystal sapphire substrate is also shown in this figure. **c** Temperature dependence of the integrated PL intensity for the range from 13 to 300 K. Reproduced from Shon et al. [46]

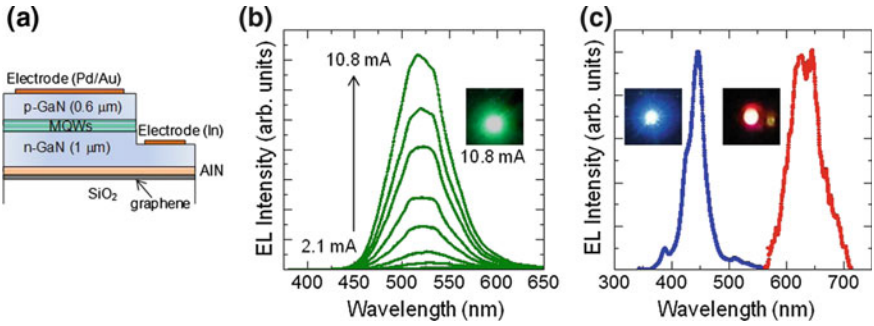

Fig. 13.21 **a** Schematic illustration and **b** EL spectra for the *green* LED structure fabricated on amorphous SiO_2 with a graphene buffer layer at various injection currents. **c** EL spectra and photographs during operation of LEDs with various in compositions. Reproduced from Shon et al. [46]

green LEDs on sapphire substrates [62, 63]. Because this value is often considered a rough indicator of the internal quantum efficiency [64], the optical properties of the film prepared via low-temperature PSD can be inferred to be not seriously degraded by the use of an amorphous substrate. In addition, the integrated intensity of the PL from the green MQW structure on amorphous SiO_2 with a multilayer graphene buffer layer was approximately 14 % of that from a commercially available reference MOCVD blue MQW on a single-crystal sapphire substrate measured with the same optical setup. Because the internal quantum efficiency of the reference blue MQW sample was approximately 50 % based on the temperature dependence of its PL intensity, this comparison is consistent with the data for the temperature dependence measurements.

After deposition of Pd/Au and In electrodes on the p- and n-type GaN surfaces, respectively, EL measurements were performed on the LED structure shown in Fig. 13.21a. As can be seen in Fig. 13.21b, green LEDs operated normally with

reasonable emission spectra, and the intensity increased with an increase in the injection current from 2.1 to 10.8 mA. Blue and red LEDs were also fabricated by changing the In composition in the PSD–InGaN layer, and both operated effectively, as shown in Fig. 13.21c.

In summary, by demonstrating that full-color LEDs can be fabricated on amorphous substrates, we suggest that because sputtering is very frequently used in the LCD industry, it is an established process that could be adapted for the fabrication of large-area inorganic LED displays on glass substrates. Notably, state-of-the-art technology in the glass industry can offer roll-to-roll processing of flexible glass foils [65]. We believe that the combination of these techniques can lead to the development of large-area flexible inorganic devices.

13.4 Conclusions

In this chapter, the feasibility of fabricating large-area inorganic crystalline devices based on group III nitrides was discussed. Using the low-temperature and high-throughput PSD, high-quality nitride films can be grown on various low-cost substrates. The low growth temperature of PSD offers various advantages in the device fabrication process, including suppression of various chemical reactions during growth and alleviation of thermal stress. In fact, operation of various nitride devices such as RGB LEDs, HEMTs, and MISFETs prepared at low process temperatures has been successfully demonstrated using PSD. Notably, using a graphene buffer layer allows the fabrication of full-color LEDs, even on amorphous substrates. These results indicate that a combination of low-temperature PSD growth of nitrides and low-cost glass substrates with the use of graphene buffer layers is quite promising for the realization of future large-area inorganic crystalline semiconductor devices.

References

1. J. Ohta, H. Fujioka, M. Oshima, Appl. Phys. Lett. **83**, 3060 (2003)
2. A. Kobayashi, H. Fujioka, J. Ohta, M. Oshima, Jpn. J. Appl. Phys. **43**, L53 (2004)
3. M.H. Kim, J. Ohta, A. Kobayashi, H. Fujioka, M. Oshima, Appl. Phys. Lett. **91**, 151903 (2007)
4. K. Sato, J. Ohta, S. Inoue, A. Kobayashi, H. Fujioka, Appl. Phys. Express **2**, 011003 (2009)
5. M.H. Kim, J. Ohta, A. Kobayashi, H. Fujioka, M. Oshima, Phys. Stat. Sol. RRL **1**, 13 (2008)
6. A. Fischer, H. Kühne, H. Richter, Phys. Rev. Lett. **20**, 2712 (1994)
7. J.H. Choi, A. Zoulkarneev, S.I. Kim, C.W. Baik, M.H. Yang, S.S. Park, H. Suh, U.J. Kim, H.B. Son, J.S. Lee, M. Kim, J.M. Kim, K. Kim, Nat. Photonics **5**, 763 (2011)
8. E. Nakamura, K. Ueno, J. Ohta, H. Fujioka, M. Oshima, Appl. Phys. Lett. **104**, 051121 (2014)
9. C.G. Van de Walle, C. Stampfl, J. Neugebauer, J. Cryst. Growth **189/190**, 505 (1998)
10. T. Tanaka, A. Watanabe, H. Amano, Y. Kobayashi, I. Akasaki, S. Yamazaki, M. Koike, Appl. Phys. Lett. **65**, 593 (1994)

11. T. Takeuchi, H. Amano, K. Hiramatsu, N. Sawaki, I. Akasaki, J. Cryst. Growth **115**, 634 (1991)
12. A. Dadgar, J. Christen, T. Riemann, S. Richter, J. Bläsing, A. Diez, A. Krost, A. Alam, M. Heuken, Appl. Phys. Lett. **78**, 2211 (2001)
13. S. Guha, N.A. Bojarczuk, Appl. Phys. Lett. **72**, 415 (1998)
14. T. Egawa, T. Moku, H. Ishikawa, K. Ohtsuka, T. Jimbo, Jpn. J. Appl. Phys. **41**, L663 (2002)
15. F. Semond, P. Lorenzini, N. Grandjean, J. Massies, Appl. Phys. Lett. **78**, 335 (2001)
16. H. Ishikawa, G.-Y. Zhao, N. Nakada, T. Egawa, T. Jimbo, M. Umeno, Jpn. J. Appl. Phys. **38**, L492 (1999)
17. X.Q. Shen, T. Takahashi, H. Kawashima, T. Ide, M. Shimizu, H. Okumura, Jpn. J. Appl. Phys. **52**, 08JB05 (2013)
18. T. Watanabe, J. Ohta, T. Kondo, M. Ohashi, K. Ueno, A. Kobayashi, H. Fujioka, Appl. Phys. Lett. **104**, 182111 (2014)
19. F. Reiher, A. Dadgar, J. Bläsing, M. Wieneke, M. Müller, A. Franke, L. Reißmann, J. Christen, A. Krost, J. Phys. D Appl. Phys. **42**, 055107 (2009)
20. B. Damilano, F. Natali, J. Brault, T. Huault, D. Lefebvre, R. Tauk, E. Frayssinet, J.C. Moreno, Y. Cordier, F. Semond, S. Chenot, J. Massies, Appl. Phys. Express **1**, 121101 (2008)
21. Y. Cordier, J.C. Moreno, N. Baron, E. Frayssinet, S. Chenot, B. Damilano, F. Semond, IEEE Electron Device Lett. **29**, 1187 (2008)
22. G. Tsutsui, T. Hiramoto, I.E.E.E. Trans, Electron Devices **53**, 2582 (2006)
23. A. Ishizaka, Y. Shiraki, J. Electrochem. Soc. **133**, 666 (1986)
24. A.R. Smith, R.M. Feenstra, D.W. Greve, M.-S. Shin, M. Skowronski, J. Neugebauer, J.E. Northrup, Appl. Phys. Lett. **72**, 2114 (1998)
25. S. Tanaka, M. Takeuchi, Y. Aoyagi, Jpn. J. Appl. Phys. **39**, L831 (2000)
26. D.S. Green, U.K. Mishra, J.S. Speck, J. Appl. Phys. **95**, 8456 (2004)
27. R. Armitage, Q. Yang, E.R. Weber, J. Appl. Phys. **97**, 073524 (2005)
28. L.G. Parratt, Phys. Rev. **95**, 359 (1954)
29. L. Nevot, P. Croce, Rev. Phys. Appl. **15**, 761 (1980)
30. N. Dharmarasu, K. Radhakrishnan, M. Agrawai, L. Ravikiran, S. Arulkmaran, K.E. Lee, N.G. Ing, Appl. Phys. Express **5**, 091003 (2012)
31. K.T. Tsen, C. Poweleit, D.K. Ferry, H. Lu, W.J. Schaff, Appl. Phys. Lett. **86**, 222103 (2005)
32. J. Kuzmik, A. Georgakilas, I.E.E.E. Trans, Electron Devices **58**, 720 (2011)
33. Y.-S. Lin, S.-H. Koa, C. Chan, S.S.H. Hsu, H.-M. Lee, S. Gwo, Appl. Phys. Lett. **90**, 142111 (2007)
34. Y.F. Ng, Y.G. Cao, M.H. Xie, X.L. Wang, S.Y. Tong, Appl. Phys. Lett. **81**, 3960 (2002)
35. X. Wang, S. Liu, N. Ma, L. Feng, G. Chen, F. Xu, N. Tang, S. Huang, K.J. Chen, S. Zhou, B. Shen, Appl. Phys. Express **5**, 015502 (2012)
36. N. Khan, A. Sedhain, J. Li, J.Y. Lin, H.X. Jiang, Appl. Phys. Lett. **92**, 172101 (2008)
37. C.J. Lu, L.A. Bendersky, H. Lu, W.J. Schaff, Appl. Phys. Lett. **83**, 2817 (2003)
38. X. Wang, S.-B. Che, Y. Ishitani, A. Yoshikawa, Appl. Phys. Lett. **90**, 151901 (2007)
39. L.F.J. Piper, T.D. Veal, C.F. McConville, H. Lu, W.J. Schaff, Appl. Phys. Lett. **88**, 252109 (2006)
40. T. Honke, H. Fujioka, J. Ohta, M. Oshima, J. Vac. Sci. Technol. A Vac. Surf. Film **22**, 2487 (2004)
41. K. Okubo, A. Kobayashi, J. Ohta, M. Oshima, H. Fujioka, Appl. Phys. Lett. **102**, 022103 (2013)
42. S. Yoshida, Phys. E Low Dimens. Syst. Nanostruct. **7**, 907 (2000)
43. H. Okumura, H. Hamaguchi, T. Koizumi, K. Balakrishnan, Y. Ishida, M. Arita, S. Chichibu, H. Nakanishi, T. Nagatomo, S. Yoshida, J. Cryst. Growth **189/190**, 390 (1998)
44. F. Dessenne, D. Cichocka, P. Desplanques, R. Fauquembergue, Mater. Sci. Eng., B **50**, 315–318 (1997)
45. J.W. Shon, J. Ohta, K. Ueno, A. Kobayashi, H. Fujioka, Appl. Phys. Express **7**, 085502 (2014)
46. J.W. Shon, J. Ohta, K. Ueno, A. Kobayashi, H. Fujioka, Sci. Rep. **4**, 5325 (2014)
47. D.P. Bour et al., Appl. Phys. Lett. **76**, 2182 (2000)

48. S. Inoue, K. Okamoto, T. Nakano, J. Ohta, H. Fujioka, Growth of single crystalline GaN on silver mirrors. Appl. Phys. Lett. **91**, 201920 (2007)
49. K. Chung, C.H. Lee, G.C. Yi, Science **330**, 655 (2010)
50. K. Chung, S.I. Park, H. Baek, J.S. Chung, G.C. Yi, NPG Asia Mater. **4**, e24 (2012)
51. X. Li, W. Cai, J. An, S. Kim, J. Nah, D. Yang, R. Piner, A. Velamakanni, I. Jung, E. Tutuc, S.K. Banerjee, L. Colombo, R.S. Ruoff, Science **324**, 1312 (2009)
52. S. Bae, H. Kim, Y. Lee, X. Xu, J.S. Park, Y. Zheng, J. Balakrishnan, T. Lei, H.R. Kim, Y.I. Song, Y.J. Kim, K.S. Kim, B. Özyilmaz, J.H. Ahn, B.H. Hong, S. Iijima, Nat. Nanotechnol. **5**, 574 (2010)
53. Q. Yu et al., Appl. Phys. Lett. **93**, 113103 (2008)
54. A. Ishii, T. Tatani, H. Asano, K. Nakada, Phys. Stat. Sol. (C) **7**, 347 (2010)
55. F. Yuan, B. Liu, Z. Wang, B. Yang, Y. Yin, B. Dierre, T. Sekiguchi, G. Zhang, X. Jiang, Appl. Mater. Interfaces **5**, 12066 (2013)
56. H. Okumura, K. Ohta, G. Feuillet, K. Balakrishnan, S. Chichibu, H. Hamaguchi, P. Hacke, S. Yoshida, J. Cryst. Growth **178**, 113 (1997)
57. M.A. Reshchikov, H. Morkoç, J. Appl. Phys. **97**, 061301 (2005)
58. F. Bernaridini, V. Fiorentini, Phys. Rev. B **57**, R9427 (1998)
59. A. Bykhovski, B. Gelmont, M. Shur, J. Appl. Phys. **74**, 6734 (1993)
60. J. Ohta, H. Fujioka, M. Oshima, K. Fujiwara, A. Ishii, Appl. Phys. Lett. **83**, 3075 (2003)
61. M.H. Wong, F. Wu, J.S. Speck, U.K. Mishra, J. Appl. Phys. **108**, 123710 (2010)
62. M. Kumar et al., Jpn. J. Appl. Phys. **47**, 839842 (2008)
63. M. Liu, B. Rong, H. Salemink, Opt. Eng. **46**, 074002 (2007)
64. A. Hangleiter et al., Phys. Stat. Sol. (A) **201**, 2808 (2006)
65. S. Garner et al., SID Symp. Dig. Tech. Pap. **43**, 342 (2012)

Chapter 14
Synthesis of Subnanoparticles Using a Dendrimer Template

Takane Imaoka and Kimihisa Yamamoto

Abstract A dendrimer-based nanoreactor that can control the number of metal ions (as the salt form) within a nanospace was employed for the synthesis of monodispersed metal subnanoparticles with a definite atomicity. Athough many other dendrimers such as polyamidoamine (PAMAM) derivatives have been used for the synthesis of larger nanoparticles, phenylazomethine dendrimers are especially the most suitable for the subnanoparticle synthesis. The typical example is the atomicity-consistent syntheses of Pt_{12} and Pt_{13} each from $PtCl_4$ through the chemical reduction by $NaBH_4$. This atomic-level precision could be achieved by the stoichiometric control of the $PtCl_4$ versus the dendrimer template. At this size scale, properties of the subnanoparticles are much different by the atomicity because the stable atomic coordination structure is significantly different by the size. Surprisingly, the Pt_{12} and Pt_{13} subnanoparticles have much different catalytic activity for an oxidation reaction reaction (ORR), and the Pt_{12} catalyst exhibited *ca.* 13-times higher mass activity than the conventionally used Pt nanoparticles ($\sim$3 nm) on a carbon support. Such size specific properties were also observed for metal oxides subnanopaticles (TiO_2).

Keywords Nanoparticles · Dendrimers · Catalysts · Macromolecular complexes

14.1 Introduction

The methodology of inorganic synthesis on a nanoscale level has been significantly developed in order to address recent requirements from the material engineering side including the applications for catalysts [1–5], light-emitting [6–8], electronic and magnetic functions [9–11]. Conventional periodic material synthesis only focused on chemical formulas and crystalline phases of the materials. In contrast, the nanoscopic discrete material synthesis also requires control with respect to other

T. Imaoka · K. Yamamoto (✉)
Chemical Resources Laboratory, Tokyo Institute of Technology, Yokohama 226-8503, Japan
e-mail: yamamoto@res.titech.ac.jp

J. Sone and S. Tsuji (eds.), *Intelligent Nanosystems for Energy, Information and Biological Technologies*, DOI 10.1007/978-4-431-56429-4_14

structural characteristics such as their sizes and shapes [4, 12]. These additional dimensions are very important for the nanomaterials because the size affects the fundamental physical and chemical properties including the band gaps [13–15] or surface chemical adsorptions [16]. As the scale became smaller, the importance of these characteristics increases. The weight of one atom in a discrete nanostructure would be significant when the structural size was reduced to a nano- and sub-nanometer scale [17].

In general, defects in a crystal lattice (excess or absence of the atoms) could affect the material property [18, 19]. What will happen when a very small discrete metal particle composed of only several tens of atoms lacks one atom? Recently, an interesting concept called "super atom" has been proposed [20–23]. The definition of "super atom" is that a cluster of metal atoms (very small metal nanoparticles) exhibits a completely different elemental property such as ionization potential, electron affinity, or reactivity to other elements as if it were a different element from the original one. The first example is an Al_{13} cluster which has the characteristic of the halogen atom family [20]. Valence electrons from each metal atom behave as free electrons within the restricted two- or three-dimensional field in the sub-nanometer particle. These electrons form new hybridized orbitals expressed as a Jellium model [24], which is similar to atomic orbitals. In this case, the property of the superatom depends on the number of valence electrons from each of the parent atoms (e.g., Na, Al, Au) and the atomicity of the cluster compound. This discovery has intrigued chemistry and material science researchers because this concept indicates the creation of a new element [25]. However, the most important and difficult challenge is to synthesize these superatoms. Because the total number of electrons in the pseudoatom strongly depends on the atomicity, the property should be much different if only one atom is present or absent in a cluster. To realize this concept based on chemistry, a true one-atom controlled synthesis is necessary.

A non-chemical approach to access such a well-defined subnanometer structure includes the gas-phase nucleation of laser-ablated atoms followed by their mass resolution [24]. Although this technique allows the one-atomic-level precise production of the discrete nanostructure, the industrial application is practically impossible due to the difficult mass production. On the contrary, the chemical approach is suitable for the mass production. Indeed, nanoparticles for catalysts, quantum dots or chemical sensors are almost ready to be commercialized. However, the conventional chemical process does not have a one-atom-level precision. Because the nanoparticle formation involves a statistical nucleation reaction in a solution or on solid surfaces, the resulting discrete particles necessarily include a statistical distribution of the size similar to the molecular-weight distribution of the as-synthesized polymers. How can we synthesize atomicity precise nanostructures (e.g. particles) using the chemical methodology for the mass production? The most promising candidate is a molecular template method using a molecular nanoreactor. This method can define the number of atoms involved in their nucleation reaction within the molecularly isolated nanospace. Various discrete molecular capsules based on supramolecular cages, complexes or natural proteins have been proposed to control the chemical reactions. Relative to these nanoreactors, dendrimers are

specifically suitable because the molecular structure from covalent bondings is relatively stable, and the number of unit structures can be easily defined. This chapter deals with the molecules that allow the precise and versatile synthesis of the metal subnanoparticles as superatomic composition.

14.2 Macromolecular Templates for Nanoparticle Synthesis

14.2.1 Dendrimers

Dendrimers are a class of macromolecules, which have regularly branched main chains spread from a core unit at the focal point (Fig. 14.1). Each monomer unit has a generation number defined as the number of branching monomer units from the focal point [26]. The definition of the ideal dendrimer is that every terminal monomer has the same generation number; therefore, the total degree of the polymerization is uniquely specified based on the generation number and the number of branches. A dendrimer could also be regarded as a hyper branch polymer having perfect branching [27]. The synthesis of such defect-free dendrimers requires a multistep organic synthesis together with the appropriate purifications, but not conventional simultaneous polymerization reactions.

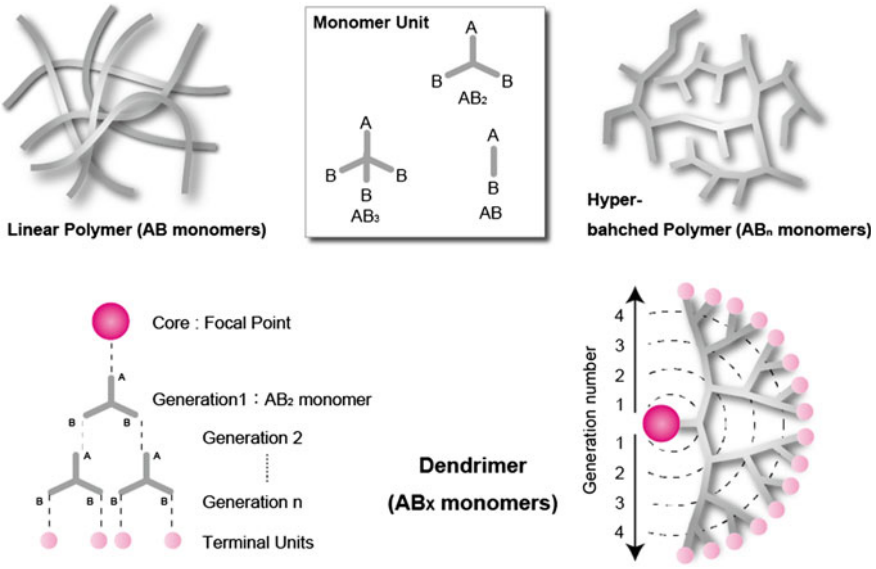

Fig. 14.1 General structures of linear polymers, hyperbranched polymers and dendrimers

In general, two typical synthetic approaches are used for the preparation of dendrimers. One is the divergent approach initially proposed by Tomalia (Fig. 14.2) [28]. This route starts from a reactive core unit, followed by the coupling with appropriate precursors of the branching monomer units. Repetitive coupling with appropriate protection/deprotection reactions and purification enables the generation number growth with minimum defect formation. However, this divergent approach has difficulty in perfect defect-free synthesis because the number of reacting points would exponentially increase with the generation number. Even if the single coupling reaction yield was 90 %, the desired product without any defect forms as the minor product when the generation number was higher than 3 or 4. A requirement for the highly quantitative reaction is very strict by the divergent approach. In contrast, the convergent approach (Fig. 14.2) proposed by Fréchet allows the synthesis of defect-free dendrimers with fewer quantitative reactions [29]. This route starts from the terminal monomer units, followed by the connection to the inner monomer units. After the growth of the branching unit (called a "dendron") repeating from the terminals to the focal point, a precursor of the core unit is finally connected to the dendrons. Because the number of reacting points at each step is limited to the number of branchings over the entire process, the major production of the defect-free dendrons is relatively easy. However, this approach requires high purity dendrons at each reacting step because a small amount of the terminal defect would be amplified after several coupling processes.

Dendrimers have an explicit definition of the topological structure as described above. The size of the dendrimers mainly depends on the number of generations and the length of the branching monomer units (Fig. 14.3). If the length was shorter

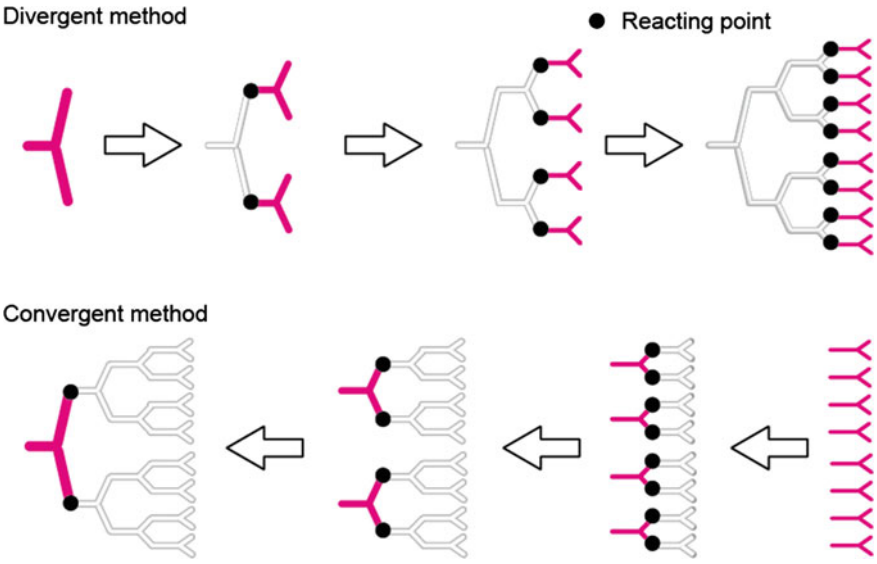

Fig. 14.2 Two synthetic approaches for defect-free dendrons

and the number of branching increased, the mass density would be higher by decreasing the inner cavity space. Many previous experimental results suggested that the hydrophobicity of the inner cavity remains constant even if the external solvent environment significantly changes [30]. This typical characteristic of the dendrimers is called "encapsulation" or the "shell" effect. The degree of the encapsulation could be flexibly controlled by the number and directions of the reactive functional groups on the core unit (Fig. 14.3). For example, the dendrimer would be "open-shell" if only one or two dendrons were connected to the core unit. When four or more dendrons were connected, the dendrimer would have a "closed-shell" configuration. Flexibility of the main chains as another important property of the dendrimer significantly affects the fundamental properties including the encapsulation [31]. If the dendrimer was composed of relatively flexible backbones based on a single-bonded covalent structure, the entire molecule tends to have a compact globular shape, in which the terminal monomers are folding back into the inner cavity. This configuration is responsive to the external environment such as temperature [32], pH [33], ionic strength or solvent [34]. Due to this flexibility, its geometric structure is difficult to design as expected at the dawn of the dendrimer chemistry. In contrast, rigid backbones allow retaining their cavity; therefore, a fine discrimination of the guest molecular shape and its design could be possible.

Implementation of functions at each part of the dendrimer (core, branch, and terminal) is possible. Especially, the core is located at a very specific site where the mass and energy transfer from the external environment is controlled by the shell. For example, enhanced or selective catalysis at the core is enabled if a catalytically active metal complex was implemented at the core unit [35]. Another example is the photoenergy conversion by controlling the vectors of the excitation energy [36] or electron transport [37] through the dendrimer shell. In this case, a photochemically active core unit is used to implement the excitation, fluorescent and photoredox properties. The terminal monomers oppositely affect the intermolecular property such as the solubility, phase stability and the formation of supramolecular structures [38]. If the hydrophilic groups were modified onto the terminal monomer units, the entire dendrimers would be water-soluble even though the physicochemical function at the core remains constant. An extreme example is the formation of the Janus-type dendrimer having an amphiphilic property when both hydrophilic and hydrophobic properties were heterolytically modified onto the terminals [39]. The branched monomer unit dominates the main part of dendrimers, and mediates the mass, energy and electro-transport between the core and external environment. As described in the next section, this part can be used as the assembling sites for the metal ions used for the nanoparticle synthesis.

Although the dendrimers are a class of macromolecules, the globular-shaped molecular morphology provides significantly different hydrodynamic properties of the solutions such as diffusion, solubilization or viscosity. Indeed, there are many insoluble polymers, such as polyphenylenes or polyphenylene ethers, used as engineering plastics. This insolubility is due to the strong intermolecular interaction between two or more polymer chains. However, dendrimers with the same molecular

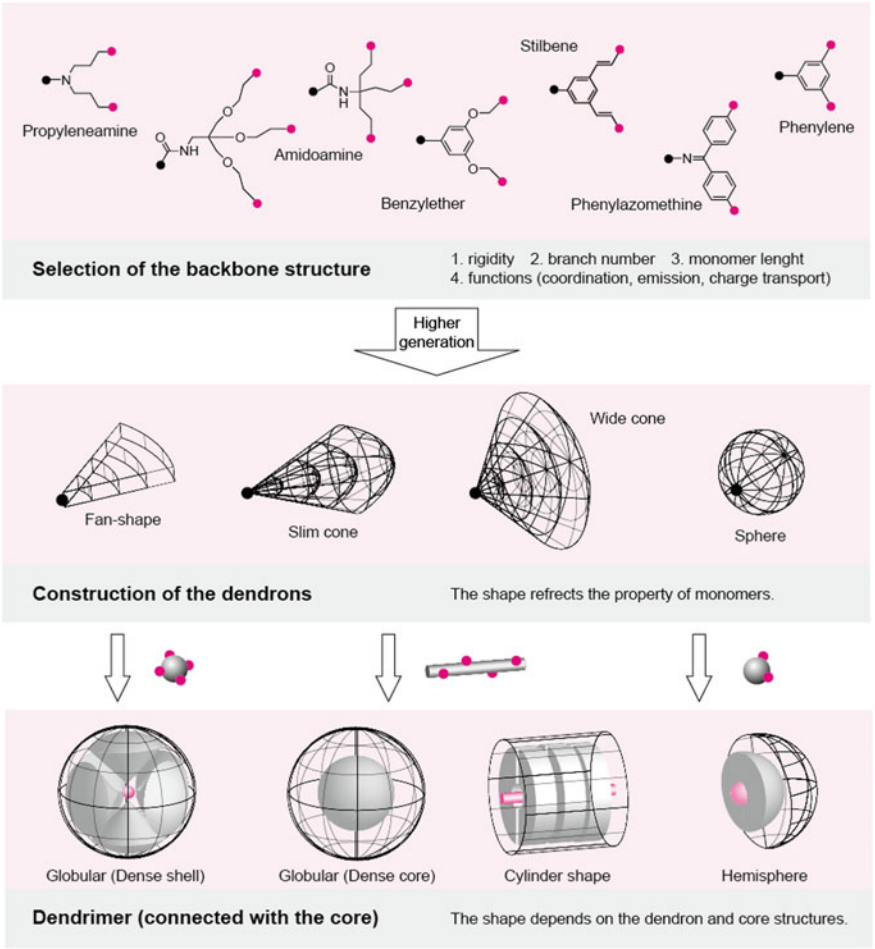

Fig. 14.3 Designing dendrimers based on the selection of the backbones and core unit

backbones are soluble in the common organic solvents (chloroform, benzene, toluene, tetrahydrofuran). The difference between the linear polymer and the dendrimer is due to the morphology. In the case of the linear polymer, a molecular thread intrudes in the hydrodynamic radius of the other molecules. One molecular thread can interact with multiple molecules; therefore, complete dissolution is very difficult. On the other hand, the dendrimers as globular-shaped molecules can interact with the other dendrimers only at the molecular surface (typically terminal monomer units). Because the surface-to-volume ratio is lower than that for linear polymers, the intermolecular interaction is much lower than that of linear ones even if the molecular weight is equivalent. The viscosity of the dendrimer solution is much lower due to the same reason. A Mark-Howink-Sakurada plot of the linear polymers shows an almost linear

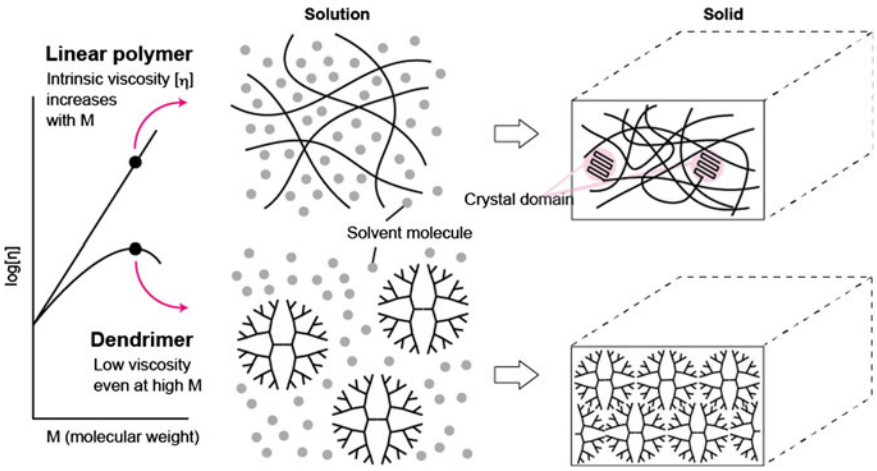

Fig. 14.4 Solution and solid-state properties of linear polymers and dendrimers

relationship between the molecular weight and the intrinsic viscosity (Fig. 14.4) [40]. In other words, the solution of linear polymers with higher molecular weights is highly viscous due to the greater intermolecular interactions. Dendrimers with higher generation numbers generally exhibit the opposite relationship between the molecular weight and viscosity [41]. When a backbone was relatively rigid, the intrinsic viscosity is almost constant (Fig. 14.4). Flexible dendrimers with backfolding character decreases their viscosity with the molecular weight. These facts suggest that the dendrimer is a much more isolated molecule relative to the linear polymers.

14.2.2 Formation of Metal-Assembling Complexes

The "dendritic box" concept [42] initially proposed by Meijer inspired fundamental interest in that the dendrimers can be employed as a large host molecule for many small molecules similar to the host-guest chemistry of proteins for various ligand molecules. Indeed, many host-guest examples involving the dendrimers have been proposed, and the dendrimers are one of the promising candidates for artificial drag delivery systems [43]. Not only small organic molecules, but also many metal ions or complexes can be assembled in the dendrimer. If the dendrimer contains many coordinating monomer units, such as amine and imines, it can assemble multiple metal ions in its interior. Although linear polymers can also assemble metal ions with these coordinating monomers, these polymers cannot isolate the metal ions into one specific domain. Dendrimers have much more discrete characteristics as described in the previous section. This is one of the primary reasons why the dendrimer is suitable for nanoparticle synthesis with precise size control.

Many coordinative dendrimers, such as polyamidoamines (PAMAM) or polypropyleneimine (PPI), can form stable metal-assembling complexes in solution [44]. However, the coordination reaction is still random because every coordination center (amines and imine nitrogen) has almost the equivalent coordinating ability within one dendrimer. This means that the multistep metal-assembling process within one dendrimer is still random and statistical reactions. Different from these frequently used dendrimers, dendritic polyphenylazomethines (DPA) undergo a stepwise coordination process upon the addition of metal ions (as chloride salts) [45]. Among many coordination sites in the dendrimer, the imine nitrogens of the first generation (on the layer closest to the core) have the highest basicity. Therefore, a metal chloride (e.g., $SnCl_2$, $GaCl_3$, $FeCl_3$, VCl_3) as a Lewis acid preferentially binds to the innermost layer in the equilibrium state [46]. In the case of a phenylazomethine dendrimer having a p-phenylene core with four generations (DPAG4), a unique stepwise reaction was found based on the UV-vis absorption spectral changes upon the addition of metal chloride to the dendrimer solution (Fig. 14.5). Overall, clear spectral changes were observed on the addition of $SnCl_2$.

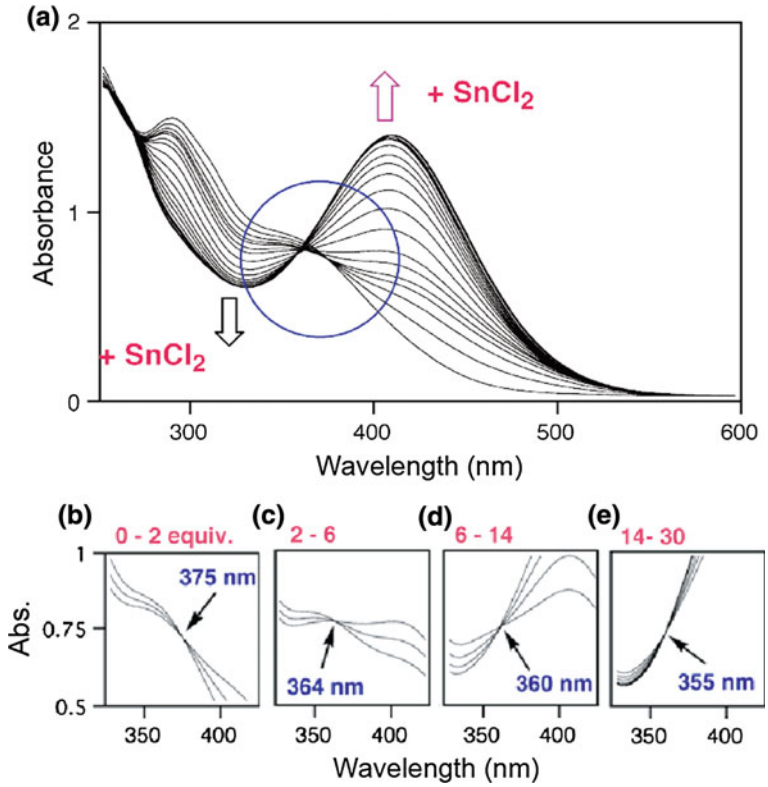

Fig. 14.5 **a** UV–Vis absorption spectra of DPAG4 upon the stepwise addition of $SnCl_2$. **b–e** Four isosbestic points appeared at different wavelengths during the titration

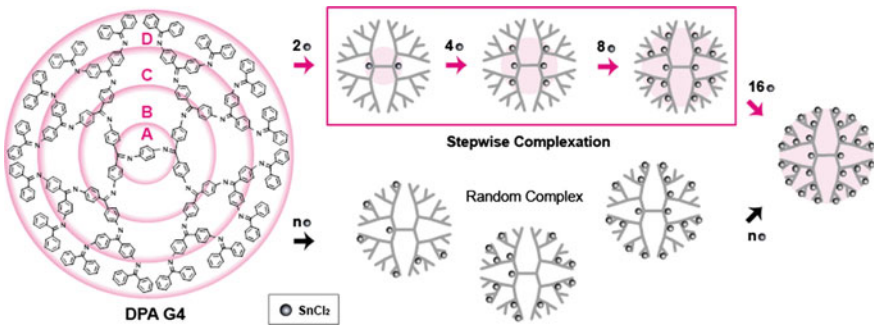

Fig. 14.6 Schematic representations of the stepwise and random complexation to DPAG4

The initial absorption band around 300 nm decreased and a new absorption around 400 nm increased accompanied by isosbestic points around 350 nm. This titration experiment initially showed a first isosbestic point at 375 nm up to the 2-equimolar addition of $SnCl_2$. The titration result suggests that $SnCl_2$ mainly binds to two equivalent imine sites on the innermost first layer. After filling up the first layer, the next $SnCl_2$ should bind to the second layer. This assumption was also supported by the titration result exhibiting an isosbestic point at 364 nm, which continues during the next 4-equimolar additions (total of 6 equivalents $SnCl_2$ to the DPAG4 molecule). The isosbestic point shifted again to 360 nm, and continued to the next 8-equimolar addition. Finally, the isosbestic point appeared at 355 nm, and the spectral change almost converged at the next 16-eqiuimolar additions. This total process of the isosbestic point completely agreed with the idea that the metal ions undergo a stepwise complexation process from the innermost layer to the outermost layer due to the preferential binding to the inner layers (Fig. 14.6). This stepwise complexation was also supported by many experimental techniques in addition to the spectroscopic investigations. For example, electrochemical probing and fluorescence quenching experiments supported that the complexation starts from the innermost layer and ends at the outermost layer [47]. Direct TEM observations suggested that $SnCl_2$ is regularly assembled from the inner layers [48].

Such a stepwise coordinating dendrimer has a significant advantage for the formation of a definitive dendrimer-metal complex. Based on the assumption of a random complexation, the number of assembling metals within one dendrimer molecule includes quite a high uncertainty due to the disproportionation reaction between two or more dendrimers. As a typical example, we assumed a dendrimer complex assembling 12 equimolar amounts of metal ions. If we could pick up one arbitrary dendrimer-metal complex, the most frequent case should be a dendrimer assembling 12 metal complexes. The average number of the metal assembly should also be 12. However, if one dendrimer complex released one metal ion and another dendrimer caught the released metal ion again, dendrimer complexes carrying 11 and 13 metal complexes should also exist. If every coordination site in the dendrimer has the equivalent affinity to the metal ion, the enthalpy change in this

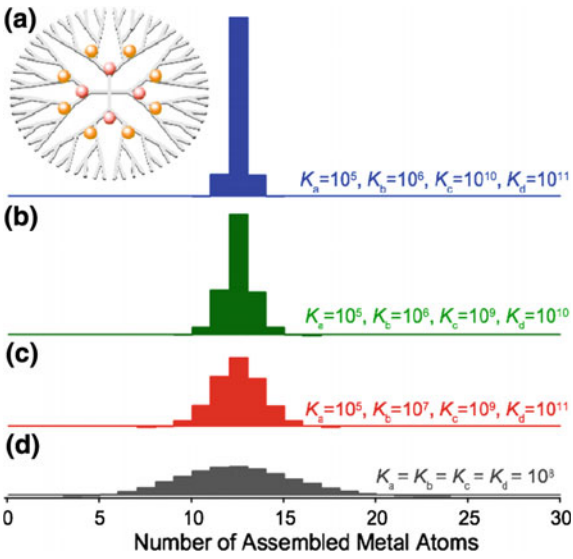

Fig. 14.7 Calculated histograms of the assembled metals in a dendrimer having 60 coordination sites assuming a 12-equimolar amount of the metal chlorides was added. If the difference between the association constants to each generation was very high, almost monodisperse (**a**). If all the coordination sites have the same association constant, the deviation is significantly high (**d**). In any case, the averaged number is 12

disproportionation reaction must be 0. Based on this circumstance, the entropic driving force would give rise to an undesirable distribution in the number of assembling metal ions (Fig. 14.7d). In contrast, the coordination would converge to an energetically stable state if there were various coordination sites with different binding affinities in one dendrimer. Such a dendrimer could provide a much narrower distribution in the assembly number (Fig. 14.7a).

14.2.3 Electron Density Gradient in Dendrimers

Assuming a dendrimer having different binding constants of the coordination sites to metal ions by the layers, the number of assembling metal ions in one arbitral dendrimer would be almost uniform. We now discuss the phenylazomethine dendrimer (DPAG4) which shows a stepwise shift of the isosbestic point in the UV–Vis absorption spectra on the stepwise addition of tin(II) chloride ($SnCl_2$). As described in the previous section, this dendrimer underwent the stepwise complexation reaction exhibiting four isosbestic points in turn. A theoretical simulation of the equilibrium reactions with the dendrimer model suggested that a 2-order of magnitude difference between the binding constants of two neighboring layers is required to reproduce the observed isosbestic points. The 1-order of magnitude difference could not exhibit such a clear shift in the isosbestic point. Similar titration experiments using trifluoroacetic acid (TFA) as a Brönsted acid also indicated such a shift in the isosbestic points [49]. This result suggests that the primary driving force of the stepwise complexation is the basicity gradient of the imine nitrogens on the respective layers of DPAG4 (Fig. 14.8c).

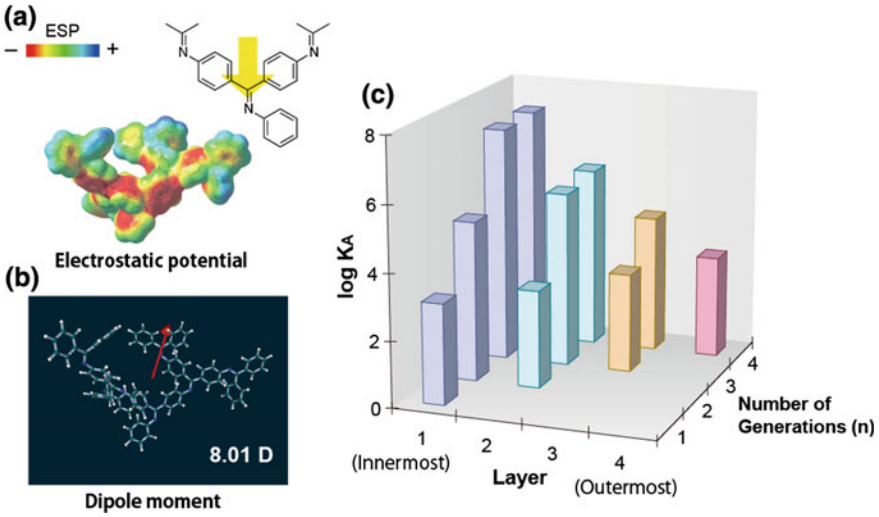

Fig. 14.8 **a** Electrostatic potential mapping and **b** a molecular dipole moment of a phenylazomethine dendrimer with a mono-substituted benzene as the core (DPAG2-Ph). **c** Experimentally estimated association constants of trifluoroacetic acid to Schiff base units on each layer number of DPAG*n*-Ph

To answer the question why such a significant difference in the basicity between the layers of a dendrimer appears in spite of almost the identical chemical structure of the coordination sites, molecular orbital calculations were carried out. The results of the calculated Mulliken charge populations and electrostatic potentials showed an obvious electron potential gradient along the layer-by-layer structure (Fig. 14.8a). Overall, the electron densities and the potentials on the inner monomers are higher than those of the outer monomers. As a result, the dendron has a relatively high dipole moment (Fig. 14.8b). Based on this characteristic, the HOMO/LUMO orbital energy also has a gradient along the dendritic structure [50]. The higher basicity of the inner imine sites can be related to the higher potential energy of the electron lone pairs on the inner monomers, which is also associated with the higher donating property. Such an electronic potential gradient appears not only in the phenylazomethine structure, but also in other dendritic architectures (carbazole dendrimer) having heteroatom-containing head-to-tail structures [51]. However, dendritic molecules involving such a stepwise characteristic are very rare at this time [52]. Although these molecular-level properties might be more universal than we initially expected, most of the previously reported dendrimers (PAMAM) having this structural characteristic did not show such a gradient property. One of the possible reasons is the unfixed molecular conformation in a solution. To obtain the electron gradient property, a molecular design from the both topological and geometrical sides is necessary.

14.3 Nanoparticle and Subnanoparticle Synthesis

14.3.1 Strategy for the Particle-Size Control

The conventional liquid-phase synthesis of metal nanoparticles has employed small molecular ligands or surfactants to control the nucleation reaction of the seed particles [53]. However, this method just controls the growth kinetics or the surface stability, but not defining the exact size. The concept of template nanoparticle synthesis using coordinating dendrimers was first reported by Crooks [54]. Using the dendrimer as a molecular flask, size-controlled nanoparticles can be synthesized because the dendrimer can regulate the nucleation reaction inside itself, followed by the stabilization of the encapsulated particles (Fig. 14.9). Especially, polyamidoamine (PAMAM) dendrimers were used for the template because they can assemble various metal ions in themselves. The PAMAM dendrimers can form stable multi-dentate complexes [44]. In addition, they can stably retain the product nanoparticles inside, and the nanoparticles can be used without any heterogeneous support for the stabilization. Indeed, there are many successful examples of the size-controlled synthesis on a single nanometer scale (typically 1.5–3 nm) [54, 55].

However, these early dendrimers cannot define the exact number of atoms because the metal-assembling process within the dendrimer is obviously random and uncontrolled. The dendrimers only regulate the average number of assembled metal ions accompanying a considerable statistical distribution. When the atomicity is higher than 100, these dendrimers work very well. On this scale, a deviation of several tens of atoms does not affect the apparent particle size and the properties such as the catalytic activity. On the contrary, a deviation of several atoms in a dozen atoms is significant for the particle properties. Previous challenges to this size scale (subnanometer) are seemingly successful. However, the resulting particle size tends to be much larger than that from the stoichiometric expectation (molar ratio between the metal and dendrimer) [56–58]. To overcome this issue, an employment of an advanced dendrimer template, which can control the multistep complexation process within the dendrimer, could be a practical solution. Actually, there were a

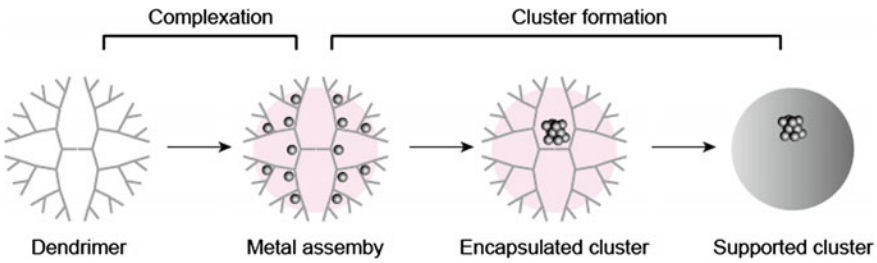

Fig. 14.9 A stragety for the preparation of precise cluster catalysts using a dendrimer as the template

lot of successful examples using phenylazomethine dendrimers as the template for subnanometer particles [59].

14.3.2 Metal Subnanoparticles

Catalytic applications of nanoparticles composed of noble platinum group metals are very important and widely studied. The size reduction has an advantage with respect to the maximum utilization of such expensive and precious metal resources. In general, the size reduction provides an increase in the surface-to-volume ratio, which contributes the higher catalytic activity per weight. In addition, extreme miniaturization to subnanometer scale can drastically change their intrinsic activity due to the modified surface adsorption properties. One of the reasons is based on an electronic mechanism. For example, smaller platinum nanoparticles have d-band center energies closer to the Fermi energy (weaker electron binding energy) relative to the larger nanoparticles [60, 61]. In most cases, the higher d-band center results in an increased vacant d-orbital state, which would strengthen the chemical adsorption by oxygen or other substrates. Another reason is structural mechanism. The surface curvature of the smaller particle would be higher, which should provide many edges and vertex atoms on the surface [62–64]. The surface-specific catalytic activity depends on the balance of an adsorption and desorption. Too strong or too weak adsorption of the substrate reduces the surface-specific activities [65]. Therefore, a comprehensive paradigm of this surface reactivity over a wide range of particle sizes is very important for designing a highly active nanoparticle catalyst. Although, larger nanoparticles (>3 nm) are well characterized, smaller nanoparticles and subnanoparticles (<1.5 nm) were hardly synthesized and their fundamental properties have not been clarified. The most practical way to access nanoparticles on this size scale is the template synthesis using a dendrimer, which can assemble metal ions as the precursor.

The syntheses of platinum subnanoparticles were carried out using a phenylazomethine dendrimer (4 generations) with a tetraphenyl methane core (TPM-DPAG4) [66]. Because the tetraphenylmethane core has four functional groups in the tetrahedral direction, a rigid and omnidirectional shell can be constructed by the connection of relatively rigid phenylazomethine dendrons around the core. This dendrimer (TPM-DPAG4) can assemble $PtCl_4$ similar to the other metal chlorides in a stepwise fashion. Four independent isosbestic points were appeared on the addition of $PtCl_4$ in turns for the 0–4, 4–12, 12–28 and 28–60 equimolar amounts, respectively. Based on the fact that fulfilling of the respective layers provides the metal-assembling complexes with narrower deviations of the atomicity. Actually, the assembling complexes carrying 12, 28 and 60 $PtCl_4$ were prepared, and chemically reduced by $NaBH_4$. The resulting solutions were quickly cast on carbon meshes. Then, transmission electron microscope (TEM) observations were then carried out for these samples. The images showed very small and uniformly size-controlled nanoparticles, of which the sizes are 0.9,

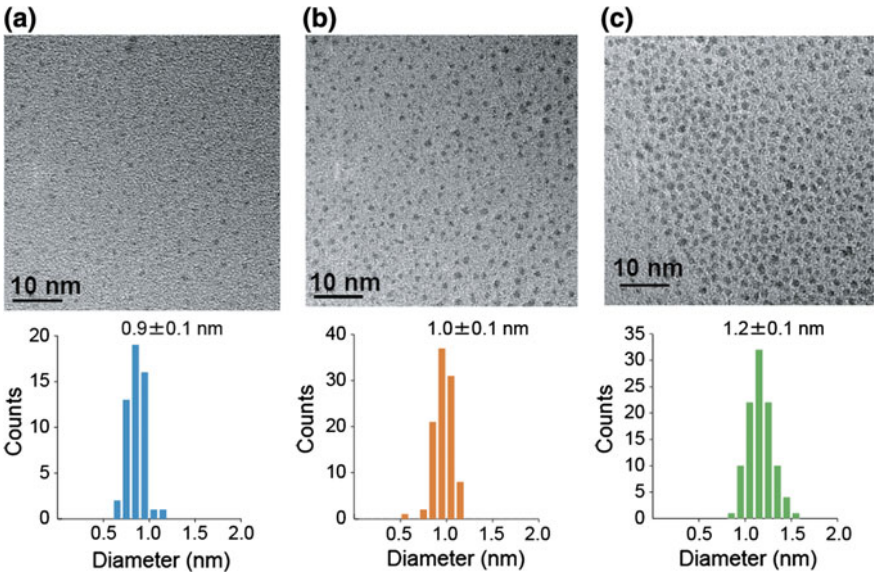

Fig. 14.10 Transmission electron microscope (TEM) images of the platinum nanoparticles synthesized with TPM-DPAG4. **a** Pt_{12}, **b** Pt_{28} and **c** Pt_{60}

1.0, and 1.2 nm for the samples synthesized from the 12, 28, and 60 equimolar $PtCl_4$, respectively (Fig. 14.10) [67]. Each observed size is in good agreement with the size expected for the Pt_{12}, $Pt_{28,}$ and Pt_{60} clusters, respectively. Extended X-ray absorption fine structure (EXAFS) spectra were also supported the formation of very small nanoparticles. X-ray photoelectron spectra (XPS) and X-ray near edge structure (XANES) spectra indicated that these smaller particles showed a slightly higher d-electron vacancy, which may be the result of a higher d-band center energy. A mass spectrum measurement of the as-synthesized platinum cluster is difficult due to their high reactivity and easy aggregation. Instead, a solution of the as-synthesized cluster was exposed to a carbon monooxide (CO) atmosphere to produce the corresponding carbonyl cluster, which is suitable for the electron spray ionization (ESI) analysis. The ESI-TOF-mass spectrum of Pt_{12} surprisingly showed monodispersed $[Pt_{12}(CO)_{16}]^{2-}$ ions (Fig. 14.11) [68]. Although partial fragmentations of the carbonyl ligands were observed, impurity peaks with different Pt-atomicities were hardly observed, suggesting an atomic-level control of the cluster size by the dendrimer template.

In principle, this template can be applied to various metal species, which are available for the metal-assembling in dendrimers. For example, rhodium nanoparticles were also synthesized. The dendrimer complex assembling a 60 equimolar amount of $RhCl_3$ was reduced by $NaBH_{4,}$ affording the size-controlled Rh_{60} nanoparticle [69]. In this case, the resulting nanoparticle was significantly stable even in the as-synthesized nanoparticle solution, probably due to the stronger interaction between the Rh_{60} nanoparticle and the dendrimer ligand. Furthermore,

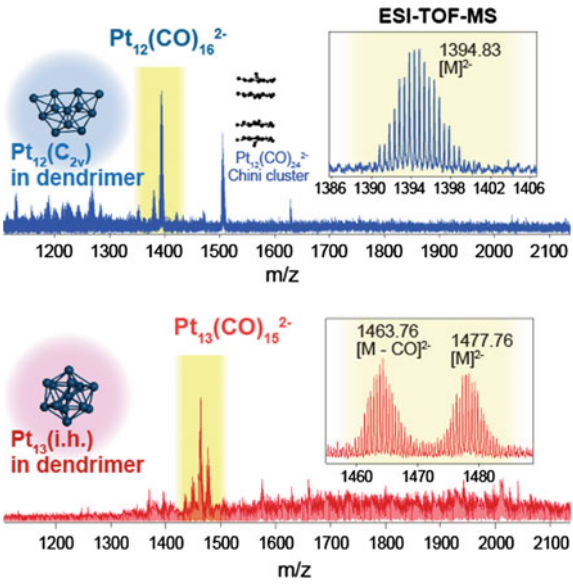

Fig. 14.11 ESI-TOF-Mass spectra of carbonyl-protected Pt_{12} and Pt_{13} subnanoparticles

bimetallic nanoparticle with additional metal elements was possible by assembling the second metal chloride ($FeCl_3$) to the dendrimer. For example, the $Rh_{32}Fe_{28}$ bimetallic nanoparticles were successfully synthesized from the binary metal-assembling precursor [70].

14.3.3 Metal Oxide Subnanoparticles

In contrast to the noble metal elements, early transition metals (e.g., Ti or V) tend to be oxidized due to their lower ionization energy. Instead, they can form very stable metal oxide compounds exhibiting unique semiconducting properties. For example, TiO_2 subnanoparticles were synthesized using a phenylazomethine dendrimer with a p-phenylene core (DPAG4) [71]. In this case, titanium chloride ($TiCl_4$) has too strong a Lewis acidity, therefore, the complexation stoichiometry with imine nitrogens in the dendrimer is not 1:1. To control the stoichiometry, the titanium acetylacetonate complex ($Ti(acac)Cl_3$) was used for the preparation of Ti assembling dendrimer complexes. Because $Ti(acac)Cl_3$ binds to the imine nitrogen at a 1:1 stoichiometry, 6, 14, and 30 equimolar $Ti(acac)Cl_3$ could be assembled into the dendrimer. These complexes were then exposed to HCl vapor affording TiO_2 nanoparticles by a hydrolysis reaction (Fig. 14.12a). Almost similar but slightly different TiO_2 nanoparticles were synthesized from a calcination reaction.

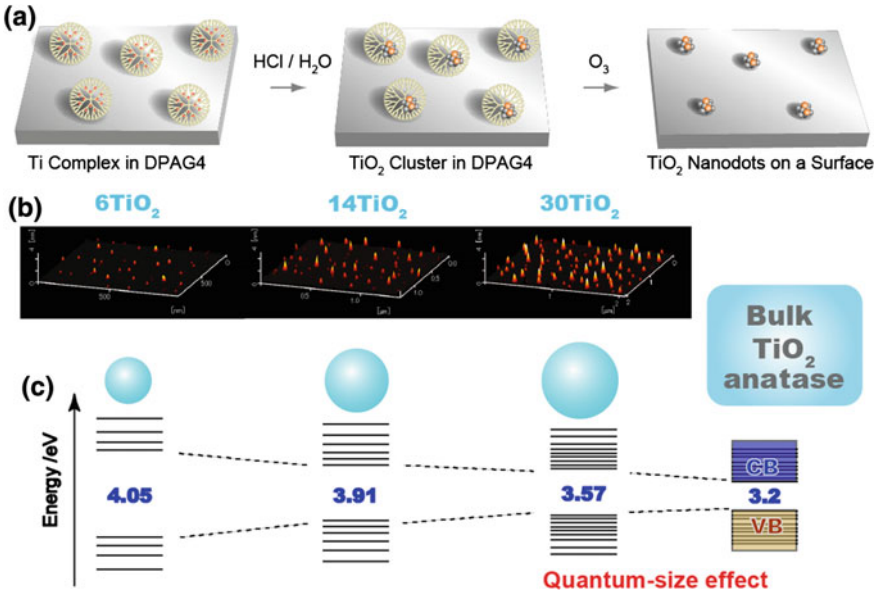

Fig. 14.12 Synthesis of the TiO_2 subnanoparticles. Smaller subnanoparticles have larger band gap energies due to the quantum size effect

Both methods (hydrolysis and calcination) successfully afforded the size-controlled TiO_2 nanoparticles containing 6, 14, and 30 Ti atoms, which could be observed by TEM and AFM (Fig. 14.12b).

The band gap energy of the TiO_2 nanoparticles observed as the near-UV absorption edges exhibited a clear dependence on the particle size (Fig. 14.12c). The relationship that smaller TiO_2 particles have a wider band gap energy suggested the quantum size effect [13] arising from the narrower quantum well size than the de Broglie wavelength of the electrons. Although there are many examples of TiO_2 nanoparticles [9], the optical band gap shift by the quantum size effect is difficult to observe or very low. Because the apparent reduced mass of an electron (or hole) of $1.63m_o$ (where m_o is the electron rest mass) is much greater than commonly used other semiconducting materials, the quantum size effect is almost negligible on the single nanometer scale [9]. In theory, the band gap shift will start from *ca*. 2.0 nm, and drastically changed when the size was reduced to the subnanometer scale. The experimental results were in good agreement with the theoretical expectation. It should be noted that TiO_2 nanoparticles synthesized from the hydrolysis and calcination reactions have different bandgap energies even if the particle size and the atomicity were equivalent. The hydrolyzed and calcined particles both showed rutile- and anatase-like properties. It was quite surprising that the two phases are still available on a subnanoscales.

14.4 Applications

14.4.1 Catalysis for Fuel-Cell Reaction

The common notion about platinum-based fuel cell catalysts was that the optimal particle size is about 3 nm, and smaller particle decreases their intrinsic activities. Based on the volcano-shaped relationship between the oxygen reduction reaction (ORR) activities and the d-band center energy of platinum and alloys, the surface adsorption of oxygen onto the pure Pt(111) surface is stronger than the optimal value. Therefore, alloying with other less noble metals (Ni, Co, Fe) would increase their ORR activity by lowering the d-band center on the platinum atoms, which leads to a weaker adsorption energy [65]. Miniaturization of the platinum particle raises the d-band center leading to a decrease in the surface-specific activity [60, 61]. Although the smaller particle size has an advantage in a higher surface-to-volume ratio, extreme miniaturization would result in a lower activity due to an electronic reason. Indeed, many previous results suggested the decreasing ORR activity of smaller particles ($\sim$1.5 nm). However, subnanoparticles of a size smaller than 1 nm are molecular-like clusters with specific structures, but not simple spherical particles. Based on this idea, it is not likely that such a simple relationship between the size and activity continues on a subnanometer scale.

Subnanoparticles synthesized by a conventional synthetic method cannot define the exact number of the atomicity. This is the reason why the precise investigation of subnanoparticles was very difficult. The significant advantage of the versatile and precise size-controlling by the dendrimer template allowed this investigation for the first time. The As-prepared platinum subnanoparticles were cast onto a glassy carbon disk electrode to determine the ORR activity using a rotating disk voltammetry method. All the platinum subnanoparticles (Pt_{12}, Pt_{28} and Pt_{60}) showed a cathodic current corresponding to the ORR. The kinetic current densities with each catalyst were determined by the Koutecky-Levich equation, and were plotted versus the weight of platinum on the electrode (Fig. 14.13a). This treatment can exclude the contribution by the mass-transfer (diffusion) limiting current. Each catalyst showed a linear relationship between the weight and the kinetic current density, indicating the intrinsic mass-specific activity as the slope of the plot. Surprisingly, Pt_{12} exhibited the highest ORR activity, and the mass activity was 13-times higher than that of a commercially available Pt/C catalyst (Fig. 14.13b) [67]. This observation completely disagrees with the common notion.

To reveal a reason for the unexpected catalytic activity, a Pt_{13} subnanoparticle, which has almost the same size but a geometric stability, was synthesized. Magic numbers (13, 55, 147…) are one of the important parameters to determine the particle stability. Clusters with this magic number have highly stable and symmetric structures such as an icosahedron or a cuboctahedron. The structure of an actually synthesized Pt_{13} subnanoparticle using a specially designed phenylazomethine dendrimer was determined to be icosahedron. In sharp contrast, Pt_{12} has a very deformed structure because it lacks one Pt atom required to form a stable icosahedral structure. More interestingly, these two subnanoparticles (Pt_{12} and Pt_{13}) have

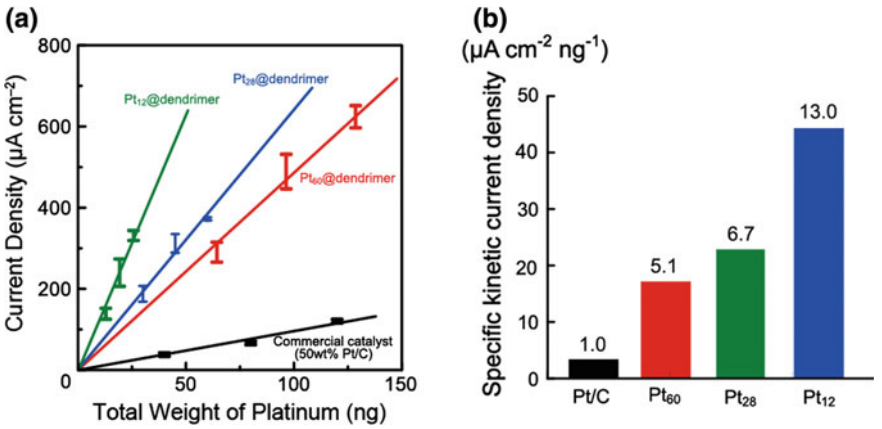

Fig. 14.13 **a** Relationship between the platinum weight on a modified electrode and observed kinetic current densities of the oxygen reduction reaction. **b** Weight-specific kinetic current densities of the different catalysts. The kinetic values normalized by the value of Pt/C are shown on each *bar* chart

significantly different catalytic activities for the ORR [68]. In spite of the almost equivalent particle size and the surface-to-volume ratio (Pt_{13}: 92 %, Pt_{12}: 100 %), Pt_{12} showed *ca*. a 2.5-times higher activity than Pt_{13}. A theoretical investigation based on the density-functional theory (DFT) suggested that several surfaces on Pt_{12} have moderate adsorption energies to oxygen suitable for the ORR. In contrast, Pt13 have to strong adsorption energies for the effective conversion. Such smaller subnanoparticles with a non-magic number atomicity can expose unique surfaces, which does not appear on the bulk or larger particles. This result suggests the significant potential of the non-magic number particles.

14.4.2 Catalysis for Organic Synthesis

Because the subnanoparticles are very reactive, they were easily aggregated producing much larger nanoparticles in a solution if there were other particles within the diffusional accessible distance. The stabilization is usually achieved by surface protection of small molecular ligands, i.e., polymers. However, this protection decreases the catalytic activity because the reactive surfaces were covered. Indeed, nanoparticles are used as the supported catalyst, which can be prepared from the precursor materials adsorbed on the surface, followed by the calcination. In contrast, the subnanoparticles temporarily stabilized in a dendrimer can be directly supported on a mesoporous carbon, and capable as the catalyst without any calcination or other post treatments (Fig. 14.14).

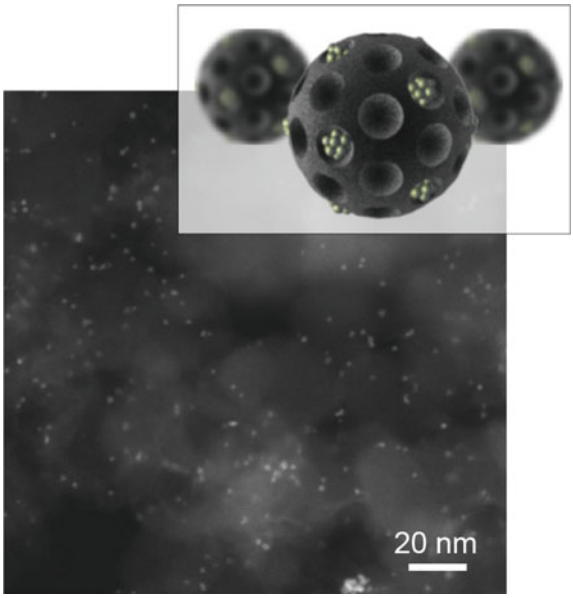

Fig. 14.14 A HAADF-STEM-image of the Pt_{28} subnanoparticle supported onto a graphitic mesoporous carbon (GMC)

Platinum subnanoparticles were supported on a graphitic mesoporous carbon (GMC) and used for the hydrogenation reactions. Relative to the larger platinum nanoparticles (diameter ~2.2 nm), the Pt_{12} catalyst exhibited a significantly high activity for the hydrogenation of olefins. The Pt-atom based turn-over-frequency of the Pt_{12} catalyst for styrene was *ca*. 3-times higher than that of the reference particle (2.2 nm diameter) [72]. It should be noted that the superiority over the larger particles was better for the styrene derivatives with an electron-withdrawing group. The same catalyst also exhibited an impressive activity over the reductive aminations of aldehydes with amines producing the tertiary amines. The product yield by Pt_{12} was much higher than that of the larger particles. Furthermore, Pt_{12} does not produce an intermediate imine or iminium species, indicating the significant reducing activity for the intermediate imines [73].

Rh subnanoparticles (Rh_{60}) also exhibited a very high hydrogenation activity for various olefinic substrates and nitroarenes (Fig. 14.15). The observed turn-over-frequency was a maximum 24-times higher than that of the Wilkinson's complex ($RhCl(PPh_3)_3$). For the olefin hydrogenation reactions, the rhodium nanoparticles prepared with phenylazomethine (DPA) dendrimers exhibited a much higher activity than that with a polyamidoamine (PAMAM) dendrimer [69]. This is probably due to the surface accessibility to the surfaces of the dendrimer-encapsulated particles. The flexible PAMAM dendrimer would fold the terminal monomers back into the inner space where the rhodium particle is encapsulated. This situation is almost similar when the linear polymers, such as polyvinyl alcohol or polyvinyl 2-pyrrolidone (PVP), were used. The catalytic performance of the rhodium particle encapsulated in DPA was much different. The rigid backbone

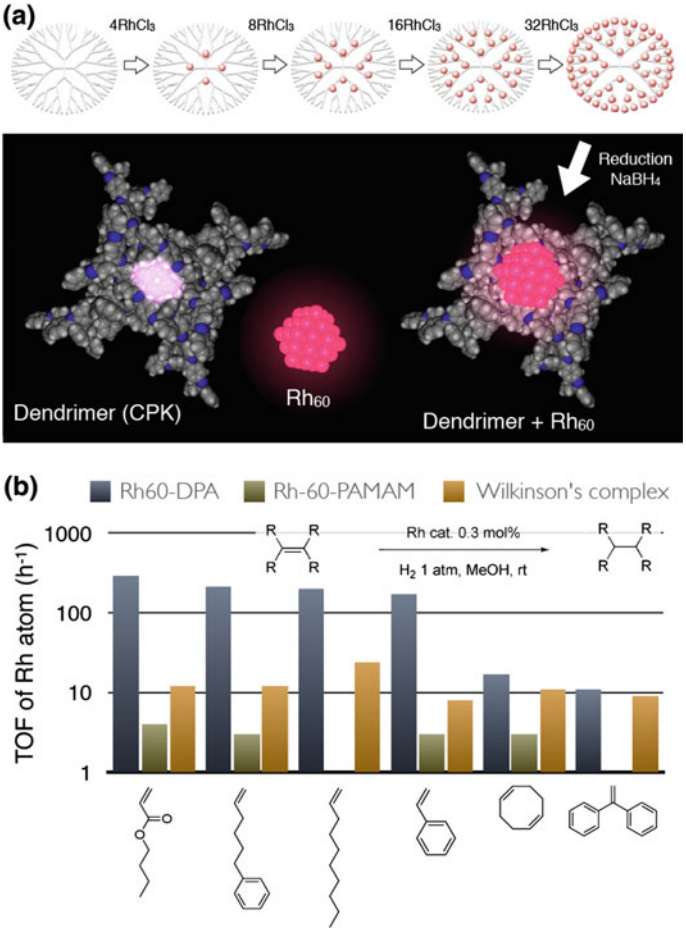

Fig. 14.15 **a** Preparation of the Rh_{60} nanoparticle using the dendrimer template. **b** Turn-over-frequency values of the catalytic hydrogenation reactions of various olefin substrates using three different catalysts. Rh_{60}-DPA and Rh_{60}-PAMAM are the rhodium nanoparticles encapsulated in a phenylazomethine dendrimer and a polyamidoamine dendrimer, respectively

structure restricting the self-backfolding might be one of the reasons why the catalyst shows such a high activity over the PAMAM dendrimer.

A noteworthy enhancement of the catalytic activity was found when the rhodium nanoparticle was alloyed with the second metallic element. One significant example is the $Rh_{32}Fe_{28}$ catalyst. Similar to the homometallic particles, the bimetallic particle can be synthesized by the dendrimer-based templating method. Although the Rh_{60} nanoparticle showed a very high catalytic activity, the $Rh_{32}Fe_{28}$ particle showed *ca*. a 3 times higher turn-over-frequency [70]. Similar enhancement was also observed for various hydrogenation reactions of olefins and nitroarenes. Because the physical mixture of Rh_{60} and Fe_{60} at the same atomic ratio did not

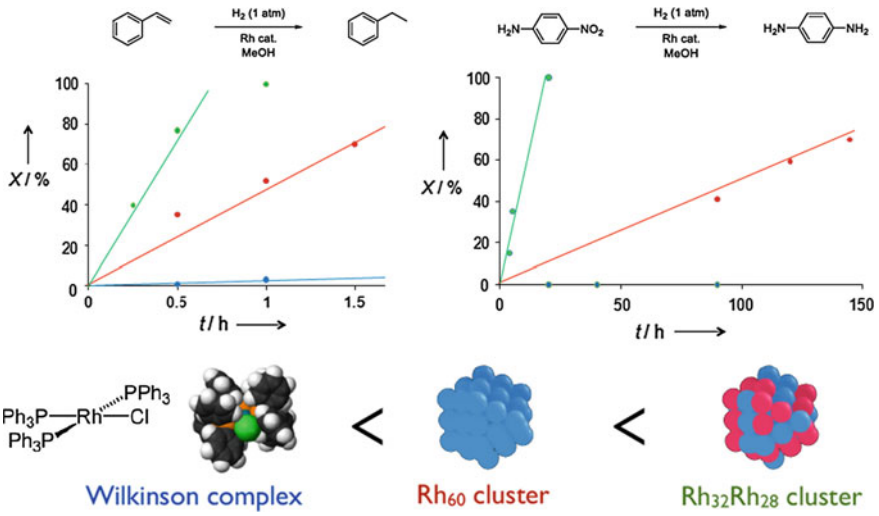

Fig. 14.16 Catalytic hydrogenation reactions of styrene and nitroarene using different Rh catalysts. A $Rh_{32}Fe_{28}$ catalyst showed a much higher activity than the other catalysts (Rh_{60} and Wilkinson's complex)

show such a high TOF value, this enhancement is considered to be the result of a synergistic catalytic enhancement (Fig. 14.16).

14.5 Summary

The molecular templating approach using a precise metal-assembling complex allows us to synthesize atomicity-controlled subnanoparticles. In addition to the platinum and titanium oxides, this modified synthesis has also been applied to the gold [74], gallium oxide [75] or iron oxide [76] subnanoparticle syntheses. The most important point of this method is versatile applications to various metallic elements and the atomicity if the precursor can be assembled in the dendrimer nanospace. Especially, non-magic number subnanoparticles (clusters) have been inaccessible with other conventional techniques because the conventional method is basically based on spontaneous nucleation and aggregations producing thermodynamically stable ones. The present template method can provide the desired nanoparticle of which the atomicity was externally controlled by the stoichiometry in the precursor material. Because the selections of the parent element(s), atomicity and their ratio are almost infinite, these novel "nanometals" could be promising materials for the next generation energy conversion and information technology.

References

1. M.-C. Daniel, D. Astruc, Gold nanoparticles: assembly, supramolecular chemistry, quantum-size-related properties, and applications toward biology, catalysis, and nanotechnology. Chem. Rev. **104**, 293–346 (2004)
2. C. Deraedt, D. Astruc, "Homeopathic" palladium nanoparticle catalysis of cross carbon–arbon coupling reactions. Acc. Chem. Res. **47**, 494–503 (2013)
3. N.S. Porter, H. Wu, Z. Quan, J. Fang, Shape-control and electrocatalytic activity-enhancement of Pt-Based bimetallic nanocrystals. Acc. Chem. Res. **46**, 1867–1877 (2013)
4. A. Taketoshi, M. Haruta, Size- and structure-specificity in catalysis by gold clusters. Chem. Lett. **43**, 380–387 (2014)
5. S. Yamazoe, K. Koyasu, T. Tsukuda, Nonscalable oxidation catalysis of gold clusters. Acc. Chem. Res. **47**, 816–824 (2014)
6. J.M. Caruge, J.E. Halpert, V. Wood, V. Bulović, M.G. Bawendi, Colloidal quantum-dot light-emitting diodes with metal-oxide charge transport layers. Nat. Photonics **2**, 247–250 (2008)
7. S. Coe, W.-K. Woo, M. Bawendi, V. Bulović, Electroluminescence from single monolayers of nanocrystals in molecular organic devices. Nature **420**, 800–803 (2002)
8. V.L. Colvin, M.C. Schlamp, A.P. Alivisatos, Light-emitting diodes made from cadmium selenide nanocrystals and a semiconducting polymer. Nature **370**, 354–357 (1994)
9. M. Cargnello, T.R. Gordon, C.B. Murray, Solution-phase synthesis of titanium dioxide nanoparticles and nanocrystals. Chem. Rev. **114**, 9319–9345 (2014)
10. J. Lai, K.V.P.M. Shafi, A. Ulman, K. Loos, R. Popovitz-Biro, Y. Lee, T. Vogt, C. Estournès, One-step synthesis of core(Cr)/shell(gamma-Fe_2O_3) nanoparticles. J. Am. Chem. Soc. **127**, 5730–5731 (2005)
11. S. Sun, C.B. Murray, D. Weller, L. Folks, A. Moser, Monodisperse FePt nanoparticles and ferromagnetic FePt nanocrystal superlattices. Science **287**, 1989–1992 (2000)
12. B.L. Cushing, V.L. Kolesnichenko, C.J. O' Connor, Recent advances in the liquid-phase syntheses of inorganic nanoparticles. Chem. Rev. **104**, 3893–3946 (2004)
13. W.P. Halperin, Quantum size effects in metal particles. Rev. Mod. Phys. **58**, 533–606 (1986)
14. H. Weller, Colloidal semiconductor Q-particles: chemistry in the transition region between solid state and molecules. Angew. Chem. Int. Ed. **32**, 41–43 (1993)
15. W.L. Wilson, P.F. Szajowski, L.E. Brus, Quantum confinement in size-selected, surface-oxidized silicon nanocrystals. Science **262**, 1242–1244 (1993)
16. M. Shao, A. Peles, K. Shoemaker, Electrocatalysis on platinum nanoparticles: particle size effect on oxygen reduction reaction activity. Nano Lett. **11**, 3714–3719 (2011)
17. H.-J. Zhai, L.-S. Wang, Probing the electronic structure and band gap evolution of titanium oxide clusters $(TiO_2)_n^-$ (n = 1–10) using photoelectron spectroscopy. J. Am. Chem. Soc. **129**, 3022–3026 (2007)
18. R.Y. Korotkov, M.A. Reshchikov, B.W. Wessels, Transient photoluminescence of defects in undoped GaN prepared by metal organic vapor phase epitaxy. Phys. B **273–274**, 80–83 (1999)
19. M.A. Reshchikov, H. Morkoç, Luminescence from defects in GaN. Phys. B **376–377**, 428–431 (2006)
20. D.E. Bergeron, P.J. Roach, A.W. Castleman, N.O. Jones, S.N. Khanna, Al cluster superatoms as halogens in polyhalides and as alkaline earths in iodide salts. Science **307**, 231–235 (2005)
21. A.W. Castleman Jr., S.N. Khanna, Clusters, superatoms, and building blocks of new materials. J. Phys. Chem. C **113**, 2664–2675 (2009)
22. H. Häkkinen, Atomic and electronic structure of gold clusters: understanding flakes, cages and superatoms from simple concepts. Chem. Soc. Rev. **37**, 1847–1859 (2008)
23. S.J. Peppernick, K.D.D. Gunaratne, A.W. Castleman, Superatom spectroscopy and the electronic state correlation between elements and isoelectronic molecular counterparts. Proc. Natl. Acad. Sci. USA **107**, 975–980 (2010)

24. W. De Heer, The physics of simple metal clusters: experimental aspects and simple models. Rev. Mod. Phys. **65**, 611–676 (1993)
25. J. Kemsley, Developing superatom science. C&En News **91**, 24–25 (2013)
26. D.A. Tomalia, A.M. Naylor, W.A. Goddard III, Starburst dendrimers: molecular-level control of size, shape, surface chemistry, topology, and flexibility from atoms to macroscopic matter. Angew. Chem. Int. Ed. **29**, 138–175 (1990)
27. B. Voit, New developments in hyperbranched polymers. J. Polym. Sci. A Polym. Chem. **38**, 2505–2525 (2000)
28. D.A. Tomalia, H. Baker, J. Dewald, M. Hall, G. Kallos, S. Martin, J. Roeck, J. Ryder, P. Smith, A new class of polymers: starburst-dendritic macromolecules. Polym. J. **17**, 117–132 (1985)
29. C. Hawker, J.M.J. Fréchet, Preparation of polymers with controlled molecular architecture. A new convergent approach to dendritic macromolecules. J. Am. Chem. Soc. **112**, 7638–7647 (1990)
30. J.M.J. Hecht Fréchet, Dendritic encapsulation of function: applying nature's site isolation principle from biomimetics to materials science. Angew. Chem. Int. Ed. **40**, 74-1 (2001)
31. M. Ballauff, C.N. Likos, Dendrimers in solution: insight from theory and simulation. Angew. Chem. Int. Ed. **43**, 2998–3020 (2004)
32. K. Kono, T. Miyoshi, Y. Haba, E. Murakami, C. Kojima, A. Harada, Temperature sensitivity control of alkylamide-terminated poly(amidoamine) dendrimers induced by guest molecule binding. J. Am. Chem. Soc. **129**, 7222–7223 (2007)
33. O. Finikova, A. Galkin, V. Rozhkov, M. Cordero, C. Hägerhäll, S. Vinogradov, Porphyrin and tetrabenzoporphyrin dendrimers: tunable membrane-impermeable fluorescent pH nanosensors. J. Am. Chem. Soc. **125**, 4882–4893 (2003)
34. M. Matos, J. Hofkens, W. Verheijen, F. Schryver, S. Hecht, K. Pollak, J.M.J. Fréchet, B. Forier, W. Dehaen, Effect of core structure on photophysical and hydrodynamic properties of porphyrin dendrimers. Macromolecules **33**, 2967–2973 (2000)
35. W. Maes, W. Dehaen, synthetic aspects of porphyrin dendrimers. Eur. J. Org. Chem. 4719–752 (2009)
36. M.-S. Choi, T. Yamazaki, I. Yamazaki, T. Aida, Bioinspired molecular design of light-harvesting multiporphyrin arrays. Angew. Chem. Int. Ed. **43**, 150–158 (2004)
37. D. Astruc, Electron-transfer processes in dendrimers and their implication in biology, catalysis, sensing and nanotechnology. Nat. Chem. **4**, 255–267 (2012)
38. F. Zeng, S.C. Zimmerman, Dendrimers in supramolecular chemistry: from molecular recognition to self-assembly. Chem. Rev. **97**, 1681–1712 (1997)
39. V. Percec, D.A. Wilson, P. Leowanawat, C.J. Wilson, A.D. Hughes, M.S. Kaucher, D.A. Hammer, D.H. Levine, A.J. Kim, F.S. Bates, K.P. Davis, T.P. Lodge, M.L. Klein, R.H. DeVane, E. Aqad, B.M. Rosen, A.O. Argintaru, M.J. Sienkowska, K. Rissanen, S. Nummelin, J. Ropponen, Self-assembly of Janus dendrimers into uniform dendrimersomes and other complex architectures. Science **328**, 1009–1014 (2010)
40. G. Behera, S. Ramakrishnan, Controlled variation of spacer segment in hyperbranched polymers: from densely branched to lightly branched systems. Macromolecules **37**, 9814–9820 (2004)
41. T. Mourey, S. Turner, M. Rubinstein, J.M.J. Fréchet, C. Hawker, K. Wooley, Unique behavior of dendritic macromolecules: intrinsic viscosity of polyether dendrimers. Macromolecules **25**, 2401–2406 (1992)
42. J.F.G.A. Jansen, E.M.M. de Brabander-van den Berg, E.W. Meijer, Encapsulation of guest molecules into a dendritic box. Science **266**, 1226–1229 (1994)
43. W.-D. Jang, N. Nishiyama, G.-D. Zhang, A. Harada, D.-L. Jiang, S. Kawauchi, Y. Morimoto, M. Kikuchi, H. Koyama, T. Aida, K. Kataoka, Supramolecular nanocarrier of anionic dendrimer porphyrins with cationic block copolymers modified with polyethylene glycol to enhance intracellular photodynamic efficacy. Angew. Chem. Int. Ed. **44**, 419–423 (2005)

44. M. Ottaviani, F. Montalti, N. Turro, D.A. Tomalia, Characterization of starburst dendrimers by the EPR technique. copper(II) ions binding full-generation dendrimers. J. Phys. Chem. B **101**, 158–166 (1997)
45. K. Yamamoto, M. Higuchi, S. Shiki, M. Tsuruta, H. Chiba, Stepwise radial complexation of imine groups in phenylazomethine dendrimers. Nature **415**, 509–511 (2002)
46. K. Takanashi, A. Fujii, R. Nakajima, H. Chiba, M. Higuchi, Y. Einaga, K. Yamamoto, Heterometal assembly in dendritic polyphenylazomethines. Bull. Chem. Soc. Jpn. **80**, 1563–1572 (2007)
47. T. Imaoka, R. Tanaka, S. Arimoto, M. Sakai, M. Fujii, K. Yamamoto, Probing stepwise complexation in phenylazomethine dendrimers by a metallo-porphyrin core. J. Am. Chem. Soc. **127**, 13896–13905 (2005)
48. M. Higuchi, M. Tsuruta, H. Chiba, S. Shiki, K. Yamamoto, Control of stepwise radial complexation in dendritic polyphenylazomethines. J. Am. Chem. Soc. **125**, 9988–9997 (2003)
49. K. Yamamoto, M. Higuchi, A. Kimoto, T. Imaoka, K. Masachika, Novel functional groups with fine-controlled metal assembling function. Bull. Chem. Soc. Jpn **78**, 349–355 (2005)
50. T. Imaoka, H. Ueda, K. Yamamoto, Enhancing the photoelectric effect with a potential-programmed molecular rectifier. J. Am. Chem. Soc. **134**, 8412–8415 (2012)
51. K. Albrecht, K. Yamamoto, Dendritic structure having a potential gradient: new synthesis and properties of carbazole dendrimers. J. Am. Chem. Soc. **131**, 2244–2251 (2009)
52. M. Wang, X. Gong, J. Hu, Y. Yu, Q. Chen, Y. Cheng, Understanding the binding interactions between dendrimer and 18 common amino acids by NMR techniques. J. Phys. Chem. B **115**, 12728–12735 (2011)
53. A. Chen, P. Holt-Hindle, Platinum-based nanostructured materials: synthesis, properties, and applications. Chem. Rev. **110**, 3767–3804 (2010)
54. V.S. Myers, M.G. Weir, E.V. Carino, D.F. Yancey, S. Pande, R.M. Crooks, Dendrimer-encapsulated nanoparticles: new synthetic and characterization methods and catalytic applications. Chem. Sci. **2**, 1632–1646 (2011)
55. R.M. Anderson, L. Zhang, J.A. Loussaert, A.I. Frenkel, G. Henkelman, R.M. Crooks, An experimental and theoretical investigation of the inversion of Pd@Pt Core@Shell dendrimer-encapsulated nanoparticles. ACS Nano **7**, 9345–9353 (2013)
56. J. Zheng, R.M. Dickson, Individual water-soluble dendrimer-encapsulated silver nanodot fluorescence. J. Am. Chem. Soc. **124**, 13982–13983 (2002)
57. J. Zheng, J.T. Petty, R.M. Dickson, High quantum yield blue emission from water-soluble Au8 nanodots. J. Am. Chem. Soc. **125**, 7780–7781 (2003)
58. S.-I. Tanaka, J. Miyazaki, D.K. Tiwari, T. Jin, Y. Inouye, Fluorescent platinum nanoclusters: synthesis, purification, characterization, and application to bioimaging. Angew. Chem. Int. Ed. **50**, 431–435 (2011)
59. K. Yamamoto, T. Imaoka, Precision synthesis of subnanoparticles using dendrimers as a superatom synthesizer. Acc. Chem. Res. **47**, 1127–1136 (2014)
60. V. Nieminen, K. Honkala, A. Taskinen, D.Y. Murzin, Intrinsic metal size effect on adsorption of organic molecules on platinum. J. Phys. Chem. C **112**, 6822–6831 (2008)
61. E. Toyoda, R. Jinnouchi, T. Hatanaka, Y. Morimoto, K. Mitsuhara, A. Visikovskiy, Y. Kido, The d-band structure of Pt nanoclusters correlated with the catalytic activity for an oxygen reduction reaction. J. Phys. Chem. C **115**, 21236–21240 (2011)
62. C. Chen, Y. Kang, Z. Huo, Z. Zhu, W. Huang, H.L. Xin, J.D. Snyder, D. Li, J.A. Herron, M. Mavrikakis, M. Chi, K.L. More, Y. Li, N.M. Markovic, G.A. Somorjai, P. Yang, V.R. Stamenkovic, Highly crystalline multimetallic nanoframes with three-dimensional electrocatalytic surfaces. Science **343**, 1339–1343 (2014)
63. B. Lim, M. Jiang, P.H.C. Camargo, E.C. Cho, J. Tao, X. Lu, Y. Zhu, Y. Xia, Pd–Pt bimetallic nanodendrites with high activity for oxygen reduction. Science **324**, 1302–1305 (2009)
64. N. Tian, Z.-Y. Zhou, S.-G. Sun, Y. Ding, Z.L. Wang, Synthesis of tetrahexahedral platinum nanocrystals with high-index facets and high electro-oxidation activity. Science **316**, 732–735 (2007)

65. V. Stamenkovic, B.S. Mun, K.J.J. Mayrhofer, P.N. Ross, N.M. Markovic, J. Rossmeisl, J. Greeley, J.K. Nøskov, Changing the activity of electrocatalysts for oxygen reduction by tuning the surface electronic structure. Angew. Chem. Int. Ed. **45**, 2897–2901 (2006)
66. O. Enoki, H. Katoh, K. Yamamoto, Synthesis and properties of a novel phenylazomethine dendrimer with a tetraphenylmethane core. Org. Lett. **8**, 569–571 (2006)
67. K. Yamamoto, T. Imaoka, W.-J. Chun, O. Enoki, H. Katoh, M. Takenaga, A. Sonoi, Size-specific catalytic activity of platinum clusters enhances oxygen reduction reactions. Nat. Chem. **1**, 397–402 (2009)
68. T. Imaoka, H. Kitazawa, W.-J. Chun, S. Omura, K. Albrecht, K. Yamamoto, Magic number Pt_{13} and misshapen Pt_{12} clusters: which one is the better catalyst? J. Am. Chem. Soc. **135**, 13089–13095 (2013)
69. I. Nakamula, Y. Yamanoi, T. Yonezawa, T. Imaoka, K. Yamamoto, H. Nishihara, Nanocage catalysts-rhodium nanoclusters encapsulated with dendrimers as accessible and stable catalysts for olefin and nitroarene hydrogenations. Chem. Commun. 5716–718 (2008)
70. I. Nakamula, Y. Yamanoi, T. Imaoka, K. Yamamoto, H. Nishihara, A uniform bimetallic rhodium/iron nanoparticle catalyst for the hydrogenation of olefins and nitroarenes. Angew. Chem. Int. Ed. **50**, 5830–5833 (2011)
71. N. Satoh, T. Nakashima, K. Kamikura, K. Yamamoto, Quantum size effect in TiO_2 nanoparticles prepared by finely controlled metal assembly on dendrimer templates. Nat. Nanotech. **3**, 106–111 (2008)
72. M. Takahashi, T. Imaoka, Y. Hongo, K. Yamamoto, Formation of a Pt_{12} cluster by single-atom control that leads to enhanced reactivity: hydrogenation of unreactive olefins. Angew. Chem. Int. Ed. **52**, 7419–7421 (2013)
73. M. Takahashi, T. Imaoka, Y. Hongo, K. Yamamoto, A highly-active and poison-tolerant Pt_{12} sub-nanocluster catalyst for the reductive amination of aldehydes with amines. Dalton Trans. **42**, 15919–15921 (2013)
74. T. Imaoka, M. Fushimi, A. Kimoto, Y. Okamoto, K. Takanashi, K. Yamamoto, Resistive switching memory based on size-controlled 1-nm gold particles. Chem. Lett. **43**, 1269–1271 (2014)
75. I. Hirano, T. Imaoka, K. Yamamoto, Deposition of gallium oxide nanodots prepared from metal-assembling dendrimer molecules isolated by the spacing of the nonmetal-assembling dendrimer molecules in the two-dendrimers mixture monolayer. Polym. Adv. Tech. **24**, 903–908 (2013)
76. I. Hirano, T. Imaoka, K. Yamamoto, Preparation of carbon nanotubes using iron oxide(III) nanoparticles size-controlled by phenylazomethine dendrimers. J. Inorg. Organomet. Polym. Mat. **23**, 223–226 (2012)

Chapter 15
Electrochemistry-Based Smart Biodevices

Matsuhiko Nishizawa

Abstract Engineering the interfacial contact between device materials and biological systems (body, tissue, cell, and protein) is of central importance to the advancement of bioelectronic devices. Here, novel possibilities of electrochemical techniques for creation of smart biodevices are discussed. Three original techniques for biocompatible interfacing will be described: (1) the electrochemical biolithography for spatiotemporal control of protein adsorption and cell adhesion even inside a microfluidic channel; (2) the hydrogel-based biocompatible electrodes prepared by electrochemical polymerization of conducting polymers; (3) the high performance enzyme electrodes made of engineered nanocarbon materials. These varieties of novel electrochemical techniques have been utilized for creating smart devices, such as on-demand biochip, contractile biochip, and self-powered biosensors and medical patches.

Keywords Electrochemistry · Biochip · Hydrogel · Conducting polymer · Biofuel cell

15.1 Introduction

Electrochemistry is the basis of battery, plating, sensing, etc., and has contributed to the progress of modern industrialized society. In this chapter, novel potential of electrochemical techniques for the creation of smart biodevices are described (Fig. 15.1). Importantly, electrochemistry could provide techniques to connect "electrical" device systems and "ionic" biosystems.

The first example of unique electrochemical technique is the electrochemical biolithography (ECBL), which is a novel surface patterning technique utilizing electrochemical reaction for spatiotemporally controlling protein adsorption and cell adhesion even inside a microfluidic channel. This ECBL technique can be used

M. Nishizawa (✉)
Department of Fine Mechanics, Tohoku University, 6-6-01 Aoba, Sendai 980-8579, Japan
e-mail: nishizawa@biomems.mech.tohoku.ac.jp

J. Sone and S. Tsuji (eds.), *Intelligent Nanosystems for Energy, Information and Biological Technologies*, DOI 10.1007/978-4-431-56429-4_15

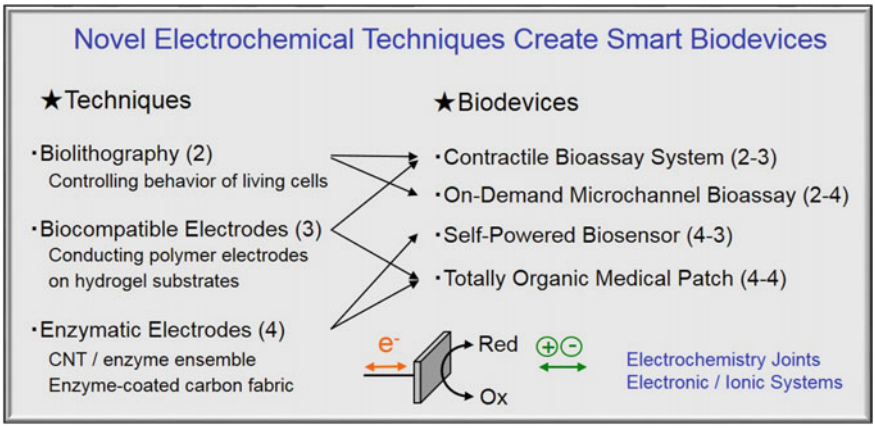

Fig. 15.1 Contents of Chap. 15

for the on-demand preparation of biochips just prior to their use. Second example is the stretchable organic electrodes on hydrogel substrates that are fabricated by electrochemical polymerization of conducting polymers. Such moist electrode shows excellent biocompatibility due to their stiffness comparable to that of cells and tissue. In addition, the molecular permeability of the hydrogel-based electrode guarantees synergy to the physiological milieu. Finally, newly designed, high-performance enzyme electrodes will be shown. The fine composite of enzyme and carbon nanotube (CNT) exhibited high performance with almost 100 % utilization of enzymes. The carbon fabric modified by enzyme layers was useful to construct flexible biological fuel cells. These varieties of novel electrochemical techniques have been utilized for creating smart devices, such as self-powered biosensors and totally organic medical devices.

15.2 Electrochemical Biolithography System

15.2.1 Microelectrode-Based Technique to Spatially Control Cell Adhesion

The interfacing between biomolecules and device materials is one of the most important subjects for both in vitro and in vivo medical devices. Especially, micropatterning of living mammalian cells has made significant contributions to fundamental cellular biology, tissue engineering, and cell-based bioelectronics [1, 2]. We have been studying the potential use of microelectrode as the tool for bio-interface engineering, and developed a technique named “electrochemical biolithography” (ECBL) that realizes in situ, spatiotemporal control of cellular adhesion, motility, and shape, by electrochemical means. The ECBL is based on

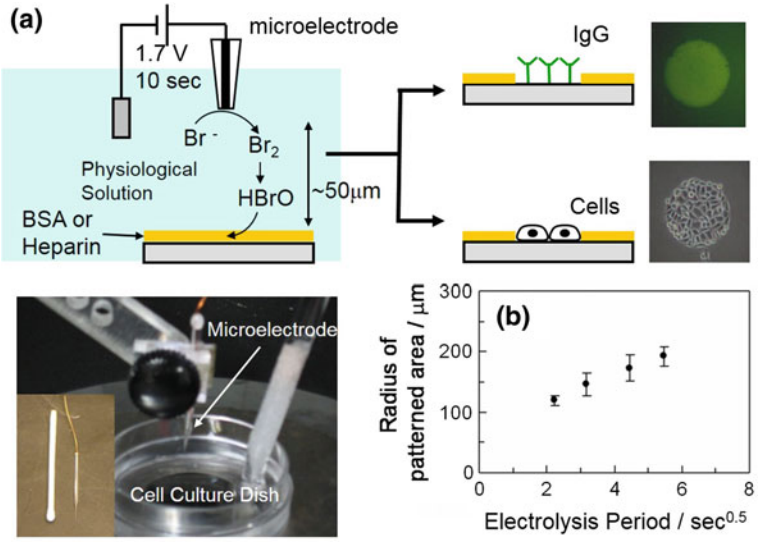

Fig. 15.2 Electrochemical biolithography (ECBL) for patterning bioadhesive area

our finding that the cytophobic nature of the albumin- or heparin-coated substrates can be rapidly switched to cell adhesive by exposure to an oxidizing agent such as HBrO, which can be easily produced by the electrochemical oxidation of a Br^--containing aqueous solution [3, 4]. As schematically illustrated in Fig. 15.2a, the tip of the fine Pt microelectrode was placed ~50 μm above an albumin- or heparin-modified substrate surface, and a potential pulse of 1.7 V with a 10 s period was applied to generate Br_2 (subsequently HBrO) in a 0.1 M phosphate buffer solution containing 25 mM KBr (pH 7.4). Here, the potential pulses were applied against the Ag/AgCl (KCl saturated) reference electrode. The electrochemically treated substrate was then incubated in the antibody IgG solution or HeLa cell-suspended serum-containing culture medium for 1 h. The micrograph shows the clear, circular patterns of IgG and HeLa cells in the area electrochemically treated using the microelectrode. The radius of the circular patterns was roughly proportional to the square root of the electrolysis period (Fig. 15.2b), suggesting that the pattern size corresponds to the diffusion layer of the electrogenerated bromine species (HBrO) which would quickly detach the BSA and heparin layer to allow protein adhesion and cell adhesion.

The cellular micropatterning can be conducted by scanning of a microelectrode as a "pen." In Fig. 15.3a, the microelectrode was scanned at 500 μm s^{-1} closely above the substrate (ca. 10 μm) so as to write a coil using a motor-driven *xyz* stage controlled by a PC, while keeping the electrode potential at 1.7 V to generate the bromine species during the writing. The width of the cellular line patterns is approximately constant and can be varied from a few hundred μm to a

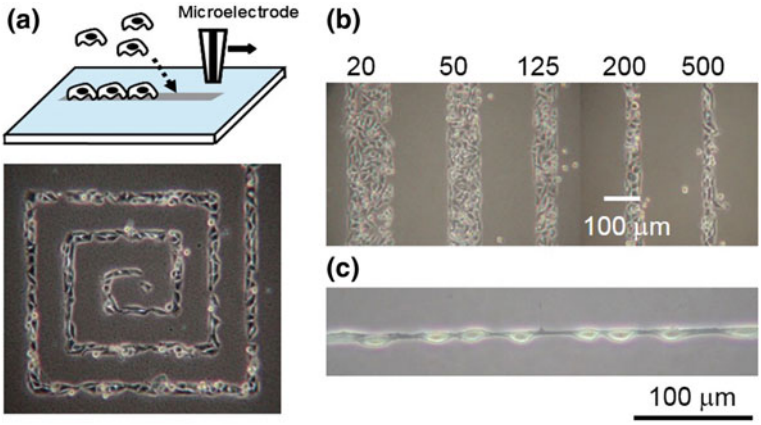

Fig. 15.3 Micropatterning of cellular adhesion by scanning a microelectrode

single-cell-width based on the rate of the scanning electrode (Fig. 15.3b). Figure 15.3c shows examples of single-cell micropatterns drawn at the higher scan rate of 1250 μm s^{-1}, in which the endothelial cells are aligning one by one.

15.2.2 In Situ Control of Cellular Mitosis and Shape

The ECBL technique can be applied even to a pre-cell-patterned substrate [1, 5]. Figure 15.4a–d demonstrates the control of cellular growth and migration possible with the microelectrode technique. The BSA-coated substrate was processed to make the first cellular pattern by a microelectrode scan and by incubation for 1 h in a serum culture medium containing suspended HeLa cells to promote cell attachment. Then, the scanning microelectrode technique was again applied to extend the cellular line pattern perpendicularly. The substrate was further incubated for 24 h in a serum-containing medium without the seeding of additional cells. The micrograph in Fig. 15.4d shows that the HeLa cells proliferated and migrated along the region electrochemically treated with the microelectrode, a finding indicating that the oxidizing agent can change the property of the BSA-coating near the cells without damaging the preexisting cells. Finally, as shown in Fig. 15.4e–g, the modification of an AFM system to accommodate ECBL enabled the in situ patterning in a few μm scale [6, 7]. Figure 15.4g demonstrates that the subcellular resolution of this system enabled the lithographic manipulation of the environment surrounding a single cultured cell (NIH-3T3 fibroblasts). An interesting future experiment using the ECBL-AFM system would be the construction of a neuronal/muscle cell network that could be used to study the interactions of cell junctions.

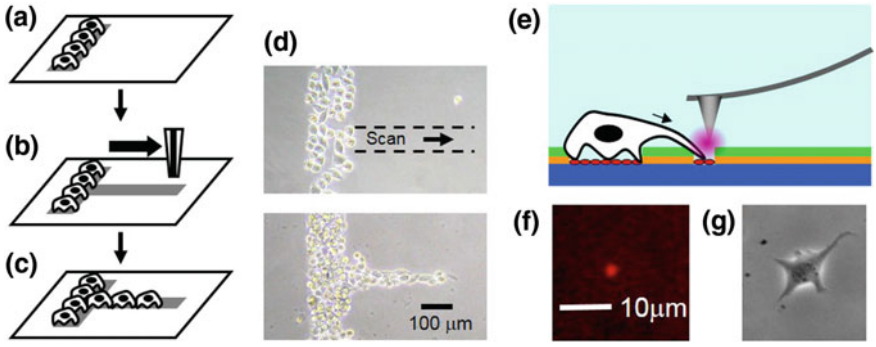

Fig. 15.4 Navigation of cellular migration and extension

15.2.3 Cellular Micropatterns on Hydrogels

The micropatterned cell cultures can be transferred into or on a fibrin gel sheet from a glass substrate with their patterns [8–10]. For example, we prepared contractile C2C12 myotube line patterns embedded in a fibrin gel. A fibrinogen mixture solution was poured over the patterned C2C12 cells, followed by facilitating fibrin gelation to allow the cell adhesion on the surface of the gel. Figure 15.5a shows fluorescent micrographs of the same myotubes pattern (250 μm width) on a glass substrate (left) and after being transferred to a fibrin gel (right). The cell transfer efficiency was almost 100 % regardless of the shape and size of C2C12 patterns, probably due to stronger adhesion to the fibrin gel than to the glass substrate. The myotubes supported by the elastic gel showed larger contractile displacement than when they were attached on a conventional culture dish. Figure 15.5b shows the degree of contractile displacements of myotubes in a fibrin gel at day 1 and day 7 during the continuous 1 week stimulation, proving that the synchronized contraction with the electrical pulse was activated and maintained for a week.

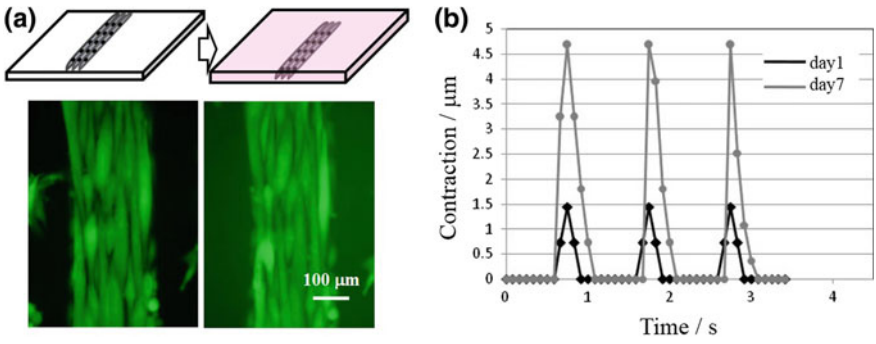

Fig. 15.5 Transfer of cellular patterns from glass substrate to hydrogel for larger contraction

The “cellular patterns on a gel” is convenient for combining microelectric devices that enables localized electrical regulation of cell cultures [10]. The myotube/fibrin gel sheet was patched onto a microelectrode array chip to construct a skeletal muscle cell-based bioassay device (Fig. 15.6a). The Pt microelectrode arrays were previously coated with a conducting polymer, poly(3,4-ethylenedioxythiophene) (PEDOT) that has a large electroactive surface area due to its fibrous structure. This modification increases the interfacial electrical capacity of the electrodes and ensures a less invasive electrical stimulation of the cells without causing faradaic reactions and gas evolution, as explained again in Sect. 15.3.1. The usefulness of this device for type 2 diabetes researches was demonstrated by fluorescent imaging of the contraction-induced translocation of the glucose transporter, GLUT4, from intracellular vesicles to the plasma membrane of the myotubes. Figure 15.6b depicts the expression assay of GLUT4 by the selective stimulation of the transfected myotube line patterns. Myotube line pattern on the left side was stimulated for 3.5 h at 10 Hz

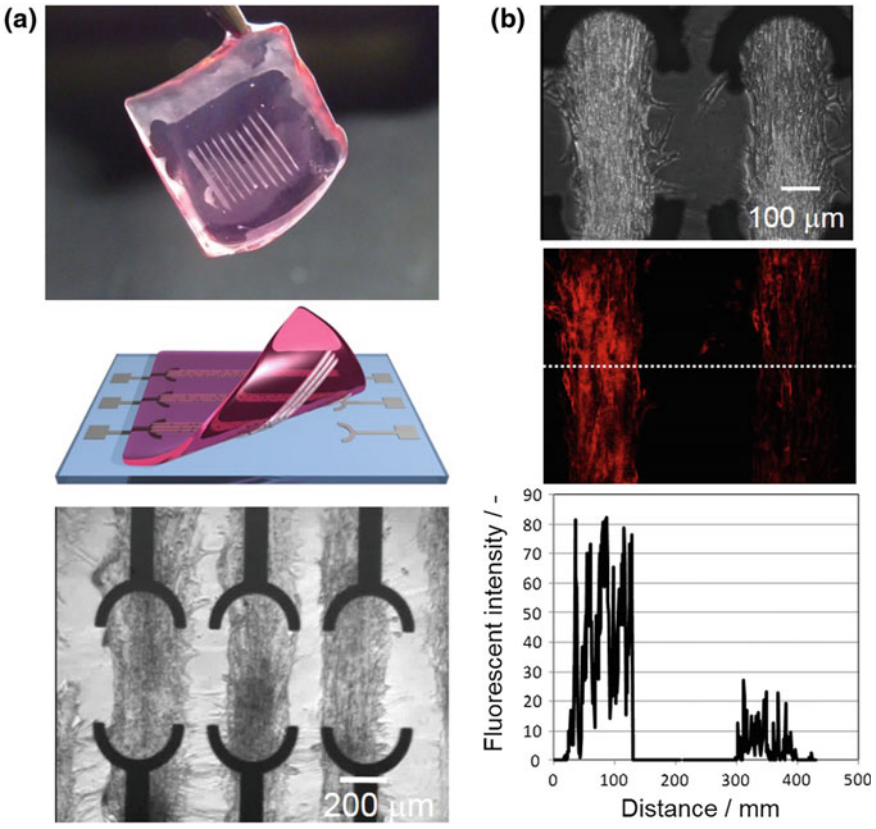

Fig. 15.6 Lamination of muscle cell array-containing gel sheet to electrode array substrate for GLUT4 assay by selective exercise

(amplitude, 2 V; duration, 3 ms; train, 1 s; interval, 10 s) and the right side pattern was rested. After the selective stimulations, the myotubes were immunostained to visualize the expression of GLUT4. The electrically stimulated myotubes displayed an obvious increase in fluorescent intensity above that of unstimulated cells by about fourfold, in agreement with previous studies using the western blot analysis of GLUT 4 translocation in a random-cultured myotube monolayer. This device would be applicable for quantitative bioassays of various contraction-induced metabolic alterations in myotubes.

15.2.4 Integration to Microfluidic Devices

The ECBL technique is simple enough to be integrated to the small and closed systems such as microfluidic devices. Microfluidic systems have been widely used in bioassays, as the microspace in a microfluidic channel allows high throughput analysis with reduced sample volumes [11–13]. On-demand immobilization of proteins at specific locations in a microfluidic device would advance many types of bioassays since most proteins are unstable to harsh solvents, desiccation, oxidation, and heat. The ECBL-based strategy to create a patterned surface within a microfluidic channel realized the site-specific immobilization of protein matrices and cells under physiological conditions even after the device is fully assembled [14–17]. As schematically illustrated in Fig. 15.7a, by locally generating hypobromous acid at a microelectrode in the microchannel, the heparin-coated channel surface rapidly switches from anti-biofouling to protein and cell adhering. Repeating the ECBL by using the array of electrodes on the roof of fluidic devices, this transformation allows compartmentalizing of multiple types of antibodies into distinct regions throughout the single microchannel. After the device was fully assembled, the

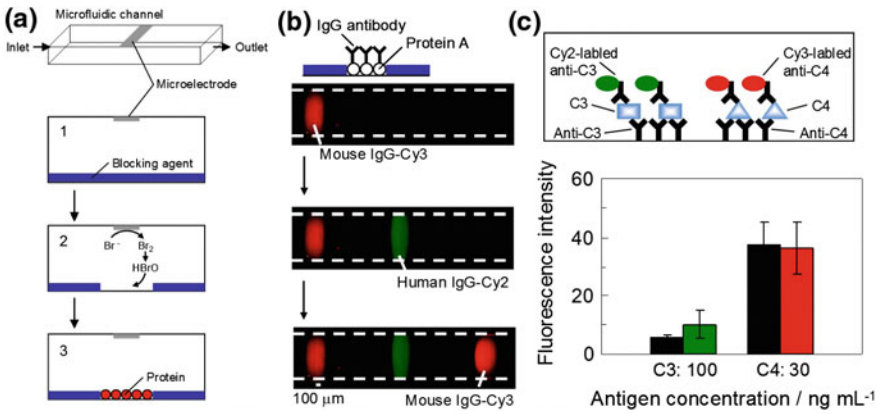

Fig. 15.7 On-demand immobilization of proteins within a microfluidic channel

solutions for heparin-coating were run through the channel. Subsequently, PBS containing 25 mM KBr was introduced into the channel, and after the flow was completely stopped, a potential pulse for ECBL was applied to each microelectrode in order to generate HbrO. Figure 15.7b shows a single microchannel in which multiple types of protein arrays have been immobilized by stepwise patterning [14, 15]. Protein A was used to get uniform orientation of IgG so as to expose the antigen-biding sites to the liquid phase. For practical demonstration, we conducted the simultaneous detention of the complement proteins, C3 protein and C4 protein. A single solution of a mixture of C3 and C4 was passed through the channel, followed by treatment with fluorescence-labeled antibodies (anti-C3-Cy2 and anti-C4-Cy3) (Fig. 15.7c). Fluorescence measurements show that the signal intensities obtained from the simultaneous detection of C3 and C4 (green and red bars) are in close agreement with those obtained from their separate detection (black bars). The results indicate the cross-contamination between the two types of primary antibodies as well as nonspecific adsorption of antigens is satisfactorily low. The clinical reference values of C3 and C4 (650–1350 and 130–350 ng mL^{-1}, respectively) indicate that the present system is sensitive enough for diluted samples in practical diagnoses.

ECBL of cell-binding proteins leads to the in-channel micropatterning or capturing of living cells [16, 17]. Such the in-channel manipulation of cells is important for cellular diagnosis and cell-based bioassay. For example, cytological examination of leucocytes and smear tests of blood samples are useful for the diagnosis of inflammatory diseases. However, preparation of blood smears is time consuming and labor-intensive because they are manually prepared on glass slides individually. As shown in Fig. 15.8a, it was demonstrated that the ECBL-integrated microfluidics is useful for the rapid capture of neutrophils from mixed leucocytes by combination with negative dielectrophoresis (DEP). We attempted selective capture of neutrophils and eosinophils from a mixture of leucocytes containing neutrophils (94.5 ± 5.9 %), eosinophils (2.6 ± 2.7 %), and basophils, lymphocytes, and monocytes (2.9 ± 3.7 %). After immobilizing the anti-neutrophil IgG and the anti-eosinophil IgG, the mixture of leucocytes (5000 cells μL^{-1}) was introduced into the channel at a flow rate of 1.5 $\mu L\ min^{-1}$, followed by the application of AC voltage (1 MHz, 20 Vpp) between the central electrode and the other two electrodes. The ratio of the mean numbers of captured cells was 24:1. Compared with the ratio of neutrophils and eosinophils (36:1) in suspension, these ratios are not greatly different, indicating that the immobilized antibody selectively recognizes the corresponding leucocyte type from the trapped cells. In typical smear test of blood samples, leucocytes are randomly distributed on a glass slide. On the other hand, the use of the microfluidic device reported herein can selectively capture a specific leucocyte type on the specific region within the channel only with simple operations.

The ECBL-integrated microfluidic system is versatile for variety of bioassays. Herein, two typical demonstrations were shown: the on-demand multi-immunoassay

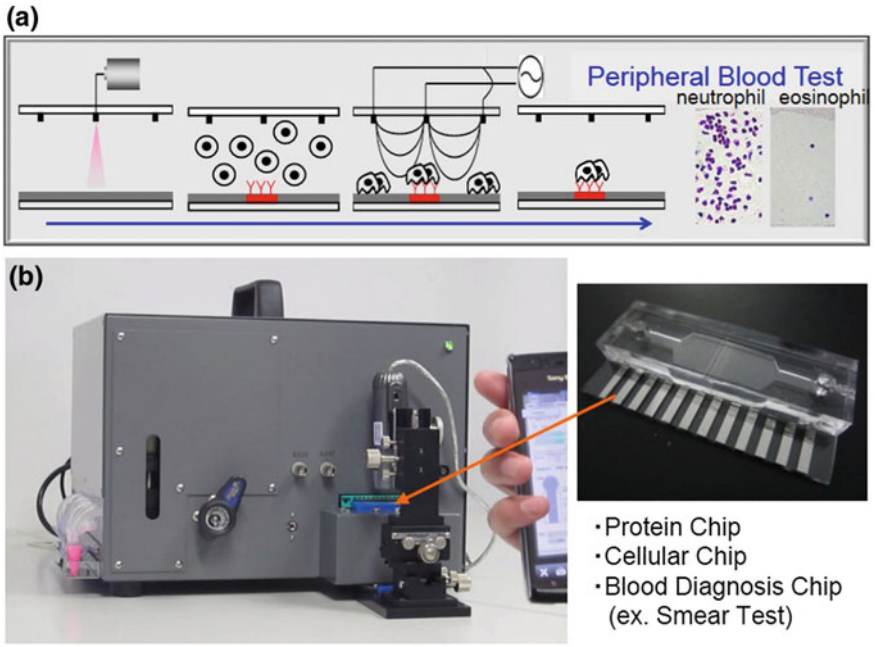

Fig. 15.8 ECBL system for selective capture of cells

for C3 and C4 detection (Fig. 15.7c); the selective capture of neutrophils and eosinophils for efficient smear test of blood samples (Fig. 15.8a). The prototype of EBCL system has been produced (Fig. 15.8b), which is computer-controlled along the preset protocol for protein chip, cell chip, diagnostic chip, etc.

15.3 Conducting Polymer-Based Electrodes

Electrical sensing and stimulation of biological systems (body, tissue, and cell) are of importance for bioengineering research, diagnosis and medical treatment. The electrical stimulation is still often technically challenging, especially when using smaller sized microelectrodes, due to limitations on the current value (charge value) which can be applied without causing a faradic reaction and gas evolution [18]. Conducting polymer (CP) such as polypyrrole (PPy) and poly (3,4-ethylenedioxythiophene) (PEDOT) have large surface area owing to its fibrous structure and thus are high capacity electrode material. Furthermore, the ease of preparation, inherent electrical conductivity, controllability of surface biochemical properties, and biocompatibility make CPs promising interfacial materials for in vivo and in vitro biodevices (Fig. 15.9) [19–21].

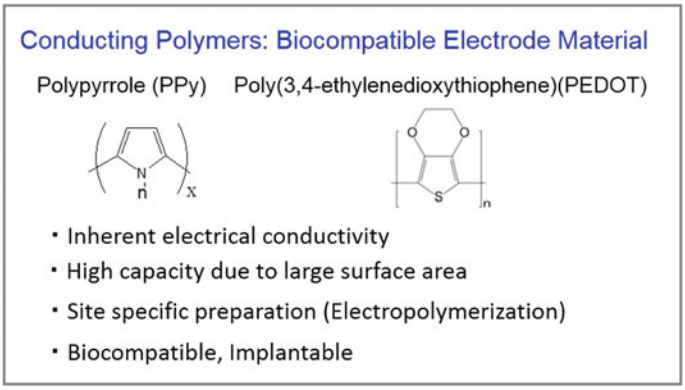

Fig. 15.9 Reasons why conducting polymers are used

Here, novel electrochemical techniques for processing CPs are explained. First, the pretreatment of the electrode substrate with a self-assembled monolayer of alkyl-silane dramatically stabilizes the CP-modified electrodes [22–25]. Next topic is the totally organic electrode devices composed of CP-based electrode and hydrogel substrate. Flexible and stretchable organic electrodes were realized by novel electrochemical process for making a soft, tough adhesion between the electrodes and hydrogel substrates [26, 27].

15.3.1 Low-Invasive Stimulation of Cells with CP-Modified Metal Electrodes

Electropolymerization of conducting polymer is effective to make conventional metal electrode low-invasive for stimulation of cells. We found that the pre-modification of the substrates (glass or polyimide) with self-assembled alkyl-silane monolayers induced anisotropic lateral growth of CP films along the substrate surface [22, 23]. The polymerization anisotropy (the ratio of lateral growth rate to vertical growth rate) was more than 20. Figure 15.10 shows the adhesive strength of the PPy film evaluated with Scotch Tape (adhesion force: 3.7 N cm^{-1}). The PPy formed on the untreated substrate was almost completely peeled off and transferred to the Scotch Tape (Fig. 15.10a). In contrast, the PPy film formed on the alkylsilane monolayer-modified substrates adhered strongly and was not peeled off by the Scotch Tape (Fig. 15.10b). As illustrated in Fig. 15.10c, the PPy film laterally grown around the electrode would anchor the whole PPy film to the substrate [24, 25].

Using the "stable" PPy-coated microelectrode, we have achieved reproducible, low-invasive, external stimulation of a cultured cardiac myocytes [24]. Confocal fluorescence Ca^{2+} imaging was performed for the fluo-3-loaded myocytes cultured

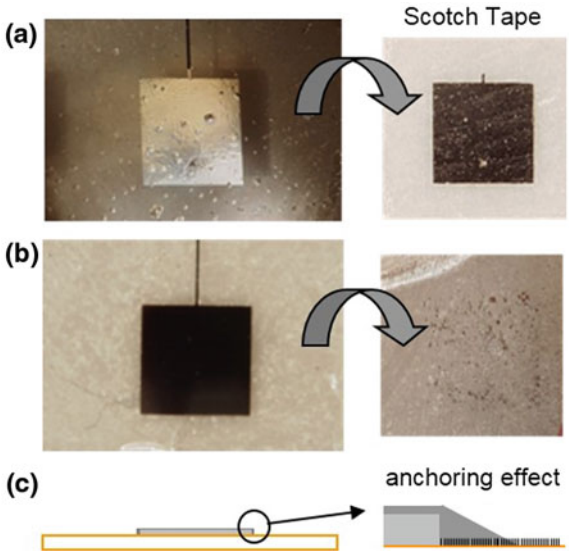

Fig. 15.10 Anchoring of PPy film to electrode substrate

over the PPy-deposited microelectrode (Fig. 15.11a). Figure 15.11b shows the time course of fluorescence intensity changes corresponding to the changes in cytosolic Ca^{2+} concentration during the beating of cardiac cells. Measurements were made at the sites 1 and 2 enclosed by dotted line in Fig. 15.11a, which shows the synchronized Ca^{2+} transients externally evoked by the current pulses delivered by the electrode. In fact, such transients were simultaneously observed throughout the culture substrate, indicating that the cardiac myocytes are electrically conjugated over the sheet through the gap junctions. Such reproducible, noninvasive, external stimulation was achieved owing to the high capacity of PPy. The surface capacity of the PPy-coated electrode (5.8 C cm^{-2}) was 38 times larger than that of bare Pt, and prevents unfavorable polarization. Polarization of the Pt electrode and the resulting faradic reaction dramatically changes surrounding conditions such as pH and temperature.

15.3.2 Totally Organic Electrodes on Hydrogel Substrates

Recent rapid progress in the fabrication of electrodes on flexible substrates has opened a new prospect in the field of future electronics [28, 29]. Hydrogels are excellent candidates of flexible substrate due to their stiffness compared to that of living tissues (a few ~tens kPa) and the molecular permeability that guarantees synergy to the physiological milieu. We have developed an electrochemical technique for micropatterning PEDOT on hydrogels to provide a fully organic, moist, and flexible electrode [26, 30]. The PEDOT/hydrogel electrodes are prepared

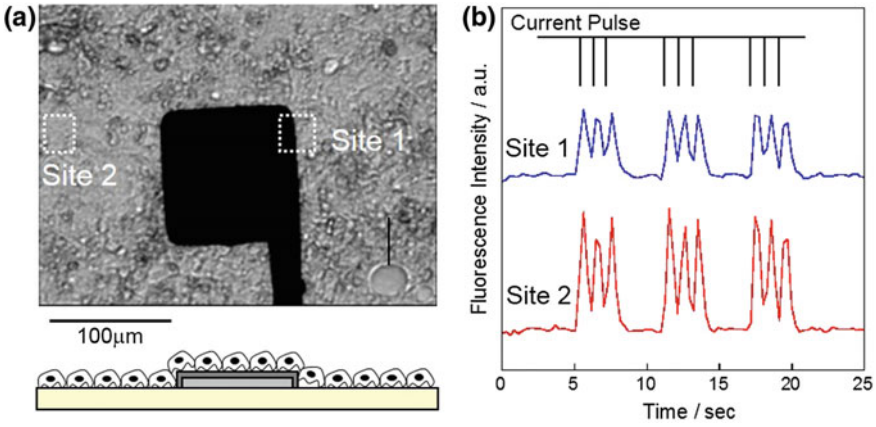

Fig. 15.11 Low-invasive stimulation of heart cells by PPy-coated electrode

through two electrochemical processes as schemed in Fig. 15.12a: the electropolymerization of PEDOT into the hydrogel and the electrochemical actuation-assisted peeling. A hydrogel film was placed over a Pt microelectrode fabricated on glass plate, followed by electropolymerization of the monomer on the Pt electrode as growing into the gel film. We found that electrochemical elastic actuation of PEDOT (±0.5 V vs. Ag/AgCl) was effective for nondestructively peeling off the PEDOT/hydrogel hybrid from the master electrodes. The volume change of PEDOT induces stress at the polymer/electrode interface, and causes detachment of the hybrid. The conductance of the PEDOT electrode attached on hydrogel was ca. 50 Ω/sq. The present technique is versatile; PEDOT microelectrodes can be prepared on a variety of hydrogels, including glucomannan (konjac), agarose, collagen and polyvinyl alcohol or on poly (hydroxyethyl methacrylate) (commercial soft contact lens), as shown in Fig. 15.12b.

"Stretchability" is a major challenge in device engineering. For example, the advances in the field of tissue engineering with integrated electronics critically require the development of all-polymeric soft and stretchable electronic platforms which are at the same time biocompatible. Although we can prepare PEDOT/hydrogel hybrid (Sect. 15.3.2), both PEDOT and conventional hydrogels such as agarose are not stretchable. Therefore, it is necessary to realize more robust electronic devices utilizing highly stable and elastic materials for both the electrode and substrate components. For example, the composite of polyurethane (PU) and PEDOT is both conductive and elastic and each of these polymers is known to be biocompatible. Additionally, soft but strong double-network (DN) hydrogels, with rupture stress exceeding 1 MPa, have recently been developed and could be used as the elastic substrate component. A tighter bonding between the components is therefore critical to minimize failure during exposure to high stress environments. We utilized electropolymerization of PEDOT as an adhesive to get tough adhesion [27]. Figure 15.13a illustrates the fabrication process of PEDOT/PU electrodes on

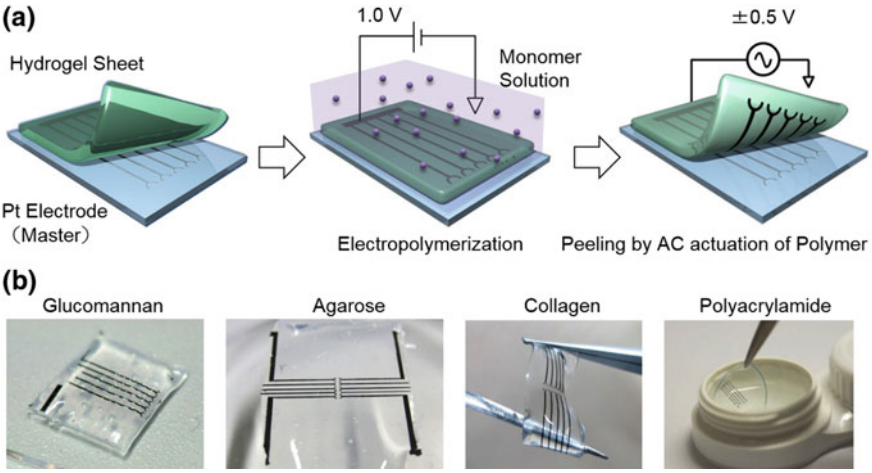

Fig. 15.12 Electropolymerization of PEDOT electrodes on hydrogels

DN hydrogel substrates. A film of PEDOT/PU composite (PEDOT 40 wt%) was initially deposited on a thin PVA-coated glass plate and cut out to the desired pattern using a cutting plotter. After laminating a DN hydrogel sheet, EDOT monomer solution was added and additional PEDOT was electropolymerized more than 0.3 C cm^{-2} to anchor the electrodes to the DN hydrogel film. Finally, the PVA sacrificial layer was dissolved to release a PEDOT/PU-patterned DN hydrogel sheet. The optical microscopic image of the cross section shows the electropolymerized PEDOT growing as an interpenetrating polymer network into the DN hydrogel. Figure 15.13b shows the dynamic change in conductivity of the PEDOT/PU-hydrogel hybrid during three repetitive stretch cycles. The PEDOT/PU composite films on DN hydrogel showed an increase in conductivity during the elongation, probably owing to the alignment of PEDOT along the direction of stretch. The conductivity change during the elongation cycles up to 10 % (orange) and 50 % (green) were satisfactorily reversible. The elongation cycle up to 100 % (purple) caused an irreversible decrease of conductivity to approximately half of the original. Significantly, electrodes displayed high and almost constant conductivity (below 11 % change) throughout repeated elongation–relaxation cycles within the biological range of mechanical elongation (10 %) experienced by contractile tissues in vivo. Even without external mechanical force, the volume of hydrogels is capable of dynamically changing in response to the environmental conditions including humidity. As shown in Fig. 15.13c, the DN hydrogel substrates were desiccated with shrinkage to approximately 25 % size of the original, accompanied by wrinkling of the PEDOT/PU electrode. The desiccated substrates show excellent re-swelling property to recover the original condition. This implies that our devices can be stored in the dry condition, allowing easy handling and transportation, making it more compliant with marketing to distant consumers. Significantly, the adhesion of the PEDOT/PU to hydrogel and the conductivity of the electrodes were

both maintained after autoclaving at 120 °C for 20 min at 2 atm pressure that offers the advantage of sterilizability of PEDOT/PU-DN hydrogel hybrids before in vitro or in vivo application.

15.4 Enzyme Fuel Cell Devices

Enzymatic fuel cells (EFCs) are power devices in which enzymes are used as electrocatalysts to directly convert biochemical energy into electricity [31]. The extremely high reaction selectivity of enzymes, as compared with metallic catalysts such as Pt, eliminates the need for fuel purification and allows a separator-free design that consists of just a pair of anode and cathode electrodes exposed to solutions containing both fuel and oxygen. Such a simple EFC system provides high flexibility in structural design and miniaturization, and as such, miniature enzymatic fuel cells could be an attractive power source for future wearable and implantable microdevices (Fig. 15.14).

Here, two kinds of enzyme-modified electrodes are explained: the film composed of the ideally aligned enzyme and carbon nanotubes (CNT) [32, 33]; the carbon fabric (CF) modified with dense enzyme layers [34, 35]. Both type of electrodes were developed by advanced engineering of carbon nanomaterials, and showed the world highest performances. These enzyme electrodes were applied to the insertion-type and the patch-type EFC devices. The insertion EFC device generates electricity directly from biofluids like fruits juice and animal bloods, and serves as a self-powered biosensor for sugar in biofluids [36]. The patch EFC device is a first totally organic iontophoresis device that generates transdermal currents to increase the efficiency of drug dosing [37].

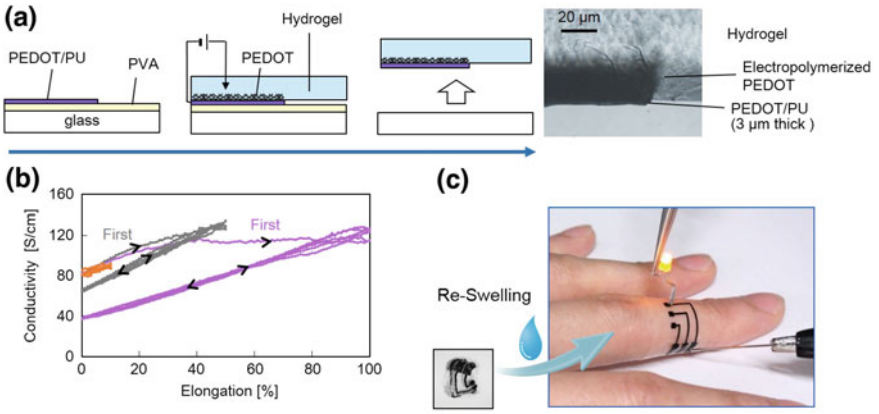

Fig. 15.13 Stretchable PEDOT/hydrogel hybrid sheet

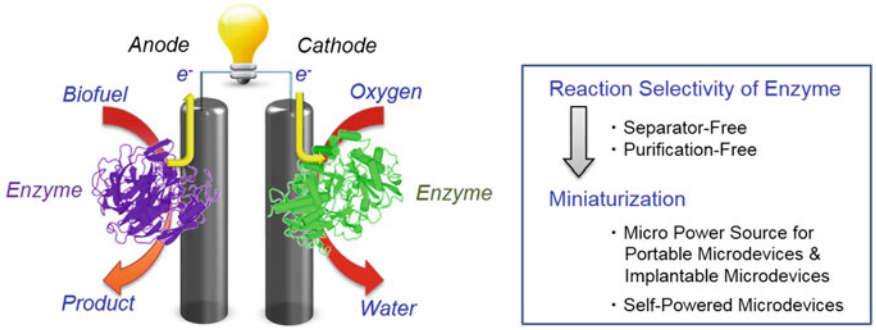

Fig. 15.14 Enzymatic fuel cell (EFC)

15.4.1 Enzyme/Carbon Nanotube Ensemble Films

A variety of nanoengineered carbon electrodes for biofuel cells have recently been developed in rapid succession due to their large specific surface area. However, all attempts to incorporate nanoengineered carbon electrodes have focused on pre-structuring electrodes before enzyme modification. If the nanostructure of the electrode can be regulated in response to the enzyme to be immobilized, the resultant enzymatic ensemble would avoid the difficulty in post-modification of enzymes. We have developed a method to achieve ideal enzyme electrodes having suitable intra-nanospace automatically regulated to the size of enzymes [32]. A carbon nanotube forest (CNTF) consisting of extremely long (~ 1 mm) single-walled CNTs was utilized as a 100 % binder-free carbon film. When liquids are introduced into the CNTF (CNTs with a pitch of 16 nm) and dried, the CNTF shrinks to a near-hexagonal close-packed structure because of the surface tension of the liquids. By using an enzyme solution as the liquid, the CNTF is expected to dynamically entrap the enzymes during the shrinkage, as illustrated in Fig. 15.15. We used two model enzymes: D-fructose dehydrogenase (FDH) and Laccase (LAC), which can directly catalyze the oxidation of D-fructose and the reduction of dioxygen, respectively, without the presence of electron mediators. The CNTF film was first treated by Triton X-100 and then immersed in a stirred buffer solution of FDH or LAC for 1 h to

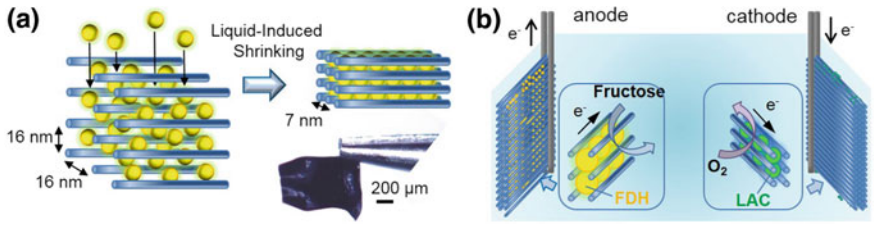

Fig. 15.15 CNT-based electrode for fructose/O_2 EFC

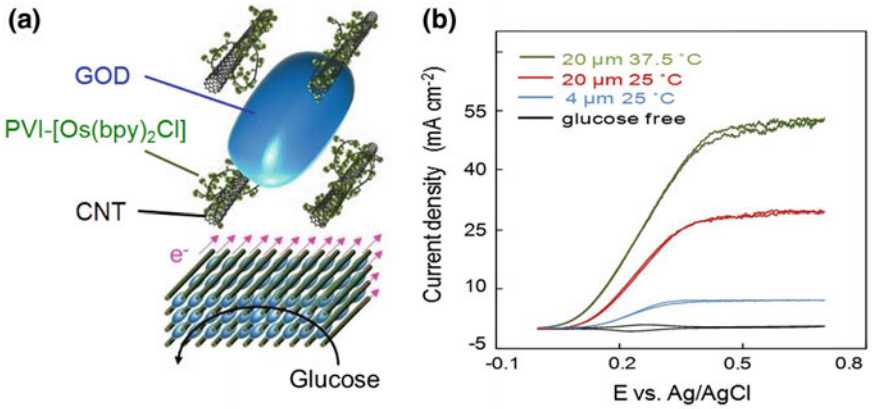

Fig. 15.16 CNT-based electrode for glucose oxidation

introduce enzymes into its void space, followed by drying on a carbon paper. The quantitative analysis of the amount of enzyme in a film indicated the structure of the ensemble as like that shown in Fig. 15.15a; enzyme molecules are aligned within the intraspace of the shrinked CNTF. The FDH-CNTF ensembles exhibited superior electrocatalytic activity for fructose oxidation by the current density of 16 mA cm^{-2} in stirred conditions. On the other hand, the LAC-entrapped CNTF cathode showed O_2 reduction with a maximum current density of ~4 mA cm^{-2}. By connecting these anode and cathode through an external resistance, the fuel cell performance was evaluated in an O_2-saturated 200 mM fructose solution. The power density reached 1.8 mW cm^{-2} (at 0.45 V) in stirred condition, 84 % of which could be maintained after continuous operation for 24 h.

Most of redox enzymes including glucose oxidase (GOD) require electron mediator for their electrode reaction. A conventional engineering for accelerating the electron transfer to the redox enzymes is the inclusive immobilization with mediator polymer matrices, such as Os-complex-pendant polymers, in which the successive electron exchange between the neighboring mediator groups connects the enzyme redox center and the electrode surface. We have developed the stepwise process to construct molecular architecture with CNTF, polyvinylimidazole-[Os(bipyridine)$_2$Cl] (PVI-[Os(bpy)$_2$Cl]) and GOD, as illustrated in Fig. 15.16a. A part of the free imidazole groups of the mediator polymer would adsorb on CNT surfaces via π-π interaction, followed by electrostatic loading of enzyme GOD. Figure 15.16b shows the cyclic voltammograms of GOD/PVI-[Os(bpy)$_2$Cl]/CNTF ensemble films at 10 mV s^{-1} in a stirred 200 mM D-glucose PBS solution. The catalytic current for glucose oxidation increased in response to the thickness of CNTF films, indicating that also GOD can entirely penetrate inside the PVI-[Os(bpy)$_2$Cl]-modified CNTF films. The current density under stirred condition was enhanced to as high as 26.7 mA cm^{-2} by turning up the buffer temperature to 37.5 °C. Importantly, more than 90 % of the electrode activity could be maintained

even after 6 days storage in a buffer solution. The electron transfer turnover rate for the 20 μm-thick film was calculated from the current value at 25 °C (0.29 mA) to be ca. 650 s^{-1}, being comparable with that of GOD in bulk solution containing the natural electron acceptor O_2 (700 s^{-1}) at 25 °C. These results indicate that most of ca. 3×10^{12} GOD units within a film could efficiently work to the fullest extent, presumably owing to the molecularly ordered structure of enzyme/mediator/electrode ensemble [33].

15.4.2 Enzyme-Modified Carbon Fabric

A flexible sheet-shaped biobattery that can be combined with advanced wearable electronics can be prepared by using carbon fabric (CF) as the flexible, conductive base for the enzyme electrodes [34, 35]. The CF strips were modified with FDH for the oxidation of fructose, or bilirubin oxidase (BOD) for the reduction of O_2 from ambient air. The pre-modifications with CNTs were found to increase the specific surface area of the CF electrodes, resulting in effective enzyme immobilization and ultimately, higher power. The FDH-modified CF anode and the BOD-modified gas-diffusion CF cathode were laminated to the opposite faces of a DN hydrogel sheet (0.5 mm thick) containing fructose (Fig. 15.17a). The enzyme-modified hydrophilic anode appeared to become moistened by blotting of the solution from the hydrogel layer. On the other hand, the O_2 reduction at the hydrophobic cathode proceeded at the three-phase boundary of the hydrogel–electrode interface. The cell performance was limited by the BOD-cathode because of its comparatively inferior activity to the FDH-anode fabric. Importantly, as shown in Fig. 15.17b, the performance of the cell bent into a circle (red plots) is almost identical to that of a cell that was not bent (green plots). Such high flexibility originates in the superior mechanical strength of both the fabric bioelectrodes and the DN hydrogel. The booster cell was fabricated simply by lamination of anode/hydrogel/cathode sheets

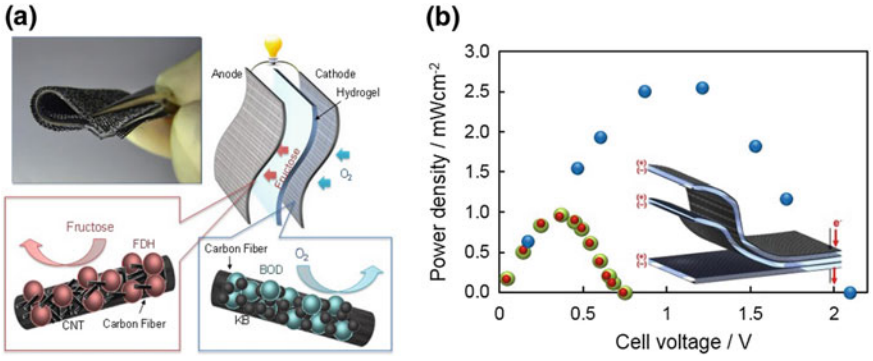

Fig. 15.17 Carbon fabric-based EFC sheet

(blue plots). The open-circuit voltage of the laminated cell was over 2 V, which is roughly threefold that of a single cell. The maximum current was quite similar to that of the single cell. These results indicate that layered cells can be connected in series without suffering from short circuit, even without packaging. Ionic isolation between the cells could be avoided by the hydrophobicity of gas-diffusion cathodes and the solid-like property of hydrogels.

15.4.3 Insertion Devices for Direct Power Generation from Biofluids

The high reaction selectivity of enzyme catalysts provides unique advantages of EFCs, including the possibility of direct power generation from carbohydrates in biofluids, such as juices or blood. Power generation from real living organisms, however, entails the consideration that natural organisms are generally covered by a skin. One possible solution is to use a needle-shaped insertion anode to approach fuels through the skins. Another important consideration is that oxygen in many organisms is limited to a lower concentration than that of sugars. Taking this consideration into account, an insertion EFC was assembled with a needle anode and a gas-diffusion cathode designed to be exposed to atmospheric air, as illustrated in Fig. 15.18a [36]. The anode and cathode are assembled using a PDMS chamber and an ion-conducting agarose hydrogel (pH 5.0) as the inner matrix. The insertion EFC was combined with a light-emitting diode (LED) device consisting of a charge pump IC, a ceramic capacitor and an LED. The blink interval of the LED is inversely proportional to the power of the biofuel cell, which is roughly proportional to the concentration of fructose. In practice, the LED blinks at a higher frequency with an increase in the fructose concentration, and as a result, the concentration of fructose within the grape was estimated to be roughly 20–40 mM (Fig. 15.18c). In fact, a separate measurement revealed that the true concentration of fructose in the grape was 35 mM.

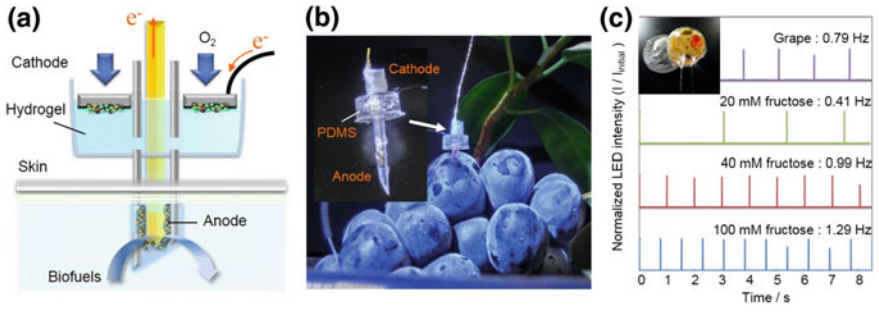

Fig. 15.18 Insertion EFC for sensing of sugar in a grape

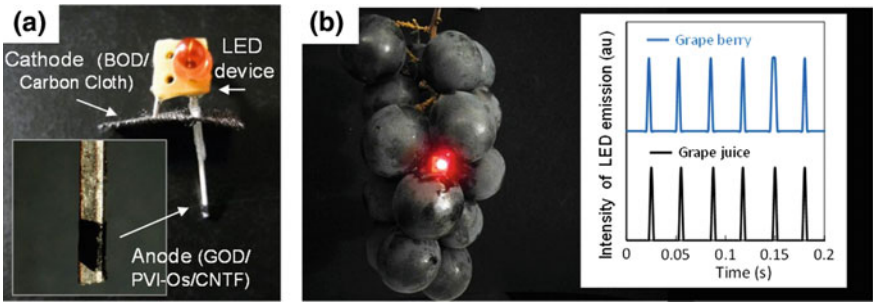

Fig. 15.19 Insertion EFC using an enzyme/CNT film anode

An insertion EFC device for power generation from blood was also developed with a needle glucose anode prepared by co-immobilization of glucose dehydrogenase (GDH), diaphorase (Dp), and vitamin K_3-pendant poly-L-lysine [36]. The fuel cell performance was evaluated by inserting the device into a vein of a rabbit ear and reached 130 μW cm^{-2} at 0.56 V. An anti-biofouling modification of the needle tip with 2-methacryloyloxyethyl phosphoryl-choline (MPC)-polymer was required, however, to stabilize the cell performance.

The enzyme-CNT ensemble film explained in Sect. 15.4.1 can be used for constructing insertion EFC devices [33]. As shown in Fig. 15.19, a piece of GOD/PVI-[$Os(bby)_2Cl$]/CNTF film anode (Fig. 15.16a) was wound on one electric lead of the LED device, whose blinking interval is inversely proportional to the flowing current. The other lead was connected to the BOD-modified CF air-breathing cathode. The blinking interval of the LED upon inserting the device to a grape was coincident with that for the extracted juice, proving that this device could serve as a sugar indicator by simply being inserted into a grape. In this case, the leaked juice was ionically connecting the anode and cathode, instead of the intra matrix (hydrogel) of the previous needle-based insertion EFC device in Fig. 15.18. The woundable enzyme-CNT film is free-standing and thus can be readily replaced when the original is degraded.

15.4.4 Patch Devices with Built-in EFC

The electric current-induced iontophoresis has been used to enhance efficiency of transdermal dosing. However, the electrically controlled skin patches need to be wired to an external power source that is usually heavy, rigid, and hazardous. The integration of a lightweight and safe power source would produce a more patient-compliant iontophoresis patch. The enzyme-modified CFs explained in Sect. 15.4.2 were used to consist the first completely organic iontophoresis patch with a built-in EFC as shown in Fig. 15.20a [37]. A FDH-modified CF anode and a BOD-modified O_2-diffusion CF cathode will be connected with the stretchable

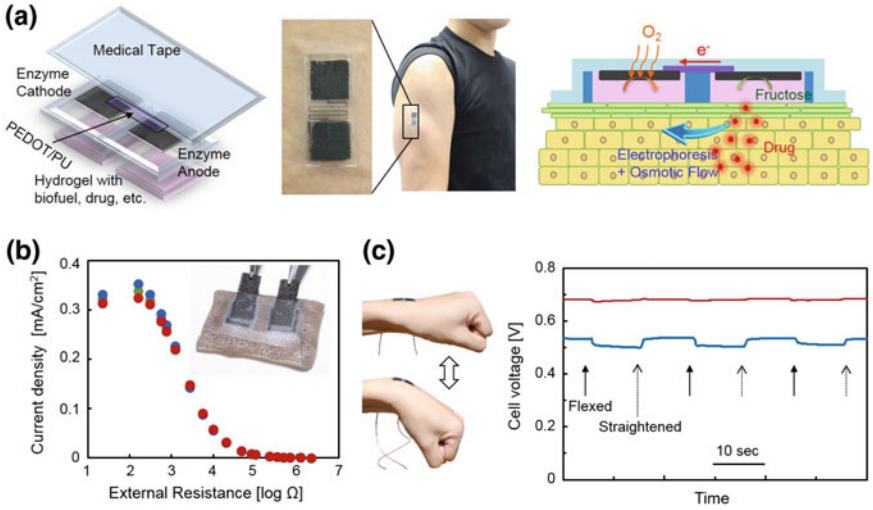

Fig. 15.20 Totally organic iontophoresis patch with built-in EFC

PEDOT/PU internal resistor, combined with hydrogel films containing fructose and the chemical to be delivered, and covered with an O_2 permeable medical tape. In Fig. 15.20b, the basic performance of the EFC patch on a piece of pig skin was measured by changing external load (without the mounting of PEDOT/PU internal resistance). The EFC patch shows the maximum current density of $\sim$300 μA cm^{-2} even at a small external load because of the presence of the skin, of which resistance was $\sim$700 Ω. As a reference, the resistance of human skin on the arms and the back of hands of three men was 270–360 Ω. Therefore, to regulate the transdermal current, regardless of the skin condition, the resistance of the built-in resistor is to be sufficiently larger than that of skin (>1 kΩ). BFC patches, placed on pigskin and under a variety of resistance conditions, maintained their activity for 6 h, indicating that the patches could possibly be used overnight. A stand-alone patch was prepared by integrating a resistor made of a PEDOT/PU composite, which is stretchable and, therefore, allows the patch to be flexible (Fig. 15.20c). The patch was mounted on a man's wrist, and the cell voltage was monitored as the man repeatedly flexed and straightened his wrist by a 40° angle. The cell voltages of the patches with the 100 kΩ resistor (red line) and the 10 kΩ resistor (blue line) were approximately 0.7 and 0.55 V, respectively, indicating that the patches were generating transdermal currents of $\sim$10 and $\sim$50 μA cm^{-2}. The cell voltages showed only slight, reversible decreases when a hand was flexed, as a consequence of minor change in performance of BFC under the flexed condition. The transdermal ionic current is known to be accompanied by a water flow from the anode to the cathode, which is generated by the preferential movement of mobile cation instead of a fixed anion, e.g., keratin, in the stratum corneum of the skin. This osmotic water flow can assist the electrophoretic movement of small molecules into the skin. We examined

the iontophoretic penetration of lidocaine (painkiller) and ascorbyl glucoside (skin care compound) by using pigskins.

15.5 Future Outlook

Precision processing of dry electronic materials (metals, semiconductors, and oxides) has been extremely progressed in this past century. On the other hand, the processing of wet materials (proteins, cells, hydrogels etc.) has not yet been well developed because the process for wet materials should be conducted in physiological mild conditions. As described in this chapter, electrochemistry can connect "dry electronic" systems and "wet ionic" systems. I deeply expect the electrochemical techniques will contribute to the progress of precision processing of wet materials and the development of future wearable and implantable devices having interfaces with biocompatible wet materials.

References

1. H. Shin, Biomaterials **28**, 126–133 (2007)
2. N. Xia, C.K. Thodeti, T.P. Hunt, Q.B. Xu, M. Ho, G.M. Whitesides, R. Westervelt, D.E. Ingber, FASEB J. **22**, 1649–1659 (2008)
3. H. Kaji, K. Tsukidate, T. Matsue, M. Nishizawa, J. Am. Chem. Soc. **126**, 15026–15027 (2004)
4. H. Kaji, K. Tsukidate, M. Hashimoto, T. Matsue, M. Nishizawa, Langmuir **21**, 6966–6969 (2005)
5. H. Kaji, T. Kawashima, M. Nishizawa, Langmuir **22**, 10784–10787 (2006)
6. S. Sekine, H. Kaji, M. Nishizawa, Anal. Bioanal. Chem. **391**, 2711–2716 (2008)
7. S. Sekine, H. Kaji, M. Nishizawa, Electrochem. Commun. **11**, 1781–1784 (2009)
8. K. Nagamine, T. Kawashima, T. Ishibashi, H. Kaji, M. Kanzaki, M. Nishizawa, Biotechnol. Bioeng. **105**, 1161–1167 (2010)
9. T. Kawashima, T. Yokoi, H. Kaji, M. Nishizawa, Chem. Commun. **46**, 2070–2072 (2010)
10. K. Nagamine, T. Kawashima, S. Sekine, Y. Ido, M. Kanzaki, M. Nishizawa, Lab Chip **11**, 513–517 (2011)
11. A. Bange, H.B. Halsall, W.R. Heineman, Biosens. Bioelectron. **20**, 2488–2503 (2005)
12. P. Mitchell, Nat. Biotechnol. **19**, 717–718 (2001)
13. D.R. Meldrum, M.R. Holl, Science **297**, 1197–1198 (2002)
14. H. Kaji, M. Hashimoto, M. Nishizawa, Anal. Chem. **78**, 5469–5473 (2006)
15. M. Hashimoto, H. Kaji, M.E. Kemppinen, M. Nishizawa, Sens. Actuators B **128**, 545–551 (2008)
16. H. Kaji, M. Hashimoto, S. Sekine, T. Kawashima, M. Nishizawa, Electrochemistry **76**, 555–558 (2008)
17. M. Hashimoto, H. Kaji, M. Nishizawa, Biosen. Bioelectron. **24**, 2892–2897 (2009)
18. T.L. Rose, L.S. Robblee, IEEE Trans. Biomed. Eng. **37**, 1118–1120 (1990)
19. P.M. George, A.W. Lyckman, D.A. LaVan, A. Hegde, Y. Leung, R. Avasare, Biomaterials **26**, 3511–3519 (2005)

20. C.E. Schmidt, V.R. Shastri, J.P. Vacanti, R. Langer, Proc. Natl. Acad. Sci. **94**, 8948–8953 (1997)
21. X. Cui, J.F. Hetke, J.A. Wiler, D.J. Anderson, D.C. Martin, Sens. Actuator A **93**, 8–18 (2001)
22. M. Nishizawa, M. Shibuya, T. Sawaguchi, T. Matsue, I. Uchida, J. Phys. Chem. **95**, 9042–9044 (1991)
23. M. Nishizawa, Y. Miwa, T. Matsue, I. Uchida, J. Electrochem. Soc. **140**, 1650–1655 (1993)
24. M. Nishizawa, H. Nozaki, H. Kaji, T. Kitazume, N. Kobayashi, T. Ishibashi, T. Abe, Biomaterials **28**, 1480–1485 (2007)
25. M. Nishizawa, T. Kamiya, H. Nozaki, H. Kaji, Langmuir **23**, 8304–8307 (2007)
26. S. Sekine, Y. Ido, T. Miyake, K. Nagamine, M. Nishizawa, J. Am. Chem. Soc. **132**, 13174–13175 (2010)
27. M. Sasaki, B.C. Karikkineth, K. Nagamine, H. Kaji, K. Torimitsu, M. Nishizawa, Adv. Healthc. Mater. **3**, 1919–1927 (2014)
28. D.-H. Kim, J.A. Rogers, Adv. Mater. **20**, 4887–4892 (2008)
29. J.A. Rogers, T. Someya, Y. Huang, Science **327**, 1603–1607 (2010)
30. Y. Ido, D. Takahashi, M. Sasaki, K. Nagamine, T. Miyake, P. Jasinski, M. Nishizawa, ACS Macro Lett. **1**, 400–403 (2012)
31. E.R. Luckarift, P. Atanassov, G.R. Johnson (eds.), *Enzymatic Fuel Cells: From Fundamentals to Applications* (Wiley, New York, 2014)
32. T. Miyake, S. Yoshino, T. Yamada, K. Hata, M. Nishizawa, J. Am. Chem. Soc. **133**, 5129–5134 (2011)
33. S. Yoshino, T. Miyake, T. Yamada, K. Hata, M. Nishizawa, Adv. Energy Mater. **3**, 60–64 (2013)
34. K. Haneda, S. Yoshino, T. Ofuji, T. Miyake, M. Nishizawa, Electrochim. Acta **82**, 175–178 (2012)
35. T. Miyake, K. Haneda, S. Yoshino, M. Nishizawa, Biosens. Bioelectron. **40**, 45–49 (2013)
36. T. Miyake, K. Haneda, N. Nagai, Y. Yatagawa, H. Ohnami, S. Yoshino, T. Abe, M. Nishizawa, Energy Environ. Sci. **4**, 5008–5012 (2011)
37. Y. Ogawa, K. Kato, T. Miyake, K. Nagamine, T. Ofuji, S. Yoshino, M. Nishizawa, Adv. Healthc. Mater. (2015). doi:10.1002/adhm.201400457

Part VI
New Concepts of Spintronics

Chapter 16
Spin Current Physics and Its Thermoelectric Application

Ken-ichi Uchida and Eiji Saitoh

Abstract Spin Seebeck effect refers to the generation of spin voltage as a result of a temperature gradient in magnetic materials. When a conductor is attached to a magnet under a temperature gradient, the thermally generated spin voltage in the magnet injects a spin current into the conductor, which in turn produces electric voltage owing to the spin–orbit interaction. The spin Seebeck effect is of increasing importance in spintronics, since it enables direct generation of a spin current from heat and appears in a variety of magnets ranging from metals and semiconductors to insulators. Recent studies on the spin Seebeck effect have been conducted mainly in paramagnetic metal/ferrimagnetic insulator junction systems in the longitudinal configuration in which a spin current flowing parallel to the temperature gradient is measured. This "longitudinal spin Seebeck effect" in insulators provides a novel and versatile pathway to thermoelectric generation in combination of the inverse spin Hall effects.

Keywords Spintronics · Spin current · Spin seebeck effect · Thermoelectric generation · Energy harvesting

16.1 Introduction

In recent years, more and more approaches to environmental and energy issues have been taken, and it is required to develop clean and reliable energy sources and power-saving electronic devices. Thermoelectric generation is one of the key

K. Uchida · E. Saitoh (✉)
Institute for Materials Research, Tohoku University, Sendai 980-8577, Japan
e-mail: eizi@imr.tohoku.ac.jp

E. Saitoh
WPI Advanced Institute for Materials Research, Tohoku University, Sendai 980-8577, Japan

E. Saitoh
Advanced Science Research Center, Japan Atomic Energy Agency, Tokai 319-1195, Japan

J. Sone and S. Tsuji (eds.), *Intelligent Nanosystems for Energy, Information and Biological Technologies*, DOI 10.1007/978-4-431-56429-4_16

technologies for solving the issues, since it can directly generate electricity from heat. The history of thermoelectric generation began with the discovery of the Seebeck effect by T. J. Seebeck in 1821, which refers to the generation of electric voltage as a result of a temperature gradient in a conductor (see Fig. 16.1a) [1]. The electric field induced by the Seebeck effect is parallel to the applied temperature gradient, and it is usually used in the form of a thermocouple, i.e., a junction of two materials with different Seebeck coefficients. Most of prevalent thermoelectric generators are based on this effect.

Spintronics is a new electronic technology which actively exploits the spin degree of freedom of electrons [2, 3]. To develop novel principles to drive electric and magnetic devices and to save their energy consumption, a lot of research on spintronics has been conducted all over the world. In this field, a spin counterpart of the Seebeck effect—the spin Seebeck effect (SSE)—was discovered in 2008 [4]. The SSE refers to the generation of 'spin voltage' as a result of a temperature gradient in ferromagnetic or ferrimagnetic materials. Here, spin voltage is a potential for electrons' spins to drive a nonequilibrium spin current [5]; when a conductor is attached to a ferromagnet with finite spin voltage, it induces spin injection into the conductor. Since the SSE appears not only in ferromagnetic metals [4, 6] and semiconductors [7] but also in ferrimagnetic insulators [8, 9], it enables the construction of "insulator-based thermoelectric generators" [10] in combination with the inverse spin Hall effect (ISHE) [11, 12], which was impossible if only conventional thermoelectric technology was used.

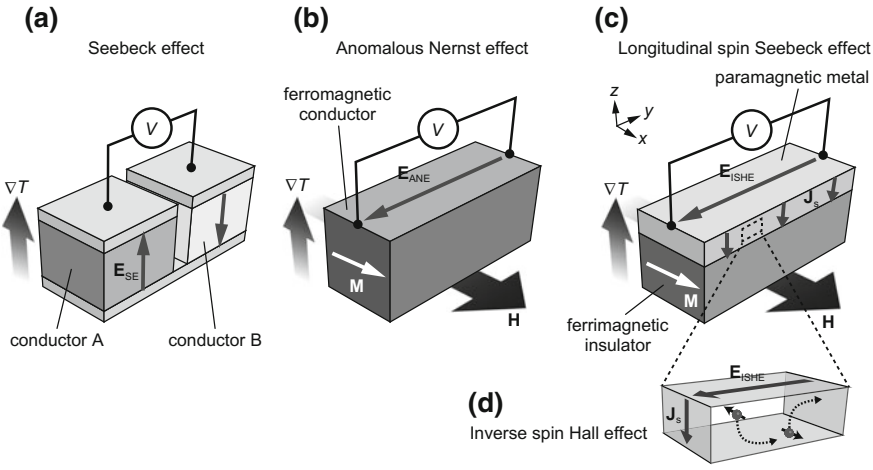

Fig. 16.1 Schematic illustrations of the conventional Seebeck effect (**a**), anomalous Nernst effect (ANE) (**b**), longitudinal spin Seebeck effect (LSSE) (**c**), and inverse spin Hall effect (ISHE) (**d**). $\mathbf{E}_{\mathrm{SE}}$, $\mathbf{E}_{\mathrm{ANE}}$, and $\mathbf{E}_{\mathrm{ISHE}}$ denote the electric fields generated by the Seebeck effect, ANE and ISHE, respectively. ∇T, $\mathbf{H}$, $\mathbf{M}$, and $\mathbf{J}_{\mathrm{s}}$ denote the temperature gradient, magnetic field (with magnitude H), magnetization vector, and spatial direction of the thermally generated spin current, respectively

The observation of the SSE has been reported in two different device structures [13]: one is a *transverse* configuration, in which a spin current *perpendicular* to a temperature gradient is measured. The first observation of the SSE in $Ni_{81}Fe_{19}$ films was reported in the transverse configuration [4] and, subsequently, this configuration has been used to measure the SSE in semiconductors [7] and insulators [8]. The other setup is a *longitudinal* configuration, in which a spin current flowing *parallel* to a temperature gradient is measured (see Fig. 16.1c). The longitudinal configuration is the simplest and most versatile structure for measuring the SSE, which was first demonstrated using $Pt/Y_3Fe_5O_{12}$ (YIG) junction systems in 2010 [9]. The longitudinal configuration is basically applicable only to magnetic insulators, since this configuration is similar to that of the anomalous Nernst effect (ANE) in ferromagnetic conductors (compare Fig. 16.1b, c) [14, 15]. Owing to its simple structure, the longitudinal configuration becomes the mainstream of the SSE research, and the longitudinal SSE (LSSE) has been observed in various magnetic materials in a wide temperature range [10, 13, 16–18].

In this chapter, we discuss the potential application of LSSE-based thermoelectric generation, which is conceptually different from that based on the conventional Seebeck effect. Here, we outline the characteristics and advantages of LSSE thermoelectric devices, followed by preliminary demonstrations for future applications.

16.2 Spin Current

Spin current, a flow of spin angular momentum in solids, is a key concept in spintronics, since a lot of spintronics functions have been discovered by using the spin current concept as a guiding principle [5]. Although spin current has realized magnetization manipulation [19], energy conversion [4, 11, 12, 20], and information transportation [21], on the other hand, its information disappears in a submicron scales in many cases. Spin current should thus be utilized in very small systems; nanotechnology was essential to give birth to spin current science and technology. In this section, some topics on spin currents in nano structures are introduced.

In nonmagnetic conductors, a spin current is mainly carried by conduction electrons [5]. An imbalance in current densities of electrons with spin ↑ and ↓ ($\mathbf{j}_\uparrow$ and $\mathbf{j}_\downarrow$) results in a spin current as shown in Fig. 16.2a. A spin current, $\mathbf{J}_s$, is represented as

$$\mathbf{J}_s = \mathbf{j}_\uparrow - \mathbf{j}_\downarrow \tag{16.1}$$

while a charge current, $\mathbf{J}_c$, is represented as

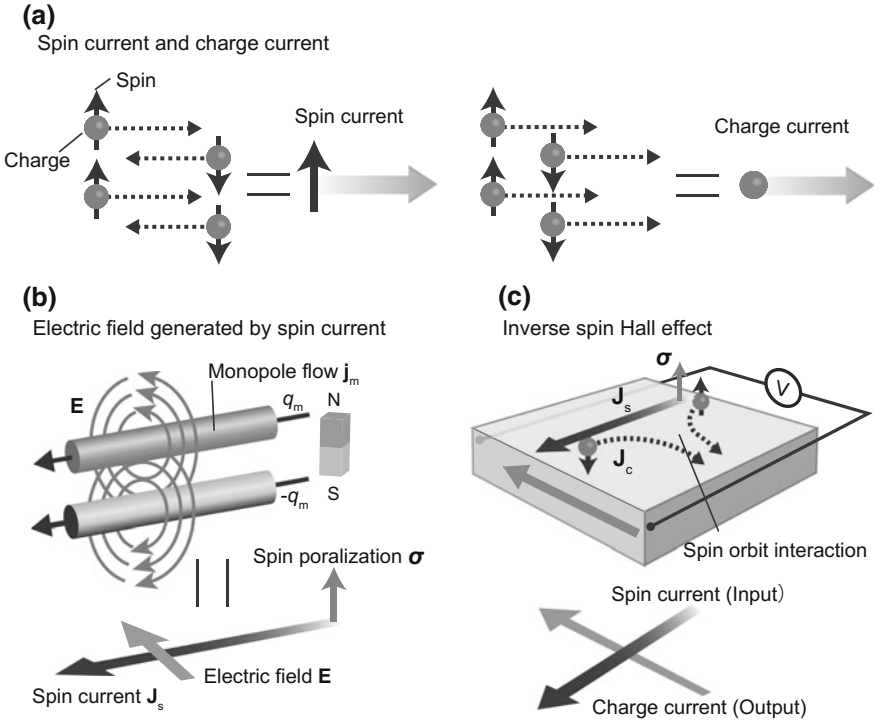

Fig. 16.2 Schematic illustrations of spin and charge currents composed of electrons with up and down spins (**a**), electric field generation by a pair of monopole currents and a spin current (**b**), and the inverse spin Hall effect (**c**). $\mathbf{J}_s$ denotes the spatial direction of the spin current and σ denotes the spin polarization of the spin current

$$\mathbf{J}_c = \mathbf{j}_\uparrow + \mathbf{j}_\downarrow \tag{16.2}$$

The spin-dependent currents $\mathbf{j}_\uparrow$ ($\mathbf{j}_\downarrow$) are driven by a spin-dependent electrochemical potential, $\mu_{\uparrow(\downarrow)}$, i.e.,

$$\mathbf{j}_{\uparrow(\downarrow)} = \frac{\sigma}{2e}\nabla\mu_{\uparrow(\downarrow)}, \tag{16.3}$$

with σ being the electric conductivity. By substituting Eq. (16.3) into Eqs. (16.1) and (16.2), the spin current is rewritten as

$$\mathbf{J}_s = \frac{\sigma}{2e}\nabla\left(\mu_\uparrow - \mu_\downarrow\right) \equiv \frac{\sigma}{2e}\nabla\mu_s. \tag{16.4}$$

Here, μ_s is the spin voltage, a driving force for the spin current.

A spin current is converted into an electric field via the spin–orbit interaction; this is the ISHE [11, 12, 20]. Owing to the relativistic effect, electricity can be

generated by a spin current. The conversion can be regarded as the spin current version of Ampere's law [22]; generation of a circular electric field $\mathbf{E}$ around a flow of hypothetical monopole $\mathbf{j}_m$. The mathematical expression should be $\nabla \times \mathbf{E} = \mathbf{j}_m$ from the electromagnetic duality [23]. As a spin current can be considered as a pair of $\mathbf{j}_m$ with positive and negative magnetic monopoles, a spin current may generate an electric field as shown in Fig. 16.2b. Accordingly, the induced field is given by the superposition of the two electric fields induced by this pair of $\mathbf{j}_m$. Thus, as depicted in Fig. 16.2c, the relation between an induced field by the ISHE, $\mathbf{E}_{ISHE}$, and $\mathbf{J}_s$ is given by

$$\mathbf{E}_{ISHE} \propto \mathbf{J}_s \times \boldsymbol{\sigma}, \tag{16.5}$$

where $\boldsymbol{\sigma}$ is the spin polarization vector of the spin current. Because the ISHE enables electric detection of spin currents and electricity generation from spin currents, it is an essential effect for harnessing spintronics with conventional electronics.

16.3 Observation of Longitudinal Spin Seebeck Effect

Figure 16.3a shows the schematic illustration of a paramagnetic metal/ferrimagnetic insulator junction system for measuring the LSSE. The sample comprises a paramagnetic metal film fabricated on the top surface of a ferrimagnetic insulator slab or film. When a temperature gradient ∇T is applied to the insulator perpendicular to the metal/insulator interface (along the z direction), the spin voltage is thermally generated and injects a spin current into the paramagnetic metal across the interface owing to thermal spin-pumping mechanism [24–26]. This thermally induced spin current is converted into an electric field $\mathbf{E}_{ISHE}$ by the ISHE in the metal (see Fig. 16.1c, d). When the magnetization $\mathbf{M}$ of the insulator is along the x direction, $\mathbf{E}_{ISHE}$ is generated in the paramagnetic metal film along the y direction according to the relation shown in Eq. (16.5), $\mathbf{E}_{ISHE} \propto \mathbf{J}_s \times \boldsymbol{\sigma}$, where $\mathbf{J}_s$ is the spatial direction of the thermally induced spin current and σ is the spin polarization vector of electrons in the paramagnetic metal. The directions of $\mathbf{J}_s$ and $\boldsymbol{\sigma}$ are perpendicular to the metal/insulator interface and parallel to $\mathbf{M}$, respectively.

Therefore, in the LSSE setup, $\mathbf{J}_s$ is parallel to the ∇T direction. The magnitude of $\mathbf{E}_{ISHE}$, E_{ISHE}, is especially large in heavy metals with strong spin–orbit interaction, such as Pt [11, 20], Ta [27], W [28], CuIr [29], and AuW [30]; by measuring the electric voltage V between the ends of the paramagnetic metal film, one can detect the ISHE induced by the LSSE as $V_{ISHE} = E_{ISHE}L_y$ with L_y being the length of the sample along the y direction. Here, when a highly resistive insulator, such as YIG, is used, extrinsic artifacts caused by the electric conduction in the ferrimagnet are eliminated.

First, we show the fundamental measurement of the LSSE using Pt/YIG junction systems [9, 14], which are widely used for measuring the SSE. The Pt/YIG sample used here consists of a single-crystalline YIG slab and a 10-nm-thick Pt film formed

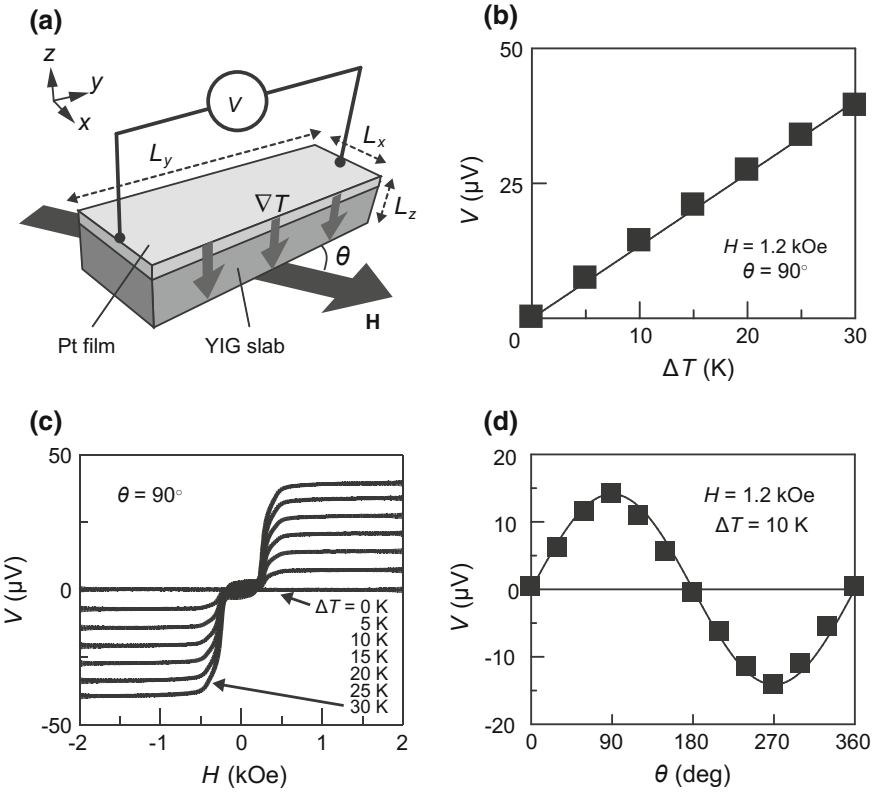

Fig. 16.3 **a** A schematic illustration of the experimental configuration for measuring the LSSE in the Pt/YIG sample. θ denotes the angle between **H** and the y direction. L_x, L_y, and L_z are the lengths of the sample along the x, y, and z directions, respectively. **b** The temperature difference ΔT dependence of the voltage V in the Pt/YIG sample at $H = 1.2$ kOe and $\theta = 90°$, measured when $\nabla T \| -\mathbf{z}$. **c** H dependence of V in the Pt/YIG sample for various values of ΔT at $\theta = 90°$. **d** θ dependence of V in the Pt/YIG sample at $\Delta T = 10$ K and $H = 1.2$ kOe

on the well-polished surface of YIG. The lengths of the Pt/YIG sample along the x, y, and z directions are $L_x = 2$ mm, $L_y = 6$ mm, and $L_z = 1$ mm, respectively. To generate ∇T along the z direction, the Pt/YIG sample was sandwiched between two heat baths of which the temperatures are stabilized to 300 and 300 K + ΔT (Fig. 16.3a). We measured V between the ends of the Pt layer with applying an external magnetic field **H** (with the magnitude H) to the Pt/YIG sample in the $x - y$ plane at an angle θ to the y direction.

Figure 16.3b shows V in the Pt/YIG sample as a function of ΔT at $H = 1.2$ kOe, where the magnetization of the YIG slab is aligned along the **H** direction at $H = 1.2$ kOe. When **H** was applied along the x direction ($\theta = 90°$), the magnitude of V was found to be proportional to ΔT. This V signal is clearly generated in the Pt layer since YIG is a very good insulator, where thermoelectric phenomena in

itinerant magnets, such as the conventional Seebeck and Nernst effects, do not exist at all. As shown in Fig. 16.3c, the sign of V for finite values of ΔT is reversed when the **H** direction is reversed, indicating that the V signal in the Pt film is affected by the magnetization direction of the YIG slab.

To confirm the origin of this signal, we measured the magnetic field angle θ dependence of V in the same Pt/YIG system at ΔT = 10 K and H = 1.2 kOe (see Fig. 16.3d). We found that the V signal varies with θ in a sinusoidal pattern and vanishes when $\theta = 0°$ and 180°, a situation consistent with the prediction of the ISHE induced by the LSSE described in Eq. (16.5).

16.4 Thermoelectric Generation Based on Longitudinal Spin Seebeck Effect

The SSE in magnetic insulators can be applied directly to the design of thermospin generators and, in combination with the ISHE, thermoelectric generators, allowing new approaches toward the improvement of thermoelectric generation efficiency. In general, the efficiency is improved by suppressing the energy loss due to heat conduction and Joule dissipation, which are realized respectively by reducing the thermal conductivity κ for the sample part where heat currents flow and by reducing the electric resistivity ρ for the part where charge currents flow. In thermoelectric metals, the Wiedemann–Franz law ($\kappa_e \rho$ = constant) [1] limits this improvement when κ is dominated by the electronic thermal conductivity κ_e. A conventional way to overcome this limitation is to use semiconductor-based thermoelectric materials, where the thermal conductance is usually dominated by phonons while the electric conductance is determined by charge carriers, and thus κ and ρ are separated according to the kind of the carriers. The SSE provides another way to overcome the Wiedemann–Franz law; in the SSE devices, the heat and charge currents flow in different parts of the sample: κ is the thermal conductivity of the magnetic insulator and ρ is the electrical resistivity of the metallic wire, such that κ and ρ in the SSE devices are segregated according to the part of the device elements [8]. Therefore, the SSE in insulators allows us to construct thermoelectric devices operated by an entirely new principle, although the thermoelectric conversion efficiency is required to be improved.

In 2012, Kirihara et al. proposed a novel thermoelectric concept based on the LSSE called "spin thermoelectric (STE) coating" [10]. The STE-coating device consists of metallic and magnetic insulator films directly coated on a heat source, as shown in Fig. 16.4. The STE coating offers not only the above characteristic but also the following features; the STE coating has a convenient scaling capability, where the thermoelectric output is increased simply by extending the coating area because the total amount of thermally induced spin currents increases as the film becomes larger. Here, the LSSE-induced electric field at each point is integrated into the thermoelectric voltage: $V_{\mathrm{ISHE}} \propto E_{\mathrm{ISHE}} L_y$. Since the internal resistance of the

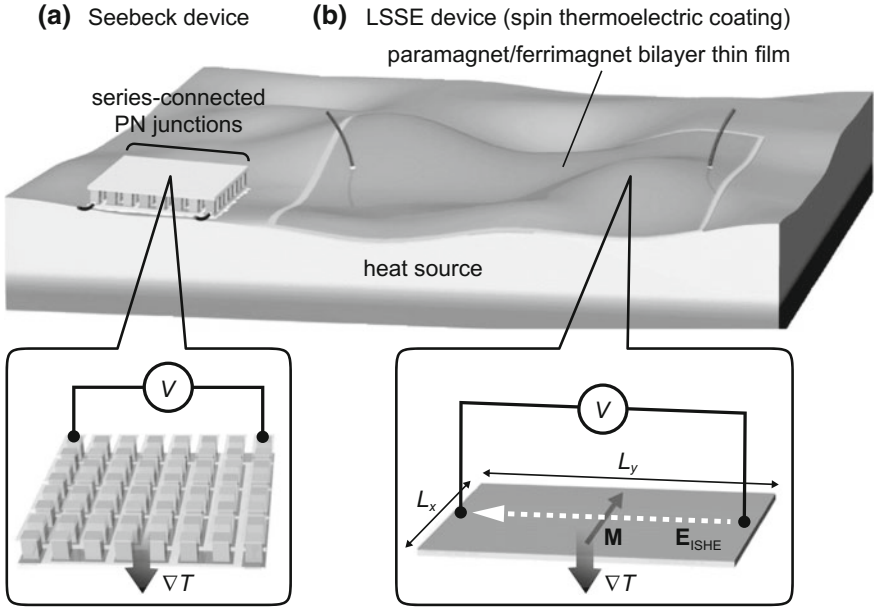

Fig. 16.4 **a** A schematic illustration of a conventional thermoelectric device based on the Seebeck effect. The Seebeck device contains a number of semiconductor PN junctions, electrically connected in series, to increase output voltage. **b** A schematic illustration of a thermoelectric device based on the LSSE called spin thermoelectric coating. The LSSE device exhibits a straightforward scaling: a larger film area leads to larger thermoelectric output. Such simple film structure can be directly coated onto heat sources with various shaped surfaces

paramagnetic metal layer of the STE-coating device is $R_{\mathrm{metal}} = \rho L_y / L_x L^z_{\mathrm{metal}}$ with L^z_{metal} being the thickness of the paramagnetic metal, the maximum extractable electric power P_{max} is proportional to the area of the STE coating: $P_{\mathrm{max}} \propto V^2 / R_{\mathrm{metal}} \propto L_x L_y$. Such a straightforward scaling law allows us to implement simple structure and large-area thermoelectric devices onto various shaped heat sources (such as electronic instruments and automobile bodies) using coating and printing technologies.

16.4.1 Demonstration of Spin Thermoelectric Coating

In this subsection, we demonstrate the STE coating based on the LSSE using magnetic insulator films fabricated using a spin coating method, which can potentially realize large-area thermoelectric systems in a highly productive way. Here, we used $BiY_2Fe_5O_{12}$ (Bi:YIG) and Pt as the magnetic insulator and metallic film layers, respectively. The STE-coating films were formed by using simple fabrication steps shown in Fig. 16.5a. First, a Bi:YIG film was formed on a

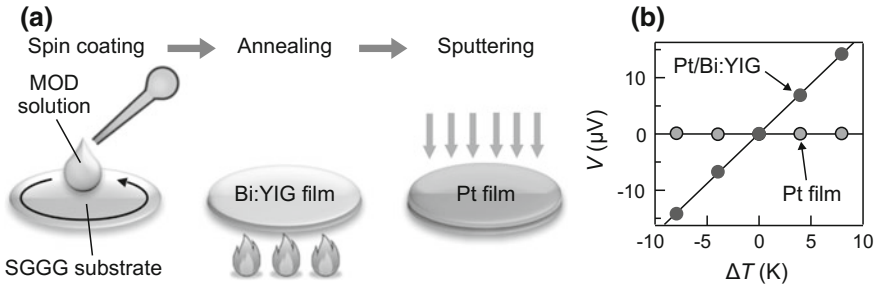

Fig. 16.5 **a** Preparation process for the Pt/Bi:YIG STE-coating device. **b** ΔT dependence of V in the Pt/Bi:YIG sample and plain Pt film

$(GdCa)_3(GaMgZr)_5O_{12}$ (substituted gadolinium gallium garnet: SGGG) substrate, which has good lattice-matching properties with Bi:YIG, by means of a metal-organic decomposition (MOD) method. The MOD method consists of two steps: spin coating and annealing of the MOD solution containing the constituent elements. Finally, the Pt film was formed by sputtering over the whole surface of the Bi:YIG film (see Fig. 16.5a). The thicknesses of the SGGG substrate, Bi:YIG film, and Pt film are 0.5 mm, 120 nm and 10 nm, respectively. The surface area of the samples is $8 \times 2\,\text{mm}^2$. Importantly, the above process can be easily applied to large-area manufacturing, as it does not require patterning steps such as photolithography.

In Fig. 16.5b, we show the ΔT dependence of V in the Pt/Bi:YIG sample. Even in this thin-film structure prepared by the MOD coating method, the clear LSSE signal was observed to appear and its magnitude is comparable to that in the conventional bulk sample systems. We also checked that no signal appears in a Pt film sputtered directly on a SGGG substrate, indicating that the thin Bi:YIG film works as a thermoelectric generator. We found that a crystalline Bi:YIG film can be grown even onto a glass substrate [10], and the STE coating is applicable onto amorphous surfaces. Such versatile implementation of thermoelectric functions may open opportunities for various applications making full use of omnipresent heat.

16.4.2 Current–Voltage–Power Characteristics

Now, we show the current–voltage–power characteristics of the Pt/Bi:YIG LSSE device. Here we attached a variable load resistance R_L to the Pt layer and measured the voltage V_L across the load resistance to estimate the output power V_L^2/R_L, while the LSSE experiments reported have been performed under the open-circuit condition. In Fig. 16.6a, we show V_L^2/R_L generated from the Pt/Bi:YIG sample at $\Delta T = 11.2$ K as a function of R_L. We found that the output power becomes maximum when R_L is equal to the resistance of the Pt layer: $R_{Pt} = 33\,\Omega$ (see also the

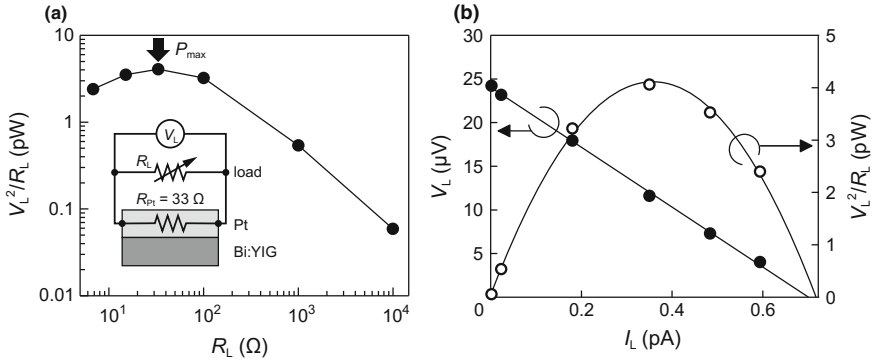

Fig. 16.6 **a** Output power V_L^2/R_L induced by the LSSE in the Pt/Bi:YIG sample as a function of the load resistance R_L. V_L denotes the output voltage between the ends of the load resistance. The length, width, and thickness of the Pt layer are 16 mm, 16 mm, and 10 nm, respectively. The Pt film was put on a 120-nm-thick Bi:YIG film. **b** V_L and V_L^2/R_L induced by the LSSE in the Pt/Bi:YIG sample as a function of the estimated current $I_L = V_L/R_L$ in the Pt layer

current–voltage and current–power curves for the Pt/Bi:YIG sample in Fig. 16.6b). This behavior is consistent with the current–voltage–power characteristics of conventional thermoelectric modules [31] and a standard impedance-matching rule; the maximum output power can be extracted when the external resistance is equal to the internal resistance.

16.4.3 Voltage Enhancement by Spin-Hall Thermopile

One of the methods of enhancing thermoelectric voltage is to use thermopile structure [32]. The thermopile for the conventional Seebeck device consists of a number of thermocouples connected electrically in series (see Fig. 16.4a), which is widely used in temperature (infrared)-measuring devices, heat flux sensors, and thermoelectric generators.

Here, we demonstrate a thermopile for the LSSE called a "spin-Hall thermopile", which allows us to enhance the ISHE voltage induced by the LSSE [33]. The basic structure of the spin-Hall thermopile is depicted in Fig. 16.7a. The sample consists of a ferrimagnetic insulator and an alternating array of two different metallic wires A and B placed on the top surface of the insulator, where the metallic wires A and B are connected in series in a zigzag configuration. In this zigzag structure, if the spin-Hall angle, i.e. charge current/spin current conversion efficiency [5], of the metallic wire A is different from that of B, the magnitude of the LSSE signals increase in proportion to the number of the A–B pairs; this zigzag structure works as a thermopile for the LSSE. Here, we note that, if the zigzag structure consists only of one material, most of the LSSE voltage is canceled out (see Fig. 16.7a).

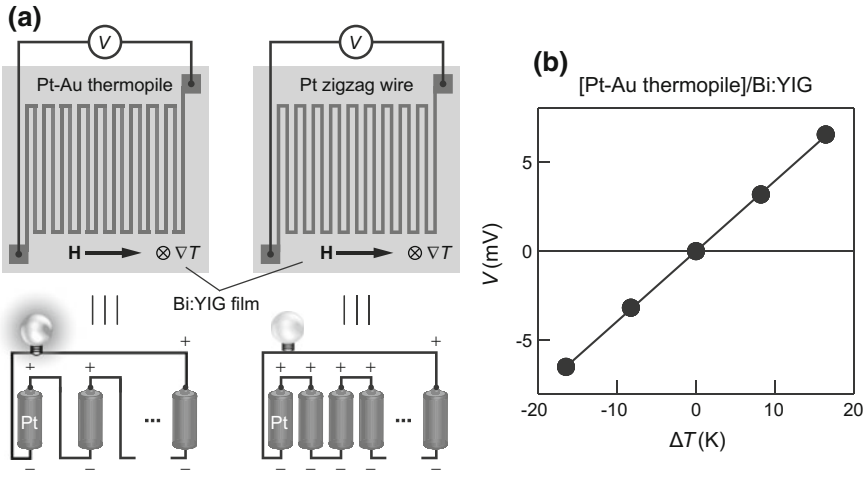

Fig. 16.7 **a** A schematic illustration of the Pt–Au spin-Hall thermopile on the Bi:YIG film. **b** ΔT dependence of V in the [Pt–Au thermopile]/Bi:YIG sample

Therefore, two different materials with different spin-Hall angles have to be used for constructing the spin-Hall thermopile [33].

To demonstrate the enhancement of the LSSE voltage by the spin-Hall thermopile, we used Pt–Au zigzag structure fabricated on a 120-nm-thick Bi:YIG film. The Bi:YIG film was formed on a SGGG substrate of 1-inch diameter and 0.5-mm thickness by means of the MOD method. The length, width, and thickness of the Pt (Au) wires are 16 mm (16 mm), 100 μm (50 μm), and 3 nm (30 nm), respectively. In the present device, 78 pairs of the Pt–Au junction are serially concatenated. Since the spin-Hall angle of Pt is greater than that of Au and the thickness of the Pt wire is much thinner than that of the Au wire, the net LSSE voltage generated in each Pt–Au junction mainly comes from the Pt layer (see Fig. 16.7a and note that the magnitude of the LSSE voltage in a metallic film increases with decreasing the thickness of the film except for ultrathin regions [15]).

Figure 16.7b shows the ΔT dependence of V in the [Pt–Au thermopile]/Bi:YIG sample. We observed the significant enhancement of the LSSE voltage in the Pt–Au spin-Hall thermopile; the thermopower induced by the LSSE in this structure is $\sim$0.4 mV/K, three-order of magnitude greater than that in the plain Pt/Bi:YIG sample (compare Figs. 16.5, 16.7). Although the spin-Hall thermopile enables significant enhancement of the LSSE *voltage*, it does not improve the *output power* of the LSSE device since the internal resistance of the metallic contact per unit area increases. However, this method may contribute to the construction of versatile spin and heat detectors, because the spin-Hall thermopile can be constructed simply by using standard thin-film formation techniques. The magnitude of the LSSE voltage in the spin-Hall thermopile will further increase by increasing the integration degree of the alternating metallic wire array, by lengthening each wire segment, and by combining materials with large positive and negative spin-Hall angles [33].

16.4.4 Position Sensing via LSSE

Possible future applications of the LSSE include not only thermoelectric generators, discussed above, but also sensing devices driven by heat. One of the candidates for sensor applications is two-dimensional (2D) position or temperature sensing. In Ref. [34], we have demonstrated the working principle of this function.

Figure 16.8a shows a schematic illustration of the device structure enabling the LSSE-based 2D position sensing. The sample consists of a polycrystalline YIG slab with a Pt-film mesh sputtered on the YIG surface. In this Pt-mesh/YIG-slab sample, since the ISHE voltage is proportional to a temperature gradient between Pt and YIG, the spatial distribution of the LSSE voltage in the Pt mesh should reflect temperature distribution of the sample surface, providing the 2D position information of heated or cooled parts of the sample. To demonstrate the LSSE-based position sensing, we measured the electric voltage between the ends of the Pt wires along the $x(y)$ direction, V_x (V_y), at different $y(x)$ positions with heating a part of the Pt-mesh/YIG-slab sample by laser light (see Fig. 16.8a). Here, **H** was applied along the diagonal direction of the Pt mesh for generating the LSSE voltage both in the x and y directions.

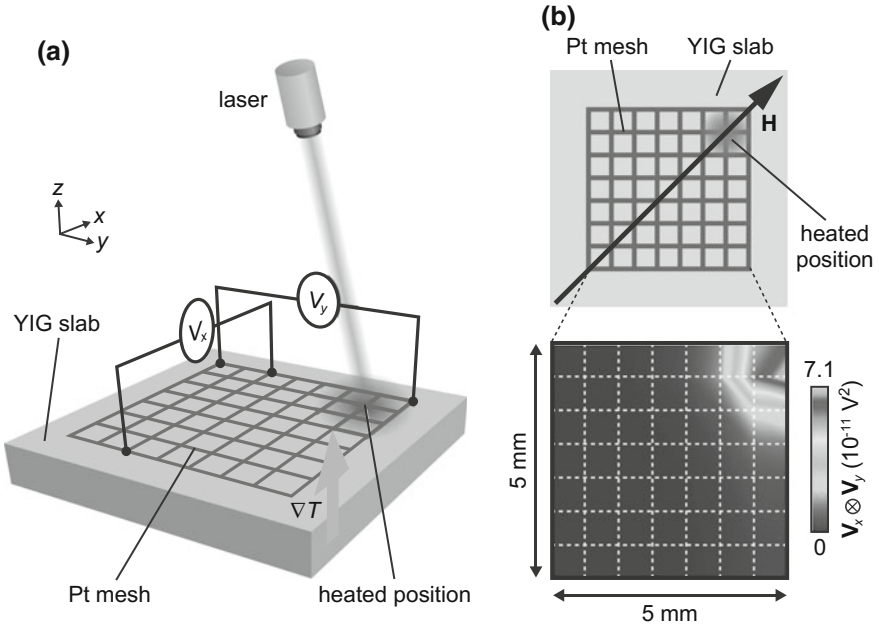

Fig. 16.8 **a** A schematic illustration of the Pt-mesh/YIG-slab sample. The YIG slab has an 8×8-mm^2 square shape and a 1-mm thickness. The Pt mesh comprises 15-nm-thick Pt wires with the width of 0.1 mm and the length of 5 mm, where the distance between the adjacent Pt wires is 0.7 mm. **b** 2D spatial distribution of the tensor product of the LSSE voltage profiles along the x and y directions: $V_x \otimes V_y$ in the Pt-mesh/YIG-slab sample

The 2D position information of the heated part of the Pt-mesh/YIG-slab sample is extracted by calculating the tensor product of the spatial profiles of the LSSE voltage along the x and y directions. We observed the large V_x and V_y signals only when the electrodes were attached across the heated area. By combining the V_x and V_y profiles, we obtained the contour plot shown in Fig. 16.8b, which reflects the 2D spatial distribution of the temperature rise of the Pt-mesh/YIG-slab sample (see Ref. [34] for details), confirming that the Pt-mesh/YIG-slab sample works as a thermally driven 2D position detector.

The advantages of the 2D position sensing based on the LSSE are the simplicity of the device structure and production cost; the device structure can be made simply by fabricating a patterned film on a commonly used magnetic insulator. The spatial resolution of the LSSE-based 2D position sensing will further be improved by increasing the density of metallic mesh and by electrically insulating the longitudinal and transverse metallic wires to suppress short circuit effects in the mesh. We also note that the output voltage can be increased by enlarging the device area and controlled by using a magnetic field or magnetic anisotropy, which is a characteristic feature of the LSSE-based position sensors. This position sensing method may provide us with realistic application perspectives of the LSSE in user interface devices and image information sensors, although the output voltage of the LSSE devices is much smaller than that of conventional devices [35, 36] at present and needs to be improved.

16.5 Conclusions and Perspectives

We have discussed the potential thermoelectric applications of the longitudinal spin Seebeck effect (LSSE). The LSSE in insulators allows us to construct thermoelectric generators or sensors operated by entirely new principles, which are characterized by simple film structure, convenient scaling capability, and easy fabrication. In an effort to realize LSSE-based thermoelectric technology, we have demonstrated the basic functionalities of the LSSE devices: (1) spin thermoelectric coating based on the metal-organic decomposition method, (2) extraction of thermoelectric output power induced by the LSSE, (3) voltage enhancement by spin-Hall thermopiles, and (4) two-dimensional position sensing based on the LSSE. The thermoelectric technology based on the LSSE is still in its infancy, and the thermoelectric conversion efficiency is very small at the present stage. However, there is plenty of scope for performance improvement; the thermoelectric conversion efficiency can be enhanced, for example, by improving the spin-Hall angle of the metal layer and spin-mixing conductance [37], i.e. spin transfer efficiency, at the metal/insulator interface and by reducing the thermal conductivity of the insulator layer. A small but great step for the realization of the LSSE devices is already in progress.

References

1. N.W. Ashcroft, N.D. Mermin, *Solid State Physics* (Saunders, Philadelphia, 1976)
2. S.A. Wolf, D.D. Awschalom, R.A. Buhrman, J.M. Daughton, S. von Molnar, M.L. Roukes, A.Y. Chtchelkanova, D.M. Treger, Science **294**, 1488 (2001)
3. Fabian J. ŽutićI, S. Das Sarma, Rev. Mod. Phys. **76**, 323 (2004)
4. K. Uchida, S. Takahashi, K. Harii, J. Ieda, W. Koshibae, K. Ando, S. Maekawa, E. Saitoh, Nature **455**, 778 (2008)
5. S. Maekawa, H. Adachi, K. Uchida, J. Ieda, E. Saitoh, J. Phys. Soc. Jpn. **82**, 102002 (2013)
6. S. Bosu, Y. Sakuraba, K. Uchida, K. Saito, T. Ota, E. Saitoh, K. Takanashi, Phys. Rev. B **83**, 224401 (2011)
7. C.M. Jaworski, J. Yang, S. Mack, D.D. Awschalom, J.P. Heremans, R.C. Myers, Nat. Mater. **9**, 898 (2010)
8. K. Uchida, J. Xiao, H. Adachi, J. Ohe, S. Takahashi, J. Ieda, T. Ota, Y. Kajiwara, H. Umezawa, H. Kawai, G.E.W. Bauer, S. Maekawa, E. Saitoh, Nat. Mater. **9**, 894 (2010)
9. K. Uchida, H. Adachi, T. Ota, H. Nakayama, S. Maekawa, E. Saitoh, Appl. Phys. Lett. **97**, 172505 (2010)
10. A. Kirihara, K. Uchida, Y. Kajiwara, M. Ishida, Y. Nakamura, T. Manako, E. Saitoh, S. Yorozu, Nat. Mater. **11**, 686 (2012)
11. E. Saitoh, M. Ueda, H. Miyajima, G. Tatara, Appl. Phys. Lett. **88**, 182509 (2006)
12. S.O. Valenzuela, M. Tinkham, Nature **442**, 176 (2006)
13. K. Uchida, T. Ota, H. Adachi, J. Xiao, T. Nonaka, Y. Kajiwara, G.E.W. Bauer, S. Maekawa, E. Saitoh, J. Appl. Phys. **111**, 103903 (2011)
14. T. Kikkawa, K. Uchida, Y. Shiomi, Z. Qiu, D. Hou, D. Tian, H. Nakayama, X.-F. Jin, E. Saitoh, Phys. Rev. Lett. **110**, 067207 (2013)
15. T. Kikkawa, K. Uchida, S. Daimon, Y. Shiomi, H. Adachi, Z. Qiu, D. Hou, X.-F. Jin, S. Maekawa, E. Saitoh, Phys. Rev. B **88**, 214403 (2013)
16. R. Ramos, T. Kikkawa, K. Uchida, H. Adachi, I. Lucas, M.H. Aguirre, P. Algarabel, L. Morellón, S. Maekawa, E. Saitoh, M.R. Ibarra, Appl. Phys. Lett. **102**, 072413 (2013)
17. D. Meier, T. Kuschel, L. Shen, A. Gupta, T. Kikkawa, K. Uchida, E. Saitoh, J.-M. Schmalhorst, G. Reiss, Phys. Rev. B **87**, 054421 (2013)
18. K. Uchida, T. Nonaka, T. Kikkawa, Y. Kajiwara, E. Saitoh, Phys. Rev. B **87**, 104412 (2013)
19. D.C. Ralph, M.D. Stiles, J. Magn. Magn. Mater. **320**, 1190 (2008)
20. T. Kimura, Y. Otani, T. Sato, S. Takahashi, S. Maekawa, Phys. Rev. Lett. **98**, 156601 (2007)
21. Y. Kajiwara, K. Harii, S. Takahashi, J. Ohe, K. Uchida, M. Mizuguchi, H. Umezawa, H. Kawai, K. Ando, K. Takanashi, S. Maekawa, E. Saitoh, Nature **464**, 262 (2010)
22. K. Harii, K. Ando, H.Y. Inoue, K. Sasage, E. Saitoh, J. Appl. Phys. **103**, 07F311 (2008)
23. P. Dirac, Phys. Rev. **74**, 817 (1948)
24. J. Xiao, G.E.W. Bauer, K. Uchida, E. Saitoh, S. Maekawa, Phys. Rev. B **81**, 214418 (2010)
25. H. Adachi, J. Ohe, S. Takahashi, S. Maekawa, Phys. Rev. B **83**, 094410 (2011)
26. H. Adachi, K. Uchida, E. Saitoh, S. Maekawa, Rep. Prog. Phys. **76**, 036501 (2013)
27. L.Q. Liu, C.-F. Pai, Y. Li, H.W. Tseng, D.C. Ralph, R.A. Buhrman, Science **336**, 555 (2012)
28. C.-F. Pai, L.Q. Liu, Y. Li, H.W. Tseng, D.C. Ralph, R.A. Buhrman, Appl. Phys. Lett. **101**, 122404 (2012)
29. Y. Niimi, M. Morota, D.H. Wei, C. Deranlot, M. Basletic, A. Hamzic, A. Fert, Y. Otani, Phys. Rev. Lett. **106**, 126601 (2011)
30. P. Laczkowski, J.C. Rojas-Sánchez, W. Savero-Torres, H. Jaffrès, N. Reyren, C. Deranlot, L. Notin, C. Beigné, A. Marty, J.-P. Attané, L. Vila, J.-M. George, A. Fert, Appl. Phys. Lett. **104**, 142403 (2014)
31. D.M. Rowe (ed.), *CRC Handbook of Thermoelectrics* (CRC Press, Boca Raton, 1995)
32. F.J. DiSalvo, Science **285**, 703 (1999)
33. K. Uchida, T. Nonaka, T. Yoshino, T. Kikkawa, D. Kikuchi, E. Saitoh, Appl. Phys. Express **5**, 093001 (2012)

34. K. Uchida, A. Kirihara, M. Ishida, R. Takahashi, E. Saitoh, J. Appl. Phys. **50**, 120211 (2011)
35. R.H. Willens, B.F. Levine, C.G. Bethea, D. Brasen, Appl. Phys. Lett. **49**, 1647 (1986)
36. J. Henry, J. Livingstone, Adv. Mater. **13**, 1022 (2001)
37. Y. Tserkovnyak, A. Brataas, G.E.W. Bauer, B.I. Halperin, Rev. Mod. Phys. **77**, 1375 (2005)